

# KURNS

# Progress Report

# 2019



Institute for Integrated Radiation and Nuclear Science,  
Kyoto University

# **KURNS Progress Report** 2019

APRIL 2019 – MARCH 2020

*Published by*  
*Institute for Integrated Radiation and Nuclear Science,*  
*Kyoto University,*  
*Kumatori-cho, Sennan-gun, Osaka 590-0494, Japan*

It is a great pleasure for us to publish the KURNS Progress Report 2019. This report contains all of the accomplishments of research and related activities at Institute for Integrated Radiation and Nuclear Science, Kyoto University (KURNS) during the fiscal year 2019 from April 2019 to March 2020. Our institute continues to play a distinctive role as a Joint Usage/Research Center, promoting an extensive range of studies from fundamental to applied research with research reactors and accelerators.

It is reassuring to note that the number of applications for Joint Research are still increasing although the reactors had sustained operations for several years. We are proud since this demonstrates that researchers and students support our activity, which endorses our facilities as indispensable tools in their research activities with quantum beam and radioisotope. In the past fiscal year, KUR was operated for 849 hours and KUCA was for 774 hours. In total, we accepted 4,477 man-day researchers and students for using research facilities and for attending scientific meetings. A large number of research subjects has been enrolled, which covers various fields of nuclear science and technology, material science, radiation life science and radiation medical science. We proudly announce that the clinical trial of the boron neutron capture therapy (BNCT) has finished successfully, and it becomes a practical medical care after long-term basic researches in KUR.

We strive for safe and stable operations for nationwide use, making it our primary mission to provide scientists the opportunity to conduct research and education. We are happy to dedicate our support to enable users conduct significant interdisciplinary research at KURNS.

Kumatori, June 8, 2020  
Yuji Kawabata  
Director, KURNS

# CONTENTS

<b>I. ANNUAL SUMMARY OF EXPERIMENTAL RESEARCH ACTIVITIES</b> .....	1
<b>I-1. PROJECT RESEARCHES</b> .....	2
<b>Project 1</b> Project Research on Nuclear Spectroscopy and Condensed Matter Physics Using Short-Lived Nuclei	
Y. Ohkubo (31P1) .....	3
<b>PR1-1</b> Technique of Transferring Radioactive Atomic Nuclei Implanted in Dry Ice Film	
A. Taniguchi <i>et al.</i> (31P1-1) .....	4
<b>PR1-2</b> $\beta$ -Decay Spectroscopic Studies of Fission Products Using a Clover Detector	
Y. Ishikawa <i>et al.</i> (31P1-2) .....	5
<b>PR1-3</b> Linear Polarization Measurement for $\gamma$ Rays from $^{148}\text{Pr}$	
Y. Kojima <i>et al.</i> (31P1-3) .....	6
<b>PR1-4</b> Measurement of the Internal Pressure in Ultrafine Bubbles by Angular Correlation Technique	
M. Tanigaki <i>et al.</i> (31P1-5) .....	7
<b>PR1-5</b> Temperature-Dependent Polaronic Local Structures in $\text{La}_{0.7}\text{Ca}_{0.3}\text{MnO}_3$ Observed through Spin Relaxation of TDPAC Probe Nuclei	
W. Sato <i>et al.</i> (31P1-6) .....	8
<b>PR1-6</b> Local Structure of In Impurities Doped in $\text{SrTiO}_3$ Studied by TDPAC Method	
S. Komatsuda <i>et al.</i> (31P1-7) .....	9
<b>Project 2</b> Project Research of Accelerator-Driven System with Spallation Neutrons at Kyoto University Critical Assembly	
C. H. Pyeon (31P2) .....	11
<b>PR2-1</b> Subcriticality Monitoring for a Reactor System Driven by Spallation Source (III)	
K. Hashimoto <i>et al.</i> (31P2-1) .....	12
<b>PR2-2</b> Measurement of Reaction Rates of Intermediate Neutrons on Accelerator-Driven System with Spallation Neutrons	
N. Aizawa <i>et al.</i> (31P2-2) .....	13
<b>PR2-3</b> Measurement of $^{243}\text{Am}$ Fission Rates in Low-Enriched Uranium Region at A-core of KUCA	
A. Oizumi <i>et al.</i> (31P2-3) .....	14
<b>PR2-4</b> Development of Real-time Subcriticality Monitor	
K. Watanabe <i>et al.</i> (31P2-5) .....	15
<b>Project 3</b> Preclinical Study for Development of New Drug for BNCT	
M. Suzuki (31P3) .....	17
<b>PR3-1</b> Screening of Boron Compound for BNCT International Collaboration Studies	
M. Takagaki and M. Suzuki. (31P3-1) .....	18
<b>PR3-2</b> The Self-assembling A6K Peptide Nanotube as BSH Delivery System	
H. Michiue <i>et al.</i> (31P3-2) .....	19
<b>PR3-3</b> Chemical Functionalization of Boron-Containing Nanoparticle and its Application to Boron Neutron Capture Therapy	
Y. Wang <i>et al.</i> (31P3-3) .....	20
<b>PR3-4</b> Examining Efficacy of Tumor Models for BNCT	
K. Matsumoto <i>et al.</i> (31P3-4) .....	21
<b>PR3-5</b> Development of New Boron Drug for Next-generation A-BNCT Treatment	
S. Ishiyama <i>et al.</i> (31P3-7) .....	22
<b>PR3-6</b> Research and Development on Next-generation A-BNCT Treatment	
S. Ishiyama <i>et al.</i> (31P3-8) .....	23
<b>PR3-7</b> Evaluation of Boron Neutron Capture Therapy (BNCT) Using Brain Tumor Bearing Rats or Mice Model	
Y. Fukuo <i>et al.</i> (31P3-11) .....	24

<b>PR3-8</b>	Intracellular Target Delivery of Cell-penetrating Peptide-conjugated Dodecaborate for Boron Neutron Capture Therapy (BNCT) I. Nakase <i>et al.</i> (31P3-12) .....	25
<b>PR3-9</b>	A Novel Carbon Nanohorns for BNCT T. Tsurubuchi <i>et al.</i> (31P3-13) .....	26
<b>PR3-10</b>	Development of a Multifunctional Nanoparticle towards Next-generation Boron Neutron Capture Therapy A. Kim <i>et al.</i> (31P3-14) .....	27
<b>PR3-11</b>	Design, Synthesis, and Evaluation of Glucose and Macrocyclic Polyamine-type Boron Carriers for BNCT S. Aoki <i>et al.</i> (31P3-15) .....	28
<b>PR3-12</b>	Boron Neutron Capture Therapy using Polymer-Based Boron Delivery Systems T. Nomoto <i>et al.</i> (31P3-16) .....	29
<b>PR3-13</b>	Development of Carrier Protein-based Boron Delivery System H. Nakamura <i>et al.</i> (31P3-17) .....	30
<b>PR3-14</b>	Development of Novel Boron Agents for BNCT against Malignant Brain Tumors A. Fujimura <i>et al.</i> (31P3-18) .....	31
<b>PR3-15</b>	Experiment on the Anti-tumor Effect of Pegylated BSH by Thermal Neutron Irradiation M. Shirakawa <i>et al.</i> (31P3-19) .....	32
<b>PR3-16</b>	Preparation and Characterization of BODIPY-Tethered Oligonucleotides for BNCT K. Tanabe <i>et al.</i> (31P3-20) .....	33
<b>PR3-17</b>	<i>In vivo</i> Evaluation of BNCT for 5-FU Resistant Oral Squamous Cell Carcinoma K. Igawa <i>et al.</i> (31P3-21) .....	34
<b>PR3-18</b>	Anti-tumor Evaluation of Gadolinium Neutron Capture Therapy through comparison of Tumor Size using Gd-DTPA-incorporated Calcium Phosphate Nanoparticles H Xuan <i>et al.</i> (31P3-22) .....	35
<b>Project 4</b>	Clinical Research on Explorations into New Application of BNCT M. Suzuki and H. Yanagie. (31P4) .....	37
<b>PR4-1</b>	Clinical Research on Explorations into New Application of BNCT M. Suzuki <i>et al.</i> (31P4-1) .....	38
<b>PR4-2</b>	Preparation of Boron entrapped WOW emulsion by Mixing Medical Device for Boron Neutron Capture Therapy to Hepatocellular Carcinoma H. Yanagie <i>et al.</i> (31P4-2) .....	39
<b>Project 5</b>	Establishment of Integrated System for Dose Estimation in BNCT Y. Sakurai (31P5) .....	41
<b>PR5-1</b>	Establishment of Characterization Estimation Method in BNCT Irradiation Field using Bonner Sphere and Ionization Chamber (III) Y. Sakurai <i>et al.</i> (31P5-1) .....	42
<b>PR5-2</b>	Study on New Type of Neutron Spectrometer for BNCT A. Uritani <i>et al.</i> (31P5-2) .....	43
<b>PR5-3</b>	Neutron Measurement by using the Self-activation of Iodine-added Plastic Scintillators A. Nohtomi <i>et al.</i> (31P5-4) .....	44
<b>PR5-4</b>	Characterization of Active Neutron Detector for Boron Neutron Capture Therapy M. Takada <i>et al.</i> (31P5-5) .....	45
<b>PR5-5</b>	Study for Microdosimetry using Silicon-on-insulator Microdosimeter in the BNCT Irradiation Field (III) Y. Sakurai <i>et al.</i> (31P5-6) .....	46
<b>PR5-6</b>	Measurement of BNCT Beam Component Fluence with Polymer Gel Detector K. Tanaka <i>et al.</i> (31P5-7) .....	47
<b>PR5-7</b>	Development of Neutron Fluence Distribution Measuring Device using Thermoluminescence Slabs K. Shinsho <i>et al.</i> (31P5-8) .....	48

<b>PR5-8</b>	The Study for Development and Application of Tissue Equivalent Neutron Dosimeter M. Oita <i>et al.</i> (31P5-9) .....	49
<b>PR5-9</b>	Development and Evaluation of 3D Gel Dosimeter for the Measurement of dose Distribution in BNCT S. Hayashi <i>et al.</i> (31P5-10) .....	50
<b>PR5-10</b>	Establishment of Beam-quality Estimation Method in BNCT Irradiation Field using Dual Phantom Technique (III) Y. Sakurai <i>et al.</i> (31P5-11) .....	51
<b>PR5-11</b>	Characteristics test of a Prpmt Gamma-ray detector using LaBr <sub>3</sub> (Ce) Scintillator and 8 x 8 Array MPPC for Boron Neutron Capture Therapy K. Okazaki <i>et al.</i> (31P5-12) .....	52
<b>PR5-12</b>	Development of Fiber-reading Radiation Monitoring System with a Red/ Infrared-emitting Scintillator at <sup>60</sup> Co Radiation Facilities S. Kurosawa <i>et al.</i> (31P5-13) .....	53
<b>PR5-13</b>	Establishment of the Imaging Technology of 478 keV Prompt Gamma-rays of Boron-neutron Capture Reaction and the Measurement of the Intensity of the Neutron Field T. Mizumoto <i>et al.</i> (31P5-14) .....	54
<b>PR5-14</b>	Feasibility Study of a Gel-dosimeter for a Quality Assurance and a Quality Control in Boron Neutron Capture Therapy S. Nakamura <i>et al.</i> (31P5-15) .....	55
<b>PR5-15</b>	Optimization of Bolus Shape for Boron Neutron Capture Therapy Using Epi-thermal Neutron Beam T. Takata <i>et al.</i> (31P5-16) .....	56
<b>PR5-16</b>	Development of Novel Radiochromic Gels for Assesing 3-Dimensional dose Distribution in Brain H. Yasuda <i>et al.</i> (31P5-17) .....	57
<b>PR5-17</b>	Measurement of Neutron Distributions in the BNCT Irradiation Field using a GEM Detector S. Uno <i>et al.</i> (31P5-18) .....	58
<b>PR5-18</b>	Development of Epi-thermal Neutron Flux Intensity Detector for BNCT I. Murata <i>et al.</i> (31P5-20) .....	59
<b>PR5-19</b>	Investigation of Thermal Neutron-Induced Soft Errors in Semiconductor Devices H. Tanaka <i>et al.</i> (31P5-21) .....	60
<b>Project 6</b>	Analyzing Tumor Microenvironment and Exploiting its Characteristics in Search of Optimizing Cancer Therapy Including Neutron Capture Therapy S. Masunaga (31P6) .....	62
<b>PR6-1</b>	Effect of a Change in Reactor Power on Response of Murine Solid Tumors <i>in vivo</i> , Especially on that of Quiescent Tumor Cells, in Boron Neutron Capture Therapy S. Masunaga <i>et al.</i> (31P6-1) .....	63
<b>PR6-2</b>	Development of New Amino Acid-type Boron Carriers for BNCT A. Matsushita <i>et al.</i> (31P6-2) .....	64
<b>PR6-3</b>	Molecular Mechanism Underlying HISP2-mediated Radioresistance of Hypoxic Tumor Cells M. Kobayashi <i>et al.</i> (31P6-3) .....	65
<b>PR6-4</b>	OH Radicals from the Indirect Actions of Neutron Beam Induce Cell Killing R. Hirayama <i>et al.</i> (31P6-4) .....	66
<b>PR6-5</b>	Intracellular Delivery of Membrane-fluidity Sensitive Boron Liposomes with Tumor-specific Cell Penetrating Peptides S. Kasaoka <i>et al.</i> (31P6-5) .....	67
<b>PR6-6</b>	Preparation and Characterization of a Novel Bispecific Antibody That Targets Her2 and BSH for Boron Neutron Capture Therapy T. Kanai <i>et al.</i> (31P6-6) .....	68

<b>PR6-7</b>	Development of Novel BPA-Tirapazamine Hybrid BNCT Agent Targeting Hypoxic Tumor Cells Y. Uto <i>et al.</i> (31P6-7).....	69
<b>PR6-8</b>	The Tumor Invasion Enhanced by the Conditioned-medium after X-irradiation H. Yasui <i>et al.</i> (31P6-8).....	70
<b>PR6-9</b>	Analysis of the Response of Tumor Tissue and Cells to BNCT S. Imamichi <i>et al.</i> (31P6-9).....	71
<b>PR6-10</b>	The Contribution of Blood Boron-neutron Reaction to Subcutaneous Tumor Growth Suppression was Equal to that of Neutrons Irradiation Only Group K. Nakai <i>et al.</i> (31P6-10) .....	72
<b>PR6-11</b>	Cell Killing Effect of BNCT with Novel Boron Compound SMA Glucosamine Complex Y. Matsumoto <i>et al.</i> (31P6-11).....	73
<b>PR6-12</b>	Attempts to Sensitize Tumor Cells by Exploiting the Tumor Microenvironment Y. Sanada <i>et al.</i> (31P6-12) .....	74
<b>Project 8</b>	Project Research on Advances in Isotope-Specific Studies Using Multi-Element Mössbauer Spectroscopy M. Seto (31P8) .....	76
<b>PR8-1</b>	Analysis of Iron-based Products Using Mössbauer Spectroscopy - Iron Oxide Scale Generated in the Boiler Feed-water in Thermal Power Plant – Y. Akiyama <i>et al.</i> (31P8-1).....	77
<b>PR8-2</b>	EFG Tensor of Fe <sup>2+</sup> in M2 site of Orthopyroxene by Single Crystal Mössbauer Microspectroscopy K. Shinoda and Y. Kobayashi. (31P8-2).....	78
<b>PR8-3</b>	Temperature Dependence of Mössbauer Spectra for Fe <sub>2</sub> O <sub>3</sub> -Al <sub>2</sub> O <sub>3</sub> Solid Solution S. Takai <i>et al.</i> (31P8-3).....	79
<b>PR8-4</b>	A Nuclear Resonance Vibrational Spectroscopic Study of Oxy Myoglobin T. Ohta <i>et al.</i> (31P8-4).....	80
<b>PR8-5</b>	Mössbauer Spectroscopy on the Antiperovskite Oxide Superconductor Sr <sub>3-x</sub> SnO Y. Maeno <i>et al.</i> (31P8-5) .....	81
<b>PR8-6</b>	Researches on Magnetism in a Novel Kondo Lattice Y. Kamihara <i>et al.</i> (31P8-6).....	82
<b>PR8-7</b>	Study on Structure of Gold Complexes Coordinated with $\alpha$ -Amino Acids by Means of <sup>197</sup> Au Mössbauer Spectroscopy H. Murayama <i>et al.</i> (31P8-7).....	83
<b>PR8-8</b>	<sup>197</sup> Au Mössbauer Study of Supported Au Nanoparticles Catalysis II Y. Kobayashi <i>et al.</i> (31P8-8).....	84
<b>PR8-9</b>	Development of Mössbauer Spectroscopy for <sup>166</sup> Er S. Kitao <i>et al.</i> (31P8-9).....	85
<b>Project 9</b>	Project Research on Boron Dynamics in Plants using Neutron Capture Reaction: Development of Boron Analytical Method and Elucidation of its Physiological Function T. Kinouchi (31P9) .....	87
<b>PR9-1</b>	Analysis of Boron Transport within Roots Using Neutron Capture Radiography M. Kobayashi and T. Kinouchi. (31P9-1).....	88
<b>PR9-2</b>	Analysis of Localization of Boron in Root Tissues by Neutron Capture Radiography S. Kitajima <i>et al.</i> (31P9-2) .....	89
<b>PR9-3</b>	Improvement of <i>In Situ</i> Visualization of Boron Distributed in Plants by Neutron Radiation T. Kinouchi (31P9-3) .....	90
<b>Project 10</b>	The Effect of Boron Neutron Capture Therapy on Normal Tissues M. Suzuki (31P10) .....	92
<b>PR10-1</b>	The Effect of Boron Neutron Capture Therapy (BNCT) on Normal Lung in Mice M. Suzuki and Y. Tamari. (31P10-1).....	93

<b>PR10-2</b>	Study of the Influence on Normal Liver tissue by BNCT Y. Tamari <i>et al.</i> (31P10-4).....	94
<b>PR10-3</b>	The Effect of Boron Neutron Capture Therapy to Normal Bones in Mice R. Iwasaki <i>et al.</i> (31P10-5) .....	95
<b>Project 11</b>	Preclinical Studies on Gadolinium Neutron Capture Therapy M. Suzuki (31P11).....	97
<b>PR11-1</b>	Investigation of Cell Killing Effect by Auger Electrons Emitted during Gadolinium Neutron Capture Therapy (Gd-NCT) M. Suzuki and H. Tanaka (31P11-1).....	98
<b>PR11-2</b>	Investigation of Gadolinium Neutron Capture Therapy (Gd-NCT) using Gadolinium-loaded Nano-particle M. Suzuki <i>et al.</i> (31P11-2).....	99
<b>PR11-3</b>	Nanoparticulate Formulations for Neutron Capture Therapy: Evaluation of Anti-tumor Effect after Intratumor Injection T. Andoh <i>et al.</i> (31P11-3).....	100
<b>PR11-4</b>	Examination on Gadolinium Neutron Capture Therapy in Mouse Malignant Melanoma Bone Metastasis Model T. Matsukawa <i>et al.</i> (31P11-4).....	101
<b>PR11-5</b>	Preparation of Drugs Bearing Hoechst unit that Target Cell Nucleus K. Tanabe <i>et al.</i> (31P11-5) .....	102
<b>PR11-6</b>	Establishment of the Chicken Egg Tumor Model for GNCT K. Matsumoto <i>et al.</i> (31P11-6).....	103
<b>PR11-7</b>	Evaluation of Antitumor Effectivity on Gd-neutron Capture Therapy with Polymeric Nanocarriers X. Hou <i>et al.</i> (31P11-7) .....	104
<b>PR11-8</b>	Development of Nano Carriers Installed with Gd(III)-Thiacalixarene Complex for Gd-NCT T. Yamatoya <i>et al.</i> (31P11-8) .....	105
<b>Project 12</b>	Enhancement of Research Methods for Material Irradiation and Defect Analysis A. Kinomura (31P12) .....	107
<b>PR12-1</b>	Study to Improve Transport and Measurement Performance of a Slow Positron Beamline A. Kinomura <i>et al.</i> (31P12-1).....	108
<b>PR12-2</b>	Electron-irradiation Induced Defects in W-Re T. Toyama <i>et al.</i> (31P12-2).....	109
<b>PR12-3</b>	Change in the Positron Annihilation Lifetime of Electron-irradiated F82H by Hydrogen Charging K. Sato <i>et al.</i> (31P12-3) .....	110
<b>PR12-4</b>	The Effect of Gamma-ray Irradiation on Luminescence Properties of Colloidal Si Nanocrystals T. Nakamura <i>et al.</i> (31P12-4) .....	111
<b>PR12-5</b>	Irradiation Technique for Study on Corrosion Resistance of Fusion Divertor Materials to liquid metal during irradiation M. Akiyoshi <i>et al.</i> (31P12-5) .....	112
<b>PR12-6</b>	Measurement of Positron Lifetimes of Various Diamond-like Carbon Thin Films K. Kanda <i>et al.</i> (31P12-6).....	113
<b>PR12-7</b>	Positron Annihilation Spectroscopy on Diamond-like Carbon Films S. Nakao <i>et al.</i> (31P12-7) .....	114
<b>Project 13</b>	Chemical and Electronic Properties of Actinide Compounds and their Applications T. Yamamura (31P13) .....	116
<b>PR13-1</b>	Synthesis and Characterization of Actinide-based Compounds with Honeycomb Layer Y. Haga <i>et al.</i> (31P13-1) .....	117

<b>PR13-2</b>	Crossover between Fermi-Liquid and Non-Fermi-Liquid States in $\text{Th}_{1-x}\text{U}_x\text{Be}_{13}$ ( $0 \leq x \leq 1$ ) H. Amitsuka <i>et al.</i> (31P13-2) .....	118
<b>PR13-3</b>	Adsorption Characterization of Actinide Chemical Species on Solid Adsorbents - Measurement of Rare Earth Elements by ICP-MS - T. Suzuki <i>et al.</i> (31P13-3) .....	119
<b>PR13-4</b>	Preparation of $^{228}\text{Ra}/^{228}\text{Ac}$ Stock Solution K. Shirasaki <i>et al.</i> (31P13-4) .....	120
<b>PR13-5</b>	Investigation on Complex Formation of Monoamide Compounds with Actinyl Ions M. Nogami and T. Yamamura (31P13-5).....	121
<b>PR13-6</b>	Consistency Verification between Relativistic Quantum Chemical Calculations and Experiments in Uranium Compounds M. Abe <i>et al.</i> (31P13-6) .....	122
<b>PR13-7</b>	Evaluation of Phase Diagram of Minor Actinide Oxides with CALPHAD H. Shishido <i>et al.</i> (31P13-7) .....	123
<b>PR13-8</b>	Synthesis of Nobel Phthaloyanine Derivatives and Effect of Substituent on Recognition of Light Actinide and Chemical Property M. Nakase <i>et al.</i> (31P13-8) .....	124
<b>I-2. COLLABORATION RESEARCHES</b> .....		125
<b>1. Slow Neutron Physics and Neutron Scattering</b>		
<b>CO1-1</b>	First Neutron Diffraction Results of Fluoride-ion Battery Materials on VCND K. Mori and F. Fujisaki (31008) .....	126
<b>CO1-2</b>	Current Status of Versatile Compact Neutron Diffractometer (VCND) on the B-3 Beam Port of KUR, 2019 K. Mori <i>et al.</i> (31016) .....	127
<b>CO1-3</b>	Neutron scattering study on microstructure of vitrified radioactive wastes K. Kaneko <i>et al.</i> (31027) .....	128
<b>CO1-4</b>	Development of neutron spin flipper with large beam acceptance M. Kitaguchi <i>et al.</i> (31030) .....	129
<b>CO1-5</b>	Development of $m=6.5$ neutron supermirror on ellipsoidal metal substrate M. Hino <i>et al.</i> (31109) .....	130
<b>CO1-6</b>	Development of high spatial resolution cold/ultracold neutron detector using nuclear emulsion N. Naganawa <i>et al.</i> (31135) .....	131
<b>2. Nuclear Physics and Nuclear Data</b>		
<b>CO2-1</b>	Measurement for thermal neutron capture cross sections and resonance integrals of the $^{243}\text{Am}(n,\gamma)^{244}\text{gAm}$ , $^{244\text{m}+\text{g}}\text{Am}$ reactions S. Nakamura <i>et al.</i> (31020) .....	132
<b>CO2-2</b>	Quantitation of Gamma Ray Emission from Capture Reaction of Uranium-238 Y. Nauchi <i>et al.</i> (31022) .....	133
<b>CO2-3</b>	Development of current-mode neutron detectors for BNCT fields T. Matsumoto <i>et al.</i> (31102) .....	134
<b>CO2-4</b>	Measurements of thermal neutron total and scattering cross section of moderator materials J. Nishiyama <i>et al.</i> (31108) .....	135
<b>CO2-5</b>	Measurement of Temperature Dependent Thermal Neutron Spectrum in Solid Moderator T. Sano <i>et al.</i> (31156) .....	136
<b>3. Reactor Physics and Reactor Engineering</b>		
<b>CO3-1</b>	Basic Research for Sophistication of High-power Reactor Noise Analysis (II) S. Hohara <i>et al.</i> (31025) .....	137
<b>CO3-2</b>	Demonstration of advanced subcritical measurements: Time-Domain Decomposition- based Integral (TDDI) method and third-order neutron-correlation technique T. Endo <i>et al.</i> (CA3101) .....	138

<b>CO3-3</b>	Measurement of Gamma Ray from Short Lived Fission Product under Background of Fission Prompt Gamma Ray Y. Nauchi <i>et al.</i> (CA3102) .....	139
<b>CO3-4</b>	Reactor Noise Power-Spectral Analysis for a Graphite-Moderated and -Reflected Core (II) A. Sakon <i>et al.</i> (CA3104) .....	140
<b>CO3-5</b>	Measurement of fundamental characteristics of nuclear reactor at KUCA (IV) Y. Kitamura (CA3106) .....	141
<b>CO3-6</b>	Reactor Physis Experiment in Graphite Moderation System for HTGR (II) Y. Fukaya <i>et al.</i> (CA3107) .....	142
<b>CO3-7</b>	Sample Worth Measurements of Lead and Bismuth in Low-enriched Uranium Region at A-core of KUCA for ADS M. Fukushima <i>et al.</i> (CA3109) .....	143
<b>CO3-8</b>	Subcriticality Measurement by using a Small Neutron Detector T. Misawa <i>et al.</i> (CA3110) .....	144
<b>CO3-9</b>	Verification of an Improved Method to Estimate Reactivity Y. Yamane <i>et al.</i> (CA3111) .....	145
<b>CO3-10</b>	Measurement of Fundamental Characteristics of Nuclear Reactor at KUCA (V) Y. Kitamura <i>et al.</i> (CA3112) .....	146
<b>CO3-11</b>	Measurement of Neutronics Characteristics for Th loaded core at KUCA (II) T. Sano <i>et al.</i> (CA3113) .....	147
<b>4. Material Science and Radiation Effects</b>		
<b>CO4-1</b>	Characterization of Additive in Lubricant using Small-Angle X-ray Scattering Y. Oba (31002).....	148
<b>CO4-2</b>	Synthesis of alloy nanoparticles in water solution by two steps reduction and one time $\gamma$ -ray irradiation F. Hori <i>et al.</i> (31004) .....	149
<b>CO4-3</b>	Defects structure and characterization of electron irradiated intermetallic alloys F. Hori <i>et al.</i> (31005) .....	150
<b>CO4-4</b>	Magnetic Scattering Contribution in Iron Characterzed by Neutron Diffraction Y. Oba <i>et al.</i> (31007) .....	151
<b>CO4-5</b>	What Exists in a 2-nm-sized Molecular Caspule Assembeld in Water? Y.-Y. Zhan <i>et al.</i> (31009) .....	152
<b>CO4-6</b>	Damage Evolution in Neutron-irradiated Metals during Neutron Irradiation at Elevated Temperatures I. Mukouda and Q. Xu. (31041) .....	153
<b>CO4-7</b>	Radiation Resistivity of Ferrite Permanent Magnets Against Neutrons Y. Iwashita <i>et al.</i> (31042) .....	154
<b>CO4-8</b>	Elucidation of the Mechanism of the Screw-sense Induction of Polymer Backbone Based on the Small Angle X-ray Scattering and Dynamic Light Scattering Measurements Y. Nagata <i>et al.</i> (31051).....	155
<b>CO4-9</b>	Crystal structure analysis of Abalone shell K. Iwase and K. Mori (31055).....	156
<b>CO4-10</b>	Radiochemical Research for the Advancement of $^{99}\text{Mo}/^{99\text{m}}\text{Tc}$ Generator by (n, $\gamma$ ) Method (2) Y. Fujita <i>et al.</i> (31065).....	157
<b>CO4-11</b>	Radiophotoluminescence phenomenon in Cu-doped silica glasses prepared from porous silica glass Y. Takada <i>et al.</i> (31066) .....	158
<b>CO4-12</b>	Study of resonant frequency change with irradiation dose of piezoelectric PZT element M. Kobayashi <i>et al.</i> (31067) .....	159
<b>CO4-13</b>	Formation of radiation defects on tungsten and their influence on effect of hydrogen isotope retention K. Tokunaga <i>et al.</i> (31086).....	160
<b>CO4-14</b>	Tritium release behavior from neutron-irradiated FLiNaBe K. Katayama <i>et al.</i> (31090).....	161

<b>CO4-15</b>	Positron Age-Momentum Correlation Measurements of $\gamma$ -rays Irradited Polystyrene H. Tsuchida <i>et al.</i> (31093) .....	162
<b>CO4-16</b>	Formation of nano-structures on Ge surfaces by ion irradiation and study on its formation mechanisms J. Yanagisawa <i>et al.</i> (31097).....	163
<b>CO4-17</b>	Evaluation of Structural Vacancies in Icosahedral Cluster Solids using Positron Annihilation J. Takahashi <i>et al.</i> (31100).....	164
<b>CO4-18</b>	Absorption Coefficient of Amino Acid in the Sub-THz region using CTR T. Takahashi <i>et al.</i> (31111).....	165
<b>CO4-19</b>	Vacancy migration behavior in CoCrFeMnNi high entropy alloys and their subsystems K. Sugita <i>et al.</i> (31112) .....	166
<b>CO4-20</b>	Observation of Gamma-ray Induced Current on Coaxial Cable for Analog Data Transfer Y. Gotoh (31118).....	167
<b>CO4-21</b>	Correlation between Damage Accumulation by Neutron Irradiation and Hydrogen isotope Retention for Plasma Facing Materials Y. Oya <i>et al.</i> (31120) .....	168
<b>CO4-22</b>	Complex Structure of Ions Coordinated with Hydrophilic Polymer 20. Ionic Diffusion in Polymeric Structure Utilized by Polyiodide Ions. (1) A. Kawaguchi and Y. Morimoto. (31122) .....	169
<b>CO4-23</b>	A study on destruction of cesium aluminosilicate cage by gamma irradiation (1) H. Ohashi <i>et al.</i> (31128) .....	170
<b>CO4-24</b>	Effects of Buffers and Salts on Nanostructure of Soybean Proteins as Revealed by SAXS N. Sato <i>et al.</i> (31137).....	171
<b>CO4-25</b>	Porosity Measurements of Sintered-Silver Bonding Plates K. Wakamoto <i>et al.</i> (31143).....	172
<b>CO4-26</b>	Differences in the Recovery Behavior of Electron-Irradiation-Induced Vacancies in Metals with Different Purities A. Yabuuchi <i>et al.</i> (31157).....	173
<b>CO4-27</b>	Differences in the Development of Vacancy-Type Defects During Annealing with Different Irradiated Ion Species A. Yabuuchi <i>et al.</i> (31158).....	174
<b>CO4-28</b>	Defect Characterization of Ion-Irradiated GdBa <sub>2</sub> Cu <sub>3</sub> O <sub>7-<math>\delta</math></sub> Superconducting Tapes Probed by a Slow Positron Beam T. Ozaki <i>et al.</i> (31159) .....	175
<b>CO4-29</b>	Neutron irradiation tests for ITER plasma diagnostics M. Ishikawa <i>et al.</i> (31167).....	176

### 5. Geochemistry and Environmental Science

<b>CO5-1</b>	Volcanic and Tectonic History of Philippine Sea Plate (South of Japan) Revealed by <sup>40</sup> Ar/ <sup>39</sup> Ar Dating Technique O. Ishizuka <i>et al.</i> (31012) .....	177
<b>CO5-2</b>	Long Term Observation of Element Concentrations in the Atmospheric Aerosols at Sakai, Osaka, 1995-2017 N. Ito <i>et al.</i> (31024) .....	178
<b>CO5-3</b>	Ar-Ar dating of submarine basalts N. Hirano <i>et al.</i> (31039) .....	179
<b>CO5-4</b>	Recrystallization of an amorphous Si layer by H <sup>+</sup> ion beam and electron beam irradiation J. Nakata <i>et al.</i> (31049) .....	180
<b>CO5-5</b>	Study on Elemental Concentration in the Atmospheric Particulate Matter by INAA N. Hagura <i>et al.</i> (31052) .....	181
<b>CO5-6</b>	Neutron activation analysis for sediments, phytoplankton, lake water of Lake Akagi Onuma Y. Okada <i>et al.</i> (31053) .....	182
<b>CO5-7</b>	Formation age of Precambrian metamorphic rocks and thermal history H. Hyodo <i>et al.</i> (31057) .....	183
<b>CO5-8</b>	A Study on Evaluation of Redox Condition of Tokyo Bay using Redox Sensitive Elements as an Indicator by Means of Instrumental Neutron Activation Analysis M. Matsuo <i>et al.</i> (31061) .....	184

<b>CO5-9</b>	Absorption of alkali metal ions by white radish sprouts M. Yanaga <i>et al.</i> (31064) .....	185
<b>CO5-10</b>	INAA and Ar-Ar Dating for Micro-sized Extraterrestrial Materials R. Okazaki and S. Sekimoto (31068) .....	186
<b>CO5-11</b>	Determination of Abundance of Rare Metal Elements in Seafloor Hydrothermal Ore Deposits by INAA Techniques-6: Evaluation of analytical accuracy J. Ishibashi <i>et al.</i> (31077) .....	187
<b>CO5-12</b>	Research on Earth Surface Processes by Use of Mineral Luminescence N. Hasebe <i>et al.</i> (31079) .....	188
<b>CO5-13</b>	Geochemistry of unbrecciated eucrite, Northwest Africa 10962 N. Shirai <i>et al.</i> (31081) .....	189
<b>CO5-14</b>	Neutron Activation Analysis of Environmental Samples Y. Oura and Md. S. Reza. (31088) .....	190
<b>CO5-15</b>	Bulk Chemical Compositions of CB and CH Chondrites M. Ebihara <i>et al.</i> (31091) .....	191
<b>CO5-16</b>	Determination of Cl, Br and I contents in geochemical reference samples by radiochemical neutron activation analysis - revisited M. Ebihara <i>et al.</i> (31092) .....	192
<b>CO5-17</b>	Spatial Distribution of Halogen Compositions in the Wedge Mantle-derived Metaserpentinite Body in Southwest Japan H. Sumino <i>et al.</i> (31113) .....	193
<b>CO5-18</b>	Fission track age and thermal history of clay deposit of the Tsuchihashi Mine H. Ohira and Y. Sampei (31119) .....	194
<b>CO5-19</b>	<sup>40</sup> Ar- <sup>39</sup> Ar Dating of Extraterrestrial Materials in KURNS N. Iwata <i>et al.</i> (31126) .....	195
<b>CO5-20</b>	Neutron activation analysis of carbonate reference materials: coral (JCp-1) and giant clam (JCt-1) S. Sekimoto <i>et al.</i> (31132) .....	196
<b>CO5-21</b>	Long term analysis of Cs isotopic ratio by thermal ionization mass spectrometry Y. Shibahara <i>et al.</i> (31160) .....	197
<b>CO5-22</b>	Analysis of Cd and As in the rice seed detected from the remains by NAA T. Inamura <i>et al.</i> (31165) .....	198
<b>CO5-23</b>	Analysis method of strontium in seawater Y. Ogata <i>et al.</i> (31168) .....	199
<b>CO5-24</b>	INAA using KUR for the determination of elemental content in air particulate samples J.H. Moon <i>et al.</i> (31169, 31170) .....	200

## 6. Life Science and Medical Science

<b>CO6-1</b>	Effect of inter-protein interaction on SAXS profile in concentrated MurD solution H. Nakagawa <i>et al.</i> (31001) .....	201
<b>CO6-2</b>	Physicochemical study on ILEI suppressing amyloid- $\beta$ generation E. Hibino <i>et al.</i> (31003) .....	202
<b>CO6-3</b>	Structural characterization of circadian clock protein complexes H. Yagi <i>et al.</i> (31006) .....	203
<b>CO6-4</b>	Interaction between Mint3 and FIH-1 involved in hypoxia stress responses R. Maeda <i>et al.</i> (31011) .....	204
<b>CO6-5</b>	Supramolecular Tholos-Like Architecture Constituted by Archaeal Proteins Without Functional Annotation M. Yagi-Utsumi <i>et al.</i> (31013) .....	205
<b>CO6-6</b>	Small Angle X-ray Scattering Measurements on Insulin B-Chain Nucleation Intermediate Complexed with Fibrinogen N. Yamamoto <i>et al.</i> (31028) .....	206
<b>CO6-7</b>	Character of DNA damage induced by nuclear plant neutron beams H. Terato <i>et al.</i> (31040) .....	207

<b>CO6-8</b>	Radiation-induced clustered DNA damage estimated by homo-FRET analysis K. Akamatsu <i>et al.</i> (31063).....	208
<b>CO6-9</b>	Photoproduction of Medical <sup>18</sup> F and <sup>99m</sup> Tc Isotopes M. Kurosawa <i>et al.</i> (31069).....	209
<b>CO6-10</b>	Small Angle X-ray Scattering Measurements on Insulin B chain; a Time-Resolved Measure-ment to Monitor the Amyloid Fibril Formation via Prefibrillar Intermediates N. Yamamoto <i>et al.</i> (31070).....	210
<b>CO6-11</b>	Generation of radioresistant Escherichia coli by adaptive evolution using gamma rays as selection pressure II T. Saito <i>et al.</i> (31072).....	211
<b>CO6-12</b>	Structural study for the nucleosome containing histone variant H2A.B R. Hirano <i>et al.</i> (31073).....	212
<b>CO6-13</b>	Effect of High-Intensity Pulsed Coherent Radiation on the Stability of the Gene Y. Tanaka <i>et al.</i> (31078).....	213
<b>CO6-14</b>	Structural analysis of multi-domain protein as studied by complementary use of molecular dynamics simulation and small-angle X-ray scattering R. Inoue <i>et al.</i> (31082).....	214
<b>CO6-15</b>	Oligomeric structure and its temperature-dependent change of HspB1 from Chinese hamster ovary cell M. Yohda <i>et al.</i> (31083).....	215
<b>CO6-16</b>	Quantitative analysis of contribution of tumor vascular damage to antitumor effect of X-ray using BNCR K. Ono <i>et al.</i> (31095).....	216
<b>CO6-17</b>	Observation of Water Uptake in Alternate Grafting of Tomato and Eggplant Using D <sub>2</sub> O as Tracer U. Matsushima <i>et al.</i> (31107).....	217
<b>CO6-18</b>	Production of medical radioisotopes using electron linear accelerator S. Sekimoto and T. Ohtsuki. (31131).....	218
<b>CO6-19</b>	N-Acetylneuraminic acid functioned as the scavenger for reactive oxygen species generated by the gamma-ray irradiation N. Fujii <i>et al.</i> (31134).....	219
<b>CO6-20</b>	Preliminary analysis of structural composition of menaquinone-7 produced by <i>Bacillus subtilis natto</i> T. Chatake <i>et al.</i> (31140).....	220
<b>CO6-21</b>	Measurement of Absorption Spectra of a Humann Calcified Aorta Tissue in the Sub-Terahertz Region, which Depended on the Thickness (III) N. Miyoshi and T. Takahashi (31162).....	221

## 7. Neutron Capture Therapy

<b>CO7-1</b>	Analyses of the immune-cell reaction and activation mechanisms in the tumor tissue after boron neutron capture therapy T. Watanabe <i>et al.</i> (31014).....	222
<b>CO7-2</b>	Boron nitride ( <sup>10</sup> BN) a prospective material for boron neutron capture therapy M. Kaur <i>et al.</i> (31017).....	223
<b>CO7-3</b>	A Fundamental Investigation on Contents of Important Elements for Activation in Various Concrete K. Kimura <i>et al.</i> (31021).....	224
<b>CO7-4</b>	Evaluation of the abscopal effect observed by mouse head irradiation following thermal neutron irradiation Y. Kinashi and T. Takata (31043).....	225
<b>CO7-5</b>	The feasibility study of Eu:LiCAF neutron detector for an accelerator-based BNCT T. Nakamura <i>et al.</i> (31076).....	226
<b>CO7-6</b>	Enhancement of the cancer cell-killing effects of boron neutron capture therapy by overexpression of <i>LATI</i> in human cancer cells K. Ohnishi <i>et al.</i> (31084).....	227
<b>CO7-7</b>	Clinical Outcome of BNCT for Advanced or Recurrent Head and Neck Cancer N. Kamitani <i>et al.</i> (31098).....	228
<b>CO7-8</b>	Establishment of a novel mutation breeding using Boron Neutron Capture Reaction (BNCR) M. Kirihata <i>et al.</i> (31104).....	229

<b>CO7-9</b>	Effects on Dissemination or Invasion of glioma cells by BNCT N. Kondo <i>et al.</i> (31144)	230
<b>CO7-10</b>	iPS cells - derived neuronal cell death and inflammation by thermal neutron irradiation N. Kondo <i>et al.</i> (31145)	231
<b>CO7-11</b>	Resistant Mechanism of Glioma Conferred by Tumor Microenvironment after BNCT N. Kondo <i>et al.</i> (31146)	232
<b>CO7-12</b>	Improvement of the method for analysis of micro boron distribution in tissues M. Suzuki <i>et al.</i> (31150)	233
<b>CO7-13</b>	Development of real-time boron-concentration estimation system for whole-organ-irradiation BNCT Y. Sakurai <i>et al.</i> (31151)	234
<b>CO7-14</b>	Establishment of protocol for neutron capture therapy for head and neck cancer I. Ota <i>et al.</i> (31152)	235
<b>CO7-15</b>	Anti-tumor evaluation of Gadolinium Neutron Capture Therapy through comparison of tumor size using with polymeric nanocarries X. Hou <i>et al.</i> (31163)	236
<b>CO7-16</b>	Accelerated deterioration assessment of SOF detector under high neutron flux environment M. Ishikawa <i>et al.</i> (31166)	237

## 8. Neutron Radiography and Radiation Application

<b>CO8-1</b>	Neutron Phase Imaging with Talbot-Lau Interferometer at CN-3 Y. Seki <i>et al.</i> (31019)	238
<b>CO8-2</b>	Study on the Visualization of Organic Matter between Metals to Contribute to the Advancement of the Industrial Products K. Hirota <i>et al.</i> (31031)	239
<b>CO8-3</b>	Measurements of multiphase flow dynamics using neutron radiography Y. Saito and D. Ito (31034)	240
<b>CO8-4</b>	Visualization of Hydrogen in Pure Palladium via Neutron Radiography and Tomography K. Shimizu <i>et al.</i> (31036)	241
<b>CO8-5</b>	Visualization and Measurement of Boiling Flow Behaviors in Parallel Mini-channel Heat Exchanger H. Asano <i>et al.</i> (31045)	242
<b>CO8-6</b>	Evaluation of Water Distribution and Electrochemical Characteristics in Polymer Electrolyte Fuel Cell H. Murakawa <i>et al.</i> (31046)	243
<b>CO8-7</b>	Meltwater Behavior During the Defrosting Process by Using Neutron Radiography R. Matsumoto <i>et al.</i> (31048)	244
<b>CO8-8</b>	Flow visualization of heavy oil in supercritical water using neutron radiography T. Tsukada <i>et al.</i> (31074)	245
<b>CO8-9</b>	Analysis of moisture transfer in high-strength concrete embedded rebar exposed to fire M. Kanematsu <i>et al.</i> (31103)	246
<b>CO8-10</b>	Development of capillary-plate-based fluorescent plates for neutron radiography T. Sakai <i>et al.</i> (31106)	247
<b>CO8-11</b>	Visualization of a Microchannel Heat Exchanger under Non-uniformly Heated Condition H. Sakai <i>et al.</i> (31121)	248
<b>CO8-12</b>	Diffusion Measurements on NASICON-Type Structured Lithium Ion Conductors by Means of Neutron Radiography S. Takai <i>et al.</i> (31130)	249
<b>CO8-13</b>	Study on the non-destructive nuclide assay for nuclear materials with a self-indication method J. Hori <i>et al.</i> (31136)	250
<b>CO8-14</b>	The measurability of photofission reaction of uranium induced by bremsstrahlung photons K.W. Chin <i>et al.</i> (31155)	251
<b>CO8-15</b>	Distribution of coolant inside a flat laminate vapor chamber in a vertical posture K. Mizuta <i>et al.</i> (31161)	252
<b>CO8-16</b>	Demonstration experiments of an innovative method to detect nuclear material M. Komeda <i>et al.</i> (CA3108)	253

## 9. TRU and Nuclear Chemistry

<b>CO9-1</b>	Leaching behavior of fission products from simulated MCCI debris T. Sasaki <i>et al.</i> (31015)	254
<b>CO9-2</b>	Complex formation of zirconium with hydroxycarboxylic acids T. Kobayashi <i>et al.</i> (31023)	255

<b>CO9-3</b>	Electrodeposition Behaviors of Uranium and Aluminum on Copper Cathode in LiCl-KCl Eutectic Melts Y. Sakamura <i>et al.</i> (31035) .....	256
<b>CO9-4</b>	Structural Change of Borosilicate Glass by Boron Isotope Composition T. Nagai <i>et al.</i> (31038) .....	257
<b>CO9-5</b>	Study on leaching behavior of carbon-14 from neutron irradiated stainless steel R. Nakabayashi <i>et al.</i> (31060) .....	258
<b>CO9-6</b>	Solvent extraction of selenium in the nitric acid solution with selected elements T. Kawakami <i>et al.</i> (31062) .....	259
<b>CO9-7</b>	Effect of $\gamma$ -Ray Irradiation in HNO <sub>3</sub> on Adsorptivity of Long-Chain 6-Membered Cyclic Monoamide Resin Y. Yoshimura <i>et al.</i> (31114) .....	260
<b>CO9-8</b>	Roll of Electrostatic Interaction in Attachment Process of Fission Products to Solution Aerosol Particles K. Takamiya <i>et al.</i> (31139) .....	261
<b>CO9-9</b>	Precipitation of alkaline earth elements toward the chemical study of Nobelium S. Hayami <i>et al.</i> (31153) .....	262
<b>10. Health Physics and Waste Management</b>		
<b>CO10-1</b>	Effective Measures on Safety, Security, Hygiene and Disaster Prevention in Laboratories T. Iimoto <i>et al.</i> (31018) .....	263
<b>CO10-2</b>	Scientific Ethnography for Nuclear Science, Part 1 -Responsibility of Science, Post 3.11, Iitate Village, Fukushima- M. Takagaki and S. Masunaga (31033) .....	264
<b>CO10-3</b>	Assessment of non-homogenous exposure of radiation workers in accelerator facility situation in the small linac facility - M. Kowatari and T. Kubota (31050) .....	265
<b>CO10-4</b>	Investigation for valiation of trace elements concentration in accelerator room concrete G. Yoshida <i>et al.</i> (31056) .....	266
<b>CO10-5</b>	Comparison of Chlorine Concentration in Each Municipal Solid Waste Fraction Measured by Neutron Activation Analysis and Bomb Calorimeter- Ion Chromatography K. Ohita <i>et al.</i> (31075) .....	267
<b>CO10-6</b>	Effect of Ammonium Ion Washing of Radiocesium Contaminated Soil K. Daiku <i>et al.</i> (31129) .....	268
<b>CO10-7</b>	Measurement of Radioactivity-Based Particle Size of Radiation-Induced Aerosols using a Diffusion Battery System in Accelerator Facilities Y. Oki. (31154) .....	269
<b>CO10-8</b>	Consideration of radon concentration measurement under natural fluctuation environment by a new monitor using two filter method Y. Igarashi <i>et al.</i> (CA3115) .....	270
<b>12. Others</b>		
<b>CO12-1</b>	Isotope Dilution-Neutron Activation Analysis for Quantifying Hafnium T. Takatsuka <i>et al.</i> (31026) .....	271
<b>CO12-2</b>	Study on Superposition of Terahertz Coherent Radiation using a Ring Resonator N. Sei and T. Takahashi (31029) .....	272
<b>CO12-3</b>	High-count-rate <sup>3</sup> He position-sensitive detector readout system S. Sato <i>et al.</i> (31044) .....	273
<b>CO12-4</b>	Neutron activation analysis of Ar in titanium metal T. Miura <i>et al.</i> (31047) .....	274
<b>CO12-5</b>	A response of inner-through type ionizaiotn chamber to <sup>41</sup> Ar A. Yunoki <i>et al.</i> (31059) .....	275
<b>CO12-6</b>	Development of neutron imager based on hole-type MPGD with glass capillary plate F. Tokanai <i>et al.</i> (31080) .....	276
<b>CO12-7</b>	Gamma ray measurement in the basement of the Kyoto University Research Reactor facility K. Okada <i>et al.</i> (31089) .....	277

<b>CO12-8</b>	Neutron efficiency of a two-dimensional neutron detector with MPPC (Mpix) H. Ohshita <i>et al.</i> (31094) .....	278
<b>CO12-9</b>	Research on Activation Assessment of a Reactor Structural Materials for Decommissioning (2) M. Seki <i>et al.</i> (31096) .....	279
<b>CO12-10</b>	Beam Test of a micro-cell MWPC for a muon-electron conversion search experiment, DeeMe M. Aoki <i>et al.</i> (31105) .....	280
<b>CO12-11</b>	An attempt to produce carrier free tracer through photonuclear reaction and hot atom effect T. Kubota <i>et al.</i> (31110) .....	281
<b>CO12-12</b>	Study of Isotope Separation via Chemical Exchange Reaction R. Hazama <i>et al.</i> (31115) .....	282
<b>CO12-13</b>	Radius of Gyration of Polymer for Viscosity Index Improver at Various Temperatures Evaluated by Small-Angle X-Ray Scattering T. Hirayama <i>et al.</i> (31116) .....	283
<b>CO12-14</b>	Friction Reduction by the Combination Use of MoDTC and Organic Friction Modifier T. Hirayama <i>et al.</i> (31117) .....	284
<b>CO12-15</b>	Multi-element neutron activation analysis of selected Japanese food samples by neutron activation analysis M. Fukushima <i>et al.</i> (31123) .....	285
<b>CO12-16</b>	Installation of Flowing Sample Neutron Activation Analysis at KUR M.A. Soliman <i>et al.</i> (31138) .....	286
<b>CO12-17</b>	Neutron Resonance Spectrometry of Urinium for Nuclear Security and Safeguards Education J. Kawarabayashi <i>et al.</i> (31141) .....	287
<b>CO12-18</b>	Evaluation test of SEL recovering system used in CubeSat by using <sup>252</sup> Cf H. Masui <i>et al.</i> (31142) .....	288

<b>II. PUBLICATION LIST (April 2019 – March 2020)</b> .....	289
---	-----

**I. ANNUAL SUMMARY OF EXPERIMENTAL  
RESEARCH ACTIVITIES**

## **I-1. PROJECT RESEARCHES**

### **Project 1**

Y. Ohkubo

*Institute for Integrated Radiation and Nuclear Science,  
Kyoto University*

### Objective and Participating Research Subjects

The main objectives of this project research are the investigation of the nuclear structure of unstable neutron-rich nuclei and also the local properties of materials using short-lived nuclei.

This period is the third and last year of the project.

The research subjects reported here are as follows:

- 31P1-1 Technique of transferring radioactive atomic nuclei implanted in dry ice film
- 31P1-2  $\beta^-$ -Decay spectroscopic studies of fission products using the clover detector
- 31P1-3 Linear polarization measurement for  $\gamma$  rays from  $^{148}\text{Pr}$
- 31P1-5 Measurement of the internal pressure in ultrafine bubbles by angular correlation technique
- 31P1-6 Temperature-dependent polaronic local structures in  $\text{La}_{0.7}\text{Ca}_{0.3}\text{MnO}_3$  observed through spin relaxation of TDPAC probe nuclei
- 31P1-7 Local structure of In impurities doped in  $\text{SrTiO}_3$  studied by TDPAC method

### Main Points Described in the Reports in the Following Six pages

As a means to measure the charge distribution of an unstable nucleus, it is promising to make a muonic atom composed of the nucleus that are trapped in deuterium film and then to measure the energies of X-ray emitted from the muonic atom. However, it is unavoidable to deal with high radioactivity. One of the technical problems is how efficiently and safely long-lived radioactivity in the apparatus is removed after such an experiment is done. A. Taniguchi *et al.* (31P1-1) has attacked this problem using a beam of  $^{146}\text{LaO}^+$  radioactive ions available at KUR-ISOL and an apparatus designed for the present work. In this period, they improved the apparatus so that the removal efficiency became much higher than that obtained previously.

M. Shibata *et al.* (31P1-2) investigated the level structures of  $^{153}\text{Nd}$  and  $^{154}\text{Nd}$ , arising via  $\beta^-$  decay, respectively, from  $^{153}\text{Pr}$  (half-life of 4.3 s) and  $^{154}\text{Pr}$  (half-life of 2.3 s), fission products of  $^{235}\text{U}$  + thermal neutron, available at KUR-ISOL. Because of the large  $Q_\beta$  values, 5752 keV for  $^{153}\text{Pr}$  and 7790 keV for  $^{154}\text{Pr}$ , it is possible to access to high excited levels of  $^{153}\text{Nd}$  and  $^{154}\text{Nd}$ . They used a clover detector consisting of 4 Ge crystals both in singles and add-back modes. For  $^{153}\text{Nd}$ , they identified eight new excited levels and also new nineteen  $\gamma$ -rays. The detailed analysis is in progress for constructing the decay schemes.

Y. Kojima *et al.* had tried to measure the linear

polarization of  $\gamma$ -rays from short-lived  $\beta^-$  decaying nuclei using a clover detector (the same detector that M. Shibata *et al.* used in 31P1-2) as a Compton polarimeter and additional coaxial Ge detectors in order to obtain the multipolarities of those  $\gamma$ -rays. In the last period, they confirmed the feasibility of their polarimeter system using the established 258-410 keV E2-E2  $\gamma$  cascade in  $^{146}\text{Ce}$  arising from  $^{146}\text{La}$  via  $\beta^-$  decay, available at KUR-ISOL. In this period, they succeeded in obtaining the preliminary result showing the E2 character of the 1358-keV  $\gamma$  ray from  $^{148}\text{Pr}$  (half-life of 2.1 m) decaying to  $^{148}\text{Nd}$ , produced at KUR-ISOL.

Ultrafine bubbles, attracting a lot of attention in various industrial fields, are of the diameter less than one micro meter. Despite the Young-Laplace equation predicting a high internal pressure for such a small bubble in water so that it should survive only very short time, it is reported to survive more than a month. Employing the time-integral perturbed angular correlation (TIPAC) technique for  $^{125}\text{I}$  arising from  $^{125}\text{Xe}$  (half-life of 17 h) produced at the slant exposure tube of KUR, M. Tanigaki *et al.* successfully obtained the internal pressure of ultrafine bubbles of the average diameter about 200 nm containing Xe gas inside, the value of which is much smaller than that the Young-Laplace equation predicts. In this period, they (31P1-5) reevaluated the value of the time-integrated perturbed angular correlation.

A perovskite manganese oxide  $\text{La}_{0.7}\text{Ca}_{0.3}\text{MnO}_3$  (for short, LCMO) is well known to exhibit colossal magnetoresistance. It is considered that polaron dynamics plays a significant role in this phenomenon. Because of the large variation in physical properties of  $\text{La}_{1-x}\text{Ca}_x\text{MnO}_3$  with  $x$ , the A-site (La or Ca) information is especially important. In order to obtain this local information for LCMO, W. Sato *et al.* (31P1-6) synthesized 2 at. % nonradioactive Cd-doped LCMO containing a tracer amount of radioactive  $^{111\text{m}}\text{Cd}$  (half-life of 49 m) produced in the pneumatic tubes of KUR and took  $^{111}\text{Cd}$  ( $\leftarrow^{111\text{m}}\text{Cd}$ ) TDPAC (time-differential perturbed angular correlation) spectra at temperatures above and below the Curie temperature of  $\sim 250$  K. They succeeded in observing the static and dynamic polarons around the probe nuclei at the A site of LCMO.

$\text{SrTiO}_3$  is a cubic perovskite oxide. Doped with metal impurity ions, it exhibits a wide variety of electronic properties. In order to obtain local information on the impurity site, S. Komatsuda *et al.* (31P1-7) synthesized  $\text{SrTiO}_3$  containing a tracer amount of commercially available  $^{111}\text{In}$  (half-life of 2.8 d) and took the room-temperature TDPAC spectrum of  $^{111}\text{Cd}$  arising from  $^{111}\text{In}$ . They found three kinds of quadrupole frequencies in the spectrum: one is zero frequency indicating  $^{111}\text{Cd}$  at the defect-free substitutional site and the other two non-zero frequencies implying  $^{111}\text{Cd}$  at the substitutional site associated with oxygen vacancy.

## PR1-1 Technique of Transferring Radioactive Atomic Nuclei Implanted in Dry Ice Film

A. Taniguchi, P. Strasser<sup>1</sup>, M. Tanigaki and Y. Ohkubo

*Institute for Integrated Radiation and Nuclear Science,  
Kyoto University*

<sup>1</sup>*Muon Science Laboratory, IMSS, KEK*

**INTRODUCTION:** Measurement of the emitted X-ray energy from muonic atoms is a powerful method for the investigation of the nuclear charge radius [1]. Recently, a new method using solid hydrogen film has been developed to produce muonic atoms. In this method, negative muons are injected to solid deuterium film in which nuclei of interest are implanted beforehand, thereby muonic atoms being formed through the highly-efficient muon transfer reaction. The feasibility of this method was demonstrated and promising results were obtained [2]. In this study, one of the problems in applying this method to unstable nuclei, concerned with handling of residual radioactivities in deuterium film after experiments, in particular their highly efficient recovery, was approached using a radioactive-isotope beam from KUR-ISOL and dry ice film instead of solid hydrogen film.

**EXPERIMENTS:** An apparatus capable of implanting radioactivities to dry ice film was installed at the beam line of KUR-ISOL [3]. This apparatus has two coolable copper blocks and one CO<sub>2</sub> gas diffuser in the vacuum chamber. Dry ice film is formed on the surface of one cooled block (catcher) by sprayed CO<sub>2</sub> gas through the diffuser and radioactivities are implanted into it. In a series of recent experiments, even if films of the same appearance were formed on the catcher, large variations were observed in the amounts of radioactivities transferred to the other block (trap). It is considered that the condition of dry ice film is important and the forming parameters should be controlled more finely in order to improve the reproducibility of the transfer efficiency. In this work, film was formed while recording the vacuum degree in the chamber with a data logger. In addition, by attaching "standing collars" on the four sides of the film formation surface, more CO<sub>2</sub> gas from the diffuser is guided to the surface during film formation, furthermore during transfer, the collars cover the catcher-trap gap so that sublimation components become less likely to escape into the chamber. About 10<sup>6</sup> ions of <sup>146</sup>LaO<sup>+</sup> were implanted into dry ice film on the catcher in every run. After the implantation, the other pre-cooled trap was moved to the frontal vicinity of the catcher, and then the catcher was warmed by stopping LN<sub>2</sub> flow. With this procedure, the atoms of <sup>146</sup>Ce and <sup>146</sup>Pr were released from the catcher and were re-trapped on the trap together with CO<sub>2</sub>. The transfer efficiency was measured by detecting the  $\gamma$ -rays emitted from each of the blocks. In each run, it took about 2 hours from the implantation to the completion of the transfer.

**RESULTS AND DISCUSSION:** The transfer efficiencies were measured by changing the amount of CO<sub>2</sub> while confirming the vacuum degree when dry ice films were formed. Although the detail data analysis including

the absolute trap efficiency for the implanted radioactivities is in progress, the higher transfer efficiency result of about 880% was obtained (see Fig.1). The efficiency is defined as the ratio of the radioactivities on the trap to those remaining on the catcher, which was deduced from the peak counts of 454 keV  $\gamma$ -ray of <sup>146</sup>Pr by taken into account of the detection efficiency of each Ge detector in its actual arrangement. This result is still poorly reproducible and the appropriate parameters for film formation have not yet been fixed, but much higher than the previous results [4]. Therefore, it can be said that the control of the vacuum degree is one of the important parameters.

**ACKNOWLEDGMENTS:** This research was partially supported by the Ministry of Education, Science, Sports and Culture, Grant-in-Aid for Scientific Research (C) (24540303, Akihiro Taniguchi, and 15K05103, Akihiro Taniguchi).

### REFERENCES:

- [1] I. Angeli and K.P. Marinova, *At. Data Nucl. Data Tables* **99** (2013) 69-95.
- [2] P. Strasser *et al.*, *Hyperfine Interact.* **193** (2009) 121-127.
- [3] A. Taniguchi *et al.*, *KURRI Prog. Rep.* 2013, p98.
- [4] A. Taniguchi *et al.*, *KURNS Prog. Rep.* 2018, p28.

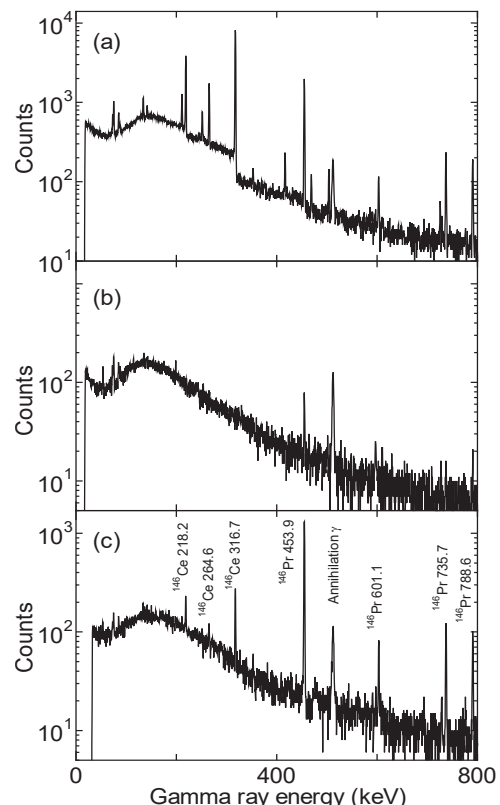


Fig.1 Transfer of radioactivities using a cold trap type recovery apparatus. (a)Gamma-ray spectrum of the catcher immediately after <sup>146</sup>La implantation. <sup>146</sup>La ( $T_{1/2} = 10$  s and 6 s) decayed out and  $\gamma$ -rays of <sup>146</sup>Ce ( $T_{1/2} = 14$  m) and <sup>146</sup>Pr ( $T_{1/2} = 24$  m) were observed. Gamma-ray spectra of (b) the catcher and (c) the trap after the transfer.

## PR1-2 $\beta$ -Decay Spectroscopic Studies of Fission Products Using a Clover Detector

Y. Ishikawa, M. Kanaji, Y. Irie<sup>1</sup>, T. Yamaguchi<sup>1</sup>,  
M. Shibata<sup>2</sup>, H. Hayashi<sup>3</sup> and A. Taniguchi<sup>4</sup>

Graduate School of Engineering, Nagoya University

<sup>1</sup>School of Engineering, Nagoya University

<sup>2</sup>Radioisotope Research Center, Nagoya University

<sup>3</sup>School of Health Science, Kanazawa University

<sup>4</sup>Institute for Integrated Radiation and Nuclear Science,  
Kyoto University

**INTRODUCTION:** Precise decay scheme of fission products are very important to study nuclear structure and also decay heat evaluation in nuclear reactor. The neutron-rich and short-lived nuclei around mass number 150 have low yields then their decay data are scarcely studied. In particular, <sup>153</sup>Pr ( $T_{1/2} = 4.3$  s) and <sup>154</sup>Pr ( $T_{1/2} = 2.3$  s) were studied by separating from the fission products of <sup>235</sup>U with isotope separator on-lines (ISOL) and was reported few  $\gamma$ -rays [1, 2], nevertheless, the  $Q_{\beta}$ -value of them are reported to be 5762 and 7790 keV [3], respectively. It means that the both daughter nuclei are expected to have much higher excited levels and also isomeric states having  $\mu$ s order of half-lives. To identify higher levels and high energy  $\gamma$ -rays and to propose detailed decay scheme, the  $\gamma$ -rays associated with the  $\beta$ -decay of <sup>153</sup>Pr and <sup>154</sup>Pr were measured with a clover detector at KUR-ISOL.

The clover detector has 4 large Ge crystals of 80 mm in diameter and 90 mm in length, they are arranged as the shape of a four-leaf clover, and it has through-hole which diameter is 15 mm in the detector. The solid angle is 98% in center of the hole, so  $\gamma$  rays can be measured with high efficiency. The list mode including time information, so-called a time-stamped list mode, data acquisition (DAQ) system was adapted to identify the  $\gamma$ - $\gamma$  coincidence relation. With this system, two types  $\gamma$ -ray spectra, those are "singles" and "add-back" spectra can be obtained by off-line analyses. In the add-back spectra compared with singles spectra, sum peaks are strongly observed, on the other hand, the cascading  $\gamma$  rays are observed weakly by coincidence summing out. The off-line analyses, the location of  $\gamma$  rays in the decay scheme can be made clear.

To deduce the half-lives of isomers with the DAQ system,  $\beta$ - $\gamma$  time difference method was applied. In this method, the time difference between the  $\gamma$ -ray of interest and a certain continuum part of spectrum which corresponds  $\beta$ -rays are extracted from the list mode data. In this method, the counting rate during the measurement is an important parameter for obtain reliable results. The isomer ( $T_{1/2} = 52.6$   $\mu$ s) at 1088 keV in <sup>95</sup>Y of daughter <sup>95</sup>Sr ( $T_{1/2} = 23.9$  s) is proper nucleus to check the effect of the counting rate on the obtained value.

**EXPERIMENTS:** The nuclei of interests were mass-separated by the KUR-ISOL from the fission products of <sup>235</sup>U. A 72 mg of 93% enriched UF<sub>4</sub> was irradiated with a thermal neutron flux of  $3 \times 10^{12}$  n/cm<sup>2</sup>/s. The radioactive sources were collected on a thin Mylar tape and were

periodically transported to the center of the detector with computer-controlled tape moving system. The tape moved periodically with two times of each half-life. In the through-hole of the detector, the two semicircle-formed 6mm thick acrylic sticks were set on the both side of Mylar tape as  $\beta$ -ray absorbers. The detector was shielded with 10 cm thick lead bricks and 5 cm thick boron-doped polyethylene bricks. The data were recorded in the DAQ system of APV8008 and APV8016 made by Techno AP Corporation. The measurements of <sup>153</sup>Pr, <sup>154</sup>Pr and <sup>95</sup>Sr were performed for 8, 11 and 8 hours, respectively.

**RESULTS:** Here, the preliminary result of each experiment was briefly described. Concerning <sup>154</sup>Pr, a typical coincidence spectrum gated by the 162.4 keV  $\gamma$ -ray, which were previously reported in ref [1], is shown in Fig.1. Ten  $\gamma$ -rays including previously proposed the 70.8, 794.4 and 895.6 keV  $\gamma$ -rays [1] and Nd Kx-rays were in coincidence with the 162.4 keV  $\gamma$ -ray. In addition, the sum peak of 162.4 + 169 keV was observed in the add-back spectrum, it means they are cascade relation each other.

Concerning <sup>153</sup>Pr, eight excited levels and nineteen  $\gamma$ -rays were newly identified in addition to the previous result [2]. The half-life value of isomeric state of 191.7 keV was determined to be 1.13(10)  $\mu$ s with the  $\beta$ - $\gamma$  time difference method. This value is in agreement with the previous value of 1.06(5)  $\mu$ s.

From the results of the half-life of the 1088 keV level in <sup>95m</sup>Y through the  $\beta$ -decay of <sup>95</sup>Sr by the  $\beta$ - $\gamma$  time difference method, the higher counting rate is, the shorter the result became. It was found desirable to keep the count rate below 5 kcps in this method.

Further analyses for construction of the decay schemes of <sup>153</sup>Pr and <sup>154</sup>Pr are in progress.

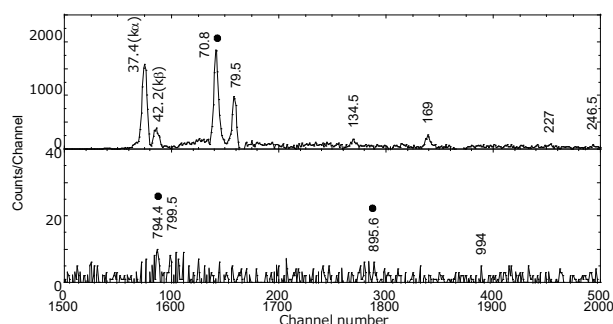


Fig. 1. Coincidence spectrum gated by the 162.4 keV  $\gamma$ -ray in the decay of <sup>154</sup>Pr. The closed circles indicate the reported  $\gamma$ -rays [1].

### REFERENCES:

- [1] Y. Toh *et al.*, Z. Phys. A 355, 345-346 (1996).
- [2] S. Yamada *et al.*, J. Phys. Soc. Jpn. 65, 3390(1996).
- [3] The 2016 Atomic Mass Evaluation.  
<http://amdc.impcas.ac.cn/web/masseval.html>.

Y. Kojima, H. Sawai<sup>1</sup>, Y. Ishikawa<sup>1</sup>, M. Kanaji<sup>1</sup>, Y. Irie<sup>2</sup>,  
T. Yamaguchi<sup>2</sup>, A. Taniguchi<sup>3</sup> and M. Shibata

*Radioisotope Research Center, Nagoya University*

<sup>1</sup>*Graduate School of Engineering, Nagoya University*

<sup>2</sup>*School of Engineering, Nagoya University*

<sup>3</sup>*Institute for Integrated Radiation and Nuclear Science, Kyoto University*

**INTRODUCTION:** Gamma-ray multiplicities are one of the most important properties for nuclei because they are necessary in discussion of nuclear structures. For determination of the  $\gamma$ -ray multiplicities, the linear polarization is useful, and is usually measured using an asymmetry of Compton scattering events. In recent years, we are trying the linear polarization measurements for short-lived  $\beta$ -decaying nuclei using a clover HPGe detector [1]. The clover detector consists of four large Ge crystals packed closely, and the size of each crystal is 80 mm in diameter and 90mm in length. In this technique, a Compton scattering asymmetry  $A$  in orthogonal directions is determined by means of coincidence measurements. After correcting the  $A$ -value using the polarimeter sensitivity  $Q$ , the value of  $A/Q$  is compared with the degree of polarization which has been calculated for various multiplicities.

In AY2018, we tried linear polarization measurements for  $^{146}\text{La}$  produced by on-line isotope separator KUR-ISOL [2], and succeeded in observation of the Compton scattering asymmetry for 258-410 keV E2-E2  $\gamma$  cascade. In this report, we present the preliminary results obtained for  $^{148}\text{Pr}$ .

**EXPERIMENTS:** The detection system consisted of the clover detector as a polarimeter, a coaxial 60% (relative efficiency) HPGe detector as a directional detector, and a coaxial 38% HPGe detector to deduce correction factors of detection efficiencies. The directional detector was placed perpendicular to the clover detector, and was used to define a *reference plane*. A detector-to-source distance was 10 cm for all detectors. The preamplifier signals from the detectors were processed by a VME-based data acquisition system, and the data on the pulse height and the detection time were recorded in event-by-event mode.

Gamma rays from the  $\beta^-$  decay of  $^{148}\text{Pr}$  (half-life of 2.1 min) were measured at KUR-ISOL. The  $^{148}\text{Pr}$  nuclei were produced by the thermal-neutron-induced fission of  $^{235}\text{U}$ . The fission products thermalized in the target chamber were transported by a He-N<sub>2</sub> mixture gas jet stream to a surface-ionization-type ion source. After ionization to the chemical form of  $^{148}\text{Pr}^{16}\text{O}^+$ , the nuclei were extracted, accelerated to 30 keV, and mass-separated. The mass-separated beams were implanted into an aluminized Mylar tape in a tape transport system. The source was periodically moved to a detector port with time intervals of 220 s. The measuring times were 73 h and 11 h under a 1-MW and 5-MW operation condition, respectively.

**RESULTS:** The list data were analyzed using an off-line sorting program. In this analysis, we considered data recorded within 460 ns as a coincident event, and focused on the 302-451 keV and 302-1358 keV  $\gamma$ -ray cascades. The former cascade is known as an E2-E2 transition, while the multipolarity of the 1358 keV  $\gamma$  ray in the latter cascade is unknown. The 1358-keV  $\gamma$  ray is a transition from a  $2^+$  to a  $2^+$  level, so that the multipolarity is expected to be M1 or E2.

From coincidence spectra gating on the 302-keV  $\gamma$  ray, we obtained the asymmetry value  $A$  of 0.045(17) for the 451-keV  $\gamma$  ray. Because the theoretical value of polarization  $P$  is 0.1667 for the E2-E2 cascade in the  $4^+-2^+-0^+$  spin-parity sequence, the sensitivity  $Q$  was found to be  $Q = A/P = 0.27(10)$ . As shown in Fig.1, this  $Q$ -value agrees with those obtained in the previous experiments. For the 1358-keV  $\gamma$  ray, the asymmetry value of  $A = -0.008(15)$  was observed. Because the sensitivity is about 0.16 for 1358 keV (Fig.1), the degree of polarization was deduced to be  $-0.05(10)$ . Here, the theoretical  $P$ -values are 0.43 and 0.08 if the 1358-keV  $\gamma$  ray is a M1 and E2 transition, respectively. Our result favors the multipolarity of the 1358-keV  $\gamma$  ray is E2, while the experimental uncertainty is large.

**CONCLUSIONS:** Compton scattering asymmetries were observed for  $\gamma$  rays from  $^{148}\text{Pr}$ . The result suggests the 1358-keV  $\gamma$ -ray is an E2 transition.

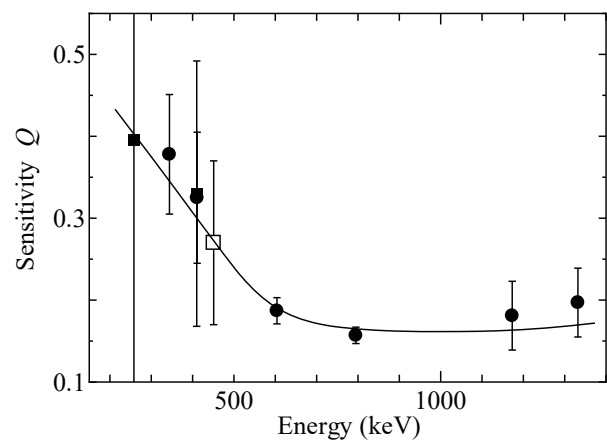


Fig. 1. Energy dependence of the polarization sensitivity. Open and filled marks show data obtained in this experiment and previous measurements using  $^{60}\text{Co}$ ,  $^{134}\text{Cs}$ ,  $^{152}\text{Eu}$  and  $^{146}\text{La}$  [3], respectively. The curve is only a guide to the eye.

**REFERENCES:**

- [1] Y. Shima *et al.*, Appl. Radiat. Isot. **91** (2014) 97-103.
- [2] A. Taniguchi *et al.*, Nucl. Instr. and Meth. A, **351** (1994) 378-382.
- [3] Y. Kojima *et al.*, KURNS Prog. Rep. 2018. PR3-3.

## Measurement of the Internal Pressure in Ultrafine Bubbles by Angular Correlation Technique

M. Tanigaki, T. Yamakura<sup>1</sup>, Y. Ueda<sup>2</sup>, A. Taniguchi, Y. Tokuda<sup>3</sup>, and Y. Ohkubo

*Institute for Integrated Radiation and Nuclear Science,  
Kyoto University*

<sup>1</sup>*Graduate School of Science, Kyoto University*

<sup>2</sup>*Research Institute for Sustainable Humanosphere, Kyoto University*

<sup>3</sup>*Faculty of Education, Shiga University*

**INTRODUCTION:** Ultrafine bubbles, the gaseous cavities with diameters less than one micrometer [1], recently attracts a lot of attention because of their multifunctionalities. While applications of ultrafine bubbles are extended in a wide variety of fields, fundamental studies on ultrafine bubbles itself are not well extended because of its small size, smaller than the wavelength of radiant rays.

In nuclear physics, the measurements of angular correlations of iodine isotopes in Xe gas reportedly show large dependences on the pressure of Xe gas [2][3][4], thus suitable as the probe for the pressure inside the gaseous cavity.

We have reported the first measurement of the angular correlation of <sup>125</sup>I induced inside the Xe ultrafine bubbles induced by the neutron irradiation at Kyoto University Research Reactor (KUR) for the determination of the internal pressure [5].

In this paper, the progress in the analysis of the previous measurement and the current status of the study are described.

**EVALUATION OF INTERNAL PRESSURE OF ULTRAFINE BUBBLE:** In the previous report,  $A_{22}G_{22}(\infty)$  for 55-188 keV cascade in <sup>125</sup>I in Xe- ultrafine bubble was determined to be  $+0.097 \pm 0.037$  by taking into account the corrections of detector solid angles, size of the source and the contribution of <sup>125</sup>I existing as the solute in the water [5]. This time, the contribution of <sup>125</sup>I existing as the solute in the water was evaluated in more detail by using the event numbers of 55-188 keV cascade in <sup>125</sup>I.

The counting number for the saturated water irradiated at 5 MW was only  $18.25 \pm 0.64\%$  of that obtained from the ultrafine bubble sample irradiated at the same time, therefore Xe was eventually maintained inside the ultrafine bubbles at the time of the angular correlation measurement for samples irradiated at 5 MW.

It should be noted that the counting number for the Xe saturated water is only  $14.53 \pm 0.50\%$  of that irradiated at 1 MW. The difference in the counting numbers observed between these Xe saturated water is the result of the difference in the elapsed time after the first repacking. The samples irradiated at 5 MW spent two days more before irradiation and Xe existed as the solute went out of the water and was accumulated at the vacant  $0.5 \text{ cm}^3$  space in the PP cylinder for this additional two days. Even though Xe

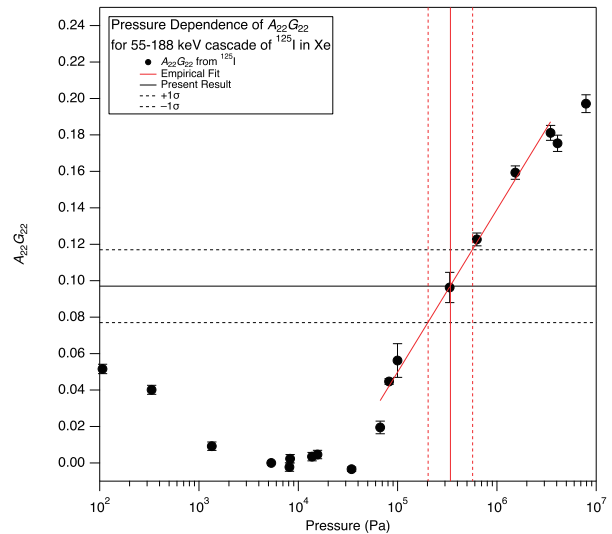


Fig. 1 Pressure dependence of  $A_{22}G_{22}(\infty)$  of <sup>125</sup>I in Xe gas.

nuclei at the vacant space were also activated at the reactor, they went away during the repacking process for the angular correlation measurement. By taking the ratio of counting numbers between the saturated water and ultrafine bubble water,  $A_{22}G_{22}(\infty)$  was re-evaluated to be  $+0.097 \pm 0.020$ . The internal pressure of the Xe-ultrafine bubble was obtained to be  $3.4^{+3.3}_{-2.3} \times 10^5 \text{ Pa}$  (Fig. 1).

### PRESSURE DEPENDENCE OF $A_{22}G_{22}(\infty)$ OF <sup>125</sup>I IN Xe-ULTRAFINE BUBBLE:

Since the internal pressure of ultrafine bubbles should be equal to the pressure from the outside including the water pressure,  $A_{22}G_{22}(\infty)$  should be changed once the outside pressure is changed. This should also give a clue to the inside temperature of ultrafine bubbles by combining the size of ultrafine bubbles. The first trial of the angular correlation measurement for the sample that was pressurized by Xe-gas was performed, and the analysis is on the way.

The present work is supported by JSPS KAKENHI Grant Number 18K03948.

- REFERENCES:**[1] E. G. Denis, The fine bubble breakthrough. <https://www.iso.org/news/2014/05/Ref1844.html>  
[2] U. Berek, W. Kreisel, H. Schneider, and E. Tierno, Phys. Lett. **A48** (1974) 79.  
[3] U. Berek, W. Kreisel, H. Schneider, E. Tierno, and H. Wagner, Phys. Lett. **A55** (1975) 22.  
[4] U. Berek, W. Kreisel, H. Schneider, and E. Tierno, Phys. Lett. **A53** (1975) 251.  
[5] M. Tanigaki, T. Yamakura, Y. Ueda, A. Taniguchi, Y. Tokuda, and Y. Ohkubo, KURNS Progress Report 2018, p.31.

W. Sato<sup>1,2</sup>, S. Komatsuda<sup>3</sup>, H. Shimizu<sup>2</sup>, R. Moriichi<sup>2</sup>, S. Abe<sup>1,2</sup>, S. Watanabe<sup>2</sup>, S. Komatsu<sup>2</sup>, T. Terai<sup>4</sup>, S. Kawata<sup>5</sup>, and Y. Ohkubo<sup>6</sup>

<sup>1</sup>*Institute of Science and Engineering, Kanazawa University*

<sup>2</sup>*Graduate School of Science and Technology, Kanazawa University*

<sup>3</sup>*Institute of Human and Social Sciences, Kanazawa University*

<sup>4</sup>*Graduate School of Engineering, Osaka University*

<sup>5</sup>*Department of Chemistry, Fukuoka University*

<sup>6</sup>*Institute for Integrated Radiation and Nuclear Science, Kyoto University*

**INTRODUCTION:** It is well known that a perovskite manganese oxide  $\text{La}_{0.7}\text{Ca}_{0.3}\text{MnO}_3$  (LCMO) exhibits the effect of colossal magnetoresistance, and it has received high expectations for application to a variety of functional magnetic materials. For its practical application, it is essential to investigate the magnetotransport phenomenon of the oxide by obtaining information on the local field at each site on an atomic scale in addition to its bulk properties. Especially, the  $A$  site information is very important because magnetoresistance of  $\text{R}_{1-x}\text{A}_x\text{MnO}_3$  is governed largely by doping of  $A$ -site ions. For a detailed investigation of the  $A$ -site field, we employed time-differential perturbed angular correlation (TDPAC) spectroscopy with the  $^{111}\text{mCd}(\rightarrow^{111}\text{Cd})$  probe [1]. Because the ionic radius of the Cd ion is close to those of La and Ca, the probe nucleus can selectively occupy the  $A$  site, which allows us to observe the change of the local fields at temperatures above and below  $T_C$  ( $\sim 250$  K). In the present work, we report a successful observation of dynamic motion and freezing of Jahn-Teller (JT) polarons formed by  $e_g$  electrons on Mn ions.

**EXPERIMENTS:** Stoichiometric amounts of  $\text{La}_2\text{O}_3$ ,  $\text{MnO}_2$ , and  $\text{CaCO}_3$  were mixed well in a mortar, and the powdery mixture was calcined at 1273 K for 12 h. The sample was again ground to uniformity, and it was pressed into a disk. The disk was then sintered at 1473 K for 96 h. Successful synthesis of LCMO was confirmed by powder X-ray diffraction patterns and magnetization measurements.

Neutron irradiation was performed for cadmium oxide (CdO) enriched with  $^{110}\text{Cd}$  in Kyoto University Reactor to produce radioactive  $^{111}\text{mCd}$  by a neutron capture reaction. The radioactive  $\text{Cd}(^{111}\text{mCd})\text{O}$  powder was mixed well with the LCMO prepared in advance, and the pressed disk was sintered in vacuum at 1373 K for 45 min. TDPAC measurements were carried out for the  $^{111}\text{mCd}(\rightarrow^{111}\text{Cd})$  probe on the 151-245 keV cascade  $\gamma$  rays with the intermediate state of  $I = 5/2$  having a half-life of 85.0 ns. In the present work, we obtained the perturbed

angular correlation as a function of the time interval of the cascade  $\gamma$ -ray emissions by the following expression:

$$A_{22}G_{22}(t) = \frac{2[N(\pi, t) - N(\pi/2, t)]}{N(\pi, t) + 2N(\pi/2, t)}, \quad (1)$$

where  $A_{22}$  denotes the angular correlation coefficient,  $G_{22}(t)$  the time-differential perturbation factor as a function of the time interval  $t$  between the cascade  $\gamma$ -ray emissions, and  $N(\theta, t)$  the number of the delayed coincidence events observed at an angle  $\theta$ . The measurements were performed at different temperatures.

**RESULTS:** The TDPAC spectra of  $^{111}\text{mCd}(\rightarrow^{111}\text{Cd})$  embedded in LCMO are shown in Fig. 1. We found that the room-temperature spectrum consists of two different components reflecting a distorted and a less distorted sites having the fractional ratio of 7 : 3. The ratio agrees with that of  $\text{Mn}^{3+}$  and  $\text{Mn}^{4+}$  abundances, suggesting that the former local distortion arises from JT polarons formed by localized  $e_g$  electrons on  $\text{Mn}^{3+}$  ions. This inference is supported by the observation that the oscillatory structure of the distorted component completely disappeared from the spectra at 201 K and 77 K ( $< T_C$ ). The disappearance of the oscillation of the distorted component below  $T_C$  can be explained by the fast relaxation of the probe nucleus caused by fluctuation of the polaronic local lattice dragged by the conduction electrons in the ferromagnetic metal phase. At helium temperature, however, the TDPAC spectrum consists of a single component with an averaged quadrupole frequency, indicating freezing of the fluctuation. This observation suggests that the lattice can no longer follow the electron movement at this low temperature. The present work shows significance of nonmagnetic probes in the study of local fields in magnetic materials.

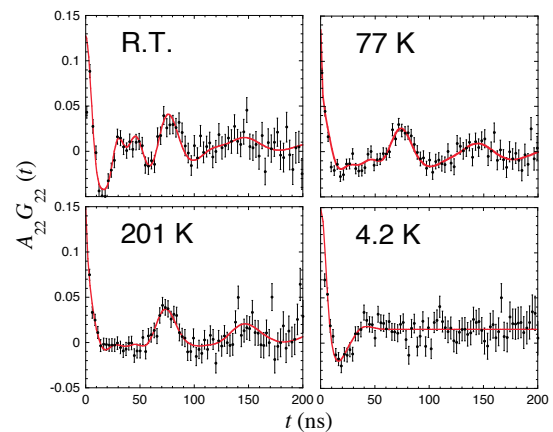


Fig. 1. TDPAC spectra of  $^{111}\text{mCd}(\rightarrow^{111}\text{Cd})$  in  $\text{La}_{0.7}\text{Ca}_{0.3}\text{MnO}_3$  measured at temperatures indicated.

**REFERENCE:**

[1] W. Sato *et al.*, Phys. Rev. B, **100** (2019) 184111(1-7).

## PR1-6 Local Structure of In Impurities Doped in SrTiO<sub>3</sub> Studied by TDPAC Method

S. Komatsuda, W. Sato<sup>1</sup> and Y. Ohkubo<sup>2</sup>

*Institute of Human and Social Sciences, Kanazawa University*

<sup>1</sup>*Institute of Science and Engineering, Kanazawa University*

<sup>2</sup>*Institute for Integrated Radiation and Nuclear Science, Kyoto University*

**INTRODUCTION:** Strontium titanate (SrTiO<sub>3</sub>) is a cubic perovskite oxide. SrTiO<sub>3</sub> doped with metal ions as impurities exhibits a wide variety of electronic properties. Especially, SrTiO<sub>3</sub> doped with trivalent metal ions at Ti<sup>4+</sup> site has been attracted much attention because of their excellent photocatalytic activity [1]. For a practical use of SrTiO<sub>3</sub>, it is necessary to obtain more microscopic information on the impurity site. Therefore, we investigated the local structures at the In<sup>3+</sup> site in SrTiO<sub>3</sub> by means of the time-differential perturbed angular correlation (TDPAC) method using the <sup>111</sup>Cd(←<sup>111</sup>In) probe.

**EXPERIMENTS:** Polycrystalline SrTiO<sub>3</sub> sample was prepared from stoichiometric mixture of SrCO<sub>3</sub> and TiO<sub>2</sub>. The powders were mixed in a mortar and pressed into a disk. For TDPAC measurements, commercially available <sup>111</sup>In solution was added in droplets onto the disk. The disk was sintered in air at 1473 K for 24 h for preparation of doped SrTiO<sub>3</sub> sample. It was confirmed from the powder XRD pattern for the nonradioactive sample that calcination at 1473 K for 24 h is sufficient to synthesize a single phase SrTiO<sub>3</sub>. The TDPAC measurement was carried out for the 171-245 keV cascade  $\gamma$  rays of <sup>111</sup>Cd(←<sup>111</sup>In) probe with the intermediate state of  $I = 5/2$  having a half-life of 85.0 ns.

**RESULTS:** Figure 1 shows the TDPAC spectrum of <sup>111</sup>Cd(←<sup>111</sup>In) probe in SrTiO<sub>3</sub>. The measurement was performed at room temperature. The directional anisotropy on the ordinate,  $A_{22}G_{22}(t)$ , was deduced with the following simple operation for delayed coincidence events of the cascade:

$$A_{22}G_{22}(t) = \frac{2[N(\pi, t) - N(\pi/2, t)]}{N(\pi, t) + 2N(\pi/2, t)}. \quad (1)$$

Here,  $A_{22}$  denotes the angular correlation coefficient,  $G_{22}(t)$  the time-differential perturbation factor as a function of the time interval,  $t$ , between the relevant cascade  $\gamma$ -ray emissions, and  $N(\theta, t)$  the number of the coincidence events observed at angle,  $\theta$ . The oscillatory structure observed in Fig.1 reflects electrostatic interactions between the probe nucleus and the extranuclear field because the sample consists of no magnetic materials. We thus performed a least-squares fit to the spectrum in Fig. 1 with  $G_{22}(t)$  expressed as

$$G_{22}(t) = \sigma_{2,0} + \sum_{n=1}^3 \sigma_{2,n} \cos(\omega_n t). \quad (2)$$

For all symbols in eq.(2), refer to our previous paper[2]. The spectrum in Fig. 1 can be reproduced by a fit with three unique quadrupole frequencies. As for one of these components, the quadrupole frequency shows a zero. On the basis of the cubic structure of SrTiO<sub>3</sub>, this signifies the <sup>111</sup>Cd(←<sup>111</sup>In) probes occupy defect-free substitutional Sr or Ti sites in SrTiO<sub>3</sub>. The remaining two components shows two well-defined EFG values which is characterized by the quadrupole frequencies and its distributions  $\omega_{Q1} = 48.9(1)$  Mrad/s,  $\delta_1 = 0\%$  and  $\omega_{Q2} = 52.1(2)$  Mrad/s,  $\delta_2 = 0\%$ , respectively. These non-zero frequencies imply that defects were associated with <sup>111</sup>In probes. It has already been reported that the oxygen vacancy is formed by substitution of trivalent metal ions such as Fe<sup>3+</sup> ion into Ti<sup>4+</sup> for charge compensation [3]. Therefore, we assume that part of the <sup>111</sup>In probes is associated with the oxygen vacancy, substituting at Ti or Sr site. For more information on the microstructure of SrTiO<sub>3</sub>, TDPAC measurements with <sup>111</sup>Cd(←<sup>111m</sup>Cd) probe are now in progress.

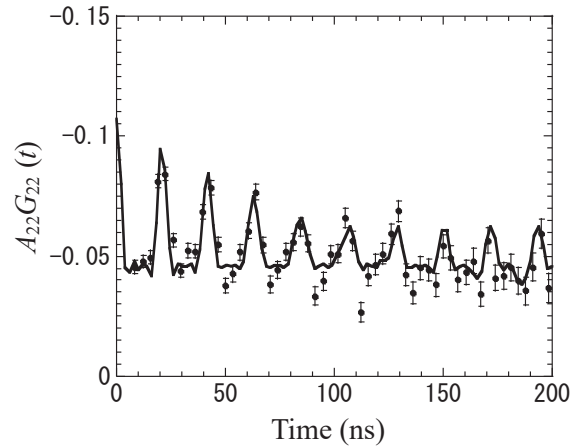


Fig. 1. TDPAC spectrum of <sup>111</sup>Cd(←<sup>111</sup>In) probe in SrTiO<sub>3</sub> at room temperature. The line is the result of a least-squares fit with eq.(2).

### REFERENCES:

- [1] Y. Goto *et al.*, *Joule*, **2** (2018) 509-520.
- [2] S. Komatsuda *et al.*, *J. Appl. Phys.*, **116** (2014) 183502 1-5.
- [3] J. S. Yoon. *et al.*, *Electron. Mater. Lett.*, **7** (2011) 209-213.

## **I-1. PROJECT RESEARCHES**

### **Project 2**

## PR2 Project Research of Accelerator-Driven System with Spallation Neutrons at Kyoto University Critical Assembly

C. H. Pyeon, M. Yamanaka, K. Hashimoto<sup>1</sup>, N. Aizawa<sup>2</sup>, A. Oizumi<sup>3</sup>, M. Fukushima<sup>3</sup>, G. Chiba<sup>4</sup>, K. Watanabe<sup>5</sup> and T. Endo<sup>5</sup>

*Institute for Integrated Radiation and Nuclear Science, Kyoto University*

<sup>1</sup> *Atomic Energy Research Institute, Kindai University*

<sup>2</sup> *Graduate School of Engineering, Tohoku University*

<sup>3</sup> *Nuclear Science and Engineering Center, Japan Atomic Energy Agency*

<sup>4</sup> *Graduate School of Engineering, Hokkaido University*

<sup>5</sup> *Graduate School of Engineering, Nagoya University*

**INTRODUCTION:** At the Kyoto University Critical Assembly (KUCA), a series of the accelerator-driven system (ADS) experiments [1]-[6] had been carried out with the combined use of A core (solid-moderated and -reflected core) and the fixed-field alternating gradient (FFAG) accelerator. Project research of “Accelerator-Driven System with Spallation Neutrons at Kyoto University Critical Assembly” was composed of six research teams in domestic: Kindai University; Tohoku University; Japan Atomic Energy Agency (JAEA); Hokkaido University, Nagoya University; Institute for Integrated Radiation and Nuclear Science, Kyoto University (KURNS). In the project research organized by KURNS, the ADS core was comprised of two zones: test zone (f) of low-enriched uranium (LEU composed of highly-enriched uranium and natural uranium) modeling core and driver zone of normal core (F: 1/8”p60EUEU) core, as shown in Fig. 1. Also, 100 MeV protons generated by the FFAG accelerator were injected onto the lead-bismuth (Pb-Bi) target. The objectives of the project research were to examine experimentally neutron characteristics of the LEU modeling core in ADS, and to investigate applicability of current measurement technologies to kinetic parameters and numerical methodologies to deterministic and stochastic calculations, in the ADS experiments with spallation neutrons at KUCA.

**EXPERIMENTS:** In the ADS experiments with spallation neutrons, main characteristic of proton beams by the FFAG accelerator were shown as follows: 100 MeV energy; 30 Hz frequency; 100 ns repetition rate; 30 pA to 1 nA intensity; 40 mm diameter beam spot. The research topics were revealed in each research team as follows:

- Subcriticality measurement by the noise method (Kindai University)
- Measurement of reaction rate of intermediate neutrons (Tohoku University)
- Am-243 irradiation (JAEA and Hokkaido University)
- On-line monitoring of kinetic parameters (Nagoya University)
- Neutronics of LEU modeling core in ADS (Kyoto University)

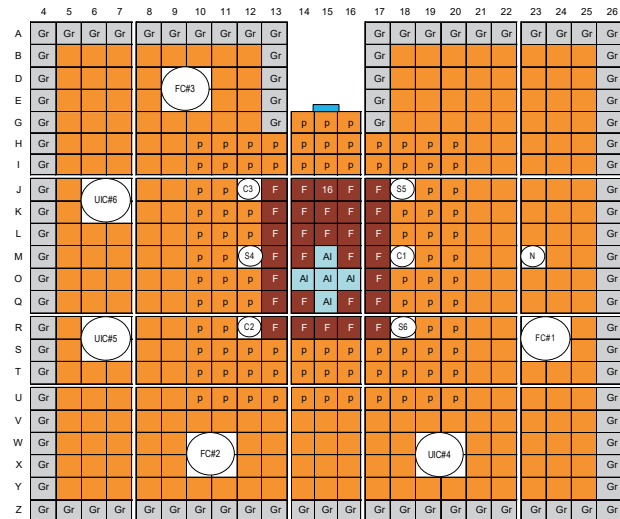


Fig. 1. Top view of core configuration with LEU test and EE1 driver zones at KUCA

**RESULTS:** From the results of a series of ADS experiments, special attention was made to the following items: applicability of the noise method to subcriticality measurement in ADS with spallation neutrons (Kindai); effect of intermediate neutrons for reaction rates in ADS (Tohoku); feasibility study on Am-243 irradiation at a critical state (JAEA and Hokkaido); applicability of advanced measurement system with optical fibers to on-line monitoring of kinetic parameters (Nagoya); benchmarks on kinetic parameters in LEU modeling core of ADS with spallation neutrons (Kyoto).

**CONCLUSION:** The project research of ADS with spallation neutrons at KUCA was successfully conducted with the combined use of LEU modeling core and FFAG accelerator at KUCA. A series of static and kinetic ADS experiments revealed importantly applicability of current measurement methodologies to upcoming actual ADS facilities in the future, demonstrating remarkable reconstruction of ADS experiments by numerical calculations.

### REFERENCES:

- [1] C. H. Pyeon, *et al.*, J. Nucl. Sci. Technol., **46**, (2009) 1091-1093.
- [2] C. H. Pyeon, *et al.*, Nucl. Eng. Technol., **45**, (2013) 81-88.
- [3] C. H. Pyeon, *et al.*, Nucl. Technol., **192**, (2013) 181-190.
- [4] C. H. Pyeon, *et al.*, Ann. Nucl. Energy, **105**, (2017) 346-354.
- [5] C. H. Pyeon, *et al.*, J. Nucl. Sci. Technol., **55**, (2018) 190-198.
- [6] C. H. Pyeon, *et al.*, J. Nucl. Sci. Technol., **57** (2020) 133-135.
- [6] M. Yamanaka, *et al.*, J. Nucl. Sci. Technol., **57** (2020) 205-215.

## PR2-1 Subcriticality Monitoring for a Reactor System Driven by Spallation Source (III)

K. Hashimoto, A. Sakon, S. Hohara, K. Nakajima<sup>1</sup>, K. Takahashi<sup>1</sup>, C. H. Pyeon<sup>2</sup>, T. Sano, M. Yamanaka<sup>2</sup>

Atomic Energy Research Institute, Kindai University  
<sup>1</sup>Graduate School of Science and Engineering, Kindai University

<sup>2</sup>Institute for Integrated Radiation and Nuclear Science, Kyoto University

**INTRODUCTION:** Feynman- $\alpha$  and Rossi- $\alpha$  Methods have been frequently employed to determine subcritical reactivity of nuclear reactor systems driven by Poisson source such as Am-Be neutron source. Recently many advanced formulas for a pulsed non-Poisson source such as spallation source have been derived. The objectives of this study are to confirm experimentally an applicability of these formulas for a subcritical reactor system driven by a spallation source and to investigate some non-Poisson character of spallation neutron source.

**EXPERIMENTS:** A subcritical system was constructed on the A loading of the Kyoto University Critical Assembly. The system had a lead-bismuth target, to which 100MeV proton beam was drawn to cause spallation reactions. The repetition frequency of the proton pulse beam was 30Hz. Time-sequence counts data from four BF<sub>3</sub> proportional counters were acquired for 30 minutes at several subcritical states referred to as A~F. The subcritical reactivity was adjusted by axial positions of 3 control rods, 3 safety rods and a central fuel loading.

**RESULTS:** Figure 1 shows a Feynman- $\alpha$  analysis result obtained from a counter B1 placed near the reactor core. The Degweker's formula [1], where a non-Poisson character and a delayed neutron contribution were considered, were fitted to these  $Y$  data to determine the prompt-neutron decay constant  $\alpha$ . These fitted curves are in very good agreement with the  $Y(T)$ . As shown in Figure 2, the decay constants  $\alpha$  determined by the present Feynman- $\alpha$  analysis is consistent with that obtained under stationary inherent neutron source, except for counter B4. Only the decay constant obtained by counter B4 has a large difference. This is because the counter B4 is placed far from the core and closely to a spallation target.

Figure 3 shows a subcriticality dependence of prompt correlation amplitudes obtained by respective Feynman- $\alpha$  analyses under stationary inherent source and spallation source. Clearly, the present non-Poisson spallation enhances the correlation amplitude, compared with the Poisson inherent source. A non-Poisson Character is responsible for this enhancement.

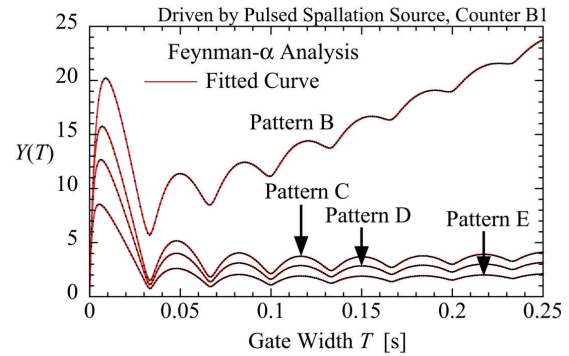


Fig.1.  $Y$  obtained by Feynman- $\alpha$  analysis.

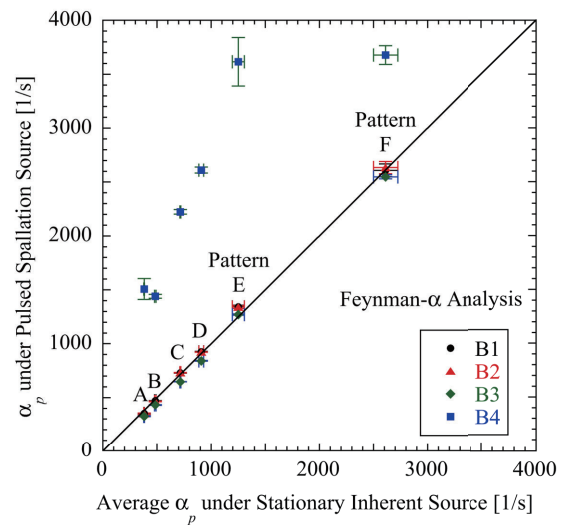


Fig.2. Prompt-neutron decay constant.

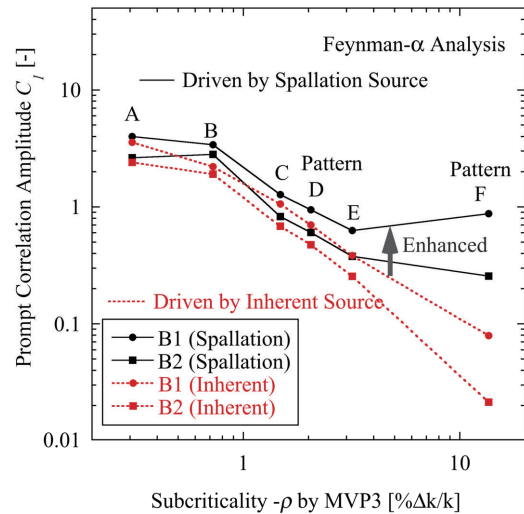


Fig.3. Feynman- $\alpha$  correlation amplitude enhanced by non-Poisson spallation source.

### REFERENCES:

[1]Y. S. Rana, S.B. Degweker, Nucl. Sci. Eng., **162** (2009) 117-133.

N. Aizawa, K. Nakamura, H. Akatsu<sup>1</sup>, T. Abe<sup>1</sup>, M. Yamanaka<sup>2</sup> and C. H. Pyeon<sup>2</sup>

Graduate School of Engineering, Tohoku University  
<sup>1</sup>School of Engineering, Tohoku University  
<sup>2</sup>Institute for Integrated Radiation and Nuclear Science, Kyoto University

**INTRODUCTION:** The accelerator-driven system (ADS) has been studied for the transmutation of minor actinides. Besides, ADS has a potential to be applicable to a neutron irradiator for an effective production of useful nuclides by providing wide range of neutron energy from ultrafast to thermal. A neutron spectrum in ADS core depends on a core structure, a neutron source and neutron multiplication factor. The previous studies have carried out the measurement of neutron reaction rates for the activation foils with the threshold of reactions at several MeV energy in the Pb-Bi zoned core [1] and polyethylene (PE) moderated core [2] driven by spallation neutron source. These results indicated that the effect of fast neutrons was increased as subcriticality became deeper. In the present study, the measurements of reaction rates for intermediate neutrons were performed through the neutron irradiation experiments in ADS with different three subcriticality level, in order to clarify the effect of subcriticality on the reaction rates by intermediate neutrons.

**EXPERIMENTS:** The ADS experiment was performed in KUCA A-core combined with spallation neutron source generated by 100 MeV protons from FFAg accelerator. Figure 1 shows the core configuration. The core was composed of the PE moderated highly-enriched uranium fuel and the low-enriched uranium mockup fuel. The activation foils of In, Ta, W and Cu employed in the experiment are sensitive to intermediate neutrons, and were set at (M-O, 15). The Au foils set at (O-P, 15) were for the measurement of thermal neutrons. The foils were set with and without Cd cover to examine the effect of thermal neutrons. The experiments were performed with one critical case and two subcritical cases (0.984 and 0.967 in  $k_{eff}$ ) by changing the positions of control rods.

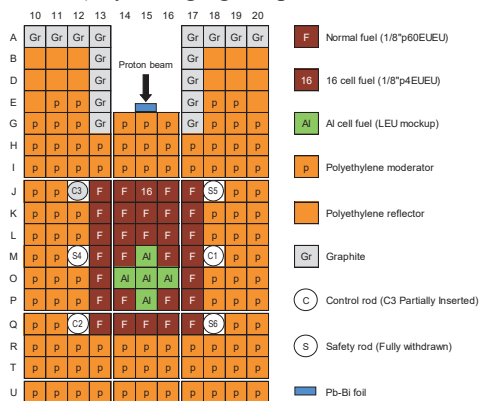
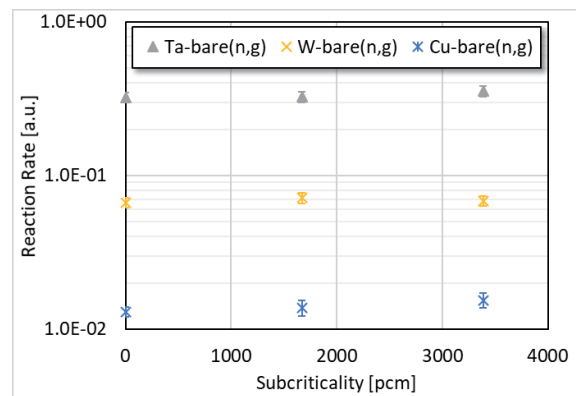
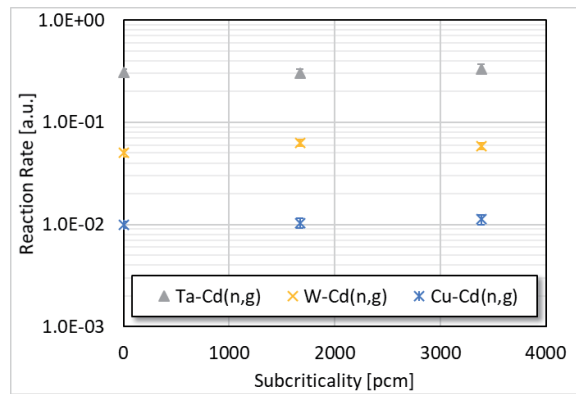


Fig. 1. Core configuration of KUCA A-core.

**RESULTS:** Figure 2 shows the reaction rates of Ta, W and Cu normalized by the Au(n,γ) reaction rates for three cases. The rates of In were excluded due to insufficient measurement accuracy. The reaction rates of bare Ta and Cu were increased slightly as subcriticality became deeper. The similar tendencies were observed in the measurement results of foils with Cd cover. The numerical calculations were also performed for the verification of the experimental results by the combined use of PHITS [3] and MVP [4]. The C/Es (the ratio of calculation result to experimental one) were almost the same values regardless of subcriticality, and the calculation results were confirmed to coincide with the measurement tendencies. These results indicated that the subcriticality change had a possibility to influence not only fast but also intermediate neutron spectrum. The tendency in the W reaction rates were remained unclear and the detailed analyses were underway.



(a) Bare foil



(b) Foil with Cd cover

Fig. 2. Reaction rates of activation foils without Cd cover normalized by Au(n,γ) reaction rate.

**REFERENCES:**

- [1] C. H. Pyeon *et al.*, J. Nucl. Sci. Technol., **55** (2) (2018) 190-198.
- [2] N. Aizawa *et al.*, KURNS Progress Report 2018, PR4-2, (2018).
- [3] T. Sato *et al.*, J. Nucl. Sci. Technol., **50** (9) (2013) 913-923.
- [4] Y. Nagaya *et al.*, JAERI 1348 (2005).

## Measurement of <sup>243</sup>Am Fission Rates in Low-Enriched Uranium Region at A-core of KUCA

A. Oizumi<sup>1</sup>, M. Fukushima<sup>1</sup>, K. Tsujimoto<sup>1</sup>,  
M. Yamanaka<sup>2</sup>, and C. H. Pyeon<sup>2</sup>

<sup>1</sup>Nuclear Science and Engineering Center, Japan Atomic Energy Agency

<sup>2</sup>Institute for Integrated Radiation and Nuclear Science, Kyoto University

**INTRODUCTION:** To transmute minor actinides (MAs) partitioned from the high-level wastes, the Japan Atomic Energy Agency has investigated neutronics of the accelerator-driven system (ADS). In the nuclear transmutation system such as ADS, the nuclear data validation of MA is required to reduce the uncertainty caused by the nuclear data of MA. To validate the nuclear data, many independent experimental data need to be mutually compared. An expansion of integral experimental data is the important issue since there is a limited number of experimental data of MA. Previously, experiments of measuring fission rate ratio of neptunium-237 (<sup>237</sup>Np) and americium-241 (<sup>241</sup>Am) to fission rate of uranium-235 (<sup>235</sup>U) were performed in a highly-enriched uranium (HEU) core [1, 2]. This study aims to measure the ratio of the americium-243 (<sup>243</sup>Am) and <sup>235</sup>U fission reaction rates in low-enriched uranium (LEU) region at the Kyoto University Critical Assembly (KUCA).

**EXPERIMENTS:** The irradiation experiment of <sup>243</sup>Am and <sup>235</sup>U was conducted at A-core in KUCA. Fission reaction rates were measured by using single fission chamber (diameter: 48 mm, height: 120 mm) having a foil such as <sup>235</sup>U (10 μg) or <sup>243</sup>Am (12 μg). The simultaneous measurement of <sup>243</sup>Am and <sup>235</sup>U fission reaction rates was conducted at the center voided region surrounded by LEU rods as shown in Fig. 1. The LEU rod composed of HEU plates, aluminum (Al) plates, and natural uranium (NU) plates shown in Fig. 2 has an averaged <sup>235</sup>U enrichment of about 17%. The pulse height distributions from the fission chambers were acquired under the condition of critical core corresponding to a reactor power of 3.5W. The irradiation time was almost 1 hour.

**RESULTS:** The distributions of pulse height of <sup>243</sup>Am and <sup>235</sup>U fission reactions were observed under the critical condition as shown in Fig. 3. The fission reaction signals need to be separated from noises due to α and γ rays in small pulse height. For example, the fission reaction events of <sup>243</sup>Am and <sup>235</sup>U in Fig. 3 were determined by integrating the counts at voltages greater than 0.589 and 0.592, respectively. As a result, the effective total fission counts of <sup>243</sup>Am and <sup>235</sup>U were estimated to be 5,208 and 118,664, respectively. Finally, the fission reaction rate ratio of <sup>243</sup>Am and <sup>235</sup>U was obtained by the total counts and the number of atoms, and a detection effi-

ciency of the fission chamber was  $0.042 \pm 0.002$ . These measured value will be used for verification of evaluated nuclear data by conducting detailed analyses.

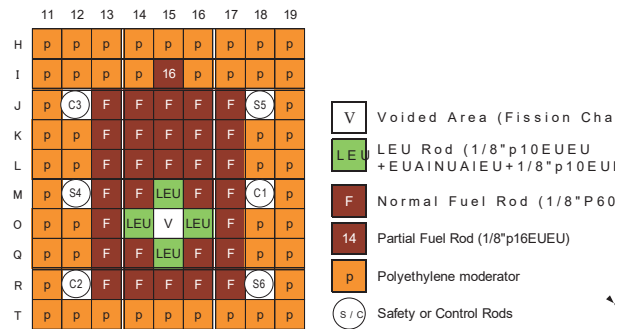


Figure 1. Loaded position of the fission chambers in the A-core of the KUCA.

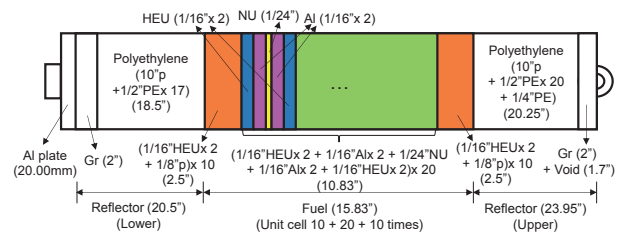


Figure 2. Schematic drawing of LEU rod in the KUCA-A core showing in Figure 1.

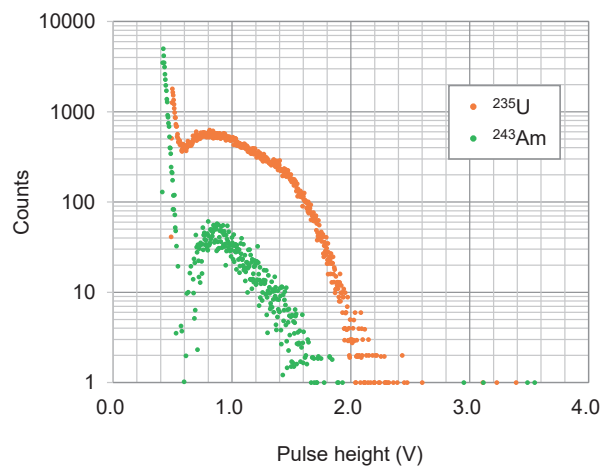


Figure 3. Fission signals of <sup>243</sup>Am and <sup>235</sup>U fission chambers.

**REFERENCES:**

[1] C. H. Pyeon, *et al.*, Nucl. Sci. Eng., **193**, pp.1023-1032 (2019).  
[2] C. H. Pyeon, *et al.*, J. Nucl. Sci. Technol., **56**, 8, pp.684-689, (2019).

K. Watanabe, T. Endo, S. Imai, A. Uritani, A. Yamazaki, M. Yamanaka<sup>1</sup> and C. H. Pyeon<sup>1</sup>

Graduate School of Engineering, Nagoya University  
<sup>1</sup> Institute for Integrated Radiation and Nuclear Science, Kyoto University

**INTRODUCTION:** The accelerator-driven subcritical (ADS) system has been developed for transmuting minor actinides and long-lived fission products [1-2]. The ADS system should keep to be subcritical condition in any case. The subcriticality is desired to be monitored in real time. We are developing a real-time subcriticality monitoring system. This system can simultaneously apply two methods: the PNS and Rossi- $\alpha$  methods, to assure validity of the measured subcriticality. In this study, we performed the subcriticality measurement experiments using the fabricated subcriticality monitoring system. In addition, we considered the experimental conditions influencing the estimated subcriticality related parameters.

**EXPERIMENTS:** Subcriticality measurements were made in A-core of Kyoto University Critical Assembly (KUCA). A Pb-Bi target bombarded with 100 MeV protons from an FFAG proton accelerator, as a pulsed neutron source. The repetition rate of the pulsed proton beam was 20Hz. We used a new optical fiber type de-

tector, in which small LiF/Eu:CaF<sub>2</sub> eutectics scintillators were dispersed on side surface of a wavelength shifting fiber. The optical fiber type detector was covered with a 2.5 mm dia. aluminum tube to protect the detection element. The PMT signal was digitized and the processed in a Field-Programmable Gate Array (FPGA). The in-formation on pulse height, rise time and detection timing were recorded and transferred to an analysis computer. In the analysis computer, these data were processed. Finally, the subcriticality was calculated in the PC every seconds. The detector was placed in a core region. The subcriticality was changed by inserting control and safety rods.

**RESULTS:** Figure 1 shows the time trends of the measured neutron count rate and subcriticality measured by the fabricated subcriticality measurement system. The estimated prompt neutron decay constant  $\alpha$  and area ratio were consistent with the reactor operation. Although the  $\alpha$  and area ratio should not depend on the count rate, the measured values slightly depend on the count rate. Figure 2 shows the relation between the ratio of the experimentally estimated parameters and calculated values, E/C, and the detector count rate. The calculated values were obtained by Monte Carlo simulation with MCNP 6.1. Difference between the estimated  $\alpha$  and area ratio and the calculated values increases with increasing the count rate. This is because the counting loss effect causes misestimation in determination of the subcriticality related parameters. Among three methods, Rossi- $\alpha$ ,  $\alpha$  fitting and area ratio in the pulsed neutron source (PNS) methods, the  $\alpha$  fitting method in the PNS took less influence compared with other methods. An error in the  $\alpha$  fitting method is evaluated to be within 20% compared with the simulation values.

**REFERENCES:**

- [1] C. H. Pyeon, J. Y. Lim, Y. Takemoto *et al.*, *Ann. Nucl. Energy*, **38** (2011) 2298–2302.
- [2] C. H. Pyeon, T. Yagi, K. Sukawa *et al.*, *Nucl. Sci. Energy*, **177** (2014) 156–168.

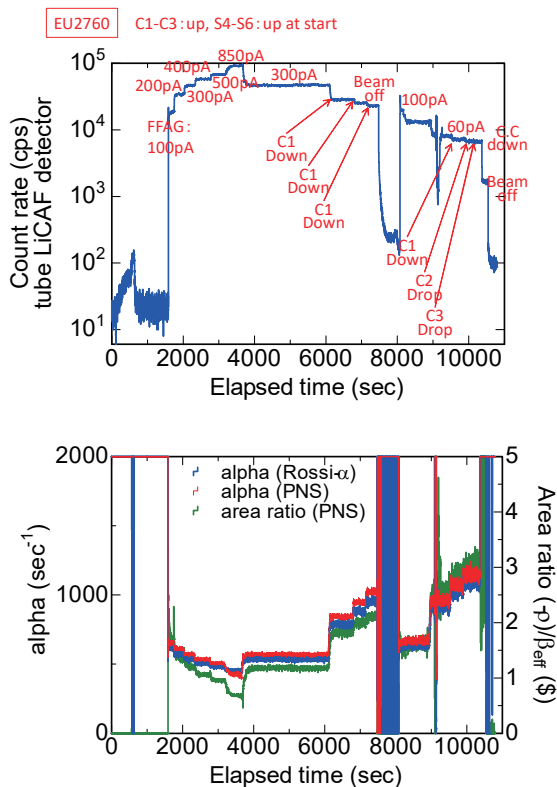


Fig. 1 Time trend of the measured neutron count rate(top) and the measured subcriticality (bottom).

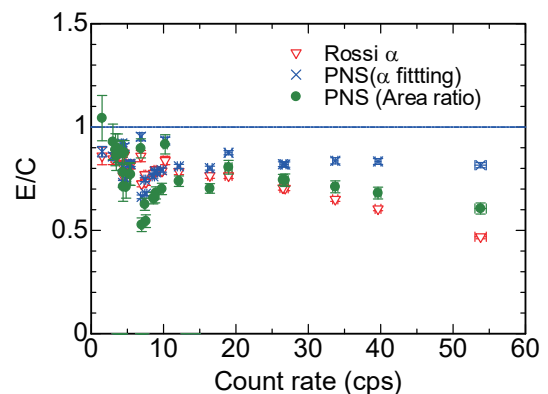


Fig. 2. Relation between the ratio of the experimentally estimated parameters and calculated values, E/C, and the detector count rate.

## **I-1. PROJECT RESEARCHES**

### **Project 3**

M. Suzuki

*Institute for Integrated Radiation and Nuclear Science, Kyoto University*

In this research project, twenty two research projects were included. In this summary, five research projects (P3-5, P3-6, P3-9, P3-10) could not be reported due to unexpected or uncontrolled events. Details of each project is referred to the following contents. Details of each project is referred to the following contents.

**P3-1:** The many novel boron compounds from China, US, Sweden and Turkey have been investigated in 2019. All of the China boron compound are extremely low toxic and highly water soluble. Some are excellent and promising B-com for BNCT.

**P3-2:** In this project, peptide DDS system with A6K peptide was focused. The new boron delivery system with A6K peptide and BSH show new direction of boron agent in next generation of BNCT.

**P3-3:** Boron-containing nanoparticle (B-NP) which is promising for which is promising nanodevice for BNCT was functionalized with polyglycerol. The resulting B-NP-PG was dispersed in a phosphate buffer saline (PBS) at very high concentration and the resulting dispersion is very stable for more than one month.

**P3-4:** The results in this project show that the chicken egg chorioallantoic membrane (CAM) model can be used as a reliable model to examine the efficacy of the BNCT therapy. The CAM tumor can be dramatically decreased by the exposure to a neutron beam. The result suggest that the CAM model is particularly suited for the BNCT experiments.

**P3-7:** In this project, the peptide series IF7-B series (IF7-BSH and IF7-BPA) newly developed as a boron drug was investigated using tumor-bearing mice. Comparing the changes in tumor size in unirradiated tumor models with IF7-BPA and IF7-BSH respectively, it seems that IF7-BPA suppresses tumor growth relatively.

**P3-8:** In this project, newly developed *in vitro* model of tumor tissue for BNCT demonstrated the pharmacokinetics of BPA and the efficacy of neutron irradiation by direct observation of  $\alpha$ -ray/recoiled Li particle tracks that are corresponding to the distribution of BxPC3 cells.

**P3-11:** In this project, the novel boron compound (BADB) was tested. The combination group of simultaneous use of both BADB (CED) and BPA (i.v.) gave the most significant prolongation of

survival (38 (36-39) days).

**P3-12:** In this research, importance of controlled intracellular locations of boron compounds was shown by the cell-penetrating peptides (CPP) conjugation for achieving their sophisticated BNCT biological activity. This experimental techniques and findings will contribute to development for BNCT methodology.

**P3-13:** In this project, a novel boron compound containing carbon nanostructure like a horn was investigated. The carbon nanohorns showed better tumor suppression effect on colony formation test *in vitro* compared to radiation only group.

**P3-14:** In this project, a phenylboronic acid (PBA)-installed polymeric nanoparticle was tested. *In vivo* evaluation on a melanoma-bearing mouse model could reveal that the PBA-NP possesses a highly potent antitumor efficacy, which could be only provoked by neutron irradiations.

**P3-16:** In this project, poly(vinyl alcohol) (PVA)-BPA was tested. PVA-BPA revealed the enhanced inhibition of the tumor growth probably because of the higher intratumoral BPA concentration than sorbitol-BPA during the thermal neutron irradiation.

**P3-17:** In this project, maleimide-functionalized *closo*-dodecaborate (MID)- transferrin (TF) conjugates was investigated regarding to their *in vivo* selective boron delivery to tumor in colon 26 tumor bearing mice.

**P3-18:** A novel boron agent OKD-001 was effective for BNCT against orthotopic xenograft glioblastoma model. As shown in Fig. 1, OKD-001 plus neutron irradiation significantly prolong the overall survival of the mice in a dose-dependent manner.

**P3-19:** Pegylated BSH (BAMP) significantly suppressed the tumor growth as compared to other control groups without remarkable side effect (e.g. weight loss).

**P3-20:** In this study, oligodeoxynucleotides (ODNs) bearing hydrophobic and fluorescent BODIPY unit at uridine base (<sup>B</sup>U) was investigated as a new boron compound.

**P3-21:** In this study, the effectiveness of BPA-BNCT for 5-FU resistance OSCC is evaluated.

**P3-22:** Arg-Gly-Aso(RGD) binding Gd-DTPA-incorporated calcium phosphate nanoparticles (Meo) was investigated as a new boron compound.

## PR3-1 Screening of boron compound for BNCT International collaboration studies

M. Takagaki and M. Suzuki<sup>1</sup>

Louis Pasteur Center for Medical Research  
<sup>1</sup>Integrated Radiation and Nuclear Science, Kyoto University

For the purpose of boron sciences, we have continuously screening the many novel boron compounds mainly for BNCT collaborating with China, US, Sweden, and Turkey in 2019. Global paucity of neutron sources is the main reason for international demands of collaboration. We investigated/ screened many compounds mainly for BNCT for Cancer. We report a brief summary of 2019 year.

### Materials and Methods.

We already uploaded our standardized experimental maneuvers on the following URL,  
<[https://1458ab30-7501-42df-8c2e-ff59d20cecb7.filesusr.com/ugd/ddd07a\\_cbe194d92fd14397a5db1690d68a185c.pdf](https://1458ab30-7501-42df-8c2e-ff59d20cecb7.filesusr.com/ugd/ddd07a_cbe194d92fd14397a5db1690d68a185c.pdf)>.

The minimum requirement for our screening protocol of Boron compound samples (B-com) for BNCT is water (and/or DMSO)-soluble 30mg for first look screening of experiments 1, 2 and 3. Whole serial steps are as follow.

1. Solubility in a physiological condition
2. Cell toxicity; IC<sub>50</sub>
3. Cellular BNCT (in-vitro BNCT)
4. Bio-distribution study (neutron induced boron autoradiography)
5. Animal BNCT (in-vivo BNCT)
6. Pre-clinical study

### Results and Discussion.

The figure 1 shows a summary of in-vitro BNCT effect of China B-coms. All of them are extremely low toxic and highly water soluble. Some are excellent and promising B-com for BNCT and following bio-distribution study of them are investigating on the step 4.

The figure 2 is a schematic drawing of tumoricidal effect of carborane-conjugated anti cancer drug, MMP inhibitor of USA. The idea of such conjugation to evaluate synergetic effect is interesting and exciting. Our data on tumoricidal effect of carborane conjugated MMP inhibitor shows MMP inhibitor is far beyond BNCT effect within acceptable dosage.

Acknowledgment: This study has been financially supported by National Research Fund No. 17Ki8536 2017-19 from the Ministry of Education, Culture, Sports, Science and Technology, Japan.

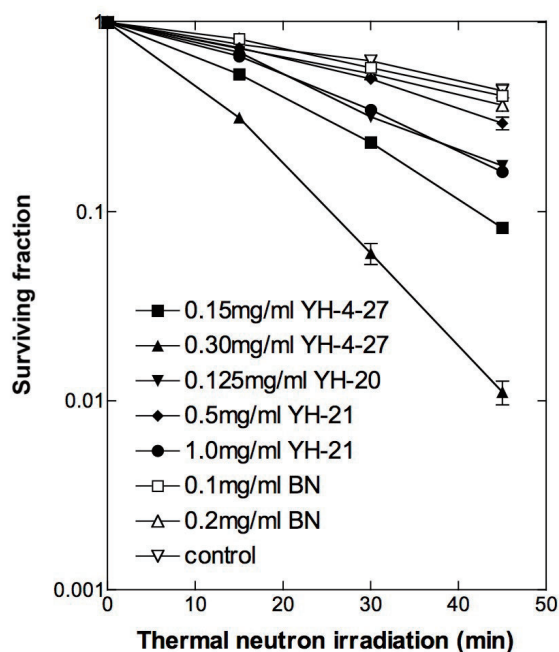


Fig.1. A summary of in-vitro BNCT effect of China B-coms.

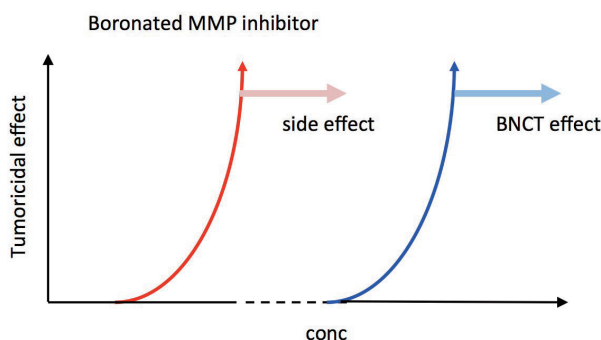


Fig.2. A schematic drawing of tumoricidal effect of carborane-conjugated anti cancer drug, MMP inhibitor of USA.

H. Michiue, N. Kondo<sup>1</sup> and M. Suzuki<sup>1</sup>

*Neutron Therapy Research Center, Okayama University, Japan*

<sup>1</sup>*Institute for Integrated Radiation and Nuclear Science, Kyoto University, Japan*

**INTRODUCTION:** In present advanced cancer therapy with surgery, chemotherapy, and radiation therapy, Glioblastoma multiforme (GBM) is the most treatment-resistant malignant primary brain tumor, with a median survival of approximately 1.5 year. Therefore, the development of novel anti-GBM treatment with the combination of drug and radiotherapy is promising method of treatment to GBM after surgery, especially for elderly GBM patients. BNCT is one of the most promising GBM treatment based on the neutron capture and fission reactions occurred by <sup>10</sup>B atoms capture with low-energy neutrons on the irradiation of brain tumor tissues with thermal or epithermal neutron beams. The BNCT reaction consists of high energy transfer alpha particle (<sup>4</sup>He) and <sup>7</sup>Li nuclei with particle range of approximately within the size cell diameter (<10 $\mu$ m). Recently, the neutron source changed to the accelerator neutron source that could be installed in hospital from reactor neutron source. One of the most difficult problem in BNCT developing has been reported the new boron drug applied to several malignant tumor except BPA. The BPA is the leading BNCT boron drug that started from amino acid analogue fused boron against malignant melanoma. Next, many researcher reported that the system L-amino acid transporter-1 (LAT-1) expressed in many malignant tumors. The BSH was used in primary malignant glioma BNCT with the combined usage of BPA. In that BNCT project, the combination use of BPA and BSH group showed significantly longer survival outcome compared to that of single BPA BNCT.

**EXPERIMENTS:** All of protocol was administrated in committee of KURNS. Before 24hr neutron irradiation, 200 $\mu$ M A6K/2mM BSH (final concentration) or 100 $\mu$ M A6K/1mM BSH (final concentration) was administrated to U87 deltaEGFR cell line. Just before neutron irradiation, all the cell sample were collected in collecting tube and got 1MW neutron irradiation (thermal neutron flux 1.4X10<sup>9</sup> neutron/cm<sup>2</sup>/sec) for 5min (thermal neutron fluence 4.4X10<sup>11</sup> neutron/cm<sup>2</sup>,  $\gamma$ -ray 0.7X10<sup>-1</sup> Gy), 15min (thermal neutron fluence 1.1X10<sup>12</sup> neutron/cm<sup>2</sup>,  $\gamma$ -ray 1.7X10<sup>-1</sup> Gy) or 30 min (thermal neutron fluence 2.8X10<sup>12</sup> neutron/cm<sup>2</sup>,  $\gamma$ -ray 3.1X10<sup>-1</sup> Gy). After irradiation, all glioma cells were re-cultured in 96 well (9 $\times$ 10<sup>3</sup> cells/well) and checked cell proliferation with Cell Proliferation Reagent WST-1 (Roche, Basel) by microplate reader (Vient XS, DS Pharma Promo Co., Ltd) for 48hr. And colony formation assay was done after 2 weeks culture with U87 delta EGFR in 60 mm culture dish (n=4)

and all culture cells were stained with 0.5% Crystal Violet (CV) in 20% methanol. The colony of CV staining sample was counted automatically with aCOLyte 3 automatic colony counter machine, (Synbiosis, A Division of Synoptics Ltd) and all data was performed statistical analysis.

**RESULTS:** As shown in Fig. 1, The boron neutron reaction in vitro with low or high dose A6K/BSH complex to U87 delta EGFR cells in KURRI: (A) The colony formation assay of U87 delta EGFR with CV staining after 2 weeks of different neutron irradiation time (blue line: control group, orange line: low dose 100 $\mu$ M A6K/ 1mM BSH and gray line: high dose of 200 $\mu$ M A6K/ 2mM BSH, each n=4).

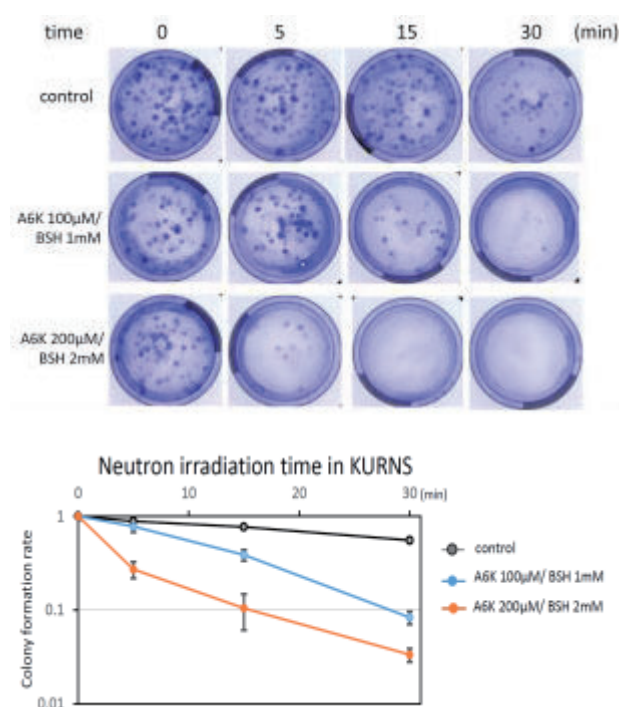


Fig. 1. The boron neutron reaction in vitro with low or high dose A6K/BSH complex to U87 delta EGFR cells in KURRI: the colony formation assay of U87 delta EGFR (blue line: control group, orange line: low dose 100 $\mu$ M A6K/ 1mM BSH and gray line: high dose of 200 $\mu$ M A6K/ 2mM BSH, each n=4) .

#### CONCLUSION:

The boron DDS agent with polymeric macromolecule DDS such as liposomes, or several boron compounds were very interesting and expansible tools in preclinical BNCT experiments. In this time, we focused peptide DDS system with A6K peptide. In this time, we tried to show the new boron delivery system with A6K peptide and BSH, and this would show new direction of boron agent in next generation of BNCT.

### PR3-3 Chemical Functionalization of Boron-Containing Nanoparticle and its Application to Boron Neutron Capture Therapy

Y. Wang, H. G. Kang, M. Nishikawa and N. Komatsu

*Graduate School of Human and Environmental Studies, Kyoto University*

Boron neutron capture therapy (BNCT) is one of the promising cancer therapy with minimized side effect, because  $^{10}\text{B}$  atoms located in the cancer tissue generate alpha particles locally upon neutron irradiation. Herein, we will report that boron-containing nanoparticle (B-NP) is functionalized with polyglycerol (B-NP-PG) and the resulting B-NP-PG exhibits good dispersibility in a physiological environment.

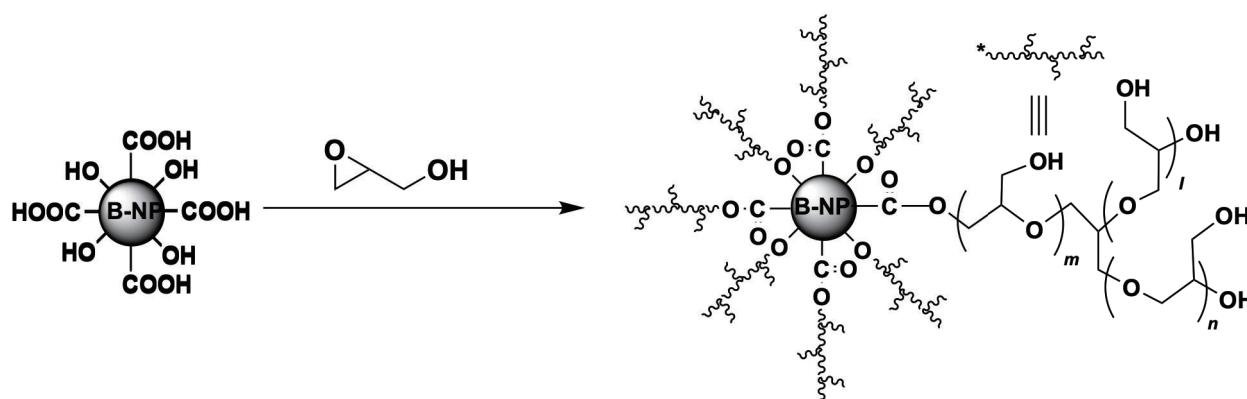
B-NP was functionalized with PG through ring-opening polymerization of glycidol, as shown in Scheme 1, according to the method previously reported by us [1-4]. The resulting B-NP-PG was fully characterized by nuclear magnetic resonance (NMR) spectroscopy, Fourier transfer infrared (FTIR) spectroscopy and thermogravimetric analysis (TGA). B-NP-PG is dispersed in a phosphate buffer saline (PBS) at very high concentration and the resulting dispersion is very stable for more than one month.

We are planning to carry out pharmacokinetic experiments to see the biodistribution; especially if B-NP-PG is trapped in the liver and/or spleen or not. If we can confirm tumor accumulation of B-NP-PG in enough amount, BNCT experiments should be carried out. We hope that the tumor decreases in size and disappears finally after neutron irradiation.

#### REFERENCES:

- [1] L. Zhao, T. Takimoto, M. Ito, N. Kitagawa, T. Kimura, and N. Komatsu,\* *Angew. Chem. Int. Ed.*, 50 (6), 1388-1392 (2011)
- [2] L. Zhao, T. Chano, S. Morikawa, Y. Saito, A. Shiino, S. Shimizu, T. Maeda, T. Irie, S. Aonuma, H. Okabe, T. Kimura, T. Inubushi, and N. Komatsu,\* *Adv. Funct. Mater.*, 22 (24), 5107-5117 (2012)
- [3] L. Zhao, Y.-H. Xu, H. Qin, S. Abe, T. Akasaka, T. Chano, F. Watari, T. Kimura, N. Komatsu,\* and X. Chen\* *Adv. Funct. Mater.*, 24 (34), 5348-5357 (2014)
- [4] L. Zhao, H. Yang, T. Amano, H. Qin, L. Zheng, A. Takahashi, S. Zhao, I. Tooyama, T. Murakami, N. Komatsu,\* *J. Mater. Chem. B*, 4(47), 7741-7748 (2016).

**Scheme 1.** Chemical Functionalization of Boron-Containing Nanoparticle (B-NP) with Polyglycerol.



K. Matsumoto, A. Komatsu, Y. Higashi, Y. Tamari, M. Suzuki<sup>1</sup> and F. Tamanoi

*Institute for Integrated Cell-Material Sciences, Institute for Advanced Study, Kyoto University*

<sup>1</sup>*Institute for Integrated Radiation and Nuclear Science, Kyoto University*

#### INTRODUCTION:

Boron Neutron Capture Therapy (BNCT) provides a promising approach for cancer treatment. While BPA and BSH have been used as a boron reagent for BNCT, we have seen development of novel boron agents in the past years. These include various nano-formulated boron agents. To evaluate the efficacy of these new agents, it is necessary to use tumor models. In the past, tissue culture cells and mouse models have been used. More recently, tumor spheroids and the CAM (chorioallantoic membrane) assay using fertilized chicken eggs have been developed [1]. We have evaluated the use of these models for BNCT.

#### EXPERIMENTS:

(Exp.1)

Tumor spheroids were prepared by growing GFP labeled ovarian cancer cells on a spheroid forming plate for fourteen days. The spheroids were incubated with boron-10 agents which resulted in the distribution of the agents throughout the spheroids. The spheroids were exposed to neutron beam at the nuclear reactor for one hour and changes to the spheroids were examined.

(Exp.2) A similar experiment was carried out with ovarian tumor formed on the CAM membrane of fertilized chicken eggs. This was prepared by transplanting human ovarian cancer cells onto the CAM membrane. After confirming tumor formation, boron-10 agents were injected intravenously and the eggs were exposed to neutron at the nuclear reactor for 1 hour. Effect on tumor growth was examined by observing tumor size as well as by examining tumor weight three days after the exposure.

#### RESULTS:

Exp.1:

Tumor spheroids were formed from human ovarian cancer cells labeled with GFP. They had uniform shape and size (0.2 x 0.2 mm). Incubation with boron agents such as BPA-loaded nanoparticle (Rhodamine-B labeled) resulted in uniform distribution of the agent throughout the spheroids as revealed by the analysis of confocal microscopy. These spheroids were then irradiated with a neutron beam for one hour at the nuclear reactor. Two days after the exposure, the spheroids were examined. The results showed that little changes have occurred by the neutron exposure.

Exp.2:

Three days after transplanting human ovarian cancer cells onto the CAM membrane, tumor was formed. Boron reagents such as BPA or BPA-loaded nanoparticles were injected intravenously into the chicken eggs. The amount of boron loaded onto the nanoparticle that was used in this experiment was examined by ICP-OES. This analysis revealed the presence of 5.47 ppm of boron in a 10 ml solution containing 2 mg of nanoparticles, which amounts to the weight of boron constituting 2.5% of the nanoparticle. The eggs were exposed to neutron beams for one hour at the nuclear reactor. Two or three days after the exposure, tumor size and weight were examined. The results showed that the tumor size was significantly decreased by the exposure.

#### CONCLUSION AND FUTURE PROSPECTS:

Our results show that the chicken egg CAM model can be used as a reliable model to examine the efficacy of the BNCT therapy. We have reproducibly demonstrated that the CAM tumor can be dramatically decreased by the exposure to a neutron beam. The tumor weight after the exposure was less than 10 mg while that of the non-exposure control was around 50 mg. This type of dramatic effect was not observed with the use of tumor spheroids. These results suggest that the CAM model is particularly suited for the BNCT experiments.

In the future, we plan to use the patient-derived chicken egg tumor model (PDcE model). We have established the PDcE model by transplanting tumor fragments from the ovarian cancer patients as well as by transplanting biopsy samples from esophageal cancer patients. This will enable testing of the BNCT efficacy with an individual patient tumor.

#### REFERENCES:

1. A. Komatsu, K. Matsumoto, T. Saito, M. Muto, F. Tamanoi. (2019) Patient Derived Chicken Egg Tumor Model (PDcE Model): Current Status and Critical Issues. *Cells*. 10;8(5).

## PR3-5 Development of new boron drug for next-generation A-BNCT treatment

S. Ishiyama, T. Hatakeyama, S. Yoneyama, C. Oyama and M. Suzuki<sup>1</sup>

Graduate School of Science, Hiroaki University  
<sup>1</sup>Institute for Integrated Radiation and Nuclear Science,  
Kyoto University

**INTRODUCTION:** Aomori Prefecture is one of the shortest-lived prefectures in Japan, and the return of short-lived prefectures is a long-cherished desire. Among them, the death rate due to cancer is the highest in both men and women nationwide, so it is an urgent task to overcome cancer death as soon as possible. Therefore, in this research, the aim is to introduce the first BNCT technology in Aomori Prefecture[1-2] and to develop original technology mainly for (1) A (advanced Aomori) -BNCT and (2) regenerative treatment using artificial tissue after BNCT[3-4]. In this report, we mainly report on (1) item mainly on the development of high-performance BNCT device and animal experiments using newly developed boron drug using this device.

**EXPERIMENTS:** For animal experiments, the QSC accelerator and irradiation facility installed by Aomori Prefecture in 2018 were used as A-BNCT devices. The peptide series IF7-B series (IF7-BSH and IF7-BPA) newly developed as a boron drug was administered to tumor model nude mice (about 80 mice) at a maximum dose of 70 mg / kg by TVI and IP. The irradiation dose was  $1.2 \times 10^{12}$  n / cm<sup>2</sup> and the maximum irradiation time was up to 1 hour.

**RESULTS:** Fig. 1 shows the tumor volume change of each tumor model injected with IF7-BPA and IF7-BSH after irradiation with A-BNCT device (indicated by Hot in the figure), respectively, and unirradiated tumor model (indicated by Cold in the figure).

According to this result, although the variation in tumor size increases with the passage of irradiation time, in the case of IF7-BPA, the tumor size rapidly increases 5 days after irradiation in the non-irradiated tumor model (Cold), whereas the irradiation(Hot), it can be seen that the growth rate in the tumor model is suppressed to some extent.

On the other hand, in the case of IF7-BSH, the tumor size rapidly increases 6 days after irradiation in the unirradiated tumor model (Cold), whereas the growth rate in the irradi-ated tumor model (Hot) is suppressed to some extent and it was after 10 days.

Comparing the changes in tumor size in unirradiated tumor models with IF7-BPA and IF7-BSH respectively, it seems that IF7-BPA suppresses tumor growth relatively.

On the other hand, when comparing the suppressive effect of tumor growth rate with IF7-BPA and IF7-BSH, almost the same suppressive effect is observed, but the time when the suppressive effect of IF7-BSH appears is slightly later than that of IF7-BPA.

### REFERENCES:

- [1] S. Ishiyama, J. of Cancer Therapy, 2014,5,1388-1398.
- [2] S. Ishiyama, Y. Imahori, J. Itami and H. Koivunoro, J. of Cancer Therapy, 2015, 6, 759-766.
- [3] S. Ishiyama, Y. Asano, M. Suzuki, M. Akashi and H. Shimada, J. of Cancer Therapy, 2019, 10, 835-845.
- [4] S. Ishiyama and M. Suzuki, J. of Cancer Therapy, 2019, 10,1025-1035.

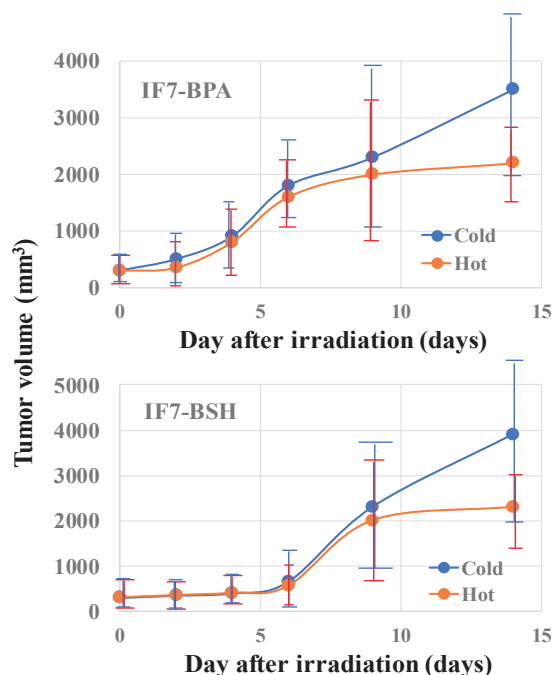


Fig. 1. Change in tumor volume of tumor seeding model after IF7-BPA and IF7-BSH dose and irradiation. In the figure, Cold shows the data of the tumor seeding model that was not irradiated after the boron drug administration, and Hot shows the data of the tumor model that was irradiated after the drug administration.

S. Ishiyama, T. Hatakeyama, S. Yoneyama, C. Oyama and M. Suzuki<sup>1</sup>

Graduate School of Science, Hiroaki University

<sup>1</sup>Institute for Integrated Radiation and Nuclear Science, Kyoto University

**INTRODUCTION:** Aomori Prefecture is one of the shortest-lived prefectures in Japan, and the return of short-lived prefectures is a long-cherished desire. Among them, the death rate due to cancer is the highest in both men and women nationwide, so it is an urgent task to overcome cancer death as soon as possible. Therefore, in this research, the aim is to introduce the first BNCT technology in Aomori Prefecture[1-2] and to develop original technology mainly for (1) A (advanced Aomori) -BNCT and (2) regenerative treatment using artificial tissue after BNCT[3-4]. In this report, we mainly report on (2) item mainly on the development of high-performance BNCT device and animal experiments using newly developed boron drug using this device.

#### EXPERIMENTS:

**2.1 Cells, reagents and instruments:** Normal human dermal-fibroblast (NHDFs) and red fluorescent protein (RFP)-labeled human pancreatic cancer line BxPC3 were used in the experiment. Dulbecco's modified Eagle's medium (DMEM) containing 10% fetal bovine serum (FBS) was used to proliferate cells prior to construction of the tumor tissue model. The cells were cultivated at 37°C, 5% carbon dioxide. Bovine plasma-derived fibronectin (FN) and porcine skin gelatin(G) were applied in this process. Cell cultivation were conducted on transwell inserts with porous polyester bottom(pore size: 0.4 μm) for 12-well culture plate(12mm diameter, 112mm<sup>2</sup> area, cat. No.3401). **2.2 Preparation of *in vitro* human three-dimensional tumor tissue model:** Human three-dimensional tumor was pre-pared by cell accumulation method. First, connective tissue-like structures were fabricated by three-dimensional lamination of NHDFs. As shown in Fig.1, NHDFs are cultured under the conditions mentioned above, then ECM-nano film (about 10nm thick) was formed on each cell surface by coating cells with fibronectin and gelatin dissolved in Tris-HCL buffer. The cells are seeded on the transwell inserts at a density of  $27.2 \times 10^5$  cells/insert (8 layers) and cultured under the conditions of 5% carbon dioxide at 37°C for 12 to 24 hours. We regarded this connective tissue-like structure as an artificial human normal tissue model, termed as NHDF3D. Next, RFP-labeled BxPC3 cells which have been cultured and proliferated were collected by trypsin treatment, washed, and uniformly seeded on the upper surface of NHDF3D at a density of 300 cells/mm<sup>2</sup>, then further cultured for 24 hours under the above culture conditions.

**2.3 BPA immersion treatment and fixation:** The BPA solution (3%w/v) was diluted to a concentration of 40ppm with DMEM containing 10% FBS. After removing the culture solution of NHDF3D or NHDF3D/BxPC3, 750 μL of BPA treatment solution was added, and incubated for 2 hours (BPA exposure) under condition of 5%

carbon dioxide at 37°C(Fig. 1). After that, the BPA treatment solution was removed and the tissues were washed 3 times with 0.01 M phosphate-buffered saline (PBS, PH 7.3). Subsequently, the tissues were fixed by 4% paraformaldehyde/0.1M phosphate buffer (PH 7.3) for 30 minutes at room temperature shading the light. After the fixation, the cellular nucleus was stained by 4',6-diamidino-2-phenyl-indole(DAPI).

**2.4 Neutron irradiation experiment:** The above-mentioned NHDF3D or NHDF3D/BxPC3 in the transwell inserts were cut out with a knife together with the polyester base, mounted on the solid track detector CR-39 with close contact, and used as a sample for track image acquisition(Fig.1(d)). Irradiation experiments using these samples were conducted at the heavy water neutron irradiation facility of Kyoto university reactor(KUR), and irradiation was performed for 30 minutes under an irradiation flux of  $1.4 \times 10^9$  n/cm<sup>2</sup>/s(Fig.1). After the neutron irradiation, the above sample was etched (6N NaOH, 70°C × 2 hours) to visualize the α-ray/recoiled Li particle tracks generated on the CR-39 surface.

**RESULTS:** From these results, our *in vitro* model of tumor tissue for BNCT demonstrated the pharmacokinetics of BPA and the efficacy of neutron irradiation by direct observation of α-ray/recoiled Li particle tracks that are corresponding to the distribution of BxPC3 cells. Moreover, the evaluated number of α-ray/recoiled Li particle tracks per single BxPC3 cell or NHDF provide the comparable value with T/N ratio of BPA in the previous studies[2-3].

#### REFERENCES:

- [1] S. Ishiyama, J. of Cancer Therapy, 2014,5,1388-1398.
- [2] S. Ishiyama, Y. Imahori, J. Itami and H. Koivunoro, J. of Cancer Therapy, 2015, 6, 759-766.
- [3] S. Ishiyama, Y. Asano, M. Suzuki, M. Akashi and H. Shimada, J. of Cancer Therapy, 2019, 10, 835-845.
- [4] S. Ishiyama and M. Suzuki, J. of Cancer Therapy, 2019, 10,1025-1035.

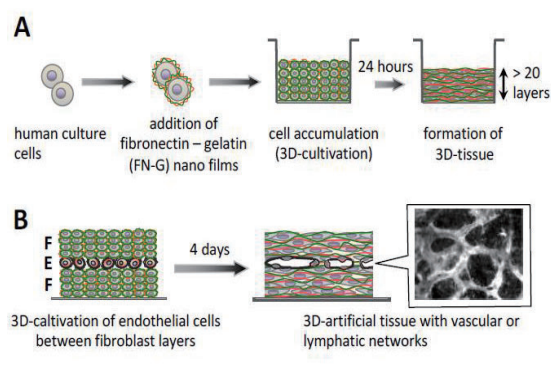


Fig. 1. Procedure for detection of BNCT reaction by using *in vitro* three-dimensional artificial human tumor tissue model.

## Evaluation of boron neutron capture therapy (BNCT) using brain tumor bearing rats or mice model

Y. Fukuo, S. Kawabata, Y. Hattori<sup>1</sup>, H. Kashiwagi, T. Kanemitsu, K. Takeuchi, R. Hiramatsu, M. Suzuki<sup>2</sup>, S-I. Masunaga<sup>2</sup>, H. Nakamura<sup>3</sup>, M. Kirihata<sup>1</sup>, M. Wanibuchi, S-I. Miyatake<sup>4</sup>

*Department of Neurosurgery, Osaka Medical College*

<sup>1</sup> *Laboratory for Chemistry and Life Science, Institute of Innovative Research, Tokyo Institute of Technology*

<sup>2</sup> *Institute for Integrated Radiation and Nuclear Science, Kyoto University*

<sup>3</sup> *Osaka Prefecture University, Research Center of Boron Neutron Capture Therapy*

<sup>4</sup> *Kansai BNCT Medical Center, Osaka Medical College*

### Introduction

Boron neutron capture therapy (BNCT) has been performed as an adjuvant therapy of malignant glioma. We treated patients with malignant glioma by surgical removal followed by BNCT, and recently reported with good results.[1]

Many new drugs have been proposed to date, but clinical experience is limited to BPA (boronophenylalanine) and BSH (borocaptate sodium).[2] The development of effective boron compounds is a major theme. We have been conducting the basic study on how the novel boron compound (BADB) that combines the advantages of using amino acid demand (BPA) and containing a large amount of <sup>10</sup>B per molecule (BSH) for BNCT will affect rat brain tumor model.

### Materials and Methods

We used two boron compounds: BPA and BADB. For in vivo BNCT study, the therapeutic effect was evaluated in terms of the survival time for all rats divided into six groups: untreated controls, neutron irradiation controls, non-neutron irradiation with BADB (CED) controls, BNCT with BPA (i.v.), BNCT with BADB (CED), and BNCT with combination of BPA (i.v.) and BADB (CED). The rats were irradiated at a reactor power of 1 MW for 1 hour.

### Results

The survival data following BNCT are summarized in Table. 1. Median survival time (MST) in all neutron irradiation groups were significantly longer than that in the untreated control group ( $p < 0.005$  by Log-rank test, respectively).

The combination group of simultaneous use of both BADB (CED) and BPA (i.v.) gave the most significant prolongation of survival (38 (36-39) days). BADB (CED) and BPA (i.v.) combined group had a significant survival prolongation compared with the single-agent group. (vs. BPA (i.v.): 34 (33-36) days,  $p < 0.05$  by Log-rank test, vs. BADB (CED): 31 (29-34) days,  $p < 0.05$  by Log-rank test). In addition, the combined group showed the highest percent increase in life span value (ILS) among all treated

groups (43.4%).

Group	n	Survival Time	
		Median	Range(95% CI)
control	6	26.5	25-28
Irradiated	5	28	27-29
BADB control	5	28	27-29
i.v. BPA	6	34	33-36
BADB (CED)	8	31	29-34
BADB (CED)+ i.v. BPA	7	38	36-39

Table 1. Survival times of F98 glioma-bearing rats after neutron irradiation

### Ongoing study

We developed another novel boron drug that human serum albumin conjugated maleimide-functionalized closo-dodecaborate (MID-HSA)[3] as <sup>10</sup>B carrier for BNCT. The MID-HSA utilizes the accumulation in the tumor through the well-established Enhanced Permeability and Retention (EPR) effect[4] of solid tumors. We evaluated the biodistribution of these following BPA, BSH, and MID-HAS. In biodistribution study, boron uptake in tumor boron concentration was confirmed by intravenous administration of MID-HSA. Blood concentration was high after i.v. administration. In vivo further therapeutic experiments of MID-HSA using intravenous and CED as a boron delivery agent are ongoing and the results will be reported soon.

### Reference

1. Kawabata S, Miyatake S, Hiramatsu *et al.*, (2011) Phase II clinical study of boron neutron capture therapy combined with X-ray radiotherapy/temozolomide in patients with newly diagnosed glioblastoma multiforme--study design and current status report. *Applied radiation and isotopes* : including data, instrumentation and methods for use in agriculture, industry and medicine 69 (12):1796-1799.
2. Miyatake S, Tamura Y, Kawabata *et al.*, (2007) Boron neutron capture therapy for malignant tumors related to meningiomas. *Neurosurgery* 61 (1):82-90.
3. Kikuchi S, Suzuki M, Nakamura H *et al.*, (2016) Maleimide-functionalized closo-dodecaborate albumin conjugates (MID-AC): Unique ligation at cysteine and lysine residues enables efficient boron delivery to tumor for neutron capture therapy. *Journal of controlled release* : official journal of the Controlled Release Society 237:160-167.
4. Matsumura Y, Maeda H (1986) A new concept for macromolecular therapeutics in cancer chemotherapy: mechanism of tumorotropic accumulation of proteins and the antitumor agent smancs. *Cancer research* 46 (12 Pt 1):6387-6392.

## PR3-8 Intracellular target delivery of cell-penetrating peptide-conjugated dodecaborate for boron neutron capture therapy (BNCT)

I. Nakase<sup>1,2</sup>, M. Katayama<sup>1,2</sup>, Y. Hattori<sup>3</sup>, M. Ishimura<sup>3</sup>, S. Inaura<sup>1</sup>, D. Fujiwara<sup>1</sup>, I. Fujii<sup>1</sup>, S. Futaki<sup>4</sup>, and M. Kirihata<sup>3</sup>

<sup>1</sup>Graduate School of Science, Osaka Prefecture University, Japan

<sup>2</sup>NanoSquare Research Institute, Osaka Prefecture University, Japan

<sup>3</sup>Research Center of BNCT, Osaka Prefecture University, Japan

<sup>4</sup>Institute for Chemical Research, Kyoto University, Japan

**INTRODUCTION:** In BNCT, internalization of <sup>10</sup>B-boron atom by cancer cells leads to the induction of cell death by generation of alpha particles and recoiling <sup>7</sup>Li nuclei with high linear energy transfer and short range when irradiated with neutrons [1]. Effective therapeutic benefits on intractable cancer, such as brain tumor and head and neck cancer have been attained through current BNCT technology. However, insufficient accumulation and cellular uptake efficacy of second-generation boron compounds such as thiododecaborate (BSH) under clinical research have been pointed out. In this research, we aim to develop BNCT technology using cell-penetrating peptides (CPPs) [2] for enhanced cellular uptake of boron compounds and their controlled locations inside cells.

**EXPERIMENTS:** Chemical synthesis of all peptides were conducted via Fmoc solid-phase peptide synthesis. Dehydration condensation of carboxyl dodecaborate derivative [B<sub>12</sub>H<sub>11</sub>S(CH<sub>2</sub>)<sub>2</sub>COOH] to the N-terminal of CPPs was conducted for their conjugation. Cellular uptake of fluorescently labeled dodecaborate-conjugated CPPs were assessed using a confocal laser microscopy. Regarding BNCT assay, after cellular treatment with each dodecaborate-conjugated CPP (30 min, 37°C), the cells were irradiated with neutrons, and cell-killing effects were detected by e.g. cellular colony assay.

**RESULTS:** When cell death is induced by organelle damage, the cell death efficacies and pathways are possibly affected by the damaged organelles (e.g. plasma membrane, mitochondria, or nucleus) by BNCT. We designed and synthesized organelle-targeted peptide-conjugated boron clusters to increase their cellular uptake and to control the intracellular locations for induction of sophisticated cancer cell-killing activity (in-

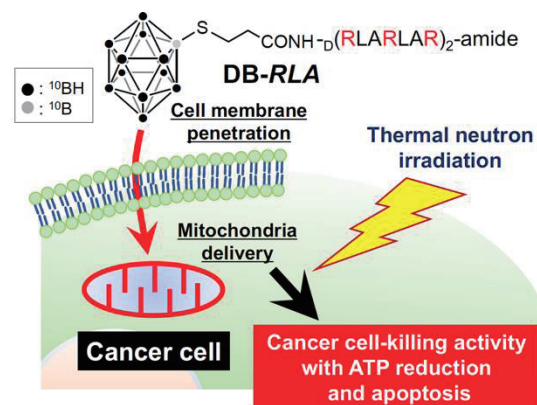


Figure 1. Schematic representation of the intracellular targeted delivery of boron compounds. Boron compounds (dodecaborates, DB) are conjugated to *RLA* peptides for mitochondria delivery. The controlled intracellular delivery by the conjugated peptide affects the efficacy of the cancer cell-killing activity and the cell death types.

cluding efficacies and mechanisms) under BNCT. For example, boron compounds conjugated with mitochondria target CPP, *RLA* (amino acid sequence: D[RLARLAR]<sub>2</sub>) [3], showed significantly enhanced cellular uptake efficacy and mitochondrial accumulation of the boron compounds (Figure 1). Once the accumulation of the boron compounds in mitochondria (30 min treatment), the compounds were highly retained even after 24 hrs incubation. In BNCT experiments, we found that *RLA* peptide-conjugated dodecaborate showed higher effects of cancer cell-killing activity than that of other CPPs (endosomes and cytosolic release) when irradiated with neutrons *in vitro* BNCT assay [4].

**CONCLUSION:** In this research, we showed importance of controlled intracellular locations of boron compounds by the CPP conjugation for achieving their sophisticated BNCT biological activity. Our experimental techniques and findings will contribute to development for BNCT methodology.

### REFERENCES:

- [1] K. Nedunchezian, *et al. J. Clin. Diagn. Res.* **10** (2016) ZE01-ZE04.
- [2] S. Futaki, I. Nakase, *Acc. Chem. Res.* **50** (2017) 2449-2456.
- [3] I. Nakase, *et al. Chem. Commun.* **48** (2012) 11097-11099.
- [4] I. Nakase, *et al. Chem. Commun.* **55** (2019) 13955-13958.

T. Tsurubuchi<sup>1</sup>, F. Yoshida<sup>1</sup>, A. Zaboronok<sup>1</sup>, K. Nakai<sup>1,2</sup>, M. Shirakawa<sup>3</sup>, Haruka Arita<sup>3</sup>, Haruna Uto<sup>3</sup>, M. Suzuki<sup>4</sup>, A. Matsumura<sup>1</sup>

Graduate School of Science, Kyoto University

<sup>1</sup> Department of Neurosurgery, Faculty of Medicine, University of Tsukuba

<sup>2</sup> Department of Radiation Oncology, Faculty of Medicine, University of Tsukuba

<sup>3</sup> Department of Pharmaceutical Sciences, University of Fukuyama

<sup>4</sup> Institute for Integrated Radiation and Nuclear science, Kyoto University

**INTRODUCTION:** For Boron Neutron Capture Therapy ( BNCT ), less toxic and tumor-selective accumulation by ideal drug delivery systems are mandatory. Many types of newly boron compound such as liposome, porphyrin, and others were developed, none of novel boron compound has been used in BNCT trials other than p-boronophenylalanine ( BPA ), sodium borocaptate ( BSH ). Moreover, only BPA proceeded to phase II trial in the field of BNCT.

We developed a novel boron compound containing carbon nanostructure like a horn provided by national institute of advanced industrial science and technology. This compound contains borons not only inside horn structure but also the outer surface of this horn. For selective accumulation in tumor cells, the BN-CN was coated with phospholipid polyethylene glycol having folate, BN-CN/PLPEG-FA [1] called carbon nanohorns. This carbon nanohorns conjugated with FA can selectively accumulate in tumor tissues. Also, it can be observed under light microscope to check whether it is in the tumor tissues and tumor cells [1].

**EXPERIMENTS:** CT26, mice colon tumor cells, and GL261, mice glioma cells were used for colony formation test. The  $1 \times 10^6$  cells were plated on wells of 6 well plate 24 hours before experiment. The drug, carbon nanohorns and BPA were added to each well respectively 24 hours before irradiation compared to control, radiation only group. The cells were trypsinized and counted. The irradiation was performed with thermal neutrons with a flux of  $1.6 \times 10^{12}$  neutrons/cm<sup>2</sup> over 15min at the Kyoto University Research Reactor (KUR). The 200 cells and 600 cells per dish were plated respectively. Plating efficiencies were checked after counting colonies on day 14. This time carbon nanohorns only contains natural boron.

**RESULTS:** The carbon nanohorns showed better tumor suppression effect on colony formation test in vitro compared to radiation only group. BPA showed the best tumor suppression effect (Figures 1&2). However, our car-

bon nanohorn consists of natural borons, not contains <sup>10</sup>B. therefore, if we use carbon nanohorns consisting of <sup>10</sup>B, we can expect better results the same as BPA or more.

Figure 1

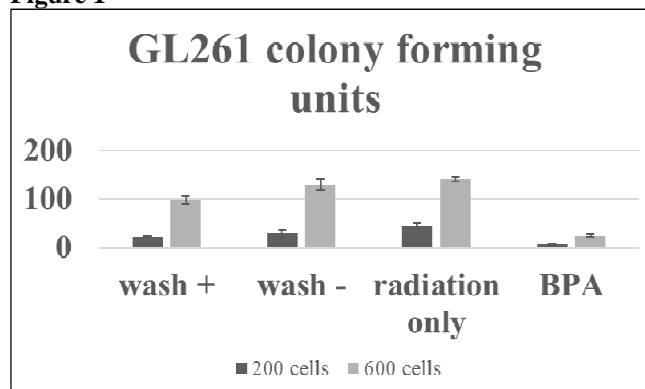
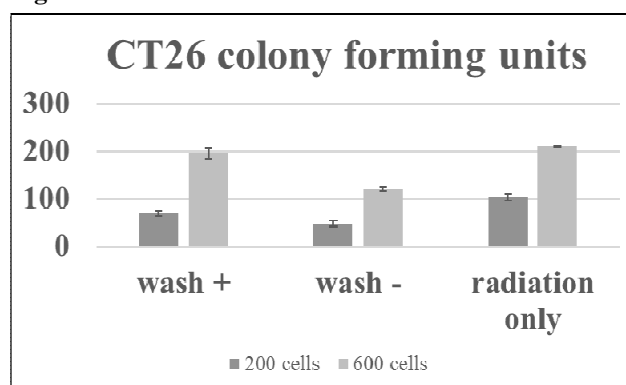


Figure 2



#### REFERENCES:

[1] Y. Iizumi *et al.*, CARBON **93** (2015) 595-603.

## PR3-10 Development of a multifunctional nanoparticle towards next-generation boron neutron capture therapy

A. Kim<sup>1</sup>, M. Suzuki<sup>2</sup>, Y. Matsumoto<sup>3,4</sup>, N. Fukumitsu<sup>5</sup>, and Y. Nagasaki<sup>1,6,7</sup>

<sup>1</sup>Department of Materials Sciences, Graduate School of Pure and Applied Sciences, University of Tsukuba, <sup>2</sup>Institute for Integrated Radiation and Nuclear Science, Kyoto University, <sup>3</sup>Faculty of Medicine, University of Tsukuba, <sup>4</sup>Proton Medical Research Center, University of Tsukuba Hospital, Radiation Oncology Research Laboratory, <sup>5</sup>Department of Radiation Oncology, Kobe Proton Center, <sup>6</sup>Masters Program in Medical Sciences, Graduate School of Comprehensive Human Sciences, University of Tsukuba, <sup>7</sup>Center for Research in Isotopes and Environmental Dynamics (CRiED), University of Tsukuba

### INTRODUCTION

Boron neutron capture therapy (BNCT) utilizes nuclear fission in a few  $\mu\text{m}$ -range to achieve target-specific tumoricidal effects. The location of the boron-10 determines where the nuclear fission takes place, thus the biodistribution of the boron-10 should be regulated to afford damage in the tumors, but not to provoke adverse effects elsewhere. To this end, we designed a phenylboronic acid (PBA)-installed polymeric nanoparticle (Fig. 1), of which tethered PBA moieties provide neutron capture capacity as well as strong affinity to sialic acids. Because hypersialylation of the cancer cells is generally accompanied by metastatic invasiveness, the PBA might facilitate accumulation and retention of the nanoparticle, especially in metastatic tumors. Furthermore, in contrast to conventional BNCT agents, polymeric nanoparticles are not prone to an acute renal clearance, due to a supramolecular structure comprised of synthetic polymers. Thus, our design is supposed to have a prolonged systemic circulation, which may result in even higher tumor accumulation.

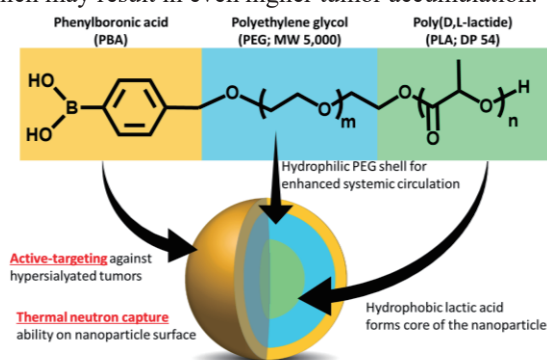


Fig. 1. Schematic design of the PBA-installed nanoparticle.

### EXPERIMENTS

Sequential anionic polymerization of ethylene oxide and D,L-lactide was carried out on a PBA pinacol ester bearing alkoxide initiator, resulted in an amphiphilic copolymer composed of pinacol-protected PBA, poly(ethylene glycol) (PEG), and poly(lactic acid) (PLA). Subsequently, the PBA-installed polymeric nanoparticle (PBA-NP) was self-assembled by dissolving aforementioned polymer in an organic solvent, followed by dialysis against distilled and ion exchanged (DI) water. The PBA-NP was then evaluated with a series of in vitro analyses, including surface plasmon resonance (SPR) technique, confocal laser scanning microscopy (CLSM) observations, and cytotoxicity

assays. In vivo feasibility of the PBA-NP was validated on a B16 melanoma-bearing C57BL/6j mouse model, by subcutaneous injection of either the PBA-NP or boronophenylalanine-fructose complex (BPA-f), subsequently irradiated with non-invasive neutrons. Furthermore, microdistribution of the boron-10 could be indirectly monitored by embedding tumor sections on a CR-39 solid state nuclear track detector, followed by thermal neutron irradiations, then observed with phase contrast microscope. Pharmacokinetics of the nanoparticles could be validated by applying an inductively coupled plasma mass spectrometry (ICP-MS) on homogenized tissue samples.

### RESULTS

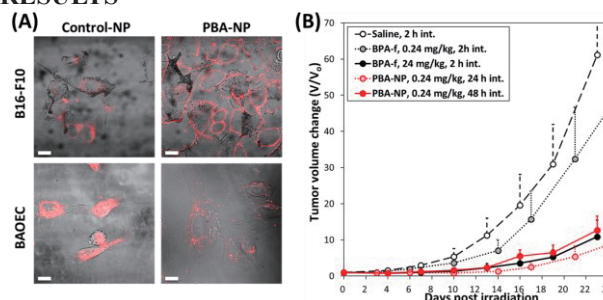


Fig. 2. (A) CLSM observation of B16-F10 cancer cell line and BAOEC primary cells treated with 5 min with rhodamine-labeled nanoparticles, scale bars represent 20  $\mu\text{m}$ . (B) Antitumor efficacy of PBA-NP on BNCT, compared with BPA-fructose (BPA-f),  $n = 6$ .

As confirmed by <sup>1</sup>H NMR spectra, although the PBA moiety on the synthetic polymer was initially protected with pinacol, it could be readily deprotected while the nanoparticle was being purified, presumably because of hydrolysis-driven deprotection on dialysis. Thus, no further procedure was required to allow functional PBA moieties to be exposed, and to obtain the PBA-NP. The hydrodynamic diameter of the PBA-NP was around 75 nm, which was stably sustained under a physiological condition in the presence of serum, for at least 24 h. With an SPR analysis, the PBA-NP demonstrated unusually strong and selective binding to a sialic acid-immobilized surface, ensured a targeting effect. This was consistent with the CLSM observation (Fig. 2A), where brief incubation of the PBA-NP with hypersialylated cancer cell lines clearly showed selective localization onto the cell membranes. Notably, in vivo evaluation on a melanoma-bearing mouse model could reveal that the PBA-NP possesses a highly potent antitumor efficacy, which could be only provoked by neutron irradiations. It is important to state although the PBA-NP was administered at a 100-folds lower effective dose (0.24 mg <sup>10</sup>B/kg) than that of the BPA-f (24 mg <sup>10</sup>B/kg), their antitumor efficacies on neutron irradiations were comparable to each other (Fig. 2B). No distinct side effect was observed in the PBA-NP injected mice, as there was no apparent body weight change in both irradiated and non-irradiated control groups. Moreover, assured with a series of cytotoxicity assays, none of the normal primary cells and cancer cell lines manifested palpable response to the PBA-NP. In conclusion, here we propose a highly efficient BNCT agent which affords an active targeting capability.

# PR3-11 Design, Synthesis, and Evaluation of Glucose and Macrocyclic Polyamine-type Boron Carriers for BNCT

S. Aoki<sup>1,2</sup>, H. Ueda<sup>1</sup>, K. Mizuno, C<sup>1</sup>. Balachandrani<sup>1</sup>, M. Suzuki<sup>3</sup>, S. Masunaga<sup>3</sup>, N. Kondo<sup>3</sup> and Y. Sakurai<sup>3</sup>

<sup>1</sup>Faculty of Pharmaceutical Sciences, Tokyo University of Science

<sup>2</sup>Research Institute for Science and Tehcnology, Tokyo University of Science

<sup>3</sup>Institute for Integrated Radiation and Nuclear Science, Kyoto University

**INTRODUCTION:** Boron neutron capture therapy (BNCT) is one of powerful therapies for local tumor control in the treatment of brain tumor, melanoma, and so on [1]. To date, only two boron-containing drugs, L-4-boronophenylalanine (BPA) and BSH (sodium mercaptoundecahydrododecaborate, Na<sub>2</sub>B<sub>12</sub>H<sub>11</sub>SH) (Fig. 1) have been approved as clinically test compounds, and development of better BNCT agents is highly required.

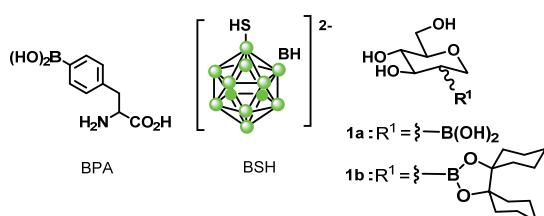


Fig. 1. Chemical structures of BSH, BSH, and 1.

An enhanced uptake of D-glucose and glucose transporter expression are common in cancer cells. In this context, we previously reported on the design and synthesis, of 2-boryl-1,2-dideoxy-D-glucose derivatives **1** (Fig. 1), although its intracellular uptake is not so high [2]. In this paper, we report on new D-glucose-based drugs **2a,b** and **3** having boryl parts at the C-2 and C-1 positions and **4a-d** having BSH unit at the C6 position of D-glucose and cationic sulfonium unit to neutralize the dianion of BSH part (Fig. 2).

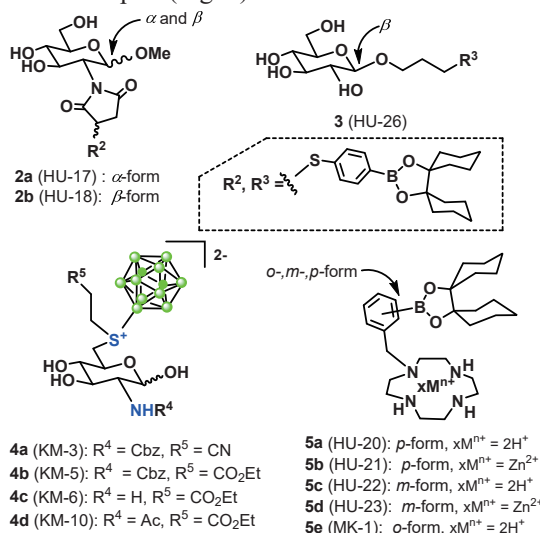


Fig. 2. Structures of boron-containing agents based on D-glucose and macrocyclic polyamine scaffolds.

**EXPERIMENTS and RESULTS:** The synthesis of **2a,b** and **3** was carried out from 2-deoxy-2-amino-D-glucose and D-glucose, respectively. The synthesis of **4a-e** was conducted from the 1,4-addition of BSH with acrylonitrile and ethyl acrylate, followed by the alkylation reaction with 6-TsO derivatives of the *N*-protected D-glucosamines (the details will be reported elsewhere). The synthesis of **5a-e** was achieved according to our previous paper [3]. Cytotoxicity and cellular uptake activity of the synthesized compounds in cancer cells were evaluated by MTT assay and ICP-MS (inductivity coupled plasma-mass spectrometer).

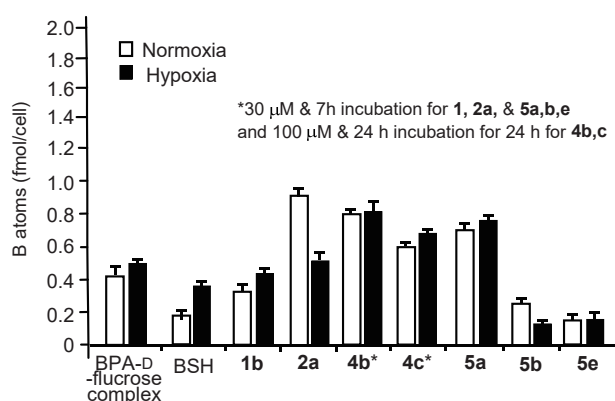


Fig. 3. The results of intracellular uptake evaluation of BPA-D-fructose complex, BSH, **1**, **2a,b**, **4b,c**, and **5a,b,e** in HeLa S3 cells, as determined on ICP-MS after the incubation with 30  $\mu$ M (for **1**, **2a,b**, and **5a,b,e**) and 100  $\mu$ M (for **4b,c**) of the drugs under normoxic and hypoxic conditions at 37 °C for 7–24 hr. Data represent the mean  $\pm$ SD of at least three replicates.

The intracellular uptake values of the aforementioned compounds are presented in Fig. 3, which implies that the intracellular uptake of **2a**, **4b**, **4c**, and **5a** is somewhat better than BPA and BSH. The uptake of **5b**, a zinc(II) complex of **5a** is lower than that of **5a**. The comparison of **5a**, **5c** (data not shown) and **5e** suggests the position of boryl unit on the benzyl groups of these compounds is important for the uptake efficiency [4]. The evaluation of BNCT effect of these molecules and the improvement of the design of these B-carriers and the attempts at <sup>11</sup>B MRI of these agents are now in progress.

## REFERENCES:

- [1] a) R. F. Barth *et al.*, *Clin. Cancer Res.*, **11** (2005) 3987-4002. b) R. F. Barth *et al.*, *Rad. Oncol.* **7** (2012) 146-166.
- [2] T. Itoh *et al.*, *Bioorg. Med. Chem.*, **26** (2018) 5922-5933.
- [3] M. Kitamura *et al.*, *Inorg. Chem.*, **50** (2011) 11568-11580.
- [4] H. Ueda *et al.*, Unpublished result.

## PR3-12 Boron Neutron Capture Therapy using Polymer-Based Boron Delivery Systems

T. Nomoto, K. Kanamori, K. Konarita, K. Uehara<sup>1</sup>, M. Ishimura<sup>1</sup>, Y. Ishino<sup>1</sup>, A. Sudani<sup>1</sup>, Y. Sakurai<sup>2</sup>, M. Suzuki<sup>2</sup> and N. Nishiyama

*Institute of Innovative Research, Tokyo Institute of Technology*

<sup>1</sup>*Stella Pharma Corporation*

<sup>2</sup>*Institute for Integrated Radiation and Nuclear Science, Kyoto University*

**INTRODUCTION:** In boron neutron capture therapy (BNCT), *p*-boronophenylalanine (BPA) has been the most powerful drug in clinical studies because it can accumulate selectively within malignant tumors by targeting LAT1 amino acid transporters overexpressed on many tumor cells. However, due to the antiport mechanism of LAT1, the intratumoral BPA concentration gradually decreases during thermal neutron irradiation in some cases [1], thereby compromising the ultimate therapeutic potential. Thus, it has been expected that the prolonged BPA retention in the tumor may enhance the BNCT effect.

In this regard, we recently found that simple mixing of biocompatible poly(vinyl alcohol) (PVA) and BPA results in the formation of PVA-BPA complexes via the formation of boronate esters. The PVA-BPA complex could be internalized into the cells through LAT1-mediated endocytosis and localized in endo-/lysosomes while conventional BPA was localized in cytosol. The PVA-BPA complex in the endo-/lysosomes eventually slowed the unfavorable efflux from the tumor cells. Even in *in vivo* study, the PVA-BPA exhibited the enhanced tumor accumulation and prolonged retention, thereby accomplishing the strong BNCT effect [2].

In these previous studies, we used PVA that was synthesized by reversible addition-fragmentation chain-transfer (RAFT) polymerization of vinyl acetate and subsequent hydrolysis. Here, to examine whether this concept can be applied to commercially available PVA, we used GMP-grade PVA (PE-05JPS provided by JAPAN VAM & POVAL CO., LTD.) for the preparation of PVA-BPA and investigated its BNCT effect.

**EXPERIMENTS:** BALB/c mice bearing subcutaneous CT26 tumors were used in this study. PVA-BPA or sorbitol-BPA complex was intravenously injected to the mouse (10 mg BPA/mouse), and the thermal and epithermal neutrons were irradiated to the tumor using KUR 3 h after the injection. Size of the tumor was measured using a caliper, and tumor volume (*V*) was calculated using the following equation:

$$V = 1/2 \times a \times b^2$$

where *a* and *b* denote major and minor axes of a tumor, respectively.

**RESULTS:** As shown in Fig. 1, both sorbitol-BPA and PVA-BPA exhibited strong BNCT effect and significantly inhibited the tumor growth. While sorbitol-BPA-treated tumors showed slight regrowth of the tumor, PVA-BPA revealed the enhanced inhibition of the tumor growth probably because of the higher intratumoral BPA concentration than sorbitol-BPA during the thermal neutron irradiation. These results strongly indicate that the concept of PVA-BPA can be applied even to commercially available PVA, which is important for smooth clinical translation of PVA-BPA.

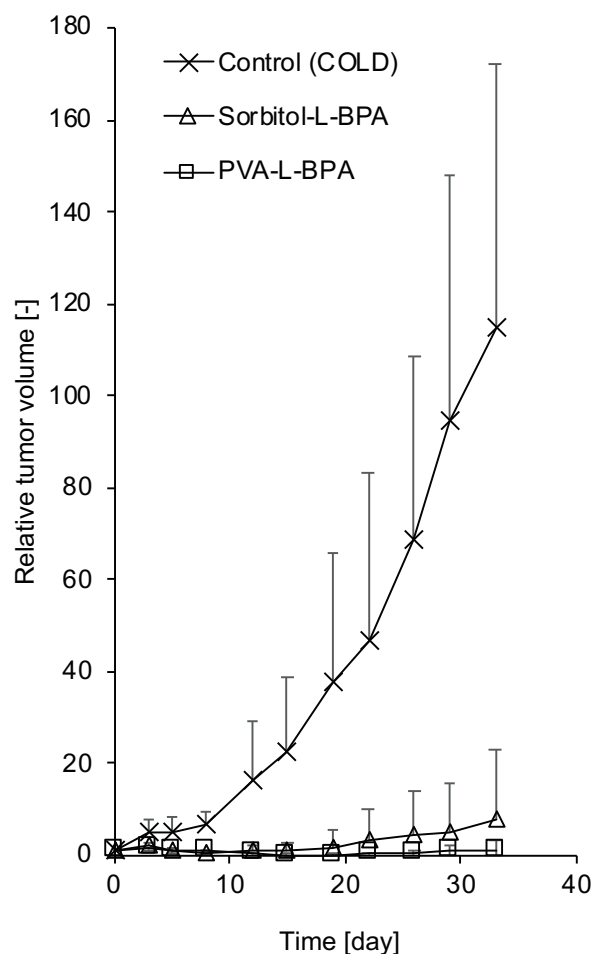


**Fig. 1. BNCT effect of sorbitol BPA and PVA-BPA.**

### REFERENCES:

- [1] A. Wittig *et al.*, *Radiat. Res.*, **153** (2000) 173-180.
- [2] T. Nomoto *et al.*, *Sci. Adv.*, **6** (2020) eaaz1722.

H. Nakamura, S. Kukichi, S. Sato and M. Suzuki<sup>1</sup>

Laboratory for Chemistry and Life Science, Institute of Innovative Research, Tokyo Institute of Technology, Yokohama, Japan

<sup>1</sup>Institute for Integrated Radiation and Nuclear Science, Kyoto University

**INTRODUCTION:** Boron Neutron Capture Therapy (BNCT) of tumor has been focused as one of the minimally invasive cancer therapies. The successful treatment of BNCT is highly dependent on the sufficient and selective accumulation of <sup>10</sup>B atoms to tumor.

We have studied carrier protein-based boron delivery system. Recently, we developed maleimide-functionalized *closo*-dodecaborate (MID) [1] aiming to conjugate to serum albumin, as known to accumulate in malignant and inflamed tissues due to the combination of leaky capillaries with the absence or defect of the lymphatic drainage system, at Cys34 which has only a free SH group among 33 cysteines. Interestingly, MID was found to conjugate not only to a free SH of cysteine residue but also to lysine residues in albumin.[2] MID was also conjugated to transferrin (TF), which does not have any free cysteine residues. TF is an iron carrier protein and accumulated into cells via TF receptor-mediated endocytosis. It is known that TF receptor is overexpressed on the surface of many tumor cells, thus TF has been used as a ligand for active targeting in drug delivery system. Herein we report the preparation of MID-TF conjugates and their *in vivo* selective boron delivery to tumor in colon 26 tumor bearing mice.[3].

**EXPERIMENTS:** MID and isothiocyanate-functionalized *closo*-dodecaborate (ISD) were synthesized from the commercially available *closo*-dodecaborate triethylammonium form, (Et<sub>3</sub>NH)<sub>2</sub>[B<sub>12</sub>H<sub>12</sub>] and <sup>10</sup>B-enriched *closo*-dodecaborate sodium form, Na<sub>2</sub>[<sup>10</sup>B<sub>12</sub>H<sub>12</sub>] according to our previously reported procedures.[1] TF was treated with MID (1.0 mM) or ISD (1.0 mM) in PBS (50 μL) at room temperature for 1 h. The mixture was subjected to SDS-polyacrylamide gel electrophoresis (PAGE). Immunoblotted with anti-B<sub>12</sub>H<sub>11</sub>SH (BSH) antibody was then carried out. After further incubation with horseradish peroxidase (HRP)-conjugated secondary antibody, MID-conjugated TF was visualized with a Molecular Imager ChemiDoc XRS System. The quantification of MID-conjugated TF was determined by image analysis program, Image J. Total proteins (MID-conjugated and unreacted TF) were visualized by coomassie brilliant blue (CBB) staining. Conjugation of MID or ISD to bovine serum albumin (BSA) was also carried out for comparison.

**RESULTS:** Figure 1(a) shows the evaluation of the conjugation of MID and ISD to TF. MID and ISD were conjugated to BSA under physiological pH conditions although the conjugation efficacy of ISD was lower than that of MID against BSA (lane 2 vs. 3). Interestingly, ISD similarly conjugated to both BSA and TF even though TF has no free SH cysteine residue (lane 5 and 6). In our previous

report, we investigated that MID binds to the lysine residues located in the drug binding sites I and II in albumin. Based on the observation, efficient conjugation of MID compared to ISD was probably caused by their different binding modes in the case of BSA.

We next examined the uptake of MID-TF conjugates by colon 26 cells which overexpress TF receptors on the cell surface. The colon 26 cells were incubated with MID-TF conjugates at 10, 30, and 300 ppm boron concentrations for 3 h and the boron accumulation was measured by inductively coupled plasma (ICP). As shown in Figure 1(b), the concentration-dependent uptake of MID-TF conjugates by colon 26 cells was observed. The uptake was not drastically arrested by addition of TF, indicating that the uptake of MID-TF conjugates is considered to be not only through the TF receptor mediated mechanism but also through other pathways.

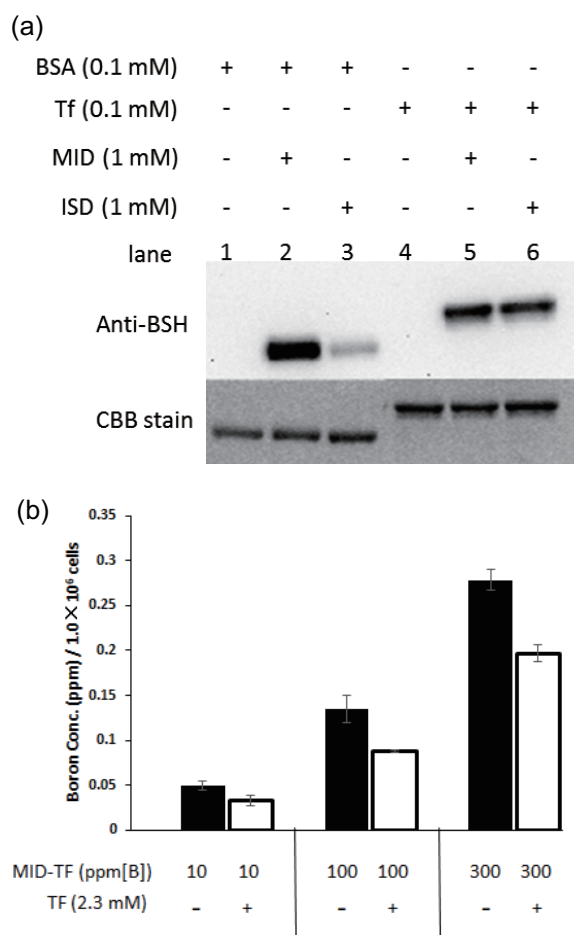


Fig. 1. (a) Western blot analysis of MID conjugation to BSA and TF. (b) Concentration-dependent uptake of MID-TF conjugates by colon 26 cells (black bars).

#### REFERENCES:

- [1] S. Kikuchi, *et al.*, *J. Control. Release*, **237** (2016) 160-167.
- [2] S. Ishii, *et al.*, *Org. Biomol. Chem.*, **17** (2019) 5496-5499.
- [3] S. Kikuchi, *et al.*, *Appl. Radiat. Isotope*, **157** (2020) 109011-109014.

## PR3-14 Development of Novel Boron Agents for BNCT against Malignant Brain Tumors

A. Fujimura<sup>1,2</sup>, K. Igawa<sup>2</sup>, H. Michiue<sup>2</sup>, A. Ueda<sup>2</sup>, and M. Suzuki<sup>3</sup>

<sup>1</sup>Graduate School of Medicine, Dentistry and Pharmaceutical Sciences, Department of Physiology, Okayama University

<sup>2</sup>Neutron Therapy Research Center, Okayama University

<sup>3</sup>Institute for Integrated Radiation and Nuclear Science, Kyoto University

**INTRODUCTION:** Boron neutron capture therapy (BNCT), a well-controlled intracellular atomic reaction of boron <sup>10</sup>B, is a cutting-edge cancer therapy. This *nanobomb* technology utilizes a combination of <sup>10</sup>B delivery and neutron irradiation, and consequent <sup>10</sup>B nuclear decay in cell, thus requires high selectivity of <sup>10</sup>B delivery into cancer cells for safety and efficacy. Currently, primary boron agent for BNCT against several kinds of cancers is BPA (4-borono-L-phenylalanine). BPA is a <sup>10</sup>B-added derivative of tyrosine/phenylalanine, and is imported through amino acid transporters such as LAT1<sup>(1)</sup>. Although LAT1 expression levels are upregulated in almost all cases of head and neck cancers or melanomas, there are many cases with low expression levels of LAT1 in the other kind of malignant tumors including glioblastoma. In these cases, the other types of boron agents are needed. Our goal of this study is to develop new boron agent for BNCT against malignant brain tumors, to cover the patients whose LAT1 expression levels are not high.

**EXPERIMENTS:** NOD-SCID mice were transplanted with 100,000 cells of patient-derived glioblastoma stem-like cells MGG8<sup>(2)</sup> 15 days before BNCT. On 14<sup>th</sup> day after transplantation, the mice were injected with 0, 10, 20, 40 mg/kg of OKD-001 (our novel boron agent). On the next day, these mice were irradiated with neutron for 1 hour at KUR. After BNCT, the mice were checked twice a week to draw the overall survival curve. Animal experiment was approved by the animal experiment ethical committees of Okayama (OKU-2019315) and Kyoto (#17) Universities.

**RESULTS:** Our novel boron agent OKD-001 was effective for BNCT against orthotopic xenograft glioblastoma model. As shown in Fig. 1, OKD-001 plus neutron irradiation significantly prolong the overall survival of the mice in a dose-dependent manner.

OKD-001-BNCT, at KUR

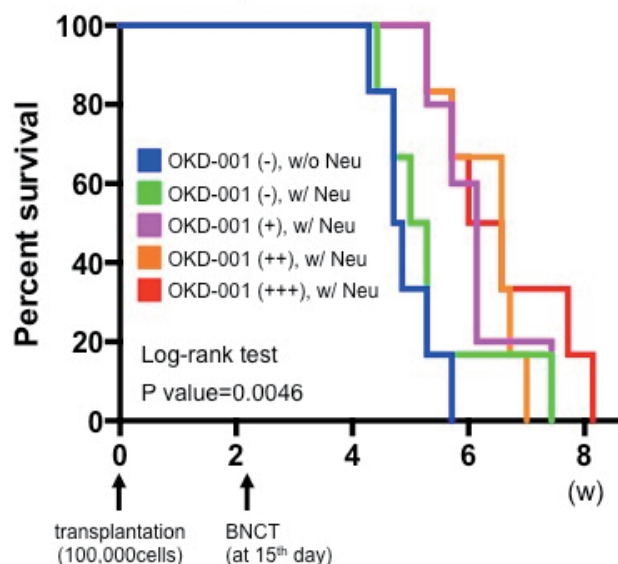


Fig. 1. Orthotopic xenograft glioblastoma model mice are treated with OKD-001-BNCT. OKD-001-BNCT significantly improves the overall survival of the mice in a dose-dependent manner.

### REFERENCES:

- 1) P. Wongthai *et al.*, "Boronophenylalanine, a boron delivery agent for boron neutron capture therapy, is transported by ATB<sup>0+</sup>, LAT1, and LAT2." *Cancer Sci.*, **106** (2015) 279-286.
- 2) M.L. Suva *et al.*, "Reconstructing and reprogramming the tumor-propagating potential of glioblastoma stem-like cells." *Cell* **157** (2014) 580-594.

## PR3-15 Experiment on the Anti-tumor Effect of Pegylated BSH by Thermal Neutron Irradiation

M. Shirakawa<sup>1,2</sup>, N. Kamegawa<sup>3</sup>, R. Takeuchi<sup>3</sup>, K. Nakai<sup>2</sup>, F. Yoshida<sup>2</sup>, T. Tsurubuchi<sup>2</sup>, T. Takata<sup>4</sup>, M. Suzuki<sup>4</sup>, A. Matsumura<sup>2</sup> and H. Hori<sup>3,5</sup>

<sup>1</sup>Department of Pharmaceutical Sciences, University of Fukuyama

<sup>2</sup>Department of Neurosurgery, Faculty of Medicine, University of Tsukuba

<sup>3</sup>Morita Pharmaceutical Ind., Ltd.

<sup>4</sup>Institute for Integrated Radiation and Nuclear Science, Kyoto University

<sup>5</sup>Niigata University of Pharmacy and Applied Life Sciences

**INTRODUCTION:** Nowadays, novel boron compounds are frequently demanded to achieve a good anti-tumor effect. Because, Boron Neutron Capture Therapy (BNCT) using *p*-boronophenylalanine (BPA) for carcinoma such as malignant glioma has a limited therapeutic effect, and there are many recurrence cases.

Therefore we synthesized novel boron compound named BAMP [1]. BAMP combined polyethylene glycol (PEG) and mercaptoundecahydrododecaborate (BSH) by covalent bond. Consequently, pegylated BSH (BAMP) leads to improvement of blood retention time and accumulation to tumor.

This paper presents the experimental results obtained on anti-tumor effect *in vivo* using BAMP.

**EXPERIMENTS:** The tumor-bearing mice were prepared by grafting  $5 \times 10^6$  of mouse colon carcinoma cells (CT26) to the right thigh of female BALB/cA mice (4 weeks old, weighing 16-20 g) to have a tumor diameter of 6-8 mm. These mice were purchased at the age of 3 weeks from CLEA Japan Inc. (Tokyo, Japan) and tamed in Institute for Integrated Radiation and Nuclear Science, Kyoto University.

About 11 days after, 200 $\mu$ L of BAMP and BPA (as control) were administrated by tail vein injection before irradiation. The dosage was 10mg<sup>10</sup>B/kg and 24mg<sup>10</sup>B/kg. At the interval BAMP was 36 hours and BPA was 2hours, the irradiation was performed with thermal neutrons with a flux of  $1.4\text{-}5.9 \times 10^{12}$  neutrons/cm<sup>2</sup> over 1 hour. The tumor size was measured over time after the irradiation until Day 24 and calculated using the general formula [2].

Also, a significant difference in tumor size on the last measurement day of each group was calculated by independent t-test. The value of the significant difference and the number of asterisks are as follows.

(\*:  $p < 0.05$ , \*\*:  $p < 0.01$ , \*\*\*:  $p < 0.005$ , \*\*\*\*:  $p < 0.001$ , ns: No significant difference)

**RESULTS:** As shown in Fig. 1, Fig. 2 and Fig. 3, BAMP significantly suppressed the tumor growth as compared to other control groups without remarkable side effect (e.g. weight loss).

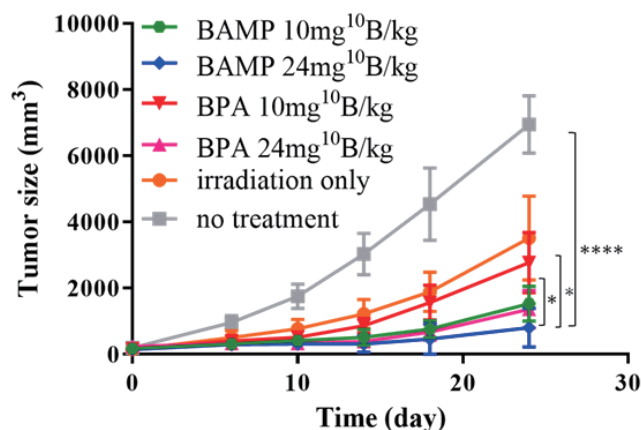


Fig.1) Anti-tumor effect of BNCT by BAMP. (BAMP 24mg<sup>10</sup>B/kg vs. BAMP 10mg<sup>10</sup>B/kg : \*, vs. BPA 10mg<sup>10</sup>B/kg : \*, vs. BPA 24mg<sup>10</sup>B/kg : ns, vs. irradiation only : \*, vs. no treatment : \*\*\*\*)

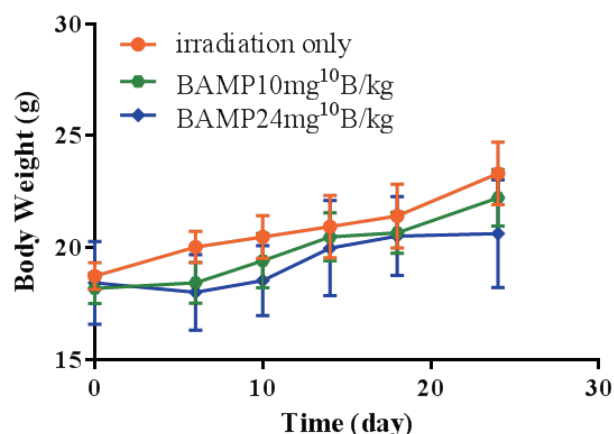


Fig.2) Body weight of mice after irradiation with the injection of BAMP.

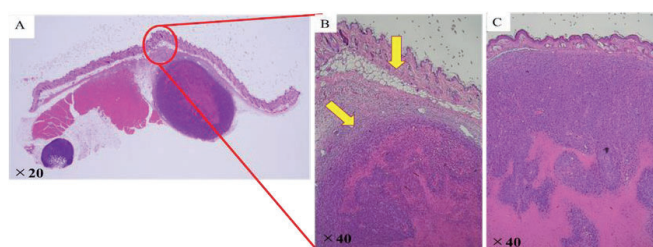


Fig.3) HE stained image of tumor including skin. (A) Image in the BAMP administration group with neutron irradiation after 24 days. (B) Enlarged image of A (x 40). (C) Image in neutron irradiation group without administration after 24 days.

### REFERENCES:

- [1] M. Shirakawa, H. Tomida, R. Takeuchi, H. Hori, Pa-tent applications 2018-156145.
- [2] M. Shirakawa, H. Tomida *et al.*, KURNS PROGRESS REPORT 2018, 55 (2019).

## PR3-16 Preparation and Characterization of BODIPY-Tethered Oligonucleotides for BNCT

K. Tanabe, M. Suzuki<sup>1</sup>, T. Nishihara and H. Yamashita

Department of Chemistry and Biological Science, College of Science and Engineering, Aoyama Gakuin University

<sup>1</sup>Institute for Integrated Radiation and Nuclear Science, Kyoto University

**INTRODUCTION:** Amphiphilic oligonucleotides with hydrophobic substituents have been widely used as functional materials, and a variety of them have important functions in biological control. For example, modifications of cell membranes, fusion of nanostructures such as liposomes, and gene manipulations have all been produced by these amphiphilic and functional oligonucleotides.

One of the most useful properties of these amphiphilic oligonucleotides is their aggregate formation that showed efficient cellular uptake and high level of biological stability within cells. In our recent studies, we demonstrated the successful delivery of the aggregate consisting of oligonucleotides into the cells to regulate the gene expression.<sup>1</sup>

In this study, we prepared oligodeoxynucleotides (ODNs) bearing hydrophobic and fluorescent BODIPY unit at uridine base (<sup>B</sup>U). We expected that the ODNs bearing BODIPY unit would form aggregate to be taken into the cells and express their cytotoxic effect upon irradiation of thermal neutron. Herein, we synthesize the ODNs and characterize their properties.

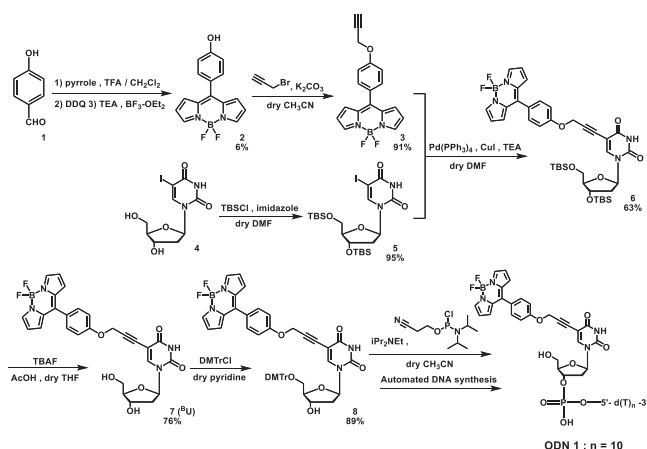
### EXPERIMENTS:

**Cellular experiments using ODNs bearing BODIPY unit.** ODN 1 (30 μM) were administered to the A549 cells and then the cells were incubated for 23 h. After incubation, the cells were irradiated (neutron, 1 MW) for 45 min at KUR. After incubation, WST 8 was added to the cells, and the cell viability assay was performed using Microplate Reader.

**RESULTS:** The synthesis of ODNs bearing <sup>B</sup>U is outlined in Scheme 1. Phenol group was introduced into BODIPY unit to give 2, which was alkylated by propargyl bromide under basic conditions. The resulting BODIPY derivative 3 and iododeoxyuridine 5 were coupled by Sonogashira reaction, and then the silyl groups were removed by treatment with TBAF. The uridine derivative 7 (<sup>B</sup>U) was tritylated and incorporated into DNA via phosphoramidite, using a DNA synthesizer. We prepared 10 mer oligodeoxynucleotides bearing one <sup>B</sup>U (ODN 1) at the 5'-end. The structures of ODNs was confirmed by MALDI-TOF mass spectrometry.

We then conducted cellular experiments with ODN 1 using a human cell line of lung adenocarcinoma, A549. A549 cells were incubated with the aggregates consisting of ODN 1 at a concentration that was sufficient to form aggregates, and the fluorescence emission of BODIPY

units from the cells was imaged by means of confocal microscopy. We observed robust emissions from all cells, indicating that the aggregates of ODNs were smoothly transported into cells.



**Scheme 1.** Synthesis of ODN 1.

Based on the above reaction characteristics, an attempt was also made to demonstrate the radiolytic onset of drug potency using A549 cells. We investigated the radiation-dependent cytotoxic effect of ODN 1 aggregates. After administration of ODN 1 aggregates to A549 cells and incubation for 23 h to allow penetration into the cells, the cells were exposed to the thermal neutrons for 45 min. As shown in Figure 1, negligible cytotoxic effect in the presence of 30 μM ODN 1, was observed. These results strongly indicate that the concentration of boron atoms in the cells are not enough to emerge their cytotoxic effects. Thus, the improvement of the drug delivery method is still challenging.

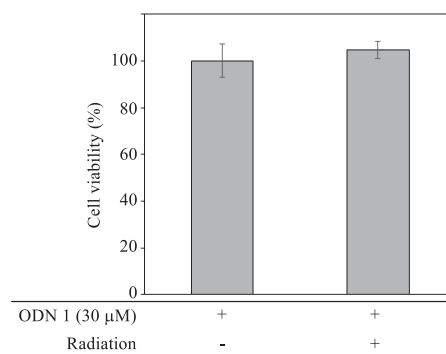


**Figure 1.** Cytotoxic effect of ODN 1 (30 μM) toward A549 cells upon thermal neutron irradiation (1 MW, 45 min).

### REFERENCES:

[1] K. Tanabe *et al.*, *ACS Applied Bio Materials* **2** (2019), 4456–4463.

## PR3-17 *In vivo* evaluation of BNCT for 5-FU resistant oral squamous cell carcinoma

K. Igawa, K. Tomizawa<sup>1</sup>, S. Wang<sup>2</sup>, A. Sasaki<sup>2</sup>, S. Ibaraki<sup>2</sup>, Y. Ichikawa, T. Takata<sup>3</sup>, M. Suzuki<sup>3</sup>

Neutron Therapy Research Center, Okayama University

<sup>1</sup> Faculty of life sciences, Kumamoto University

<sup>2</sup> Graduate School of medicine, Dentistry and Pharmaceutical Sciences, Okayama University

<sup>3</sup> Institute for Integrated Radiation and Nuclear Science, Kyoto University

**INTRODUCTION:** The incidence of oral squamous cell carcinoma (OSCC) is increasing gradually with aging society in Japan. In consideration of the preservation of organ function, as well as appearance, Boron Neutron Capture Therapy (BNCT) for head and neck cancer is one of the effective treatments instead of surgical procedures, radiotherapy, chemotherapy and combined therapy. OSCC is the most common malignant neoplasm of the oral cavity and has been treated with 5-fluorouracil (5-FU) as an anticancer drug. However, the acquisition of resistance to 5-FU is a major problem for successful cancer treatment. In this study, the effectiveness of BNCT for 5-FU resistance OSCC is evaluated.

**EXPERIMENTS:** 5-FU resistant oral squamous cell carcinoma cell line [2] were subcutaneously injected into the left hind legs of 6-week-old female Balb/c nude mice (Clea Japan Inc., Japan). Using L-boronophenylalanine (BPA, Katchem, Czech), fructose-BPA complex (200 mg/kg) was injected to the tumor bearing mouse before 40 minutes' irradiation. After neutron irradiation, the body weight and the diameter of tumor were measured. The tumor size was calculated according to the following formula.

Tumor volume [mm<sup>3</sup>] = (Long diameter [mm]) x (Short diameter [mm])<sup>2</sup> / 2

**RESULTS and DISCUSSION:** As shown in Fig. 1, BPA group showed significantly decrease in tumor size compared to non-boron group at 2 weeks after BNCT for 5-FU resistant SCC bearing mice. The mortality of 5-FU resistant SCC bearing mice is 80 % in non-boron group and 0 % in BPA group.

These results indicate that BNCT is effective to 5-FU resistant OSCC. Moreover, it is important to validate the BNCT for cisplatin resistant OSCC [3]. In near future, the multidisciplinary approach including BNCT is proposed for refractory OSCC.

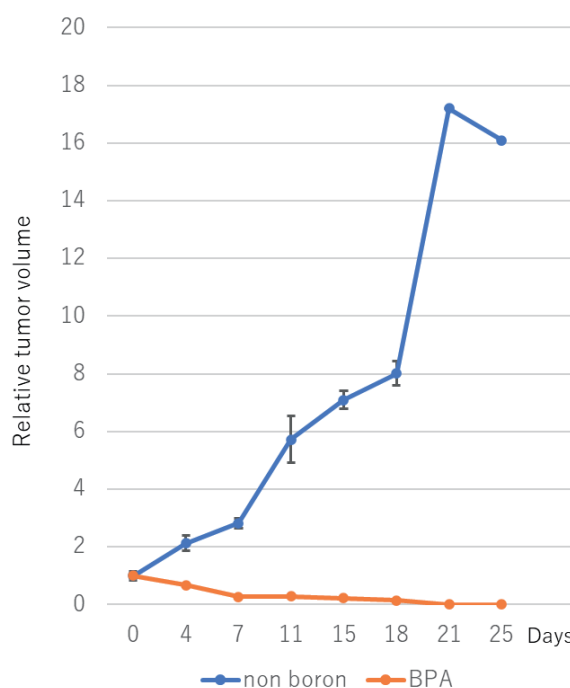


Fig. 1. Tumor growth ratio after thermal neutron irradiation with or without BPA (each group n=5) .

### REFERENCES:

- [1]Kato I, Fujita Y, Maruhashi A *et al.*, Effectiveness of boron neutron capture therapy for recurrent head and neck malignancies. *Appl Radiat Isot* 67(Suppl.):S37–S42, 2009.
- [2]Harada K, Ferdous T and Uneyama Y. Establishment of 5-fluorouracil-resistant oral squamous cell carcinoma cell lines with epithelial to mesenchymal transition changes *International Journal of Oncology* 44: 1302-1308, 2014.
- [3]Miyazaki H, Takahashi R, Vila M *et al.*, CD44 exerts a functional role during EMT induction in cisplatin-resistant head and neck cancer cells *Oncotarget*, Vol. 9, (No. 11), pp: 10029-10041, 2018.

## PR3-18 Anti-tumor evaluation of Gadolinium Neutron Capture Therapy through comparison of tumor size using Gd-DTPA-incorporated calcium phosphate nanoparticles

H. Xuan<sup>1,2</sup>, H. Yanagie<sup>1,3,4</sup>, M. Yanagawa<sup>5</sup>,  
Y. Sakurai<sup>3,4</sup>, K. Mouri<sup>3,4</sup>, N. Dewi<sup>3,4</sup>, H. Cabral<sup>2</sup>,  
S. Dowaki<sup>6</sup>, T. Nagasaki<sup>6</sup>, Y. Sakurai<sup>7</sup>, H. Tanaka<sup>7</sup>,  
M. Suzuki<sup>7</sup>, S. Masunaga<sup>7</sup>, and H. Takahashi<sup>1,2,3</sup>

<sup>1</sup>Dept of Nuclear Engineering & Management, School of Engineering, Univ of Tokyo, <sup>2</sup>Dept of Bioengineering, School of Engineering, Univ of Tokyo, <sup>3</sup>Cooperative Unit of Medicine & Engineering, Univ of Tokyo Hospital, <sup>4</sup>Nii-gata Univ of Pharmacy & Applied Life Sciences, <sup>5</sup>Obihiro Univ of Agriculture and Veterinary Medicine, <sup>6</sup>Osaka City University Graduate School of Engineering, <sup>7</sup>Kyoto Univ Institute for Integrated Radiation & Nuclear Science

### INTRODUCTION:

In our previous report, the anti-tumor effect of Gd-DTPA-incorporated calcium phosphate nanoparticles (Meo) was improved, and it had the possibility to be applied to the intensive cancer treatment in the future [1,2,3].

However, although the Gd-DTPA-incorporated calcium phosphate nanoparticle can bind tumor tissues through the EPR pathway, considering to improve the tumor targeting ability and drug accumulation in tumor, we introduced Arg-Gly-Aso(RGD), which is a peptides that can target many kinds of cancer cells through the integrin.

In this work, we checked the antitumor effect of this material again and focused on the change of the tumor size. We took the photos at the 30st day after irradiation to compare the antitumor effect of each samples.

### EXPERIMENTS:

Tumor-bearing mouse models were developed with colon 26 tumor cells and after synthesis of Meo and RGD binding Meo, they were injected into mice, respectively.

At the 24h after administration, these mice received thermal neutron irradiation at Nuclear Reactor Facility of Kyoto Univ Institute for Integrated Radiation & Nuclear Science with average neutron fluence of  $2.0 \times 10^{12}$  n/cm<sup>2</sup>. Moreover, considering the influence of neutron, the same samples were also injected into mice but without irradiation.

After almost one-month observation, the situation of all mice was recorded and the conclusion about antitumor effect was showed below according to the tumor size comparison photos.

### RESULTS:

In this experiment, tumor growth was suppressed in the groups of RGD sequence binding Meo nanomicelle and Meo nanomicelle compared with the non-irradiated groups with the injection of same DDS. In this time, the tumour decrease by RGD nanomicelle and Meo nanomicelle was almost same effect by NCT.

We will check the expression of integrin receptors in Colon 26 cancer cell line, and evaluate the uptake of Gd atoms in the cancer cells by endocytosis. We also evaluate

the possibility of RGD sequence binding Meo nanomicelle for clinical applications of NCT.

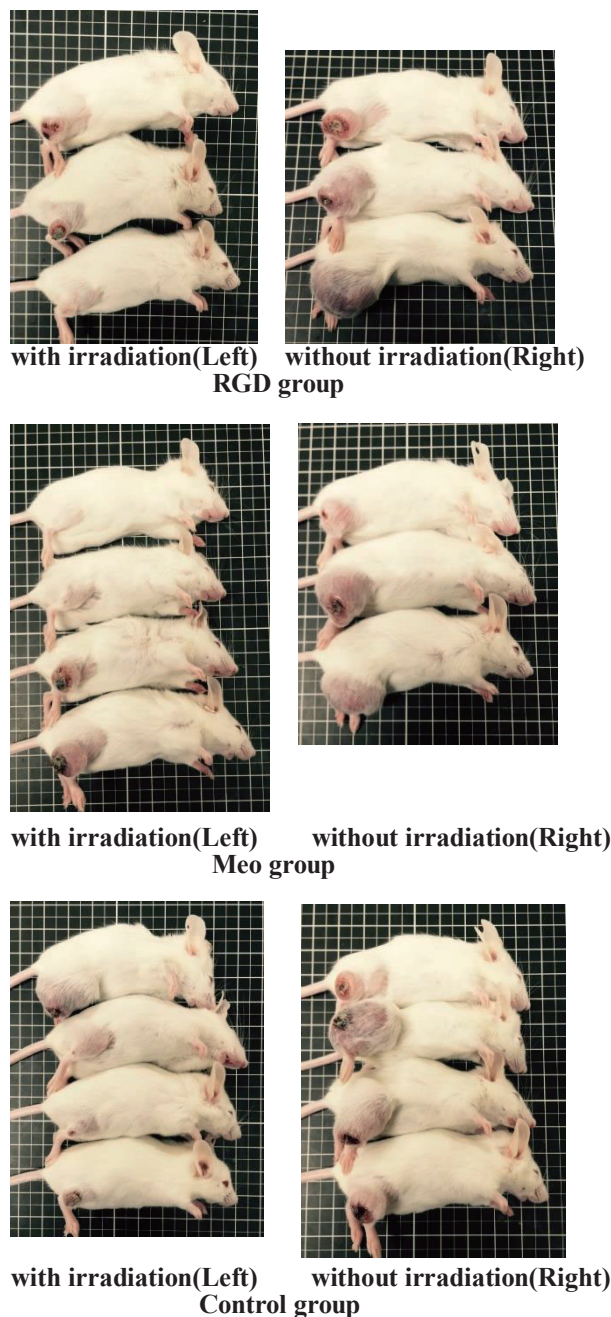


Figure 1. Tumor growth suppression by GdNCT using RGD-Meo / Meo nanomicelle.

### REFERENCES:

- [1] Dewi N *et al.*, Biomed & Pharmacother (2013) 67:451-7.
- [2] Dewi N *et al.*, J Can.Res.Clin.Oncol. (2016) 142(4):767-75.
- [3] Mi P *et al.*: J Cont. Release (2014) 174:63-71.

## **I-1. PROJECT RESEARCHES**

### **Project 4**

M. Suzuki and H. Yanagie<sup>1,2,3</sup>

*Institute for Integrated Radiation and Nuclear Science, Kyoto University*

<sup>1</sup>*Institute of Engineering Innovation, School of Engineering, The University of Tokyo,*

<sup>2</sup>*Cooperative Unit of Medicine & Engineering, The University of Tokyo Hospital,*

<sup>3</sup>*Research Institute of Healthy Living, Niigata University of Pharmacy & Applied Life Sciences,*

porous glass (SPG) membrane to the preparation of <sup>10</sup>BSH-entrapped WOW emulsion for clinical use. Details in this case report is referred to the P4-2 report.

An accelerator-based boron neutron capture therapy (BNCT) system and boronophenylalanine (BPA)-based new drug were approved by the Ministry of Health, Labour and Welfare of Japan for the treatment of locally unresectable recurrent or unresectable advanced head and neck cancer on March 2020. Since BNCT will be carried out at the medical institute, the accessibility of BNCT will improve dramatically and much greater patients will be treated with accelerator-BNCT compared with reactor-BNCT.

In 2019, under the Law on Clinical research\* (*rinsho kenkyu hou*), clinical researches on BNCT for local recurrent breast cancer and angiosarcoma have been approved.

\***Law on Clinical research (*rinsho kenkyu hou*)** New regulation on clinical research, Law on clinical Research (*rinsho kenkyu hou*), has come into effect since April in 2018. Clinical researches conducted by using Drugs and Medical Devices not approved under the Pharmaceutical and Medical Device LAW are categorized into Specified Clinical Research (*tokutei rinsho kenkyu*). Specified Clinical Research Plan should be reviewed by Certified Clinical Research Review Committee. Since BNCT is carried out using unapproved drug (boron compound) and research reactor, BNCT study is categorized into Specific Clinical Research. Six clinical researches on BNCT have been approved as Specific Clinical Research by Certified Clinical Research Review Committee established in medical institutes.

In this research projects, two researches are included.

**P4-1:** We treated one patient suffering from angiosarcoma of the face in this research program. Since the patient treated with BNCT in this research problem are under-observation, no detailed report is available.

**P4-2:** No patient was enrolled in this clinical research program. Yanagie et al. reported a preclinical study on syringe-shaped medical device attached with Shirasu

M. Suzuki, M. Iwamoto<sup>1</sup>, J. Sugawara<sup>2</sup>, S. Moriwaki<sup>3</sup>, H. Tanizaki<sup>3</sup>, K. Yoshida<sup>4</sup>, S. Kawabata<sup>5</sup>, S. Miyatade<sup>6</sup>, S. Masunaga, Y. Kinashi, H. Tanaka, Y. Sakurai, N. Kondo, Y. Tamari, T. Fujimoto<sup>7</sup>

*Institute for Integrated Radiation and Nuclear Science, Kyoto University*

<sup>1</sup>*Department of Breast and endocrine surgery, Osaka Medical Collage*

<sup>2</sup>*Department of Ophthalmology, Osaka Medical Collage*

<sup>3</sup>*Departement of dermatology, Osaka Medical College*

<sup>4</sup>*Department of Radiology Osaka Medical College*

<sup>5</sup>*Department of Neurosurgery, Osaka Medical College,*

<sup>6</sup>*Cancer center, Osaka Medical College*

<sup>7</sup>*Department of Orthopedic Surgery, Hyogo Cancer Center*

An accelerator-based boron neutron capture therapy (BNCT) system and boronophenylalanine (BPA)-based new drug were approved by the Ministry of Health, Labour and Welfare of Japan for the treatment of locally unresectable recurrent or unresectable advanced head and neck cancer on March 2020. Since BNCT will be carried out at the medical institute, the accessibility of BNCT will improve dramatically and much greater patients will be treated with accelerator-BNCT compared with reactor-BNCT. One of the drawbacks of BNCT is that thermal neutrons necessary for tumor control cannot be delivered to the deep portion of the tumor which is located at > 6 cm in depth from the skin surface.

For BNCT to be recognized as effective treatment modality for malignant tumor, expanding indication of BNCT is very important.

We treated one patient suffering from angiosarcoma of the face in this research program. Since the patient treated with BNCT in this research problem are under-observation, no detailed report is available.

## PR4-2 Preparation of Boron entrapped WOW emulsion by Mixing Medical Device for Boron Neutron Capture Therapy to Hepatocellular Carcinoma

Hironobu Yanagie<sup>1,2,3</sup>, Mitsuteru Fujihara<sup>4</sup>, Ryouji Mizumachi<sup>5</sup>, Yuji Murata<sup>5</sup>, Yuriko Sakurai<sup>1,2,3</sup>, Atsuko Shinohara<sup>6,7</sup>, Takehisa Matsukawa<sup>7</sup>, Ayano Kubota<sup>7</sup>, Yasuyuki Morishita<sup>8</sup>, Novriana Dewi<sup>3</sup>, Masashi Yanagawa<sup>9</sup>, Kazuhito Yokoyama<sup>7</sup>, Shushi Higashi<sup>10</sup>, Kouji Seguchi<sup>10</sup>, Ichiro Ikushima<sup>11</sup>, Yoshinori Sakurai<sup>12</sup>, Hiroki Tanaka<sup>12</sup>, Minoru Suzuki<sup>12</sup>, Shinichiro Masunaga<sup>12</sup>, Koji Ono<sup>13</sup>, Minoru Ono<sup>2,14</sup>, Jun Nakajima<sup>2,15</sup>, and Hiroyuki Takahashi<sup>1,2</sup>

<sup>1</sup>Institute of Engineering Innovation, School of Engineering, The University of Tokyo, <sup>2</sup>Cooperative Unit of Medicine & Engineering, The University of Tokyo Hospital, <sup>3</sup>Research Institute of Healthy Living, Niigata University of Pharmacy & Applied Life Sciences, <sup>4</sup>SPG Techno Ltd. Co., <sup>5</sup>LSI Medience Ltd Co, <sup>6</sup>The Graduate School of Seisen University, <sup>7</sup>Jyuntendo University, <sup>8</sup>Dept. of Human & Molecular Pathology, Graduate School of Medicine, The University of Tokyo, <sup>9</sup>Veterinary Medical Center, Obihiro University of Agriculture & Veterinary Medicine, <sup>10</sup>Dept. of Surgery, Kojin-kai Medical City East Hospital, <sup>11</sup>Dept. of Radiology, Miyakonojo Meteropolitan Hospital, <sup>12</sup> Kyoto Univ. Institute for Integrated Radiation & Nuclear Science, <sup>13</sup>Kansai BNCT Medical Center, Osaka Medical College, <sup>14</sup>Dept. of Cardiac Surgery, The University of Tokyo Hospital, <sup>15</sup>Dept. of Pulmonary Surgery, The University of Tokyo Hospital, JAPAN.

**INTRODUCTION:** Hepatocellular carcinoma (HCC) is one of the difficult cancers to cure with conventional treatment. Higashi et al prepared a long term inseparable Water-in-oil-in-water(WOW) emulsion for use in arterial injection therapy to treat patients with HCC by the double emulcificating technique[1]. Suzuki et al. had reported the tumor growth suppression by BNCT using boron compound with IPSO administered intra-arterially[2]. We performed preclinical BNCT study using <sup>10</sup>BSH entrapped WOW [3], and had experienced clinical BNCT study for HCC using this system[4].

In this study, we developed syringe-shaped medical device attached with Shirasu porous glass (SPG) membrane to the preparation of <sup>10</sup>BSH-entrapped WOW emulsion for clinical use, and evaluated the boron encapsulating activity to measure the <sup>10</sup>B concentrations of WOW emulsion by using ICP-Mas.

**EXPERIMENTS:** We developed the syringe-shaped medical device by attaching to SPG Millipore membrane. <sup>10</sup>BSH (262.5 mg) was dissolved in 1.5 ml of a 5% glucose solution, which was first filtered through an SPG controlled pore glass membrane and then emulsified in 1.5 ml IPSO containing surfactant to form the water-in-oil emulsion (WO). The WO emulsion was then emulsified again with an aqueous phase containing 3 ml

saline solution and surfactant through a second SPG controlled pore glass membrane using this medical device. The <sup>10</sup>B concentration in WOW vesicles was determined by ICP-AES of Jyuntendo University.

**RESULTS:** By using this device, we were able to produce the WOW emulsion of the same size even after changing the persons who perform the experiment more than ten times. About 7300 ppm <sup>10</sup>B concentrations were recognized in the <sup>10</sup>BSH-WOW emulsion as same as Day 0 and Day 1 after preparation using Mixing medical device (Table 1).

In the conventional preparation of WOW emulsion, the procedure takes about 6 hours. By using this device, we were able to prepare the WOW emulsion with the single peak of 100 μm in about 30 minutes.

Since WOW emulsion can deliver high amounts of <sup>10</sup>B to tumor as the first targeting delivery to tumor. We hope to develop the second targeting delivery to cancer cells with the increase of mechanism by endocytosis, fusion, etc.

**Table 1. <sup>10</sup>B concentration in <sup>10</sup>BSH-entrapped WOW emulsion prepared with Mixing medical device**

	<sup>10</sup> B	<sup>11</sup> B	<sup>10</sup> B	<sup>11</sup> B
<sup>10</sup> BSH-WOW	DAY0		DAY1	
1	6626.3	N.D.	7586.3	N.D.
2	7333.0	N.D.	7360.8	N.D.
3	7213.0	N.D.	6663.2	N.D.
4	7829.6	N.D.	7510.5	N.D.
5	7726.0	N.D.	7813.6	N.D.
Mean	7345.6		7386.9	
S.D.	478.0		436.3	
Lactose-WOW	DAY0		DAY1	
1	0.07	0.19	0.02	0.25
2	0.04	0.2	0.11	0.45
3	0.05	0.18	0.07	0.32
4	0.05	0.29	0.08	0.34
5	0.05	0.20	0.08	0.32
Mean	0.05	0.21	0.07	0.33
S.D.	0.01	0.04	0.03	0.07

**The original <sup>10</sup>B concentration (ppm) in WOW emulsion was determined using ICP-AES at Juntendo University.**

### REFERENCES:

- [1] S Higashi S *et al.*, Cancer, **75**(1995):1245–1254.
- [2] M Suzuki *et al.*, Jpn J Clin Oncol. **37**(2007):376- 81.
- [3] H Yanagie *et al.*, Br J Radiol.,doi: 10.1259/bjr.20170004.
- [4] H Yanagie *et al.*, Appl Radiat Isot., **88**(2014):32-7.

## **I-1. PROJECT RESEARCHES**

### **Project 5**

Y. Sakurai

*Institute for Integrated Radiation and Nuclear Science,  
Kyoto University*

#### BACKGROUNDS AND PURPOSES:

There are a number of subjects, which should be improved for the further advance and generalization of boron neutron capture therapy (BNCT). In the viewpoints of medical physics and engineering, the advance for dose estimation is one of the important subjects. The purposes of this project research are the advance for various dose estimation methods, and the establishment of an integrated system for dose estimation in BNCT.

In the third year of this research project, 2019, the advancement for the respective dose estimation methods were forwarded mainly using Heavy Water Neutron Irradiation Facility (HWNIF) and E-3 Neutron Guide Tube (E-3) at KUR, sequentially the previous year. In addition, the integrated system was considered for the simultaneous usage of several dose estimation methods.

#### RESEARCH SUBJECTS:

The collaboration and allotted research subjects (ARS) were organized as follows;

- ARS-1 (31P5-1):** Establishment of characterization estimation method in BNCT irradiation field using Bonner sphere and ionization chamber (III). (Y. Sakurai, S. Shiraishi, N. Matsubayashi, K. Okazaki, A. Sasaki, Y. Kumagai, T. Naito, T. Nakamura, Y. Kakimoto, H. Matsunaga, T. Takata and H. Tanaka)
- ARS-2 (31P5-2):** Study on new type of neutron spectrometer for BNCT. (A. Uritani, A. Ishikawa, K. Watanabe, S. Yoshihashi, A. Yamazaki and Y. Sakurai)
- ARS-4 (31P5-4):** Neutron measurement by using the self-activation of iodine-added plastic scintillators. (A. Nohtomi, Y. Hanada, G. Wakabayashi, Y. Sakurai and T. Takata)
- ARS-5 (31P5-5):** Characterization of active neutron detector for boron neutron capture therapy. (M. Takada, S. Endo, H. Tanaka, T. Matsumoto, A. Masuda, T. Nunomiya, K. Aoyama and T. Nakamura)
- ARS-6 (31P5-6):** Study for microdosimetry using silicon-on-insulator microdosimeter in the BNCT irradiation field (III). (Y. Sakurai, N. Ko, T. Takata, H. Tanaka, T. L. Tran, J. Davis, S. Guatelli, A. Rozenfeld, N. Kondo and M. Suzuki)
- ARS-7 (31P5-7):** Measurement of BNCT beam component fluence with polymer gel detector. (K. Tanaka, Y. Sakurai, T. Kajimoto, Y. Ito, H. Tanaka, T. Takata and S. Endo)
- ARS-8 (31P5-8):** Development of neutron fluence distribution measuring device using Thermoluminescence slabs. (K. Shinsho, R. Oh, M. Tanaka, S. Yanagisawa, H. Tanaka, T. Takata, G. Wakabayashi and Y. Koba)
- ARS-9 (31P5-9):** The study for development and application of tissue equivalent neutron dosimeter. (M. Oita, T. Kamomae, T. Takada and Y. Sakurai)
- ARS-10 (31P5-10):** Development and evaluation of 3D gel dosimeter for the measurement of dose distribution in BNCT. (S. Hayashi, Y. Sakurai, M. Suzuki and T. Takata)
- ARS-11 (31P5-11):** Establishment of beam-quality estimation method in BNCT irradiation field using dual phantom technique (III). (Y. Sakurai, T. Takata, H. Tanaka, N. Kondo and M. Suzuki)
- ARS-12 (31P5-12):** Characteristics test of a prompt gamma-ray detector using LaBr<sub>3</sub>(Ce) scintillator and 8×8 array MPPC for boron neutron capture therapy. (K. Okazaki, K. Akabori, T. Takata, S. Kawabata, Y. Sakurai and H. Tanaka)
- ARS-13 (31P5-13):** Development of fiber-reading radiation monitoring system with a red/infrared-emitting scintillator at <sup>60</sup>Co radiation facilities. (S. Kurosawa, S. Kodama, T. Takada, Y. Sakurai and H. Tanaka)
- ARS-14 (31P5-14):** Establishment of the imaging technology of 478 keV prompt gamma-rays of boron-neutron capture reaction and the measurement of the intensity of the neutron field. (T. Mizumoto, S. Komura, Y. Sakurai, A. Takada, T. Takata and T. Tanimori)
- ARS-15 (31P5-15):** Feasibility study of a gel-dosimeter for a quality assurance and a quality control in boron neutron capture therapy. (S. Nakamura, K. Iijima, M. Takemori, H. Nakayama, S. Nishioka, H. Okamoto, Y. Sakurai, H. Tanaka, T. Takata, M. Suzuki, H. Igaki and J. Itami)
- ARS-16 (31P5-16):** Optimization of bolus shape for boron neutron capture therapy using epi-thermal neutron beam. (T. Takata, H. Tanaka, A. Sasaki, Y. Sakurai, A. Maruhashi and M. Suzuki)
- ARS-17 (31P5-17):** Development of novel radiochromic gels for assessing 3-dimensional dose distribution in brain. (H. Yasuda, J.E. Tano, C.A.B. Gonzales and Y. Sakurai)
- ARS-18 (31P5-18):** Measurement of neutron distributions in the BNCT irradiation field using a GEM detector. (S. Uno, T. Koike, K. Miyamoto, K. Nobori and H. Tanaka)
- ARS-20 (31P5-20):** Development of epi-thermal neutron flux intensity detector for BNCT. (I. Murata, K. Aoki, Y. Miyaji, S. Kusaka, H. Tanaka, Y. Sakurai and T. Takada)
- ARS-21 (31P5-21):** Investigation of thermal neutron-induced soft errors in semiconductor devices. (H. Tanaka, T. Kato, H. Matsuyama, T. Takata and Y. Sakurai)

For ARS-3, no results were obtained because the insufficient neutron intensities of HWNIF for this subject. For ARS-19, the animal experiments at E-3 were originally planned but could not be performed, because the registration of E-3 as an animal experimental room was not in time. So, the reports of these subjects are not appeared.

## PR5-1 Establishment of characterization estimation method in BNCT irradiation field using Bonner sphere and ionization chamber (III)

Y. Sakurai, S. Shiraishi<sup>1</sup>, N. Matsubayashi<sup>1</sup>, K. Okazaki<sup>1</sup>, A. Sasaki<sup>1</sup>, Y. Kumagai<sup>1</sup>, T. Naito<sup>1</sup>, T. Nakamura<sup>1</sup>, Y. Kakimoto<sup>1</sup>, H. Matsunaga<sup>1</sup>, T. Takata, H. Tanaka

*Institute for Integrated Radiation and Nuclear Science,  
Kyoto University*

<sup>1</sup>*Graduate School of Engineering, Kyoto University*

<sup>2</sup>*Osaka Medical School*

**INTRODUCTION:** Research and development into several types of accelerator-based irradiation systems for boron neutron capture therapy (BNCT) is underway [1,2]. In the near future, BNCT using these newly developed irradiation systems may be carried out at multiple facilities across the world. Considering this situation, it is important that the estimations for dose quantity and quality are performed consistently among several irradiation fields, and that the equivalency of BNCT is guaranteed, within and across BNCT systems. Then, we are establishing the quality assurance and quality control (QA/QC) system for BNCT irradiation field.

As part of the QA/QC system, we are developing estimation method for neutron energy spectrum using Bonner sphere [3]. For our spectrometer using Bonner sphere, liquid such as pure water and/or boric acid solution is used as the moderator. A multi-layer concentric-sphere case with several sphere shells is prepared. The moderator and its diameter are changeable without entering the irradiation room, by the remote supply and drainage of liquid moderator in the several layers. For the detector, activation foils are remotely changed, or online measurement is performed using SOF (scintillator with optical fiber) detector containing boron, etc. [4].

In 2019, a prototype of the Remote-changeable Bonner-sphere Spectrometer (RBS) was made. An experiment was performed for the characteristic verification of the prototype RBS at Heavy Water Neutron Irradiation Facility of Kyoto University Reactor (KUR-HWNIF).

**METHODS:** In the neutron energy spectrometry by Bonner-sphere, the combinations of the moderator material and diameter should be previously decided and prepared. Of course, the more information can be obtained as the more moderators and detectors are prepared. However, the information number from those measured data is less than the combination number, because of the overlapped regions among the combinations. The selection is important, in which the more information number is obtained for the combination number.

The combination of moderator and detector is decided, for that the response functions cannot be approximated by the linear functions of the other response functions. The accuracy and precision for the spectrometry can be higher, because the independent information can be obtained from the measurement by the respective combinations. We were developed the selection method, High

Independence Selection (HIS) [5].

On the assumption of the application in the standard epi-thermal neutron irradiation mode of KUR-HWNIF, the combination of the moderators for boron-10 concentration and diameter was optimized by HIS. Based on this optimization, a configuration of an RBS was decided and a prototype of RBS was made. An experiment was performed for the characteristic verification of the prototype RBS in the standard epi-thermal neutron irradiation mode of KUR-HWNIF.

**RESULTS:** The configuration of the RBS was decided as follows. A five-layer concentric spherical acrylic shell is used as a container. Each acrylic wall is 1 mm in thickness. The moderator injection part is 9 mm in thickness for each layer. Pure water and 0.15-weight-percent boric acid water for boron-10 (45 g/l solubility for H<sub>3</sub>BO<sub>3</sub> at 20 degree Centigrade) were used as liquid moderators. A LiCaF scintillation detector is used.

Figure 1 shows an example of the optimized combination of moderator injection patterns for RBS. Photo 1 shows a prototype RBS, which was made based on the optimization. It was confirmed that the experimental results were in good agreement with the simulation results for the ratios of the detector responses for the respective moderator injection patterns.

**CONCLUSION:** We plan to further analyze the experimental data, and improve the prototype RBS.

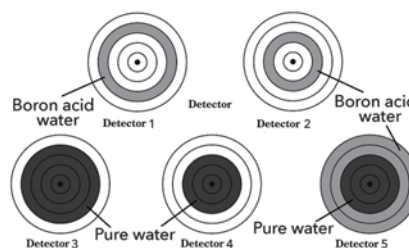


Fig. 1. An example of the optimized combination of moderator injection patterns for RBS.



Photo 1. A prototype RBS.

### REFERENCES:

- [1] H. Tanaka *et al.*, Nucl. Instr. Meth. B **267** (2009) 1970-1977.
- [2] H. Kumada *et al.*, Appl. Radiat. Isot. **88** (2014) 211-215.
- [3] H. Ueda *et al.*, Appl. Radiat. Isot. **104** (2015) 25-28.
- [4] M. Ishikawa *et al.*, Radiat. Oncol. **11** (2016) 105(1-10).
- [5] H. Ueda, Doctoral Thesis (2016).

A. Uritani, A. Ishikawa, K. Watanabe, S. Yoshihashi, A. Yamazaki and Y. Sakurai<sup>1</sup>

Graduate School of Engineering, Nagoya University  
<sup>1</sup> Institute for Integrated Radiation and Nuclear Science, Kyoto University

**INTRODUCTION:** Boron neutron capture therapy (BNCT) is a promising treatment method for cancers such as brain tumors. Recently, an accelerator-driven neutron source has actively been developed owing to its simplicity of management. In commissioning phase of the facilities, specifications of the irradiation field, such as neutron intensity, the neutron energy spectrum and gamma-ray contamination, should be characterized in order to assure designed ones.

We are developing a new neutron energy spectrometer using the optical fiber type detector. The conventional technique for neutron spectrometry is the Bonner sphere method. Generally, moderation based neutron spectrometers should be improved in energy response especially for epi-thermal neutron energy region. In order to improve the energy response, the number of detectors with different responses should be increased. We propose the spectrometer consisting of liquid moderator and thermal neutron flux profile scanner using the optical fiber type detector. So far, we has developed the optical fiber type detector showing a neutron peak in the pulse height spectrum [1]. The detector used the Eu:LiCaAlF<sub>6</sub> scintillator, which has relatively slow decay time of 1.6  $\mu$ s. In order to expand the dynamic range of the neutron detector, it is desired to use faster scintillator to improve the counting rate capability. As a fast neutron scintillator, the Li glass scintillator is well known. However, the light yield of the Li glass is quite low compared with the Eu:LiCaAlF<sub>6</sub> scintillator. Therefore, it was considered to be difficult to fabricate the optical fiber type detector showing a neutron peak.

**EXPERIMENTS:** We fabricated the optical fiber type neutron detector using Li glass scintillator. A small piece of the Li glass scintillator was mounted at a tip of the optical fiber. The scintillator was coated with a reflector powder and then covered with a heat shrink tube for light shielding. Figure 1 shows the fabrication procedure of the optical fiber type detector using the Li glass scintillator.

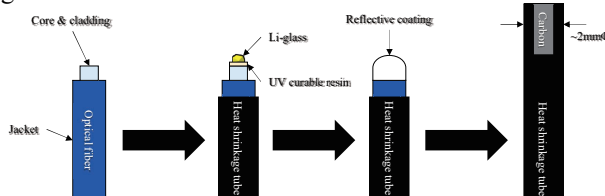


Fig. 1. Fabrication procedure of the optical fiber type detector using the Li glass scintillator.

First of all, we evaluated the detector response at the E3 port of the Kyoto University Reactor. And then, the fab-

ricated detector was irradiated with intense neutrons with the flux of  $4 \times 10^8$  n/cm<sup>2</sup>/s at Heavy Water Irradiation Facility of Kyoto University Reactor.

**RESULTS:** Figure 1 shows pulse height spectrum obtained from the fabricated optical fiber type detector using the Li glass scintillator. The detector shows a clear neutron peak. This is because a high NA optical fiber is used in the detector. The high NA optical fiber helps to efficiently collect scintillation photons from low light yield scintillator.

Figure 2 shows the time trend of the neutron peak channel during irradiation with intense neutrons with the flux of  $4 \times 10^8$  n/cm<sup>2</sup>/s. No significant deterioration of the signal gain was confirmed. Since the fabricated detector used the silica fiber, the detector is considered to show sufficient radiation hardness.

#### REFERENCES:

- [1] K. Watanabe *et al.*, Nuclear Instruments and Methods in Physics Research Section A, **802**, 1 (2015).

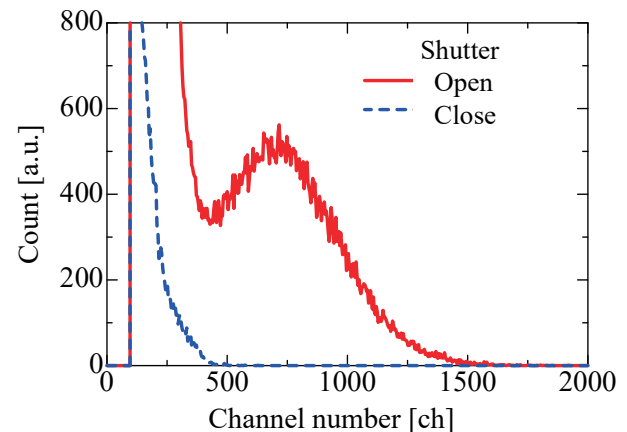


Fig. 2. Pulse height spectrum obtained from the optical fiber neutron detector using the Li glass scintillator.

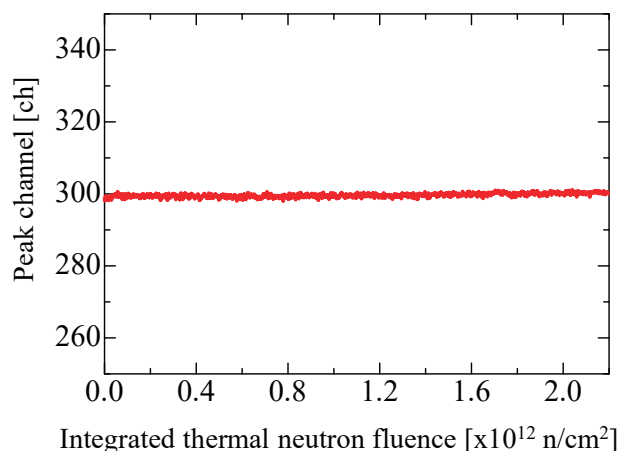


Fig. 3. Time trend of the neutron peak channel during irradiation with intense neutrons with the flux of  $4 \times 10^8$  n/cm<sup>2</sup>/s.

## PR5-3 Neutron measurement by using the self-activation of iodine-added plastic scintillators

A. Nohtomi, Y. Hanada, G. Wakabayashi<sup>1</sup>, Y. Sakurai<sup>2</sup> and T. Takata<sup>2</sup>

Graduate School of Medicine, Kyushu University

<sup>1</sup> Atomic Energy Research Institute, Kindai University

<sup>2</sup> Institute for Integrated Radiation and Nuclear Science, Kyoto University

**INTRODUCTION:** In our previous works, thermal neutron was measured by using the self-activation of iodine-containing inorganic scintillators such as NaI and CsI [1, 2]. The method is highly sensitive even for short time irradiation, but not appropriate for very intense neutron field like the BNCT treatment, because the tuning of sensitivity is not possible. Another drawback is the production of byproduct activity, <sup>24</sup>Na and <sup>134m</sup>Cs. In the present work, the applicability of iodine-added plastic scintillator was studied at rather intense neutron field like BNCT one of KUR irradiation facility

**EXPERIMENTS:** Iodine-added plastic scintillator was fabricated with an optical modeling type 3D printer (MiiCraft: MiiCraft Corp.). The base component was M211-B and PPO; small amount of Bis-MSB and Irgacure TPO are also mixed. In addition, iodobenzene (C<sub>6</sub>H<sub>5</sub>I) was added to the base material of plastic scintillator by 1 wt% and 0.1 wt% (Fig.1). Two plastic scintillators were irradiated at Rail Device of the Heavy Water Neutron Irradiation Facility with OO-0000F mode (1MW) [3]. Those scintillators were put at the Bismuth Surface (thermal neutron flux : ~10<sup>9</sup> n/cm<sup>2</sup>/s) during 10 seconds for 1 wt% scintillator and 100 seconds for 0.1 wt% one. After the termination of each irradiation, the output signal of scintillators was read out by PMT and MCA every one minute continuously.

**RESULTS:** Figure 2 shows pulse height distributions observed by the two iodine-added plastic scintillators: 1 wt% and 0.1 wt%. Reference spectrum of <sup>128</sup>I beta-rays is also indicated for comparison. Although iodobenzene is known one of the strongest chemical quenchers, the shift of pulse-height distribution towards low energy region is not so significant because the amount added to plastic scintillator is very small, but negligible.



Fig. 1. Appearance of iodine-added plastic scintillator. (diameter : 25 mm, height : 25 mm)

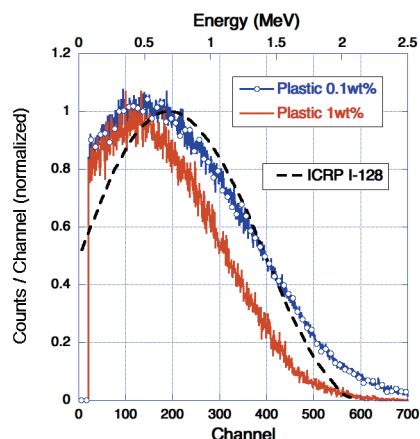


Fig. 2. Pulse height distributions observed by the iodine-added plastic scintillators.

Figure 3 shows decay curves of count rate observed by the iodine-added plastic scintillators. Only <sup>128</sup>I decaying components with half-life of 25 min are seen for both 1 wt% and 0.1 wt% scintillators. As clearly indicated in the figure, no byproduct radio-activity is produced. This property is very desirable for the application of iodine-added plastic scintillator to intense BNCT neutron field.

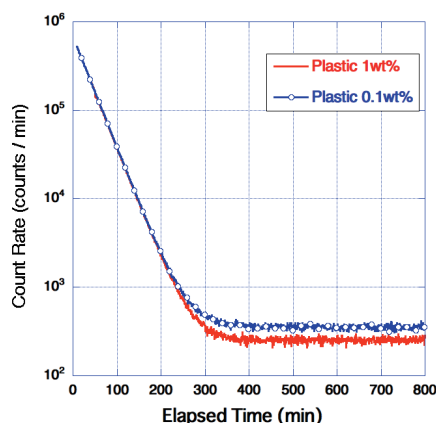


Fig. 3. Decay curves of count rate observed by the iodine-added plastic scintillators.

**ACKNOWLEDGEMENT:** This work was supported by JSPS KAKENHI Grant Number JP19K08202.

Dr. T. Kin and Mr. Y. Shinjyo of Kyushu University are deeply appreciated for their fabrication of iodine-added plastic scintillators.

### REFERENCES:

- [1] G. Wakabayashi *et al.*, Radiol. Phys. Technol., **8** (2015) 125-134.
- [2] A. Nohtomi *et al.*, JPS Conf. Proc., **24** (2019) 011041.
- [3] Y. Sakurai and T. Kobayashi, Nucl. Instr. and Meth., **A453** (2000) 569-596.

## PR5-4 Characterization of Active Neutron Detector for Boron Neutron Capture Therapy

M. Takada, S. Endo<sup>1</sup>, H. Tanaka<sup>2</sup>, T. Matsumoto<sup>3</sup>,  
A. Masuda<sup>3</sup>, T. Nunomiya<sup>4</sup>, K. Aoyama<sup>4</sup>, T. Nakamura<sup>4</sup>

Department of Applied Physics, National Defense  
Academy of Japan

<sup>1</sup>Graduate School of Engineering, Hiroshima University

<sup>2</sup>Institute for Integrated Radiation and Nuclear Science,  
Kyoto University

<sup>3</sup>National Metrology Institute of Japan, National Institute  
of Advanced Industrial Science and Technology

<sup>4</sup>Fuji Electric Co. Ltd.

**INTRODUCTION:** Boron Neutron Capture Therapy (BNCT) is a binary radiotherapy method developed to treat patients with certain malignant tumors. BNCT has been widely used at nuclear reactors. Recently, several accelerator-based BNCT facilities have been developed, or ready to clinical treatment for more accessible for patients. Intensity of neutron beam produced from the neutron accelerator could be varied with time due to instability of the accelerator condition and the neutron target degeneration. The neutron beam should be continuously measured in a real time.

The active neutron detector, which composes of thin silicon sensor with a 40  $\mu\text{m}$  thickness and ultra thin LiF neutron converter with around 0.1  $\mu\text{m}$  thickness, have been developed to measure the BNCT neutron beam. Using this neutron detector, intense neutron beam over  $1 \times 10^9 \text{ (cm}^{-2} \text{ s}^{-1})$  and high dose-rate gamma rays around 500 mGy/h were measured separately at the two BNCT facilities in KURNS (Institute for Integrated Radiation and Nuclear Science, Kyoto University) and NCC (National Cancer Research Center) [1-3]. Although it is said that the silicon detector is sensitive to neutron irradiation, no neutron damage have been observed.

At the NCC BNCT neutron facility, relative neutron depth distribution in an acrylic block was measured. The neutron detection efficiency is required to evaluate absolute neutron depth distribution. In this study, the detection efficiency of the real-time neutron detector for thermal neutron was experimentally obtained.

In the BNCT neutron beam, fast neutron component is included other than thermal neutrons. The patients could be affected by fast neutrons. The fast neutron component is preferred to be measured in addition to thermal neutron measurement. In this study, the fast neutron components were measured by exchanging the LiF neutron converter to polyethylene sheet. The 30- $\mu\text{m}$ -thick thin silicon sensor was applied to deduce another gamma sensitivity.

**EXPERIMENTS:** The neutron measurements were performed at the heavy water irradiation facility of research reactor of KURNS. The neutron detector was located in the center of neutron beam area. Signals from the neutron sensor were fed to a preamplifier outside of the irradiation room, and then, acquired using fast digital pulse-shaping processor. The thermal neutron beam fluxes and cadmium ratios are changed by opening a Cd

aperture slit at an upward of the irradiation location. Neutron flux at the irradiation position was, also, measured using gold neutron activation analysis. In the measurements of fast neutrons, the fast neutron detector was located at the same positions as the thermal neutron detector. The Cd slit was closed to decrease the thermal neutron flux. The thickness of depletion layer was changed with bias voltages.

**RESULTS:** The response functions normalized with the thermal neutron flux, which was evaluated from the gold neutron activation analysis, were obtained. The neutron peak in the response function is created by detecting triton events produced from the  $n\text{-}^6\text{Li}$  reaction. The detection efficiency for thermal neutron was experimentally obtained by integrating the neutron peak counts. The neutron detection efficiency was evaluated,  $3.5 \times 10^{-5} \text{ (cm}^{-2})$ . This results will be used to evaluate the absolute neutron depth distribution.

The pulse heights detecting the fast neutron were shown in **Fig.1**. The measurements show edges around 1100 ch, indicated by an arrow. Events from 500 ch to 1400 ch are created by detecting protons recoiled by fast neutrons at polyethylene converter. Black, red, and light green solid line show the measurement results, applying the bias voltage, -4, -0.5, and 0V, respectively. The -4 V voltage creates the thickest depletion layer. These edge positions are dependent on bias voltage, equivalent to thickness of depletion layer. Without polyethylene converter, this edge was not observed, shown as a blue solid line. From this result, fast neutron components in the BNCT neutron beam can be measured.

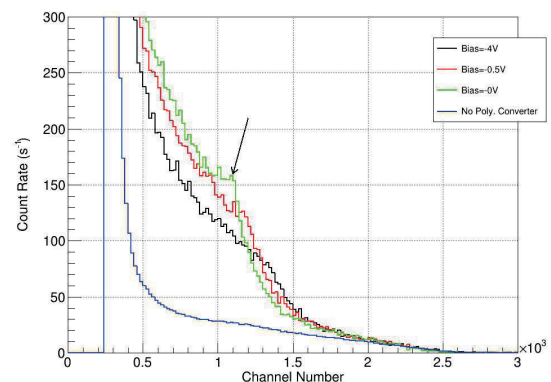


**Figure 1. Pulse heights detecting fast neutrons, using thin Si detector attached with a polyethylene neutron converter and applied with several bias voltages, compared to measurement without neutron converter.**

### REFERENCES:

- [1] M. Takada *et al.*, Radiat. Meas., 99, 33-54 (2017).
- [2] M. Takada *et al.*, Appl. Radiat. Isotopes (submitted).
- [3] M. Takada *et al.*, Radiat. Meas. (submitted).

Y. Sakurai<sup>1</sup>, N. Ko<sup>1,2</sup>, T. Takata<sup>1</sup>, H. Tanaka<sup>1</sup>, T. L. Tran<sup>3</sup>, J. Davis<sup>3</sup>, S. Guatelli<sup>3</sup>, A. Rozenfeld<sup>3</sup>, N. Kondo<sup>1</sup>, M. Suzuki<sup>1</sup>

<sup>1</sup>Institute for Integrated Radiation and Nuclear Science, Kyoto University

<sup>2</sup>Kansai BNCT Medical Center, Osaka Medical College

<sup>3</sup>Centre for Medical Radiation Physics, University of Wollongong

**INTRODUCTION:** Research and development into several types of accelerator-based irradiation systems for boron neutron capture therapy (BNCT) is underway [1,2]. In the near future, BNCT using these newly developed irradiation systems may be carried out at multiple facilities across the world. In contrast to conventional radiotherapy, the types of radiation present in BNCT consists of many distinct radiation components, each having a different biological weighting factor.

Microdosimetry is an effective dosimetry technique in a mixed radiation environment. Using this technique, it is possible to derive the relative contributions of different radiation modalities. The feasibility study of a novel 3D mesa bridge silicon-on-insulator microdosimeter (SIM) in BNCT [3], developed by University of Wollongong (UOW).

In 2019, a new design silicon microdosimeter and its use for dosimetry in boron neutron capture therapy (BNCT) were investigated by Monte Carlo simulation.

**METHODS:** Two detector configurations were investigated, based on the current 3D mushroom microdosimeter. The first structure consists of a cylindrical p<sup>+</sup> core electrode through the center of the SV with n<sup>+</sup> ring electrode wrapped around the outside of the SV. The second structure consists of a cylindrical n<sup>+</sup> core electrode through the center of the SV with p<sup>+</sup> ring electrode wrapped around the outside of the SV. Each SV has a diameter and height of 10 μm and the pitch between each individual SV is 40 μm to reduce cross talk between neighboring row of detectors. A total of 2500 individual SVs were connected in an array with odd and even detector row readout channels.

PHITS was used for this study. The T-deposit tally, which scores dose and event-by-event deposition energy distribution was used to calculate the energy deposited inside the SV of the mushroom microdosimeter. The microdosimetric spectrum (frequency mean and dose mean lineal energy distribution) were calculated by dividing the deposited energy by the average chord length of the SV. The detectors response to neutrons were investigated using the neutron source for the mixed neutron irradiation of Heavy Water Neutron Irradiation Facility installed in Kyoto University Reactor (KUR-HWNIF).

**RESULTS:** The deposit energy spectrum obtained with

the p<sup>+</sup> core and p<sup>+</sup> ring detector when irradiated by the mix irradiation mode of KUR-HWNIF are shown in Figs. 1 and 2, respectively. Higher events were observed with the p<sup>+</sup> ring detector, due to the larger surface area of the p<sup>+</sup> region (i.e. absolute number of <sup>10</sup>B atoms were larger). The dominant component was the 1.47 MeV alpha particle, followed by the 840 keV <sup>7</sup>Li ion. A small amount of recoil silicon was observed. The lineal energy was calculated and the yd(y) versus log(y) distribution was calculated, as shown in Fig. 3. From this spectrum, the p<sup>+</sup> core design had a higher lineal energy than the p<sup>+</sup> ring and the previous version microdosimeter (3D bridge).

**CONCLUSION:** It was confirmed that the new detector can accurately measure the lineal energy of alpha particles emitted from the <sup>10</sup>B(n,α)<sup>7</sup>Li reaction.

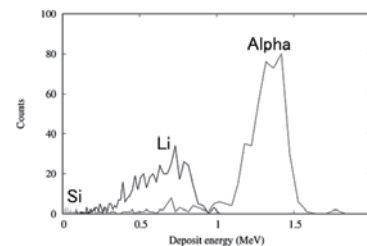


Fig. 1. Deposit energy spectrum for the p<sup>+</sup> core.

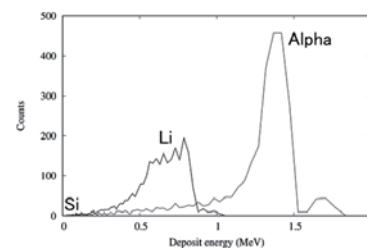


Fig. 2. Deposit energy spectrum for the p<sup>+</sup> ring.

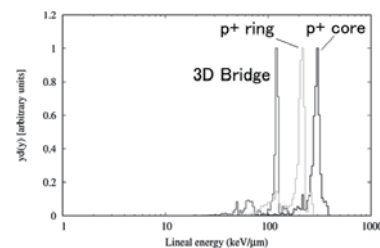


Fig. 3. Microdosimetric yd(y) spectrum of the p<sup>+</sup> core and p<sup>+</sup> ring detector, normalised to maximum.

#### REFERENCES:

- [1] H. Tanaka *et al.*, Nucl. Instr. Meth. B **267** (2009) 1970-1977.
- [2] H. Kumada *et al.*, Appl. Radiat. Isot. **88** (2014) 211-215.
- [3] L. T. Tran *et al.*, IEEE Trans. Nucl. Sci. **62** (2015) 3027-3033.

## PR5-6 Measurement of BNCT beam component fluence with polymer gel detector

K. Tanaka, Y. Sakurai<sup>1</sup>, T. Kajimoto, Y. Ito, H. Tanaka<sup>1</sup>,  
T. Takata<sup>1</sup>, S. Endo

Graduate School of Engineering, Hiroshima University  
<sup>1</sup> Institute for Integrated Radiation and Nuclear Science,  
Kyoto University

**INTRODUCTION:** Evaluation of dose is required for quality assurance in the irradiation field used for boron neutron capture therapy. This study investigated the use of the MAGAT polymer gel detector in the QA by estimation of dose and position resolution.

**EXPERIMENTS:** The experiment was performed with the standard epithermal neutron irradiation mode of KUR-HWNIF at 1 MW. The beam size was set to about  $120 \times 120 \text{ mm}^2$  using the collimator. The irradiation was performed for 2 minutes. The nominal value of the flux at the center of the collimator aperture was  $7.07 \times 10^6 \text{ cm}^{-2}\text{s}^{-1}$ ,  $1.33 \times 10^8 \text{ cm}^{-2}\text{s}^{-1}$  and  $1.38 \times 10^7 \text{ cm}^{-2}\text{s}^{-1}$  for thermal, epithermal and fast neutrons, respectively. The gamma ray flux was  $1.25 \times 10^7 \text{ cm}^{-2}\text{s}^{-1}$ .

In the experiments for the present study, the MAGAT-type gel detector was infused with LiCl, where the naturally abundant isotope  $^6\text{Li}$  was used. The  $^6\text{Li}$  concentrations were set at 0, 10 and 100 ppm. The dimension of the gel detector was  $60 \times 60 \times 60 \text{ mm}^3$ . The gel detector was encased in a box made of 5 mm thick acrylic acid resin. The box was set inside a  $200 \times 200 \times 200 \text{ mm}^3$  acrylic acid resin phantom, to simulate a human head in a brain tumor treatment.

The response of the MAGAT to dose was measured. The irradiation was performed by using Co gamma rays irradiation facility at Hiroshima University. The transverse relaxation rate ( $R_2$ ) was determined using a 0.3T MRI scanner (AIRIS II comfort, Hitachi Medical Corp.) with a standards head coil.

The fluence  $\phi_j$  of each component was determined using the following model;

$$S = \begin{pmatrix} S_1 \\ S_2 \\ S_3 \end{pmatrix} = \begin{pmatrix} a_{11} & a_{12} & a_{13} \\ a_{21} & a_{22} & a_{22} \\ a_{31} & a_{32} & a_{33} \end{pmatrix} \begin{pmatrix} \Phi_1 \\ \Phi_2 \\ \Phi_3 \end{pmatrix} = A \cdot \Phi \quad (1),$$

$$\Phi = A^{-1} \cdot S \quad (2),$$

where  $a_{ij}$  denotes the sensitivity of the  $i$ th gel for the component  $j$ .

**RESULTS:** The raw signal intensity of the gel detector is shown in Figure 1(a). The data in Figure 1 (a) was corrected so that all the gel detectors would have the same dose-response as the gel detector without  $^6\text{Li}$ , and the background signal intensity was subtracted. The corrected result is shown in Figure 1 (b). The data at the depths of 2.5 and 57.5 mm, which are within the regions 0 to 5 mm away from the wall of the acrylic

acid resin box, were omitted from further analysis since the oxygen penetrating the wall reduced the polymerization and thus the signal intensity.

The results for the two-component estimation are shown in Figure 2. In this case, both the gamma rays and thermal neutrons are positive. The standard deviation is about 2% for gold activation, 10% for TLD, and 0.5% for the PHITS calculation. The fluence distribution measured by the gel detector agrees to within 20% to 30% of other estimates. This suggests the potential usability of polymer gel detector in spatial measurement of fluence in BNCT beam.

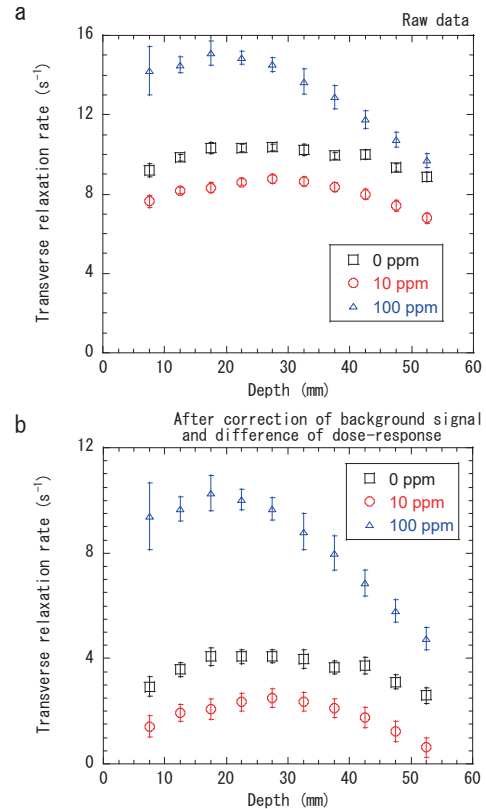


Fig. 1. Signal intensity ( $s^{-1}$ ), of the gel detector; (a) raw data, (b) after correction of background signal and difference of dose-response.

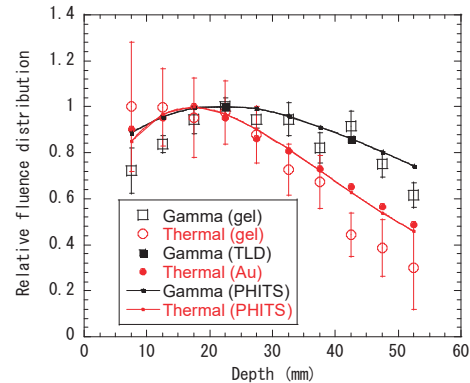


Fig. 2. Relative distribution of fluence estimated with two gel detectors with  $^6\text{Li}$  at 0 and 100 ppm.

K. Shinsho, R. Oh, M. Tanaka, S. Yanagisawa, H. Tanaka<sup>1</sup>, T. Takata<sup>1</sup>, G. Wakabayashi<sup>2</sup> and Y. Koba<sup>3</sup>

Graduate School of Human Health Science, Tokyo Metropolitan University

<sup>1</sup>Institute for Integrated Radiation and Nuclear Science, Kyoto University

<sup>2</sup>Graduate school of Science and Engineering Research, Kindai University

<sup>3</sup>Center for Radiation Protection Knowledge, QST-NIRS

**INTRODUCTION:** Boron Neutron Capture Therapy (BNCT) is one of the radiation therapies using neutrons and <sup>10</sup>B drugs which are attracted to tumors. BNCT is expected to be next-generation cancer therapy which will improve the QOL of patient because it is able to irradiate a cancer cell at the molecular level selectively. However, dosimetry techniques in mixed neutron-gamma fields have not been established yet. Therefore, we focused on reusable two-dimensional thermoluminescence dosimeter (2D-TLD). The 2D-TLD which we used is thermoluminescence (TL) phosphor Cr doped Al<sub>2</sub>O<sub>3</sub> ceramic plate (2-D Al<sub>2</sub>O<sub>3</sub>: Cr TLD).[1] 2-D Al<sub>2</sub>O<sub>3</sub>: Cr TLD that can acquire radiation images with high spatial resolution. In addition, it has high solidity and can be used under water. In this study, we investigated that neutron imaging using 2-D Al<sub>2</sub>O<sub>3</sub>: Cr TLD and Cd neutron-gamma ray converter technique in mixed neutron-gamma fields. The Cd neutron-gamma ray converter lets the sensitivity of the neutron increase selectively. As a result, we can acquire the neutron images easily without discrimination of gamma ray.

**EXPERIMENTS:** Low melting point Al<sub>2</sub>O<sub>3</sub> of Chibac ceramic MFG Co. LTD., which was composed of Al<sub>2</sub>O<sub>3</sub> > 99.5 wt% was used. The bulk density of the plates was 3.7g·cm<sup>-3</sup>. The dimensions used for the glow curve measurements were 10 × 10 × 0.7 mm<sup>3</sup>. The concentration of Cr<sub>2</sub>O<sub>3</sub> in the present study was 0.05 wt%. The assumed irradiation fields are the mixed neutron irradiation mode in KUR-HWNIF, with a power of 1MW. The glow curves were recorded from room temperature up to 400 °C at a heating rate of 0.1 °C·s<sup>-1</sup>. Fig.1 shows the Diagram of TLD irradiation arrangement for glow curve measurements. The Two - dimensional TL measurement system consists of a CMOS camera, 80 × 80 mm<sup>2</sup> heater, and a dark box. After exposure, the TL slabs were heated to 400 °C for 5 min. The TL images were captured using a CMOS camera equipped with a thermal cut filter.

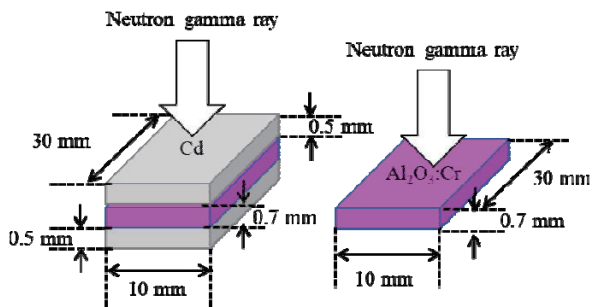


Fig.1. Diagram of TLD irradiation arrangement for glow curve measurements.

**RESULTS:** Figure2 shows the glow curve of Al<sub>2</sub>O<sub>3</sub>: Cr using Cd converter at mixed neutron irradiation mode in KUR-HWNIF. The glow peak of Al<sub>2</sub>O<sub>3</sub>: Cr was observed at 310 °C with and without Cd converter. In addition, the glow peak intensity was increased by installing the Cd converter. The TL sensitivity increased approximately 150 times using Cd converter. Table shows the relations between the thermal neutron fluencies and the γ- ray dose. The irradiation field contains gamma rays as well as neutrons, but the TL intensity of the TLD using the Cd converter is almost derived from neutrons.

Figure 3 shows the arrangement of TL slabs (Al<sub>2</sub>O<sub>3</sub>: Cr using Cd converter) irradiation arrangement for TL imaging and the TL image. We could take the thermal neutron image easily in the mixed neutron-gamma fields without to discriminate.

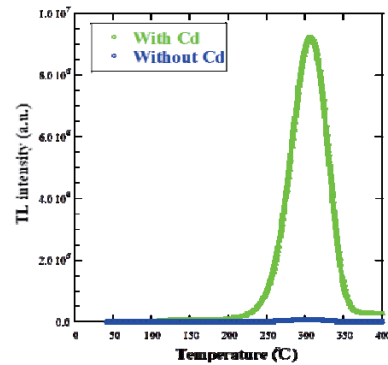


Fig.2. Glow curve of Al<sub>2</sub>O<sub>3</sub>: Cr using Cd converter at mixed neutron irradiation mode in KUR-HWNIF.

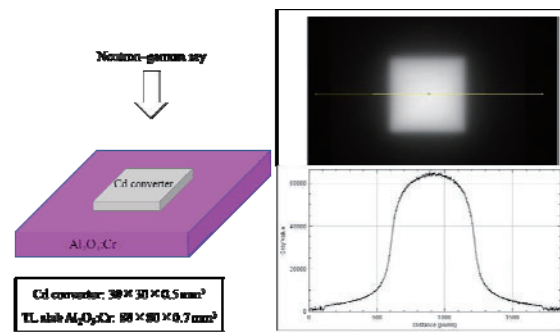


Fig.3. Left: Arrangement of TL slabs (Al<sub>2</sub>O<sub>3</sub>: Cr using Cd converter) irradiation arrangement for TL imaging. Right: TL image of the slab and the off axis ratio.

Table. Thermal neutron fluencies and γ- ray dose.

Thermal neutron fluencies[cm <sup>-2</sup> ]	Gamma-ray dose[Gy]
$7.2 \times 10^{15}$	0.61

**REFERENCES:** [1]K. Shinsho *et al.*, Sensors and Materials., 30 (2018) 1591-1.

## PR5-8 The Study for Development and Application of Tissue Equivalent Neutron Dosimeter

M. Oita, T. Kamomae<sup>1</sup>, T. Takata<sup>2</sup> and Y. Sakurai<sup>2</sup>

Graduate School of Interdisciplinary Science and Engineering in Health Systems, Okayama University

<sup>1</sup>Graduate School of Medicine, Department of Radiology, Nagoya University

<sup>2</sup>Institute for Integrated Radiation and Nuclear Science, Kyoto University

**INTRODUCTION:** Recent years, the clinical application of Accelerator-Based Boron Neutron Capture Therapy (AB-BNCT) has been introduced to make significant contributions to treatment for intractable cancer such as glioblastoma multiforme, superficial head and neck cancer, and melanoma in Japan.

In BNCT, the boron ( $n,\alpha$ )-reaction of the isotope  $^{10}\text{B}$  has a high cross-section toward thermal neutrons, and the produced alpha and lithium particles have a short-range on the micrometer scale. However, the neutron spectrum always spans a broad energy range, which results in different dose distribution and biological effects in tissue. A radiochromic film (RCF) is one of the most useful dosimetry tools in the advantages of high spatial resolution, small energy dependence, tissue equivalence, and self-development without processing in a darkroom<sup>1-3</sup>. The hydrogel material is also expected to use for a patient bolus in clinical radiotherapy<sup>4</sup>. In this work, the authors have developed new nanocomposite hydrogel for BNCT, which is highly expected to use for a patient bolus in clinical BNCT. Moreover, the hydrogel can improve dose distribution as well as can be manufactured arbitrary size and thickness using a 3D printer. Therefore, we have investigated to develop a system that enables dose optimization by optimally modulating the neutron beam for each patient using the hydrogel and RCFs.

**EXPERIMENTS:** Firstly, a reflective-type RCF, GAFCHROMIC® EBT3 (Ashland Inc., Wayne, NJ, USA) using a KUR neutron source was evaluated in this study. For irradiation,  $1.0 \times 1.0 \text{ cm}^2$  pieces of the RCF were placed at a depth of 0 cm to 24.2 cm in the air, water with 50ppm of boron, and water using the standard epithermal neutron irradiation mode of the Heavy Water Neutron Irradiation Facility at Kyoto University Research Reactor (KUR-HWNIF). Then, to assess the shielding effect of the 3D printed hydrogel for neutron beam, test slabs were fabricated. The thickness and clay nanoparticles concentration of the test slabs were varied from 2.5 to 5.2 wt%, respectively. The irradiation experiment was performed using KUR-HWNIF. Gold wires were used to estimate the neutron flux at the entrance and exit plane of the test slabs. Thermo-luminescent dosimeters

were used for the estimation of gamma-ray doses. The measured data were normalized by the values at the entrance plane of the test slabs.

**RESULTS:** Fig.1 shows the change of relative pixel values of RCFs irradiated by the KUR- HWNIF neutron source. Further analysis was needed for the response of RCFs with neutron components and contributions of gamma rays using Monte Carlo simulation and additional experiments with a cadmium filter. Fig. 2 shows a depth neutron flux and gamma-ray distribution with a change in the clay nanoparticles concentration (left: 2.6 wt%, right: 5.2 wt%). The results showed that the influence of NC gel was mainly the neutron thermalization (Epithermal neutrons loss their kinetic energy). The influence of the change in the clay nanoparticles concentration was almost unconfirmed. These phenomena would be affected by the buildup of neutron and gamma-ray doses. Our results demonstrated the feasibility of utilizing the 3D printed compensator to modulate the neutron beam intensity for clinical BNCT.

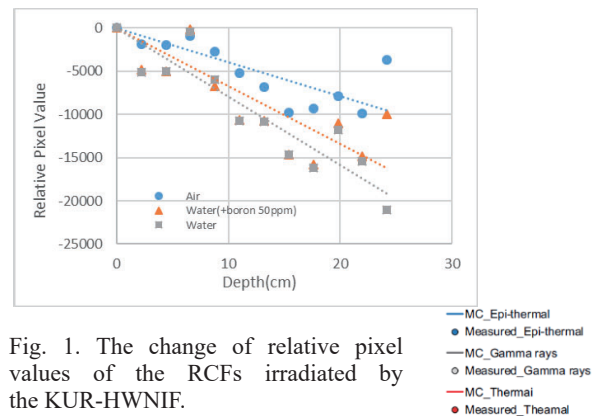


Fig. 1. The change of relative pixel values of the RCFs irradiated by the KUR-HWNIF.

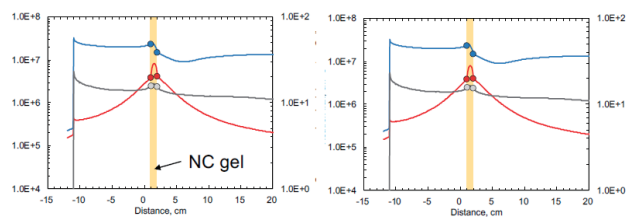


Fig. 2. Depth neutron flux and gamma-ray distribution with change in the clay nanoparticles concentration. (left: 2.6 wt%, right: 5.2 wt%)

### REFERENCES:

- [1] Niroomand-Rad, Azam *et al.*, Medical physics **25** (1998), 2093-2115.
- [2] Borca, Valeria Casanova *et al.*, Journal of applied clinical medical physics **14** (2013).
- [3] Fiandra, Christian *et al.*, Medical physics **40** (2013).
- [4] K Tanaka, Y Sakurai *et al.*, Applied Radiation and Isotopes **127** (2017), 253-259.

S. Hayashi, Y. Sakurai<sup>1</sup>, M. Suzuki<sup>1</sup>, and T. Takata<sup>1</sup>

Department of Clinical Radiology, Hiroshima International University

<sup>1</sup> Institute for Integrated Radiation and Nuclear Science, Kyoto University

**INTRODUCTION:** Three-dimensional (3D) gel dosimeters have been investigated for the 3D dose measurement of the complex conformal dose distributions in the clinical applications [1]. These devices utilize radiation-induced chemical reactions in the gel to preserve information about the radiation dose. The 3D absorbed dose distribution is deduced from the distribution of the reactant measured by imaging modalities, such as MRI, X-ray and optical computed tomography (CT). The applications to neutron irradiation have been also investigated, and the potential as a 3D dosimeter has been suggested [1].

Recently, we developed a novel radiochromic gel dosimeter that utilizes red color development due to the complexation of polyvinyl alcohol (PVA) with iodide ( $I_3^-$ ) formed in an aqueous solution by irradiation [2]. This gel dosimeter has excellent dose properties such as high sensitivity, dose rate independence, and a wide dose range, on X- and gamma-rays.

In this preliminary study, the optical-dose-response of the novel PVA-I (PVA-GTA-I) gel dosimeters [3] containing boron and lithium in the irradiation of neutron beams with different energy spectra from a nuclear reactor was examined and its availability was investigated.

**EXPERIMENTS:** As sensitizers, boric acid,  $B(OH)_3$ , containing  $^{10}B$  of 20% naturally, and lithium sulfate,  $Li_2SO_4$ , containing  $^6Li$  of 100% approximately, were added into the standard PVA-GTA-I gel, respectively. The concentrations in the gel were approximately 25, 50 mM of  $^{10}B(OH)_3$ , and 10, 20 mM of  $^6Li_2SO_4$ . The resulting solution was subdivided by pouring into PMMA cuvettes (4.5 mL, 1 cm path length).

The neutron irradiations were performed using Heavy Water Neutron Irradiation Facility (HWNIF) of Kyoto University Research Reactor (KUR, power of 1 MW). The samples were irradiated at 1, 2, 3, and 4 cm depths from surface in air at room temperature. The three different modes (thermal neutron rich for 30 min, epi-thermal and fast neutron rich for 50 min, and the mixed modes for 10 min) of neutron beams made by

heavy water spectrum shifter and cadmium thermal-neutron filters were applied to the samples.

The measurements were performed at room temperature using a UV-Vis spectrophotometer (SHIMADZU, UV-1600PC, Japan). The change in the absorbance ( $\Delta Abs.$ ) at the peak wavelength (486 nm) was investigated as the dose-response.

**RESULTS:** As examples, Figures 1(a) and 1(b) show that the depth-absorbance profiles obtained from our PVA-GTA-I gel dosimeters containing boron and lithium exposed to neutron beam of the epi-thermal and fast mode, respectively.

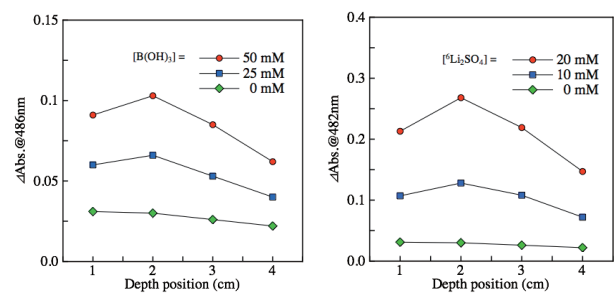


**Figure 1** Depth-absorbance distributions in epi-thermal and fast neutron mode of gel dosimeters with (a) boron and (b) lithium from the phantom surface.

The broad peaks were observed around 2 cm of depth in both dosimeters. The changes increased with the concentration of sensitizers. It is suggested that the peaks correspond to the distribution of the thermal neutron due to the moderation of epi-thermal neutron. It is noteworthy that the effect of lithium is larger than that boron in spite of the difference in their concentrations and absorption cross-sections. The effect was also observed in the other spectra modes.

These results suggest that both boron and lithium work as effective sensitizers on the thermal neutron in the PVA-I gel dosimeters.

#### REFERENCES:

- [1] C. Baldock *et al.*, *Phys. Med. Biol.* **55** (2010) R1–63.
- [2] S. Hayashi *et al.*, *Radiat. Meas.* **131** (2020) 106226.
- [3] J. E. Taño *et al.*, *Radiat. Meas.* (in press) (2020) 106311.

# PR5-10 Establishment of beam-quality estimation method in BNCT irradiation field using dual phantom technique (III)

Y. Sakurai, T. Takata, H. Tanaka, N. Kondo, M. Suzuki

*Institute for Integrated Radiation and Nuclear Science,  
Kyoto University*

**INTRODUCTION:** Research and development into several types of accelerator-based irradiation systems for boron neutron capture therapy (BNCT) is underway [1,2]. Many of these systems are nearing or have started clinical trials. Before the start of treatment with BNCT, the relative biological effectiveness (RBE) for the fast neutrons (over 10 keV) incident to the irradiation field must be estimated.

Measurements of RBE are typically performed by biological experiments with a phantom. Although the dose deposition due to secondary gamma rays is dominant, the relative contributions of thermal neutrons and fast neutrons are virtually equivalent under typical irradiation conditions in a water and/or acrylic phantom. Uniform contributions to the dose deposited from thermal and fast neutrons is based in part on relatively inaccurate dose information for fast neutrons.

The aim of this study is the establishment of accurate beam-quality estimation method mainly for fast neutrons by using two phantoms made of different materials, in which the dose components can be separated according to differences in the interaction cross-sections. The fundamental study of a “dual phantom technique” for measuring the fast neutron component of dose is reported [3].

In 2019, verification experiments for the dual phantom technique were performed using Heavy Water Neutron Irradiation Facility installed in Kyoto University Reactor (KUR-HWNIF). Biological experiments were performed using the solid phantoms, which were made based on the simulation results in 2018.

**METHODS:** One of the dual solid phantoms was made of polyethylene with natural lithium fluoride for 30 weight percent (LiF-polyethylene phantom), and the other phantom was made of polyethylene with 95%-enriched lithium-6 fluoride for 30 weight percent (<sup>6</sup>LiF-polyethylene phantom).

Vials containing one kind of human brain cell, such as U87ΔEGFR, were placed at the surface, 2-cm depth, 5-cm depth and 8-cm depth in the phantoms on the center axis of the beam line. Cell growth assay was performed for the irradiated cells.

The neutron flux and gamma-ray dose rate along the central axis in the phantoms were measured using activation foils and thermo-luminescent dosimeter, respectively. The depth dose distributions for the thermal neutron, fast neutron and gamma-ray components were determined based on the simulation calculation results normalized referring to the measured values.

Figure 1 shows a schematic of the experimental setup.

**RESULTS:** Figures 2 and 3 show the depth distributions for the thermal neutron dose, fast neutron dose, gamma-ray dose, and total dose in the LiF-polyethylene phantom and the <sup>6</sup>LiF-polyethylene phantom, respectively. It was confirmed that the dose contribution of fast neutrons is improved from approximately 10% in the LiF-polyethylene phantom, to approximately 50% in the <sup>6</sup>LiF-polyethylene phantom.

**CONCLUSION:** The assay results are presently being analyzed in association with the data of the depth dose distribution for the thermal neutrons, fast neutrons and gamma-rays. The biological experiments using the other cell lines are under planning.

**ACKNOWLEDGMENT:** This work was supported by JSPS KAKENHI Grant Number JP 16H05237.

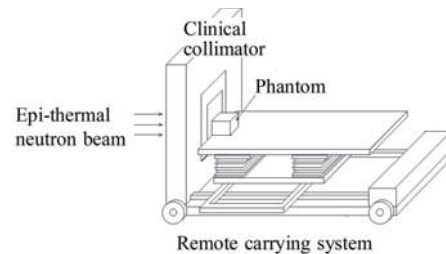


Fig. 1. A schematic of the experimental setup.

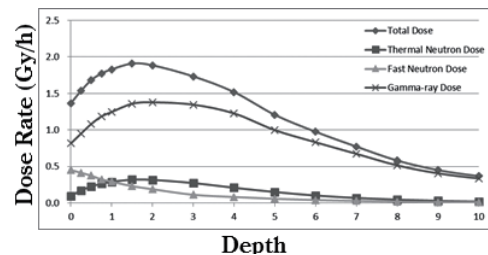


Fig. 2. Depth dose distributions in the LiF-poly phantom.

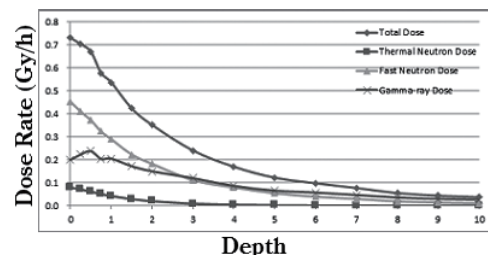


Fig. 3. Depth dose distributions in the <sup>6</sup>LiF-poly phantom.

## REFERENCES:

- [1] H. Tanaka *et al.*, Nucl. Instr. Meth. B **267** (2009) 1970-1977.
- [2] H. Kumada *et al.*, Appl. Radiat. Isot. **88** (2014) 211-215.
- [3] Y. Sakurai *et al.*, Med. Phys. **42** (2015) 6651-6657.

## PR5-11 Characteristics test of a Prompt Gamma-ray detector using LaBr<sub>3</sub>(Ce) Scintillator and 8 x 8 Array MPPC for Boron Neutron Capture Therapy

K. Okazaki, K. Akabori<sup>1</sup>, T. Takata<sup>2</sup>, S. Kawabata<sup>3</sup>, Y. Sakurai<sup>2</sup>, H. Tanaka<sup>2</sup>

Graduate School of Engineering, Kyoto University

<sup>1</sup>Sumitomo Heavy Industries

<sup>2</sup>Institute for Radiation and Nuclear Science, Kyoto University

<sup>3</sup>Osaka Medical College

**INTRODUCTION:** Boron neutron capture therapy (BNCT) is employed to treat cancer cells using a <sup>10</sup>B compound and a neutron beam. Basically, the range of the heavy particles, which are produced by the (n,  $\alpha$ ) reaction between <sup>10</sup>B and thermal neutrons, is shorter than the diameter of a cell. A <sup>10</sup>B compound accumulates <sup>10</sup>B into tumor cells, and into normal cells slightly. To determine the prescript dose during the treatment, it is necessary to measure the <sup>10</sup>B concentration in tumor and normal tissue in real-time. At present, it is obtained using a high purity germanium detector with prompt gamma-ray analysis at the Institute for Integrated of Radiation and Nuclear Science, Kyoto University Integrated for Radiation and Nuclear Science (KURNS)[1,2]. However, this method is not able to attain the <sup>10</sup>B concentration during the irradiation. Thus, a prompt gamma-ray imaging detector system has been developed. It consists of a LaBr<sub>3</sub>(Ce) scintillator and an 8 x 8 channel multi-pixel photon counter (MPPC), 64 channels amplifiers, a shaper and analog-to-digital converters (ADCs). This paper reports the concept underlying this system and the results of characterizing this system.

**EXPERIMENTS:** The size of the LaBr<sub>3</sub>(Ce) scintillator was 50 mm x 50 mm x 10 mm[3]. The scintillator was put in front of an 8 x 8 array MPPC. An MPPC is a type of silicon photomultiplier, and the effective active area of one channel of an MPPC is 6 x 6 mm<sup>2</sup>. The outputs of 64 channels were fed to an amplifier unit. The 64 analog outputs were digitalized by ADCs. These digital signals were stored in a PC. Firstly, gain in each channel of the MPPC was adjusted. Secondly, gamma ray spectra from an Na-22 source, which emitted 511 keV gamma rays, were attained in order to confirm that the energy resolution at 511 keV. Finally, gamma ray spectra using samples with 25 and 50 ppm were obtained by irradiating thermal neutrons at the Kyoto University Reactor neutron guide tube. To discriminate between 478 keV and 511 keV gamma rays, the Gaussian distribution for the two gamma rays was defined.

**RESULTS:** The average energy resolution of this detector system at 511 keV gamma rays was approximately 5.0 $\pm$ 0.2 %. Fig.1 shows the spectrum at the center channel of the MPPC obtained with 25 ppm and the region of interest (ROI) in the Gaussian distribution for 478 keV gamma rays set up as  $-3\sigma$  to the median. In addition, the count rate of 478 keV gamma rays with 25 and 50 ppm samples were calculated in the ROI. Moreover, gamma

ray peak at 511 keV did not overlap 478 keV peak so much. The count rate of 478 keV gamma rays with 25 ppm sample in the ROI was 0.23 that was sufficient to obtain counts to be below 10 % statistic error within an hour. In addition, the linearity of the count rate at 478 keV gamma rays and <sup>10</sup>B concentration was confirmed as shown as Fig. 2.

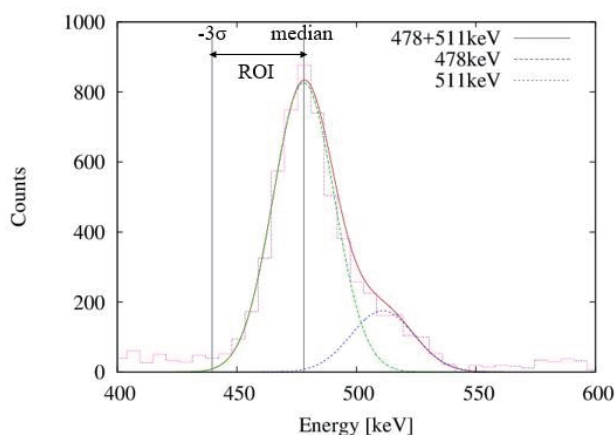


Fig. 1. Gamma rays spectrum at the center channel with 25 ppm.

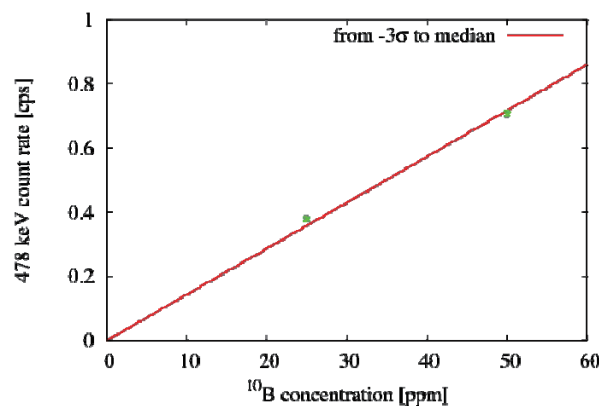


Fig. 2. The linearity between <sup>10</sup>B concentration and 478 keV count rate.

### REFERENCES:

- [1] T. Kobayashi and K. Kanda, Nucl. Instruments Methods Phys. Res., vol. 204, pp. 525-531, 1983.
- [2] J. Laakso, M. Kulvik, I. Ruokonen, and J. Va, Clin. Chem, vol 47, No. 10, pp. 1796-1803, 2001.
- [3] E. V. D. van Loef, P. Dorenbos, C. W. E. van Eijk, K. Krämer, and H. U. Güdel, Appl. Phys. Lett., vol. 1573, pp. 1-4, 2013.

S. Kurosawa<sup>1,2</sup>, S. Kodama<sup>2</sup>, T. Takada<sup>3</sup>, Y. Sakurai<sup>3</sup>, H. Tanaka<sup>3</sup>

<sup>1</sup>New Industry Creation Hatchery Center, Tohoku University

<sup>2</sup>Institute for Materials Research Tohoku University

<sup>3</sup>Institute for Integrated Radiation and Nuclear Science, Kyoto University

**INTRODUCTION:** In the extremely high radiation dose condition such as inside of nuclear powerplant after the accident (decommissioning), a real-time-remote radiation-monitor is required to survey the internal condition. To avoid the radiation damage of the detectors or circuits, the use of a long silica optical fiber (over ~100-m-length) is proposed to read scintillation photons from the high dose condition [1] as shown in Fig. 1. To detect the scintillation photons efficiently through such a long optical fiber, high-light output and red- or NIR-emitting scintillators are suitable than blue or yellow photons to suppress the transmission loss.

We suggest to apply our developed red-emitting scintillator  $\text{Cs}_2\text{HfI}_6$  (CHI) to the fiber-read radiation monitor for the decommissioning. CHI has a broad scintillation emission from 500 nm up to 800 nm with a peak at around 700 nm, a short decay time of ~1.9  $\mu\text{s}$  among the red-phosphors and high light output of 64,000 photons/MeV [2]. In this study, we demonstrated such fiber-reading systems under the high-dose condition at the  $^{60}\text{Co}$  Gamma-ray Irradiation Facility in Institute for Integrated Radiation and Nuclear Science, Kyoto University.

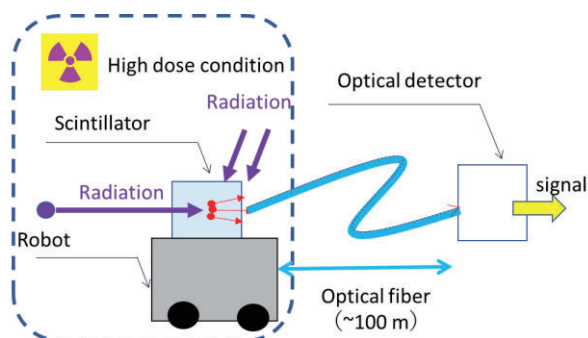


Fig. 1. Schematic view of real-time dose monitor.

**EXPERIMENTS:** We prepared a small CHI piece with a size of 2 mm x 3 mm x 1 mm by Bridgeman method. Due to hygroscopic nature, CHI was embedded in the optical cement (BC-600, Saint-Gobain Crystal) with a size of 3 mm x 4 mm x 1.5 mm. The CHI-cement sample was irradiated with gamma-rays from a  $^{60}\text{Co}$  source with an activity of ~100 TBq, and the gamma-ray air dose rates at certain points on the experimental apparatus were estimated by Sato et al. [3]. Also, we fabricated Cr-doped  $\alpha\text{-Al}_2\text{O}_3$  sample (Ruby) with the same size and shape including the cement as that of CHI to compare the scin-

tillation photons.

The CHI and ruby-cement specimens were put on the tip of an optical fiber (S.600/600B, Fujikura) with a length of 20 m and pure  $\text{SiO}_2$  core diameter of  $600 \pm 30 \mu\text{m}$ . The scintillation light was transmitted through the fiber and measured with a CCD spectrometer (Blue-UVNb, StellarNet). We determined the scintillation signal intensity from the emission spectrum: integration of the emission area. The exposure time of the CCD camera was 5 sec for one time, and the measurements were repeated three times for each dose rate position.

**RESULTS:** We succeeded in observation of emission for CHI and also ruby with monitorable dynamic range of  $10^{-2}$  up to 1 kSv/h for the first time, and emission intensities as a function of the dose rate are displayed in Fig. 2. The data was linear-fitted by  $I = ax + b$ , where  $I$  and  $x$  are the intensity and the dose rate, respectively, and coefficients ( $a$ ,  $b$ ) is  $(9.4 \times 10^5, 3 \times 10^3)$  and  $(1.4 \times 10^5, 3 \times 10^3)$  for CHI and ruby, respectively.

The transition loss through the optical fiber for CHI was larger than that of ruby due to slightly shorter emission peak; nevertheless, the scintillation signal of emission integrated area of CHI was the highest due to the high light output. Combining with the quick response against gamma-rays with no afterglow, we should obtain a more accurate and reliable signal when CHI is used as a scintillation probe than ruby. The detail of this collaboration study is described in [4].

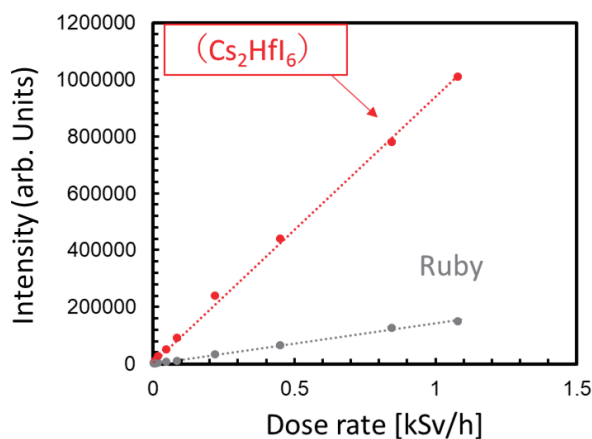


Fig. 2. Emission intensities for CHI and ruby excited by gamma rays ( $^{60}\text{Co}$ ) as a function of the dose rate.

#### REFERENCES:

- [1] C. Ito, *et al.*, J. Nucl. Sci. Technol. **51** (2014) 944.
- [2] S. Kodama, S. Kurosawa *et al.*, Radiat. Meas. **124**, (2019) 54.
- [3] N. Sato *et al.*, (2008). at <http://www.rii.kyoto-u.ac.jp/gamma/doseratesheet.pdf>
- [4] S. Kodama, S. Kurosawa and H. Tanaka *et al.*, Applied Physics Express **13**, (2020) 047002.

# PR5-13 Establishment of the Imaging Technology of 478 keV Prompt Gamma-rays of Boron-neutron Capture Reaction and the Measurement of the Intensity of the Neutron Field

T. Mizumoto, S. Komura, Y. Sakurai<sup>1</sup>, A. Takada<sup>2</sup>,  
T. Takata<sup>1</sup>, T. Tanimori<sup>2</sup>

Fukushima SiC Applied Engineering Inc.

<sup>1</sup>KURNS

<sup>2</sup>Graduate School of Science, Kyoto University

**INTRODUCTION:** BNCT is one of the promising cancer treatment methods. However, we have not yet obtained a good monitoring method of the treatment effect in real-time during BNCT. The main reason is that it is difficult to know precisely both the boron concentration and neutron flux intensity in tumor cells and healthy ones. If we get images of 478 keV gamma-rays generated by the boron-neutron capture reaction, and measure their intensity and generation positions, we can check the treatment effect on BNCT. To get gamma-ray images, several detectors such as SPECT and Compton cameras have been proposed. However, they have not been established due to their weaknesses [1]. To overcome the current situation, we have been developing electron tracking Compton cameras (ETCCs) which can uniquely determine the arrival direction of sub-MeV/MeV gamma ray event by event. An ETCC is the complex detector of two sub detectors: a time projection chamber TPC (Compton scatterer and recoil electron detector) and a scintillation camera (scattering gamma-ray absorber)[2][3].

**EXPERIMENTS:** We developed an ETCC which has a scintillation camera constructed with 576 pixelated GSO scintillators, whose pixel size is 6 mm×6 mm (26 mm in high), and a TPC whose size is 330 cm<sup>2</sup> (20 cm in high). As the performance measurement of the ETCC, we carried out two types of measurements at the Institute for Integrated Radiation and Nuclear Science, Kyoto University (KURNS). The first type was performed with E3 neutron guide tube of Kyoto University Reactor (KUR) (1 MW). We irradiated a Boron target (high concentration Boron solution) with a thermal neutron beam from E3 tube. We set the ETCC near the target and measured gamma rays from the target. The exposure time was a few hours. Another type of measurement was performed at KUR heavy water neutron irradiation facility. We set a (20 cm)<sup>3</sup> Boron solution target in the irradiation room, and the ETCC on the ceiling of the room. We set both the target and the ETCC on the axis of the cylindrical hole about 11 cm in diameter in the ceiling. We also set a LiF-containing Teflon plate between the ETCC and the hole as the shielding of thermal neutrons.

**RESULTS:** Fig. 1 shows the photograph and meas-

urement results with E3 tube. Measurement was performed for two target positions. From the result, we can see a clear positional difference between the two 478 keV gamma-ray images. We confirm 478 keV clear peak in spectra. Fig. 2 shows the schematic, photograph and measurement results with Heavy Water Neutron Irradiation Facility (epithermal neutron irradiation mode). The gamma-ray flux is approximately 10<sup>3</sup> /cm<sup>2</sup>/sec in front of the ETCC. Despite such the intense gamma-ray radiation environment, where the conventional Compton cameras are disturbed by random coincidence noise, our ETCC succeeded to detect the 478 keV prompt gamma rays arrived from the water phantom target as we can see in the spectra (a) and (b). In the prospects, we also need to try the measurement test in the high neutron flux condition.

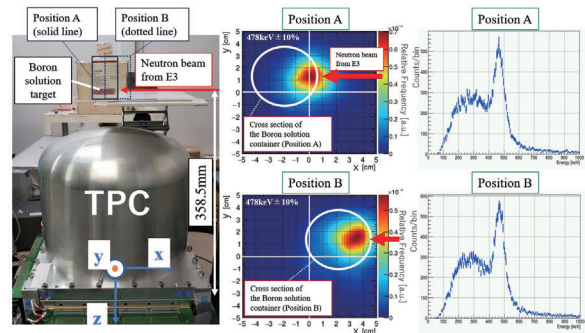


**Fig.1. Photo and results of the experiment with E3 tube. Left: photo taken on the measurement. Right: back-projection 478 keV gamma-ray images using the ML-EM method and spectra taken by the ETCC. Measurement was performed for two target positions. The positional difference between A and B is 4 cm.**

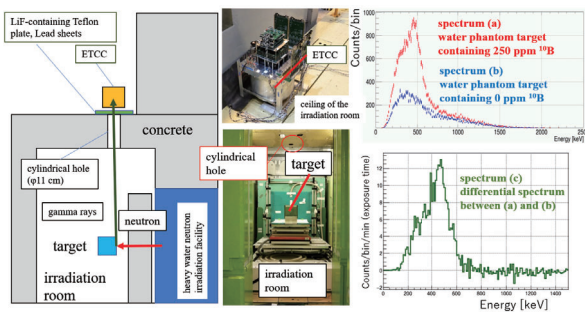


**Fig.2. Schematic view, photograph and gamma-ray energy spectra of the experiment with heavy water neutron irradiation facility. ETCC measured gamma-rays from the treatment room. <sup>10</sup>B concentration of water phantom target is 250 ppm and 0 ppm.**

**REFERENCES:**

- [1] T. Mizumoto, KURNS Progress Report 2018 (2019).
- [2] Y. Mizumura, JINST, 9, (2014) C05045.
- [3] T. Mizumoto, JINST 10 (2015) C06003.

## PR5-14 Feasibility study of a gel-dosimeter for a quality assurance and a quality control in boron neutron capture therapy

S. Nakamura<sup>1,2</sup>, K. Iijima<sup>1</sup>, M. Takemori, H<sup>1</sup>. Nakayama<sup>1</sup>, S. Nishioka<sup>1,2</sup>, H. Okamoto<sup>1,2</sup>, Y. Sakurai<sup>3</sup>, H. Tanaka<sup>3</sup>, N. T. Takata<sup>3</sup>, M. Suzuki<sup>3</sup>, H. Igaki<sup>2,4</sup>, and J. Itami<sup>2,4</sup>

<sup>1</sup>Department of Medical Physics, National Cancer Center Hospital

<sup>2</sup>Division of Research and Development for Boron Neutron Capture Therapy, National Cancer Center Exploratory Oncology Research & Clinical Trial Center

<sup>3</sup>Institute for Integrated Radiation and Nuclear Science, Kyoto University

<sup>4</sup>Department of Radiation Oncology, National Cancer Center Hospital

**INTRODUCTION:** In boron neutron capture therapy (BNCT), the neutron irradiation to the patient is performed after a sufficient accumulation of <sup>10</sup>B to tumor cells because the treatment efficacy is based on the <sup>10</sup>B(n,α)<sup>7</sup>Li reaction. It is important for the radiation therapy that the delivered dose is verified as a quality assurance before the treatment. However, it is a difficult for the existing detector that the three dimensional dose distribution is measured in BNCT with considering a non-uniformity of <sup>10</sup>B on the actual patient. Thus, this study focuses on the gel-dosimeter for the three dimensional dosimetry in BNCT. There are some reasons. First, the gel-dosimeter can mix a few <sup>10</sup>B with keeping the dose response. Second, the gel-dosimeter is generally used for the three dimensional dosimeter. Third, the gel-dosimeter is not expensive, and the quality assurance using the gel-dosimeter may not affect the medical costs in BNCT. Therefore, this study aims to evaluate the dose response dependence of the gel-dosimeter which contains a certain boron-10 density in BNCT.

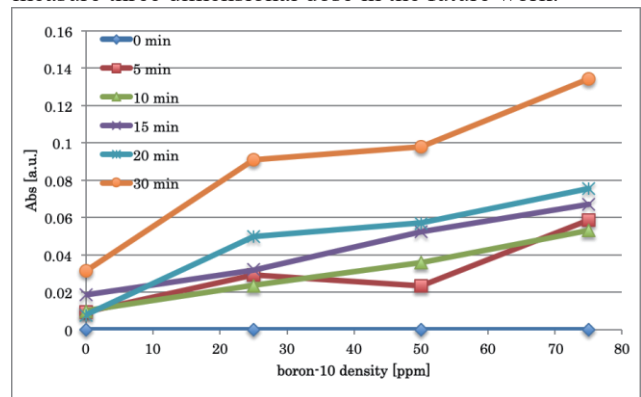
**EXPERIMENTS:** The experiment was performed in the Heavy Water Neutron Irradiation Facility (Kyoto University Reactor, KUR). The KUR was operated at a power of 1 MW. The neutrons were delivered to the gel-dosimeter which composed of water, PVA, KI, KCl, Gellan gum, Fructose, and boron solutions. The boron-10 density of the gel-dosimeter was 0, 25, 50, and 75 ppm. The irradiation time was set to 0, 5, 10, 15, 20, 30 min in each gel-dosimeter. After the neutron irradiation, the dose response in each gel-dosimeter was read by an optical scanner. The dose response dependence in each gel-dosimeter was evaluated.

**RESULTS:** Figure 1 (a) shows the dose responses of gel-dosimeter in each boron-10 density and (b) shows those in each irradiation time. According to Fig.1, the dose response increases with boron-10 density and irradiation time. Figure 2 shows the difference of dose response among the irradiation positions on the beam port. The dose response of gel-dosimeter positioned at the center on the beam port was higher than that positioned at the edge.

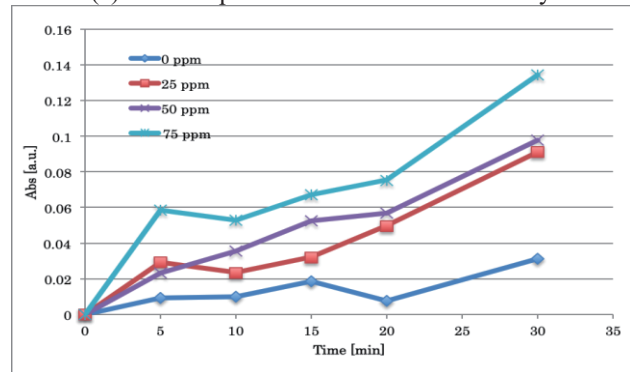
**Discussion:** This study suggests that the gel-dosimeter has a sufficient sensitivity for the reaction

of <sup>10</sup>B(n,α)<sup>7</sup>Li in BNCT although the boron-10 density expects very low (25 ppm, etc...). According to fig. 1, the dose response in the gel-dosimeter increases with the boron-10 density and the irradiation time, and it seems that the dose response can evaluate the actual dose delivered to the gel-dosimeter (Fig. 2). On the other hand, linearity of the dose response against the boron-10 density is not sufficient. It may relate to a creating method of the gel-dosimeter. Some different method will be tried to seek the best method for creating the gel-dosimeter in the future work.

**Conclusion:** We performed the feasibility test of the gel-dosimeter whether it could evaluate the three dimensional dose distribution in BNCT. The possibility for the evaluation could be indicated in this study. We will try to measure three dimensional dose in the future work.



(a) Dose response in each boron-10 density



(b) Dose response in each irradiation time

Fig. 1. Dose response of gel dosimeter.

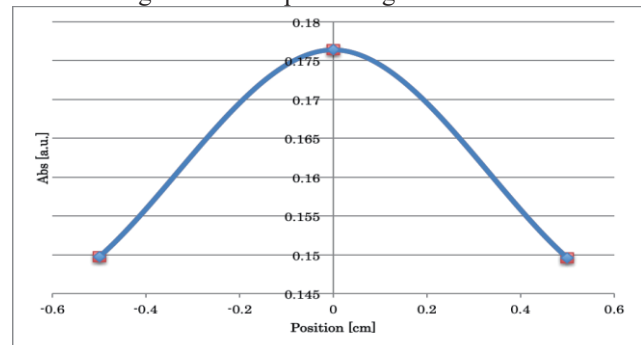


Fig.2. Dependence of position.

T. Takata, H. Tanaka, A. Sasaki<sup>1</sup>, Y. Sakurai, A. Maruhashi and M. Suzuki

*Institute for Integrated Radiation and Nuclear Science, Kyoto University*

<sup>1</sup>*Graduate School of Engineering, Kyoto University*

**INTRODUCTION:** In Boron Neutron Capture Therapy (BNCT), epithermal neutron beam has been utilized to treat a deep-seated tumor due to its high penetration ability based on thermalization within a patient. However, thermal neutron buildup causes dose deficiency in a case for a tumor locating in a vicinity of a patient surface. In such a case, a bolus consisting of a hydrogen-rich material has been utilized to improve the dose distribution. In present clinical BNCT, a bolus with a uniform thickness and a simple shape has been adopted. Aiming to more aggressively increase tumor dose, an optimizing method of bolus shape was studied.

**MATERIALS AND METHODS:** The optimization was performed as following. At first, a beam incident direction was determined according to location of a planning target volume (PTV) and organs at risk (OARs). Then, control points to define bolus thicknesses were assigned on the beam incident surface. A bolus region was modeled in a patient geometry by interpolating the thicknesses defined at the control points. These procedures were illustrated in Fig. 1. The thicknesses at the control points were adjusted to maximize a PTV dose under OAR dose regulations through an optimization calculation. As an example, a case for parotid cancer extended into a subcutaneous region was examined.

*Patient geometry modelling:* A PTV around a parotid gland and an OAR for an oral mucosa were delineated on X-ray CT images of a head phantom by a radiation oncologist. Then, a patient geometry model was constructed for radiation transport calculations. A beam direction was determined so that the PTV was centered in an irradiation field while locating the OAR in a deeper side.

*Bolus formation:* A bolus forming area was limited within a surface area in a 5-cm distance from the beam incident point. Control points were assigned to voxels in the area by using a  $1.5 \times 1.5 \times 1.5 \text{ cm}^3$  mesh-grid down sampling method. A bolus region was generated in the patient geometry by using an inverse-distance weighted interpolation of the thicknesses of the control points.

*Neutron and photon transport calculation:* The transport calculations were performed by using a Monte Carlo transport calculation module implemented in SERA; the treatment planning system for BNCT [1]. An epithermal neutron beam of the KUR heavy water neutron irradiation facility with an aperture diameter of 12 cm was assumed in the calculations [2]. The results were analyzed by using a dose evaluation module of SERA.

*Optimization calculation:* The maximum dose of the

oral mucosa was fixed to be 12 Gy-Eq according to the treatment protocol of BNCT for a head and neck cancer performed at KUR. Under this condition, an objective function was defined as the minimum dose of the PTV. The bolus thicknesses were adjusted to maximize the objective function by using a steepest gradient descent method.

**RESULTS:** The location of the PTV and OAR is shown in Fig. 2. The control points were assigned to 43 surface voxels by using the method described above. The iterative calculation was started from bolus thicknesses of zero at all control points. The result is shown in Fig. 3, where increase and convergence in the PTV dose according to iteration are confirmed. Fig. 2 also shows the resulting bolus shape at the 5<sup>th</sup> iteration, at which the objective function is almost converged. The growth of the bolus was observed around the area under which the PTV was extended into the subcutaneous region.

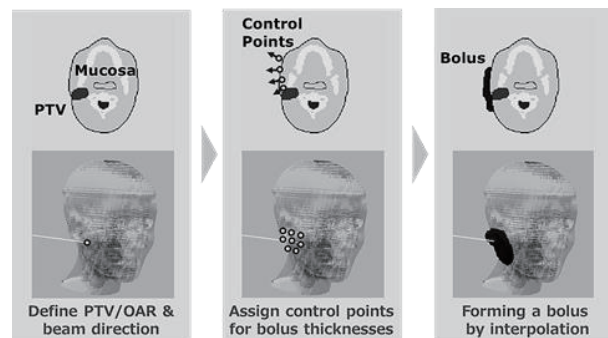


Fig. 1. Procedure of bolus formation.

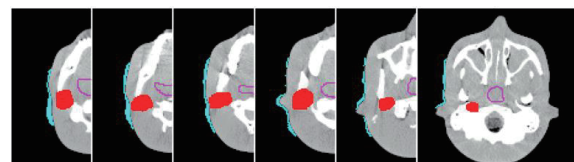


Fig. 2. Patient geometry with an optimized bolus.

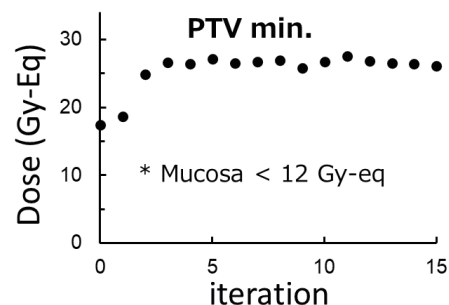


Fig. 3. Change in the objective function according to an iterative calculation.

### REFERENCES:

- [1] D. E. Wessel *et al.*, INEEL/EXT-02-00698 (2002).
- [2] Y. Sakurai, T. Kobayashi, *Med. Phys.* **29** (2002), 2328-2337.

H. Yasuda<sup>1</sup>, JE. Tano<sup>1,2,3</sup>, CAB. Gonzales<sup>1</sup>, Y. Sakurai<sup>4</sup><sup>1</sup>Department of Radiation Biophysics, RIRBM, Hiroshima University<sup>2</sup>Graduate School of Biomedical and Health Sciences, Hiroshima University<sup>3</sup>Phoenix Leader Education Program for Renaissance from Radiation Disaster, Hiroshima University<sup>4</sup>Institute for Integrated Radiation and Nuclear Science, Kyoto University (KURNS)

**INTRODUCTION:** The flexibility of a gel dosimeter offers the advantage of providing 3D dose distribution in brain formed with complex geometries in the boron neutron capture therapy (BNCT) which is a chemically targeted treatment based on the nuclear reaction  $^{10}\text{B}(n,\alpha)^7\text{Li}$ . The authors have investigated application of a novel radiochromic gel made of polyvinyl alcohol (PVA), glutaraldehyde (GTA), and iodide (I) using gamma rays [1,2]. The present study explores the feasibility of the PVA-GTA-I gels infused with boric acid by evaluating their dose responses and sensitivities to epithermal neutron beams that are used for brain tumor treatment.

**EXPERIMENTS:** The gel samples were produced using analytical grade from Fujifilm Wako Pure Chemical Co., Japan and prepared one day before irradiation. The formula of each sample set is summarized in Table 1. Boric acid contains approximately 20% of  $^{10}\text{B}$  which equates to ~50 ppm and 200 ppm for 25 and 100 mM, respectively. The solution was poured into PMMA cuvettes and stored inside a vacuum chamber (-0.08 MPa) for 1-hour to remove the dissolved oxygen. Then, the samples are covered with lids and placed inside an oven at 45°C for 12 hours to allow gelation.

The neutron irradiation of the gel samples was carried out at the Heavy Water Neutron Irradiation Facility of Institute (HWNIF) for Integrated Radiation and Nuclear Science, Kyoto University with a nominal power of 1MW. The samples were fixed on an acrylic plate such that the axes of the cuvettes are perpendicular to the source and irradiated at different periods: 15, 30, and 60 min. Optical absorbance of the gel was measured with a UV-Vis spectrometer (Thermo Fisher Scientific Inc., USA).

Table 1. Compositions of PVA-GTA-I gels infused with different boric acid concentrations

Reagent	Concentration
Polyvinyl alcohol (PVA)	10 wt%
Ultrapure water	90 wt%
Glutaraldehyde (GTA)	0.01 M
Potassium Iodide (KI)	0.1 M
Glucono- $\delta$ -lactone (GDL)	0.1 M
Fructose	0.1 M
Boric acid	0, 25, and 100 mM

**RESULTS:** As shown in Fig. 1, optical absorbance of the PVA-GTA-I gels with higher boron concentration increased significantly after neutron exposure. Moreover, all the samples exhibited good dose-response linearities despite the low sensitivity from the standard formula of the PVA-GTA-I gel (i.e, without boric acid). This is further visualized in Fig. 2 wherein an increasing color intensity gradient is seen from the samples with 100 mM of boric acid.

These data indicate the feasibility of the boron-infused PVA-GTA-I gel for 3D dose assessment in BNCT. In addition, the results implied that the potential of combination of two or three PVA-GTA-I gels having different boron concentrations could enable us to distinguish the doses from neutrons and gamma rays. Further investigations are now under way.

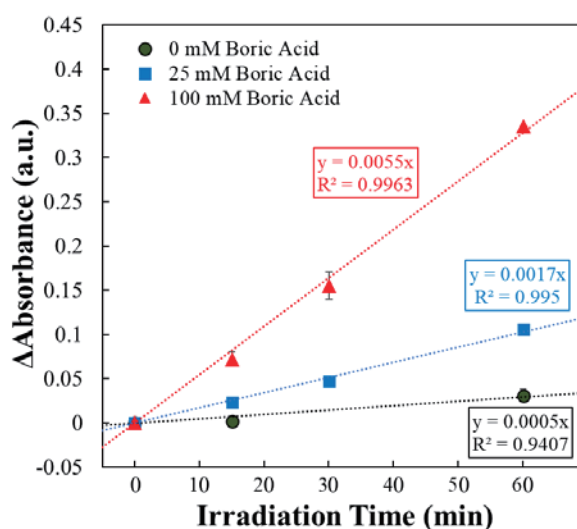


Fig. 1. Increments of the optical absorbances of the PVA-GTA-I gels infused with different-level boric acid concentrations as a function of irradiation time. Each data set is fitted with a linear function curve.



Fig. 2. A photo image of the PVA-GTA-I gel with 100 mM boric acid at 15, 30, and 60 min after neutron irradiation.

**REFERENCES:**

- [1] Taño JE *et al.*, 2019. *J Phys Conf Ser.*, **1305** 012034.
- [2] Taño JE *et al.*, 2020. *Radiat Meas* 106311.

## PR5-17 Measurement of neutron distributions in the BNCT irradiation field using a GEM detector

S. Uno, T. Koike<sup>1</sup>, K. Miyamoto<sup>2</sup>, K. Nobori<sup>2</sup>, H. Tanaka<sup>3</sup>

High Energy Accelerator Research Organization (KEK)

<sup>1</sup> Faculty of Health Sciences, Kyorin University

<sup>2</sup> BeeBeans Technologies Co.Ltd

<sup>3</sup> Institute for Integrated Radiation and Nuclear Science, Kyoto University

**INTRODUCTION:** The boron neutron capture therapy (BNCT) is a radiation therapy to destroy tumor cells selectively based on a nuclear reaction when  $^{10}\text{B}$  is irradiated with thermal neutrons. Epithermal neutrons are suitable for the BNCT, because thermal neutrons are effectively irradiated on tumor cells after epithermal neutrons are moderated in the tissue. Therefore, it is important to know the spatial distribution of epithermal neutrons in the treatment planning. For a measurement of the spatial distribution in thermal and epithermal neutrons irradiation field in the BNCT, we have been developing a two-dimensional real time imaging detector with the gas electron multiplier (GEM) [1]. The GEM is a position-sensitive device with the gas amplification to detect charged particles, photons, and neutrons. In this study, the performance of the GEM detector was evaluated using the Heavy Water Neutron Irradiation Facility (HWNIF) of the Kyoto University Research Reactor (KUR) [2].

**EXPERIMENTS:** Our GEM detector has a compact body with dimensions, 444 mm × 270 mm × 41 mm. It consists of a GEM chamber and a readout electronics board [3]. The effective detection area is 100 mm × 100 mm. The ASIC for the amplification and the FPGA for the online processing are mounted on the electronics board, which is able to transfer data directly to a PC via the net-work. Fig. 1 shows a schematic cross-section of the GEM chamber with a  $^{10}\text{B}$ -coated cathode plate. The detector works as a gas radiation detector for neutrons by detecting the charged particles emitted through a  $^{10}\text{B}(n, \alpha)^7\text{Li}$  nuclear reaction. Ionization electrons are created through the interaction of the charged particle with the chamber gas in the drift region and the electrons are amplified by the electron avalanche process which occurs at high electric field in GEM holes. The GEM is the double-side printed circuit board, which consists of low temperature co-fired ceramic (LTCC) with 100  $\mu\text{m}$  thickness as an insulator and gold layers with 6  $\mu\text{m}$  thickness on both sides as an electrode. It has also a large number of holes with 100  $\mu\text{m}$  diameter and 200  $\mu\text{m}$  pitch (LTCC-GEM [4]). The LTCC-GEM is quite robust against the large discharge. Fig. 2 shows the experimental setup of the GEM detector. In the clinical practice of the BNCT, a collimator with a diameter of 120 mm is normally used. In this study, the irradiation was performed using an additional collimator with smaller aperture than the effective detection area to demonstrate whether the detector can measure the neutron spatial distribution. In addition, the measurements were performed while changing the detector position in order to observe the neutron flux distributions.

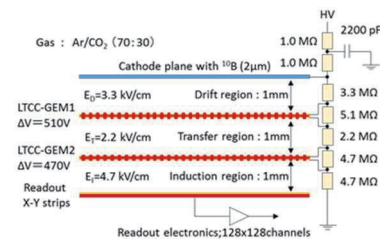


Fig. 1. Cross-section of the GEM detector; electrons are amplified in a succession of steps.

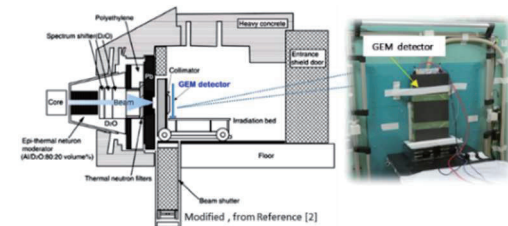


Fig. 2. Schematic diagram of experimental layout and appearance of irradiation geometry at the HWNIF of the KUR.

**RESULTS:** Fig. 3 shows the neutron spatial distribution at a distance of 640 mm from the collimator surface and the horizontal intensity profile at the beam center. The beam condition of the neutron irradiation field could be evaluated in real time and the collimator shape could be clearly seen. Since the detector is not sensitive against gamma-ray, we guess that the tail of the distribution was caused by neutron leaking from the collimator. For pulsed neutron sources, the detector can measure the neutron energy distribution in the time-of-flight method, but for reactor neutron sources, the neutron generation time cannot be determined because neutrons are randomly generated, so the neutron energy distribution cannot be measured. In the future, we plan to make improvements so that the energy distribution of the reactor neutron sources can be evaluated.

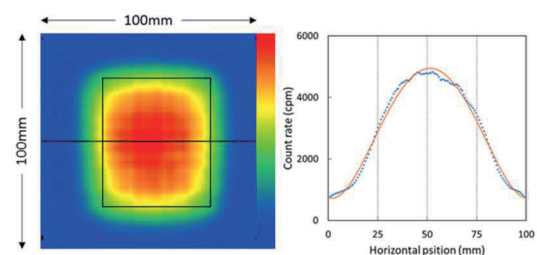


Fig. 3. The neutron spatial distribution and the intensity profile at the beam center. The square black line indicates the collimator size (60 mm × 50 mm).

### REFERENCES:

- [1] F. Sauli, Nucl. Instrum. Meth., A **386** (1997) 531.
- [2] Y. Sakurai *et al*, Nucl. Instrum. Meth., A **453** (2000) 569.
- [3] S. Uno *et al*, Physics Procedia **26** (2012) 142.
- [4] K. Komiya *et al*, J. Jpn. Soc. Prec. Eng., **84**.11 (2018) 936.

## PR5-18 Development of Epi-thermal Neutron Flux Intensity Detector for BNCT

I. Murata, K. Aoki, Y. Miyaji, S. Kusaka, H. Tanaka<sup>1</sup>, Y. Sakurai<sup>1</sup> and T. Takada<sup>1</sup>

Graduate School of Engineering, Osaka University  
<sup>1</sup>Institute for Integrated Radiation and Nuclear Science, Kyoto University

**INTRODUCTION:** BNCT is a promising cancer therapy which kills tumor cells while suppressing exposure dose to normal tissues. Normally, BNCT neutron field, produced by a nuclear reactor or an accelerator-based neutron source, has energy distribution spreading within thermal, epi-thermal and fast neutron region. Because epi-thermal neutrons ( $0.5 \text{ eV} < E_n < 10 \text{ keV}$ ) are generally used for BNCT, we must measure the epi-thermal neutron flux intensity to evaluate therapeutic effect and patients' exposure dose. However, it is quite difficult to measure it directly and accurately because there is no available method to measure the neutron spectrum and no activation materials covering only epi-thermal region. The objective of this work is hence to design a new detector to precisely measure the absolute integral flux intensity of epi-thermal neutrons.

**EXPERIMENTS:** The present epi-thermal neutron detector needs to reduce sensitivities to thermal and fast neutrons by using cadmium and polyethylene. We carried out numerical simulations by MCNP5. As a result,  $^{71}\text{Ga}$  ( $n, \gamma$ )  $^{72}\text{Ga}$  reaction was selected as the activation detector and the shape of the epi-thermal neutron detector was fixed to be a rectangular polyethylene (5.52 cm cubic) covered with a cadmium sheet (Fig.1). The epi-thermal neutron detector is however a little sensitive to fast neutrons (Fig.2). In order to test the performance of the epi-thermal neutron detector, a verification experiment was conducted at KUR. After the experiment, we can know the epi-thermal neutron flux intensity by Eq. (1). All we have to do is to measure radioactivity of  $^{72}\text{Ga}$ , meaning it is easy and it takes a short time.

$$\Phi_{\text{epi}} = \frac{Q}{Y \times (1 - e^{-\lambda t_1})} \quad (1)$$

$\Phi_{\text{epi}}$ [n / cm <sup>2</sup> / sec]	epi-thermal neutron flux intensity
Q [Bq]	$^{72}\text{Ga}$ radioactivity
Y [atoms / (source_neutron / cm <sup>2</sup> )]	$^{72}\text{Ga}$ production sensitivity
$\lambda$ [1 / sec]	decay constant of $^{72}\text{Ga}$
$t_1$ [sec]	irradiation time

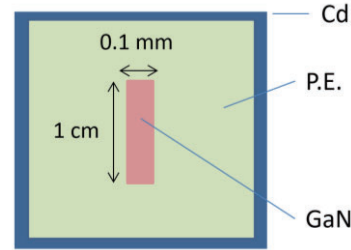


Fig. 1. Calculation model.

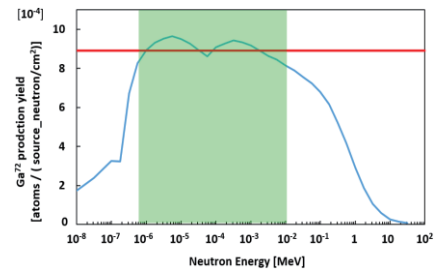


Fig. 2. Sensitivity of epi-thermal neutron detector.

**RESULTS:** Measurement conditions are shown in Table. 1. The radioactivity immediately after irradiation of GaN obtained by the experiment was 1.31 kBq. Therefore, the epi-thermal neutron flux intensity is estimated to be  $1.76 \times 10^8 \text{ n/cm}^2/\text{sec}$  by using Eq. (1). The nominal value of epi-thermal neutron ( $0.5 \text{ eV} < E_n < 10 \text{ keV}$ ) flux intensity is estimated to be  $1.62 \times 10^8 \text{ n/cm}^2/\text{sec}$ . Because this detector is a little sensitive to fast neutrons, it is probable that a discrepancy seen between the experimental value and the nominal value.

To investigate the contribution from fast neutrons, we carried out a correction calculation by MCNP5. As a result, the amount of activation by fast neutrons was estimated to be 50 Bq. Removing the contribution from fast neutron, the radioactivity becomes 1.26 kBq. Then, the epi-thermal neutron flux intensity is finally estimated to be  $1.69 \times 10^8 \text{ n/cm}^2/\text{sec}$ . It shows an excellent good agreement of  $\sim 4\%$ .

Table. 1. Measurement conditions.

Measuring Equipment HP-Ge detector	
Irradiation Time	10 min
Cooling Time	26 min
Measuring Time	55 min
Equipment Efficiency	0.00383741

**CONCLUSION:** The epi-thermal neutron flux intensity could be measured with an error of 4.2 % by correcting with the calculated value in the experiment at KUR. In order not to carry out a correction, we are developing a fast neutron ( $10 \text{ keV} < E_n < 1 \text{ MeV}$ ) flux intensity detector.

## PR5-19 Investigation of Thermal Neutron-Induced Soft Errors in Semiconductor Devices

H. Tanaka, T. Kato<sup>1</sup>, H. Matsuyama<sup>1</sup> and T. Takata and Y. Sakurai

*Institute for Integrated Radiation and Nuclear Science, Kyoto University*  
<sup>1</sup>*Reliability and Quality Assurance Department, Socionext Inc.*

**INTRODUCTION:** Soft errors are radiation-induced errors in semiconductor devices. Although the soft errors can be recovered by reset or power cycle of the devices, this is a critical issue in high reliability applications, such as automated driving and factory automation.

In the terrestrial environment, the major radiation source for the soft error is cosmic-ray-induced neutrons. The energy spectrum of the terrestrial neutron ranges from thermal to high-energy (GeV). The semiconductor device is sensitive to the thermal neutrons when it contains a number of <sup>10</sup>B atoms. The key mechanism is neutron-induced <sup>10</sup>B fission, which produces He and Li ions. These ions deposit charges in transistors, leading to the occurrence of the soft errors [1].

Historically, the thermal neutron-induced soft errors were suppressed by eliminating a borophosphosilicate glass (BPSG) layer, which contained <sup>10</sup>B atoms. However, in recent semiconductor devices, the thermal neutron sensitivity reappeared due to a change in the manufacturing process [2, 3]. Therefore, it is important to explore the thermal neutron sensitivity in advanced devices.

In this study, the thermal neutron-induced soft errors are investigated by irradiation testing. Soft error rates (SERs), which are the occurrence rates of radiation-induced error events, are statistically analyzed in advanced static random access memories (SRAMs).

**EXPERIMENTS:** Irradiation tests were performed using Heavy Water Neutron Irradiation Facility (HWNIF) of KUR [4]. The irradiation mode was “OO-0000F.” Fig. 1 shows the energy spectrum of this mode (black solid line) together with that of the terrestrial environment (gray dashed line) [5]. It is seen that these two spectra are similar to each other. In other words, this neutron source is suitable for the accelerated test of the terrestrial neutron-induced soft errors.

The samples were SRAM chips manufactured in advanced CMOS processes. Two types of SRAM chips, which were labeled as Device A and Device B, were irradiated. The number of error events occurred during irradiation were analyzed. The SERs were then calculated according to the JEDEC standard [6]. To estimate thermal neutron fluxes at the locations of samples, gold wires were attached on the SRAM chips. The fluxes were determined based on the activation of the gold.

Additionally, irradiation tests with boron shields were conducted for Device A. The boron shields were placed surrounding the SRAM chip to attenuate thermal neutrons. To clarify the sensitivity to thermal neutrons, the SERs with and without the boron shields were compared.

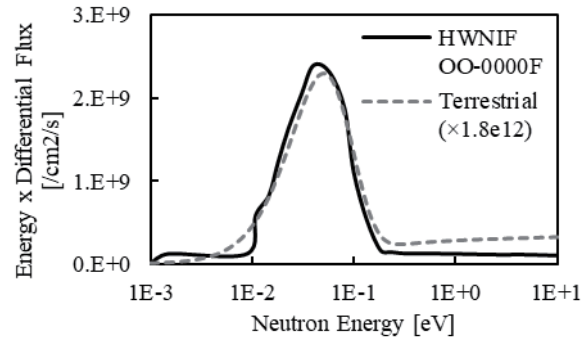


Fig. 1. Neutron energy spectra of HWNIF OO-0000F [4] and terrestrial environment [5]

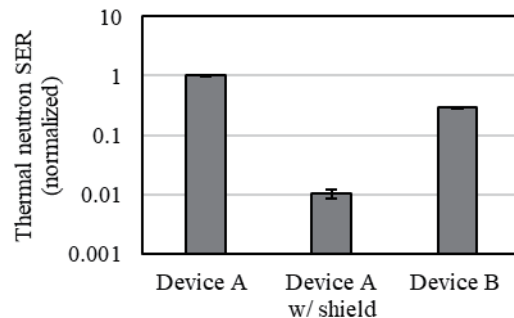


Fig. 2. Thermal neutron SERs of Device A, Device A with boron shield, and Device B.

**RESULTS:** Fig. 2 presents the thermal neutron SERs of Device A and Device B, where the SER values are normalized by the value of Device A. As for Device A, the SER with the boron shields is also shown.

In the comparison between the SERs of Device A with and without the boron shields, it was demonstrated that the SER with the shields was significantly reduced by two orders of magnitude.

As for the comparison between Device A and Device B, the SER of Device B was lower by 70%. This is probably due to the difference in the manufacturing process between them.

We have demonstrated that the advanced SRAMs are sensitive to thermal neutrons and that the SERs are different device-to-device, indicating the importance of thermal neutron irradiation testing.

### REFERENCES:

- [1] R. Baumann *et al.*, Proc. IEEE Int. Reliab. Phys. Symp. (IRPS), 152 (2000).
- [2] S. Wen *et al.*, Proc. IEEE Int. Reliab. Phys. Symp. (IRPS), SE.5.2 (2010).
- [3] Y. Fang *et al.*, IEEE Trans. Device Mater. Rel., **14**, 583 (2014).
- [4] Y. Sakurai *et al.*, Nucl. Instr. Meth. A, **453**, 569 (2000).
- [5] T. Sato, PLoS ONE, **10(12)** (2015).
- [6] JEDEC Standard JESD89A (2006).

## **I-1. PROJECT RESEARCHES**

### **Project 6**

## PR6 Analyzing Tumor Microenvironment and Exploiting its Characteristics in Search of Optimizing Cancer Therapy Including Neutron Capture Therapy

Shin-ichiro Masunaga

*Institute for Integrated Radiation and Nuclear Science,  
Kyoto University*

**BACKGROUNDS AND PURPOSES:** Human solid tumors contain moderately large fractions of quiescent (Q) tumor cells that are out of the cell cycle and stop cell division, but are viable compared with established experimental animal tumor cell lines. The presence of Q cells is probably due, in part, to hypoxia and the depletion of nutrition in the tumor core, which is another consequence of poor vascular supply. As a result, Q cells are viable and clonogenic, but stop cell division. In general, radiation and many DNA-damaging chemotherapeutic agents kill proliferating (P) tumor cells more efficiently than Q tumor cells, resulting in many clonogenic Q cells remaining following radiotherapy or chemotherapy. Therefore, it is harder to control Q tumor cells than to control P tumor cells, and many post-radiotherapy recurrent tumors result partly from the regrowth of Q tumor cells that could not be killed by radiotherapy. Similarly, sufficient doses of drugs cannot be distributed into Q tumor cells mainly due to heterogeneous and poor vascularity within solid tumors. Thus, one of the major causes of post-chemotherapy recurrent tumors is an insufficient dose distribution into the Q cell fractions.

With regard to boron neutron capture therapy (BNCT), with  $^{10}\text{B}$ -compounds, boronophenylalanine- $^{10}\text{B}$  (BPA) increased the sensitivity of the total cells to a greater extent than mercaptoundecahydrododecaborate- $^{10}\text{B}$  (BSH). However, the sensitivity of Q cells treated with BPA was lower than that in BSH-treated Q cells. The difference in the sensitivity between the total and Q cells was greater with  $^{10}\text{B}$ -compounds, especially with BPA. These findings concerning the difference in sensitivity, including other recovery and reoxygenation following neutron irradiation after  $^{10}\text{B}$ -compound administration were mainly based on the fact that it is difficult to deliver a therapeutic amount of  $^{10}\text{B}$  from  $^{10}\text{B}$ -carriers throughout the target tumors, especially into intratumor hypoxic cells with low uptake capacities.

Hypoxia is suggested to enhance metastasis by increasing genetic instability. Acute, but not chronic, hypoxia was reported to increase the number of macroscopic metastases in mouse lungs. We recently reported the significance of the injection of an acute hypoxia-releasing agent, nicotinamide, into tumor-bearing mice as a combined treatment with  $\gamma$ -ray irradiation in terms of repressing lung metastasis. As the delivered total dose increased with irradiation, the number of macroscopic lung metastases decreased reflecting the decrease in the number of clonogenically viable tumor cells in the primary tumor. The metastasis-repressing effect achieved through a reduction in the number of clonogenic tumor cells by irradiation is much greater than that achieved by releasing tumor cells from acute hypoxia. On the other hand, more  $^{10}\text{B}$  from BPA than from BSH could be distributed into the acute hypoxia-rich total tumor cell population, resulting in a greater decrease in the number of highly clonogenic P tumor cells with BPA-BNCT than with BSH-BNCT and with neutron beam irradiation only. BPA-BNCT rather than BSH-BNCT has some potential to decrease the number of lung metastases, and an acute hypoxia-releasing treatment such as the administration of nicotinamide, bevacizumab, wortmannin

or thalidomide may be promising for reducing numbers of lung metastases. Consequently, BPA-BNCT in combination with the treatment using these agents may show a little more potential to reduce the number of metastases. Now, it has been elucidated that control of the chronic hypoxia-rich Q cell population in the primary solid tumor has the potential to impact the control of local tumors as a whole, and that control of the acute hypoxia-rich total tumor cell population in the primary solid tumor has the potential to impact the control of lung metastases.

The aim of this research project is focused on clarifying and analyzing the characteristics of intratumor microenvironment including hypoxia within malignant solid tumors and optimizing cancer therapeutic modalities, especially radiotherapy including BNCT in the use of newly-developed  $^{10}\text{B}$ -carriers based on the revealed findings on intratumor microenvironmental characteristics.

### RESEARCH SUBJECTS:

The collaborators and allotted research subjects (ARS) were organized as follows;

**ARS-1 (31P6-1):** Optimization of Radiation Therapy Including BNCT in terms of the Effect on a Specific Cell Fraction within a Solid Tumor and the Suppressing Effect of Distant Metastasis. (S. Masunaga, et al.)

**ARS-2 (31P6-2):** Development of Hypoxic Microenvironment-Oriented  $^{10}\text{B}$ -Carriers. (H. Nagasawa, et al.)

**ARS-3 (31P6-3)\*:** Search and Functional Analysis of Novel Genes that Activate HIF-1, and Development into Local Tumor Control. (H. Harada, et al.)

**ARS-4 (31P6-4):** Radiochemical Analysis of Cell Lethality Mechanism in Neutron Capture Reaction. (R. Hirayama, et al.)

**ARS-5 (31P6-5):** Development of Neutron Capture Therapy Using Cell-Membrane Fluidity Recognition Type Novel Boron Hybrid Liposome. (S. Kasaoka, et al.)

**ARS-6 (31P6-6):** Drug Delivery System Aimed at Adaptation to Neutron Capture Therapy for Melanoma. (T. Nagasaki, et al.)

**ARS-7 (31P6-7):** Molecular Design, Synthesis and Functional Evaluation of Hypoxic Cytotoxin Including Boron. (Y. Uto, et al.)

**ARS-8 (30P8-8):** Bystander Effect on Malignant Trait of Tumor Cells by Irradiation. (H. Yasui, et al.)

**ARS-9 (31P6-9):** Analysis of the Response of Malignant Tumor to BNCT. (M. Masutani, et al.)

**ARS-10 (31P6-10):** Cell Survival Test by Neutron Capture Reaction Using Boron Compound and Inhibitory Effect on Tumor Growth. (K. Nakai, et al.)

**ARS-11 (31P6-11):** Multilateral Approach Toward Realization of Next Generation Boron Neutron Capture Therapy. (Y. Matsumoto, et al.)

**ARS-12 (31P6-12):** Analysis of Radiosensitization Effect through Targeting Intratumoral Environmental. (Y. Sanada, et al.)

**ARS-13 (31P6-13)\*:** Exploratory Research on the Optimal Administration of  $^{10}\text{B}$  Compound Aiming at New Enforcement Method of Neutron Capture Therapy (S. Masunaga et al.)

**ARS-14 (31P6-14)\*:** Examination of Cancer Cell Accumulation Property of New Boron Agent (CbaP14). (J. Hiratsuka, et al.)

(\*There was no allocated time for experiments using reactor facilities during their operation periods of FY 2019.

## PR6-1 Effect of a change in reactor power on response of murine solid tumors *in vivo*, especially on that of quiescent tumor cells, in boron neutron capture therapy

S. Masunaga, Y. Sakurai, H. Tanaka, T. Takata, M. Suzuki, Y. Sanada, K. Tano, A. Maruhashi and K. Ono<sup>1</sup>

*Institute for Integrated Radiation and Nuclear Science, Kyoto University*

<sup>1</sup>*Kansai BNCT Medical Center, Osaka Medical College*

**INTRODUCTION:** Neutron beams, that are essential for performing BNCT, have been supplied at some research reactors. In Japan, based on legal regulations, more reactor operation personnel have to be in place at the time of high power reactor operation (5 MW), than with low output operation (1 MW). In our reactor, to prevent nuclear fuel from being depleted during the reactor operable period, the output power during reactor operation for research use has been reduced from 5 to 1MW since 2010. However, reactor operation output remains at 5MW at the time of clinical boron neutron capture therapy (BNCT) to prevent prolongation of irradiation time.

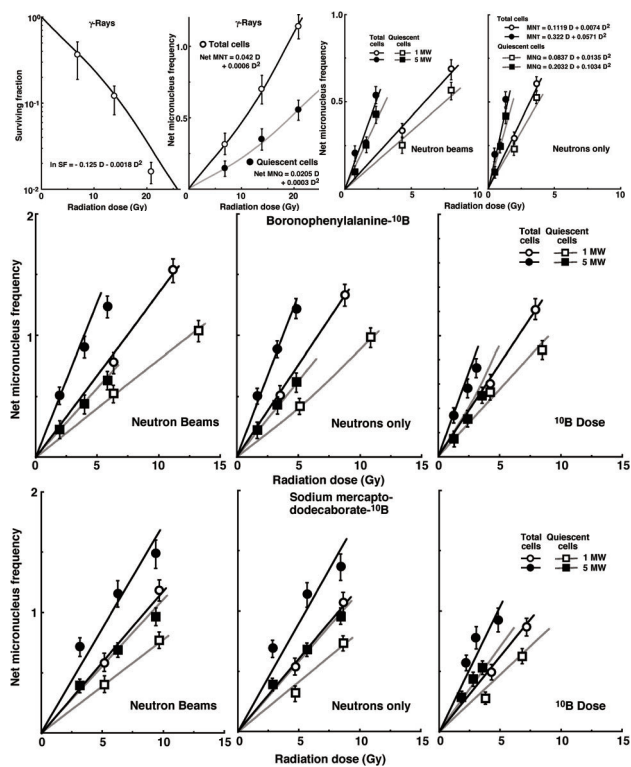
We analyzed the changes in the values of relative biological effectiveness (RBE) for neutron-only irradiation and compound biological effectiveness (CBE) factors for employed <sup>10</sup>B-carriers according to the value of a power of the operated reactor [1,2]. The neutron capture reaction was performed with two kinds of <sup>10</sup>B-carriers, boronophenylalanine-<sup>10</sup>B (BPA, C<sub>9</sub>H<sub>12</sub><sup>10</sup>BNO<sub>4</sub>) or sodium mercaptoundecahydrododecaborate-<sup>10</sup>B (sodium borocaptate-10B, BSH, Na<sup>2</sup><sup>10</sup>B<sub>12</sub>H<sub>11</sub>SH). Regarding local tumor response, the effect not only on the total [proliferating (P) + quiescent (Q)] tumor cell population, but also on the Q cell population, was evaluated using our original method for selectively detecting the response of Q cells in solid tumors [3].

**MATERIALS AND METHODS:** SCC VII tumor-bearing mice continuously received 5-bromo-2'-deoxyuridine (BrdU) to label all P tumor cells, and were treated with BPA or BSH. After reactor neutron beam irradiation at a power of 1 or 5MW with an identical beam spectrum, cells from tumors were isolated and incubated with a cytokinesis blocker. The responses of BrdU-unlabeled Q and total (P + Q) tumor cells were assessed based on the frequencies of micronucleation using immunofluorescence staining for BrdU.

**RESULTS:** After neutron irradiation with or without <sup>10</sup>B-carrier, radio-sensitivity was reduced by decreasing reactor power in both cells, especially in Q cells and after irradiation with BPA. The values of RBE and CBE were larger at a power of 5MW and in Q cells than at a

power of 1MW and in total cells, respectively. The sensitivity difference between total and Q cells was widened when combined with <sup>10</sup>B-carrier, especially with BPA, and through decreasing reactor power.

**CONCLUSION:** In actual clinical situations, it takes approximately 5 times longer time at a power of 1MW than 5MW to carry out one session of BNCT. Patients cannot move their body at the optimum treatment position all through the treatment time for BNCT. Thus, it is very reasonable that reactor power was maintained at 5MW for BNCT even after the power during reactor operation for research use was reduced to 1 MW. Consequently, taking these findings obtained in the current *in vivo* studies and clinical realities into consideration, 5MW is more useful, convenient, appropriate, advantageous and practical than 1MW as a reactor operation power in clinical BNCT [4].



### REFERENCES:

- [1] R. F. Barth *et al.*, *Radiat. Oncol.*, **7** (2012) 146–166.
- [2] J. W. Hopewell *et al.*, in *Neutron capture therapy. Principles and applications*. Edited by W. Sauerwein, A. Wittig, R. Moss, Y. Nakagawa (Springer-Verlag, Berlin, 2012) pp. 329–358.
- [3] S. Masunaga and K. Ono *J. Radiat. Res.*, **43** (2002) 11–25.
- [4] S. Masunaga *et al.*, *Int. J. Radiat. Biol.*, **95** (2019) 635–645.

A. Matsushita, M. Tsuji, Y. Sanada<sup>1</sup>, T. Hirayama, S. Masunaga<sup>1</sup> and H. Nagasawa

Laboratory of Medicinal & Pharmaceutical Chemistry, Gifu Pharmaceutical University

<sup>1</sup> Institute for Integrated Radiation and Nuclear Science, Kyoto University

**INTRODUCTION:** In malignant tumor cells, there is a significant increase in the demand for amino acids to maintain rapid growth and energy metabolism, and in particular such cancer cells show glutamine addiction.

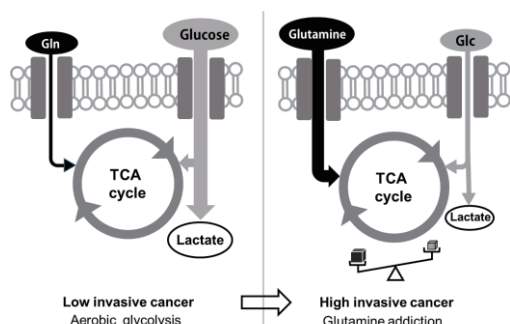
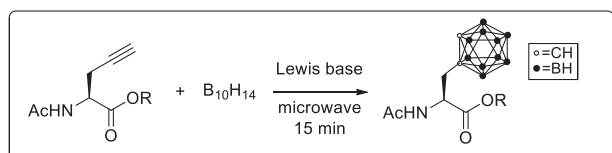


Fig. 1. Metabolic shift in malignant tumor cells.

Thus, such tumor cells overexpress transporters (ASCT2 and LAT1) that transport glutamine and neutral amino acids with aromatic or branched side chains. In this study, we designed and synthesized boron cluster-containing amino acid derivatives for the purpose of developing boron carriers that can efficiently capture <sup>10</sup>B atoms in tumors using tumor-specific amino acid transporters, focusing on glutamine addiction in cancer.

**EXPERIMENTS AND RESULTS:** First, utilizing boron clusters as unique hydrophobic pharmacophores, we synthesized carborane(C<sub>2</sub>B<sub>10</sub>H<sub>12</sub>)-containing amino acid derivatives L-*o*-carboranylalanine (**1**) and *O*-(*o*-carboran-1-ylmethyl) -L-tyrosine (**2**), which mimic the transport substrate of LAT1. They were efficiently obtained from the corresponding amino acid alkynes and decaboran in a short step using our microwave-assisted reaction, with total yields of 53% and 46%, respectively. R<sub>m</sub> values of all compounds were examined by TLC method (RP-8 modified silica gel TLC, 20 mM phosphate buffer (pH 7.2) : methanol = 7:3) as hydrophobic parameter.



Next, the uptake of boron atoms was evaluated after treatment of T98G with these compounds and L-boronophenylalanine(BPA). Intracellular boron uptake was measured by ICP-AES after 20 h of treatment with 10 μg <sup>10</sup>B/mL of the boron carriers. As a result, it was

found that compound **1** (41 ng <sup>10</sup>B/10<sup>6</sup> cells) and **2** (206 ng <sup>10</sup>B/10<sup>6</sup> cells) showed significantly higher uptake than BPA (23 ng <sup>10</sup>B/10<sup>6</sup> cells).

To evaluate neutron sensitizing ability of the compounds, T98G cells were treated with 10 μg <sup>10</sup>B/mL boron carriers for 24 h. Then the cells were washed with PBS, suspended in serum containing medium and aliquoted into Teflon tubes for irradiation. Cells were irradiated using the neutron beam at the Heavy Water Facility of the Kyoto University Research Reactor (KUR) operated at 1 MW power output. The survival rates of the irradiated cells were determined using conventional colony assays. The D<sub>10</sub> of BNCT was calculated from survival curve shown in Fig. 2.

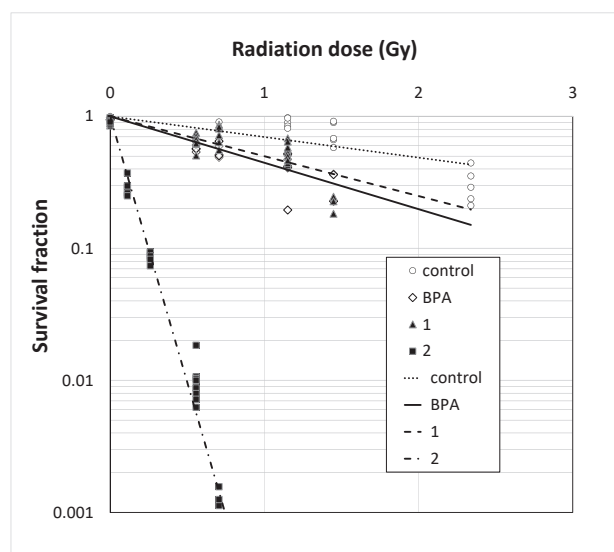


Fig. 2. Survival fraction of T98G cells treated with compound **1**, **2** and BPA and irradiated by mixed-neutron beam for BNCT.

Table 1. Intracellular uptake of <sup>10</sup>B atom, R<sub>m</sub> values, D<sub>10</sub> values and the enhancement ratios of boron carriers.

Compound	<sup>10</sup> B uptake ( <sup>10</sup> B ng/10 <sup>6</sup> cells)	R <sub>m</sub> value	D <sub>10</sub> value (Gy)	enhancement ratio
control	nd	—	6.41	1.00
BPA	23	nd	3.31	1.94
<b>1</b>	41	0.302	2.85	2.25
<b>2</b>	203	1.09	0.25	25.8

In summary, Compound **2** showed approximately 9-fold higher intracellular <sup>10</sup>B uptake than BPA. In addition, compound **2** enhanced the inhibition of cell survival of T98G cells irradiated with thermal neutrons by 13-fold compared to BPA. These results suggest that **2** is a promising candidate for new boron carrier. We are now synthesizing more diverse derivatives and investigating the structure-activity relationship analysis in BNCT.

## PR6-3 Molecular mechanism underlying HISP2-mediated radioresistance of hypoxic tumor cells

M. Kobayashi<sup>1,2</sup>, S. Masunaga<sup>3</sup>, A. Morinibu<sup>1,2</sup> and H. Harada<sup>1,2</sup>

<sup>1</sup>Laboratory of Cancer Cell Biology, Graduate School of Biostudies, Kyoto University

<sup>2</sup>Department of Genome Dynamics, Radiation Biology Center, Graduate School of Biostudies, Kyoto University

<sup>3</sup>Institute for Integrated Radiation and Nuclear Science, Kyoto University

**INTRODUCTION:** Cancer cells acquire 2-3 times more radioresistance under hypoxia compared to normoxia, which causes poor prognosis, e.g. poor overall survival and poor local control, of patients with more hypoxic regions in their tumor tissues [1]. Although the radioresistance is known to be enhanced by biological mechanisms, at least in part, in a hypoxia-inducible factor 1 (HIF-1)-dependent manner, further studies are needed for better understanding of the nature of hypoxic cell radioresistance [2, 3].

### EXPERIMENTS & RESULTS:

We conducted a DNA microarray analysis to explore novel genes whose expression are induced under hypoxic conditions. We found that not only expression but also secretion of one of the genes is markedly upregulated upon hypoxia; and therefore, we designated it as hypoxia-inducible secretory protein 2 (HISP2). The hypoxia-dependent increase in the HISP2 mRNA levels was abrogated by a transcription inhibitor, actinomycin D, suggesting that HISP2 were upregulated under hypoxia at transcription initiation levels. A loss-of-function study found that the hypoxia-dependent increase in the HISP-2 mRNA levels was significantly abrogated by silencing of HIF-1 $\beta$ , but not by that of HIF-1 $\alpha$  and HIF-2 $\alpha$ , suggested that the hypoxia-mediated expression is dependent on HIF-1 $\beta$ . A reporter gene assay with the use of an expression vector for EGFP-53BP1M fusion protein demonstrated that HISP2-overexpression decreased the number of DNA double strand breaks after irradiation. Clonogenic cell survival assay showed that cancer cells acquired radioresistance when transfected with HISP2-overexpression vector. We preliminary found that the radioresistance was dependent on EGFR and Nrf2. All of these data suggested that HISP2 proteins are secreted under hypoxic conditions in a HIF-1-independent but HIF-1 $\beta$ -dependent manner and decrease the number of double-strand break after irradiation, leading to radioresistance of cancer cells in an autocrine fashion. In combination with our recent findings about HIF-1- and hypoxia-mediated malignant phenotypes and therapy resistance of cancer cells [4-6], we elucidated one aspect of biological mechanism behind radioresistance of cancer cells.

### REFERENCES:

[1] Harada H. Hypoxia-inducible factor 1-mediated

characteristic features of cancer cells for tumor radioresistance. *J Radiat Res.* 57:99-105. 2016.

- [2] Koyasu S, Kobayashi M, Goto Y, Hiraoka M, Harada H. Regulatory mechanisms of hypoxia-inducible factor 1 activity: Two decades of knowledge. *Cancer Sci.* 109:560-571. 2018.
- [3] Nagao A, Kobayashi M, Koyasu S, Chow CCT, Harada H. HIF-1-dependent reprogramming of glucose metabolic pathway of cancer cells and its therapeutic significance. *Int J Mol Sci.* 20:238. 2019.
- [4] Koyasu S, Shimizu Y, Morinibu A, Saga T, Nakamoto Y, Togashi K, Harada H. Increased 14C-acetate accumulation in IDH-mutated human glioblastoma: implications for detecting IDH-mutated glioblastoma with 11C-acetate PET imaging. *Journal of Neurooncol.* 145:441-447. 2019.
- [5] Li X, Hattori A, Takahashi S, Goto Y, Harada H, Takeya H. UCHL1 promotes HIF-1-dependent tumor cell malignancy in spheroid models. *Cancer Sci.* 111:239-252. 2020.
- [6] Roudkenar MH, Fukumoto M, Roushandeh AM, Kuwahara Y, Uroshihara Y, Harada H, Fukumoto M. Disturbance in the regulation of miR17-92 cluster on HIF-1 $\alpha$  expression contributes to clinically relevant radioresistant cells: an in vitro study. *Cytotechnology.* 72:141-153. 2020.

## PR6-4 OH radicals from the indirect actions of neutron beam induce cell killing

R. Hirayama, Y. Sanada<sup>1</sup>, A. Uzawa, M. Suzuki<sup>1</sup>, S. Masunaga<sup>1</sup> and S. Hasegawa

National Institute of Radiological Sciences (NIRS), National Institutes for Quantum and Radiological Science and Technology (QST)

<sup>1</sup> Institute for Integrated Radiation and Nuclear Science, Kyoto University (KURNS)

**INTRODUCTION:** Excellent dose distribution in a cell of neutron capture reaction of boron atom induces high relative biological effectiveness. These phenomena are commonly assumed to be an interaction between cells and low energy heavy particles ( $\alpha$  and Li) resulting from the boron atom fissions in the cells. However, there has been little study done concerning the action of the particles on living cells. We have investigated contributions of indirect actions of radiation in cell killing by heavy ions with radical scavenger that selectively reduces the indirect action [1].

Therefore, it is important that how these mechanisms can be made to clear through a thorough basic research in boron neutron capture therapy is urgently discussed. The main object of this year is to make clear the contribution of indirect action of neutron beam to cell killing using mammalian cells.

**EXPERIMENTS:** We used HSGc-C5 (JCRB1070, here after call as HSG) cells. HSG cells were grown in Eagle's minimum essential medium supplemented with 10% fetal bovine serum and antibiotics (100 U/ml penicillin and 100  $\mu$ g/ml streptomycin) under humidified air with 5% CO<sub>2</sub> at 37°C. The cells were suspended at a density of about  $3 \times 10^5$  cells/ml. The cells in Polypropylene tubes were irradiated at the remodeled heavy water facility at the KURRI.

Total fluencies of thermal neutron, epithermal neutron and fast neutron were measured by means of gold foil activation analysis. The gamma ray dose including secondary gamma rays was measured with a thermo luminescence dosimeter. Boron concentrations in the cells were taken to be equivalent to those in the medium as reported previously [2].

After irradiation, cells were seeded in triplicate onto 100 mm ( $\Phi$ ) culture dishes at densities to give approximately 100 colonies per dish. After 14 days of incubation, the colonies were fixed with 10 % formalin solution and stained with 1 % methylene blue in water. Colonies consisting of more than 50 surviving cells were scored.

The contribution of indirect action on cell killing can be estimated from the maximum degree of protection by dimethylsulfoxide (DMSO) [1], which suppresses indirect action by quenching OH radicals without affecting the direct action of neutron beam on cell killing.

**RESULTS:** The surviving fractions of HSG cells irradiated with 5.85 Gy dose initially increased with increas-

ing DMSO concentration and then plateaued at higher concentrations (Fig.1A). Degrees of protection (DP:  $(\ln SF_0 - \ln SF_x) / \ln SF_0$ ) defined was calculated and plotted as a function of the DMSO concentration (Fig. 1B). Since the curve were upper concave in nature, DP curve was approached saturation as the concentration of DMSO increased. The maximum DP (i.e., saturation level) for DMSO concentrations was 0.29. Namely, the OH radical-mediated indirect action contributions to cell killing by neutron beam was 29%.

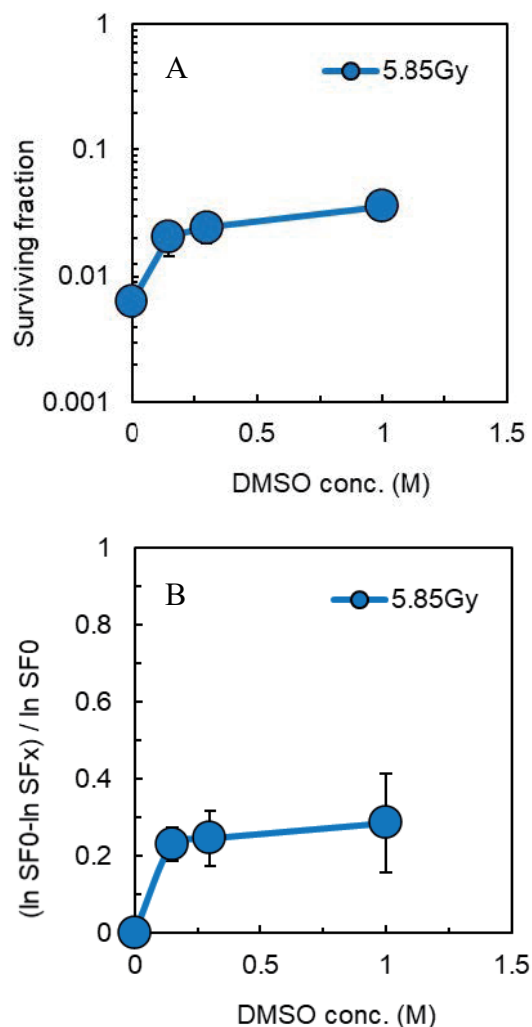


Fig. 1. Effects of DMSO on the survival of HSG cells after exposure to neutron beam. (A) HSG cell survival irradiated with neutron beam in the presence of various concentration of DMSO. (B) Degrees of protections were determined from panel A. The curve was fitted by MichaelisMenten kinetics. The error bars represent the standard errors.

### REFERENCES:

- [1] R. Hirayama *et al.*, Radiat. Res., **171** (2009) 212-218.
- [2] Y. Sakurai and T. Kobayashi, Nucl. Instrum. Methods Phys. Res. Sect. A., **453** (2000) 569-596.

S. Kasaoka, M. Saruwatari, Y. Tanaka, Y. Sanada<sup>1</sup>, Y. Sakurai<sup>1</sup>, H. Tanaka<sup>1</sup> and S. Masunaga<sup>1</sup>

*Department of Pharmaceutical Science, Hiroshima International University*

<sup>1</sup>*Institute for Integrated Radiation and Nuclear Science, Kyoto University*

**INTRODUCTION:** There are many reports that membranes in cancer cells are relatively more fluid compared to healthy cells. Higher membrane fluidity in cancer cells closely relates to their invasive potential, proliferation, and metastatic ability [1]. Liposomes composed of dimyristoylphosphatidylcholine (DMPC) and polyoxyethylenedodecylether were found to inhibit the growth of human promyelocytic leukemia cells without using any drugs [2]. Cell-penetrating peptides (CPPs) have been studied for their capacity to translocate across the lipid membrane of several cell types. 17-amino acid cell penetrating peptide (BR2) was found to have cancer-specificity without toxicity to normal cells [3]. In this study, we have developed a novel boron delivery system using the membrane-fluidity sensitive boron liposomes (MFSBLs) composed of DMPC and borocaptate (BSH)-conjugated chemical compounds with cell penetrating peptides (BR2) for boron neutron capture therapy.

**EXPERIMENTS:** Octadecylamine and 1,2-dimyristoyl-sn-glycero-3-phosphorylethanolamine were conjugated with BSH using the optimal heterocrosslinking agents for boron compounds. BR2-conjugated MFSBLs composed of DMPC, polyoxyethylenedodecylether, boron compounds and BR2 at mole ratios of 8:0.9:1.1:0.1 were prepared by sonication method in 5% glucose solution at 45°C. The diameter of MFSBLs was measured with a light scattering spectrometer. The boron concentration was measured by inductively coupled plasma atomic emission spectrometry. B16F10 murine melanoma cells and human fibroblast cells were incubated with 2 ppm of <sup>10</sup>B at 37°C for 14 hours before neutron irradiation. The cells were rinsed twice in PBS and suspended in fresh medium. After neutron irradiation the cells were plated into plastic Petri dishes 60 mm in diameter at 200 cells per dish. They were incubated for an additional 7 days to allow colony formation.

**RESULTS:** Tumor-specific CPPs (BR2) conjugated MFSBLs had a mean diameter of 78.5 nm. High encapsulation efficiency value from 48% to 74% of <sup>10</sup>B in MFSBLs were obtained. BRs-conjugated MFSBLs had high stability (92-97%) in the retention of <sup>10</sup>B during storage at 4°C for 4 weeks. All borocaptate-loaded formulations had low cytotoxic effects in human fibroblast cells. BR2-conjugated were efficiently fused to melanoma cells, but were inefficiently fused to human fibroblast cells. As shown in Fig. 1, BR2-conjugated MFSBLs showed higher suppression of growth of murine and human melanoma cells than BSH solution. This result suggested novel BR2-conjugated MFSBLs is useful for <sup>10</sup>B carrier on BNCT for melanoma.

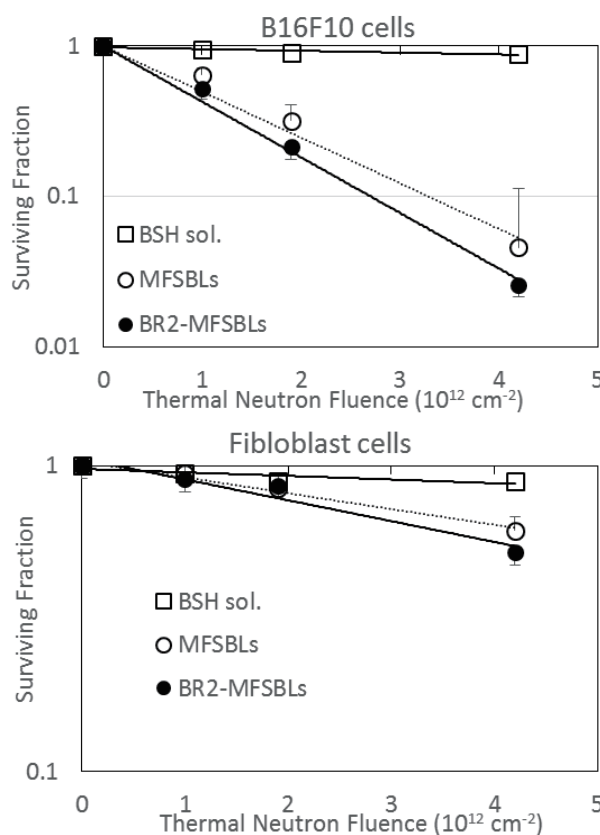


Fig. 1. Suppression of the colony formation of B16F10 cells and fibroblast cells after in vitro BNCT.

**REFERENCES:**

- [1] Sherbet GV, Magalit, *Exp Cell Biol.* **57** (1989).
- [2] Y. Matsumoto *et al.*, *Int. J. Cancer*, **115** (2005).
- [3] K. Lim *et al.*, *PLoS One*, **8** (2013).

## Preparation and Characterization of a Novel Bispecific Antibody That Targets Her2 and BSH for Boron Neutron Capture Therapy

T. Kanai, T. Tachibana, T. Nakanishi, T. Nagasaki, M. Kirihata<sup>1</sup>, Y. Hattori<sup>1</sup>, Y. Sanada<sup>2</sup>, Y. Sakurai<sup>2</sup> and S. Masunaga<sup>2</sup>

Graduate School of Engineering, Osaka City University

<sup>1</sup> BNCT Research Center, Osaka Prefecture University,

<sup>2</sup> Institute for Integrated Radiation and Nuclear Science, Kyoto University

**INTRODUCTION:** Boron neutron capture therapy (BNCT) is a cancer treatment that specifically kills cancer cells with the energy of particle beams generated by a nuclear reaction between boron (<sup>10</sup>B) and thermal neutrons. The key to successful BNCT is how to selectively deliver boron atoms into cancer cells. However, conventional boron drugs are poor in water solubility, tumor selectivity, and accumulation. Therefore, the development of effective boron delivery system is serious issue for the spread of BNCT. In this study, we developed novel bispecific antibodies against BSH, a water-soluble boron drug with a high boron content, and Her2 that is overexpressed on the surface of cancer cells. Moreover, we aim to construct a boron drug delivery system with high tumor selectivity and tumor accumulation by using it.

**EXPERIMENTS:** Rabbits were immunized with BSH-modified KLH, anti-BSH antibody-producing lymphocytes were obtained by the single cell method using ASONE Cell Picking System, and anti-BSH antibody was successfully produced genetically (Fig. 1A). The prepared antibody was confirmed for its binding ability to BSH by the ELISA method. In addition, colon 26 cells internalized with BSH-modified BSA were immunostained to evaluate the function of the anti-BSH antibody.

A bispecific antibody light chain expression vector was constructed by linking the prepared rabbit anti-BSH antibody light chain variable region gene with a human antibody CL region gene. In addition, the rabbit anti-BSH antibody heavy chain variable region gene was incorporated into an expression vector containing the Her2 binding site gene that had been successfully constructed to construct a bispecific antibody heavy chain expression vector (Fig. 1B). Bispecific antibodies against BSH and Her2 were prepared using the prepared bispecific antibody expression vector, and the binding ability to BSH was confirmed by ELISA evaluation, and the binding ability to Her2 was confirmed by flow cytometry evaluation.

**RESULTS:** First, we succeeded in producing an anti-BSH antibody using rabbits and decoded the gene sequence. By using the ELISA evaluation with BSH-modified BSA immobilized, it was confirmed that the prepared bispecific antibody binds to BSH (Fig. 2). In the flow cytometric evaluation, SKBR3 cells as Her2

positive cells and NIH3T3 cells as Her2 negative cells were used. The binding could be confirmed only when the prepared bispecific antibody treated with SKBR3 cells. From this, the affinity for Her2 was confirmed (Fig. 3).

These results suggest that the prepared bispecific antibody against BSH and Her2 is expected as a potent boron drug delivery tool.

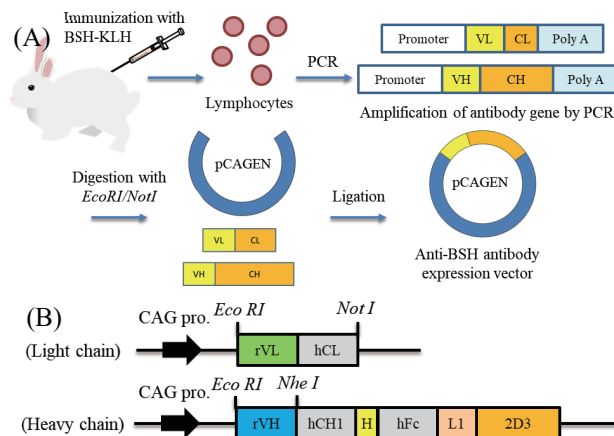


Fig. 1. (A) Construction of anti-BSH antibody expression vector (B) Sequences of light and heavy chains.

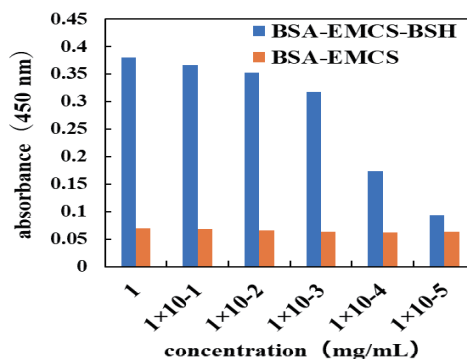


Fig. 2. ELISA evaluation of prepared bispecific antibodies against BSH and Her2.

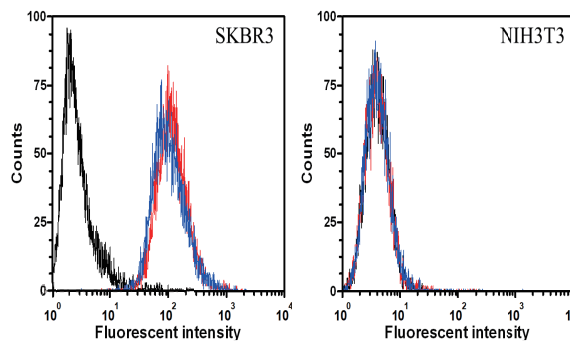


Fig. 3. Flow cytometric evaluation of prepared bispecific antibodies against BSH and Her2.

### REFERENCE

- [1] K. Ono *et al.*, *Int. J. S. Radiation Oncol. Biol. Phys.*, **43** (1999)431.

Y. Uto, Y. Tanaka, S. Masunaga<sup>1</sup>, Y. Sanada<sup>1</sup>

Graduate School of Technology, Industrial and Social Sciences, Tokushima University

<sup>1</sup> Institute for Integrated Radiation and Nuclear Science, Kuoyo University

## INTRODUCTION:

Hypoxia is a ubiquitous environment of cancer, it has a resistance to anticancer drugs and X ray, and accelerated infiltration / metastasis is a problem. Boron neutron capture therapy (BNCT), a kind of radiotherapy, is a treatment method utilizing neutron capture reaction in tumor cells by accumulating <sup>10</sup>B in tumor tissue. Hybrid molecules of Tirapazamine (TPZ), as a hypoxic cytotoxin and the neutron scavenger *p*-borono-L-phenylalanine (BPA) are useful as selective neutron scavengers for hypoxic tumors. Since boron neutron capture therapy depends on <sup>10</sup>B concentration, it is expected to provide an effective therapeutic effect for hypoxic cancer.

In this study, UTX-117 with amide linkage of TPZ and BPA and UTX-118 with ester linkage of TPZ and BPA were designed and synthesized, and antitumor activity and neutron sensitizing activity were evaluated. UTX-118 exhibited hypoxia selective cytotoxicity. Further, UTX-118 showed neutron sensitizing activity.

## EXPERIMENTS:

Tirapazamine derivatives and BPA were condensed to synthesize UTX-117 and UTX-118 (Fig.1). Using HeLa cells, the uptake amount of UTX-117 and UTX-118 was measured by ICP-AES, and the intracellular boron concentration was calculated. The IC<sub>50</sub> values of UTX-117 and UTX-118 were calculated by WST-1 assay. After adding <sup>10</sup>B enriched UTX-117, <sup>10</sup>B enriched UTX-118 and <sup>10</sup>B enriched BPA-F (>99.5% <sup>10</sup>B) to HeLa cells, neutrons were irradiated to calculate cell viability.

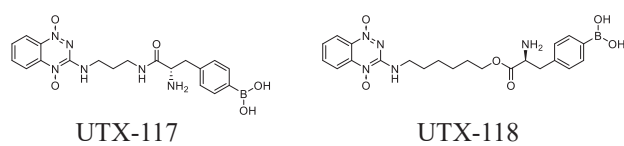


Fig.1

## RESULTS:

The uptake test of UTX-117, UTX-118 and BPA-F was performed using HeLa cells (Fig. 2). The boron concentration required for BNCT is  $1.0 \times 10^9$  atoms / cell.<sup>[1]</sup> since the maximum uptake of UTX-118 was approximately  $1.0 \times 10^9$  atoms / cell, a neutron sensitization effect can be expected for UTX-118. On the other hand, UTX-117 was below the detection limit of ICP-AES.

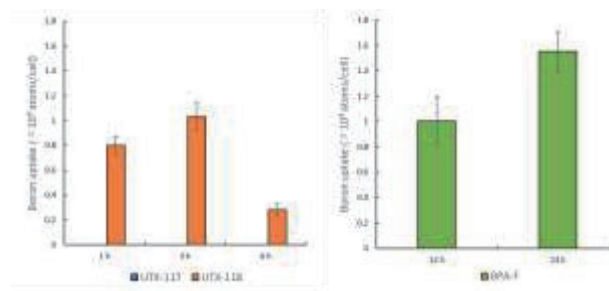


Fig.2

Toxicity test was performed by WST-1 assay using HeLa cells. As shown in Table 1, UTX-118 exhibited hypoxia-selective toxicity. The low toxicity of UTX-117 may be due to low uptake.

	Normoxia	Hypoxia	N/H ratio
UTX-117	>1000 μM	299 μM	-
UTX-118	24.4 μM	7.17 μM	3.40
TPZ	346 μM	21.1 μM	16.4

N/H ratio=the IC<sub>50</sub> value of Normoxia  
/ the IC<sub>50</sub> value of Hypoxia

Table. 1

Neutron sensitizing activity of <sup>10</sup>B enriched UTX-117, <sup>10</sup>B enriched UTX-118 and <sup>10</sup>B enriched BPA-F was evaluated using HeLa cells (Fig. 3). <sup>10</sup>B enriched UTX-118 showed the neutron sensitizing activity (sensitization ratio: 4.15 compared to the neutron irradiation control group). Since the sensitization ratio of <sup>10</sup>B enriched BPA-F was 3.27, <sup>10</sup>B enriched UTX-118 showed higher neutron sensitization activity than <sup>10</sup>B enriched BPA-F.

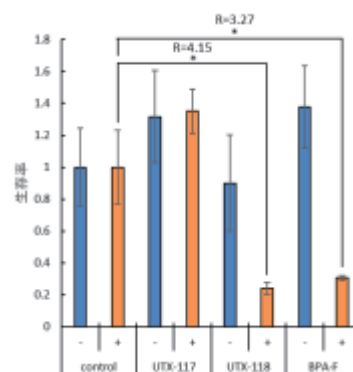


Fig.3. +:Irradiation, -:Non-irradiation

## REFERENCES:

- [1] F. F. Flores *et al. Radiat. Environ. Biophys.* **51** (2012) 329.

## PR6-8 The tumor invasion enhanced by the conditioned-medium after X-irradiation

H. Yasui, M. Eitaki, S. Masunaga<sup>1</sup> and O. Inanami

Laboratory of Radiation Biology, Graduate School of Veterinary Medicine, Hokkaido University

<sup>1</sup>Institute for Integrated Radiation and Nuclear Science, Kyoto University

**INTRODUCTION:** In cancer studies, it has been suggested that irradiation sometimes enhances invasion of tumor cells. Wild-Bode et al. reported that sublethal dose of  $\gamma$ -ray irradiation enhanced invasiveness of human glioblastoma, and the enhancement was accompanied by the activation and/or up-regulation of integrin and matrix metalloproteinase (MMP) contributed to cellular adhesion and degradation of extracellular matrix (ECM) [1]. Fujita et al. also reported that X-ray irradiation enhanced cellular invasive ability via up-regulation of MMP in some human pancreatic tumors [2]. Including these reports, a number of studies suggested that ECM degradation activity was involved in the irradiation-enhanced invasiveness of tumor cells. However, although there are many studies that estimate effects of direct irradiation on tumor cell invasiveness, not so many reports did by-stander effects of irradiated tumor cell conditioned medium (CM) on it. Furthermore, the same effect of high LET radiation therapy such as boron neutron capture reaction (BNCT) has not been reported. In this study, we conducted the experiments to examine effects of X-irradiated tumor cell CM on cellular invasiveness in breast cancer and lung cancer-derived cells, prior to BNCT challenge. In 2018, using human breast adenocarcinoma MDA-MB-231 cells and human lung adenocarcinoma A549 cells, we reported the X-ray irradiated cell-derived CM promotes cell infiltration ability even if taken into consideration cell proliferation activity [3]. In this year, we examined the expressions of growth factors such as Epidermal growth factor (EGF), Vascular endothelial growth factor (VEGF) and Transforming Growth Factor- $\beta$ 1 (TGF- $\beta$ 1) in X-irradiated MDA-MB-231 cells.

**EXPERIMENTS:** The expression of growth factors was evaluated using real-time PCR. Cells were seeded on 60 mm dishes ( $1 \times 10^6$  cells/dish), and incubated with RPMI1640/10% FBS overnight. After washing by PBS, 2 ml of serum-free RPMI1640 medium was added to the dishes followed by 0 or 4 Gy X-irradiation immediately. After 0-24 h incubation, the cells were collected with time. Total RNA of the cells was extracted by SV Total RNA Isolation System (Promega, Madison, WI.) according to the manufacture's instruction. RNA concentration was measured by DU 800 (BECKMAN COULTER, CA.). Reverse transcription was performed by Reverse Transcription System (Promega) according to the manufacture's instruction. Real-time PCR was performed by LightCycler® Nano System (Roche Diagnostics GmbH, Mannheim, Germany) and FastStart Essential DNA

Green Master (Roche) according to the manufacture's instruction. GAPDH was used as an internal control. Amount of mRNA was expressed as relative values which set that of non-treated cells to 1.

**RESULTS:** Since the CM derived from X-ray-irradiated cells promoted the cell invasion ability [3], it was considered that some bystander factor that promotes the cell-infiltrated ability exists in the CM derived from X-irradiated cells. Therefore, using MDA-MB-231 cells, which showed a large effect of promoting invasion ability by CM derived from X-ray-irradiated cells, the expression of mRNA for several proteins related to invasion ability in non-irradiated and 4 Gy-irradiated cells was measured using real-time PCR method. As shown in Fig. 1., the mRNA levels of TGF- $\beta$  and VEGF were not increased by at least 24 hours in 4 Gy-irradiated cells compared to non-irradiated cells. On the other hand, the amount of EGF mRNA was significantly increased in the 4 Gy-irradiated cells with a peak at 18 hours after X-irradiation. This result suggested that EGF acts as a bystander factor to promote the cell invasion ability.

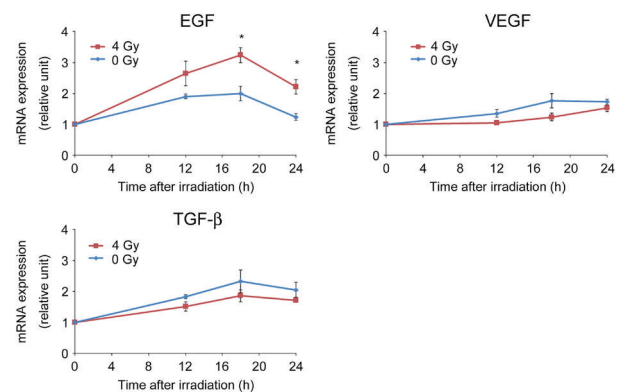


Fig. 1. The time-course of the mRNA expression of EGF, VEGF, and TGF- $\beta$  in X-irradiated MDA-MB231 cells. \*;  $p < 0.05$  vs. non-irradiated cells.

### REFERENCES:

- [1] C. Wild-Bode *et al.*, Cancer Res., **61** (2001) 2744-50.
- [2] M. Fujita *et al.*, Cancer Sci., **102** (2011) 729-8.
- [3] H. Yasui *et al.*, KURNS Progress Report 2018, PR8-7.

S. Imamichi<sup>1,2,3</sup>, L. Chen<sup>2,3</sup>, N. Toriya<sup>3</sup>, A. Takahira<sup>3</sup>, Y. Mitsuhashi<sup>3</sup>, T. Onodera<sup>2,3</sup>, Y. Sasaki<sup>2,3</sup>, M. Ihara<sup>2,3</sup>, Y. Sanada<sup>4</sup>, S. Masunaga<sup>4</sup> and M. Masutani<sup>1,2,3</sup>

1 Division of Boron Neutron Capture Therapy, EPOC, National Cancer Center

2 Lab. of Collaborative Research, Division of Cell Signaling, Research Institute, National Cancer Center

3 Department of Molecular and Genomic Biomedicine, Center for Bioinformatics and Molecular Medicine, Nagasaki University Graduate School of Biomedical Sciences

4 Institute for Integrated Radiation and Nuclear Science, Kyoto University

**INTRODUCTION:** Boron neutron capture therapy (BNCT) is based on nuclear reactions and preferential killing of cancer cells. The reaction is occurred between thermal neutron and boron-10 and causes alpha particle and lithium nuclei in a short length. For the clinical trials, boron compounds such as <sup>10</sup>B-boronophenylalanine (BPA) have been used in nuclear reactor or accelerator-based BNCT systems, which have been developed recently. Boron neutron capture reaction (BNCR) efficiently introduces DNA damages, however, it is still difficult to measure or calculate the irradiated dose. This is because BNCT dose is composed by various factors including boron uptake in tumors and irradiated thermal neutron fluence, and furthermore, these factors are variable depending on the irradiation system. We previously observed extensive DNA damage as gamma-H2AX foci, and poly(ADP-ribose) level in the rat lymphosarcoma model after BNCR<sup>1)</sup>. We also performed comprehensive analysis of proteome for human squamous carcinoma SAS cells after BNCR<sup>2)</sup>. The results suggested that the changes in the particular protein levels may be involved in the early response of BNCT. In this study, we investigated the changes and the dynamics of genes and proteins after BNCR or neutron beam irradiation in comparison with the gamma-ray irradiation.

**EXPERIMENTS:** We used human squamous cell line SAS, human melanoma A375 cells, and mouse melanoma B16 cells. BALB/c nude male mice of 5 weeks old were used for xenograft models after subcutaneous injection of tumor cells. Approximately ten days before irradiation, SAS and A375 cells were subcutaneously transplanted at hind legs of mice. For BNCR experiment, <sup>10</sup>B-BPA fructose complex (BPA) were used as a boron compound, and neutron irradiations at KUR reactor was operated at 1 MW. Irradiation experiments were carried out on July 31, September 4, November 12 of 2019. Cells were irradiated 2 hrs after incubation in the presence or absence of BPA at 25 ppm concentration of boron. Local irradiations to mouse legs were operated using <sup>6</sup>LiF containing thermal neutron shield approximately 30 min after intraperitoneal administration.

We used gold foil activation analysis for the meas-

urement of thermal neutron fluences and thermoluminescence dosimeter (TLD) for the measurement of the  $\gamma$ -ray doses including secondary  $\gamma$ -ray. Gold foils are placed on the surface and backside of the cell vials. Total absorbed dose calculation was carried out using the flux-to-dose conversion factor by the sum of the absorbed doses resulting from <sup>1</sup>H(n,  $\gamma$ )<sup>2</sup>D, <sup>14</sup>N(n, p)<sup>14</sup>C, and <sup>10</sup>B(n,  $\alpha$ )<sup>7</sup>Li reactions, as previously described. To analyze the acute cellular responses including factors and metabolites, cell culture supernatants were filtrated and analyzed 6 and 24 hrs after irradiation. RNA and proteins were also isolated and RNA expression levels were validated using real-time PCR and protein levels were analyzed by western blot and ELISA.

**RESULTS:** The irradiated thermal neutron fluence and total doses (Gy-Eq) are exemplified in Table 1. According to the previous microarray analysis in SAS, we analyzed gene expression profiles of *CSF2* gene, that encodes GM-CSF, *GM-CSF receptor*, genes in NF- $\kappa$ B-dependent pathway. We observed the increase of *CSF2* mRNA and its protein level in culture supernatant after the therapeutic dose irradiation. Changes in NF- $\kappa$ B-dependent pathway was also observed within 24 hrs. The results suggest that roles of GM-CSF cascade and NF- $\kappa$ B-dependent pathway in cellular response after BNCT.

**Table 1. Irradiated neutron fluence and doses on cells.**

Irradiation time [min]	Position	Thermal neutron [ $\mu\text{cm}^2$ ]	Thermal neutron [Gy]	Epi-thermal neutron [Gy]	Fast neutron [Gy]	Gamma-ray [Gy]	Total dose [Gy-Eq]
20	S, U	1.9E+12	0.26	0.027	0.19	0.26	4.21
	B, U	2.0E+12	0.26	0.028	0.19	0.25	4.48
	S, C	1.9E+12	0.26	0.027	0.19	0.25	4.22
	B, C	1.2E+12	0.16	0.017	0.12	0.25	2.83
	S, L	1.6E+12	0.21	0.022	0.16	0.25	3.63
	B, L	1.4E+12	0.18	0.02	0.14	0.25	3.09
13	S, C	1.2E+12	0.17	0.018	0.12	0.14	2.78
	B, C	9.0E+11	0.12	0.013	0.089	0.14	2.05
7	S, U	7.5E+11	0.099	0.011	0.074	0.11	1.67
	B, U	6.8E+11	0.091	0.0097	0.067	0.11	1.53
	S, C	5.0E+11	0.067	0.0071	0.049	0.11	1.16
	B, C	5.7E+11	0.077	0.0082	0.057	0.11	1.33
	S, L	7.3E+11	0.098	0.01	0.072	0.11	1.64
	B, L	6.0E+11	0.08	0.0085	0.059	0.11	1.39
4	S, C	4.5E+11	0.06	0.0064	0.045	0.066	1.03
	B, C	2.6E+11	0.035	0.0037	0.026	0.066	0.61
2	S, C	2.0E+11	0.027	0.0029	0.02	0.039	0.46
	B, C	1.4E+11	0.018	0.0019	0.013	0.039	0.32
60	S, L	6.3E+12	0.84	0.089	0.62	0.9	14.15
	B, L	6.5E+12	0.87	0.092	0.64	0.9	14.50
	S, R	3.8E+12	0.5	0.053	0.37	0.9	8.80
	B, R	3.2E+12	0.43	0.045	0.32	0.9	7.70
	B, R	3.7E+12	0.5	0.053	0.37	0.9	8.80
	S, L	1.1E+12	0.14	0.015	0.1	0.17	2.38
10	B, L	1.0E+12	0.13	0.014	0.099	0.17	2.27
	S, R	5.9E+11	0.079	0.0084	0.059	0.17	1.42
	B, R	6.1E+11	0.081	0.0087	0.06	0.17	1.45
	S, R	5.9E+11	0.079	0.0084	0.059	0.17	1.42

Irradiation was carried out in cell vials on September 4<sup>th</sup> 2019. S, surface; B, back-side; U, upper position; C, center position; L, left position; R, right position. Total dose was calculated for the presence of 25 ppm boron concentration.

## REFERENCES:

- [1] M. Masutani *et al.*, Appl. Rad. Iso., 104 (2014) 104-108.
- [2] A. Sato *et al.*, Appl. Rad. Iso., 106 (2015) 213-219.

## PR6-10 The contribution of blood boron-neutron reaction to subcutaneous tumor growth suppression was equal to that of neutrons irradiation only group

K. Nakai, M. Shirakawa<sup>1</sup>, S. Masunaga<sup>2</sup>, Y. Sakurai<sup>2</sup>, H. Tanaka<sup>2</sup>, T. Tsurubuchi<sup>3</sup>, F. Yoshida<sup>3</sup>, Y. Matsumoto, H. Kumada and H. Sakurai

Department of Radiation oncology, Faculty of Medicine, University of Tsukuba

<sup>1</sup>Department of Pharmaceutical Sciences, University of Fukuyama

<sup>2</sup>Institute for Integrated Radiation and Nuclear Science, Kyoto University

<sup>3</sup>Department of Neurosurgery, Faculty of Medicine, University of Tsukuba

### INTRODUCTION:

Boron Neutron Capture Therapy (BNCT) is a particle radiation therapy for malignant diseases[1]. However, Boron distribution of extra-cellular fluid or interstitial tumor tissue during the neutron irradiation and radiobiological effect of extracellular boron neutron reaction is still unclear. In the previous studies, we have focused on intra-cellular boron concentration and average boron concentrations of tumor tissue. There has intrinsic heterogeneity. The goal of this study is, to clarify a role of extra-cellular/peri-tumoral boron neutron reaction in BNCT.

### EXPERIMENTS:

**Materials:** Boron agent was designed and synthesized by Dr. M. Shirakawa[2]. The concept of this boron particle was that has only blood retention and has not pass through the vascular endothelium. The diameter of the liposome was 400nm, and pegylated, containing BSH solutions. Boron concentration of these solution were about 1400ppm.

**Cell Lines:** CT-26 murine colon cancer cell lines were cultured in D-MEM supplemented with 10% fetal bovine serum and maintained at 37°C in a humidified atmosphere with 5% CO<sub>2</sub>. After trypsinized and counted, cells were suspended in culture medium.

**Tumor models:** 4w female bulb/c mice were used. 1.0x10<sup>7</sup> cells were implanted to rt. thigh subcutaneously.

### Boron Neutron Reaction:

PEG liposome was administrated via tail vein injection 1hr before neutron irradiation(n=4). Thermal neutron dose was 2.2x10<sup>12</sup> n/cm<sup>2</sup>. At KUR, 50min of thermal mode irradiation was performed, Gamma ray dose was 0.18 to 0.32Gy. As a control, Neutron irradiation only group(n=5) and no treatment group(n=6) were also analyzed. Tumor progression were measured by tumor size.

**RESULTS and DISCUSSIONS:** As shown in Fig. 1, the contribution of PEG liposomal boron-neutron reaction to subcutaneous tumor growth suppression was equal to that of neutrons irradiation only group. This liposome was large sized, and pegylated to have a characteristics of blood retention. It means that boron neutron reaction in the blood vessels were not contribute to tumor suppression. Therefore, it is considered that the boron compound distributed in the stroma or tumor cells during 1hour ex-

erts an effect. To clarify this inference, the detailed boron distribution of intra and extra tumor cells, and interstitial peritumoral tissue should be examined. And also, it is suggested that BNCT is effective for tumor histopathology with early distribution of boron compounds in tumor cells.

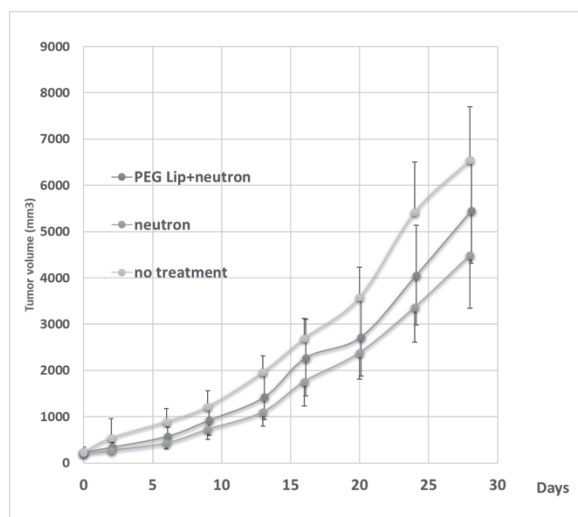


**Fig. 1** Subcutaneous CT-26 Tumor volume after Boron containing PEG liposome administration and neutron irradiation. Three groups of animals underwent the irradiation treatment at KUR. The first group (irradiated and i.v. PEG liposome group, n=4) received PEG liposome a dose of 250mg<sup>10</sup>B/kg, i.v. via tail vein 1 hour before neutron exposure. The second mice group (irradiated only group, n=5) received neutron exposure only. The third group (no treatment, n=6), six mice were followed up as non-treatment group.

### REFERENCES:

- [1] 石川仁ら、癌と化学療法. 46(2019)1219-25.
- [2] Shirakawa M. et al, Appl Radiat Isot. 67(2009) S88-90.

## PR6-11 Cell killing effect of BNCT with novel boron compound SMA glucosamine complex

Y. Matsumoto<sup>1,2</sup>, W. Islam<sup>3,4</sup>, J. Fang<sup>3,5</sup>, N. Fukumitsu<sup>6</sup>,  
Y. Sanada<sup>7</sup>, S.i. Masunaga<sup>7</sup>, H. Maeda<sup>3,4</sup> and H. Sakurai<sup>1,2</sup>

<sup>1</sup>Radiation Oncology, Faculty of Medicine, University of Tsukuba

<sup>2</sup>Proton Medical Research Center, University of Tsukuba Hospital

<sup>3</sup>BioDynamics Research Institute

<sup>4</sup>Department of Microbiology, School of Medicine, Kumamoto University

<sup>5</sup>Faculty of Pharmaceutical Sciences, Sojo University

<sup>6</sup>Proton Medical Research Center, Kobe University

<sup>7</sup>Institute for Integrated Radiation and Nuclear Science, Kyoto University

**INTRODUCTION:** Tumor vessels usually showed a special characteristic such as active angiogenesis, incomplete anatomy from normal tissue vasculature, highly occluded or embolized, or high or low vessel density compared with normal vessels. Therefore, the vascular permeability of the polymer compound is selectively promoted. Nanoparticles can remain in tumor tissue for extended periods of days to weeks, in contrast to the behavior of small compounds. The enhanced permeability and retention (EPR) effect can be used for tumor-selective delivery of nanopharmaceuticals, leading to avoidance of side effects and enhanced therapeutic effect. Boron neutron capture therapy (BNCT) has been known for more than 60 years, and its basic mechanism of action depends on  $\alpha$  rays emitted from  $^{10}\text{B}$  when neutrons collide with  $^{10}\text{B}$  atoms. A major challenge in the BNCT area is that most of the  $^{10}\text{B}$  compounds used for BNCT are low molecular weight compounds such as f-BPA and BSH, and they do not produce EPR effects, so they do not selectively accumulate in solid tumor. We developed a synthetic polymer (SMA, styrene-co-maleic acid)-conjugated glucosamine via amide bond, which was then complexed with boric acid, thus SMA-Glc-NH<sub>2</sub>-borate (SGB) showed 10-30 nm in hydrodynamic size and contains about 6-7% boron (w/w). SGB was also shown to stay in circulation for long time (> 6h), and exhibited good tumor selectivity (Tumor/blood ratio: 5-10). Thus, it will be ideal to use for BNCT. The effect of this drug on BNCT was verified, the difference with existing low molecular weight compounds was clarified, and its usefulness was evaluated.

**EXPERIMENTS:** The following endpoints were examined. 1) Synthesis of SMA polymer, SMA-glucosamine conjugate (SG) and SG-borate complex (SGB), 2) Particle size measurement by UV spectrum method (XYZ-001) and dynamic light scattering method (ELSZ-2000ZS), 3) Zeta potential measurement, 4) Shape and size measurement of nanoparticles by phase contrast electron microscopy (TEM), 5) Quantification of boron containing SGB complex by IPC-MS, 6) Boric acid (BA) from SGB by carmine method Correlation between

release amount and pH, 7) Stability of SGB complex in serum, 8) Toxicity evaluation by C26 and S180 tumor-bearing mice, 9) Pharmacokinetics of SGB complex by ICP-MS, 10) Hypoxia treatment Glycolytic changes and X-ray sensitivity after administration of BA, SG and SGB to cells, 11) Cell killing effect by combined use of BA and SGB with thermal neutrons

SAS cells were treated with BPA for 2 hours and BA, SG and SGB complex for 24 hours before irradiation. Cells were collected, placed in a cryotube (FG-CRY-05S), and irradiated with a neutron beam (1 MW) in the reactor. Thermal neutron fluence and  $\gamma$ -dose were measured by activation analysis of gold foil (diameter 3 mm, thickness 0.05 mm) and thermoluminescence dosimeter, respectively. The total absorbed dose due to neutrons was calculated as the sum of the individual absorbed doses, which are mainly the result of  $^1\text{H}(n, c)^2\text{D}$ ,  $^{14}\text{N}(n, p)^{14}\text{C}$  and  $^{10}\text{B}(n, \alpha)^7\text{Li}$  reactions. The fluences of thermal neutrons and epithermal neutrons were  $2.32 \times 10^{12} \pm 1.94 \times 10^{11}$  (n/cm<sup>2</sup>) and  $4.09 \times 10^{11} \pm 3.38 \times 10^{10}$  (n/cm<sup>2</sup>), respectively.

**RESULTS:** The SGB complex showed rapid uptake into tumor cells, liberating free boric acid at weakly acidic pH (5-7) of tumor tissue or cytosol. The free boric acid competed with phosphate for phosphorylation of glucose and inhibited tumor growth by inhibiting the tumor glycolysis system. It was found that the 15 mg/kg SGB complex significantly suppressed tumor growth compared with the untreated control group for S180 and C26 tumors and was not toxic during the experimental period. SGB also suppressed the enhanced glycolysis by hypoxia treatment (Fig. 1A-B) and decreased the enhanced radioresistance (Fig. 1C). Furthermore, it was revealed that SGB induces cell death after BNCT extremely efficiently as compared with the amount of  $^{10}\text{B}$  contained (Fig. 2).

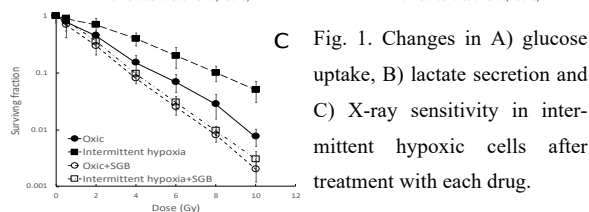
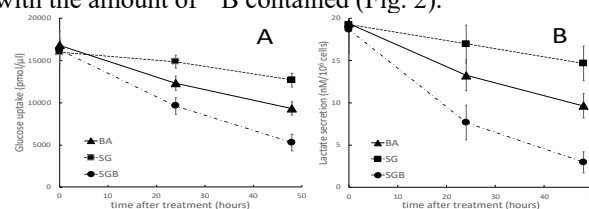


Fig. 1. Changes in A) glucose uptake, B) lactate secretion and C) X-ray sensitivity in intermittent hypoxic cells after treatment with each drug.

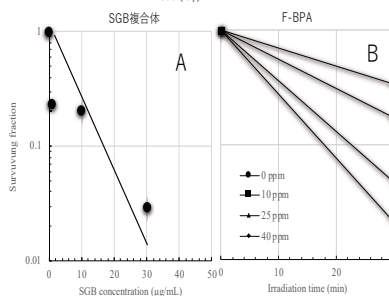


Fig. 2. Cell killing effect by A) SGB complex and B) f-BPA treatment with neutron irradiation.

## PR6-12 Attempts to sensitize tumor cells by exploiting the tumor microenvironment

Y. Sanada, T. Takata, Y. Sakurai, H. Tanaka and S. Masunaga

*Institute for Integrated Radiation and Nuclear Science,  
Kyoto University*

**INTRODUCTION:** Hypoxia and glucose deprivation have been suggested to play important roles in resistance to radiation [1]. Attempts to sensitize tumor cells by exploiting the tumor microenvironment have been studied. A major mediator of the cellular hypoxic response, hypoxia inducible factor 1 (HIF-1), is a potential target for cancer therapy, because it transcriptionally regulates a number of genes, including those involved in glucose metabolism, angiogenesis and resistance to chemotherapy and radiation therapy [2]. We previously reported that the disruption of Hif-1 $\alpha$  enhanced the sensitivity of murine squamous cell carcinoma (SCC-VII) cells to gamma-ray [3]. In the present study, we investigated whether the disruption of Hif-1 $\alpha$  affects the radiosensitivity of SCC-VII cells to the boron neutron capture reaction (BNCR). Previous studies reported that HIF-1 is likely involved in DNA damage and DNA repair. We first examined the extent of DNA damage after exposure to ionizing radiation or neutron beams. Furthermore, in order to determine the intracellular  $^{10}\text{B}$  levels in tumor cells, neutron-induced autoradiography was performed.

**EXPERIMENTS:** In order to mark the sites of DNA damage signaling, we established SCC-VII cells expressing EGFP-fused 53BP1 fragment (SCC-VII-BP1 cells). SCC-VII-BP1 cells and SCC-VII-BP1 Hif-1 $\alpha$ -deficient ( $\Delta\text{Hif-1}\alpha$ ) cell suspensions were exposed to gamma-rays (Co-60 Gamma-ray Irradiation Facility) or neutron beam (KUR Heavy Water Facility). The irradiated cells were seeded onto coverslips, and fixed with 4% formaldehyde. The intracellular localization of the EGFP-BP1 proteins was monitored by fluorescence microscopy.

In order to estimate the uptake of boron 10 ( $^{10}\text{B}$ ), neutron autoradiography was performed using CR-39 detectors. Cells grown under normoxia or hypoxia on CR-39 were treated with BPA (60 ppm), and then fixed. CR-39 detectors were exposed to thermal neutrons at a fluency of  $3 \times 10^{12} \text{ n} \cdot \text{cm}^{-2}$  (60 min), and etched in 6 N NaOH solution at 70°C for 45 min. The etched pits were counted using light microscope.

### RESULTS:

53BP1 is an early participant in the DNA damage response, and a fusion protein consisting of 53BP1 and GFP (GFP-53BP1) is used as a marker of the DNA damage response. In this study, we established SCC-VII cells expressing EGFP-fused 53BP1 fragment, and counted the number of BP1 foci formed in response to ionizing radia-

tion- or neutron beams-induced DNA damage. We first tested whether the BP1 foci can be detected in the SCC-VII-BP1 cells. It was found that the number of foci after gamma irradiation was formed in a dose dependent manner (Fig 1A). Next, SCC-VII-BP1 cells and SCC-VII-BP1  $\Delta\text{Hif-1}\alpha$  cells were cultured under normoxic or hypoxic condition, incubated with BPA, and then exposed to neutron beams. As shown in Fig. 1B, fewer 53BP1 foci occurred in SCC-VII-BP1 (hypoxia) cells than in SCC-VII-BP1 (normoxia) cells. On the other hand, the number of foci did not differ significantly in SCC-VII-BP1  $\Delta\text{Hif-1}\alpha$  cells (hypoxia and normoxia).

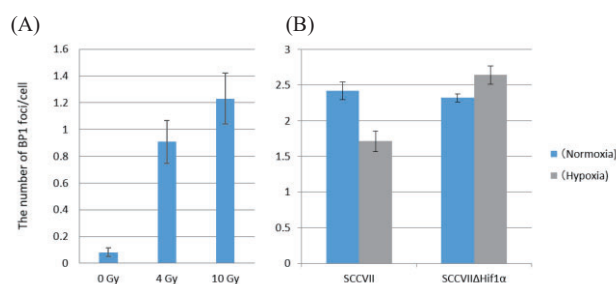


Figure. 1: (A) The number of BP1 foci 60 min after gamma irradiation. (B) The number of BP1 foci 30 min after neutron beam irradiation. The cells were exposed to neutrons at a fluency of  $4.0 \times 10^{11} \text{ n} \cdot \text{cm}^{-2}$ .

We also examined whether the disruption of Hif-1 $\alpha$  affects the uptake of BPA by calculating the average tracks on CR-39 per cell. The average tracks per cell were 3.5 tracks for SCC-VII (normoxia) cells and 1.8 tracks for SCC-VII (hypoxia) cells, suggesting that BPA was accumulated in SCC-VII (normoxia) cells more than in SCC-VII (hypoxia) cells. The average tracks per cell were 4.31 tracks for SCC-VII  $\Delta\text{Hif-1}\alpha$  (normoxia) cells and 4.72 tracks for SCC-VII  $\Delta\text{Hif-1}\alpha$  (hypoxia) cells. The results indicate that, if Hif-1 $\alpha$  is disrupted, there was little difference in  $^{10}\text{B}$  concentration in normoxia-treated and hypoxia-treated cells.

### REFERENCES:

- [1] S. Masunaga *et al.*, *Int. J. Rad. Biol.*, **92** (2016) 187–194.
- [2] Z. Luo *et al.*, *Neuropharmacology*. **89** (2015) 168–174.
- [3] Y. Sanada *et al.*, *Int. J. Rad. Biol.*, **94** (2018) 88–96.

## **I-1. PROJECT RESEARCHES**

### **Project 8**

## PR8 Project Research on Advances in Isotope-Specific Studies Using Multi-Element Mössbauer Spectroscopy

M. Seto

*Institute for Integrated Radiation and Nuclear Science,  
Kyoto University*

### OBJECTIVES AND PERFORMED RESEARCH SUBJECTS:

The main objectives of this project research are the investigation of the fundamental properties of new materials and the development of the advanced experimental methods by using multi-element Mössbauer spectroscopy. One of the most irreplaceable features of the Mössbauer spectroscopy is to extract element-specific or isotope-specific information. As the Mössbauer resonance line is extremely narrow, hyperfine interactions are well resolved and give us the information on the surrounding electronic states and magnetism. Therefore, promotion of the variety of Mössbauer isotope provides more useful and valuable methods for modern precise materials science of complex systems, such as biological substances, multi-layer films, and complicated-structured matter.

In this project research, each group performed their research by specifying a certain isotope:

$^{57}\text{Fe}$  in P8-1, P8-2, P8-3 and P8-4

$^{119}\text{Sn}$  in P8-5

$^{119}\text{Sn}$  and  $^{151}\text{Eu}$  in P8-6

$^{197}\text{Au}$  in P8-7 and P8-8

Development for other isotopes in P8-9

The subjects of research are as follows:

P8-1 Analysis of iron-based products using Mössbauer spectroscopy – iron oxide scale generated in the boiler feed-water in thermal power plant – (Y. Akiyama *et al.*)

P8-2 EFG tensor of  $\text{Fe}^{2+}$  in M2 site of orthopyroxene by single crystal Mössbauer microspectroscopy (K. Shinoda *et al.*)

P8-3 Temperature dependence of Mössbauer spectra for  $\text{Fe}_2\text{O}_3\text{-Al}_2\text{O}_3$  solid solution (S. Takai *et al.*)

P8-4 A nuclear resonance vibrational spectroscopic study of oxy-myoglobin (Y. Yamamoto *et al.*)

P8-5 Mössbauer spectroscopy on the antiperovskite oxide superconductor  $\text{Sr}_{3-x}\text{SnO}$  (Y. Maeno *et al.*)

P8-6 Researches on magnetism in a novel Kondo lattice (Y. Kamihara *et al.*)

P8-7 Study on structure of gold complexes coordinated with  $\alpha$ -amino acids by means of  $^{197}\text{Au}$  Mössbauer spectroscopy (H. Murayama *et al.*)

P8-8  $^{197}\text{Au}$  Mössbauer study of supported Au nanoparticles catalysis II (Y. Kobayashi *et al.*)

P8-9 Development of Mössbauer spectroscopy for  $^{166}\text{Er}$  (S. Kitao *et al.*)

### MAIN RESULTS AND CONTENTS OF THIS REPORT:

Y. Akiyama *et al.* (P8-1) investigated iron oxide scales generated in the pipe of the boiler feed-water system in the thermal power plant with oxygenated treatment. The information of chemical components of the iron oxide resolved by Mössbauer spectroscopy is necessary for magnetic separation system to remove the scales.

K. Shinoda *et al.* (P8-2) have developed Mössbauer microspectrometer and applied it to the studies of M2 site of orthopyroxene in a crystallographically-oriented enstatite crystal. The EFG tensor of the  $\text{Fe}^{2+}$  at the M2 site was successfully determined.

S. Takai *et al.* (P8-3) studied temperature dependence of  $(\text{Fe}_2\text{O}_3)_{1-x}(\text{Al}_2\text{O}_3)_x$  solid solutions with  $x = 0.5$  by Mössbauer spectroscopy. The temperature dependence of the spectra apparently showed a spectral change due to thermally distributed spin interaction with an effect of small particle size.

T. Ohta and Y. Yamamoto *et al.* (P8-4) have been investigating on oxymyoglobin through vibrational studies to reveal the relationship between the function and the conformation of Fe-O<sub>2</sub> bond in oxymyoglobin.

Y. Maeno *et al.* (P8-5) studied antiperovskite oxide superconductors  $\text{Sr}_{3-x}\text{SnO}$ . Temperature dependence of  $^{119}\text{Sn}$  Mössbauer spectra of  $\text{Sr}_{3-x}\text{SnO}$  ( $x \sim 0.5$ ) have revealed the presence of  $\text{Sn}^{4+}$  site and a site of  $\text{Sn}^{4+}$  hole-doped by Sr deficiency.

Y. Kamihara *et al.* (P8-6) have studied magnetic phases in novel Kondo Lattice,  $\text{EuSn}_2\text{As}_2$  though  $^{151}\text{Eu}$  and  $^{119}\text{Sn}$  Mössbauer spectroscopies. Temperature dependences clearly showed the magnetic splitting below 20K both in Eu and Sn spectra.

H. Murayama *et al.* (P8-7) investigated gold complexes coordinated with amino acids by  $^{197}\text{Au}$ -Mössbauer spectroscopy and obtained the characterization of Au(III) and Au(I) components. This information is helpful for producing Au nanoparticles deposited on various supports.

Y. Kobayashi *et al.* (P8-8) applied  $^{197}\text{Au}$ -Mössbauer spectroscopy to the studies on Au nanoparticles catalysis supported with Hydroxyapatite. The comparison of the catalysis prepared by several calcination temperatures showed a slight effect by this treatment.

S. Kitao *et al.* (P8-9) have developed Mössbauer sources for several less-common Mössbauer spectroscopy. As for source materials of  $^{166}\text{Er}$ -Mössbauer spectroscopy, improvement of source activity in  $\text{HoAl}_2$  was successfully confirmed. This source is useful for various researches for Er compounds.

## Analysis of Iron-based Products Using Mössbauer Spectroscopy - Iron Oxide Scale Generated in the Boiler Feed-water in Thermal Power Plant -

Y. Akiyama, M. Hiramatsu, K. Akiyama, F. Mishima<sup>1</sup>, S. Nishijima<sup>1</sup>, H. Okada<sup>2</sup>, N. Hirota<sup>2</sup>, T. Yamaji<sup>3</sup>, H. Matsuura<sup>3</sup>, S. Namba<sup>3</sup>, T. Sekine<sup>4</sup>, Y. Kobayashi<sup>5</sup>, M. Seto<sup>5</sup>

*Graduate School of Engineering, Osaka University*  
<sup>1</sup> *Department of Nuclear Technology and Applied Engineering, Fukui University of Technology*  
<sup>2</sup> *National Institute for Materials Science*  
<sup>3</sup> *Shikoku Research Institute Inc.,*  
<sup>4</sup> *Ebara Industrial Cleaning Co., Ltd.,*  
<sup>5</sup> *Institute for Integrated Radiation and Nuclear Science, Kyoto University*

**INTRODUCTION:** One of the reasons for deterioration of power generation efficiency of the thermal power generation is adhesion of the iron oxide scale generated by the corrosion of the pipe to the inner wall of the boiler feed-water system. Focusing on the magnetic properties of the scale, we have studied the removal of scales in the feed-water system by high gradient magnetic separation (HGMS) using the superconducting magnet. In this study, we targeted the thermal power plants adopting oxygenated treatment (OT). In order to determine the installation site and the magnetic separation conditions of the HGMS system, we analyzed the composition of the actual OT scale, which is considered to be the mixture of several kinds of iron oxides, by Mössbauer spectrometry.

**EXPERIMENTS:** The scale was sampled at 6 sampling points in the feed-water system of the power plant adopting OT. The composition was analyzed with Mössbauer spectrometry, and magnetization was analyzed by a physical property measurement system (Quantum Design Inc.). Fig. 1. shows the sampling points in the feed-water system of the thermal power plant. The sampling points were as follows; (1) outlet of condensate pump, (2) outlet of condensate demineralize, (3) drain of low-pressure feed-water heater, (4) inlet of deaerator, (5) storage tank of deaerator and (6) inlet of the economizer.

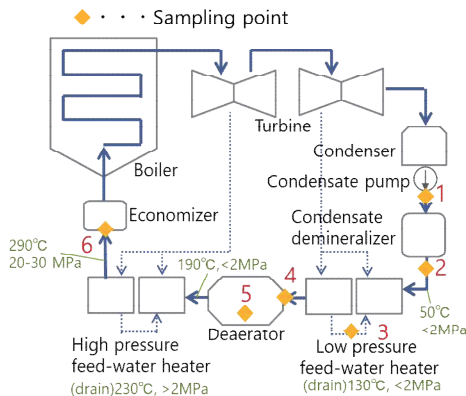


Fig. 1. The sampling points in the feed-water system of the thermal power generation [1].

**RESULTS:** Fig. 2. show the composition of the actual scales at 6 sampling points, respectively. The peaks were clearly separated from the Mössbauer spectrum, indicating that composite crystals may not exist. 6 major components; magnetite ( $\text{Fe}_3\text{O}_4$ ), maghemite ( $\gamma\text{-Fe}_2\text{O}_3$ ), hematite ( $\alpha\text{-Fe}_2\text{O}_3$ ), goethite ( $\alpha\text{-FeOOH}$ ) and lepidocrocite ( $\gamma\text{-FeOOH}$ ) were found in the scale. The composition of the scale was different depending on the sampling points. The scale sampled from the low-pressure feed-water heater drain (LPD) most contained the ferromagnetic magnetite and maghemite, compared with the scales of other sampling points. The sample also showed the highest magnetic susceptibility.

As a next step, the aggregation states of the ferromagnetic and the paramagnetic particles were investigated by lab-scale magnetic separation experiments by superconducting magnet. The experiments were conducted both for the actual scale sampled at low-pressure feed-water heater drain and the simulated sample by mixing commercially available iron oxide and hydroxide according to the result of Fig. 2. The result of the magnetic separation experiment showed that the capture rates showed similar results in actual and simulated scale, indicating the aggregation states of the particles in the simulated and the actual scale were similar. It was also shown that homogeneous aggregation existed in the OT scale, because a part of the paramagnetic particles were captured even in the separation conditions that the pure paramagnetic particles cannot be captured. Based on the results, we are currently designing HGMS system for removing the OT scale.

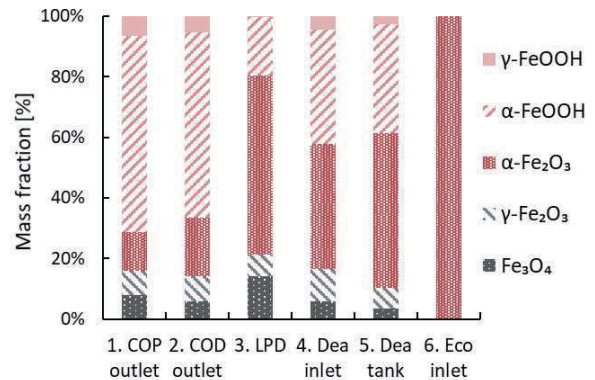


Fig. 2. The composition of the actual scales at 6 sampling points estimated by Mössbauer spectrometry [1].

**Acknowledgments:** This work is partly supported by Advanced Low Carbon Technology Research and Development Program (ALCA) of JST Strategic Basic Research Programs (JPMJAL1304).

**REFERENCES:**

[1] M. Hiramatsu *et al.*, J. Phys. Conf. Ser., **1293** (2019) 012079.

K. Shinoda and Y. Kobayashi<sup>1</sup>

Department of Geosciences,  
Graduate School of Science, Osaka City University

<sup>1</sup>Institute for Integrated Radiation and Nuclear Science,  
Kyoto University

**INTRODUCTION:** <sup>57</sup>Fe Mössbauer spectroscopy has been widely used for the analysis of Fe in Fe-bearing minerals. Powdered mineral is generally used as a Mössbauer sample, in spite of the usefulness of the conventional method, it is not useful for the Mössbauer analysis of any narrow area in a crystal or mineral grain. To overcome the disadvantage of spatial resolution by powder method, several Mössbauer microspectrometers have been proposed. Mössbauer microspectroscopy will be widely used for measuring spectra of a grain in a thin section in future. Intensities of component peaks in a quadrupole doublet of a thin section as a single crystal are asymmetric and vary depending on the angle between the direction of incident  $\gamma$ -rays and the crystallographic orientation of the thin section. Intensity of quadrupole doublet ( $I^h / I^{total}$ ) means a ratio between area of the peak of the higher energy ( $I^h$ ) and total area of the doublet ( $I^{total} = I^h + I^l$ ) (sum of  $I^h$  and area of the lower energy ( $I^l$ )). The intensity of component peaks of a <sup>57</sup>Fe Mössbauer doublet is related to an electronic field gradient (EFG) tensor of the site containing Fe<sup>2+</sup> and Fe<sup>3+</sup> (Zimmermann, 1975 and 1983). Thus, EFG determination is important in Mössbauer measurements of thin section as a single crystal. Zimmermann (1975, 1983) introduced experimental determination of EFG tensor from the Mössbauer spectrum of a single crystal, and proposed a formulation of the EFG tensor from the intensities of the component peaks of asymmetric Mössbauer doublet.

In pyroxene, Fe<sup>2+</sup> in M1, Fe<sup>2+</sup> in M2 and Fe<sup>3+</sup> in M1 sites are possible. As three doublets overlap in Mössbauer spectrum of pyroxene, it is important to reveal EFG of three doublets to analyze Mössbauer spectrum of pyroxene thin section. Tennant *et al.* (2000) revealed the EFG tensor of Fe<sup>2+</sup> at the octahedral M1 site of clinopyroxene. Shinoda and Kobayashi (2019) revealed EFG the tensor due to Fe<sup>3+</sup> in M1 site of clinopyroxene. In this study, Zimmermann's method was applied for single crystal <sup>57</sup>Fe Mössbauer spectra of an enstatite crystal on oriented thin sections to determine the EFG tensor of Fe<sup>2+</sup> at the M2 site of *Pbca* orthopyroxene of orthorhombic crystal system. Chemical formula of this sample was (Mg<sub>2.03</sub>, Fe<sub>0.16</sub>)(Si<sub>1.78</sub>, Al<sub>0.13</sub>)O<sub>6</sub> by EDS analyses.

**EXPERIMENTS and RESULTS:** A single crystal of enstatite from Turiani, Morogoro, Tanzania was used for this study. Three crystallographically oriented thin sections which are perpendicular to  $a^*$ ,  $b^*$  and  $c^*$  were prepared by measuring X-ray diffraction using precession camera. Nine Mössbauer spectra of oriented thin sections were measured. In this study, Cartesian coordinate ( $X Y Z$ ) is set as  $X//c^*$ ,  $Y//a^*$ ,  $Z//b^*$ , where  $a^*$ ,  $b^*$ ,  $c^*$  are reciprocal lattice vectors of enstatite. Mössbauer measurements were carried out in transmission mode on a constant acceleration spectrometer with an Si-PIN semiconductor detector (XR-100CR, AMPTEK Inc.) and multi-channel analyzer of 1024 channels. A 3.7GBq <sup>57</sup>Co/Rh of 4mm $\phi$  in diameter was used as  $\gamma$ -ray source. An <sup>57</sup>Fe-enriched iron foil was used as velocity calibrant. The two symmetric spectra were folded and velocity range was  $\pm 5$ mm/s. Thickness corrections of raw spectra were not done.

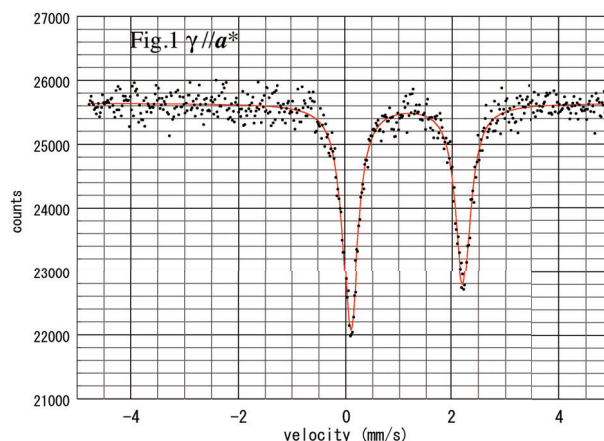


Fig.1 shows representative Mössbauer spectrum of enstatite measured under incident  $\gamma$ -ray parallel to  $a^*$ -axis. A doublet due to Fe<sup>2+</sup> in M2 site of orthopyroxene was observed. Isomer shift, Q-splitting, and line width were 1.06 2.11 and 0.34 mm/s, respectively. From nine sets of intensity of quadrupole doublet, three components of traceless tensor were calculated as 0.116, -0.045 and -0.075. Asymmetric parameter  $\eta$  was 0.266.

#### REFERENCES

- [1] R. Zimmermann (1983) Advances in Mössbauer spectroscopy (Thosar, B.V. Ed.). pp.273-315, Elsevier Scientific Publishing Co. Amsterdam.
- [2] R. Zimmermann (1975) Nucl. Instr. and Meth. **128**, 537-543.
- [3] W.C. Tennant, C. A. McCammon and R. Miletich (2000) Phys. Chem. Min., **27**, 156-163.
- [4] K. Shinoda, Y. Kobayashi (2019) J. Min. Petro. Sci., **114**, 130-141.

### PR8-3 Temperature Dependence of Mössbauer Spectra for Fe<sub>2</sub>O<sub>3</sub>-Al<sub>2</sub>O<sub>3</sub> Solid Solution

S. Takai<sup>1</sup>, H. Nakaishi<sup>1</sup>, K. Ota<sup>1</sup>, T. Yabutsuka<sup>1</sup>, T. Yao<sup>2</sup>,  
S. Kitao<sup>3</sup>, M. Seto<sup>3</sup>

<sup>1</sup>Graduate School of Energy Science, Kyoto University

<sup>2</sup>Kyoto University

<sup>3</sup>Institute for Integrated Radiation and Nuclear Science,  
Kyoto University

**INTRODUCTION:** Although both  $\alpha$ -Fe<sub>2</sub>O<sub>3</sub> and  $\alpha$ -Al<sub>2</sub>O<sub>3</sub> possess corundum-type structure, the solid solution range is so restricted as approximately 10 % from the terminal compositions due to 5.6 % smaller  $c$ -length for Al<sub>2</sub>O<sub>3</sub> in comparison with Fe<sub>2</sub>O<sub>3</sub> [1]. We have recently revealed that corundum-type structured solid solution can be obtained in the hole compositional range of Fe<sub>2</sub>O<sub>3</sub>-Al<sub>2</sub>O<sub>3</sub> system by means of mechanochemical method using high-energy ball milling technique. In terms of the continuous substitution of non-magnetic aluminum ions instead of iron in Fe<sub>2</sub>O<sub>3</sub>, dilution of spin interaction can be achieved in corundum-type structure, which would result in the variation of magnetic properties of (Fe<sub>2</sub>O<sub>3</sub>)<sub>1-x</sub>(Al<sub>2</sub>O<sub>3</sub>)<sub>x</sub> solid solution system.

$\alpha$ -Fe<sub>2</sub>O<sub>3</sub> exhibits antiferromagnetic properties at low temperatures, which undergo Morin transition at 265 K on heating to show a weak ferromagnetic. In the previous study (30121), Mössbauer spectroscopy experiments have been carried out on (Fe<sub>2</sub>O<sub>3</sub>)<sub>1-x</sub>(Al<sub>2</sub>O<sub>3</sub>)<sub>x</sub> solid solutions at room temperature. It is found that the Mössbauer spectra varies from sextet peaks at  $x = 0$  into almost doublet at  $x = 0.50$ . This indicates that substitution of aluminum ions allows the change in magnetic properties from weak ferromagnetism to paramagnetic state by reducing the spin interactions. It is also expected that spin ordering would be attributed by temperature, i.e. the Mössbauer spectra should be altered by reducing temperature. In the present study, we measured the Mössbauer spectra in the temperature range from 4 K up to the room temperature to investigate the variation of magnetic properties of (Fe<sub>2</sub>O<sub>3</sub>)<sub>0.5</sub>(Al<sub>2</sub>O<sub>3</sub>)<sub>0.5</sub>.

**EXPERIMENTS:** Stoichiometric mixture of  $\gamma$ -Fe<sub>2</sub>O<sub>3</sub> and  $\gamma$ -Al<sub>2</sub>O<sub>3</sub> reagents were put into a silicon nitride milling pod with 10 milling balls with the diameter of  $\phi 10$ . In the present study, the compositions were selected as  $x = 0.50$  for (Fe<sub>2</sub>O<sub>3</sub>)<sub>1-x</sub>(Al<sub>2</sub>O<sub>3</sub>)<sub>x</sub> system. Mechanical alloying has been carried out using a planetary ball milling machine operated at 800 rpm for 240 min. The crystalline phase of the obtained sample was confirmed by X-ray diffraction.

For the measurement of Mössbauer spectroscopy, <sup>57</sup>Co in Rh was employed as the  $\gamma$ -ray source. Doppler velocity scale has been calibrated by using Fe foil. The Mössbauer spectra were collected at various temperatures below 300K. Low temperature has been achieved by using He gas flow type refrigerator or liquid N<sub>2</sub> cryostat.

**RESULTS:** The Mössbauer spectra measured at various temperatures are represented in Fig. 1. At 300 K,

apparent doublet peaks are observed as the previous investigation of last year (30121). The doublet diminishes with decreasing temperature, while the sextet grows around 200 K, and almost sextet peaks are remained below 40 K. It is supposed that spin interaction thermally disturbed and attributed by small particle size would bring about the ordering at lower temperatures. Further precise analysis is now carried out accompanied by the neutron diffraction. Moreover, additional low temperature Mössbauer experiments are planning with other compositions.

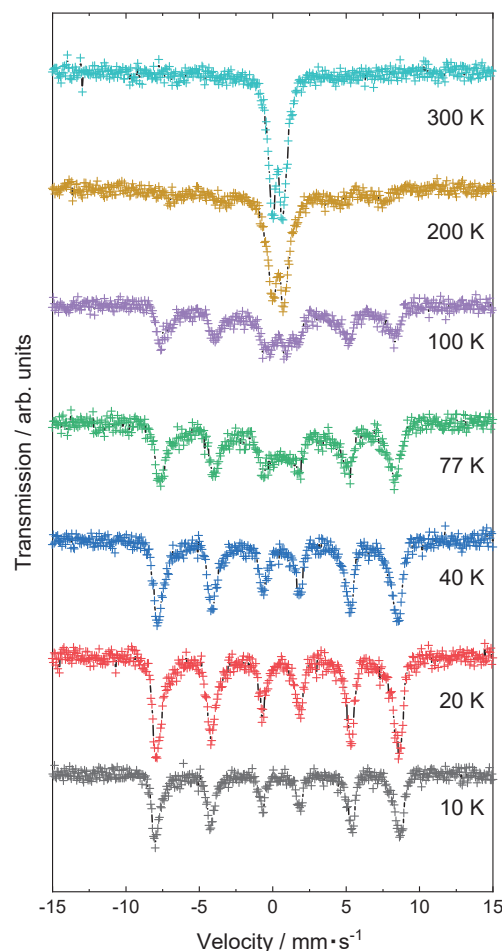


Fig. 1. Temperature dependence of Mössbauer spectra for (Fe<sub>2</sub>O<sub>3</sub>)<sub>0.5</sub>(Al<sub>2</sub>O<sub>3</sub>)<sub>0.5</sub>.

#### REFERENCES:

- [1] A. Muan *et al.*, *J. Am. Ceram. Soc.*, 39 (1956) 207-214.
- [2] S. Takai *et al.*, *Solid State Ionics*, 313 (2017) 1-6.

## PR8-4 A Nuclear Resonance Vibrational Spectroscopic Study of Oxy Myoglobin

T. Ohta, T. Shibata<sup>1</sup>, M. Saito<sup>2</sup>, M. Seto<sup>2</sup>, Y. Kobayashi<sup>2</sup>, S. Yanagisawa<sup>3</sup>, T. Ogura<sup>3</sup>, Y. Yamamoto<sup>1</sup>, S. Neya<sup>4</sup> and A. Suzuki<sup>5</sup>

Department of Applied Chemistry, Faculty of Engineering, Sanyo-Onoda City University

<sup>1</sup>Department of Chemistry, University of Tsukuba

<sup>2</sup>Integrated Radiation and Nuclear Science, Kyoto University

<sup>3</sup>Graduate School of Life Science, University of Hyogo

<sup>4</sup>Graduate School of Pharmaceutical Sciences, Chiba University

<sup>5</sup>Department of Materials Engineering, National Institute of Technology, Nagaoka College

**INTRODUCTION:** Myoglobin (Mb), an oxygen (O<sub>2</sub>) storage hemoprotein, has been served as a paradigm for the structure-function relationship of metalloproteins. O<sub>2</sub> is reversibly bound to a ferrous heme Fe atom (Fe(II)) in Mb. Although the reaction between O<sub>2</sub> and heme Fe(II) of Mb is often considered as one of the simplest biological reactions, in fact, the reaction is much more complicated than it appears. Upon oxygenation of the protein, ground state triplet O<sub>2</sub> is bound to a high-spin quintet heme Fe(II) in Mb to yield a low-spin singlet heme Fe(II) in oxy Mb (MbO<sub>2</sub>), which is considered as a mixture of Weiss (Fe<sup>3+</sup>(*S* = 1/2)-O<sub>2</sub><sup>-</sup>(*S* = 1/2)),<sup>1</sup> Pauling (Fe<sup>2+</sup>(*S* = 0)-O<sub>2</sub>(*S* = 0)),<sup>2</sup> and McClure forms (Fe<sup>2+</sup>(*S* = 1)-O<sub>2</sub>(*S* = 1)).<sup>3</sup> We characterized MbO<sub>2</sub>s possessing <sup>57</sup>Fe-enriched heme cofactors (Figure 1) using nuclear resonance vibrational spectroscopy (NRVS) to elucidate the electronic nature of the Fe-O<sub>2</sub> bond.<sup>4</sup>

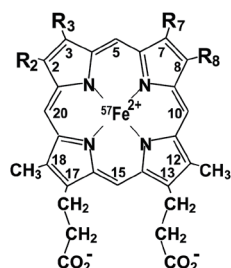


Figure 1. The structures and numbering system for the heme cofactors used in the study. Proto (R<sub>2</sub> = R<sub>7</sub> = CH<sub>3</sub>, R<sub>3</sub> = R<sub>8</sub> = CH=CH<sub>2</sub>), Meso (R<sub>2</sub> = R<sub>7</sub> = CH<sub>3</sub>, R<sub>3</sub> = R<sub>8</sub> = C<sub>2</sub>H<sub>5</sub>), and 7-PF (R<sub>2</sub> = CH<sub>3</sub>, R<sub>3</sub> = R<sub>8</sub> = C<sub>2</sub>H<sub>5</sub>, R<sub>7</sub> = CF<sub>3</sub>).

**EXPERIMENTS:** Iron-<sup>57</sup>Fe (95 atom%, Merck) was used to prepare <sup>57</sup>Fe-enriched heme cofactors. Sperm whale Mb was purchased as a lyophilized powder from Biozyme and used without further purification. Apoprotein of Mb was prepared using the procedure of Teale<sup>5</sup>. <sup>57</sup>Fe-enriched Proto, Meso, and 7-PF (Figure 1) were incorporated into apoprotein, and then the obtained proteins were converted to oxy forms, i.e., MbO<sub>2</sub>(Proto), MbO<sub>2</sub>(Meso), and MbO<sub>2</sub>(7-PF), respectively, using the standard procedure. NRVS measurements were performed at SPring-8, BL09XU<sup>6</sup>. During the data collection, the protein samples were maintained at low temperature using a liquid He cryostat (head temperature <10 K). Spectra were recorded between -20 and 80 meV in 0.25 meV steps. <sup>57</sup>Fe partial vibrational density of states (<sup>57</sup>Fe PVDOS) was calculated using a program PHOENIX<sup>7</sup>.

**RESULTS:** Based on the <sup>57</sup>Fe PVDOS of the proteins (Figure 2A), we found that the vibrational spectrum of MbO<sub>2</sub>(Proto) can be better reproduced by the spin polarized Fe<sup>3+</sup>-O<sub>2</sub><sup>-</sup> state calculated on the basis of broken-symmetry singlet state, rather than the Fe<sup>2+</sup>-O<sub>2</sub> closed-shell singlet one, in terms of the vibrational energies and peak intensities of the major bands due to the Fe-O<sub>2</sub> bond and the bonds between heme Fe and pyrrole nitrogen atoms. This finding supported the dominance of the Weiss form<sup>1</sup> in the nature of the Fe-O<sub>2</sub> bond in the protein.

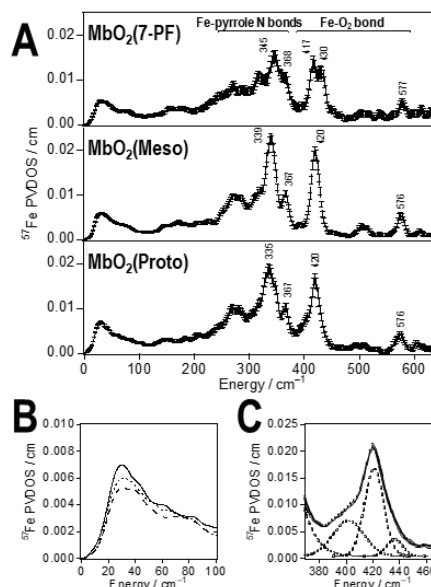


Figure 2. <sup>57</sup>Fe PVDOS of MbO<sub>2</sub>(Proto) at 43 K (bottom), MbO<sub>2</sub>(Meso) at 27 K (middle) and MbO<sub>2</sub>(7-PF) at 26 K (top) (A), expanded <sup>57</sup>Fe PVDOS of MbO<sub>2</sub>(Proto) (solid line), MbO<sub>2</sub>(Meso) (dotted line) and MbO<sub>2</sub>(7-PF) (broken line) in 0–100 cm<sup>-1</sup> (B), and deconvolution of Fe-O<sub>2</sub> band region, 370–470 cm<sup>-1</sup>, of MbO<sub>2</sub>(Proto) (C).

The comparison of the <sup>57</sup>Fe PVDOS below 100 cm<sup>-1</sup> between the proteins (Figure 2B) indicated that translational motion of heme cofactor is larger in MbO<sub>2</sub>(Proto) compared with those in MbO<sub>2</sub>(Meso) and MbO<sub>2</sub>(7-PF). The large conformational flexibility of MbO<sub>2</sub>(Proto) would be due to the presence of multiple conformations of the Fe-O<sub>2</sub> bond, because deconvolution of the Fe-O<sub>2</sub> band region of the <sup>57</sup>Fe PVDOS of MbO<sub>2</sub>(Proto), i.e., 400–430 cm<sup>-1</sup>, yielded at least three peaks at 402, 421 and 436 cm<sup>-1</sup> (Figure 2C), indicative of the presence of multiple conformations.

### REFERENCES:

- [1] J. J. Weiss, *Nature*, **202**, 83-84 (1964).
- [2] L. Pauling, *Nature*, **203**, 182-183 (1964).
- [3] D. S. McClure, *Radiation. Res. Suppl.*, **2**, 218-242 (1960).
- [4] T. Ohta *et al.*, *Biochemistry*, **57**, 6649-6652 (2018).
- [5] F. W. J. Teale, *Biochim. Biophys. Acta*, **35**, 543 (1959).
- [6] Y. Yoda *et al.*, *Hyperfine Interact.*, **206**, 83-86 (2012).
- [7] J. T. Sage *et al.*, *J. Phys.: Condens. Matter.*, **13**, 7707–7722 (2001).

Y. Maeno, M. Seto<sup>1</sup>, S. Kitao<sup>1</sup>, S. Yonezawa, A. Ikeda,  
S. Koibuchi, and M. Oudah.<sup>2</sup>

Graduate School of Science, Kyoto University

<sup>1</sup>Institute for Integrated Radiation and Nuclear Science,  
Kyoto University

<sup>2</sup>Stewart Blusson Quantum Matter Institute, University of  
British Columbia

**INTRODUCTION:** Antiperovskite (inverse perovskite) oxides  $A_3BO$  ( $A$ : group-2 element,  $B$ : group-14 element) crystalize in the same structure as the ordinary perovskite oxides, but with inverted positions of the cations and anions [1]. In those materials, a metallic anion  $B^{4-}$  ( $\text{Sn}^{4-}$ ,  $\text{Pb}^{4-}$ , etc.) is expected to satisfy the charge neutrality, assuming the ionic states of  $A^{2+}$  and  $\text{O}^{2-}$ . Metallic anions are rare especially in oxides. Originating from the unusual oxidation state, antiperovskite oxides are candidates for topological crystalline insulators [2, 3]. In 2016, some of the present authors discovered the first superconductor among antiperovskite oxides,  $\text{Sr}_{3-x}\text{SnO}$  [4]. Reflecting the nontrivial topology in the normal state, topological superconductivity is theoretically possible in this compound [5]. To investigate the unusual properties of this material, we performed Mössbauer spectroscopy on the Sn nucleus.

**EXPERIMENTS:** The sample was prepared from Sr (Sigma-Aldrich, 99.99%) and SnO (Sigma-Aldrich 99.99%) using the reaction  $(3-x)\text{Sr} + \text{SnO} \rightarrow \text{Sr}_{3-x}\text{SnO}$ , with a condition of  $x \sim 0.5$  [6]. From powder x-ray diffraction, we confirmed that the sample is dominated by  $\text{Sr}_{3-x}\text{SnO}$ . Superconductivity with a volume fraction of about 10% was observed below 5 K in a magnetization measurement. We also observed superconductivity of  $\beta$ -Sn impurity. From the diamagnetic signal, we estimated the amount of  $\beta$ -Sn impurity to be 14 mol %. We conducted Mössbauer spectroscopy at the Institute for Integrated Radiation and Nuclear Science, Kyoto University.  $^{119\text{m}}\text{Sn}$  in the form of  $\text{CaSnO}_3$  (Ritverc GmbH, 740 MBq) was used as the  $\gamma$ -ray source.

**RESULTS:** We present the Mössbauer spectra of  $\text{Sr}_{3-x}\text{SnO}$  in Fig. 1. We observed a clear  $\gamma$ -ray absorption with a shoulder at high temperatures, and the relative intensity of the shoulder increases at low temperatures.

To analyze the data, we fitted the spectra with three Lorentz functions, corresponding to the main and shoulder absorptions as well as  $\beta$ -Sn impurity. The isomer shift and intensity of one of three Lorentzians were fixed to that of the reported value for  $\beta$ -Sn and 14%, respectively. As a result, the isomer shifts at 3 K are fitted to be 1.960(6) mm/s for the main absorption and 2.973(11) mm/s for the shoulder. Since the isomer shift of the main absorption is close to that of  $\text{Mg}_2\text{Sn}$ , in which  $\text{Sn}^{4-}$  is anticipated, this result evidences presence of  $\text{Sn}^{4-}$  in

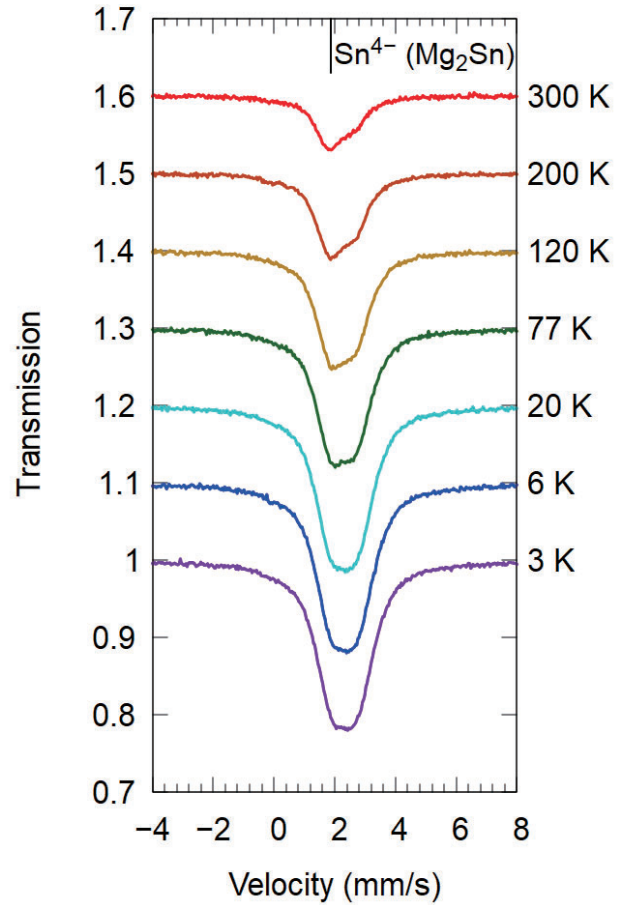


Fig. 1. Mössbauer spectra of  $\text{Sr}_{3-x}\text{SnO}$  ( $x \sim 0.5$ ) with respect to the isomer shift of  $\text{BaSnO}_3$ . Each spectrum is shifted upward by 0.1 for visibility.  $\gamma$ -ray absorption with an isomer shift similar to that of  $\text{Mg}_2\text{Sn}$  evidences presence of  $\text{Sn}^{4-}$ . In addition, another absorption with a larger isomer shift originating from Sr deficiency was observed.

$\text{Sr}_{3-x}\text{SnO}$ . The shoulder with a larger isomer shift originates from a modified ionic state of  $\text{Sn}^{4-}$  hole-doped by Sr deficiency. The greater temperature evolution of the shoulder, corresponding to a higher local Debye temperature, is consistent with the Sn atoms neighboring the Sr vacancies.

Detailed results were published in Ref. [6], where we evaluated the isomer shift and the Debye temperature using the first-principles calculation.

#### REFERENCES:

- [1] A. Widera and H. Schafer, *Mater. Res. Bull.* **15** (1980) 1805–1809.
- [2] T. Kariyado and M. Ogata, *J. Phys. Soc. Jpn.* **80** (2011) 083704.
- [3] T. H. Hsieh *et al.*, *Phys. Rev. B* **90** (2014) 081112(R).
- [4] M. Oudah *et al.*, *Nat. Commun.* **7** (2016) 13617.
- [5] T. Kawakami *et al.*, *Phys. Rev. X* **8** (2018) 041026.
- [6] A. Ikeda *et al.*, *Phys. Rev. B* **100** (2019) 245145.

Y. Kamihara, R. Sakagami, S. Kitao<sup>1</sup>, M. Seto<sup>1</sup>

Department of Applied Physics and Physico-Informatics,  
Keio University

<sup>1</sup>Institute for Integrated Radiation and Nuclear Science,  
Kyoto University

**INTRODUCTION:** In this research, we demonstrate the magnetic phases in a novel Kondo lattice,  $\text{EuSn}_2\text{As}_2$ .  $\text{EuSn}_2\text{As}_2$  is an inter-metallic compound, which is reported by Arguilla *et al.*[1] and is a 2 dimensional layered magnetic compound composed by Eu cation and negative charged  $\text{Sn}_2\text{As}_2$ . In a unit cell of  $\text{EuSn}_2\text{As}_2$ , van der Waals interaction is dominant force to make chemical bonding along  $c$ -axis. Such characteristic chemical bonds are similar to those of "state of art" 2 dimensional topological insulator,  $\text{Bi}_2(\text{Se}, \text{Te})_3$  [2,3,4], which have been focused as thermo electric materials since 1961 or earlier. In 2019, we unveiled a complex magnetic phases in  $\text{EuSn}_2\text{As}_2$ .

In undoped  $\text{EuSn}_2\text{As}_2$ , density functional theory (DFT) demonstrates that a sublattice of Eu orders antiferromagnetically at temperature ( $T$ ) = 0 K, although Eu ions ferromagnetically ordered along  $a / b$  axes; i.e. the Eu orders ferromagnetic intra layer.

In 2019, we demonstrated spontaneous magnetic moments of undoped  $\text{EuSn}_2\text{As}_2$  using DC-magnetic moment measurements. The spontaneous magnetic moments verify a ferromagnetic phase of undoped  $\text{EuSn}_2\text{As}_2$  under weak finite magnetic fields at low  $T$ . [5]

These results indicate that a magnetic phase of undoped  $\text{EuSn}_2\text{As}_2$  is changed to the ferromagnetic order under finite magnetic fields from the antiferromagnetic order under a zero field. In the ferromagnetic order phase, the Eu ion exhibits  $\sim 5 \mu_B$  at  $T < \sim 20$  K. The magnetic moment of Eu is smaller than that of representative  $\text{Eu}^{2+}$ .

The small magnetic moment of Eu suggests a highly hybridized electronic orbital among Eu and Sn atomic orbitals, although direct measurements of internal magnetic fields have not been reported for  $\text{EuSn}_2\text{As}_2$ .

In this research, we have measured  $^{151}\text{Eu}$  and  $^{119}\text{Sn}$  Mössbauer spectroscopy, and demonstrate an appearance of internal magnetic fields at low  $T$  in undoped  $\text{EuSn}_2\text{As}_2$ .

**EXPERIMENTS:** Synthesis procedure of the polycrystalline undoped  $\text{EuSn}_2\text{As}_2$  has been reported in ref.[6]. Optical systems for the Mössbauer spectroscopy are conventional.[7]

**RESULTS:** As shown in Fig. 1, Mössbauer spectra of  $^{151}\text{Eu}$  demonstrate a clear magnetic splitting at  $T = 4.2$  K for undoped  $\text{EuSn}_2\text{As}_2$ . As shown in Fig. 2, the  $^{119}\text{Sn}$  Mössbauer spectra also demonstrate magnetic splitting at  $T < 20$  K. A quantitative analysis on internal magnetic field should be performed in the collaborative research in 2020.

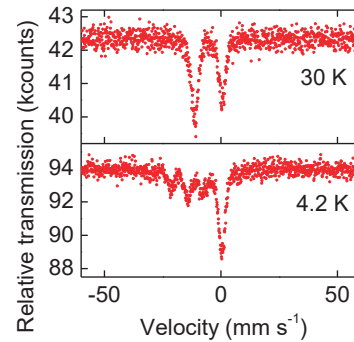


Fig. 1.  $^{151}\text{Eu}$  Mössbauer spectra for polycrystalline undoped  $\text{EuSn}_2\text{As}_2$ .

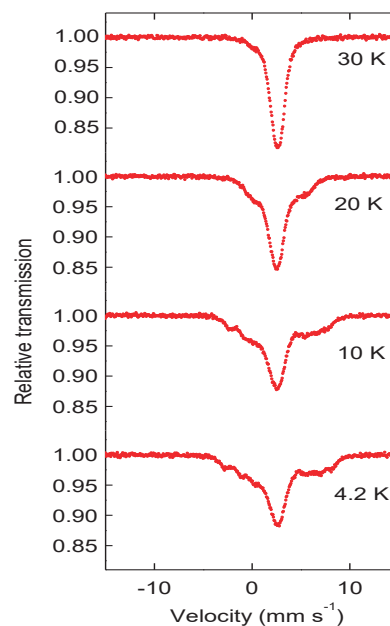


Fig. 2.  $^{119}\text{Sn}$  Mössbauer spectra for polycrystalline undoped  $\text{EuSn}_2\text{As}_2$ .

#### REFERENCES:

- [1] M. Q. Arguilla, *et al.*, Inorg. Chem. Front. 4, 378-386 (2017).
- [2] C. L. Kane and E. J. Mele, Phys. Rev. Lett. 95, 146802 (2005).
- [3] H. Zhang, *et al.*, Nature Phys. 5, 438-442 (2009).
- [4] H. J. Goldsmid and R. T. Delves, G.E.C. Journal 28, 102 (1961).
- [5] K. Hirata, *et al.*, "Spontaneous magnetic polarization of a layered hexagonal compound,  $\text{EuSn}_2\text{As}_2$ ", The 6th Japan-Korean International Symposium on Materials Science and Technology (JKMST2019), Sapporo, Japan: 26th August 2019.
- [6] R. Sakagami, *et al.*, Mater. Sci. Tech. Jpn. 55, 72-76 (2018). In Japanese
- [7] S. Kitao, *et al.*, J. Phys. Soc. Jpn. 77, 103706 (2008).

## PR8-7 Study on Structure of Gold Complexes Coordinated with $\alpha$ -Amino Acids by Means of $^{197}\text{Au}$ Mössbauer Spectroscopy

H. Murayama, M. Takaki, Y. Kobayashi<sup>1</sup>, H. Ohashi<sup>2</sup>, T. Ishida<sup>3</sup>, D. Kawamoto<sup>4</sup> and M. Tokunaga

Department of Chemistry, Kyushu University

<sup>1</sup>Institute for Integrated Radiation and Nuclear Science, Kyoto University

<sup>2</sup>Faculty of Symbiotic Systems Science, Fukushima University

<sup>3</sup>Department of Applied Chemistry for Environment, Tokyo Metropolitan University

<sup>4</sup>Department of Chemistry, Okayama University of Science

**INTRODUCTION:** Gold nanoparticles show catalytic activities when their sizes were less than 5 nm. We have reported a simple and easy impregnation method for the preparation of small gold nanoparticles deposited on various supports [1]. A gold complex coordinated with  $\beta$ -alanine (Au- $\beta$ -ala) was synthesized as a chloride-free and water-soluble precursor for this method. A molecular structure of Au- $\beta$ -ala was determined as mononuclear complexes of  $\text{Au}^{3+}$  with square-planar coordination by means of in situ X-ray absorption fine structure, TG-DTA, and DFT calculations (Fig. 1). Recently, the gold complexes coordinated with various kinds of amino acids were synthesized to realize better precursor than Au- $\beta$ -ala. In this study, the structures of the gold complexes were analyzed by  $^{197}\text{Au}$  Mössbauer spectra.

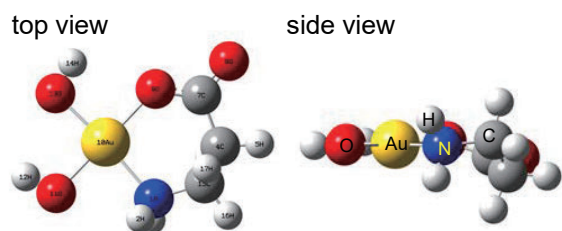


Fig. 1. The geometry of Au- $\beta$ -ala optimized by DFT calculation.

**EXPERIMENTS:** Gold complexes coordinated with amino acid ( $\beta$ -ala,  $\gamma$ -aminobutyric acid (GABA),  $\delta$ -aminovaleric acid (DAVA),  $\epsilon$ -aminocaproic acid (EAHA), tryptophan (Trp), histidine (His), and tyrosine (Tyr)) were synthesized as follows: ethanol was added to a NaOH aqueous solution in which amino acid was dissolved. The amino acid solution was then added to the  $\text{HAuCl}_4$  ethanol/water mixed solution. The mixed solution was left at  $-18^\circ\text{C}$  for 12 h. The precipitates were collected and washed with ethanol/water. The solid was dried to obtain Au-amino acid complex powder [1].  $^{197}\text{Au}$  Mössbauer spectra of the synthesized Au-amino acid complexes were collected at Institute for Integrated Radiation and Nuclear Science, Kyoto University. The  $\gamma$ -ray source ( $^{197}\text{Pt}$ ) feeding the 77.3 keV Mössbauer tran-

sition of  $^{197}\text{Au}$ , was prepared by neutron irradiation of isotopically enriched  $^{196}\text{Pt}$  metal at the Kyoto University Reactor. The  $\gamma$ -ray source and the samples were cooled to a temperature below 20K. The isomer shift ( $IS$ ) of Au foil was referenced to 0 mm/s.

**RESULTS:** As shown in Fig. 2a, the  $^{197}\text{Au}$  Mössbauer spectrum for Au- $\beta$ -ala, which consisted of doublet peaks, was analyzed and then the  $IS$  and the quadrupole splitting ( $QS$ ) were obtained as 4.29 mm/s and 4.93 mm/s, respectively. Similar values were obtained from analyses of the spectra for Au-GABA, Au-DAVA, and Au-EAHA. The values of  $IS$ - $QS$  were in the range of data given by various four-coordinate gold(III) compounds [2]. In addition to the doublet as same as that in the spectrum for Au- $\beta$ -ala, another doublet was observed in the spectrum for Au-Trp (Fig. 2b). The values of  $IS$  and  $QS$  were 3.44 mm/s and 7.83 mm/s, respectively. The characteristic double doublets were also observed in the spectra for gold complexes coordinated with  $\alpha$ -amino acid (His and Tyr) indicating that those gold complexes were mixtures of gold(III) and gold(I).

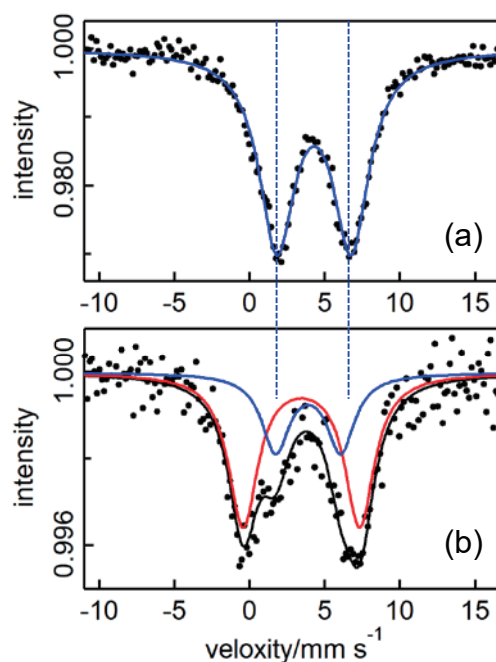


Fig. 2.  $^{197}\text{Au}$  Mössbauer spectra for (a) Au- $\beta$ -ala and (b) Au-Trp.

### REFERENCES:

- [1] H. Murayama *et al.*, J. Catal., **353** (2017) 74-80.
- [2] R. V. Parish, Gold Bull., **15** (1982) 51-63.

Y. Kobayashi, J. Wang<sup>1</sup> and M. Seto

*Institute for Integrated Radiation and Nuclear Science,  
Kyoto University*

<sup>1</sup>*Dalian Institute of Chemical Physics, Chinese Academy  
of Sciences*

**INTRODUCTION:** The normal surface of metallic gold does not adsorb small molecules like hydrogen and oxygen; thus, gold is not generally considered as a good catalyst. Small particles have many edges, corners, and metastable surfaces, and they are different from bulk for catalytic activities. Dispersing the small particles on supports, the catalytic activity of gold increases. Au small particles supported on some materials show high catalytic activity to oxidize CO to CO<sub>2</sub> at temperatures as low as 197K [1,2].

The interaction between particles and supports may give new activity to the catalysts. Hydroxyapatite (HAp) is known as bone mineral, and it is nature friendly. Further-more, it is good support for nanoparticles [3]. HAp binds strongly with Au, and it avoids the fusion of the nanoparticles. This binding with HAp may change the charge of Au, which is expected to show different properties from the bulk.

We have studied the supported Au nanoparticles catalysis using <sup>197</sup>Au Mössbauer spectroscopy. We can observe the signals from Au atoms without disturbance from supports by <sup>197</sup>Au Mössbauer spectroscopy. Moreover, it is sensitive to the electronic states of Au atoms. Thus, Mössbauer spectroscopy is powerful for the study of supported catalysts.

**EXPERIMENTS:** The supported Au nanoparticles catalysis was prepared by the deposition precipitation method and calcination. The mixed solution of HAuCl<sub>4</sub> and HAp was kept on pH 9 and 65°C, thus the Au ions were precipitate on HAp as Au(OH)<sub>3</sub>. After precipitation, the specimens were washed with distilled water, and dried. These specimens were calcined for 4 hours at 200~800°C in air. At that time, Au(OH)<sub>3</sub> was degraded into Au metal, and the Au nanoparticles were firmly fixed on HAp.

<sup>197</sup>Au Mössbauer measurement was conducted using a constant-acceleration spectrometer with a NaI scintillation counter. The <sup>197</sup>Au  $\gamma$ -ray source (77.3 keV) was obtained from <sup>197</sup>Pt (half-life; 18.3 hrs) generated by irradiation of neutron to 98%-enriched <sup>196</sup>Pt metal foil using KUR. The  $\gamma$ -ray source and samples were cooled to 16 K, and the spectra were recorded in a transmission geometry. The isomer shift value of a gold foil was referenced to 0 mm/s.

**RESULTS:** Figure 1 shows the <sup>197</sup>Au Mössbauer spectra of the Au nanoparticle catalysis prepared by several calcination temperatures. All observed spectra show almost the same shape and peak position. This result indicates that the electronic states of the nanoparticles are nearly the same as that of metallic bulk Au. However, in detail, the value of the isomer shift slightly changes from 0.09 mm/s to 0.04 mm/s from the 200°C calcined sample to the 800°C calcined sample. The direction of this change is the direction in which the charge of the Au atom decreases; however, the difference is only slightly above the error, and further verification is necessary.

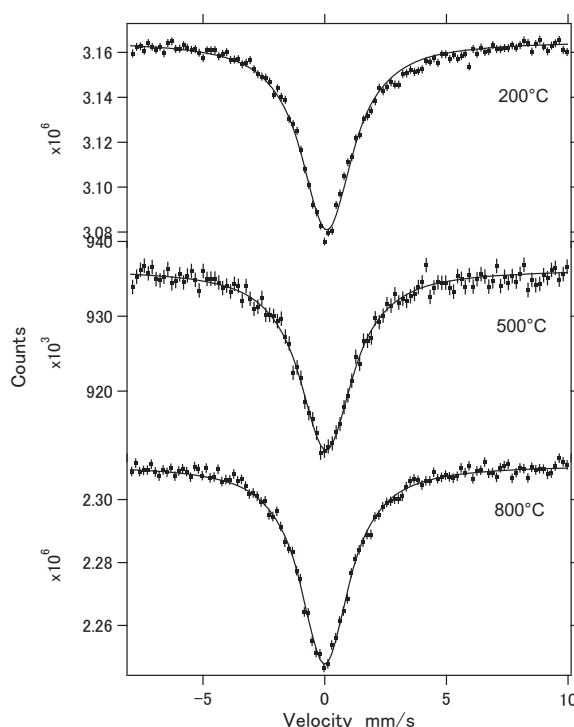


Fig. 1 <sup>197</sup>Au Mössbauer spectra of Au nano-particles catalysis prepared by several calcination temperatures. The measurement temperature was 16K.

**REFERENCES:**

- [1] M. Haruta, T. Kobayashi, H. Sano and N. Yamada, *Chem. Lett.*, **16** (1987) 405.
- [2] M. Haruta, N. Yamada, T. Kobayashi and S. Iijima, *J. Catal.*, **115** (1989) 301.
- [3] Yanjie Zhang, Junhu Wang, Jie Yin, Kunfeng Zhao, Changzi Jin, Yuying Huang, Zheng Jiang, and Tao Zhang, *J. Phys. Chem. C*, **114** (2010) 16443-16450.

S. Kitao<sup>1</sup>, M. Kobayashi<sup>1</sup>, T. Kubota<sup>1</sup>, M. Kurokuzu<sup>1</sup>, H. Tajima<sup>2</sup>, and M. Seto<sup>1</sup>

<sup>1</sup>*Institute for Integrated Radiation and Nuclear Science, Kyoto University*

<sup>2</sup>*Graduate School of Science, Kyoto University*

### INTRODUCTION:

The Mössbauer spectroscopy is one of the most powerful methods for investigation of electronic states, magnetic properties, chemical properties, and so on. A remarkable feature of this method is to extract the information of the specific isotope. Although about one hundred of Mössbauer energy levels are known, research activities in Mössbauer studies so far are quite limited, except  $^{57}\text{Fe}$  and  $^{119}\text{Sn}$ . It is partly because commercially available sources at present are only  $^{57}\text{Co}$  and  $^{119\text{m}}\text{Sn}$  for the Mössbauer spectroscopy of  $^{57}\text{Fe}$  and  $^{119}\text{Sn}$ , respectively.

On the contrary, at the Institute for Integrated Radiation and Nuclear Science, various short-lived isotopes can be obtained by neutron irradiation at Kyoto University Research Reactor(KUR). Moreover, some short-lived isotopes can be complementarily produced by high-energy  $\gamma$ -ray irradiation at the electron linear accelerator(KURNS-LINAC). Thus, we have already been performing Mössbauer spectroscopy with various isotopes(by source nuclides in parentheses):  $^{61}\text{Ni}$ ( $^{61}\text{Co}$ ),  $^{125}\text{Te}$ ( $^{125\text{m}}\text{Te}$ ),  $^{129}\text{I}$ ( $^{129}\text{Te}$ ,  $^{129\text{m}}\text{Te}$ ),  $^{161}\text{Dy}$ ( $^{161}\text{Tb}$ ),  $^{166}\text{Er}$ ( $^{166}\text{Ho}$ ),  $^{169}\text{Tm}$ ( $^{169}\text{Er}$ ),  $^{170}\text{Yb}$ ( $^{170}\text{Tm}$ ),  $^{197}\text{Au}$ ( $^{197}\text{Pt}$ ), etc.

The main purpose of this research is to develop effective Mössbauer sources for various isotopes and to apply this spectroscopy to many fields of researches. Among these researches, an improvement of  $^{166}\text{Er}$  Mössbauer spectroscopy is described in this report.

### EXPERIMENTS AND RESULTS:

Although several levels are known in the Mössbauer spectroscopy of Er, the 80.6 keV level of  $^{166}\text{Er}$  is the most useful level. Since the natural abundance of  $^{165}\text{Ho}$  is 100 %, by neutron irradiation of natural Ho,  $^{166}\text{Ho}$  with a half-life of 26.8 hours can be obtained for the Mössbauer source without by-product nuclides. As for the source material, we have synthesized  $\text{HoAl}_2$ , by arc-melting

method from Ho and Al. The obtained  $\text{HoAl}_2$  powder was sealed in polypropylene capsule with polystyrene resin. The neutron irradiation has been done by the pneumatic tube station(Pn) at KUR.

Since  $\text{HoAl}_2$  has a Curie temperature of about 25 K[1,2], the source temperature had better to be kept above 40 K to avoid line broadening by magnetic splitting. Since the recoilless fraction of Er compounds is low at high temperature, the sample and the source were usually cooled at the temperature of 40 K by using He-closed-cycle refrigerator. The gamma-rays with the energy of 80.6 keV have been measured by  $\text{CeBr}_3$  scintillation detector.

Until last year, several  $^{166}\text{Er}$  experiments have already been performed at KUR by users from other research groups[3]. However, because of the limitation from radiation safety regulations, the radioactivity of  $^{166}\text{Ho}$  was limited to 20 MBq. Some experiments had suffered from poor statistics. Therefore, in order to promote the  $^{166}\text{Er}$  experiments, we requested to extend the limitation and it was approved to be extended to 500 MBq.

In order to check the effectiveness of the gain of source activity and the radiation safety of experimental condition, a comparison was done using  $\text{Er}_2\text{O}_3$  absorber with the same source material of  $\text{HoAl}_2$  at about 18 to 20 K. The obtained activity was controlled by irradiation time. Similar measurements have been performed by 20 MBq and 98 MBq source as shown in Fig.1 and Fig.2, respectively. The experiment was successfully performed without any problem in radiation safety. The statistics of the spectra was well improved by the gain of radioactivity. The results showed the improvement of the  $^{166}\text{Ho}$  source was successful. The observed Mössbauer spectra showed the line broadening due to magnetic splitting of  $\text{HoAl}_2$  below Curie temperature. This source will be useful for various application in Er compounds, when measured at 40 K.

### REFERENCES:

- [1] E. Munck, D. Quitmann, S. Hufner, Z. Naturforsch. **21A**, 847 (1966).
- [2] E. Munck, D. Quitmann, S. Hufner, Phys. Lett. **24B**, 392 (1967).
- [3] S. Nakamura, H. Yokota, S. Kitao, Y. Kobayashi, M. Saito, R. Masuda, M. Seto, Hyperfine Interact. **240**, 75 (2019).

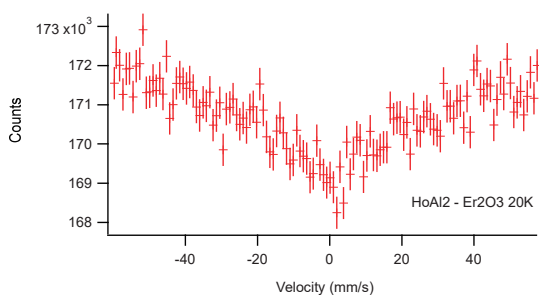


Fig. 1.  $^{166}\text{Er}$ -Mössbauer spectrum of  $\text{Er}_2\text{O}_3$  at 20 K using 20MBq  $^{166}\text{Ho}$  source in  $\text{HoAl}_2$ .

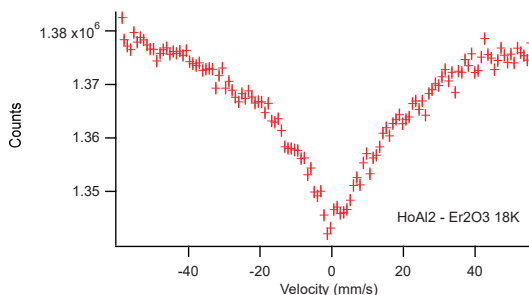


Fig. 2.  $^{166}\text{Er}$ -Mössbauer spectrum of  $\text{Er}_2\text{O}_3$  at 18 K using 98MBq  $^{166}\text{Ho}$  source in  $\text{HoAl}_2$ .

## **I-1. PROJECT RESEARCHES**

### **Project 9**

## PR9 Project Research on Boron Dynamics in Plants using Neutron Capture Reaction: Development of Boron Analytical Method and Elucidation of its Physiological Function

T. Kinouchi

*Institute for Integrated Radiation and Nuclear Science,  
Kyoto University*

### BACKGROUND AND OBJECTIVE

Boron is an essential micronutrient for all plants. In general, boron in the soil dissolves in rainwater to form boric acid, which migrates into the groundwater. Therefore, in Japan or Southeast Asia, where there is a large amount of precipitation, the concentration of boron in the soil tends to decrease. As a result, various crops suffer from a growth disorder, called “boron deficiency,” and it significantly reduces the value and productivity as the agricultural products. While the use of fertilizers, which contain boron, can restore them from its deficiency, boron overload causes other disorders for plants, such as sterility. Especially in semi-arid areas such as central Asia, in which the amount of precipitation is small, in fact the agricultural damage caused by the boron overload stress is more serious rather than by a simple lack of water. Despite this situation, drastic measures have not made, since there is not enough information on the physiological functions of boron to develop the effective measures compared to other essential micronutrients. In order to understand the physiological functions of micronutrients, research has often been carried out to investigate their kinetics in plants by tracer experiments using their radioisotopes. In fact, Tsukamoto *et al.* revealed that iron (Fe) distribution was different depending on the process of plant growth by a tracer experiment using  $^{52}\text{Fe}$  (*Plant Cell Physiol.* 2009; 50(1): 48–57). On the other hand, recently it was put to practical use for a novel method by injecting boric-acid water into wood building material. This method is an epoch-making one that incorporates antiseptic properties to the wood by applying the insecticidal activity and cross-linking function in the cell wall of boron. However, if this development goes on without paying due attention to the leaching of boron from this wood, it may cause great adverse impacts on the environment.

If a method to analyze multi-dimensional information of boron in plants is developed, the productivity of agricultural products will be improved by advancing understanding of the physiological functions of boron. Moreover, it is very promising in the contribution to the public interest in many ways, such as reinforcing historical wooden buildings by the injection of a proper dose of boron. Therefore, we decided to establish a method to perform precise detection and quantification of boron in plant tissue using a neutron capturing reaction.

### ALLOTTED RESEARCH SUBJECTS

This project research is composed by three individual subjects as follows;

**PR-1:** Analysis of boron transport within roots using neutron capture radiography (M. Kobayashi and T. Kinouchi)

**PR-2:** Analysis of Localization of Boron in Root Tissues by Neutron Capture Radiography (S. Kitajima, M. Kobayashi and T. Kinouchi)

**PR-3:** Improvement of *In Situ* Visualization of Boron Distributed in Plants by Neutron Capture Reaction (T. Kinouchi)

### MAIN RESULTS

**PR-1:** Kobayashi *et al.* performed a time-course analysis of the localization of boron newly taken up into tap roots of radish seedlings. The result suggests that the delivery of boron to the innermost pith and medullary ray takes more time compared to the other parts, as the endodermis blocks an influx of boron from the external medium, and hence the acquisition relies on the diffusion of boric acid from xylem.

**PR-2:** Kitajima analyzed vertical distribution of boron in Arabidopsis tap roots by neutron capture radiography. High amount of boron was observed in the root cap and apical meristem.

**PR-3:** Kinouchi tried to improve *in situ* visualization technique of boron distribution in plants, which was grown in a boron-10 enriched medium, by neutron capture radiography. As a result, it was visualized that a large amount of boron was detected at the center tissues and cambium of the radish tap root.

## PR9-1 Analysis of Boron Transport within Roots using Neutron Capture Radiography

M. Kobayashi and T. Kinouchi<sup>1</sup>

Graduate School of Agriculture, Kyoto University

<sup>1</sup> Institute for Integrated Radiation and Nuclear Science, Kyoto University

**INTRODUCTION:** Boron (B) is one of the essential micronutrients for vascular plants. At cellular level, B occurs mainly in apoplast to form a borate diester with the rhamnogalacturonan II regions of pectin. In addition to this “bound form” of B, plants contain free boric acid as well, under the condition of sufficient B supply. However, it still remains unclear how B in these forms distribute within plant tissues. To address the issue, we have been trying to develop a technique for *in situ* visualization of B in plants using neutron capture radiography [1-3]. Results of our previous analyses suggest that B distributes unevenly within roots. To understand the physiological relevance of the uneven distribution, it would be useful to analyze the movement of B within the roots. Thus, in this study we performed a time-course analysis of the localization of B newly taken up into tap roots of radish seedlings.

**EXPERIMENTS:** Seeds of radish (*Raphanus sativus* L. *sativus*) were germinated on vermiculite and cultivated under a 16-h light/8-h dark cycle in a growth chamber set at 23°C and 60% relative humidity. A week later, the seedlings were transferred to the hydroponic media containing 1 mM Ca(NO<sub>3</sub>)<sub>2</sub>, 0.5 mM KH<sub>2</sub>PO<sub>4</sub>, 0.5 mM K<sub>2</sub>SO<sub>4</sub>, 1 mM MgSO<sub>4</sub>, 1.5 mM NH<sub>4</sub>NO<sub>3</sub>, 75 μM EDTA-Fe, 46 μM H<sub>3</sub><sup>11</sup>BO<sub>3</sub>, 9 μM MnSO<sub>4</sub>, 0.8 μM ZnSO<sub>4</sub>, 0.3 μM CuSO<sub>4</sub>, and 0.8 μM Na<sub>2</sub>MoO<sub>4</sub> under the same cultivation condition. After 6 days of cultivation, seedlings were transferred to the hydroponic medium of the same composition except that H<sub>3</sub><sup>11</sup>BO<sub>3</sub> was replaced with H<sub>3</sub><sup>10</sup>BO<sub>3</sub>, then cultivated further for additional 24–96 h. Detached tap roots were fixed with glutaraldehyde and embedded in OCT compound (Tissue-Tek), frozen in liquid nitrogen, and sectioned at 10-μm thickness with a sliding microtome. The section was mounted on CR-39 nuclear tracker detector (20 mm×30 mm) and irradiated with epithermal neutron by applying to the pneumatic tube in the graphite thermal column (Tc-Pn) of Kyoto University Research Reactor (KUR). The CR-39 plate after irradiation was etched in 6 M NaOH solution for 90 min, and the resulting etch-pits were observed under an optical microscope.

**RESULTS:** The boron neutron capture technique detects <sup>10</sup>B but not <sup>11</sup>B. In this study, radish seedlings were grown in an <sup>11</sup>B-enriched medium and then transferred to the medium containing <sup>10</sup>B, hence the time-course change of the signal should represent the movement of B taken up after the treatment. Figure 1 shows a representative set of radiographs of the roots sampled at 48–96 h after the treatment. Etch pits could be observed clearly in the sec-

tion of the roots sampled at 48 h after treatment (Fig. 1B), indicating that significant amount of <sup>10</sup>B had already been taken up by that time. Nonetheless, further intensification of the signal was discernible over time, especially in the innermost pith and medullary ray inside the endodermis (Fig. 1D, F). The result suggests that the delivery of B to the regions takes more time compared to the other parts, as the endodermis blocks an influx of B from the external medium, and hence the acquisition relies on the diffusion of boric acid from xylem. The regions seem to coincide with the area where brown heart of tap roots, which has been suspected to be related with B deficiency, occurs in Japanese radish. Further analyses with shorter periods of <sup>10</sup>B feeding may give better resolution of the movement of B within tissues.

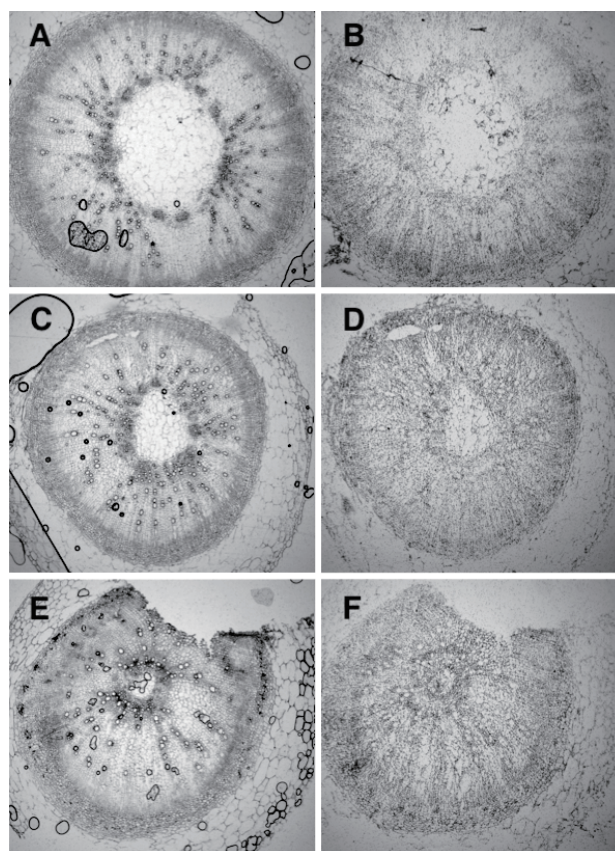


Fig. 1. Detection of B in radish roots using neutron capture radiography. (A), (C), and (E): Optical microscopic images of cross-sections of radish tap roots taken before irradiation; (B), (D), and (F): etch-pit images of (A), (C), and (E) after irradiation, respectively. (A) and (B): 48 h, (C) and (D): 72 h, (E) and (F): 96 h after transfer to <sup>10</sup>B-medium, respectively.

### REFERENCES:

- [1] M. Kobayashi and T. Kinouchi, KURRI Progress Report, 2014 12929-12929 (2014).
- [2] T. Kinouchi and M. Kobayashi, KURNS Progress Report 2018, 122 (2019).
- [3] T. Kinouchi, KURNS Progress Report 2018, 121 (2019).

## PR9-2 Analysis of Localization of Boron in Root Tissues by Neutron Capture Radiography

S. Kitajima<sup>1</sup>, M. Kobayashi<sup>2</sup> and T. Kinouchi<sup>3</sup>

<sup>1</sup> Department of Applied Biology, Kyoto Institute of Technology

<sup>2</sup> Graduate School of Agriculture, Kyoto University

<sup>3</sup> Institute for Integrated Radiation and Nuclear Science, Kyoto University

**INTRODUCTION:** In plant primary cell walls, boron provides a cross-link as a borate ester between apiose residues of rhamnogalacturonan II (RG-II) in pectin [1]. Thus Borate-RG-II complex is an essential factor in the formation of the pectic network, which contributes to cell adhesion or physical characteristics of plants. In fact, boron deficiency causes various physiological disorders in plants, such as necrosis of tap roots or reduced fertility. On the other hand, the distribution of boron within plant tissues still remains unclear. In our previous analyses, it was suggested that a large amount of boron would be distributed in the central part and cambium of radish tap roots. In order to study the vertical distribution of boron in plants, we tried to analyze *Arabidopsis* tap roots by neutron capture radiography.

**EXPERIMENTS:** Plant material> Seeds of *Arabidopsis thaliana* were germinated in the hydroponic media containing 1 mM  $\text{Ca}(\text{NO}_3)_2$ , 0.5 mM  $\text{KH}_2\text{PO}_4$ , 0.5 mM  $\text{K}_2\text{SO}_4$ , 1 mM  $\text{MgSO}_4$ , 1.5 mM  $\text{NH}_4\text{NO}_3$ , 75  $\mu\text{M}$  EDTA-Fe, 46  $\mu\text{M}$   $\text{H}_3\text{BO}_3$ , 9  $\mu\text{M}$   $\text{MnSO}_4$ , 0.8  $\mu\text{M}$   $\text{ZnSO}_4$ , 0.3  $\mu\text{M}$   $\text{CuSO}_4$ , and 0.8  $\mu\text{M}$   $\text{Na}_2\text{MoO}_4$ , and cultivated at 23°C under a 16-h light/8-h dark cycle in a 60%-humidified growth chamber.

*In situ* visualization of boron by neutron capture radiography> After 6 days of cultivation, seedlings were fixed with 3% glutaraldehyde solution containing 250 mM sucrose. Chilled *Arabidopsis* in liquid nitrogen was sectioned at 10- $\mu\text{m}$  thickness by a cryostat. The section was mounted onto CR-39 nuclear track detector and irradiated with epithermal neutron for 15 min by application to the pneumatic tube in the graphite thermal column (Tc-Pn) of Kyoto University Research Reactor (KUR). The irradiated CR-39 was etched in 6 M NaOH solution, and the resulting etch-pits were observed under an optical microscope.

**RESULTS:** Etch pit could be observed clearly in the vertical section of the *Arabidopsis* roots (Fig. 1C). As well as radish tap roots [1], boron in *Arabidopsis* roots was concentrated at the center and outer peripheral tissues as indicated by arrows. Interestingly, at the tip of the root, high amounts of boron were observed (Fig. 1E, G). Fig. 1D and F shows the root cap and apical meristem, which consists of undifferentiated cells (meristematic cells). Since both tissues cause cell division actively and require physical strength by synthesizing new cell walls, a large amount of boron would be applied. Recently, we improved the resolution of this visualization technique by culturing plants in a special solution replac-

ing natural boron with boron-10. Further analyses based on the detailed boron-distribution might help understand the molecular mechanism regarding controlling root elongation growth.

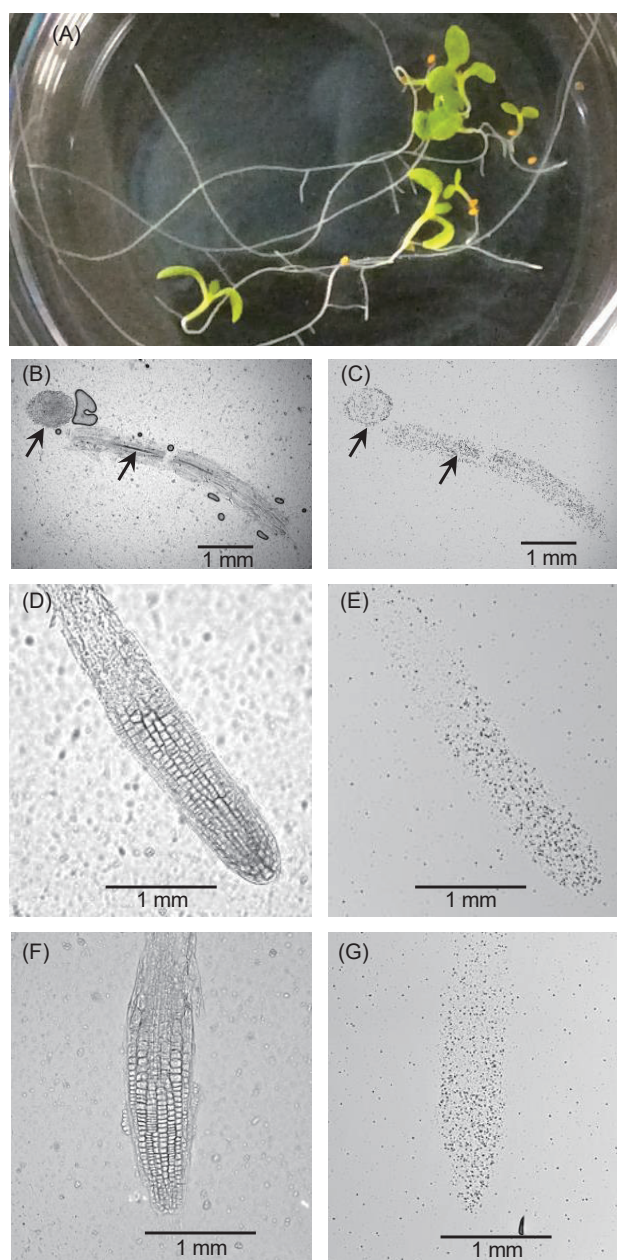


Fig. 1 Detection of boron in *Arabidopsis* tap roots using neutron capture radiography. (A): Stereomicroscopic image of *Arabidopsis* on the sixth day after seeding. Tap roots applied with neutron capture radiography. (B), (D) and (F): Optical microscopic images of cross-sections of *Arabidopsis* roots taken before irradiation; (C), (E), and (G): etch-pit images of (B), (D), and (F) after irradiation, respectively.

### REFERENCES:

- [1] M. Kobayashi, T. Matoh, J. Azuma, *Plant Physiol.*, **110**:1017–1020 (1996).

T. Kinouchi

*Institute for Integrated Radiation and Nuclear Science,  
Kyoto University*

**INTRODUCTION:** Boron is an essential nutritional element for all plants, however, a deficiency or an excess of boron causes various growth disorders of them. For all crops due to boron-toxicity which occurs frequently all over the world, a drastic solution has not been developed, because boron analysis methods with high resolution has not yet been well-developed. We still have a poor understanding about physiological functions of boron in plants. Thus, in order to collect multidimensional information on how much boron is localized in which tissue/cell at any stage of growth, we are developing an *in situ* visualization technique capable of detecting the localization of boron with high resolution, by applying neutron capture radiography with a solid-state nuclear track detector, CR-39[1,2]. On the other hand, boron captured by neutron is only boron-10, which is a stable isotope, and the ratio of these existing in nature is 20%. It means that, among boron absorbed from the roots of the plants, their ratio visualized by neutron capture radiography is also 20% at maximum. Since the low content of boron-10 made it difficult for visualization of the localization of boron in the tissue of a plant, we tried to increase the resolution by culturing the plant in a special solution replacing natural boron with boron-10 as a nutrient.

**EXPERIMENTS:** Plant materials and growth conditions> Seeds of radish (*Raphanus sativus* L.) were seeded on the moderately moisturized vermiculite and cultivated at 23°C under a 16-h light/8-h dark cycle in a 60%-humidified growth chamber. A week later, their seedlings were transferred to the hydroponic media containing major nutrients (1 mM Ca(NO<sub>3</sub>)<sub>2</sub>, 0.5 mM KH<sub>2</sub>PO<sub>4</sub>, 0.5 mM K<sub>2</sub>SO<sub>4</sub>, 1 mM MgSO<sub>4</sub>, and 1.5 mM NH<sub>4</sub>NO<sub>3</sub>) and micronutrients (75 μM EDTA-Fe, 46 μM H<sub>3</sub><sup>10</sup>BO<sub>3</sub>, 9 μM MnSO<sub>4</sub>, 0.8 μM ZnSO<sub>4</sub>, 0.3 μM CuSO<sub>4</sub>, and 0.8 μM Na<sub>2</sub>MoO<sub>4</sub>) under the same condition, and cultured for 10 days.

*In situ* visualization of boron in plants using neutron capture radiography> Mounted slice (10-μm thickness) of the radish tap root onto CR-39 (20 mm×30 mm) was irradiated with epithermal neutron for 15 min by applying to the pneumatic tube in the graphite thermal column (Tc-Pn) of Kyoto University Research Reactor (KUR).

The irradiated CR-39 plate was etched in 6 M NaOH solution, and the resulting etch-pits were observed under an optical microscope [1].

**RESULTS:** Both Fig. 1(B) and 1(D) are radiographs of the radish tap root, which were cultured with natural boron and boron-10 including culture media respectively. As expected, a large of etch-pits, which were generated from boron-10 on CR-39 by boron-neutron capture reaction, were imaged as small black spots. Especially, Fig. 1(D) showed quite a number of etch-pit which were not equally distributed, but were concentrated at the center and outer peripheral tissues as indicated by arrows. To judge from the optical microscopic image of the original cross section (Fig. 1(C)), the outer peripheral tissues were supposed as cambium, and the vascular bundles arranged in ring shape were observed. The concentrated formation of etch-pits was considered as evidence for the distribution of a large numbers of boron, indicating cell dividing actively in such tissues.

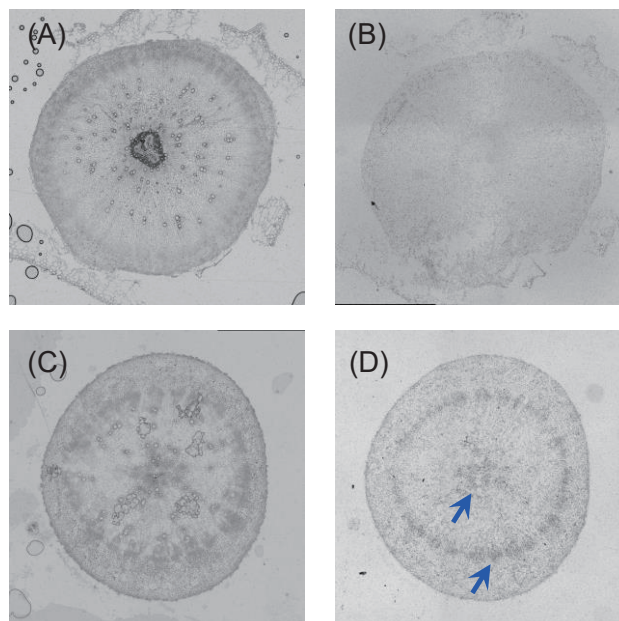


Fig.1 Distribution of boron in the radish tap root. (A) and (C): Optical microscopic images of cross sections of the radish tap root. Each root has a diameter of ~5 mm. (B) and (D): Etch-pit images of (A) and (C) after neutron radiation, respectively.

#### REFERENCES:

- [1] M. Kobayashi and T. Kinouchi, KURRI Progress Report 2014, 129 (2015).
- [2] T. Kinouchi, KURNS Progress Report 2018, 121 (2019).

## **I-1. PROJECT RESEARCHES**

### **Project 10**

M. Suzuki

*Institute for Integrated Radiation and Nuclear Science, Kyoto University*

In this research project, five research projects were included. In this summary, two research projects (P10-2 and P10-3) could not be reported due to unexpected or uncontrolled events. Details of each project is referred to the following contents.

**P10-1:** “The effect of boron neutron capture therapy (BNCT) on normal lung in mice.”

We have already reported the survival fraction following whole thorax irradiation with X-ray irradiation. In 2020, the effect of thermal neutron beam at KUR on normal lung was investigated. The mice were sorted into four treatment groups, 40-min, 50-min, 60 min, and 70-min irradiation groups. In each group, six to seven mice were irradiated. In 40-min and 50-min irradiation groups, all the mice survived within an observation period of 40 to 140 days. In 60-min irradiation group, six mice died within an observation period of 12 days, three mice survive within an observation period of 140 to 180 days, and one mouse died at 146 days after the treatment. In 70-min irradiation group, all the three mice died within 10 days.

**P10-4:** “Study of the influence on normal liver tissue by BNCT.”

The purpose of this study is to establish systematically and continuously technique that can analyze the harmful phenomenon in the normal liver tissue of BNCT.

Female C57BL6 mice at 6weeks of age were injected 1000mg/kg p-boronophenylalanine (BPA) solution subcutaneously 2 hours before neutron irradiation. The mice were irradiated for 60 minutes at the 1MW output. One week after irradiation, mice were sacrificed, and the blood and livers were analyzed. Blood and liver boron concentrations 2 hours and 3 hours after the administration of 1000 mg / kg BPA were quantified using Inductively Coupled Plasma Spectrometer (ICP). The livers of the mice 6 months after neutron irradiation were stained with Masson trichrome. HE staining and triglyceride quantification were performed to investigate degree of the steatosis in the mouse normal liver tissue after BNCT. Western blotting was performed to determine the expression level of Sonic Hedgehog protein. In addition, Masson

trichrome staining was performed to determine the degree of liver fibrosis six months after neutron irradiation.

**P10-5:** “The Effect of Boron Neutron Capture Therapy to Normal Bones in Mice.”

In this study, the effect of BNCT on normal bone in mice were evaluated regarding to their bone strengths. The tibial bending strength was decreased by reactor-producing radiation including thermal neutron, epithermal neutron, fast neutron, and  $\gamma$ -ray. However, the effect of BPA administration on bone strength was expected to be minimal.

## PR10-1 The effect of boron neutron capture therapy (BNCT) on normal lung in mice

M. Suzuki and Y. Tamari  
*Institute for Integrated Radiation and Nuclear Science  
Kyoto University*

**INTRODUCTION:** An accelerator-based boron neutron capture therapy (BNCT) system and boronophenylalanine (BPA)-based new drug were approved by the Ministry of Health, Labour and Welfare of Japan for the treatment of locally unresectable recurrent or unresectable advanced head and neck cancer on March 2020. Since BNCT will be carried out at the medical institute, the accessibility of BNCT will improve dramatically and much greater patients will be treated with accelerator-BNCT compared with reactor-BNCT. One of the drawbacks of BNCT is that thermal neutrons necessary for tumor control cannot be delivered to the deep portion of the tumor which is located at > 6 cm in depth from the skin surface.

For BNCT to be recognized as effective treatment modality for malignant tumors, to expand indication of BNCT is very important. We have investigated the possibility of BNCT for malignant tumors in body trunk such as liver and lung cancers. In these body trunk tumors, multiple lung metastatic tumor is good candidate for new application. Since the lung contains air, thermal neutron is delivered to the lung tissues in deep portion. In BNCT for multiple lung tumors, whole lung is irradiated with boron thermal neutron capture irradiation.

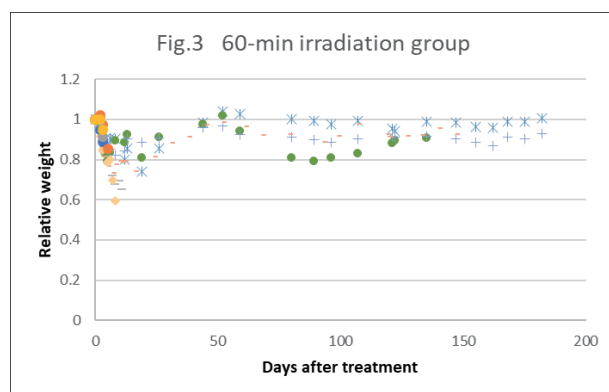
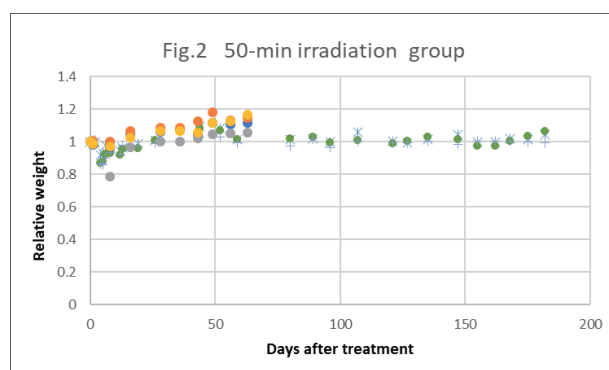
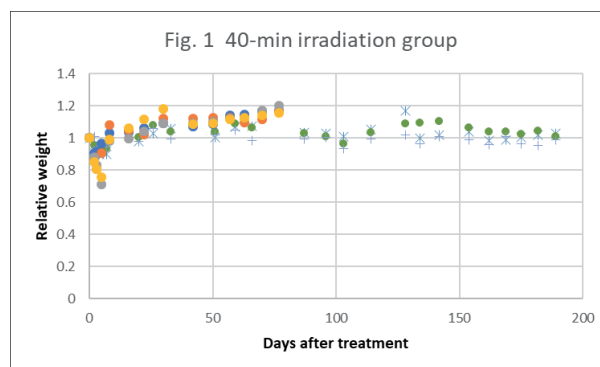
We have investigated the compound biological effectiveness (CBE) factor for normal lung tissues. The CBE factors depend on the biological or clinical endpoint. The CBE factor for normal lung tissue had been reported at 2.3 from the Massachusetts Institute of Technology (MIT) group. In MIT study, the biological endpoint for the CBE factor was the occurrence of lung fibrosis. In our study, the clinical endpoint for the CBE was the death.

We have already reported the survival fraction following whole thorax irradiation with X-ray irradiation. In 2020, the effect of thermal neutron beam at KUR on normal lung was investigated.

**EXPERIMENTS:** Ten to twelve-week old female C3H/He mice were used. Since, in this experiment, a large amount of thermal neutrons were needed to cause equivalent biological effect with X-ray irradiation, the irradiations were carried out at the 5MW reactor power. The mice were anesthetized by intraperitoneal injection of pentobarbital solution (5 mg/ml in saline) at the dose of 10  $\mu$ l/g. The three or four mice were fixed in the paper box and the body except for the thorax were shielded with LiF plate. The mice were sorted into four treatment groups, 40-min, 50-min, 60 min, and 70-min irradiation groups. In each group, six to seven mice were treated. The acryl box containing mice were irradiated with thermal neutron beam at the thermal neutron flux of  $7.5E+09$  n/cm<sup>2</sup>/s which was measured by analysis of activation of gold foil attached to the surface of the box. Survival and change of weight have been observed twice or three times a week in the first one month and once a week after the second

month.

**RESULTS:** In 40-min and 50-min irradiation groups, all the mice survive within an observation period of 40 to 140 days. In 60-min irradiation group, six mice died within an observation period of 12 days, three mice survive within an observation period of 140 to 180 days, and one mouse died at 146 days after the treatment. In 70-min irradiation group, all the three mice died within 10 days. Figures.1-3 show the weight change of the 40-min, 50-min, and 60-min treatment groups. In all the groups, 20 to 40% weight reduction was observed within two weeks.



**DISCUSSION:** In X-ray irradiation group, the mice treated with 16-17 Gy died within an observation period of 120 to 300 days. The survival of mice irradiated with thermal neutron beam will be compared with that of mice treated with X-ray irradiation in 2020.

Y. Tamari<sup>1</sup>, S. Takeno, T. Takata, M. Suzuki

*Institute for Integrated Radiation and Nuclear Science,  
Kyoto University*

<sup>1</sup> *Department of Radiology, Kyoto Prefectural University  
of Medicine*

**INTRODUCTION:** Boron neutron capture therapy (BNCT) for liver tumor, which has been conducted up to the present, has used the compound effectiveness factor (CBE) determined by using genotoxicity for hepatocytes as an indicator, which has been clarified by Suzuki et al [1]. But there is a problem whether it is appropriate as a real clinical endpoint. Fundamental researches of liver fibrosis that are the late effect of radiation therapy are necessary. It is necessary to do basic research that uses liver fibrosis, which is a late radiation injury to the liver, as an evaluation index. The hedgehog signaling pathway is one of the important processes involved in animal development, and has been implicated in the maintenance and regeneration of adult tissues. The hedgehog signaling pathway is activated in the damaged liver and affects tissue remodeling. It has also been reported that cell proliferation is promoted and epithelial-mesenchymal transition leading to fibrosis is induced [2][3]. A purpose of this study is to establish systematically and continuously technique that can analyze the harmful phenomenon in the normal liver tissue of BNCT.

**EXPERIMENTS:** Female C57BL6 mice at 6 weeks of age were injected 1000mg/kg p-boronophenylalanine (BPA) solution Subcutaneously 2 hours before neutron irradiation. The mice were irradiated for 60 minutes at the 1MW output. One week after irradiation, mice were sacrificed and the blood and livers were analyzed. Blood and liver boron concentrations 2 hours and 3 hours after the administration of 1000 mg / kg BPA were quantified using Inductively Coupled Plasma Spectrometer (ICP). The livers of the mice 6 months after neutron irradiation were stained with Masson trichrome. HE staining and triglyceride quantification were performed to investigate degree of the steatosis in the mouse normal liver tissue after BNCT. Western blotting was performed to determine the expression level of Sonic Hedgehog protein. In addition, Masson trichrome staining was performed to determine the degree of liver fibrosis six months after neutron irradiation.

**RESULTS:** Two hours after the administration of BPA, the liver boron concentration was about 8.1  $\mu\text{g/g}$ , and the blood boron concentration was about 9.2  $\mu\text{g/g}$ . Three hours after BPA administration, the liver boron concentration was about 4.1  $\mu\text{g/g}$ , and the blood boron concentration was about 4.4  $\mu\text{g/g}$ . Masson trichrome staining

showed a tendency for increased liver fibrosis in the neutron-irradiated group receiving BPA (BNCT group). The result of HE staining demonstrated that the steatosis of the BNCT group was increased. Furthermore, quantification of triglyceride was performed to determine the degree of steatosis of normal mouse liver tissue after BNCT. Triglycerides in mouse normal liver tissue after BNCT tended to be increased compared to control. Furthermore, as a result of Western blotting, the expression of sonic hedgehog protein in the BNCT group was higher than in the group only irradiated with neutrons.

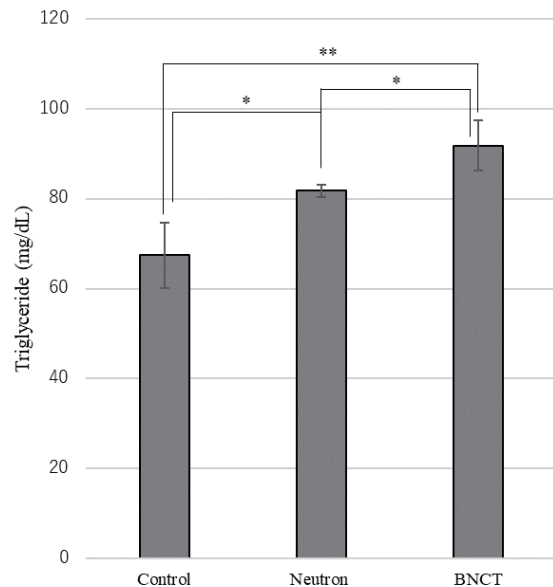


Fig.1. Triglyceride concentration of mouse liver. A significant difference was observed comparing the control and BNCT groups. (\*\*). Error bars indicate standard deviations.

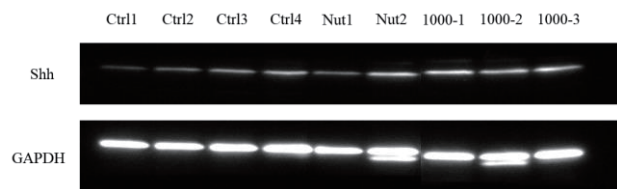


Fig.2. Shh expression level after neutron irradiation. Upper bar is Shh and Under bar is GAPDH of Ctrl (Control) and Nut (Neutron alone), 1000 (BNCT group).

#### REFERENCES:

- [1] M. Suzuki *et al.*, Jpn. j. Cancer. Res., **91** (2000) 1058-1064.
- [2] Y. jung *et al.*, Gut, **59** (2010) 655-665.
- [3] F. Rangwala *et al.*, J. Pathol., **224** (2011) 401-410.

## PR10-3 The Effect of Boron Neutron Capture Therapy to Normal Bones in Mice

R. Iwasaki, R. Yoshikawa<sup>1</sup>, T. Mori, Y. Tamari<sup>2</sup>, Y. Sakurai<sup>2</sup>, M. Suzuki<sup>2</sup> and K. Ono<sup>3</sup>

Faculty of Applied Biological Sciences, Gifu University  
<sup>1</sup>United Graduate School of Veterinary Sciences, Gifu University

<sup>2</sup>Institute for Integrated Radiation and Nuclear Science, Kyoto University

<sup>3</sup>Kansai BNCT Medical Center, Osaka Medical College

**INTRODUCTION:** Primary malignant bone tumors have been mainly treated with preoperative chemotherapy followed by surgery. Wide or radical margins including limb amputation are required for local control. Although surgical techniques named limb-salvage therapy become a mainstay of treatment to avoid the limb amputation, complications such as postoperative infection, fracture, or local recurrence often occurred.

Although primary bone tumors have been generally considered as radio-resistant tumors, radiation therapy has been used for the purpose of the functional and cosmetic status of patients. When a large single dose of photon radiation therapy is delivered to achieve the effective tumor control, clinically relevant late effects in the surrounding normal tissues include skin ulceration, neuropathy, and fracture.

Boron neutron capture therapy (BNCT), a tumor cell-selective particle radiation therapy, is considered to be effective for the tumors without any late effects to the normal bone. However, an appropriate BNCT dose irradiated safely to the normal bone, that is evaluated using experiment animals, is not determined.

In this study, we performed BNCT to normal bone in mice, and evaluated the influence on their bone strengths.

**EXPERIMENTS:** Female eight-week-old C3H/He mice were used for the study. As boron compound, p-boronophenylalanine (BPA) was prepared at a dose of 25 mg/ml. Irradiation was carried out using X-ray and thermal neutron at Gifu University and Kyoto University Reactor, respectively.

**X-ray irradiation** Mice were irradiated to their right hind limb at a single dose of 24 Gy, which was the dose that did not affect the bone strength, based on our previous study. Five mice were used for each group.

**Neutron irradiation** On the next day after X-ray irradiation of 24 Gy, mice were irradiated with a reactor neutron beam at a power of 1 MW. Irradiation was carried out as follows; neutron beam only (for 60, 90, and 120 min in each group), neutron beams for 60 min after subcutaneously injected into mice at doses of 125, 250, and 500 mg/kg of BPA. Based on a preliminary study of the biodistribution of BPA, irradiation was performed between 30 and 90 min after the injection. Five mice were used for each group.

**Bone strength analyses** Tibias were collected at 12 weeks

post-irradiation. Subsequently, they were mechanically tested by three-point bending to determine the bone strength. Tests were performed at HAMRI CO., LTD.

**RESULTS:** As shown in Figure 1, additional neutron irradiation reduced tibial bending strength 12 weeks after irradiation compared to X-ray irradiation alone. Although the tibial bending strength reduced irradiation-time dependently, the strength of the tibia irradiated for 120 min was not different from that of the tibia irradiated for 90 min.

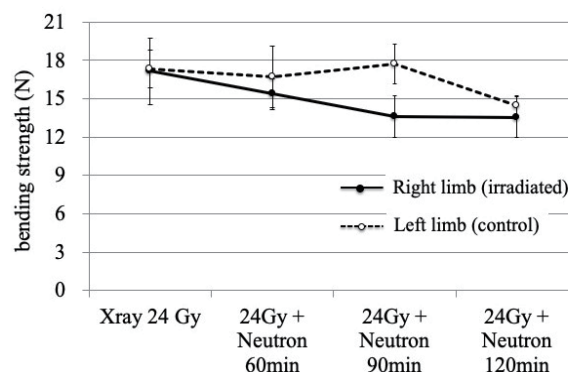


Fig. 1. Tibial strength at 12 weeks after neutron irradiation.

Subsequently, X-ray irradiation followed by neutron irradiation for 60 min with BPA administration was performed (Figure 2). The results showed that neutron irradiation with any dose of BPA administration hardly decreased the tibial strength compared with neutron irradiation alone.

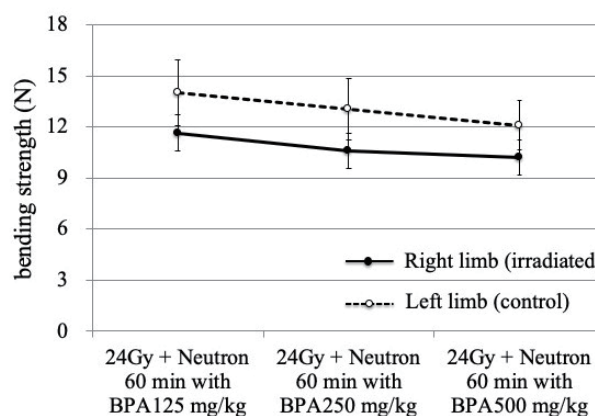


Fig. 2. Bone strengths at 12 weeks after X-ray irradiation followed by neutron irradiation with BPA administration.

**CONCLUSION:** The tibial bending strength was decreased by reactor-producing radiation including thermal neutron, epithermal neutron, fast neutron, and  $\gamma$ -ray. However, the effect of BPA administration on bone strength was expected to be minimal. Further investigation will be able to elucidate the Compound Biological Effectiveness (CBE) factor in normal bone.

## **I-1. PROJECT RESEARCHES**

### **Project 11**

M. Suzuki

*Institute for Integrated Radiation and Nuclear Science, Kyoto University*

The isotope of gadolinium-157 ( $^{157}\text{Gd}$ ) has the highest thermal neutron capture cross-section about 254,000 barn which is about 66 times higher compared with that of boron-10 ( $^{10}\text{B}$ ). The gadolinium neutron capture reaction is as follows,  $^{157}\text{Gd} + n = ^{158}\text{Gd} + \text{gamma-ray} + \text{internal conversion electrons} + \text{Auger electrons}$ . Among the byproducts, Auger electrons is categorized as a high linear energy transfer radiation which can induce double strand break of DNA. Since the range of the Auger electron is the order of a few nanometers, cell killing effect by the electron is evoked at when  $^{157}\text{Gd}$  is incorporated into the target such as DNA. Combination therapy with BNCT and Gd-NCT may help to raise the radiation dose for the deep portion of the tumors.

In this research project, eight research projects were included. Details of each project is referred to the following contents.

**P11-1:** In the case of irradiation to the cell incorporating  $^{157}\text{Gd}$  compound which are suspended liquid, the cells are irradiated with gamma-ray (range is  $>100 \mu\text{m}$ ) which are emitted from surrounding the cells. To eliminate the irradiation by gamma-ray as much as possible, the irradiation system as follows is effective; the cells adhered to the well of the microplate which stands upright are irradiated with thermal neutrons. A preliminary experiment study was carried out to confirm the feasibility of the irradiation system. Since the point to notice is occurrence of contamination, the microplate should be sealed by sterilized seat to keep the medium in the well of microplate. During the observation time for one week, no contamination was experienced. With respect to the cell killing effect, the BPA-treated cells were morphologically destructed and decreased in number compared with no treatment and irradiation alone control groups.

**P11-2:** In this study, the effectiveness of new Gd-loaded nanoparticle was tested in vivo study. Since this study was carried out as preliminary study, only one mouse was used. The GdXX-NCT showed a little growth inhibition compared with that of thermal neutron irradiation.

**P11-3:** In this study, we investigate the in vivo antitumor effects after NCT with intra-tumoral injected nanoparticulate formulations. Gd-nanoCPs with different particle sizes were prepared by using chitosan with molecular weights of 10 k (Gd-nanoCP 200) or 950 k (Gd-nanoCP 400) and Gd-DTPA through the previously developed w/o emulsion-droplet coalescence technique. The Gd-nanoCP 200 exhibited a stronger tumor-killing effect than the Gd-nanoCP 400. This significance in tumor-killing

effect would be ascribed from a higher Gd retention in the tumor tissue and improved distribution of Gd with intratumorally administered Gd-nanoCP 200.

**P11-4:** Tetra (methylene phosphonic acid) chelate of Gd (Gd-EDTMP) were evaluated with reference to tissue distribution and effects of thermal neutron irradiation using tumor animal models. Malignant melanoma B16 cells administered through the caudal artery infiltrated the bone marrow in all of the mice. In addition,  $^{157}\text{Gd}$  was distributed in the bone matrix around the bony edge line and malignant melanoma. When the distribution of malignant melanoma was compared according to the distribution of melanin in the thermal neutron irradiated and non-thermal neutron irradiated groups, no significant difference was found in the present study.

**P11-5:** In this study, to construct the molecular system to take drugs into cell nucleus was attempted by using Hoechst molecules. Since the Hoechst group has high DNA-binding function and accumulates in the cell nucleus, it was expected that this molecule act as a courier molecule to deliver drugs into the nucleus. Herein, we designed the reaction protocols to couple the drugs with Hoechst unit by Huisgen cycloaddition reaction.

**P11-6:** The results showed that the chicken egg CAM model can be used as a model to examine the efficacy of the GNCT therapy. The results of gadolinium-loaded nanoparticles compared with that of free gadolinium compound show that the nanoparticle formulation increases efficacy of GNCT.

**P11-7:** In this study, a series of nanocarriers in sub-50 nm scale and researched its antitumor effect though the change of tumor size was investigated as a novel Gd-compound. The growth rate of the C26 tumors was significantly inhibited after injection of PEG272 and PEG454 with irradiation compared with non-irradiation group.

**P11-8:** In this study, a silica nano-particle (SiNP,  $61.6 \pm 3.8 \text{ nm}$  in diameter) containing 55 ng/mg Gd3TCAS2, which is promising as a carrier for Gd-NCT was investigated as a new Gd-compound.

M. Suzuki and H. Tanaka

*Institute for Integrated Radiation and Nuclear Science  
Kyoto University*

**INTRODUCTION:** An accelerator-based boron neutron capture therapy (BNCT) system and boronophenylalanine (BPA)-based new drug were approved by the Ministry of Health, Labour and Welfare of Japan for the treatment of locally unresectable recurrent or unresectable advanced head and neck cancer on March 2020. Since BNCT will be carried out at the medical institute, the accessibility of BNCT will improve dramatically.

One of the drawbacks of BNCT is that thermal neutrons necessary for tumor control cannot be delivered to the deep portion of the tumor which is located at > 6 cm in depth from the skin surface. To overcome the drawback, in the clinical study on BNCT for malignant glioma, X-ray irradiation to the deep portion of the tumor was followed by BNCT.

The isotope of gadolinium-157 ( $^{157}\text{Gd}$ ) has the highest thermal neutron capture cross-section about 254,000 barn which is about 66 times higher compared with that of boron-10 ( $^{10}\text{B}$ ). The gadolinium neutron capture reaction is as follows,  $^{157}\text{Gd} + n = ^{158}\text{Gd} + \text{gamma-ray} + \text{internal conversion electrons} + \text{Auger electrons}$ . Among the byproducts, Auger electrons is categorized as a high linear energy transfer radiation which can induce double strand break of DNA. Since the range of the Auger electron is the order of a few nanometers, cell killing effect by the electron is evoked at when  $^{157}\text{Gd}$  is incorporated into the target such as DNA. Combination therapy with BNCT and Gd-NCT may help to raise the radiation dose for the deep portion of the tumors.

To investigate the cell killing effect by Auger electron, irradiation by other byproducts yielded by  $^{157}\text{Gd}$  neutron capture reaction should be eliminated as much as possible from the site of the reaction. In the case of irradiation to the cell incorporating  $^{157}\text{Gd}$  compound which are suspended liquid, the cells are irradiated with gamma-ray (range is >100  $\mu\text{m}$ ) which are emitted from surrounding the cells. To eliminate the irradiation by gamma-ray as much as possible, the irradiation system as follows is effective; the cells adhered to the well of the microplate which stands upright are irradiated with thermal neutrons.

A preliminary experiment study was carried out to confirm the feasibility of the irradiation system. Since the point to notice is occurrence of contamination, the microplate should be sealed by sterilized seat to keep the medium in the well of microplate.

**EXPERIMENTS:** The colon-26 cells were maintained in RPMI-1640 supplemented with L-glutamine and 10% fetal bovine serum (FBS). The 1,000 cells per well were seeded in the 96-well microplates. After overnight incubation, the medium of each well was replaced by BPA-containing medium at the  $^{10}\text{B}$  concentration of 100 ppm for 2 hours before irradiation with thermal neutron. The

microplate was sealed with sterilized seat and kept standing upright. The microplate was irradiated with thermal neutron beam at the flux of  $1 \times 10^9 \text{ n/cm}^2/\text{s}^{-1}$  for 30 minutes. After the irradiation, the medium in each well was replaced with fresh medium. To confirm the feasibility of this experiment, the microplate was kept in the incubator for one week. The occurrence of contamination was visually checked and the cell killing effect by BPA-treated cells was inspected thorough a microscope.

**RESULTS:** During the observation time for one week, no contamination was experienced. With respect to the cell killing effect, the BPA-treated cells were morphologically destructed and decreased in number compared with no treatment and irradiation alone control groups.

**DISCUSSION:** To irradiate the cells attached to the culture device vertically against the thermal neutron beam, the irradiation system in which microplate was standing upright was used in this experiment. Although some additional procedure such as sealing the plate with sterilized seat is needed, the analysis of the cell-toxic effects such as WST-1 assay is easily carried out by using microplate reader. Since the feasibility of this irradiation system was confirmed, we will investigate the cell killing effect of the positive-charged  $^{157}\text{Gd}$ -compound which was attached to the cell membrane.

## Investigation of gadolinium neutron capture therapy (Gd-NCT) using gadolinium-loaded nano-particle

M. Suzuki, Li. Peng<sup>1</sup>, N. Komatsu<sup>1</sup>, Li. Zhao<sup>2</sup>

*Institute for Integrated Radiation and Nuclear Science  
Kyoto University*

<sup>1</sup>*Graduate School of Human and Environmental Studies,  
Kyoto University*

<sup>2</sup>*Medical College, Soochow University*

**INTRODUCTION:** An accelerator-based boron neutron capture therapy (BNCT) system and boronophenylalanine (BPA)-based new drug were approved by the Ministry of Health, Labour and Welfare of Japan for the treatment of locally unresectable recurrent or unresectable advanced head and neck cancer on March 2020. Since BNCT will be carried out at the medical institute, the accessibility of BNCT will improve dramatically.

One of the drawbacks of BNCT is that thermal neutrons necessary for tumor control cannot be delivered to the deep portion of the tumor which is located at > 6 cm in depth from the skin surface. To overcome the drawback, in the clinical study on BNCT for malignant glioma, X-ray irradiation to the deep portion of the tumor was followed by BNCT.

The isotope of gadolinium-157 (<sup>157</sup>Gd) has the highest thermal neutron capture cross-section about 254,000 barn which is about 66 times higher compared with that of boron-10 (<sup>10</sup>B). The gadolinium neutron capture reaction is as follows, <sup>157</sup>Gd+n = <sup>158</sup>Gd+gamma-ray+internal conversion electrons +Auger electrons. Among the byproducts, Auger electrons is categorized as a high linear energy transfer radiation which can induce double strand break of DNA. Since the range of the Auger electron is the order of a few nanometers, cell killing effect by the electron is evoked at when <sup>157</sup>Gd is incorporated into the target such as DNA. Combination therapy with BNCT and Gd-NCT may help to raise the radiation dose for the deep portion of the tumors.

In this study, the effectiveness of new Gd-loaded nanoparticle was tested in vivo study. Since this study was carried out as preliminary study, only one mouse was used.

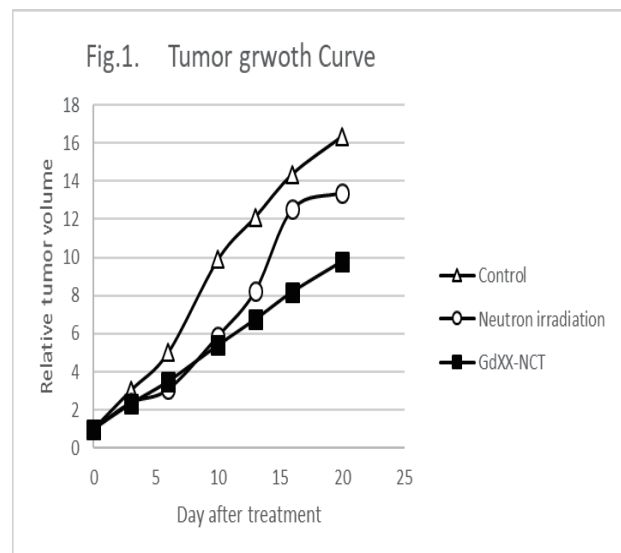
**EXPERIMENTS:** The colon-26 cells were maintained in RPMI-1640 supplemented with L-glutamine and 10% fetal bovine serum (FBS) in cell culture flasks (T-75). The cells were processed into single cells by exposure of 0.05% trypsin. The single cell suspended medium was prepared at the concentration of four million cells per 100 μm. At 10 days before the irradiation, four million colon-26 cells in 100 μm FBS-free medium were implanted to the left hind leg of 8-week old female Balb/c mice. At the irradiation, size of the tumors ranged from 10 cm to 15 cm. The new Gd-loaded nanoparticle (GdXX) was injected to one mouse intravenously via tail vein at 24 hours before the irradiation. The mouse was irradiated at the heavy water facility of Kyoto University Research Reactor (KUR) at the thermal neutron flux of 5.1E10+8 (n/cm<sup>2</sup>/s) for 60 minutes. The long and short diameter of the tumor

and the weight of the mouse was measured twice a week. The tumor volume was calculated by the following equation:

The tumor volume = (long diameter x short diameter x short diameter) / 2.

Since this preliminary experiment was carried out in accompanied with other experiment using 50-60 mice, the tumor growth curve for GdXX was compared with those of no-treatment control and thermal neutron irradiation control in the other experiment.

**RESULTS:** Decrease of the weight of the GdXX-NCT treated mouse 10% greater than that of the treatment day was not observed. Fig.1 shows the tumor growth curves for no-treatment control, thermal neutron irradiation, and GdXX -NCT treated mice. The GdXX-NCT showed a little growth inhibition compared with that of thermal neutron irradiation.



**DISCUSSION:** No suggestion was drawn from this preliminary experiment in which only one mouse was treated with GdXX-NCT. In 2020, the pharmacokinetic and GdXX-NCT in vivo studies were planned.

T. Andoh<sup>1</sup>, T. Fujimoto<sup>2</sup>, M. Suzuki<sup>3</sup>, T. Takata<sup>4</sup>, Y. Sakurai<sup>4</sup> and H. Ichikawa<sup>1</sup>

<sup>1</sup>Faculty of Pharmaceutical Sciences, Kobe Gakuin University, Japan.

<sup>2</sup>Department of Orthopaedic Surgery, Hyogo Cancer Center, Japan.

<sup>3</sup>Particle Radiation Oncology Research Center, Institute for Integrated Radiation and Nuclear Science, Kyoto University, Japan.

<sup>4</sup>Division of Radiation Life Science, Institute for Integrated Radiation and Nuclear Science, Kyoto University, Japan

**INTRODUCTION:** The successful treatment of cancer by neutron capture therapy (NCT) requires selective delivery of large amounts of <sup>10</sup>B or <sup>157</sup>Gd isotope to tumor cells. In the previous study, we developed two types nanoparticulate formulations for NCT. One is formulated nanosuspension (NS) composed of *p*-borono-L-phenylalanine (L-BPA) itself. In this BPA-NS formulation, solid particles of L-BPA are dispersed in water with a surface-active stabilizer. The other one is gadolinium-loaded chitosan nanoparticles (Gd-nanoCPs). Gd in Gd-nanoCP-treated tumors is based primarily on the bioadhesive (cationic), biocompatible (nontoxic), and biodegradable (bioerodible) properties of chitosan nanoparticles. In the present study, we investigate the *in vivo* antitumor effects after NCT with intratumoral injected nanoparticulate formulations.

**EXPERIMENTS:** Macrogol 15 hydroxystearate (Solutol® HS 15, SO) and soybean lecithin (SL) were used as stabilizers. BPA-NS using SO and SL was prepared by a wet-milling method with the use of a Pulverisette-7 planetary ball mill (Fritsch). The obtained BPA-NS was sonicated using a 2510J-DTH water-bath sonicator (Branson Ultrasonics Co.) for 5 min at room temperature. Gd-nanoCPs with different particle sizes were prepared by using chitosan with molecular weights of 10 k (Gd-nanoCP 200) or 950 k (Gd-nanoCP 400) and Gd-DTPA through the previously developed w/o emulsion-droplet coalescence technique [1]. In the NCT trial, male B16F10 melanoma bearing C57BL/6J mice were used. The mice were divided into NCT group and HOT control group. BPA-Fructose complex (BPA-Fr), BPA-NS (500 mg BPA/kg), Gd-nanoCP 200 and 400 (2.4 mg Gd/kg) were administered intratumoral (i.t.) injection to the mice. The tumors in the left hind legs were exposed to thermal neutron irradiation at the Institute for Integrated Radiation and Nuclear Science, Kyoto University. For determining the tumor volume, two bisecting diame-

ters of the tumor were measured with a slide caliper, and calculation with the longest and shortest length of the tumor in millimeters (mm). The tumor-growth suppressing effect was assessed by the ratio of tumor volume before and after neutron irradiation.

**RESULTS:** BPA-NS displayed a mass median diameter of 176 nm. After i.t. administration, BPA-NS gave rise to the remarkably prolonged retention of <sup>10</sup>B in tumor tissue possibly due to the slow diffusion and/or dissolution of solid BPA-nanoparticles in a tumor. Gd-nanoCPs prepared using chitosan with a higher MW (950 kDa) had a mean particle size of 468 nm; Gd-nanoCPs prepared using chitosan with a lower MW (10 kDa) had a mean particle size of 185 nm. After i.t. administration, Gd-nanoCP 200 showed significantly higher Gd concentration in tumor tissue in comparison to Gd-nanoCP 400. In the NCT trial, growth of tumor masses was observed in the control group, while the NCT groups showed an equivalent suppression of tumor growth (Fig. 1). In BNCT, two BPA formulations had been similar tumor-killing effect. These results suggested that boron accumulates specifically in the tumor after i.t. administration of BPA formulations and that BNCT after i.t. dosing of BPA-NS is equally efficacious in the treatment of BNCT after i.t. administration of BPA-Fr. In GdNCT, the Gd-nanoCP 200 exhibited a stronger tumor-killing effect than the Gd-nanoCP 400. This significance in tumor-killing effect would be ascribed from a higher Gd retention in the tumor tissue and improved distribution of Gd with intratumorally administered Gd-nanoCP 200.

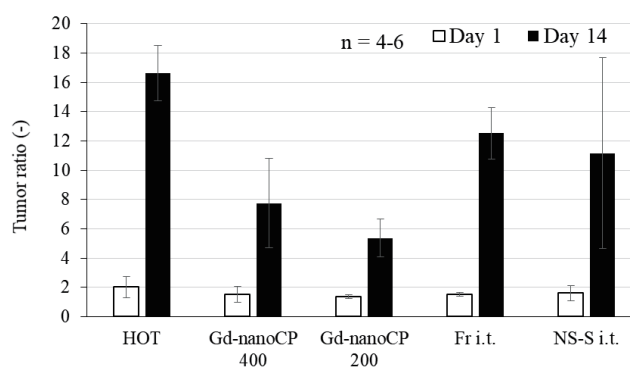


Fig. 1. Tumor volumes after thermal neutron beam irradiation of NCT and HOT control groups.

### REFERENCES:

- [1] H. Tokumitsu *et al.*, Pharm. Res., 16, 1830–1835 (1999).

T. Matsukawa<sup>1</sup>, A. Kubota<sup>1</sup>, M. Suzuki<sup>2</sup>, A. Shinohara<sup>1,3</sup>, K. Kajino<sup>1</sup>, K. Yokoyama<sup>1,4</sup>

<sup>1</sup> Juntendo University Faculty of Medicine

<sup>2</sup> Institute for Integrated Radiation and Nuclear Science, Kyoto University

<sup>3</sup> Research Institute for Cultural Studies, Seisen University

<sup>4</sup> International University of Health and Welfare

**INTRODUCTION:** To develop the next generation of cancer radiotherapy, we evaluated tissue distribution and effects of thermal neutron irradiation on tumor animal models of tetra (methylene phosphonic acid) chelate of Gd (Gd-EDTMP), a neutron capture therapy formulation containing gadolinium. The distribution of <sup>157</sup>Gd in the tissue was imaged by laser ablation inductively coupled plasma mass spectrometry (LA-ICP-MS).

**EXPERIMENTS:** Gd-EDTMP solutions were prepared from gadolinium chloride and EDTMP; C57BL/6Jcl female mice (6 weeks old) were obtained from CLEA Japan, Inc. (Tokyo, Japan). Mouse malignant melanoma B16 cells (JCRB0202) were purchased from JCRB Cell Bank (Ibaraki, Japan). Cultured B16 cells were injected from the tail artery of C57BL mice anesthetized with isoflurane and transplanted into the lower limbs ( $1 \times 10^6$  cells per mouse). On day 7 after transplantation, a saline dilution solution of Gd-EDTMP was administered intraperitoneally at a concentration of 20.0 mg-Gd/kg. After 24 h of injection, mice were randomly divided into two groups (n = 3) and one group was irradiated with thermal neutrons at the Kyoto University reactor at  $6.0 \times 10^8 \text{ cm}^{-2}$  for 60 min. The remaining one group was not irradiated. After 7 days, mice were sacrificed and femur and tibia were sampled. For each mouse, the left femur was demineralized for 24 h, paraffin-embedded, and 5  $\mu\text{m}$  sections were made in thin sections parallel to the long axis of the bone and stained with hematoxylin and eosin (H.E.). The right femur was cut into thin sections every 5  $\mu\text{m}$  using the Kawamoto method, a non-demineralized frozen section preparation method, and the <sup>157</sup>Gd distribution was determined by LA-ICP-MS<sup>[1]</sup>. The invasion of the tumor into the bone was assessed by micrographs of H.E. stained sections of the femur and tibia.

**RESULTS:** Malignant melanoma B16 cells administered through the caudal artery infiltrated the bone marrow in all of the mice studied here. In addition, <sup>157</sup>Gd was distributed in the bone matrix around the bony edge line and malignant melanoma. When the distribution of malignant melanoma was compared according to the distribution of melanin in the thermal neutron irradiated and non-thermal neutron irradiated groups, no significant difference was found in the present study. Although bone is hard tissue, it is actually undergoing

constant remodeling by osteoblasts and osteoclasts. Gd-EDTMP may have been included in this remodeling. In bone metastatic tumors, tumor cells that flow into the bloodstream create a foothold in the bone marrow, disrupting the balance between osteoclasts and osteoblasts and proliferating. It is known that there are many cases of osteoclastic enhancement due to tumor growth, and it is thought that <sup>157</sup>Gd is enriched by the incorporation of Gd-EDTMP into the bone tissue generated by osteoblasts that work for repair in the vicinity of these osteoclasts. In particular, the acidic environment caused by osteolysis is known to be one of the causes of pain, so this formulation, which can capture neutrons in the vicinity, may have an effect on the pain of bone metastases. In the present study, there was no significant difference in the distribution of melanin in malignant melanoma caused by thermal neutron irradiation, which may be due to the small number of animal models produced and the fact that we could not compare the malignant melanoma cells themselves because we used pigment as an indicator. In the future, it is necessary to study the experimental animal model system that can follow the therapeutic effect of neutron capture more strictly, especially the model focusing on the pain of bone metastasis.

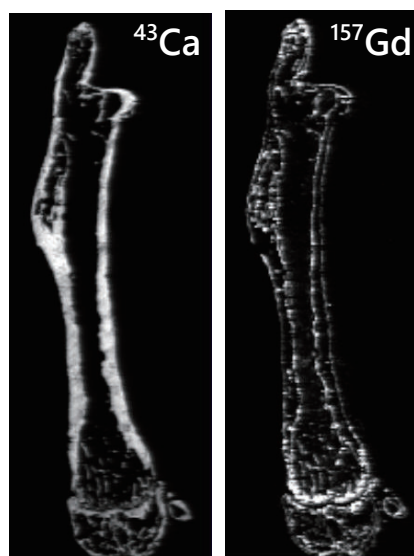


Fig. 1.  
Distribution of <sup>43</sup>Ca and <sup>157</sup>Gd in the tumor bearing mice femur 24h after injection of Gd-EDTMP.

#### REFERENCES:

- [1] A. Kubota *et al.*, Juntendo Medical Journal., **65** (2019) 461-467.

K. Tanabe, M. Suzuki<sup>1</sup>, T. Nishihara and J. Meguro

Department of Chemistry and Biological Science, College of Science and Engineering, Aoyama Gakuin University

<sup>1</sup>Institute for Integrated Radiation and Nuclear Science, Kyoto University

**INTRODUCTION:** The cell nucleus has been recognized as an important target in boron neutron capture therapy (BNCT). Therefore, there are increasing demands for the development of the methods to take drugs for BNCT to cell nucleus.

In this study, we attempted to construct the molecular system to take drugs into cell nucleus by using Hoechst molecules. Since the Hoechst group has high DNA-binding function and accumulates in the cell nucleus,<sup>1,2</sup> it was expected that this molecule act as a courier molecule to deliver drugs into the nucleus. Herein, we designed the reaction protocols to couple the drugs with Hoechst unit by Huisgen cycloaddition reaction.

#### EXPERIMENTS:

**Huisgen cycloaddition reaction between A-Hoechst and 9-azidemethylantracene 11.** A-Hoechst (1.0 mg, 2.2  $\mu\text{mol}$ ) was added to the solution of 9-azidemethylantracene (0.5 mg, 2.1  $\mu\text{mol}$ ) in DMF-H<sub>2</sub>O. Then, CuSO<sub>4</sub>, TBTA and sodium ascorbate were added to the solution. The resulting mixture was stirred for 20 h at ambient temperature. After the reaction, the mixture was extracted with ethyl acetate. The organic layer was washed with brine, dried over MgSO<sub>4</sub>, filtered and concentrated in vacuo. The crude product was purified by silica gel column chromatography to give anthracene derivative with Hoechst unit 12.

**RESULTS:** We designed the synthetic protocols of the Hoechst-tethered molecules by using Huisgen cycloaddition. It is well-known that azide group is coupled with acetylene unit in the presence of Cu(I) catalyst via a formation of triazole ring. Thus, we designed Hoechst unit with acetylene group (A-Hoechst in Scheme 1) and drugs with azide substituent.

The synthesis of A-Hoechst is outlined in Scheme 1. Phenol derivative 1 was alkylated by propargyl bromide under basic conditions to form 2. On the other hand, dinitro benzoic acid 3 was converted to amide 4, and then 4 was reduced to give diamine 5. The diamine 5 was treated with aldehyde 2 to form benzimidazole derivative 6, which was reduced to give formyl benzimidazole 7. The Hoechst skeleton was synthesized as follows. Nitroaniline 8 was coupled with 1-methylpiperazine under basic conditions and following reduction gave diaminobenzene 10. The coupling of 7 and 10 furnished the desired A-Hoechst.

We next evaluated the Huisgen reaction of A-Hoechst. As a phantom drug, we employed 9-azidemethylantracene 11 and conducted the cycloaddition reaction. The reaction

of A-Hoechst and anthracene 11 was conducted at ambient temperature in the presence of catalytic CuSO<sub>4</sub> and ascorbic acid. Efficiently, the triazole ring formation occurred, and anthracene derivative with Hoechst unit 12 was formed. These results strongly indicate that A-Hoechst will be a promising molecule to prepare Hoechst-tethered molecules. At present, introduction of Gadolinium complexes or boron compounds into A-Hoechst is in progress.

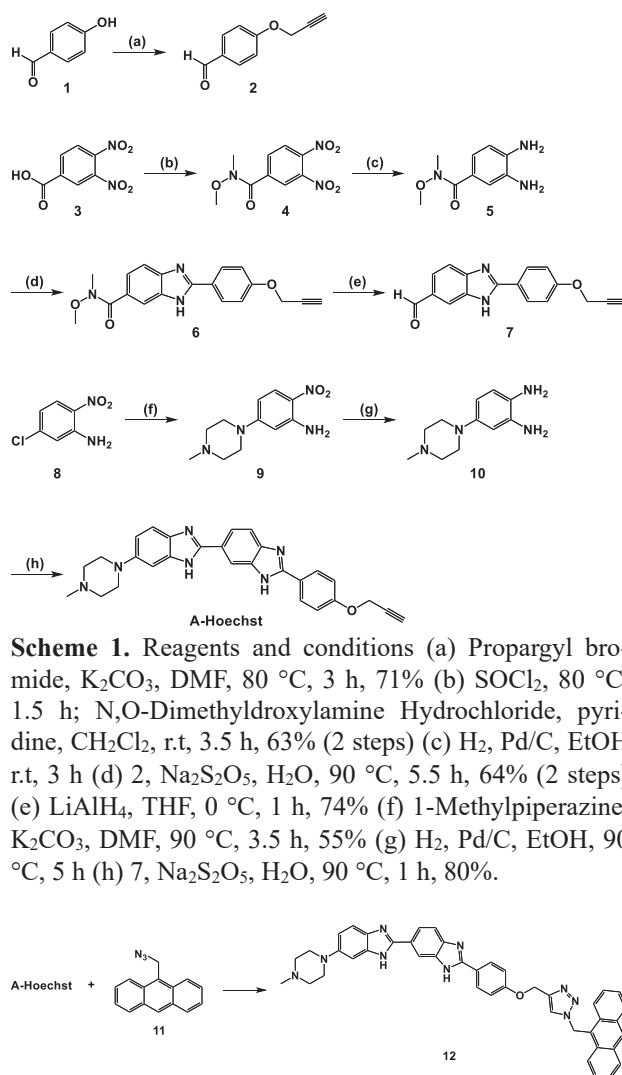


**Figure 1.** Huisgen reaction between A-Hoechst and 11.

#### REFERENCES:

- [1] Tsukiji, S. *et al.*, *Chem. Comm.* **50** (2014) 6149–6152.
- [2] Tanabe, K. *et al.*, *ChemBioChem*, **19** (2018) 956-962.

K. Matsumoto, A. Komatsu, Y. Higashi, M. Tamari<sup>1</sup>, M. Suzuki<sup>1</sup> and F. Tamanoi

*Institute for Integrated Cell-Material Sciences, Institute for Advanced Study, Kyoto University*

<sup>1</sup>*Particle Radiation Oncology Research Center, Institute for Integrated Radiation and Nuclear Science, Kyoto University*

## INTRODUCTION:

Gadolinium Neutron Capture Therapy (GNCT) provides a promising alternative to BNCT. Because gadolinium is used as an MRI enhancing reagent, various compounds containing gadolinium have been developed. Our aim is to establish a capability to test various gadolinium containing reagents for GNCT at the Kyoto University Research Nuclear Reactor. In this study, we have evaluated the possibility to use the chicken egg tumor model that has been shown to be effective for the study of BNCT.

Nanoparticles can be tuned to accumulate in the tumor. This feature is attractive for GNCT, as tumor accumulation of gadolinium may dramatically enhance GNCT efficacy. We chose mesoporous silica-based nanoparticles as a carrier for gadolinium. This material is a homogeneous preparation of nanoparticles with a diameter of 40-400 nm. Approximately 1400 pores are present in one particle. Because the wall of the pore can be considered as a part of the surface area, they have a large surface area; it is reported that 1g of the nanoparticle contains 400 square meter of surface area.

## EXPERIMENTS:

(Exp.1) The CAM assay was established by using fertilized chicken eggs. After incubation for ten days, a window was made on the egg shell and ovarian cancer cells were transplanted onto the CAM membrane of fertilized chicken eggs. Tumor formation was examined.

(Exp.2) Mesoporous silica-based nanoparticles were synthesized by incubating TEOS in an alkaline solution which promotes the formation of the Si-O-Si framework as a base structure of the nanoparticle. CTAB was added as a templating agent. Surface modification was carried out by the grafting method that enabled attachment of gadolinium to the surface of the nanoparticles. Stability of the gadolinium attachment was examined.

(Exp.3) The CAM model established as described in Exp. 1 was used to intravenously inject gadolinium-loaded nanoparticles and the eggs were exposed to neutron at the nuclear reactor for 1 hour. Effect on tumor growth was examined by observing tumor size as well as by examining tumor weight three days after the exposure.

## RESULTS:

Exp.1:

Three days after transplanting human ovarian cancer cells onto the CAM membrane, tumor formation was confirmed. The tumor was examined by green fluorescence of ovarian cancer cells that express GFP. In addition, H&E staining of the tumor was carried out.

Exp.2:

Successful synthesis of gadolinium-loaded silica-based nanoparticles was confirmed by SEM, TEM and elemental mapping using TEM (EDX-TEM). The size of the nanoparticle was 120 nm. Loading of gadolinium was 4% of the weight of the nanoparticle, as determined by ICP.

Exp.3:

We carried out a GNCT experiment using the nuclear reactor. Gadolinium-loaded nanoparticles were intravenously injected into the chicken egg and irradiated with a neutron beam for one hour two days after the injection. Three days after the irradiation, the size and weight of the tumor was examined. The results showed that the weight of the tumor after injection of gadolinium-loaded nanoparticles was 27% of the control tumor (no injection). This contrasts with the injection of free gadolinium compound in which case the weight of the tumor was 75% of the control. Nanoparticles without gadolinium gave results that were similar to that of the control.

## CONCLUSION AND FUTURE PROSPECTS:

Our results show that the chicken egg CAM model can be used as a model to examine the efficacy of the GNCT therapy. The results of gadolinium-loaded nanoparticles compared with that of free gadolinium compound show that the nanoparticle formulation increases efficacy of GNCT. However, this should be taken as a preliminary result, as the experiment was carried out only once. Further experiments are planned using different conditions such as varying irradiation time.

X. Hou<sup>1,2</sup>, C. Qin<sup>2</sup>, H. Yanagie<sup>1,3,4</sup>, M. Yanagawa<sup>5</sup>, Y. Sakurai<sup>3,4</sup>, K. Mouri<sup>3,4</sup>, Y. Ueda<sup>6</sup>, N. Dewi<sup>4</sup>, H. Cabral<sup>2</sup>, Y. Morishita<sup>7</sup>, T. Kanai<sup>8</sup>, S. Dowaki<sup>8</sup>, T. Nagasaki<sup>8</sup>, Y. Sakura<sup>9</sup>, H. Tanaka<sup>9</sup>, M. Suzuki<sup>9</sup>, S. Masunaga<sup>9</sup>, and H. Takahashi<sup>1,2,3</sup>

<sup>1</sup>Dept of Nuclear Engineering & Management, School of Engineering, Univ of Tokyo, <sup>2</sup>Dept of Bioengineering, School of Engineering, Univ of Tokyo, <sup>3</sup>Cooperative Unit of Medicine & Engineering, Univ of Tokyo Hospital, <sup>4</sup>Niigata Univ of Pharmacy & Applied Life Sciences, <sup>5</sup>Obihiro Univ of Agriculture and Veterinary Medicine, <sup>6</sup>Kumatori Veterinary Hospital, <sup>7</sup>Dept of Human & Molecular Pathology, Graduate School of Medicine, The University of Tokyo, <sup>8</sup>Osaka City University Graduate School of Engineering, <sup>9</sup>Kyoto Univ Institute for Integrated Radiation & Nuclear Science, JAPAN

## INTRODUCTION:

Gadolinium neutron capture therapy (GdNCT) is a promising cancer treatment. Compared with the conventional boron NCT, because Gd compound can be used as MRI contrast agent [1], it allowed for MRI-guided GdNCT. However, clinical Gd-chelates lack high and selective accumulation in tumors for electing safe and potent GdNCT [2].

Nanoscale drug carriers are a promising way to promote the accumulation of Gd agents in tumors through the enhanced permeability and retention (EPR) effect, which is based on the leaky vasculature of tumor tissues and their impaired lymphatic drainage. For developing successful nanocarriers for GdNCT, it is necessary to design systems with high Gd loading capacity that avoid leakage of free Gd. Thus, we developed a series of nanocarriers in sub-50 nm scale and researched its anti-tumor effect though the change of tumor size.

## EXPERIMENTS:

We developed nanocarriers based on poly(aspartic acid) (P(Asp)) and were modified with poly(ethylene glycol) (PEG) chains having different molecular weight (Mw). After chelating Gd-DOTA, the final products, which are PEG<sub>272</sub>(PEG<sub>272</sub>-P(Asp-Gd-DOTA)) and PEG<sub>454</sub>(PEG<sub>454</sub>-P(Asp-Gd-DOTA)), were made.

Colon 26 cancer cell was used for the *in vivo* anti-tumor effect evaluation. After 24h administration, the tumor-bearing mice received neutron irradiation 60 minutes at Nuclear Reactor Facility of Kyoto Univ Institute for Integrated Radiation & Nuclear Science with average neutron fluence of  $2.0 \times 10^{12}$  n/cm<sup>2</sup>. the change in tumor growth and survival rate of the mice reflected the anti-tumor effect of nanocarriers. Considering the influence of irradiation, we also set the mice injected

same samples but without receiving irradiation as controls groups. Besides, while measuring the size of tumor, the weight change was also recorded for evaluation of the toxicity of these samples.

## RESULTS:

The result of tumor growth showed at Figure 1. From the results of antitumor effect after GdNCT (Fig. 1), the growth rate of the C26 tumors was significantly inhibited after injection of PEG<sub>272</sub> and PEG<sub>454</sub> with irradiation compared with non-irradiation group. However, PEG<sub>272</sub> showed more potent antitumor ability. From day 9, the relative tumor volume became smaller than before irradiation, and until day 24, the relative tumor volume was 0.27 of the initial size. Despite PEG<sub>454</sub> showed higher tumor accumulation, the enhancement of the antitumor activity of PEG<sub>272</sub> could be attributed to the higher cellular uptake, as intracellular delivery of Gd has been indicated to be critical for effective cell killing [3].

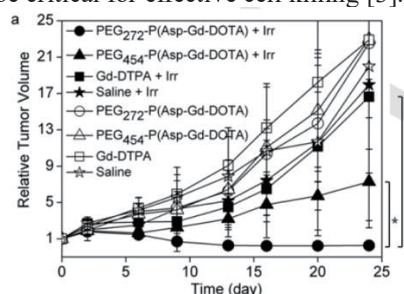


Fig. 1. Tumor growth suppression result.

Moreover, the body weight of the mice did not decrease after the treatments, which indicate the safety of these polymers and the GdNCT (Fig. 2).

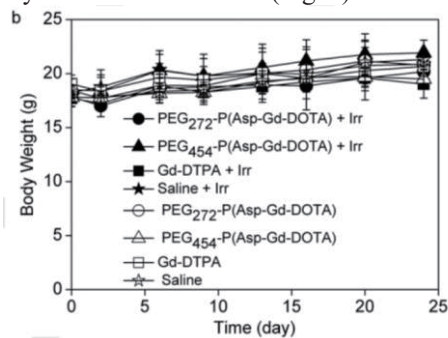


Fig. 2. The weight loss.

## REFERENCES:

- [1] A. Narmani *et al.* J. Drug Deliv. Sci. Technol., **44** (2018) 457-466.
- [2] H. Tokumitsu *et al.* Pharm. Res., **16** (1999) 1830-1835.
- [3] K. H. Jung *et al.* Contrast Media Mol. Imaging, **01** (2018) 3727109.

## PR 11-8 Development of Nano Carriers Installed with Gd(III)-Thiacalixarene Complex for Gd-NCT

T. Yamatoya<sup>1</sup>, T. Nagasaki<sup>2</sup>, N. Iki<sup>1</sup> and M. Suzuki<sup>3</sup>

<sup>1</sup>Graduate School of Environmental Studies, Tohoku University

<sup>2</sup>Graduate School of Engineering, Osaka City University

<sup>3</sup>Institute for Integrated Radiation and Nuclear Science, Kyoto University

**INTRODUCTION:** Owing to a large thermal neutron capture cross section and total kinetic energy of  $^{157}\text{Gd}(n,\gamma)^{158}\text{Gd}$  larger than that of  $^{10}\text{B}(n,\alpha)^7\text{Li}$ , gadolinium attracts growing attention as an alternative to boron in neutron capture therapy [1]. Because free gadolinium ( $\text{Gd}(\text{OH}_2)_9$ ) has toxicity, a safe carrier of Gd to tumor not to release free Gd is required. We recently found that thiacalix[4]arene-*p*-tetrasulfonate (TCAS) self-assembled three lanthanide (Ln) cores including Gd to form a sandwich-type complex,  $\text{Ln}_3\text{TCAS}_2$  (Fig. 1) [2], the characteristic features of which are high kinetic stability, luminescence signal [3], and  $^1\text{H}$  relaxation arising from the Ln center [4]. Nano-sized particles are frequently used as a drug carrier toward tumor by enhanced permeability and retention (EPR) effect. Previously, we obtained a silica nano-particle (SiNP,  $61.6 \pm 3.8$  nm in diameter) containing 55 ng/mg  $\text{Gd}_3\text{TCAS}_2$ , which is promising as a carrier for Gd-NCT. Here we attempted to evaluate the ability to kill cancer cell upon neutron irradiation by comparison with the cases of  $\text{Gd}_3\text{TCAS}_2$ , BSA- $\text{Gd}_3\text{TCAS}_2$  complex, Gd-DTPA, and PBS control.

**EXPERIMENTS:** *Preparation of SiNP installed with Ln.* The trinuclear complexes  $\text{Ln}_3\text{TCAS}_2$  (Ln = Gd, Tb) were prepared as reported elsewhere [2]. The  $\text{Ln}_3\text{TCAS}_2$ -installed SiNP was prepared by a Stöber's method [5], which was modified with using 3-aminopropyltrimethoxysilane (APTES) as an anchor of negatively charged  $\text{Ln}_3\text{TCAS}_2$ . Furthermore, the surface was modified with poly(ethylene glycol) (PEG) by PEG-NHS (MW 2000) to retain water-dispersibility and biocompatibility.

*Cell experiments.* MCF-7 cells were seeded in a 6-well plate at a cell concentration of  $1.0 \times 10^5$  cells/mL and incubated for 24 h. After supernatant was removed, DMEM and solution of SiNP loaded with  $\text{Gd}_3\text{TCAS}_2$  ( $5.0 \times 10^5$  M as Gd) were added to each well and incubated for 24 hr. After washing with PBS, the cells were detached from the well and transferred to tubes to be irradiated with thermal neutron ( $8.6 \times 10^{12}$  n/cm<sup>2</sup>) for 90 min. Assay: To the wells containing 2 mL of RPMI medium in 6-well plates, irradiated cells were seeded at the concentration of 1,000 cells/well. After incubation for 14 days, the colony was stained with crystal violet.

### RESULTS:

The images of 6-well plates for samples without irradiation showed formation of colonies (Fig. 2). This implies that  $\text{Gd}_3\text{TCAS}_2$ , BSA- $\text{Gd}_3\text{TCAS}_2$ , and  $\text{Gd}_3\text{TCAS}_2$ -loaded SiNP are not toxic. By contrast, no colony was found for

those samples with irradiation of thermal neutron, suggesting that the experimental conditions such as irradiation time were too harsh for the cell. Optimization of the irradiation conditions is necessary for further survey of the potential of the Gd-carrier.

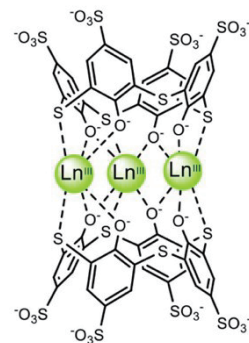


Fig. 1 Structure of  $\text{Ln}_3\text{TCAS}_2$  complex.



Fig. 2 Images of plates for the colony assay of MCF-7 cells with and without irradiation of thermal neutron.

### REFERENCES:

- [1] M. Takagaki *et al.*, Future Application of Boron and Gadolinium Neutron Capture Therapy, in *Boron Science*, Ed N. S. Hosmane (CRC Press) (2012) 243.
- [2] N. Iki *et al.*, *Eur. J. Inorg. Chem.*, **2016** (2016) 5020-5027.
- [3] R. Karashimada *et al.*, *Chem. Commun.* **52** (2016) 3139-3142.
- [4] N. Iki *et al.*, *Inorg. Chem.* **55** (2016) 4000-4005.
- [5] W. Stöber *et al.*, *J. Colloid Interface Sci.*, **26**, (1968) 62-69.

## **I-1. PROJECT RESEARCHES**

### **Project 12**

## PR12 Enhancement of research methods for material irradiation and defect analysis

A. Kinomura

*Institute for Integrated Radiation and Nuclear Science,  
Kyoto University*

**OBJECTIVES:** Irradiation facilities of high-energy particles for neutrons (Material Controlled irradiation Facility), ions (e.g., Heavy ion irradiation facility) and electrons (Temperature-controlled irradiation facilities, KUR-LINAC) have been extensively developed at the Institute for Integrated Radiation and Nuclear Science. The developed facilities have been in operation and opened for joint research projects. One of the objectives of this project is to further improve or optimize irradiation facilities for advanced irradiation experiments.

As characterization techniques for irradiated materials, a slow positron-beam system and a focused ion beam system have been developed and introduced, respectively, in addition to previous characterization facilities such as an electron microscope, an electron-spin-resonance spectrometer, a bulk positron annihilation spectrometer and a thermal desorption spectrometer. Another objective is to introduce new techniques or reconsider analytical methods of previously used characterization techniques.

Based on these two objectives, we expect the enhancement of previous studies and the attraction of new users for the joint research program.

The allotted research subject (ARS) and individual co-researchers are listed below. Note that the titles of research subjects are based on individual reports.

ARS-1:

Study to improve transport and measurement performance of a slow positron beamline (A. Kinomura et al.)

ARS-2:

Electron-irradiation induced defects in W-Re (K. Inoue et al.)

ARS-3:

Change in the positron annihilation lifetime of electron-irradiated F82H by hydrogen charging (K. Sato et al.)

ARS-4:

The effect of gamma-ray irradiation on luminescence properties of colloidal Si nanocrystals (T. Nishimura et al.)

ARS-5:

Irradiation technique for study on corrosion resistance of fusion divertor materials to liquid metal during irradiation (M. Akiyoshi et al.)

ARS-6:

Measurement of positron lifetimes of various diamond-like carbon thin films (K. Kanda et al.)

ARS-7

Positron annihilation spectroscopy on diamond-like carbon films (S. Nakao et al.)

**RESULTS:** In ARS-1, transport and measurement

performance of the KUR slow positron system was evaluated with a positron beam during the KUR operation. The brightness enhancement system and positron lifetime measurement system were confirmed to be effective.

In ARS-2, electron-irradiation to introduce only a simple Frenkel pair to W or W-5%Re (in weight %) was performed. The effect of Re addition on the defect formation is investigated by the positron annihilation method. Positron lifetime spectra before and after electron-irradiation were well fitted with one component both even after irradiation.

In ARS-3, the quantity of hydrogen atoms trapped at vacancy clusters in electron-irradiated F82H was evaluated by positron annihilation spectroscopy. The samples were soaked with liquid nitrogen within 5 min from the end of hydrogen charging. Isochronal annealing for 0.5 h was conducted every 25 K from 123 to 298 K. Subsequently, isothermal annealing was also conducted at room temperature (298 K).

In ARS-4, the effect of gamma-ray irradiation on luminescence properties of colloidal Si nanocrystals was investigated. The heavy dose irradiation of gamma-ray on the colloidal Si nanocrystals causes the decrease in photoluminescence intensity. A Compton effect on the Si core of nanocrystal is attributed to the photoluminescence quenching.

In ARS-5, irradiation techniques for study on corrosion resistance of fusion divertor materials to liquid metal during irradiation have been developed. Aluminum rich ferritic steel (Fe-18Cr-3.3Al-0.4Si) NTK04L in liquid Sn and FeCrAl-ODS in liquid Pb-Li were irradiated by KURNS-LINAC in 1<sup>st</sup> and 2<sup>nd</sup> experiments in this year. The validity of the developed specimen holders and measurement circuits was examined.

In ARS-6, free volume in the 4 kinds of DLC films was evaluated by the results of positron annihilation spectroscopy (PAS) and nano-indentation hardness. Positron lifetime decreases with increasing hardness. The relative S parameter also shows a tendency similar to a positron lifetime, but does not completely agree.

In ARS-7, several types of DLC and carbon films were also examined by PAS measurement for as-grown and thermally-annealed films. The results suggest that the structural changes, possibly caused by hydrogen desorption, may depend on the source gases and the films prepared by C<sub>2</sub>H<sub>2</sub> should be less stable than those prepared by C<sub>7</sub>H<sub>8</sub>.

**SUMMARY:** Several new developments on irradiation (electron-beam and gamma-rays) and analytical techniques (beam and bulk positron measurements) for new materials have been continuously performed in the line of the objectives of this project. Such studies may enhance developments of new materials in various scientific fields.

## PR12-1 Study to improve transport and measurement performance of a slow positron beamline

A. Kinomura, N. Oshima<sup>1</sup>, Y. Kuzuya and A. Yabuuchi

*Institute for Integrated Radiation and Nuclear Science,  
Kyoto University*

<sup>1</sup>*National Institute of Advanced Industrial Science and  
Technology (AIST)*

**INTRODUCTION:** Positron annihilation spectroscopy is an important analytical method to detect vacancy-type defects and vacant spaces of materials. Energy-variable mono-energetic positron beams (slow positron beams) are essential to perform depth-dependent positron annihilation spectroscopy of surface layers such as ion-implanted layers or thin films formed on substrates. Intense positron sources are necessary to obtain slow positron beams applicable for practical use. Positron sources based on pair creation, in general, provide higher intensity than radioisotope-based positron sources. A positron source using pair-creation by gamma-rays from a nuclear reactor have been developed by using Kyoto University research Reactor (KUR) to obtain a slow positron beam for materials analysis. In the KUR slow positron beamline, the source size (converter and moderator assembly) is approximately 30 mm in diameter. For typical sample sizes of materials analysis ( $\leq 10$  mm), it is necessary to reduce beam sizes efficiently while keeping beam intensity as high as possible. For this purpose, brightness enhancement techniques have been developed for the KUR slow positron beamline [1]. In addition, measurement systems for positron annihilation lifetime spectroscopy have been optimized in this study.

**EXPERIMENTS:** The brightness enhancement system of the KUR slow positron beam system has been evaluated in terms of the spot size and the beam intensity. A single-crystalline Ni thin film annealed in vacuum at 750 °C for 1h was used as a remoderator of the brightness enhancement system. The Ni remoderator film was cleaned by thermally excited hydrogen atoms after installation in vacuum to remove contamination during handling in air.

In addition to the detailed studies of last year, the performance of the brightness enhancement system was re-evaluated. In particular, transport of a brightness-enhanced beam to the downstream and efficiency of remoderator thin films were investigated again after careful treatments of the remoderator film and measurements of beam intensities.

**RESULTS:** The trajectories of the beam were optimized by adjusting voltages for the source components and currents for transport coils by observing images of phosphor screens on microchannel plates (MCP's). In particular, the excitation current of the focusing lens of the brightness enhancement system was optimized by observing the spot images on the MCP screen positioned at the focal point of the lens. The spot sizes at individual MCP screens were evaluated using photographs of the spot images taken by a digital single-lens reflex camera with a CMOS CCD (charge coupled device) image sensor.

To avoid unnecessary data processing in the camera, a RAW-mode (a raw-data mode without data processing) was selected for this experiment. Linearity of used devices such as the MCP, the phosphor screen and the CCD was taken into account. Parameters of image acquisition were appropriately selected to keep the linearity of the combination of these three devices.

Figure 1 shows the images of the beam spots before and after the brightness enhancement. The distribution of the beam spot were different for horizontal and vertical directions. Furthermore, the positron source near the reactor core has a circular shape but the images of Fig. 1(a) was uneven (not circular). We believe that the original beam (i.e., circular beam) extracted from the source was cut several times by the walls of vacuum ducts during beam transportation. Regardless of these results, we evaluated spot size as a full-width at half-maximum (FWHM) value for horizontal and vertical directions.

Demagnification factors calculated from the spot image were close to 1/10. The efficiency of the remoderator in the case of an extraction energy of 6.5 keV was measured to be  $\sim 4\%$  by gamma-ray intensities measured from the MCPs placed before and after the brightness enhancement system. As the beam loss at the acceleration mesh before the brightness enhancement was assumed to be 80%, the actual remoderation efficiency of the Ni film was estimated to be higher than the measured efficiency. The estimated efficiency value is acceptable but the contribution of high energy positrons (i.e., insufficiently remoderated positrons) should be taken into account for further discussion.

Finally, positron annihilation lifetime spectroscopy was examined by optimizing a positron pulsing and measurement systems. Trial measurements for Kapton and crystalline Si samples were successfully performed.

In summary, transport and measurement performance of the KUR slow positron system was evaluated with a positron beam during the KUR operation. The brightness enhancement system and positron lifetime measurement system were confirmed to be effective.

### REFERENCE:

[1] Y. Kuzuya et al. J. Phys. Conf. Series 791 (2017) 012012.

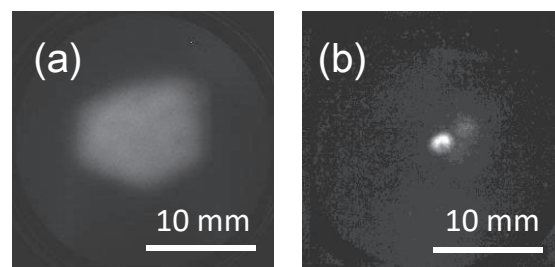


Fig. 1 Beam spot images before (a) and after (b) brightness enhancement.

T. Toyama, Y. Hatano<sup>1</sup>, C. Zhao, A. Yabuuchi<sup>2</sup>, A. Kinomura<sup>2</sup>, K. Inoue and Y. Nagai

*Institute for Materials Research, Tohoku University*

<sup>1</sup>*Organization for Promotion of Research, University of Toyama*

<sup>2</sup>*Institute for Integrated Radiation and Nuclear Science, Kyoto University*

## INTRODUCTION:

Tungsten (W) is a primary candidate material for the plasma-facing components (PFCs) due to its high melting point and high sputtering resistance to energetic particles. Furthermore, the very low solubility of hydrogen isotopes in W is a notable advantage in reducing tritium (T) retention during the operation of fusion reactors. However, recent studies have reported that neutron-irradiation and ion-irradiation cause significant enhancement of hydrogen isotope retention in W, due to hydrogen trapping at irradiation-induced defects such as vacancies, vacancy clusters, and dislocation loops. Recently it was found that the addition of rhenium (Re) to W drastically reduces the hydrogen isotope accumulation [1]. As a mechanism for this, quantum chemical calculation has been performed [2]; it is suggested that Re is strongly bound to interstitial atoms, so that recombination of interstitial atoms and vacancies is promoted, and the formation of vacancy-type defects that become hydrogen capture sites is suppressed. However, no experimental studies on this has been obtained.

In this study, we performed electron-irradiation to introduce only a simple Frenkel pair to W or W-Re alloy. The effect of Re addition on the defect formation is investigated by the positron annihilation method.

## EXPERIMENTS:

Electron-irradiation to pure W and W-5%Re (in weight %) was performed at LINAC at KUR at 8 MeV, at temperature of < 100 °C to the fluence of about  $5E+23$  e-/m<sup>2</sup>. Positron annihilation measurements (lifetime measurement and coincidence Doppler broadening measurement) were performed.

## RESULTS:

Figure 1 shows results of positron lifetime measurement before and after electron-irradiation for pure W and W-5%Re. Calculated values of positron lifetime at W bulk, mono-vacancy in W and di-vacancy in W are also shown by dashed lines. In pure W, the average lifetime,  $\tau_{ave}$ , was about 120 ps before electron-irradiation, which is close to the value in W bulk. After electron-irradiation,  $\tau_{ave}$  was about 140 ps, showing positron trapping to vacancy-type defects induced by electron-irradiation. The lifetime spectrum after irradiation was analyzed with two components; the shorter component,  $\tau_1$ , and the longer component,  $\tau_2$ .  $\tau_2$  was 215 ps, suggesting positron trapping at mono-vacancies and/or di-vacancies.

In W-5% Re alloy,  $\tau_{ave}$  before electron-irradiation was 158 ps, longer than that for pure W before electron-

irradiation. This implies an existence of defects before irradiation.  $\tau_{ave}$  after electron-irradiation was 162 ps, only 4 ps longer than that for W-5%Re before irradiation. Remarkable increase of  $\tau_{ave}$  was not observed after irradiation. Different from the case of pure W, the lifetime spectrum was well fitted with one component both even after irradiation, and Positron trapping at mono-vacancy was not clearly observed. The possible candidate for positron trapping site for W-5%Re after irradiation could be dislocations in which positron lifetime value may be shorter than mono-vacancy. Other candidate could be vacancy-Re complexes, however, positron lifetime value at vacancy-Re complex might be almost same as at mono-vacancy in W because Re and W are the “neighborhood” in the periodic table. Further studies by chemical analysis of positron annihilation sites with coincidence Doppler broadening measurements are now in progress to discuss electron-irradiation induced defects in W-Re.

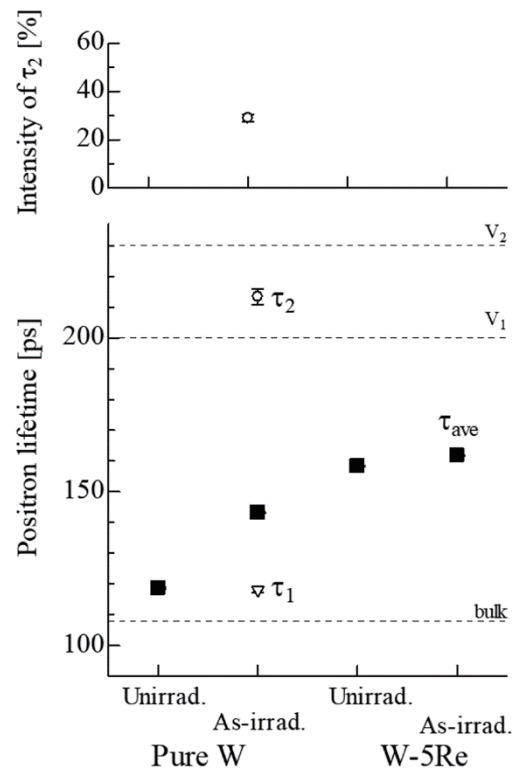


Fig. 1. Results of positron lifetime measurements for pure W and W-5%Re alloy; before electron-irradiation (Unirrad.) and after electron-irradiation (As-irrad.).

## REFERENCES:

- [1] Y. Hatano *et al.*, Nucl. Mater. Energy **9** (2016) 93.
- [2] T. Suzudo, A. Hasegawa, Sci. Rep. **6** (2016) 36738.

## PR12-3 Change in the Positron Annihilation Lifetime of Electron-irradiated F82H by Hydrogen Charging

K. Sato, Y. Kondo, M. Ohta, Q. Xu<sup>1</sup>, A. Yabuuchi<sup>1</sup> and A. Kinomura<sup>1</sup>

Graduate School of Science and Engineering,  
Kagoshima University

<sup>1</sup>Institute for Integrated Radiation and Nuclear Science,  
Kyoto University

**INTRODUCTION:** The structural materials of spallation neutron sources (SNS) cause more serious irradiation damage than fission reactors due to high-energy protons or spallation neutrons and the formation of extremely larger amount of gas atoms by nuclear transmutation [1, 2]. Therefore, irradiation resistance is required. Reduced activation ferritic/martensitic steel F82H, one of the candidates for fusion reactor structural materials, has good thermal and mechanical properties [3]. Using this steel, many researchers have investigated the effect of He or H on its microstructural evolution [4–6]. The increase in hydrogen retention caused by the interaction with defects has an influence on the mechanical properties of structural materials [7, 8]. Vacancy-type defects are detected well by positron annihilation spectroscopy (PAS). Sato et al. determined the change in the positron annihilation life-time (PAL) through experiments and simulations [9]. Comparison and estimation of the number of hydrogen atoms trapped at single vacancies in electron-irradiated tungsten by PAS were performed [9]. In this study, the quantity of hydrogen atoms trapped at vacancy clusters in electron-irradiated F82H will be estimated by PAS.

**EXPERIMENTS:** Reduced activation ferritic/martensitic steel F82H IEA heat was used. Samples with diameters of 5 mm were cut from 0.4 mm-thick sheets using a wire electric discharge machine. Samples were irradiated with an 8 MeV electron linear accelerator from the Institute for Integrated Radiation and Nuclear Science, Kyoto University. The irradiation temperature was  $333 \pm 10$  K, and the irradiation dose was  $2.74 \times 10^{27} / \text{m}^2$  ( $1.75 \times 10^{-4}$  dpa). Cathodic electrolysis charging was performed in an aqueous solution of 0.1 mol/L NaOH with the addition of 0.5 mass%  $\text{NH}_4\text{SCN}$ . The current density, temperature, and time for hydrogen charging were 50 A/m<sup>2</sup>, 303 K, and 4 h, respectively. After hydrogen charging, the sample surface was mechanically polished using polishing paper #2400. Subsequently, samples were soaked with liquid nitrogen within 5 min from the end of hydrogen charging. The PAL measurements were conducted at a liquid nitrogen temperature of 77 K using a fast digital oscilloscope with a time resolution of 150 ps, i.e., full width at half maximum (FWHM) [11]. The PAL spectra were accumulated with a total count of approximately  $3 \times 10^6$  and analysed using the PALSfit package [12]. Isochronal annealing for 0.5 h was conducted every 25 K from 123 to 298 K. Subsequently, isothermal annealing was also conducted at room temperature (298 K). To investigate the repeatability, the same

samples used in the first experiment, which were left at room temperature for approximately 14 days, were subjected to the second hydrogen charging.

**RESULTS:** As dislocations, packet/block/lath boundaries, and precipitates exist in unirradiated F82H, a  $\tau_1$  of 140 ps, which denotes the PAL of dislocations [13], was fixed. After electron irradiation, a  $\tau_2$  of 254 ps was obtained. This PAL is almost the same as the calculated PAL of vacancy clusters composed of five vacancies ( $V_5$ ). After hydrogen charging,  $\tau_2$  decreased to approximately 230 ps, and was constant until isochronal annealing at 273 K. After isochronal annealing at 298 K for 0.5 h,  $\tau_2$  started to increase during isothermal annealing for 1 h, 2 h, and 4 h, and was higher than the value before hydrogen charging (254 ps). When the isothermal annealing time reached 8 h,  $\tau_2$  decreased to the value before hydrogen charging. Almost the same trend of the change in PAL was observed in the second experiment. The cause of the increase in the PAL after annealing at 298 K from 0.5 to 4 h cannot be identified; therefore, it will be investigated in the near future.

From the theoretical estimation, the number of hydrogen atoms trapped at  $V_5$  of 14.5 ( $\theta = 0.805$ ) is obtained. After the first and second hydrogen charging, the PAL decreases by 22 ps and 18 ps, respectively. Compared with the calculated result, each  $V_5$  contains 4 hydrogen atoms ( $\theta = 0.22$ ). This value is significantly lower than the theoretical value. Analysis of the PAL spectra without fixing  $\tau_1$  of 140 ps was also performed, because it is better to obtain a stable PAL. The difference in the PAL between before hydrogen charging and after annealing at 148 K for 0.5 h was more than 50 ps. In this case, more than 14 hydrogen atoms can be trapped at each  $V_5$ . However, both  $\tau_1$  and  $\tau_2$  significantly change in each treatment. As F82H contains a variety of positron trapping sites such as dislocations, interfaces of precipitates, packet/block/lath boundaries, and vacancy clusters, identification of the positron trapping sites may be difficult in F82H. For future studies, samples with a different number of hydrogen atoms trapped at vacancy clusters will be prepared, and PAL spectra of F82H will be carefully analysed.

### REFERENCES:

- [1] Y. Dai, G.S. Bauer, *J. Nucl. Mater.* **296** (2001) 43.
- [2] Y. Dai *et al.*, *J. Nucl. Mater.*, **343** (2005) 33.
- [3] M. Tamura *et al.*, *J. Nucl. Mater.*, **141–143** (1986) 1067.
- [4] X. Jia, Y. Dai, *J. Nucl. Mater.*, **318** (2003) 207.
- [5] Z. Tong, Y. Dai, *J. Nucl. Mater.*, **385** (2009) 258.
- [6] Z. Tong, Y. Dai, *T. J. Nucl. Mater.*, **398** (2010) 43.
- [7] H.K. Birnbaum, P. Sofronis, *Mater., Sci. Eng., A* **176** (1994) 191.
- [8] M. Nagumo *et al.*, *Metall. Mater. Trans., A* **32** (2001) 339.
- [9] K. Sato *et al.*, *J. Nucl. Mater.*, **496** (2017) 9.

T. Nakamura, J. Otsubo, K. Kuriyama and A. Kinomura<sup>1</sup>,

College of Engineering and Research Center of Ion Beam Technology, Hosei University

<sup>1</sup> Institute for Integrated Radiation and Nuclear Science, Kyoto University

**INTRODUCTION:** Colloidal crystalline silicon (Si) nanocrystals is known to exhibit a size tunable and efficient visible luminescence at room temperature due to quantum confinement effect. Because of its environmental friendliness and earth-abundancy, colloidal Si nanocrystals are a promising material for future light-emitting devices and biomedical applications. Various fabrication techniques for colloidal Si nanoparticles have been developed, such as wet-chemical synthesis and high-temperature thermal processing. Recently, we developed an efficient formation process of colloidal Si nanocrystals from porous Si, which is an interconnected wire-nanostructure assembly, as a raw material with low energy cost treatments. This process produces a large amount of colloidal nanocrystals per batch, and thus it allows us to utilize the Si nanocrystals in practical applications.

Optical properties of Si nanocrystals including luminescence properties are strongly affected by surface chemistry [1]. In particular, insufficient surface terminations causes the notable decrease in the luminescence efficiencies due to the formation of nonradiative centers i.e., dangling bonds. Thus, ambient condition is one of the most important key parameters to determine the luminescence efficiency. There are many reports on the effects of various environments on luminescence properties of Si nanocrystals. For example, it has been reported that a highly oxidant condition such as high humidity environment promotes inhomogeneous oxidation as well as removal of terminated species on the Si nanocrystals and resultantly the decreases in luminescence intensity occurs. However, the effect of extreme conditions such as high level radiation environment on Si nanocrystals luminescence properties is not known.

In this work, we investigate the effect of gamma-ray irradiation on luminescence properties of colloidal Si nanocrystals. The heavy dose irradiation of gamma-ray on the colloidal Si nanocrystals causes the decrease in photoluminescence intensity. However, we find that, comparing with compound semiconductor nanocrystals such as CdSe, the decreasing effect is much weaker.

**EXPERIMENTS:** The porous Si used was prepared by a chemical etching of bulk Si. After the etching, porous layer was formed on the wafer surface, and then, samples were obtained. The formed sample exhibited a weak red photoluminescence. For preparing the colloidal Si nanoparticles, porous Si were firstly dispersed in an organic solvent with a quartz cuvette. Then, pulsed laser light at 266 or 532 nm from a Q-switched Nd:YAG laser (Continuum) was irradiated with a pulse duration of 5 ns and a repetition rate of 15 Hz. During laser irradiation, the po-

rous Si dispersed in the organic solution were constantly stirred by a magnetic stirrer. After the pulsed laser irradiation of porous Si, the colloidal solution sample is obtained. Under UV illumination, the colloidal Si nanocrystal solution exhibits red luminescence.

For gamma ray irradiation experiments, we spin-coated the Si nanocrystals solution on the Si surface and the colloidal Si nanocrystal films were obtained. The prepared film samples were irradiated at room temperature with gamma-rays of 1.17 and 1.33 MeV from a cobalt-60 source of Institute of Integrated Radiation and Nuclear Science, Kyoto University. The dose rate of the irradiation was 1.771 KGy/h. Total gamma-ray dose was ~150 kGy.

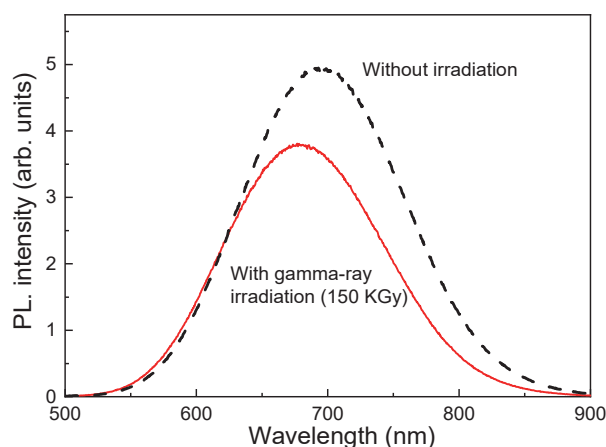


Fig. 1. PL spectra of colloidal Si nanocrystal films with and without gamma-ray irradiation.

**RESULTS:** Figure 1 shows PL spectra of colloidal Si nanocrystal films with and without gamma-ray irradiation. As shown in the figure, the heavy dose irradiation of gamma-ray on the colloidal Si nanocrystals causes the decrease in photoluminescence intensity. This may be due to the formation of defect centers formed by gamma-ray irradiation. However, the degree of the intensity decrease is much smaller than colloidal CdSe nanocrystals where the origin of the photoluminescence quenching is gamma-ray induced losses of surface ligands [2]. In our previous work, it was shown that Compton electrons emitted by the gamma-ray irradiation causes lattice defects of ZnO crystals [3], where the degree of the luminescence intensity change is trivial in spite of heavily dose. Thus, in the present case, such a Compton effect on the Si core of nanocrystal is attributed to the photoluminescence quenching.

#### REFERENCES:

- [1] Dohnalová, K. *et al.*, J. Phys. Condens. Matter **26** (2014) 173201.
- [2] Stodilka, R. Z. *et al.*, J. Phys. Chem. C **113** (2009) 2580–2585.
- [3] Tashiro, J. *et al.*, Solid State Commun. **292** (2019) 24–26.

## PR12-5 Irradiation technique for study on corrosion resistance of fusion divertor materials to liquid metal during irradiation

M. Akiyoshi, M. Kondo<sup>1</sup> and A. Kinomura<sup>2</sup>

Radiation Research Center, Osaka Prefecture University  
<sup>1</sup>. Lab. for Nucl. Reactors, Tokyo Institute of Technology  
<sup>2</sup>Inst. for Integrated Radiation and Nuclear Science, Kyoto University

### INTRODUCTION:

Development of divertor material is one of the most important issues for future fusion reactor, where high thermal conductivity in severe neutron irradiation environment, sputtering resistance, and low radioactivity is required. Although development of SiC ceramics, tungsten, and its composite material is furthered, neither has resulted in the solution of this problem.

The liquid divertor is completely different approach from the conventional divertor material development, that is covering a surface of material with coolant liquid metal, and it can expect to moderate damage to the structure material. There is little study on the compatibility of liquid metal and structure material, and furthermore, compatibility study during irradiation is quite limited.

### EXPERIMENTS and RESULTS:

In the previous year, it was planned to perform the corrosion experiment after an electron irradiation. However, it is impossible to avoid corrosion on the surface by underwater or in air irradiation. Therefore, tin (Sn) was sealed in a small irradiation container ( $30 \times 34 \times 4$ mm) manufactured by SUS316L stainless steel, and inside of the container, aluminum rich ferritic steel (Fe-18Cr-3.3Al-0.4Si) NTK04L with  $100\mu\text{m}$   $\text{Al}_2\text{O}_3$  oxidation coating was enclosed to performed electron irradiation by KURUNS-LINAC that achieved the corrosion action inner side of the container under irradiation environment.

In this year, at the first MT, NTK04L specimen (pre oxidation  $1000^\circ\text{C}$  10h) was irradiated during  $1.1 \times 10^5$  sec (32.5h) to a dose of  $5.8 \times 10^{19}$ e that corresponds to 2.3 mdpa (for Fe  $E_d=40\text{keV}$ ) and also ODS sp-10 specimen (pre oxidation  $1000^\circ\text{C}$  10h) was irradiated during  $1.1 \times 10^5$  sec (32.5h)  $6.5 \times 10^{19}$ e that corresponds to 2.6 mdpa. With this irradiation, rear heat sink was rather small to make a difference small between front side and rear side temperature. However, for the first specimen, temperature at the front-side was increased to  $500^\circ\text{C}$  while at the rear-side was only  $300^\circ\text{C}$ . In the case of the second specimen, air blower was settled at the front side while it was settle rear side at the first specimen. With this treatment, temperature at the front side was same

$500^\circ\text{C}$  but rear side was kept  $400^\circ\text{C}$ .

At the second MT, FeCrAl-ODS specimen was irradiated in Pb-Li liquid metal during  $1.1 \times 10^5$  sec (32.5h) to a dose of  $6.6 \times 10^{19}$ e that correspond to 2.6 mdpa, and also JLF-1-SS430 specimen was irradiated in Pb-Li during  $1.1 \times 10^5$  sec (32.5h) to a dose of  $6.8 \times 10^{19}$ e that corresponds to 2.7 mdpa.

In this irradiation, temperature measurement was failed because of failure of several AD8495 thermo-couple amplifier IC. Only rear-side temperature was measured and kept it to  $370^\circ\text{C}$ , but after the irradiation, some liquid metal was over spilled from the container.

To measure the electron current, the specimen holder was connected to current meter and not connected to ground directly and also thermo couple was not connected to ground to measure electron current. It is better to connect the thermocouple to ground with temperature measurement, and disconnect them when current measurement is performed.

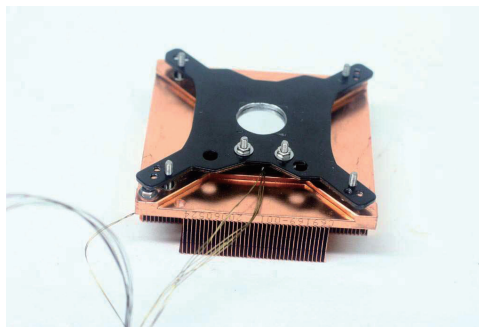


Fig.1. Cu heat sink and retention plate used for the electron irradiation. The irradiation container was placed between heat sink and the retention plate.



Fig. 2. In the second MT, over heat was assumed and some liquid metal was over spilled from the container.

## PR12-6 Measurement of Positron Lifetimes of Various Diamond-like Carbon Thin Films

K. Kanda, F. Hori<sup>1</sup>, A. Yabuuchi<sup>2</sup> and A. Kinomura<sup>2</sup>

Laboratory of Advanced Science and Technology for Industry, University of Hyogo

<sup>1</sup>Department of Materials Science, Osaka Prefecture University

<sup>2</sup>Institute for Integrated Radiation and Nuclear Science, Kyoto University

**INTRODUCTION:** Diamond-like carbon (DLC) film, which is amorphous carbon film consisting of carbon and hydrogen, has several excellent properties, such as high mechanical hardness, chemical inertness, low frictional coefficient, and abrasion resistance [1]. The film properties of DLC film is depended on its three kinds of structural factors, that is,  $sp^2/sp^3$  ratio of carbon atom, hydrogen content, and free volume [2]. Free volume in the DLC film has been macroscopically evaluated as film density, but microscopic discussion on it has not been carried out yet. In the present study, free volume in the 4 kinds of DLC films, which were synthesized by various deposition methods and deposition conditions, was discussed on the results of positron annihilation spectroscopy (PAS). We also measured the nano-indentation hardness of these DLC films. Indentation hardness is expected to decrease as quantity and the size of the free volume increase.

**EXPERIMENTS:** We prepared 4 kinds of DLC films for the present study. The first DLC film was deposited by using a plasma-enhanced chemical vapor deposition (PE-CVD) method. On the present plasma condition, hydrogen-rich soft DLC film is expected to be deposited. The second DLC film was prepared by the ion plating (IP) method, which is very familiar to the industrial field as a hard protective coating. Last DLC films were is synthesized by filtered cathodic vacuum arc (FCVA) method. Two kinds of DLC films were deposited using this method with the different bias voltage, 100 and 400 V. All DLC films were deposited on Si wafer with the film thickness of several hundred nm. Indentation hardness of these DLC films was estimated by using a nano-indenter. PAS measurement was performed at the slow positron beam system (B-1) at Kyoto University research Reactor (KUR). Doppler broadening profiles of annihilation  $\gamma$ -rays were obtained using a Ge detector for each positron energy. The-low momentum part of spectra was characterized by the line-shape  $S$  parameter, which is defined as the number of annihilation events over the range of  $511 \pm 0.80$  keV.  $S$  parameters as a function of energy (S-E curves) were measured in the range of 0 - 30 keV. Positron annihilation lifetime spectroscopy (PALS) was performed at an energy of 2 keV, corresponding to the DLC film on Si. Figure 1 shows lifetime spectra for the DLC films formed by the FCVA method. A Kapton (polyimide) film was measured before and after measurements of the DLC samples as a control sample. Obtained lifetime spectra were analyzed by the PALSfit code assuming one-lifetime component.

**RESULTS:** Experimental results obtained from PAS measurements were summarized in Table with indentation hardness. Relative  $S$  parameter of each DLC film was obtained in comparison with that of and Si.

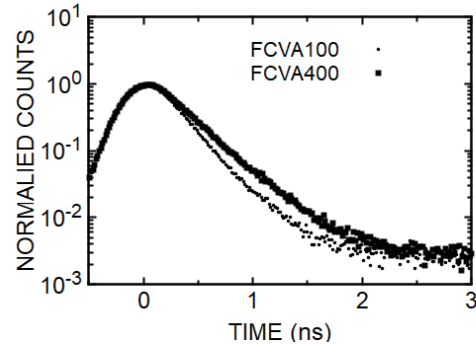


Fig. 1 Lifetime spectra for the DLC samples formed by the FCVA method with different bias voltage.

Table 1. positron lifetime and  $S$  parameter obtained from PAS measurements with nano-indentation hardness of each DLC films.

Deposition method	Bias voltage [V]	Positron lifetime [ns]	Relative $S$ parameter	Indentation hardness [N/mm <sup>2</sup> ]
PE-CVD		0.379	0.932	2488
IP		0.339	0.952	75960
FCVA	400	0.267	0.914	62303
FCVA	100	0.202	0.891	211795

The DLC film, which is synthesized by the FCVA method with the bias voltage of 100 V, has very high indentation hardness and its positron lifetime and relative  $S$  parameter are smaller than those of other DLC films. The DLC film deposited by the PE-CVD method, which has low hardness, has a large positron lifetime and relative  $S$  parameter. As described above, positron lifetime decreases with increasing hardness. The relative  $S$  parameter also shows a tendency similar to a positron lifetime, but does not completely agree. PAS techniques give information on voids consisting of the free volume. It should be noted that positron lifetimes reflect void sizes but  $S$  parameters reflect void densities in addition to void sizes. We think that the hydrogen in the DLC film influenced the results of the  $S$  parameter. We are planning to obtain the hydrogen content and the  $sp^2/sp^3$  ratio of carbon atom in these films by measuring elastic recoil detection analysis (ERDA) and near-edge x-ray fine structure (NEXAFS), respectively.

### REFERENCES:

- [1] S. Aisenberg *et al.*, J. Appl. Phys., **42** (1971) 3963.
- [2] J. Robertson, Surf. Coat. Technol., **50** (1992) 185.

S. Nakao, Q. Xu<sup>1</sup>, A. Yabuuchi<sup>1</sup> and A. Kinomura<sup>1</sup>

*Innovative Functional Materials Research Institute, National Institute of Advanced Industrial Science and Technology*

<sup>1</sup>*Institute for Integrated Radiation and Nuclear Science, Kyoto University*

**INTRODUCTION:** Diamond-like carbon (DLC) films have attracted much attention because of their excellent mechanical properties, such as high hardness, high wear resistance and low friction coefficients. However, the properties strongly depend on the microstructure of the films which is varied by the deposition conditions and methods. Recently, DLC or carbon films are categorized from type I to VI, which includes graphite-like carbon (GLC) and polymer-like carbon (PLC).

The thermal stability of the films is of importance for practical applications. However, the thermal stability is not always enough to use it at high temperature. It is considered that the changes of the microstructure at high temperature should be responsible for the degradation of the properties. The structural changes are related to H desorption and the behavior of defects at high temperature. Many studies have been carried out on the thermal stability of DLC films. However, the principal phenomena, such as defect behavior, are not always clear. Therefore, to make clear the thermal stability of DLC or carbon films, the examination on the defect behavior is necessary for every type of DLC films (type I to VI) because of different microstructure and hydrogen content. The positron annihilation spectroscopy (PAS) is one of the useful methods to clarify the defect behavior in materials.

In a previous report [1, 2], the films of type I, III, IV, V and VI were examined by thermal desorption spectroscopy (TDS) measurement. From the results, it was found that hydrogen desorption clearly started around 400°C in the case of PLC (type VI) films. On the other hand, ta-C (type I) films did not change significantly until 800°C. The result, thus, suggested that defects may be created by hydrogen desorption and the behavior may play important role for the durability of the films. Several types of DLC and carbon films were also examined by PAS measurement for as-grown films [3]. It was found that the situation of the defect in the type III – VI films may be similar among as grown films except for ta-C (type I) films. In this study, thermal annealing and PAS measurement is carried out for a-C:H films (type IV) to make clear the effect of annealing temperature (hydrogen desorption).

**EXPERIMENTS:** Type IV (a-C:H) films were deposited using C<sub>2</sub>H<sub>2</sub> and C<sub>7</sub>H<sub>8</sub> source gases by plasma-based ion implantation (PBII) under the different conditions. Si wafer was used as substrate. The details on the PBII system were reported elsewhere [4]. The samples were heated at 400 and 800 °C for 1 h in vacuum by an infrared image furnace. The S-parameter was obtained at dif-

ferent positron energies ranging from 0 to 30 keV.

**RESULTS:** Figure 1 shows the change in S-parameter obtained from the PAS spectra of the samples prepared by (a) C<sub>2</sub>H<sub>2</sub> and (b) C<sub>7</sub>H<sub>8</sub> gases, which are annealed at different temperature. The sample prepared by C<sub>2</sub>H<sub>2</sub> gas was peeled off after 800 °C annealing so that the one was not available for PAS measurement. In Fig. 1(a), the S-parameter of the as-grown film using C<sub>2</sub>H<sub>2</sub> gas is around 0.50 and then that decreases to around 0.48 after annealed at 400 °C, which is close to that of graphite [3]. A similar trend is also observed in the sample prepared using C<sub>7</sub>H<sub>8</sub> gas, as shown in Fig. 1(b). However, the changes of the S-parameter of sample (a) seems to be larger than those of sample (b) at 400 °C. These results suggest that the structural changes, possibly caused by hydrogen desorption, may depend on the source gases and the films prepared by C<sub>2</sub>H<sub>2</sub> should be less stable than those prepared by C<sub>7</sub>H<sub>8</sub>. To make clear this point of view, more detail investigations are underway.

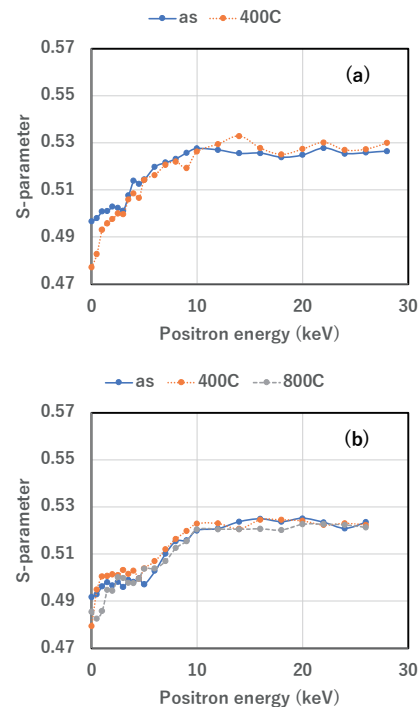


Fig.1. Changes in S-parameters of the samples after annealed at different temperature.

#### REFERENCES:

- [1] S. Nakao *et al.*, KURRI Progress Report 2016, 28P12-8 (2016) 57.
- [2] S. Nakao *et al.*, KURRI Progress Report 2017, 29P6-8 (2017) 32.
- [3] S. Nakao *et al.*, KURNS Progress Report 2018, 30P1-8 (2018) 11.
- [4] S. Miyagawa *et al.*, Surf. Coat. Technol., **156** (2002) 322-327.

## **I-1. PROJECT RESEARCHES**

### **Project 13**

## PR13 Chemical and electronic properties of Actinide compounds and their applications

T. Yamamura<sup>1</sup>, C. Tabata<sup>1</sup>, Y. Haga<sup>2</sup>, H. Amitsuka<sup>3</sup>, T. Suzuki<sup>4</sup>, K. Shirasaki<sup>5</sup>, M. Abe<sup>6</sup>, A. Sunaga<sup>1,6</sup>, M. Nogami<sup>7</sup>, H. Shishido<sup>8</sup>, M. Nakase<sup>9</sup>

<sup>1</sup>Institute for Integrated Radiation and Nuclear Science, Kyoto University

<sup>2</sup>Advanced Science Research Center, JAEA

<sup>3</sup>Graduate School of Science, Hokkaido University

<sup>4</sup>Ngaoka University of Technology

<sup>5</sup>Institute for Materials Research, Tohoku University

<sup>6</sup>Department of Chemistry, Tokyo Metropolitan University

<sup>7</sup>Graduate school of Electronic Eng., Kindai University

<sup>8</sup>Graduate School of Engineering, Tohoku University

<sup>9</sup>Lab. for Adv. Nuclear Energy, Tokyo Inst. of Tech.

### INTRODUCTION:

Actinide compounds shows a unique chemical and electronic nature due to the partial and insufficient shield of 5f orbital electrons as inner transition elements. We have a deep interest in the aspect of the electronic properties of the actinide compounds and formed the group consisting of three major fields: (1) inorganic and coordination chemistry, (2) electronic properties and (3) theoretical chemistry and its users. The methodology should have substantial applications to the issues of the IF debris, the transmutation of the long-lived radioactive wastes. Also, since the epochal clinical effect of <sup>225</sup>Ac nuclear medicine against the propagated prostate cancer, the demands for such actinide nuclides and for research environments are increasing. Such research environments as well as obtaining such actinide nuclides are extremely difficult to prepare in ordinary university institutes. The hot laboratory of the KURNS offers precious opportunities for the above-mentioned research group to carry out their characteristic research activities.

### EXPERIMENTS:

The first fiscal year of the project has been devoted to the preparatory discussions on the equipment and the environment of the KURNS to start a series of researches. Each of research fields has made their progress as followings:

(1) K. Shirasaki has investigated the key separation step of <sup>225</sup>Ac generation from <sup>229</sup>Th. The fact that <sup>229</sup>Th-<sup>225</sup>Ac system shows too many  $\gamma$ -ray emissions lead us difficulties in monitoring the separation factors, and improve the step. M. Nakase has synthesized the Zn-based porphyrin (ZnPc) complex as a prototype for the actinide porphyrins such as <sup>225</sup>Ac complexes. T. Suzuki and M. Nogami has carried out the preparatory experiments on the extraction behavior of actinides, by using corresponding lanthanide ions and by using ICP-MS.

(2) The single-crystalline samples of a series of uranium intermetallic compounds were prepared and their magnetic and crystallographic properties were characterized.

(3) The calculation of the atomic orbitals for various uranium ions (e.g., U<sup>6+</sup>, U<sup>5+</sup>, and U<sup>4+</sup>) is crucial in chemical nature. The GRASP program [2] is used to calculate the radial distribution functions at the four-component relativistic method.

### RESULTS:

(1) K. Shirasaki et al have proposed the use of <sup>232</sup>Th-<sup>228</sup>Ac system and successfully revealed 40% of <sup>228</sup>Ra remained in the starting <sup>232</sup>Th. Figure 1 shows the synthesis of ZnPc. (2) A newly synthesized compound U<sub>2</sub>Pt<sub>6</sub>Al<sub>15</sub>, characterized in a hexagonal crystal structure, shows disorder to have honey-comb structure. Also, a certain anomalous state of the conduction electron system in Th<sub>1-x</sub>U<sub>x</sub>Be<sub>13</sub> was unveiled from the magnetization measurements (Fig. 2). (3) From Fig. 3, the order of spread of 7s orbital is U<sup>6+</sup> < U<sup>5+</sup> < U<sup>4+</sup>, which indicates that 7s orbital becomes more spread as the number of 5f electrons is increased. Also, minor actinides (MA) phase diagrams for actinide transmutation based on CALPHAD is now underway by H. Shishido.

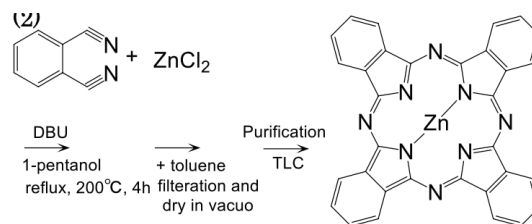


Fig. 1. Synthesis of the prototype Zn porphyrin complex.

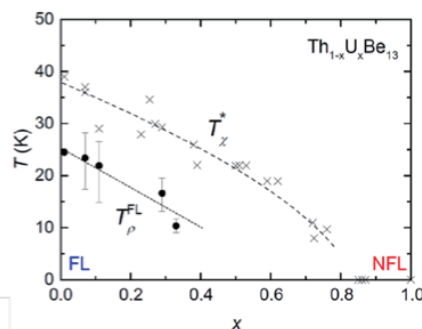


Fig.2. The U concentration dependence of the characteristic temperatures of Th<sub>1-x</sub>U<sub>x</sub>Be<sub>13</sub>.

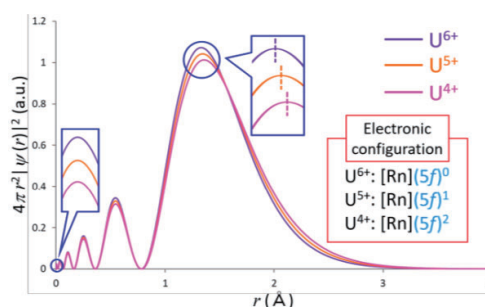


Fig. 3. Radial distribution function of 6s orbitals in U<sup>6+</sup>, U<sup>5+</sup>, and U<sup>4+</sup> ions.

### REFERENCES:

- [1] S. S. Saxena *et al.*, Nature, **406** (2000) 587-592.
- [2] P. Jönsson, *et al.*, Comput. Phys. Commun. **177**, 597 (2007).

## PR13-1 Synthesis and characterization of actinide-based compounds with honeycomb layer

Y. Haga<sup>1</sup>, T. Sugai<sup>2</sup>, Y. Matsumoto<sup>3</sup> and E. Yamamoto<sup>1</sup>

<sup>1</sup>Advanced Science Research Center, Japan Atomic Energy Agency

<sup>2</sup>Graduate School of Science, Tohoku University

<sup>3</sup>Department of Physics, Toyama University

**INTRODUCTION:** A series of ternary compounds having chemical composition close to 2:6:15 crystallizing in the hexagonal structure are known to form rare earth [1,2] and actinide [3-5] intermetallics. Although an apparent structural disorder in the rare earth/actinide containing layer is observed in X-ray diffraction, a possible honeycomb arrangement of rare earth atom is suggested in earlier investigations on rare earth analogues [6]. In this paper, we report characterization of both crystallographic and magnetic properties of  $U_2Pt_6Al_{15}$ . [7]

**EXPERIMENTS:** The sample was prepared either by arc-melting the constituent elements or Al-flux method. Obtained samples were characterized by electron-probe microanalysis for stoichiometry and homogeneity. Crystal structure was investigated by the single-crystal X-ray diffraction using a tiny single crystal extracted from ingots. Magnetization was measured using a SQUID magnetometer.

**RESULTS:** X-ray diffraction successfully identified a hexagonal unit cell ( $P6_3/mmc$ ,  $a = 4.2957 \text{ \AA}$ ,  $c = 16.2211 \text{ \AA}$ ). The structural disorder is reflected in the partial occupation on uranium 0.667(6) and one of the aluminum sites 0.33(2), in agreement with the previous report. Furthermore, additional weak peaks are observed at  $(h/3 \ l/3 \ 0)$  in the basal plane, corresponding to a superstructure with a larger lattice parameter. These superstructure peaks are elongated along the  $c^*$  direction suggesting that the periodicity along the  $c$ -axis is lost. A honeycomb layer model with a planer disorder well describes experimental observation above. Similar model is also reported in rare earth analogue. A more complex superstructure is recently reported in europium analogue [8]. The present honeycomb arrangement of neighboring uranium layer is shown in Fig. 1. The neighboring uranium layers have a displacement  $(-1/3, 1/3)$  or equivalent directions in the hexagonal cell, keeping hexagonal symmetry in the average structure.

Despite the disordered structure, a relatively sharp magnetic phase transition due to uranium 5f electrons was observed. [7] Considering the fact that each honeycomb layer is separated by  $8.1 \text{ \AA}$  and U-U distance ( $4.3 \text{ \AA}$ ) within the layer is much shorter than that, magnetic interaction within the layer is considered to be primarily dominant. The disorder of the stacking between the layers less influences the magnetic transition.

In summary, we established the honeycomb uranium arrangements in a uranium compound  $U_2Pt_6Al_{15}$ . A well-defined magnetic ordering is found in this compound. The detailed magnetic property investigation is in

progress.

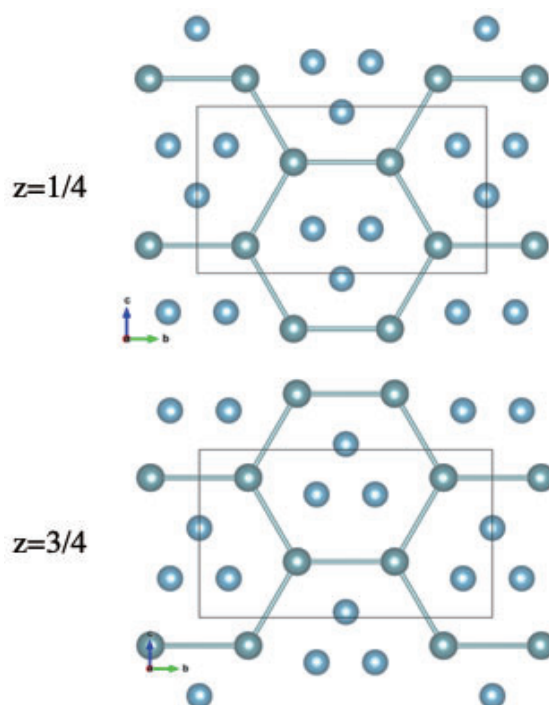


Fig. 1. Local arrangement of neighboring uranium layers located at  $z = 1/4$  and  $3/4$  in  $U_2Pt_6Al_{15}$ . Solid square denotes the local unit structure corresponding to orthorhombic symmetry.

### REFERENCES:

- [1] A. Lacerda *et al.*, J. Alloys Compds., **181** (1992) 191-196.
- [2] S. Lattner *et al.*, Inorg. Chem. **41** (2002) 5479-5486.
- [3] S. Noguchi *et al.*, Physica B, **246-247** (1998) 456-459.
- [4] S. Bobev *et al.*, Acta Cryst. E, **62** (2006) i77-i79.
- [5] Y. Haga *et al.*, J. Phys. Soc. Jpn. **77 Suppl. A** (2008) 365-367.
- [6] G. Kwei *et al.*, Acta Cryst. B, **52** (1996) 580-585.
- [7] Y. Haga *et al.*, JPS Conf. Ser., **29** (2020) 013003-1-5.
- [8] M. Radziejowski *et al.*, J. Am. Chem. Soc. **140** (2018) 8950-8957.

## PR13-2 Crossover between Fermi-liquid and non-Fermi-liquid states in $\text{Th}_{1-x}\text{U}_x\text{Be}_{13}$ ( $0 \leq x \leq 1$ )

H. Amitsuka, N. Miura, H. Hidaka, T. Yanagisawa,  
C. Tabata<sup>1</sup>, Y. Shimizu<sup>2</sup>, K. Uhlířová<sup>3</sup> and V. Sechovský<sup>3</sup>

*Graduate School of Science, Hokkaido University*  
<sup>1</sup>*Institute for Integrated Radiation and Nuclear Science, Kyoto University*

<sup>2</sup>*Institute for Materials Research, Tohoku University*  
<sup>3</sup>*Faculty of Mathematics and Physics, Charles University*

**INTRODUCTION:**  $\text{UBe}_{13}$  (the cubic  $\text{NaZn}_{13}$  structure) is well known as the second heavy-electron superconductor discovered by Ott et al. in 1983 [1]. It becomes superconducting (SC) at  $T_c \sim 0.85$  K, where  $C(T)$  shows a large jump ( $\Delta C/\gamma T_c \sim 2.6$ ) followed by a non-exponential temperature dependence below  $T_c$ . Numerous experimental studies during the last three decades have revealed many anomalous SC properties which are incompatible with the BCS framework. Despite intensive efforts, however, the exact nature of the SC state, including the symmetry of order parameter, still remains unresolved. This puzzle may mainly stem from the difficulty in understanding the normal state of this system: Though many properties of  $\text{UBe}_{13}$  at high temperature resemble those of typical Kondo lattice, the low-temperature behavior shows a significant deviation from Landau's Fermi liquid theory. It is expected that the origin of this so-called "non-Fermi-liquid" (NFL) could be crucial to understand the unconventional SC of this system. Our previous studies on the diluted magnetic system  $\text{Th}_{1-x}\text{U}_x\text{Be}_{13}$  ( $x \leq 0.11$ ) revealed that the low-temperature properties in the dilute U limit is described as Fermi liquid (FL), and imply that the NFL state in the pure  $\text{UBe}_{13}$  could be attributed to a quantum criticality due to the competition between the crystalline-electric-field (CEF) singlet state versus the Kondo-Yosida singlet and/or CEF triplet states [2].

**EXPERIMENTS:** In order to see how the low-temperature state changes from FL to NFL with  $x$ , we have performed magnetic susceptibility ( $\chi$ ), specific heat ( $C$ ), and electric resistivity ( $\rho$ ) measurements on the  $\text{Th}_{1-x}\text{U}_x\text{Be}_{13}$  single crystals in the entire range of U concentration:  $0 \leq x \leq 1$  for temperatures down to 0.1 K at Hokkaido University. A part of the crystal growth for  $x \leq 0.11$  and the follow up experiments were done in MGML (<https://mgml.eu>) at Charles University, Czech Republic.

**RESULTS and DISCUSSION:** Weiss temperatures derived from fitting the high-temperature susceptibility data by Curie-Weiss law are all negative in the whole range of  $x$ , and its absolute value increases with increasing  $x$ . The  $\gamma$  value at low temperature also increases monotonically with increasing  $x$ . Interestingly, the characteristic temperature of the FL state estimated from  $\chi(T)$  and  $\rho(T)$  data decreases continuously and monotonically with increasing  $x$ , and shows a tendency to vanish at  $x^* \sim 0.8$ , above which the NFL behavior becomes significant

in  $C(T)/T$  and  $\rho(T)$  (Fig. 1). These results strongly suggest that a crossover of the low- $T$  states between FL and NFL occurs around  $x^*$ . Together with our high-pressure  $\rho(T)$  measurements for some concentrations, we suggest that the anomalous metallic state in  $\text{UBe}_{13}$  is mainly ascribed to the inter-U-site electronic correlations. We plan to make further detailed discussion by checking the U concentration  $x$  using ICP-MS at the Institute for Integrated Radiation and Nuclear Science, Kyoto University.

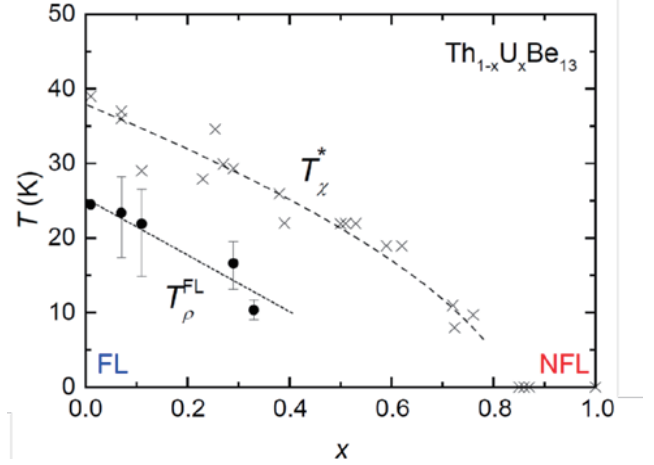


Fig. 1. The U concentration dependence of the characteristic temperatures  $T_{\chi}^*$  and  $T_{\rho}^{\text{FL}}$ , below which  $\chi$  and  $\rho$  show a tendency to behave like Fermi liquid, respectively.

### ACKNOWLEDGEMENT:

We are grateful to Dr. J. Prchal for his assistance in the low-temperature experiments. The present work was supported by JSPS KAKENHI Grant Number JP15H05882, JP15H05885 and JP15K21732 (J-Physics), and the Strategic Young Researcher Overseas Visits Program for Accelerating Brain Circulation from the Japan Society for the Promotion of Science. The Prague group was supported by the Czech Science Foundation by the Grant No. P204/15/03777S.

### REFERENCES:

- [1] H. R. Ott, H. Rudigier, Z. Fisk, and J. L. Smith, Phys. Rev. Lett., 50 (1983) 1595 .
- [2] S. Yotsuhashi, K. Miyake, and H. Kusunose, J. Phys. Soc. Jpn., 71 (2002) 389.

### PR13-3 Adsorption Characterization of Actinide Chemical Species on Solid Adsorbents - Measurement of Rare Earth Elements by ICP-MS -

T. Suzuki<sup>1</sup>, Z. Ma<sup>1</sup>, S. Fukutani<sup>2</sup> and T. Yamamura<sup>2</sup>

<sup>1</sup>Department of Nuclear System Safety Engineering,  
Nagaoka University of Technology

<sup>2</sup>Institute for Integrated Radiation and Nuclear Science,  
Kyoto University

**INTRODUCTION:** The accurate and precise analyses of actinides and many kinds of fission products in the spent fuels and/or nuclear debris are important issue for nuclear fuel management and the radioactive waste management. The separation or removal of the actinides is required before the above analyses. Especially, for the quantitative actinide analysis and the actinide isotope ratio analysis by using mass spectrometry such as ICP-MS (inductivity coupled plasma mass spectrometry) or TIMS (thermal ionization mass spectrometry), the mutual separation of actinides is highly important from the viewpoint of removal of isobaric interferences. And also, for the analyses of fission product nuclides, the removal of uranium and plutonium, which are dominant elements in the spent fuel or nuclear debris, is important. We have been studying the separation and removal of actinides by using the solid type adsorbents such as amine type resin, amino type resin. By the way, the light actinides have many valences, and the adsorption behaviors of actinides on solid adsorbents depend on their valences. We must study the adsorption behaviors of each valences of actinides on solid adsorbents. For this study, the control and confirmation of actinide valences, the adsorption experiments, and the detection and measurement methods of actinides are necessary. However, now, the preparation for application of actinides in Institute for Integrated Radiation and Nuclear Science (IRNS), Kyoto University, has not been readied enough to carried out the experiment. In consideration under such a situation, we confirmed the fundamental characteristics of ICP-MS set in hot laboratory of IRNS.

**ICP-MS EXPERIMENTS:** We use the ICP-MS (Analytik jena, Plasma Quant MS) set in a hot laboratory of IRNS. The standard solution of europium for ICP-MS (AccuStandard Inc.) was used as the sample. The lanthanides are one of the targets of our study. Some lanthanides are mono-isotope elements, and some lanthanides have many isotopes. Europium has two isotopes; <sup>151</sup>Eu and <sup>153</sup>Eu. Number of isotopes is appropriate, because of not too many. It is also desirable that the mass numbers of isotopes are alternate, that is, if the mass numbers are continuous, it is difficult to distinguish the mass of the heavier isotope ion and the mass of hydrate ion of lighter isotope. The confirmations in this year are the spectrum profile, the detection limitation, and the generation of molecular ions. The concentration of europium for the spectrum profile and the molecular ion generation was 1 ppb, and for the detection limitation was 1ppb, 10 ppt,

and 0.1 ppb, and blank. The upper limitation of sample concentration which can be feed into this ICP-MS is defined as 1 ppb. The repetition of measurements is 5.

**RESULTS:** Mass spectrum around mass number of 151 and 153 is shown in Fig. 1. The good peak curves on 151 and 153 are obtained. Although peak points are little difference from the real mass, the peaks are corrected by mass calibration.

The relationship of europium sample concentration and cps is shown in Fig. 2. We confirmed that the cps of concentration of 0.1 ppt is same level of background..

We confirmed the generation of molecular ions; hydrate ion, monoxide ion. We didn't observed the dioxide ion. The generation ratios of molecular ions and atomic ion are about 10<sup>-3</sup>. However, the cps of every detected molecular ion was so small that we should carry out further precise measurement.

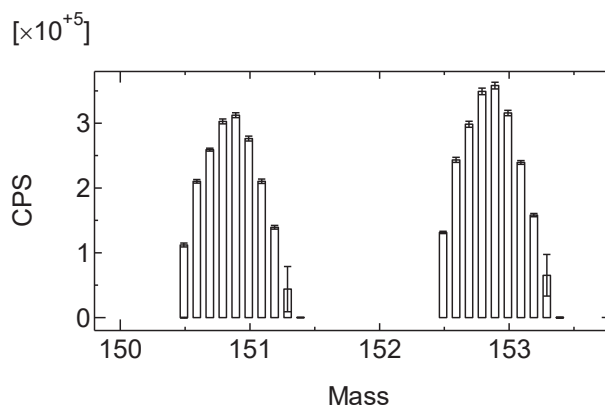


Fig. 1. Mass spectrum of europium by ICP-MS.

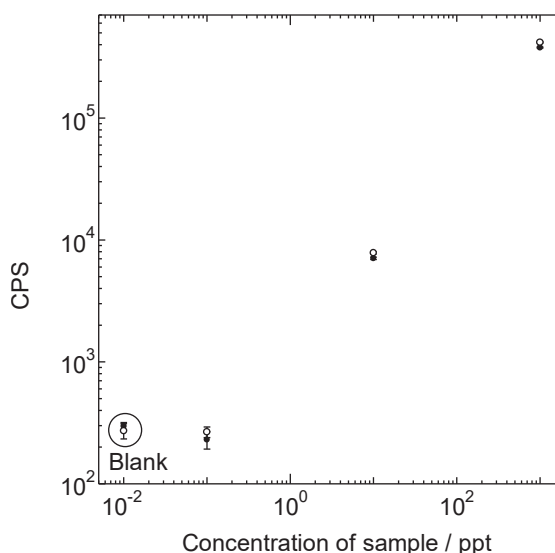


Fig. 2. Relationship of europium sample concentration and cps. Solid circles and open circles are data of <sup>151</sup>Eu and <sup>153</sup>Eu, respectively. Datum of blank sample was set on 10<sup>-2</sup> ppt.

K. Shirasaki, H. Kikunaga<sup>1</sup>, K. Washiyama<sup>2</sup>, A. Shinohara<sup>3</sup>, T. Yoshimura<sup>4</sup>, K. Nagata<sup>4</sup>, C. Tabata<sup>5</sup>, and T. Yamamura<sup>5</sup>

*Institute for Materials Research, Tohoku University*

<sup>1</sup>*Research Center for Electron Photon Science, Tohoku University*

<sup>2</sup>*Advanced Clinical Research Center, Fukushima Medical University*

<sup>3</sup>*Department of Chemistry, Graduate School of Science, Osaka University*

<sup>4</sup>*Radioisotope Research Center, Institute for Radiation Sciences, Osaka University*

<sup>5</sup>*Institute for Integrated Radiation and Nuclear Science, Kyoto University*

**INTRODUCTION:** In the past decade,  $^{225}\text{Ac}$  ( $T_{1/2} = 10$  d) which decays through a chain of four  $\alpha$ -emissions and two  $\beta$ -emissions to the stable  $^{209}\text{Bi}$ , has been receiving constant attention as a targeted alpha therapy (TAT) nuclide due to its ability to kill considerably high efficiency of tumor cell [1]. By contrast,  $\gamma$ -rays of  $^{225}\text{Ac}$  suffer from low emission ratios and are often unresolved from the  $\gamma$ -emissions associated with its daughter nuclides. Thus  $\gamma$ -ray spectrometry, which is a convenient method for identification of radionuclides, has an uncertainty about the application to  $^{225}\text{Ac}$ . This fact makes it difficult to study chemical properties of actinium complexes using a tracer amount of  $^{225}\text{Ac}$ .

In terms of emission ratios of  $\gamma$ -rays,  $^{228}\text{Ac}$  ( $T_{1/2} = 6.15$  h, daughter nuclide of  $^{228}\text{Ra}$ ) has potential value because it emits well-defined and intense  $\gamma$ -rays that are easily resolved from the daughter nuclides. Aldrich *et al.* reported the preparation method of  $^{228}\text{Ac}$  generator from natural thorium salts in 2020 [2]. Their method was composed of two parts with the bulk thorium separation by the precipitation of thorium hydroxide, and purification of  $^{228}\text{Ra}$  by the column chromatography using ion-exchange resins. In the handling of thorium hydroxide, the voluminous slurry precipitate complicates the convenient separation from the daughter nuclides.

Hence, we studied simple bulk thorium separation by cation exchange chromatography.

**EXPERIMENTS:** The separation method was based on a technique used in conjunction with  $^{223}\text{Ra}$  separation from irradiated thorium [3]. Thorium oxide was dissolved in conc.  $\text{HNO}_3$  spiked with a slight amount of conc.  $\text{HF}$  with heating ( $\sim 230^\circ\text{C}$ ) for approximately 5 min. The solution was evaporated near dryness and added mili-Q water (18.2  $\text{M}\Omega$ , repeated two times). Then, the solution was brought to dryness and reconstituted in mili-Q water with citric acid. Finally, the solution volume was adjusted by the addition of mili-Q water.

The thorium citrate solution was processed according to the following steps. The solution passed through an ion exchange column containing 2.5 mL cation exchange resin,

which was preconditioned with a 1 M (mol/L) citric acid solution. The eluate from the column was collected (fraction 1), then an additional 1 M citric acid solution was passed through for washing the column (fraction 2 and fraction 3). The column was then washed with 0.1 M  $\text{HNO}_3$  to remove residual citric acid (fraction 4) and flowed 6M  $\text{HNO}_3$  (fraction 5). These fractions were subjected to the  $\gamma$ -ray spectrometry using a high-pure Ge-detector (ORTEC). The  $^{228}\text{Ac}$  activity was determined by  $\gamma$ -emission of 911 keV. The distribution ratio ( $D_i$ ) of  $^{228}\text{Ra}$  in each fraction ( $i = 1-5$ ) was calculated by the equation:

$$D_i = A_i / (\sum_{i=1}^5 A_i) \quad (1)$$

Here,  $A_i$  is an activity obtained from  $\gamma$ -ray spectrometry of fraction  $i$ .

**RESULTS:** As shown in Fig. 1, almost all of  $^{232}\text{Th}$  daughters were found in fraction 1, which was assumed to be contained thorium as a major eluted nuclide.

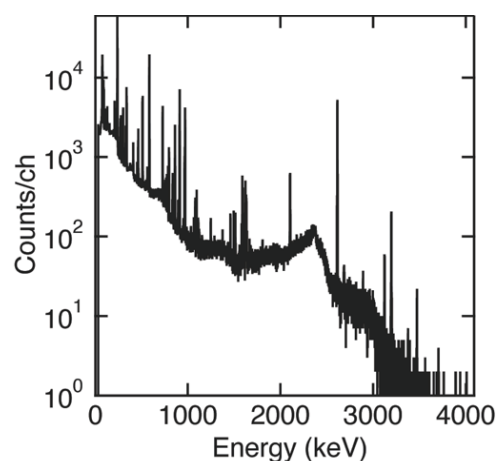


Fig. 1.  $\gamma$ -ray spectra of a sample of fraction 1.

The initial  $^{228}\text{Ra}$  atomicity ( $N_1$ ) of each fraction can be estimated by the equation:

$$N_2' = \lambda_1 / (\lambda_2 - \lambda_1) \cdot N_1 (e^{-\lambda_1 t} - e^{-\lambda_2 t}) + N_2 e^{-\lambda_2 t} \quad (2)$$

Here,  $N_2$  and  $N_2'$  are the number of  $^{228}\text{Ac}$  atom at initial and elapsed time  $t$ , respectively,  $\lambda_1$  and  $\lambda_2$  are the decay constant of  $^{228}\text{Ra}$  and  $^{228}\text{Ac}$ , respectively. The distribution ratios ( $D$ ) of  $^{228}\text{Ra}$  in the fractions 1-5 were determined by  $^{228}\text{Ac}$  activities and summarized in Table 1. This result indicates that approximately 40% of  $^{228}\text{Ra}$  is remained in bulk thorium.

Table 1.  $^{228}\text{Ra}$  distribution ratio ( $D$ ) in the separation steps.

Fraction no.	1	2	3	4	5
$D$	0.431	0.075	0.001	0.005	0.489

#### REFERENCES:

- [1] C. Kratochwil *et al.*, *J. Nucl. Med.*, **57** (2016) 1941-1944.
- [2] K. E. Aldrich *et al.*, *Inorg. Chem.*, **59** (2020) 3200-3206.
- [3] T. Mastren *et al.*, *Scientific Reports*, **7** (2017) 8216.

## PR13-5 Investigation on complex formation of monoamide compounds with actinyl ions

M. Nogami<sup>1</sup> and T. Yamamura<sup>2</sup>

<sup>1</sup>Faculty of Science and Engineering, Kindai University

<sup>2</sup>Institute for Integrated Radiation and Nuclear Science, Kyoto University

**INTRODUCTION:** Development of highly selective compounds for actinyl ions has been important. We have been focusing on monoamide compounds as promising candidates, considering the possibility of complete incineration of waste compounds (so-called “CHON principle”[1]). This year, as the first year of the project, we made a summary on various monoamides we have been investigating. In addition, some subjects which should be investigated during the next few years and environments necessary for experiments to be carried out in KUR were extracted.

**RESULTS: (1) Monoamide compounds :** We have clarified that adsorptivity of various synthetic organic resins with a monoamide structure as the functional group to uranium(VI) species in acidic nitric acid solutions greatly differs depending on the chemical structure of the functional monoamide[2,3]. There seems to be two factors for interaction between monoamides and actinyl ions; one is “chelating effect” of the ring formed by polymer monoamides and actinyl ion(s), and the other is “flexibility” of monoamide.

For chelating effect, it is well known that five- or six-membered rings are most stable for common metal complexes. While, situation seems different for our resins. For example, polymerized dimethylacrylamide (DMAA), one of resins with high adsorptivity and selectivity for U(VI) in HNO<sub>3</sub>, is expected to form eight-membered ring when it adsorbs U(VI) (UO<sub>2</sub><sup>2+</sup>), where five carbon atoms and two carbonyl oxygen atoms of two DMAA molecules, and one uranium atom are composed of the ring (Fig.1)[2]. In addition, eight would be the minimum number for the chelating ring formed by our synthetic resins. These things suggest that detailed investigations on cheating effect for resins with a larger ring than common complexes are necessary.

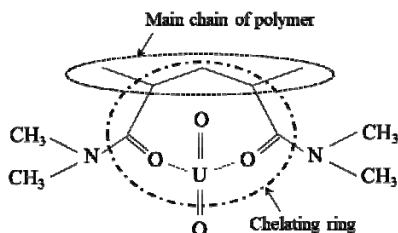


Fig. 1. Expected bond style between DMAA resin and UO<sub>2</sub><sup>2+</sup>.

Flexibility is somewhat an opposite relationship to chelating effect. Functional groups are expected to improve the ability to capture metal ions more easily with an increase in flexibility, *i.e.*, the length between the

functional group and the main polymer chain. Flexibility would be very effective in case that adsorption occurs by, *e.g.*, ion exchange, namely, the approach of plural ions with positive and negative charges, respectively. On the other hand, for monoamide resins, two monoamide carbonyl groups are in general necessary to capture one UO<sub>2</sub><sup>2+</sup> ion, as can be seen in, *e.g.*, Fig. 1. Effect of flexibility of monoamide resins might be, therefore, suppressed compared with that of ion exchange resins. Moreover, functional groups with longer chains must be disadvantageous from the viewpoint of chelating effect, because the number of atoms consisting of chelating rings becomes larger as mentioned above.

We have been accumulating adsorption data of our monoamide resins for U(VI), but we have not found any clear tendency between the chemical structure of functional monoamide and the adsorptivity. We have also take into account the fact adsorption of U(VI) by monoamide resins occurs not only at oxygen atom of monoamide but also at other sites, which was clarified by the Scatchard plot analysis[4].

**(2) Future studies for monoamide compounds :** The above things were examples on resins. Current status for the development of our monoamide resins was introduced at the symposium held at KUR on Feb. 7, 2020, and fruitful discussions were made.

We have also been developing monoamide extractants and precipitants as well as resins. Based on the above knowledge, we will carry out the following studies at KUR.

Experimental areas treating actinide species are under preparation. Determination of concentration of actinide species is essential for our study, and an ICP-MS instrument has been introduced. We would like to establish the determination condition for ICP-MS with our colleagues.

Theoretical approach would also be necessary for understanding the interaction between monoamide compounds and actinyl ions. We would like to make frequent discussions with our colleagues in this regard.

### REFERENCES:

- [1] M. G. B. Drew *et al.*, Dalton Trans. (2007) 244-251.
- [2] M. Nogami *et al.*, J. Radioanal. Nucl. Chem., **273** (2007) 37-41.
- [3] M. Nogami *et al.*, Prog. Nucl. Energy, **50** (2008) 462-465.
- [4] M. Nogami *et al.*, J. Radioanal. Nucl. Chem., **273** (2010) 541-546.

## PR13-6 Consistency verification between relativistic quantum chemical calculations and experiments in uranium compounds

M. Abe<sup>1</sup>, M. Hada<sup>1</sup>, A. Sunaga<sup>1</sup>, A. Sato<sup>1</sup>, T. Yamamura<sup>2</sup>,  
C. Tabata<sup>2</sup>

<sup>1</sup>Department of Chemistry, Tokyo Metropolitan University  
<sup>2</sup>Institute for Integrated Radiation and Nuclear Science,  
Kyoto University

**INTRODUCTION:** Theoretical calculations of actinide compounds are very important to understand or predict new phenomenon in these compounds. We have developed computational methods based on the relativistic quantum chemistry and applied it to uranium (U) isotope fractionation, which is widely discussed in geochemistry [1]. In the present work, we evaluated equilibrium isotope fractionation coefficients ( $\epsilon$ ) for 54 U species in U(VI), U(V), and U(IV) states with various ligands (e.g., H<sub>2</sub>O, CO<sub>3</sub><sup>2-</sup>, CH<sub>3</sub>COO<sup>-</sup>, Cl<sup>-</sup>, NO<sub>3</sub><sup>-</sup>, etc.) using accurate relativistic quantum chemical methods to verify the accuracy of the computational results and predict  $\epsilon$  for new species.

**METHODS:** We calculated  $\epsilon$  between <sup>235</sup>U and <sup>238</sup>U as the sum of the nuclear volume term ( $\ln K_{nv}$ ) and the nuclear mass term ( $\ln K_{nm}$ ) [2-4].  $\ln K_{nv}$  is due to the electronic energy difference caused by the different size and shape of nucleus of isotopes [2,3], while  $\ln K_{nm}$  is due to the vibrational level caused by the different reduced mass of isotopologues [4]. In the heavy element system,  $\ln K_{nv}$  is dominant in  $\epsilon$ . Because  $\ln K_{nv}$  is highly affected by relativity, we used the exact two-component (X2C) relativistic method with the Gaussian finite nucleus model, implemented in the DIRAC16 program.

**RESULTS:** As a calibration, we calculated  $\epsilon$  for U(IV)-U(VI) in chlorides and obtained as 1.72‰, which agrees well with the experimentally reported  $\epsilon$  (1.64‰) [5]. As shown in Fig. 1,  $\epsilon$  strongly depends on the uranium valence state, and its general order is U(VI) > U(V) > U(IV). Also, we can confirm that the magnitude of  $\ln K_{nv}$  is much larger than  $\ln K_{nm}$  from Fig.1. This is consistent with the fact that  $\ln K_{nv}$  is the dominant term in U isotope fractionation. To explain the strong dependence of  $\epsilon$  on U valence, we depicted the radial distribution function of 6s orbital of U<sup>6+</sup>, U<sup>5+</sup>, and U<sup>4+</sup> atomic ions (Fig. 2) because this orbital significantly affects the magnitude of  $\ln K_{nv}$ . The order of spread of 6s orbital is U<sup>6+</sup> < U<sup>5+</sup> < U<sup>4+</sup>, indicating that 6s orbital is more spread as more 5f electrons are added. This causes the decrease in electron density at the nucleus, leading to the large  $\ln K_{nv}$  [3], and consequently,  $\epsilon$  shows large value. Besides, the largest difference in  $\epsilon$  between U(VI) and U(IV) is about 3‰, which indicates that the U speciation significantly affects isotope fractionation. The present theoretical data set of  $\epsilon$  including various specification would be very helpful for the accurate discussions of U isotope fractionation in geochemistry.

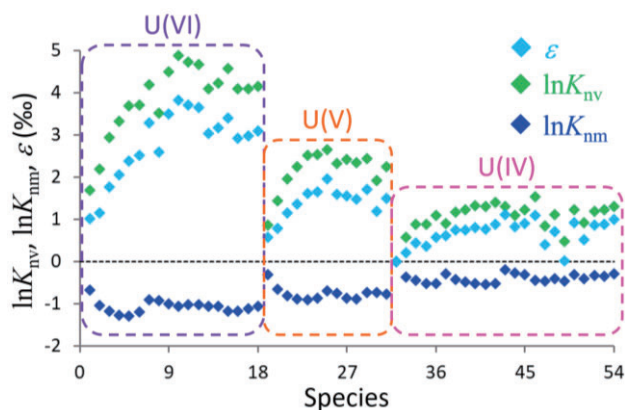


Fig. 1.  $\ln K_{nv}$ ,  $\ln K_{nm}$ , and  $\epsilon$  of 54 U species. The light blue, green, and deep blue plots represent  $\epsilon$ ,  $\ln K_{nv}$ , and  $\ln K_{nm}$ , respectively. These plots for U(VI), U(V), and U(IV) species are surrounded by the purple, orange, and pink rounded squares, respectively. [6]

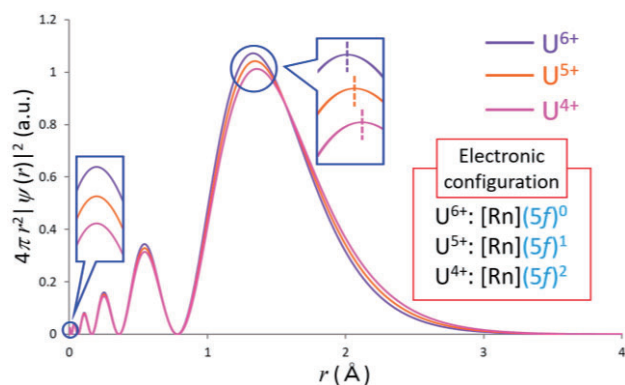


Fig. 2. Radial distribution function of 6s orbitals in U<sup>6+</sup>, U<sup>5+</sup>, and U<sup>4+</sup> atomic ions. Purple, orange, and pink lines represent the functions of U<sup>6+</sup>, U<sup>5+</sup>, and U<sup>4+</sup>, respectively. Electronic configuration of these ions are shown in the red box. [6]

### REFERENCES:

- [1] C. H. Stirling *et al.*, *Geochim. Cosmochim. Acta*, **163** (2015) 200-218.
- [2] M. Nomura *et al.*, *J. Am. Chem. Soc.*, **118** (1996) 9127-9130.
- [3] J. Bigeleisen, *J. Am. Chem. Soc.*, **118** (1996) 3676-3680.
- [4] J. Bigeleisen and M. G. Mayer, *J. Chem. Phys.*, **15** (1947) 261-267.
- [5] Wang *et al.* *Geochim. Cosmochim. Acta*, **158**, 262 (2015)
- [6] A. Sato, R. Bernier-Latmani, M. Hada, and M. Abe, to be submitted.

H. Shishido, H. Hashizume, C. Tabata<sup>1</sup> and T. Yamamura<sup>1</sup>

Graduate School of Engineering, Tohoku University

<sup>1</sup>Institute for Integrated Radiation and Nuclear Science, Kyoto University

**INTRODUCTION:** Partitioning and transmuting is presently regarded as an effective method to address the issue of high-level radioactive waste disposal. The most efficient way to transmute minor actinide (MA) nuclides is to cause fission reactions with neutrons, and such studies have been reported since almost the beginning of the use of nuclear energy [1]. Neutrons generated by fusion reactors are most preferred for transmutation because of their high energy and monochromaticity. We have proposed to transmute MA rather moderately, namely with a low fission reaction rate to avoid imposing severe engineering challenges on the system design [2].

In this concept, MA mixed oxides (e.g., Am-Cm-O) are loaded into limited space in fusion reactors, where sufficient neutron flux can be secured with relatively lower heat flux. Whereas some studies have reported the phase diagram of U or Pu based MA oxides, no reports have provided the diagrams of the MA-only mixed oxides. It is vital to reveal the properties and construct a database for realization of the transmutation system.

The objective of this study is to evaluate the phase diagram of the MA-only mixed oxides. Measurement of the phase diagrams is not a straightforward task because the toxicity, radioactivity, scarcity and the short lifetime of many actinides impede experimental studies. Thus, we aim to develop a method to evaluate the phase diagrams. In the first year, we discussed the research direction and important issues to be solved each other. We also examined the phase diagrams of MA from earlier studies.

**DISCUSSION:** We had a meeting at Research Reactor Institute in Kyoto University and the concept of this research and important issues have been confirmed each other. The most focused point was the idea of MA transmutation to Plutonium even number nuclides in the research concept. We have proposed a rather moderately transmuting MA in a fusion reactor to reduce the heat generation from fission reactions [2], which results in the production of many Pu-238 nuclides. However, one important issue—the decay heat from Pu-238—was indicated in the meeting. The nuclide Pu-238 has large decay heat and is utilized as a heat source in radioisotope thermoelectric generators. We have concerned a possibility to handle the large quantity of the targets having large and continuously decay heat in a huge fusion reactor system. The research direction is still under debate and we proceed with the research from a general point of view to solve the crucial issue.

**RESEARCH REVIEW:** The term CALPHAD (CALCulation of PHase Diagram) means calculating phase diagrams from thermodynamic models with parameters

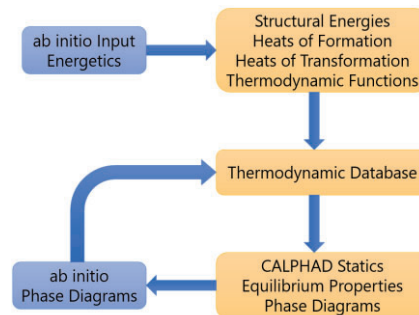


Fig. 1. Schematic flow chart for the numerical simulation of the statics of phase transformation [6].

adjusted to available measured data. Few researches have evaluated the phase diagrams and thermodynamic models of the MA mixed oxides (U-Pu-Np-O, Pu-Am-O) [3-5]. These studies were based on very limited experimental values to derive the thermodynamic models. Unfortunately, there are no thermodynamic data of the MA-only mixed oxides; thus, ab initio calculation needs to be performed to provide inputs for CALPHAD.

Figure 1 schematically depicts the situation of ab initio with respect to CALPHAD [6]. The ab initio calculation can provide energetics and phase diagram information. The energetics (structural energies, heats formation) of existing or hypothetical compounds can be easily evaluated and directly input in a CALPHAD database. The ab initio outputs can be also converted to a Redlich-Kister format and combined with the thermodynamics database in use with CALPHAD. This procedure has been successfully applied to some cases of binary metal alloys [7]. We consider that the phase diagrams of the MA-only mixed oxides can be predicted with a certain accuracy based on the examination above.

**FUTURE TASKS:** We move forward with the ab initio calculations to evaluate the energetics of the MA oxides. It is important, as well known, that the values provided by ab initio calculations must be assessed critically because the values depend on the methods and approximations used and they scatter similarly to how experimental values do. Because we do not have expert knowledge that guarantees the best results for the issues, prudent and critical study is under way.

#### REFERENCES:

- [1] S. L. Beaman *et al.*, NR-CONF-001, United States Nuclear Regulatory Commission, (1976).
- [2] Y. Furudate *et al.*, Prog. Nucl. Energ. **103** (2018) 28-32.
- [3] C. Guéneau *et al.*, in *Comprehensive Nuclear Materials*, edited by R. J. M. Konings (Elsevier, 2012), Vol. 2.
- [4] M. Hirota *et al.*, J. Nucl. Mater. **344** (2005) 84-88.
- [5] P. Gotcu-Freis *et al.*, J. Nucl. Mater. **414** (2011) 408-421.
- [6] P. E. A. Turchi *et al.*, CALPHAD **31** (2007) 4-27.
- [7] L. Kaufman *et al.*, CALPHAD **25** (2001) 419-433.

## PR13-8 Synthesis of nobel phthaloyanine derivatives and effect of substituent on recognition of light actinide and chemical property

M. Nakase<sup>1</sup>, M. Harigai<sup>1</sup>, C. Tabata<sup>2</sup>, T. Yamamura<sup>2</sup>

<sup>1</sup>Laboratory for Advanced Nuclear Energy, Tokyo Institute of Technology

<sup>2</sup>Institute for Integrated Radiation and Nuclear Science, Kyoto University

**INTRODUCTION:** In Th fuel cycle, effective separation of U from Th and other fission products in spent Th fuels is needed. To enable that, an extraction method similar to plutonium–uranium redox extraction (PUREX) has been studied, namely, thorium–uranium extraction (THOREX)[1]. In the THOREX process,  $\text{UO}_2^{2+}$  is extracted by tri-*n*-butyl phosphate (TBP) with the aid of  $\text{Al}(\text{NO}_3)_3$ . Some of the other ligands such as monoamide is recently reported for U/Th separation [2]. In both the cases, extractability of  $\text{UO}_2^{2+}$  is high, but that of  $\text{Th}^{4+}$  is also high, leading to low selectivity of  $\text{UO}_2^{2+}$  over  $\text{Th}^{4+}$ . Therefore, study on highly selective ligands to specific light actinide is needed. In this study, Phthalocyanine (Pc) was selected as the main structure of the ligand. Pc is known as forming stable complex with U and there are many reports on mechanism and characterization study. However, the Pc has low solubility in organic solvent which limit the utilization in solvent extraction. Therefore, the Pc derivatives with substituent modification was planned and metal free Pc and Pc-Zn complex were synthesized in fiscal year of 2019. Zinc was selected because of the relatively weak interaction of Zn and N of Pc. One of the most famous complexes of Pc is Pc-Cu complex but the covalent bond of Cu and N of Pc is too strong to exchange to other metal ions. Also, N is easily protonated under acidic condition, hence the O-derivatized Pc will also be synthesized. During this study, applicability of Pc derivatives to solvent extraction will be surveyed.

**EXPERIMENTS AND RESULTS:** Synthesis of Pc was done at Tokyo Tech and test-run of hydrothermal synthesis of U-complex was done at Koyo University. To synthesize the Pc, literature survey was firstly done and some preliminary experiments were conducted. The simple metal free Pc and Pc-Zinc complex were synthesized as following schemes in (1) and (2) of Figure 1. In both the schemes, the starting building block of phthalonitrile can be replaced into derivatized one and the combination of different building blocks can make the synthesis of other Pc derivatives easily possible. Also, Zn in the Pc-Zn complex can be easily replaced into other metals. For purification of metal free Pc and Pc-Zn, Soxhlet extractor and thin layer chromatography (TLC) were used respectively. The color of metal free Pc and Pc-Zn were white and dark blue, respectively as shown in Figure 2. By <sup>1</sup>H-NMR measurement, successful synthesis of the desired products was confirmed. The purities of both products were not high enough for characterization study, hence, further purification methods such as distillation

will be tested and the synthetic scale will also be enlarged.

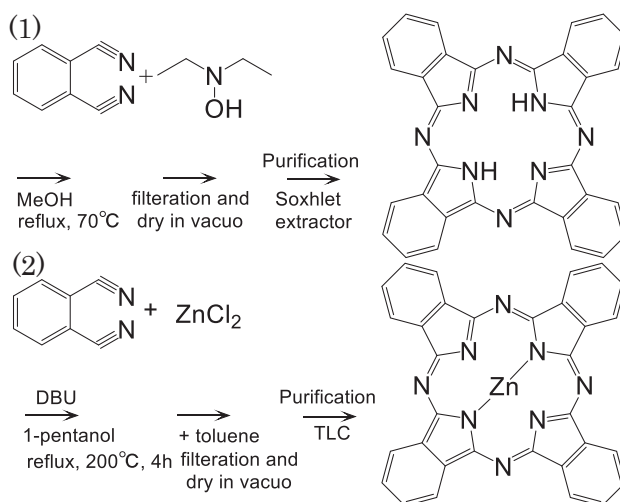


Figure 1 Synthetic scheme of (1) metal free Pc and (2)Pc-Zn

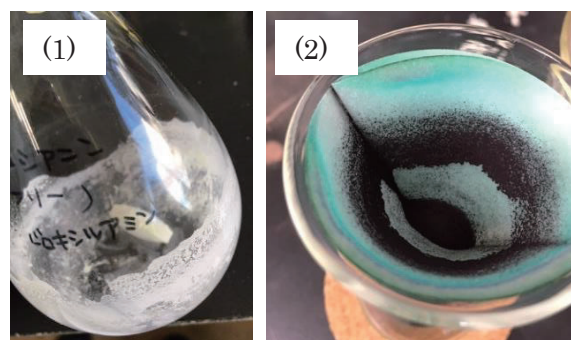


Figure 2 Pictures of synthesized chemicals, (1) metal free Pc and (2)Pc-Zn

**FUTURE PLAN:** From next fiscal year, the following experiments are planned;

- 1.Synthesis of Pc derivatives with long alkyl chain to increase solubility in organic phase.
- 2.Survey of the synthetic scheme of Pc derivatives-U complexes.
- 3.Survey of the synthetic scheme of Pc derivatives to make the Pc *N,O*-hybrid donor ligand
4. Trial of single crystal synthesis of Pc derivatives and some metals and their characterization

**CONCLUSIONS:** The synthetic schemes of metal free Pc and Pc-Zn complex were established and the further synthetic strategy was made clear. The characterization study will also be started from next fiscal year.

### REFERENCES:

- [1] R.H.Rainey and J.G.Moore, *Nucl Sci Eng*, 10(4), 367–371, 1961.
- [2] P.N.Pathak, *Solv Ext Ion Exch*, 20(3), 293–311, 2002.

## **I-2. COLLABORATION RESEARCHES**

- 1. Slow Neutron Physics and Neutron Scattering**
- 2. Nuclear Physics and Nuclear Data**
- 3. Reactor Physics and Reactor Engineering**
- 4. Material Science and Radiation Effects**
- 5. Geochemistry and Environmental Science**
- 6. Life Science and Medical Science**
- 7. Neutron Capture Therapy**
- 8. Neutron Radiography and Radiation Application**
- 9. TRU and Nuclear Chemistry**
- 10. Health Physics and Waste Management**
- 12. Others**

## CO1-1 First Neutron Diffraction Results of Fluoride-ion Battery Materials on VCND

K. Mori<sup>1</sup> and F. Fujisaki<sup>2</sup>

<sup>1</sup>Institute for Integrated Radiation and Nuclear Science, Kyoto University (KURNS)

<sup>2</sup>Office of Society-Academia Collaboration for Innovation, Kyoto University

**INTRODUCTION:** The all-solid-state rechargeable battery is a key technology for large-scale applications such as electric vehicles, plug-in hybrid vehicles, and electrical energy-storage systems in future smart grids. The use of solid electrolytes is critical for improving the battery performance parameters: energy density, power capacity, lifespan, and reliability. In the last decade, fluoride-ion batteries (FIBs) have attracted much attention as alternative candidates for lithium-ion batteries, nickel-metal hydride batteries, sodium-ion batteries, and so on. However, no standard choice for FIB materials has been established. For the realization of all-solid-state FIBs, it is very important to explore new fluoride-based solid electrodes and electrolytes. In this work, we performed structural studies for fluoride-ion battery materials such as Cu nanoparticle with BaF<sub>2</sub> (hereafter referred to as nano-Cu + BaF<sub>2</sub>), AlF<sub>3</sub> nanoparticle (hereafter referred to as nano-nano-AlF<sub>3</sub>), AlF<sub>3</sub> nanoparticle with Li (hereafter referred to as nano-AlF<sub>3</sub> + Li), using the VCND on the B-3 beam port of KUR.

**EXPERIMENTS:** Powder samples of the “nano-Cu + BaF<sub>2</sub>”, the “nano-AlF<sub>3</sub>”, and the “nano-AlF<sub>3</sub> + Li” were put into a cylindrical vanadium-nickel-alloy holder (diameter: 6 mm, thickness: 0.1 mm) under a high-purity argon atmosphere. ND experiments were performed using the VCND, as shown in Fig. 1. The neutron wavelength,  $\lambda$ , which is monochromatized by the (220) plane of a Cu single crystal (i.e., Cu monochromator), is 1.0 Å. Their ND data were collected in the  $2\theta$  range of 10–115° at room temperature. In addition, their X-ray diffraction (XRD) data were recorded on an X-ray diffractometer with CuK $\alpha$  radiation ( $\lambda = 1.54$  Å; SmartLab, Rigaku Co.) at room temperature.

**RESULTS:** The ND data of the “nano-Cu + BaF<sub>2</sub>”, the “nano-AlF<sub>3</sub>”, and the “nano-AlF<sub>3</sub> + Li” were shown in Fig. 2(a). Obviously, Bragg reflections were clearly observed in the higher  $2\theta$  range of ND data, compared with XRD data (see Fig. 2(b)). It is most likely that the ND data enable us to offer the precise atomic positions and thermal factors of F<sup>-</sup> ions, since the scattering amplitude (or coherent scattering length) of F is as large as those of other elements. Further analysis (e.g. Rietveld analysis) is now in progress to determine their structures.

The authors acknowledge Mr. Tanaka of Kyoto University for his help with the sample preparation.

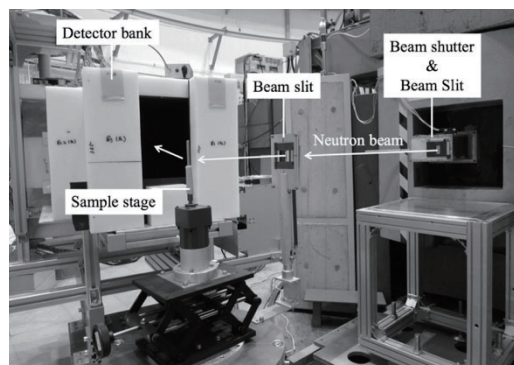
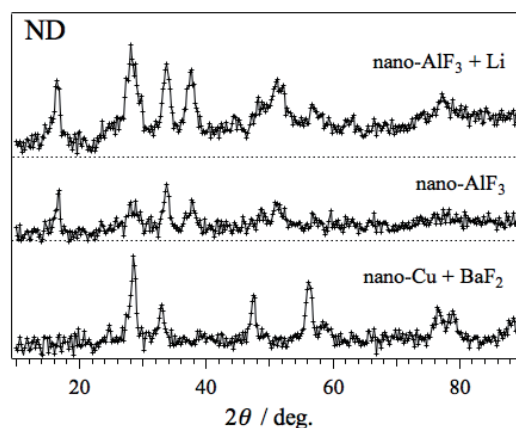


Fig. 1. Versatile compact neutron diffractometer (VCND) installed at the B-3 beam port of Kyoto University Research Reactor (KUR).

(a)



(b)

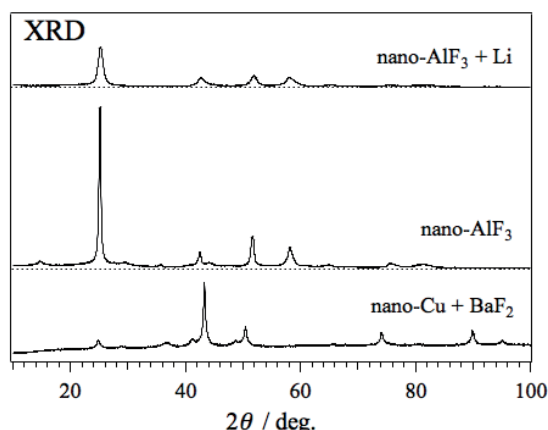


Fig. 2. (a) Neutron diffraction data of Cu nanoparticle with BaF<sub>2</sub> (nano-Cu + BaF<sub>2</sub>), AlF<sub>3</sub> nanoparticle (nano-AlF<sub>3</sub>), AlF<sub>3</sub> nanoparticle with Li (nano-AlF<sub>3</sub> + Li) collected at the VCND. (b) X-ray diffraction data of the “nano-Cu + BaF<sub>2</sub>”, the “nano-AlF<sub>3</sub>”, and the “nano-AlF<sub>3</sub> + Li” collected at the X-ray diffractometer with CuK $\alpha$  radiation.

K. Mori, R. Okumura, H. Yoshino, M. Kanayama, S. Sato<sup>1</sup>,  
K. Iwase<sup>2</sup>, Y. Oba<sup>3</sup>, H. Hiraka<sup>4</sup>, F. Fujisaki<sup>5</sup>, F. Kobayashi<sup>6</sup>,  
and T. Emoto<sup>6</sup>

*Institute for Integrated Radiation and Nuclear Science,  
Kyoto University (KURNS)*

<sup>1</sup>*High Energy Accelerator Research Organization (KEK)*

<sup>2</sup>*Department of Materials and Engineering, Ibaraki Uni-  
versity*

<sup>3</sup>*Materials Sciences Research Center, Japan Atomic En-  
ergy Agency (JAEA)*

<sup>4</sup>*Neutron Science Center, Korea Atomic Energy Research  
Institute*

<sup>5</sup>*Office of Society-Academia Collaboration for Innovation,  
Kyoto University*

<sup>6</sup>*Graduate School of Engineering, Kyoto University*

**INTRODUCTION:** Neutron diffraction is a powerful tool to precisely determine the positions of light elements (e.g., hydrogen and lithium) in solids. This is the main reason why neutron powder diffractometers are critical for structural investigations of energy storage materials, for example, rechargeable lithium-ion batteries and hydrogen absorbing alloys. The B-3 beam port of Kyoto University Research Reactor (KUR) had long been used as a four-circle single-crystal neutron diffractometer (4CND). For the last decade, however, the 4CND was so old that its research activity on neutron science was quite low. Now, the versatile compact neutron diffractometer (VCND) is installed on the B-3 beam port of KUR.

**SPECIFICATIONS:** Figure 1 shows the current state of the VCND. The neutron wavelength,  $\lambda$ , which is monochromatized by the (220) plane of a Cu single crystal (i.e., Cu monochromator), is 1.0 Å. To cover the detector area of  $6^\circ \leq 2\theta \leq 130^\circ$ , twenty-five <sup>3</sup>He tube detectors (1/2 inch in diameter) are used, where  $2\theta$  is the scattering angle. A detector bank including twenty-five <sup>3</sup>He tube detectors is placed on the arm of the HUBER-440 goniometer. The distance from the Cu monochromator to the sample is approximately 2 m, and the distance from the sample to the detector is 1.2 m.

**CRYSTAL STRUCTURE ANALYSIS:** Strontium fluoride (SrF<sub>2</sub>) is a key material for the solid electrolytes of all-solid-state fluoride-ion batteries. The crystal structure of SrF<sub>2</sub> is well-known as the fluorite-type structure, comprising a metal site and a fluorine site: Sr(0, 0, 0) in the 4a site and F(1/4, 1/4, 1/4) in the 8c site (Wyckoff notation in space group  $Fm\bar{3}m$ ). To assess the ability of the VCND, we performed the ND experiment using SrF<sub>2</sub> powder. Figure 2 shows the ND data of SrF<sub>2</sub> at room temperature. In the figure, a good fit was obtained between the observed and calculated intensities. The lattice constant,  $a$ , was estimated to be 5.85(15) Å.

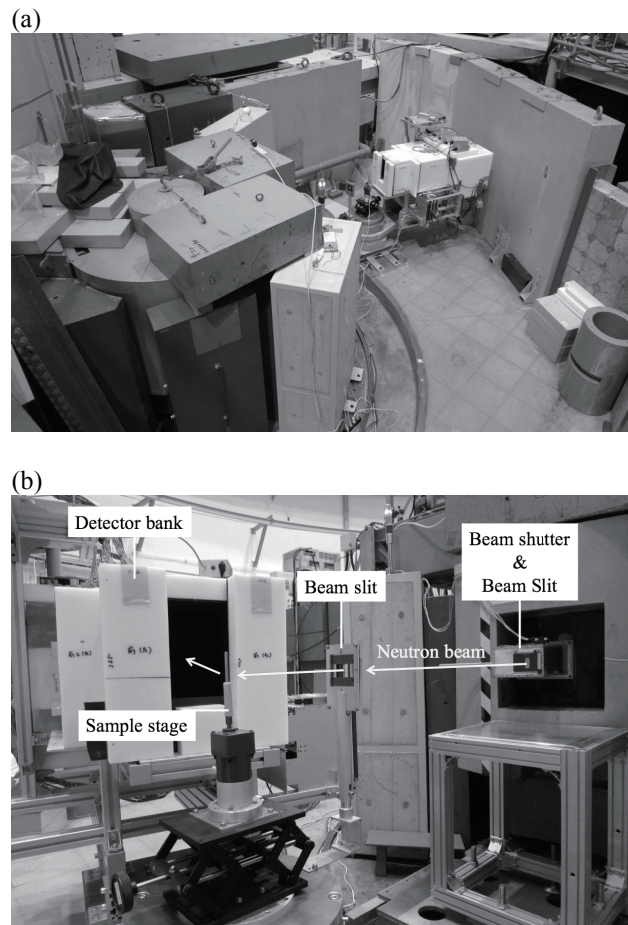


Fig. 1. Versatile compact neutron diffractometer (VCND) installed at the B-3 beam port of Kyoto University Research Reactor (KUR): (a) bird's-eye-view photograph and (b) partial view (around the sample stage) of the VCND.

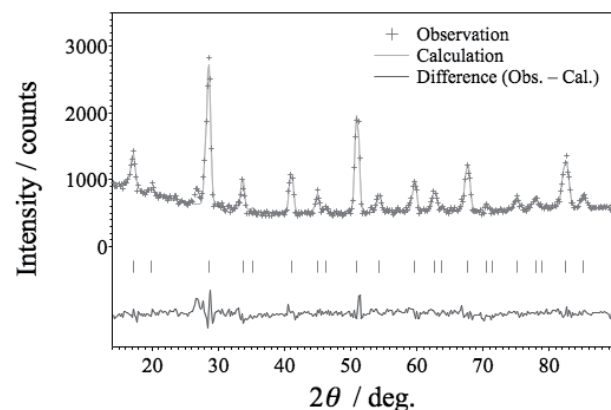


Fig. 2. The crystal structure refinement of SrF<sub>2</sub> using neutron diffraction data collected at the VCND.

K. Kaneko, R. Motokawa, Y. Oba, K. Mori<sup>1</sup> and R. Okumura<sup>1</sup>

Materials Sciences Research Center, Japan Atomic Energy Agency  
<sup>1</sup>Institute for Integrated Radiation and Nuclear Science, Kyoto University

## INTRODUCTION:

The vitrification technique with borosilicate glass is used to immobilize high-level radioactive liquid wastes, which is produced during the reprocessing of nuclear fuels[1]. The high-level wastes is mixed with the borosilicate glass and melted, that results in forming an oxide. In order to have a long-term stability, details of this vitrification process are important. Among the constituents, molybdate tends to precipitate that lowers durability[2]. The segregation of platinoids also cause issues on fabrication[3].

In order to fabricate stable vitrified radioactive waste, microscopic insights into the structure are required. Neutron diffraction is suitable to structure of the glass as it can access to high- $Q$  range. In addition, thanks to its high transmission, the vitrified waste can be investigated without crashing into a powder form. The latter could be essential to obtain an actual form of the waste.

Since the research reactor JRR-3 has not been in operation for roughly 10 years, the B-3 diffractometer offers an unique opportunity to perform neutron diffraction with the monochromatic beam. As a first step, we performed neutron diffraction experiments to check feasibility to study the vitrified nuclear waste using the simulated waste.

## EXPERIMENTS:

The borosilicate glass samples with and without simulated radioactive wastes were prepared to have cylindrical form with several diameters ranging from 6 mm to 20 mm. In order to reduce neutron absorption of boron, one of the main constituent of the glass, enriched <sup>11</sup>B was used.

Neutron diffraction experiments were performed on the versatile compact diffractometer installed at the B-3 beam port. Neutrons with a wavelength of 1Å are provided by a Cu monochromator. An array of the <sup>3</sup>He detectors which covers 25° in the scattering angle allows efficient measurements. The sample was mounted on the continuous rotation stage which increases homogeneity.

## RESULTS:

Figure 1 shows a representative neutron diffraction pattern of the borosilicate glass for vitrification without the simulated radioactive waste measured on the B-3. The inset of the figure displays the neutron transmission image for the same sample taken by the CCD camera. This

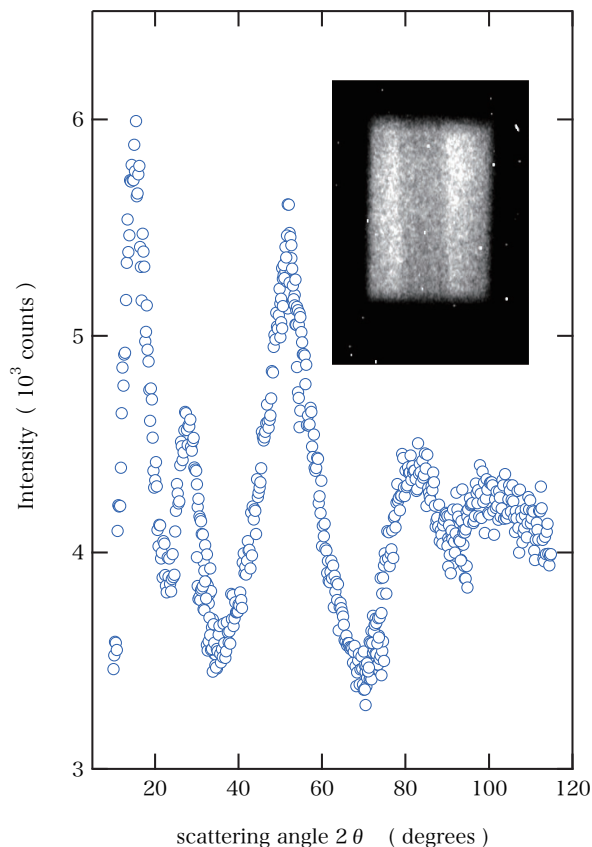


Fig. 1. Neutron diffraction pattern of the borosilicate glass for vitrification without simulated radioactive waste recorded on the B-3 diffractometer. The inset shows a neutron transmission image for the same sample.

image proves that a sufficient transmission was obtained owing to the <sup>11</sup>B enrichment. The suppression of the neutron absorption leads to obtain a clear neutron diffraction pattern shown in the figure, which was taken for a few hours at 5MW. In addition to first sharp diffraction peak around 15°, the higher-order peaks were clearly observed around 27°, 52° and 83° as well. This high quality data with the high S/N ratio should be sufficient for quantitative analysis and is in progress.

The present result demonstrates that the B-3 diffractometer is suitable for the study on the vitrified radioactive waste. We plan to extend our study on the simulated radioactive waste with different compositions and fabrication conditions in order to reveal its impact on the structure in a microscopic scale.

## REFERENCES:

- [1] G. Roth, S. Weisenburger, Nucl. Eng. Des. **202**, 197e207 (2000).
- [2] S. Morgan *et al.*, Mater. Res. Soc. Symp. Proc. **807**, 151e156 (2003).
- [3] H. Mitamura *et al.*, Nucl. Chem. Waste Manag. **4**, 245e251 (1983).

M. Kitaguchi, H. Okabe<sup>1</sup>, K. Morikawa<sup>1</sup>, T. Oda<sup>2</sup>  
and M. Hino<sup>2</sup>

KMI, Nagoya University

<sup>1</sup>Department of Physics, Nagoya University

<sup>2</sup>Institute for Integrated Radiation and Nuclear Science,  
Kyoto University

**INTRODUCTION:** The recent values of neutron lifetime deviate far beyond the systematic errors claimed in the past and require the further improvement for the neutron lifetime puzzle. We are continuing neutron lifetime measurement at the polarized beam branch of the NOP beamline installed at the port BL05 in J-PARC. The system consists of a neutron chopper (SFC) and a gas chamber (TPC) for detecting the electrons from the neutron beta decays. The TPC contains small amount of <sup>3</sup>He. The rate of the <sup>3</sup>He(n,p)<sup>3</sup>H reaction is measured by counting the protons. The neutron lifetime is measured as the ratio of the electron events to the proton events [1].

The large background via neutron-induced reactions is suppressed by introducing small neutron bunches into the TPC and selectively detecting decay electrons and reaction protons only when neutron bunches are traveling inside the sensitive volume and they were not transmitting through chamber windows and other materials on the beam path. The SFC is a spin-selective optics to switch the neutron beam using the combination of magnetic supermirrors and spin flippers[2]. Polarized neutrons are injected into the SFC. Controlling the timing of spin-flip makes neutron bunches at the exit of the SFC, which can be reflected by the magnetic mirrors successively. By employing the triple series reflection, the present version of the SFC chops the neutron beam with the intensity contrast of about 400. During the lifetime measurement, the bunch length is adjusted as about 50 cm, which is half of the length of TPC sensitive region for maximizing the signal statistics. The cross section of the output bunches is 2 cm × 2 cm. In order to reduce the statistical uncertainties for the lifetime measurement to the order of 1 s, the incident neutron flux into the TPC must be increased. Although the new mirrors have been already assembled to accept large cross section of the neutron beam, large scale of spin flippers are also required. New mirrors and flippers with the beam acceptance of 4 cm × 4 cm can transfer neutrons with the intensity of 9 times larger than that before upgrade.

We have developed the precision simulation of neutron spin behavior to design the flipper. Composed magnetic field of the static field and the radio frequency field for the resonance spin-flip affects the spin-flip probability. To avoid the effect, the asymmetrical shape of the flipper coil was designed (Figure 1).

**EXPERIMENTS:** The experiments were performed at cold neutron beamline CN3 in KUR. Figure 2 shows the experimental setup. Disk chopper provided pulsed neutrons. Magnetic supermirrors were used for neutron polarizer and analyzer. The position and time-of-flight from the chopper to the detector were measured. The behavior of the spin of each neutron was investigated by scanning the position and magnetic field of the flipper coil.

**RESULTS:** The dependence of spin flipping probability for neutron beam position was clearly observed. It was consistent with the simulation. The probability achieved 0.95 for the required area of the acceptance (Figure 3). This type of the flipper is suitable for the new SFC. It will be installed into NOP beamline.

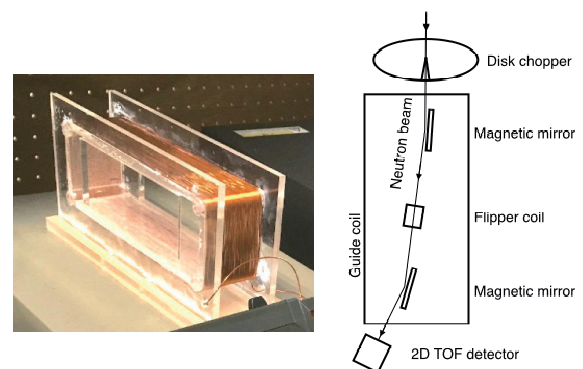


Fig. 1. New flipper coil with large acceptance.

Fig. 2. Experimental setup with polarized neutron beam at CN3 beamline.

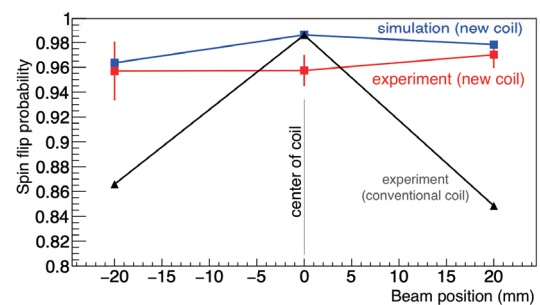


Fig. 3. Position dependence of spin flip probability.

#### REFERENCES:

- [1] K.Mishima *et al.*, Nucl. Instrum. Methods A600 (2009) 342.
- [2] K. Taketani *et al.*, Nucl. Instr. and Meth. A634 (2011) S134–S137.

## CO1-5 Development of $m=6.5$ neutron supermirror on ellipsoidal metal substrate

M. Hino<sup>1</sup>, T.Hosobata<sup>2</sup>, T.Oda<sup>1</sup>, Y.Yamagata<sup>2</sup>, H.Endo<sup>3</sup>, N.L.Yamada<sup>3</sup>, F. Funama<sup>4</sup>, H.Yoshinaga<sup>1</sup>, Y. Kawabata<sup>1</sup>

<sup>1</sup>Institute for Integrated Radiation and Nuclear Science, Kyoto University (KURNS), Japan

<sup>2</sup>RAP, RIKEN, Japan

<sup>3</sup>IMSS, KEK, Japan

<sup>4</sup>Dept., Nucl. Eng., Kyoto University, Japan

**INTRODUCTION:** Progress of neutron optical devices is very significant. We have established fabrication method for aspherical focusing supermirror with metal substrate [1-3]. The metallic substrate is robust and ductile, to which able to fabricate steeply curved surface with high form accuracy. It is also applicable to use under high radiation irradiation and high-temperature field, even at a place close to the neutron target and moderator. Furthermore, it is possible to fabricate a large focusing mirror by combining multiple segmented mirrors with mechanical fastening entailing the usage of screw holes and fixture tabs. We have solved the problem of required surface roughness for neutron mirror. The roughness should be smaller than 0.3 nm for high- $m$  supermirror coating. Here  $m$  is the maximum critical angle of the mirror in units of critical angle of natural nickel. By using electroless nickel-phosphorus (Ni-P) plating, we overcame the problem and are establishing fabrication process for aspherical focusing supermirror. There is still a problem of peeling off for high- $m$  supermirror coating on metal substrate with steep curvature. In this study, we reported an improvement of higher- $m$  NiC/Ti(SiC) ellipsoidal supermirror. Here the (SiC) means thin interlayers in which thickness are less than 1 nm. The NiC layers were sandwiched by the SiC thin inter-layers in to reduce compressive stress of layer and to improve interface roughness possibly.

**EXPERIMENTS:** We fabricated ellipsoidal metallic substrates with the Ni-P plating, based on the technology using ultrahigh precision cutting with correction processing, followed by mechanical precision polishing. The first precise manufacturing was conducted at a CNC machine for development of neutron optical devices at workshop of the KURNS. The ultra-precise manufacturing, polishing and cleaning of the metallic substrate were conducted at RIKEN. The supermirror coating was conducted with ion beam sputtering machine at the KURNS (KUR-IBS) [4]. The neutron experiments were conducted at CN-3 beam line at the KURNS and the BL16 (SOFIA) beam port at J-PARC MLF. We have succeeded in fabricating a couple of NiC/Ti ellipsoidal supermirrors in which length of 900mm. The semi-major and semi-minor axes of the ellipsoidal supermirror were 1250 mm and 65.4 mm, respectively. The acceptable angle of the minor axis arc of the ellipsoidal supermirror is 20 degree [5]. We have fabricated  $m=6.5$  NiC/Ti supermirrors in which total number of layers was 8900, where the half of the layers were SiC interlayers.

**RESULTS:** Figure 1 shows reflectivity profiles of neutrons by the  $m=6.5$  NiC/Ti (SiC) supermirror fabricated by the KUR-IBS. As shown in Fig. 1 (a), the profile by the supermirror on metal substrate was almost same with that on a well-polished silicon wafer. There is no big difference for the reflectivity profiles on each metal elements which corresponds to upstream, center, downstream parts shown in Fig.1(b). By using the new layer structure, we have realized  $m=6.5$  supermirror, which is difficult even on a flat surface, on a curved surface with a steep curvature. Here the required number of periodic layers of high- $m$  supermirror increases with the proportional of  $m^4$ , in which principle is well known as Porod's law. The number of effective periodic layers of the supermirror was 4450 and it was not much enough number for  $m=6.5$  supermirror. It is also still preliminary measurement and we will report more detail in our future work.

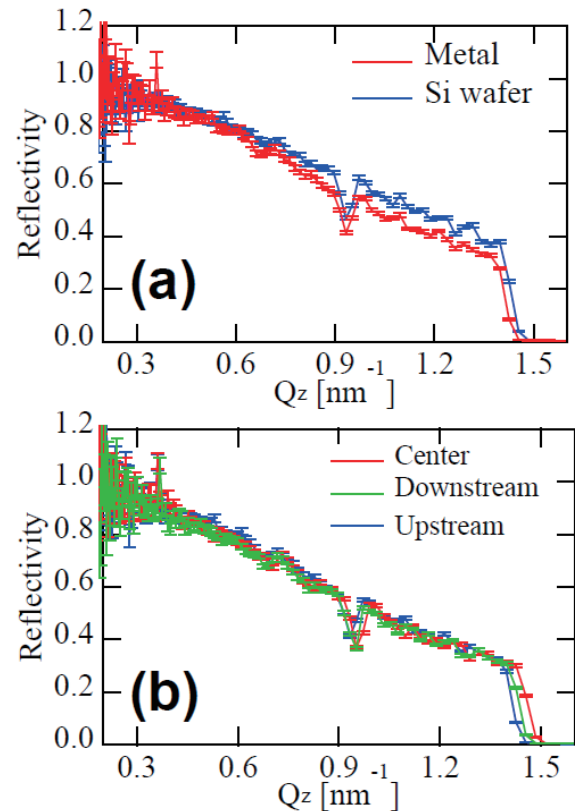


Fig. 1. Neutron reflectivity of  $m=6.5$  NiC/Ti (SiC) supermirror deposited simultaneously on (a) metal substrate and silicon wafer. (b) Those on different metal elements (upstream, center downstream parts).

### REFERENCES:

- [1] J.Guo, *et al.*, Optics Express 22(2014) 063108.
- [2] T.Hosobata, *et al.*, Optics Express 25(2017) 20012.
- [3] T.Hosobata, *et al.*, Optics Express 27(2019)26807.
- [4] M.Hino, *et al.*, Nucl. Instr. and Meth., **797**(2015) 265.
- [5] T.Hosobata, *et al.*, JPS Conf. Proc. 22, 011010 (2018).

## CO1-6 Development of high spatial resolution cold/ultracold neutron detector using nuclear emulsion

N. Naganawa, M. Hino<sup>1</sup>, K. Hirota<sup>2</sup>, H. Kawahara<sup>2</sup>,  
M. Kitaguchi<sup>3</sup>, K. Mishima<sup>4</sup>, N. Muto<sup>2</sup>, A. Umemoto<sup>2</sup>

*Institute of Materials and Systems for Sustainability*

<sup>1</sup>*Institute for Integrated Radiation and Nuclear Science,  
Kyoto University*

<sup>2</sup>*Graduate School of Science, Nagoya University*

<sup>3</sup>*Kobayashi-Maskawa Institute for the Origin of Particles  
and the Universe*

<sup>4</sup>*High Energy Accelerator Research Organization, KEK*

**INTRODUCTION:** Experiments measuring position distributions of ultracold neutrons under the earth's gravitation [1-3] have been carried out to study gravitation or short-range forces. For those purposes, ultracold neutron (UCN) detectors with high spatial resolution are useful. Conventional best detectors had resolutions of 1-2  $\mu\text{m}$  [4,5]. To improve the ability to study gravitation, we successfully developed a detector with spatial resolution of less than 100 nm [6] using fine-grained nuclear emulsion [7]. It was fabricated by sputtering a converter layer with a structure of  $^{10}\text{B}_4\text{C}(50\text{ nm})\text{-NiC-C}$  on a side of silicon wafer at KURRI using the ion beam sputtering system (KUR-IBS) and applying the fine-grained nuclear emulsion with the thickness of 10  $\mu\text{m}$  on the layer. The detector can also be used in neutron imaging. In order to obtain position distributions of neutrons with a high accuracy of submicron, a method to connect images between microscopic views with high accuracy is necessary. We developed a method using microscopic marks formed on silicon substrates for the purpose. In this experiment, we sputtered a converter layer with a structure of  $^{10}\text{B}_4\text{C-NiC-C}$  on silicon wafers with those marks, applied fine-grained nuclear emulsion on them, exposed one of them to cold neutrons at J-PARC, and checked the stability of sputtered layer and the emulsion layer. The rest of the samples were used in an experiment measuring position distributions of UCNs under the earth's gravitation at Institut Laue-Langevin (ILL).

**EXPERIMENTS:** The detectors were fabricated as follows. The microscopic marks for fine alignment with their diameter of 1  $\mu\text{m}$ , a pitch of 50  $\mu\text{m}$ , and a depth of 0.5  $\mu\text{m}$  were formed on areas of 10 mm by 70 mm on single sides of silicon wafers by electron beam lithography at Nanofabrication Platform in Nagoya University. After that, wafers were cut into the size of 20 mm by 90 mm and washed. Next, layers of  $^{10}\text{B}_4\text{C}(200\text{ nm})\text{-NiC}(60\text{ nm})\text{-C}(20\text{ nm})$  were formed on those wafers at KURRI using KUR-IBS. After that, fine-grained nuclear emulsion gel was applied on those wafers with final thickness of 10  $\mu\text{m}$  at Lab. F, Physics Department, Nagoya University. A detector was exposed to cold neutrons of 1000 m/s at BL05, MLF, J-PARC. The exposure density was approximately  $2.7 \times 10^7$  neutrons/cm<sup>2</sup>. After the exposure, it was developed and checked on stabilities of sputtered layer and adhesion between the layer of the emulsion. Observation of tracks was also done with epi-illumination optical microscope at Nagoya University.

**RESULTS:** Stability of sputtered layer was confirmed to be enough that the layer did not separate from silicon substrate after the application of fine-grained nuclear emulsion and development. Adhesion between the layer and the emulsion layer was also strong enough that the emulsion layer did not separate from the sputtered layer during the development. Tracks of alpha particles and  $^7\text{Li}$  nuclei from neutron absorption by  $^{10}\text{B}$  in the converter layer were clearly seen as shown in Fig. 1 with an expected density. Marks for fine alignment were also clearly seen as shown in the same figure.

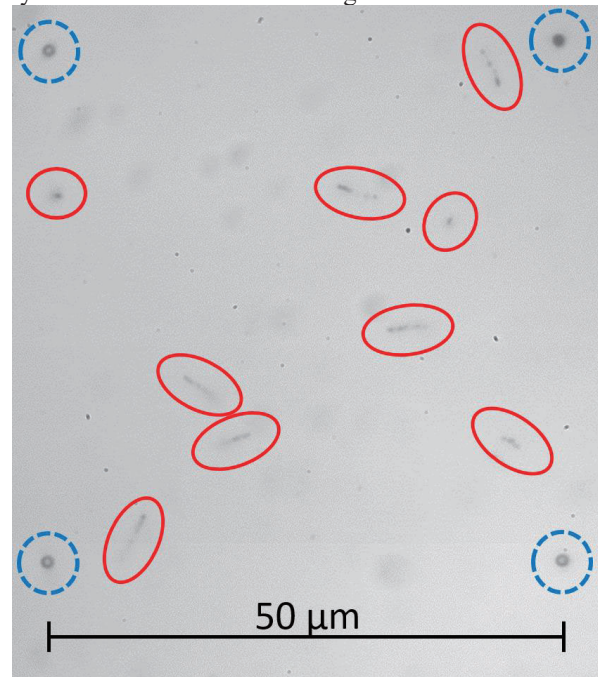


Fig. 1. Microscopic image of the detector after development. Observed tracks are surrounded by red ellipses. Marks for fine alignment are surrounded by dashed blue circles. Tracks and marks were clearly seen after development.

Thus, stability and functionality of the detector was confirmed, and the rest of the detectors were used in an experiment for measuring position distributions of quantized UCNs under the earth's gravitational field at PF2, ILL, whose analysis is going on.

### REFERENCES:

- [1] V. V. Nesvizhevsky *et al.*, *Nature*, **415** (2002) 297.
- [2] H. Abele *et al.*, *Nucl. Phys. A* 827, 593c-595c (2009).
- [3] G. Ichikawa *et al.*, *Phys. Rev. Lett.*, 112, 071101 (2014).
- [4] V.V. Nesvizhevsky *et al.*, *Nucl. Instrum. Methods Phys. Res. A* 440, 754-759 (2000).
- [5] T. Jenke *et al.*, *Nucl. Instrum. Methods Phys. Res. A*, 732, 1-8 (2013).
- [6] N. Naganawa *et al.*, *Eur. Phys. J. C*, 78 (2018)959.
- [7] T.Asada *et al.*, *Prog. Thor. Exp. Phys.*, 2017 (2017) 063H01.

## CO2-1 Measurement for thermal neutron capture cross sections and resonance integrals of the $^{243}\text{Am}(n,\gamma)^{244g}\text{Am}$ , $^{244m+g}\text{Am}$ reactions

S. Nakamura, S. Endo, A. Kimura and Y. Shibahara<sup>1</sup>

Japan Atomic Energy Agency

<sup>1</sup>Institute for Integrated Radiation and Nuclear Science, Kyoto University

**Introduction:** Americium-243 has the half-life of 7367 yr [1] and contributes to the production of  $^{244}\text{Cm}$  (18.11 yr [1]) through neutron capture reaction. The neutron capture cross-section data of  $^{243}\text{Am}$  are important in considering the amount of  $^{244}\text{Cm}$  accumulated in spent nuclear fuels. For the prediction of  $^{244}\text{Cm}$  production, a difference of 10% between calculated and experimental values was reported.[2] Thus the neutron capture cross sections of  $^{243}\text{Am}$  were measured by a neutron activation method.

**Experiments:** Nitric acid solutions of  $^{243}\text{Am}$  equivalent to 1 kBq were dropped onto fiber filters and dried. To monitor neutron fluxes, a set of Au/Al and Co/Al alloy wires was attached to the Am sample as an irradiation target. Neutron irradiation was performed using irradiation systems of the KUR. Gamma- and alpha-ray spectrometry were applied to measurements of irradiated samples.

First, for the  $^{243}\text{Am}(n,\gamma)^{244g}\text{Am}$  reaction, measurements of emission probabilities of  $\gamma$  rays emitted from the ground state  $^{244g}\text{Am}$  (10.1 h[1]) had been performed under the project 25P1-16 in 2014. The previous 29% uncertainty [3] in the emission probability had been improved to 2% uncertainty [4]. The  $^{243}\text{Am}$  targets were irradiated in 1 MW power operation with the pneumatic tube Pn-2. The bare target was irradiated for 30 min, and that with a Gd filter for 5 min. Gamma rays emitted from irradiated Am samples and alloy wires were measured with a high-purity Ge detector.

Next, for the  $^{243}\text{Am}(n,\gamma)^{244m+g}\text{Am}$  reaction, the amounts of  $^{244m}\text{Am}$  and  $^{244g}\text{Am}$  produced via neutron capture reaction were determined from the  $\alpha$ -ray yield of their daughter nucleus  $^{244}\text{Cm}$ . The  $^{243}\text{Am}$  targets with and without a Gd shield were irradiated for 6 hours by the hydraulic conveyer in 5 MW power operation. After irradiation, a cooling time for 5 days caused  $^{244g}\text{Am}$  sufficiently to decay to  $^{244}\text{Cm}$ . At this time, the amount of  $^{244g}\text{Am}$  was reduced to about 1/4000. Irradiated fiber filters were rinsed with 3M  $\text{HNO}_3$  solution and the solution was centrifuged. The separated supernatants were dropped onto Petri dishes, and dried to make  $\alpha$ -ray samples. Alpha-ray measurements were done with the model 7401 alpha spectrometer (Canberra, Inc.).

**Analysis:** Neutron fluxes at the irradiation positions were obtained from the induced activities of the monitor wires.

**Figure 1** shows an example of  $\gamma$ -ray spectrum due to the decay  $\gamma$ -rays emitted from  $^{244g}\text{Am}$  produced by the  $^{243}\text{Am}(n,\gamma)^{244g}\text{Am}$  reaction. Its measurement time was 16 hours. For the  $^{243}\text{Am}(n,\gamma)^{244m+g}\text{Am}$  reaction, **Figure 2** shows an  $\alpha$ -ray spectrum obtained by 168-hours measurement. Reaction rates of the  $^{243}\text{Am}$  were obtained from amounts of the  $^{243}\text{Am}$  samples and produced nuclides. Their reaction rates and neutron flux information were analyzed on the basis of Westcott's convention [5] to derive neutron capture cross sections. Data analysis is in progress.

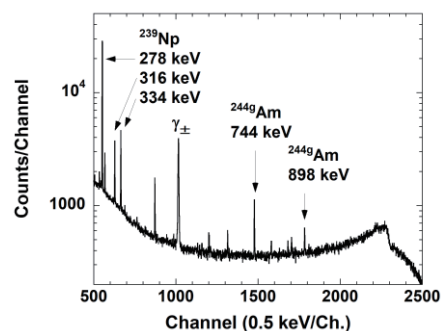


**Fig.1** An example of  $\gamma$ -ray spectrum of irradiated  $^{243}\text{Am}$  sample.

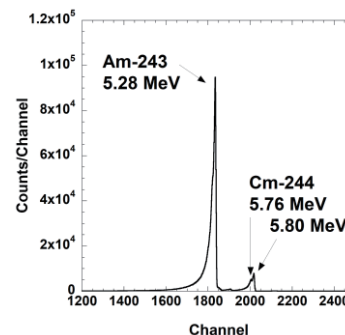


**Fig.2** An example of  $\alpha$ -ray spectrum of irradiated  $^{243}\text{Am}$  sample.

### Acknowledgement

Present study includes the result of “Research and Development for accuracy improvement of neutron nuclear data on minor actinides” entrusted to the Japan Atomic Energy Agency by the Ministry of Education, Culture, Sports, Science and Technology of Japan (MEXT).

### References:

- [1] <http://www.nucleide.org/Laraweb/index.php>
- [2] K.Okumura *et al.*, JAERI-Research 2004-025.
- [3] R.W.Hoff *et al.*, *Phys. Rev. C.*, **29** (1984) 618.
- [4] S.Nakamura *et al.*, *J. Nucl. Sci. Technol.*, **56** (2019) 123.
- [5] C.H. Westcott *et al.*, “*Proc.2nd Int. Conf.Peaceful Use of Atomic Energy, Geneva*”, **16** (1958) 70.

## CO2-2 Quantitation of Gamma Ray Emission from Capture Reaction of Uranium-238

Y. Nauchi, J. Hori<sup>1</sup> and T. Sano<sup>2</sup>

*Nuclear Technology Research Laboratory, Central Research Institute of Electric Power Industry*

<sup>1</sup>*Kyoto University Institute for Integrated Radiation and Nuclear Science*

<sup>2</sup>*Atomic Energy Research Institute, Kindai University*

**INTRODUCTION:** For the criticality control and the safeguards of fuel debris formed in the Fukushima Dai-Ichi nuclear power station, quantification of the mass of nuclear materials and its residual fissile enrichment is desirable. However, non-destructive quantification techniques have never been developed even for intact spent nuclear fuel assemblies. In the conventional fuels for light water reactor utilization, the dominant nuclide of the fuel mass is <sup>238</sup>U. Thus, we have focused on measurement of  $\gamma$  rays from capture reactions of <sup>238</sup>U by neutron induced  $\gamma$  ray spectroscopy (NIGS). We have succeeded in detection of 4060 keV  $\gamma$  rays from capture reaction of <sup>238</sup>U from a sub-critical core [1]. Furthermore, we found that the count rate ratios of the 4060 keV  $\gamma$  ray to fission prompt ones are consistent with <sup>238</sup>U/<sup>235</sup>U ratios in two sub-critical cores of different average <sup>235</sup>U enrichments [2]. However, the  $\gamma$  ray spectrum from the reaction has been reported to vary with the incident neutron energy [3]. To utilize the NIGS spectrum for the quantification of the nuclear material and the enrichment, the  $\gamma$  ray spectrum measurement was conducted in this work.

**EXPERIMENTS:** The measurement was conducted in LINAC pulsed neutron source facility in KURNS. A tungsten (W) target was irradiated by accelerated electron and the Bremsstrahlung photons were radiated. Then the photon interacted with W and photo nuclear reactions were induced. The beam frequency was adjusted to 50 Hz and the pulse width was 1  $\mu$ s (nominally). The beam current was stabilized to 27  $\mu$ A. The target was located on center of a cylindrical tank of 20 cm in diameter and 30 cm in height. The tank was filled with light water. The neutrons generated in the W target was moderated in the water. We used the neutron at “12 m room” which is located on 135 deg axis from the electron beam line. In the room, a square shaped sample of metallic U was irradiated by the moderated neutron. Its geometry was 4 cm  $\times$  4 cm and the thickness corresponds to 2.91 g/cm<sup>2</sup>. A HP-Ge detector of 35% relative efficiency was set on 90 deg axis from the neutron flying axis. The distance from the center of the sample to the head of the detector was 5 cm. The detector was carefully shielded from the  $\gamma$  - flash from the target. The  $\gamma$  ray pulse height in the detector was acquired together with the time of flight (TOF) information. The pulse height was calibrated with additional measurement of <sup>35</sup>Cl(n, $\gamma$ ) reactions. The energy of the neutron inducing the <sup>238</sup>U(n, $\gamma$ ) reaction was deduced from the TOF information. TOF spectra was calibrated with additional transmission measurements through Mn, In,

Ag, Cd. The effective length of the flight path was deduced to be 11.3m.

**RESULTS:** In figure 1, the  $\gamma$  ray pulse height spectra are given for several neutron energy regions: the thermal, the epi-thermal, and the resonances of <sup>238</sup>U(n, $\gamma$ ) reactions. In the thermal and epi-thermal regions, <sup>238</sup>U(n, $\gamma$ )  $\gamma$  rays were measured simultaneously with prompt and delayed ones from fission reactions of <sup>235</sup>U. For the resonance energies, it is considered that the <sup>238</sup>U(n, $\gamma$ )  $\gamma$  rays are dominant. In every region, 4060 keV  $\gamma$  ray was detected. The energy resolution of this experiment was better so that 3982 and 3991 keV components are resolved, which has never been done with 4 $\pi$  type HP-Ge detector [3]. 3583 and 3197 keV  $\gamma$  rays were measured especially for the En=6.67 eV resonance. However, 3567, 3541 and 3482 keV  $\gamma$  rays [3] were not clearly resolved due to the counting statistics and the single escape peaks. In CapGam [4], yield of 3296.5 keV  $\gamma$  ray is evaluated larger than that of 4060 keV  $\gamma$  ray for the thermal neutron capture of <sup>238</sup>U. However, the 3296.5 keV  $\gamma$  ray peak was not found for reactions for every neutron energy region.

The  $\gamma$  ray spectra were observed differently for incident neutron energies. On account of the difference, ratio of some resonances to the thermal <sup>238</sup>U(n, $\gamma$ ) reaction might be unfolded by spectra obtained by NIGS. Thus, NIGS would be a new validation tool for neutron spectrum calculation in the reactor physics field, which has never been achieved. For the purpose, <sup>238</sup>U(n, $\gamma$ )  $\gamma$  ray measurements with better statistical accuracy is further desired as well as nuclear data evaluation.

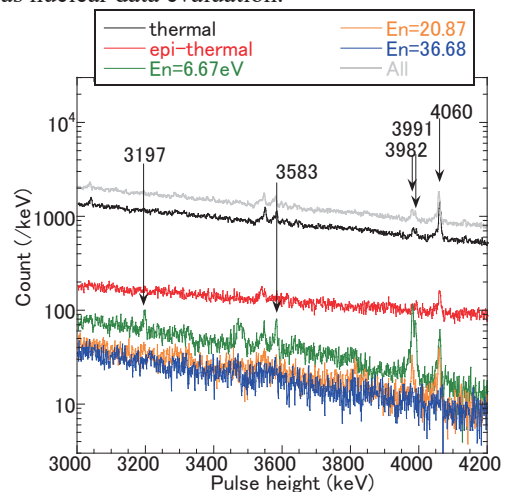


Fig. 1 Measured pulse height spectrum for U sample.

### REFERENCES:

- [1] Y. Nauchi, T. Sano, H. Unesaki, S. Sato, M. Suzuki, H. Ohta. Proc. ICNC2019.
- [2] Y. Nauchi, S. Sato, M. Suzuki et al., KURNS progress report 2018, CO3-10.
- [3] H. Harada, S. Goko, A. Kimura, et al, J. Korean Phys. Society 59(2) 1547-1552, 2011.
- [4] E. A. McCutchan manages, “Thermal Neutron Capture  $\gamma$ 's by Target”, browse on Jan5, 2020.

T. Matsumoto, A. Masuda, H. Harano, J. Hori<sup>1</sup> and T. Sano<sup>2</sup>

National Metrology Institute of Japan, National Institute of Advanced Industrial Science and Technology

<sup>1</sup>Institute for Integrated Radiation and Nuclear Science, Kyoto University

<sup>2</sup>Atomic Energy Research Institute, Kindai University

**INTRODUCTION:** Evaluation of neutron fluence and neutron dose equivalent for the epi-thermal neutron region is very important to manage workplaces with neutron sources or nuclear fuels as well as irradiation fields in a boron neutron capture therapy (BNCT). In the pre-sent study, we have developed a current-mode neutron detector [1] that can be used in intense neutron flux field such as BNCT fields. The neutron detector is composed of a pair of <sup>6</sup>Li-glass and <sup>7</sup>Li-glass scintillators (10-mm diameter and 2-mm thickness). The current outputs from photomultipliers are directly used to evaluate the neutron fluence in the detector. We have tried to apply the current-mode detectors to sensors used in a neutron detection device with a moderator. We fabricated four pairs of the current-mode detector (four <sup>6</sup>Li-glass and four <sup>7</sup>Li-glass scintillation detectors). The individual difference was evaluated to precisely measure neutrons using the neutron detector device with the moderator. Moreover, we fabricate a prototype of <sup>6</sup>Li-glass scintillation detector with a photodiode (Fig. 1). We also experimentally verified the <sup>6</sup>Li-glass scintillation detector with the photodiode

**EXPERIMENTS:** A collimated neutron beam with 30 mm diameter was obtained by the photo neutron reaction using a tantalum target with a water moderator at the KURRI Linac [2]. Figure 2 shows the experimental setup. The detector was set at 12 m away from the target. An enriched <sup>10</sup>B<sub>4</sub>C sample with 10-mm thickness was also used to subtract background thermal neutrons in the measurement room. The <sup>10</sup>B<sub>4</sub>C sample was set between the detector and end of the collimator in the beam line. A BF<sub>3</sub> proportional counter was used as a neutron monitor. All data were normalized using counts obtained with the BF<sub>3</sub> proportional counter. Characteristics of the neutron detection were experimentally evaluated by means of the time-of-flight (TOF) method.

**RESULTS:** Figure 3 shows the relative sensitivity of the <sup>6</sup>Li-glass and <sup>7</sup>Li-glass scintillation detectors for thermal neutron region, respectively. The thermal neutron sensitivities for the <sup>6</sup>Li-glass scintillation detectors were agreed within 0.5 %. The sensitivities for the <sup>7</sup>Li-glass scintillation detectors had variation within 6 %.

It is guessed that the neutron sensitivity of the <sup>6</sup>Li-glass scintillation detector with the photodiode is lower than that with the photomultiplier, because of difference of photon sensitivities of the photon detectors for 470 nm photon from the <sup>6</sup>Li-glass scintillator. In the first experiments of 2019, signals due to neutrons were not observed

clearly, although signals due to gamma flash from the target were successfully observed.



Fig. 1. Prototype of the <sup>6</sup>Li-glass scintillation detector with the photodiode.

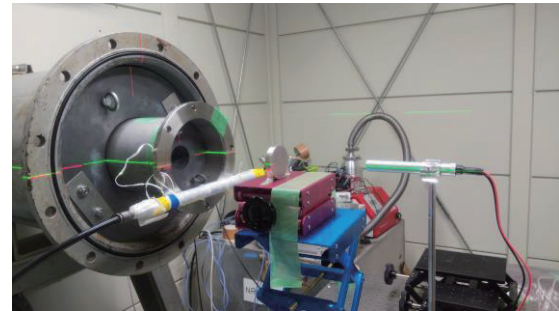


Fig. 2. Experimental setup for the <sup>6</sup>Li-glass scintillation detector. The detector was set at 12 m away from the target.

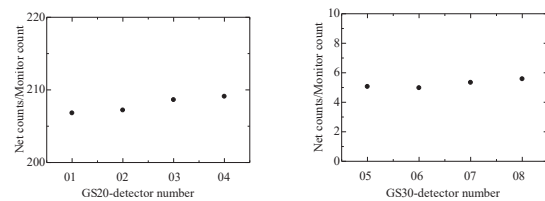


Fig. 3. Results of neutron sensitivities for the <sup>6</sup>Li-glass (GS20) and <sup>7</sup>Li-glass (GS30) scintillation detector.

#### REFERENCES:

- [1] K. Kobayashi *et al.*, Annu. Rep. Res. Reactorinst. Kyoto Univ. 22, 142 (1989).
- [2] T. Matsumoto *et al.*, Radiat. Prot. Dosim. in press (<https://doi.org/10.1093/rpd/ncz266>)

This work was supported by JSPS KAKENHI(JP16K21679, JP16K09030, 19K12638).

## CO2-4 Measurements of thermal neutron total and scattering cross section of moderator materials

Jun Nishiyama<sup>1</sup>, Jaehong Lee<sup>2,4</sup>, Tadafumi Sano<sup>3</sup> and Jun-ichi Hori<sup>2</sup>

<sup>1</sup>Laboratory for Advanced Nuclear Energy, Institute of Innovative Research, Tokyo Institute of Technology

<sup>2</sup>Institute for Integrated Radiation and Nuclear Science, Kyoto University

<sup>3</sup>Atomic Energy Research Institute, Kindai University

<sup>4</sup>Japan Atomic Energy Agency (June 2019~)

**INTRODUCTION:** The high temperature gas-cooled reactor is a Generation IV reactor concept that use a graphite moderator. The design takes advantage of the inherent safety characteristics with specific design optimizations. The treatment of thermal scattering caused by crystalline is important for graphite to improve the prediction accuracy of graphite moderated core analysis. There is sufficient thermal scattering law for single crystal graphite, but there is no method has been established to reconstruct thermal scattering cross section for polycrystalline graphite. On the other hand, a new concept of small modular reactor using CaH<sub>2</sub> as solid moderator has been developed [1]. The experimental and evaluated data of the thermal scattering law for CaH<sub>2</sub> are insufficient. In order to provide basic data for thermal neutron scattering law evaluation, the total and scattering cross sections of moderator materials were measured.

**EXPERIMENTS:** The total and scattering cross sections of moderator materials were measured in the incident neutron energy region from 0.001 to 10 eV by transmission and scattering experiments at the KURNS-LINAC. An experimental arrangement is shown in Fig. 1. Pulsed neutrons were produced from a water-cooled Ta-target by ( $\gamma$ ,n) reaction with a pulsed electron beam. The incident neutron spectrum on a sample, the transmitted and scattering neutron spectrum were measured by means of a time-of-flight (TOF) method with a <sup>6</sup>Li-glass scintillation detector. A 5.0 mm diameter by 5.0 mm thick <sup>6</sup>Li-glass was located 12.0 m from the neutron source. The scattering neutrons were measured by a 50 mm diameter by 5.0 mm thick <sup>6</sup>Li-glass scintillation detector. The scattering neutron spectra were observed at angle of 45 degrees with respect to the neutron beam direction.

The characteristics of the samples are shown in Table 1. The graphite and polyethylene sample are used as a moderator in the KUCA facility.

**RESULTS:** The total cross sections of moderator materials were derived in the incident neutron energy region from 0.001 to 10 eV. Figure shows the scattering neutron spectra. The result of graphite had a structure caused by thermal scattering crystalline. Figure 3 shows the scattering neutron spectrum with the resonance filter (Cd, In, Ag, Mn). It was shown that it is possible to measure quasi-monochromatic neutrons from a white neutron source.

**ACKNOWLEDGEMENTS:** This research is a collaborative effort of Toshiba Energy Systems & Solutions, Kindai University, Kyoto University and Tokyo Institute of Technology.

### REFERENCES:

- [1] R. Kimura and S. Wada, Nucl. Sci. Eng., Vol.193, p.1013-1022, (2019).

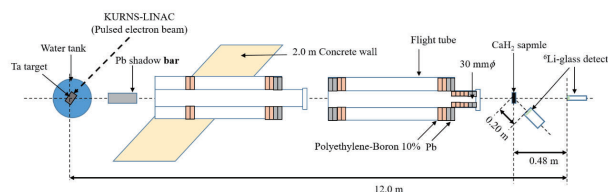


Fig 1. Experimental arrangement.

Table 1. Characteristics of samples.

Sample	Polyethylene	Graphite	CaH <sub>2</sub>
Structure	High molecular	Polycrystalline	Powder
Sample shape	Square plate	Square plate	Disk in Al case
Density [g/cm <sup>3</sup> ]	0.949	1.754	1.200
Size [mm]	50.8 × 50.8	50.8 × 50.8	φ50
Thickness [mm]	3.18	12.7	5.0
[atoms/b]	1.26 × 10 <sup>-2</sup>	1.12 × 10 <sup>-1</sup>	8.63 × 10 <sup>-3</sup>

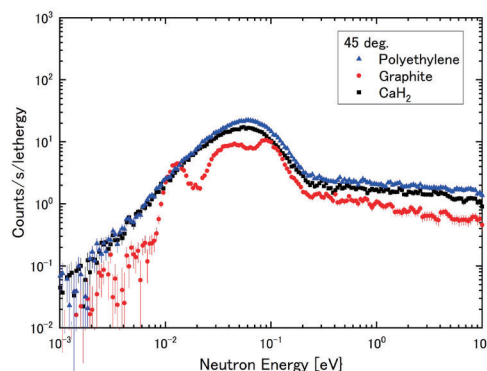


Fig. 2. Scattering neutron energy spectra.

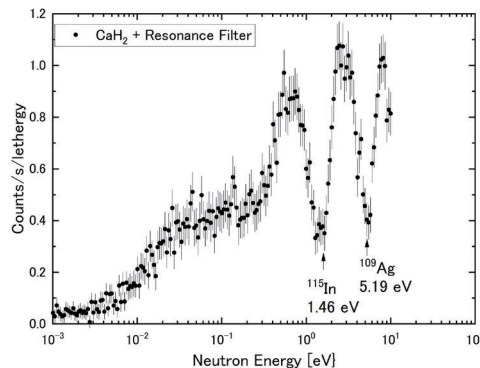


Fig. 3. Scattering neutron energy spectrum with resonance filter (Cd, In, Ag, Mn).

# CO2-5 Measurement of Temperature depended Thermal Neutron Spectrum in Solid Moderator

T. Sano, J. Lee<sup>1,3</sup>, J. Hori<sup>1</sup>, J. Nishiyama<sup>2</sup>

Atomic Energy Research Institute, Kindai University  
<sup>1</sup>Institute for Integrated Radiation and Nuclear Science, Kyoto University  
<sup>2</sup>Laboratory for Advanced Nuclear Energy, Tokyo Institute of Technology  
<sup>3</sup>Japan Atomic Energy Agency (Jun 2019~)

## INTRODUCTION:

In recent years, small modular reactors (SMR) have been studied intensively. Those SMR are employed existing technologies such as light-water moderator and coolant and so on. On the other hand, a new concept of SMR using solid moderator has been developed [1]. Here, the moderator in a nuclear reactor is common material such as light-water, researchers and engineers could calculate the accurate neutron spectrum in the moderator by using evaluate nuclear data libraries such as the JENDL-4.0 [2]. However, if evaluate nuclear data libraries has poor data for moderator materials, the calculations of accurate neutron spectrum in the moderator will be difficult. The new concept of SMR is employed CaH<sub>2</sub> as solid moderator [1].

Therefore, in order to perform a nuclear design for the reactor with CaH<sub>2</sub>, it is necessary to experimentally investigate the temperature-dependent neutron spectrum in the moderator. In last year, a preliminary experiment of temperature-dependent neutron spectrum measurements was carried out [3]. In the present study, the experimental geometry and condition were optimized based on the results of preliminary experiment and the temperature-dependent neutron spectrum measurements were performed.

## EXPERIMENTS:

To measure the temperature-dependent thermal neutron spectrum in CaH<sub>2</sub> sample, a preliminary experiment was conducted method in KURNS-LINAC. The CaH<sub>2</sub> sample was set in a heater to be increased the sample temperature from 21°C to 470°C. Figure 1 shows an experimental geometry of present study. The heater was installed at a position of 12.6 m from the pulsed neutron source at KURNS-LINAC. In this experiment, a GEM type neutron detector was employed. The neutron flight length between the CaH<sub>2</sub> and the GEM detector was 60 cm. Table 1 shows the experimental conditions and Table 2 is the sample information. The transmitted neutron flux from the sample was observed by the TOF method in the present study.

## RESULTS:

The obtained thermal neutron TOF spectrum of the CaH<sub>2</sub> at room temperature (21°C) and 470°C are shown in the Fig. 1. The difference of thermal neutron spectrum between 21°C and 470°C was clearly observed.

## ACKNOWLEDGEMENTS

This research is a collaborative effort of Toshiba Energy Systems & Solutions, Kindai University, Tokyo Institute of Technology and Kyoto University.

## REFERENCES:

- [1] R. Kimura and S. Wada, Nucl. Sci. Eng., Vol.193, p.1013-1022, (2019).
- [2] K. Shibata, *et. al.*, J. Nucl. Sci. Technol., 39(11), (2002).
- [3] J. Lee, *et. al.*, Proc. on ND 2019, Beijing, China, May 19-24, (2019).

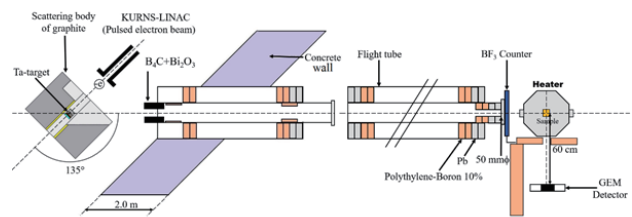


Fig.1. Experimental geometry.

Table 1 Experimental condition.

Sample	LINAC operational condition (Frequency, pulse width, current)	Sample temperature (degree)	Measuring time (h)
CaH <sub>2</sub>	35Hz, 3 μs, 53 μA	21	10
CaH <sub>2</sub>	35Hz, 3 μs, 53 μA	470	16
Blank	35Hz, 3 μs, 53 μA	21	5.5

Table 2 Sample information.

Chemical formula	CaH <sub>2</sub>
Density	1.33 g/cm <sup>3</sup>
Geometry	70 mm × 70 mm × 60 mm

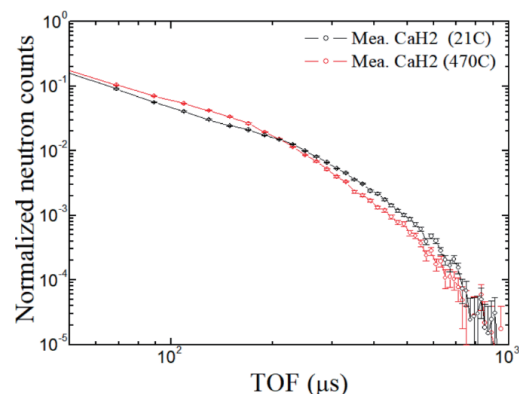


Fig.1. Obtained thermal neutron TOF spectrum of CaH<sub>2</sub> sample at 21°C and 470°C.

## CO3-1 Basic Research for Sophistication of High-power Reactor Noise Analysis (II)

S. Hohara<sup>1</sup>, T. Sano<sup>1</sup>, A. Sakon<sup>1</sup>, K. Nakajima<sup>2</sup>, K. Takahashi<sup>2</sup>, K. Hashimoto<sup>1</sup>

<sup>1</sup>Atomic Energy Research Institute, Kindai University

<sup>2</sup>Interdisciplinary Graduate School of Science and Engineering, Kindai University

**INTRODUCTION:** Reactor noise for high-power reactors were actively measured in the 1960's and 1970's. The major focuses of those researches were for the abnormality diagnosis or the output stabilization diagnosis, and almost researchers were in the field of system control engineering or instrumentation engineering. High-power reactor noise measurements for dynamics' analysis of reactivity change, reactivity feedback or reactor characteristics itself were few in the time (1960's and 1970's), because of the powerless measurement system. In this research, we plan to measure KUR's output with present-day measurement system and plan to analyze with several analysis methods. The results of this work will supply some knowledges and technics in the aspect of sophistication of reactor noise analysis or simulation methods.

In this year, we tried to measure the reactor nuclide noise of the critical state KUR core via a 1-inch <sup>3</sup>He counter at CN-1 port. The experimental work was done in 7th November 2019. As the result of the experiment, a result looks like the nuclear reactor noise was observed.

**EXPERIMENTS:** In this experiment, the output signal of the <sup>3</sup>He counter was put into a Spectro Scopy AMP (2022: Canberra), and the output of the SSA was measured with a time-series measurement system (HSM-CA4106\_LC: ANSeeN Inc.). A schematic view of the measurement is shown in Fig.1, and the counter installation overview is shown in Pic.1.

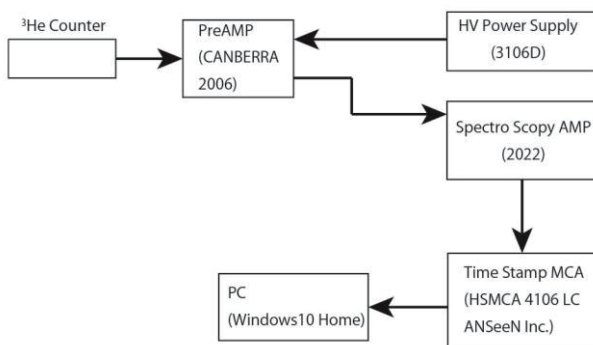


Fig. 1. Schematic view of the measurement.

The experimental condition is shown in Table.1. The reactor Power was set from 20W to 1kW. The measurement time was 800 – 3,600 sec.



Fig. 2. An overview of the counter installation.

Table 1. Experimental condition.

No.	Reactor Power [W]	Measurement Time [sec]	Count Rate [cps]
1	20	800	0.54
2	100	600	2.73
3	300	1,000	7.92
4	1k	3,600	26.33

### RESULTS:

The measurement results were analyzed by Feynman- $\alpha$  / bunching method. As a result of the analysis, good results were not obtained for 20W, 100W and 300W. However, a plot shape similar to Feynman's theoretical formula was obtained for 1kW. The analysis result is shown in Fig.3. From the result, the prompt neutron decay constant was 97.7 [sec<sup>-1</sup>], and y value was very small (~0.09). From the smallness of the Y value, it is considered necessary to verify whether it is a nuclear noise by other techniques (e.g., covariance to mean ratio method, etc.).

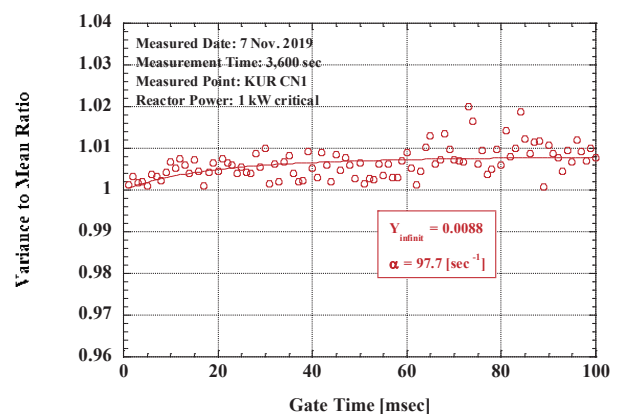


Fig. 3. A Feynman- $\alpha$ /Bunching analysis result for the 1kW KUR operation.

## CO3-2 Demonstration of advanced subcritical measurements: Time-Domain Decomposition-based Integral (TDDI) method and third-order neutron-correlation technique

T. Endo<sup>1</sup>, K. Watanabe<sup>1</sup>, A. Nonaka<sup>1</sup>, S. Imai<sup>1</sup>, F. Nishioka<sup>1</sup>, H. Oike<sup>1</sup>, M. Yamanaka<sup>2</sup>, C.H. Pyeon<sup>2</sup>

<sup>1</sup>Graduate School of Engineering, Nagoya University

<sup>2</sup>Institute for Integrated Radiation and Nuclear Science, Kyoto University

**INTRODUCTION:** In a general transient in a subcritical system, reactivity, neutron source intensity  $S$ , and point kinetic parameters ( $\Lambda$  and  $\beta_{\text{eff}}$ ) can change simultaneously. For such a simultaneous transient, the subcriticality measurement by the conventional neutron source multiplication method or inverse kinetics method is difficult because  $S$  and point kinetics parameters are generally assumed to be constant. To address this issue, we developed the time-domain decomposition-based integral (TDDI) method [1] to measure the subcriticality in dollar units after the transient. Furthermore, for an unknown target system with a steady-state, it is not easy to estimate an absolute value of subcriticality,  $-\rho$ , without additional information such as detector efficiency, source strength, and preliminary numerical analysis. To roughly estimate  $-\rho$  in the stationary unknown system, we have been investigating the third-order neutron correlation technique [2], which is a zero-power reactor noise analysis method using the second- and third-order factorial moments of neutron counts. In this study, advanced subcritical measurements using the TDDI method and third-order neutron correlation technique were conducted to confirm these applicability in subcritical cores at the Kyoto University Critical Assembly (KUCA). This report mainly presents experimental results using the TDDI method.

**METHODOLOGY:** The TDDI method was proposed using the point kinetics theory based on the fundamental mode approximation. This method assumes that a target subcritical system changes from a steady-state into another steady-state via an arbitrary transient of state change (e.g. subcriticality, source strength, and point kinetics parameters) during  $t_0 < t < t_1$ . Using the measured time variation in neutron count rate  $n(t)$  under such a situation, an absolute value of subcriticality in dollar units after the transient ( $-\rho_1/\beta_{\text{eff},1}$ ) can be evaluated by the following formula:

$$\frac{-\rho_1}{\beta_{\text{eff},1}} = \frac{\sum_{i=1}^6 \frac{a_i}{\lambda_i} (n_0 e^{-\lambda_i(t_1-t_0)} - n_\infty + \lambda_i \int_{t_0}^{t_1} n(t) e^{-\lambda_i(t_1-t)} dt)}{\int_{t_1}^{\infty} (n(t) - n_\infty) dt}, \quad (1)$$

where  $n_0$  and  $n_\infty$  means the stationary neutron count rates before and after the transient;  $a_i$  and  $\lambda_i$  represent relative delayed neutron yields and decay constant for  $i$ th precursor group. The TDDI method has advantages to approximately estimate the subcriticality without the following information: (1) the reference subcriticality  $-\rho_0$  before the transient, (2) the absolute values of neutron source intensity and the point kinetics parameters before and after the transient, and (3) the time variation in them. The statistical error of  $-\rho_1/\beta_{\text{eff},1}$  using the TDDI method can be approximately estimated using the random sampling

method [1] with the assumption where the probability distribution of neutron counts approximately follows the Poisson distribution.

**EXPERIMENTS:** The subcritical transient experiments were carried out in a deep subcritical core (A(1/8”p60EUEU(3)+1/8”p10EUEU<EUEU-AIAI-NU-AIAI-EUEU>)) driven by a spallation neutron source, which was generated by colliding a 100MeV proton beam from the FFAG accelerator with a Pb-Bi target. All control and safety rods were fully inserted. Time series data of neutron count rate,  $n(t)$ , was continuously measured using neutron detectors (LiFCaF and LiF/Eu:CaF<sub>2</sub> fiber-type detectors (#1,4) in the core region and BF<sub>3</sub> counters (#1,3,4) in the polyethylene reflector region) with list-mode data acquisition systems. First, the subcritical core was kept under the steady-state driven by the spallation source to obtain the stationary count rate  $n_0$  before the transient. Second, a ramp-wise transient was given by withdrawing 3×3 fuel and reflector assemblies in approximately 15 seconds. Thereby, not only the subcriticality but also point kinetics parameters simultaneously changed over the withdrawing time. After the transient, the core was kept as-is for a sufficiently long time until the subcritical core reached another steady-state to measure stationary count rate  $n_\infty$  after the transient. Based on Eq. (1),  $-\rho_1/\beta_{\text{eff},1}$  was estimated from the measured  $n(t)$ . For comparison, the subcriticality using the conventional integral method was also estimated.

**RESULTS:** Figure 1 shows experimental results of  $-\rho_1/\beta_{\text{eff},1}$  by the conventional integral and TDDI methods for five neutron detectors, and the numerical result by MCNP6.2 with ENDF/B-VII.1 (10.20±0.08 [\$]). In the case of the conventional integral method,  $-\rho_1/\beta_{\text{eff},1}$  values were significantly underestimated compared with the MCNP6.2 result, and these differences were larger than the statistical errors. On the other hand,  $-\rho_1/\beta_{\text{eff},1}$  of the TDDI method well agreed with the MCNP6.2 result. Consequently, the applicability of the TDDI method was demonstrated through this KUCA subcritical transient.

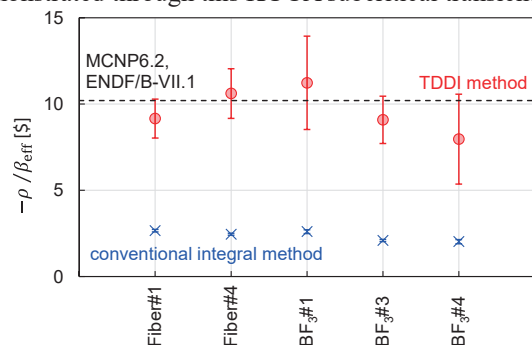


Figure 1. Experimental results of TDDI method.

### REFERENCES:

- [1] T. Endo, *et al.*, J. Nucl. Sci. Technol., (2019). DOI:10.1080/00223131.2019.1706658
- [2] T. Endo, *et al.*, J. Nucl. Sci. Technol., **56** (2019) 322–336.



# CO3-4 Reactor Noise Power-Spectral Analysis for a Graphite-Moderated and -Reflected Core (II)

A. Sakon, K. Hashimoto, S. Hohara, K. Nakajima<sup>1</sup>, K. Takahashi<sup>1</sup>, T. Sano<sup>1</sup>, Y. Fukaya<sup>2</sup>, N. Fujimoto<sup>3</sup>, and Y. Takahashi<sup>4</sup>

*Kindai University Atomic Energy Research Institute*  
<sup>1</sup>*Graduate School of Science and Engineering, Kindai University*  
<sup>2</sup>*Sector of Fast Reactor and Advanced Reactor Research and Development, Japan Atomic Energy Agency*  
<sup>3</sup>*Faculty of Engineering, Kyushu University*  
<sup>4</sup>*Institute for Integrated Radiation and Nuclear Science, Kyoto University*

**INTRODUCTION:** In the last study, the prompt neutron decay constants measured by the detectors about 30cm and 35cm away from core region agreed with the calculated results by the continuous-energy Monte Carlo code MVP version 3[1]. The location of these detectors is farther than the location in the light water moderation reactor. The objective of this study is experimentally to confirm a high flexibility of neutron detector placement in graphite reflector for reactor noise analysis.

**EXPERIMENTS:** The core configuration is shown in Fig. 1. “F” denoted a low-enriched fuel assembly, whose average enrichment is 5.41wt%. “D” is a driver highly-enriched fuel assembly. “G” is graphite reflector. Orange cell is polyethylene reflector. “1”, “2”, “3”, and black dots are BF<sub>3</sub> proportional neutron counters. Withe dot is <sup>3</sup>H proportional neutron counter. These counters are 1.0 in. diameter and 15.47 in. length. In a critical state, reactor noise analysis was carried out using BF<sub>3</sub> detector “1”, “2”, and “3”. The distance from core region to detector “1” is about 20cm, that to detector “2” is about 35cm, that to detector “3” is about 55cm.

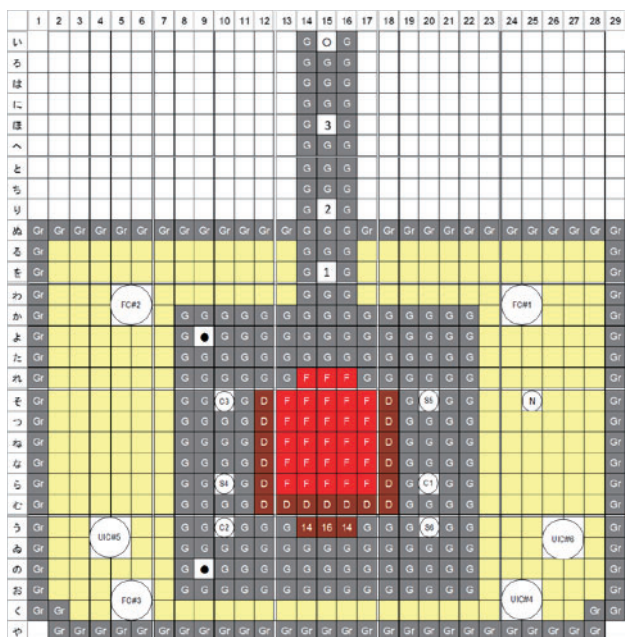


Fig. 1 Core configuration (B7/4”G2/8”p8EUNU+3/8”p38EU)

Reactor noise analysis by power spectrum method was performed in the critical state of suitable reactor power for each detector. The reactor power during measurement was adjusted so that the count rate of each detector was about 3,000[cps].

**RESULTS:** The auto power spectral densities by detector “2” and detector “3” are shown in Fig. 2 and Fig. 3, respectively. These figures also include least-squares fits of a conventional formula [2] to the spectral densities to determine the prompt-neutron decay constant  $\alpha_0$  ( $\beta_{\text{eff}}/\Lambda$ ), where the fitting was confined to a frequency range from 1.25 to 100 Hz. The derived decay constant of detector “2” was  $65.8 \pm 3.4$  [1/s], which was about the same as that the graphite core of last year. However, the derived decay constant of detector “3” was  $96.3 \pm 14.3$  [1/s]. In order to obtain the prompt-neutron decay constant using a detector more than 35cm away from core regions, it is necessary to efficiently measure neutrons that information on fission reaction.

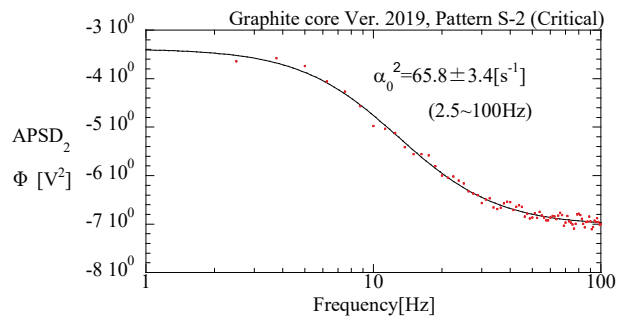


Fig. 2 Auto-Power Spectral Density (Detector “2”)

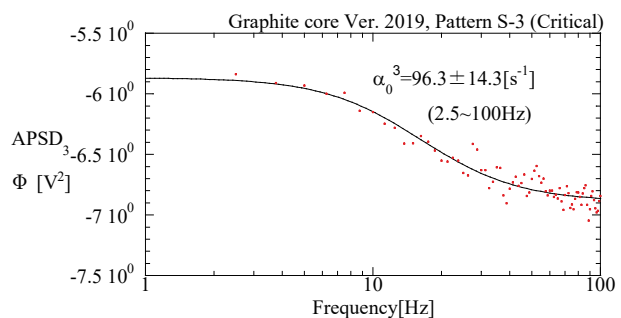


Fig. 3 Auto-Power Spectral Density (Detector “3”)

**REFERENCES:**

[1] Y. Nagaya, K. Okumura, T. Sakurai and T. Mori, MVP/GMVP Version 3 : General Purpose Monte Carlo Codes for Neutron and Photon Transport Calculations Based on Continuous Energy and Multigroup Methods, Tokai-mura: Japan Atomic Energy Agency; 2017, (JAEA-Data/Code 2016-018).  
 [2] M. M. R. Williams, Random Processes in Nuclear Reactors, (Pergamon Press, Oxford,1974), section 3.6.

## CO3-5 Measurement of fundamental characteristics of nuclear reactor at KUCA (IV)

Y. Kitamura<sup>1</sup>, T. Misawa<sup>1</sup>, M. Szieberth<sup>2</sup> and G. Klujber<sup>2</sup>

<sup>1</sup>*Institute for Integrated Radiation and Nuclear Science, Kyoto University*

<sup>2</sup>*Institute of Nuclear Techniques, Budapest University of Technology and Economics*

**INTRODUCTION:** The reactor noise methods can measure the subcriticality through determination of the prompt neutron decay constant. Owing to a great amount of efforts devoted by many researchers, they are now regarded to be one of the most established methods. However, these methods still have one serious problem; the dead time effect that deteriorates the information from the neutron detector and disables the conventional theoretical formula. In 2014, Kitamura and Fukushima hence derived theoretical formulae of two major methods, i.e., Feynman- and Rossi-alpha ones by rigorously considering the dead time effect[1]. However, unfortunately, it was found that their formulae are too complicated to practically apply. Hence, in the present study, another technique for overcoming the dead time effect and its experimental investigation performed at the KUCA are reported.

**METHOD:** In the Feynman-alpha method, neutron detection signals from the neutron detector arising within a certain length of the time interval, i.e., the gate width, are counted. By using thus obtained neutron counts, a correlation index  $Y$  is calculated to quantify the temporal fluctuations in neutron population in the subcritical multiplying system. The neutron counts with respect to various gate widths are further obtained to calculate the  $Y$  values as a function of the gate width, i.e., the Feynman- $Y$  curve. This curve is fitted by the theoretical formula of the Feynman-alpha method to infer the prompt neutron decay constant. However, under high counting-rate conditions, the  $Y$  values with respect to shorter gate widths take negative values as shown in Fig. 1. Owing to this fact, the prompt neutron decay constant inferred under such conditions is biased.

In Fig. 2, a couple of neutron detection signals (red and blue dashed lines) overlapping with each other are shown. In the conventional technique, these signals are regarded to be one signal. On the other hand, in the present technique, before counting the neutron detection signals, the overlapped signals (yellow dots) are resolved. To realize such an analysis, in the present technique, a row signal wave-form recording system is introduced.

**RESULTS:** In Fig. 3, the Feynman- $Y$  curve after resolving overlapping signals is shown. One sees that even the  $Y$  values with respect to short gate widths take positive values.

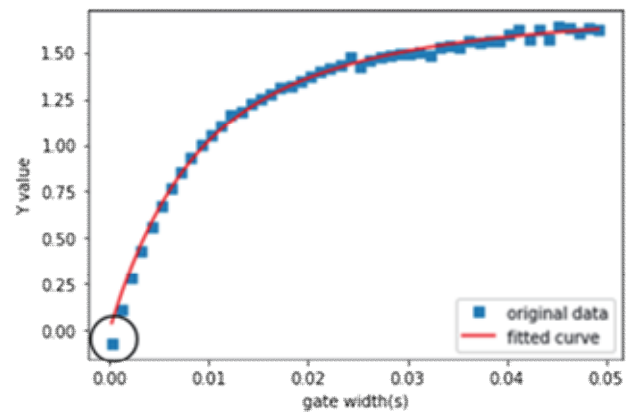


Fig. 1: Example of conventional Feynman- $Y$  curve.

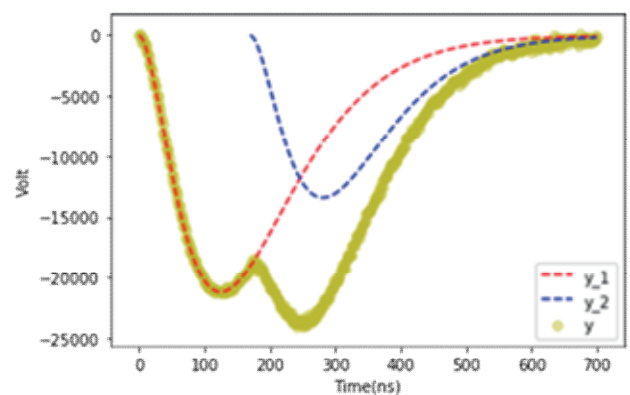


Fig. 2: Signal resolving by wave-form analysis.

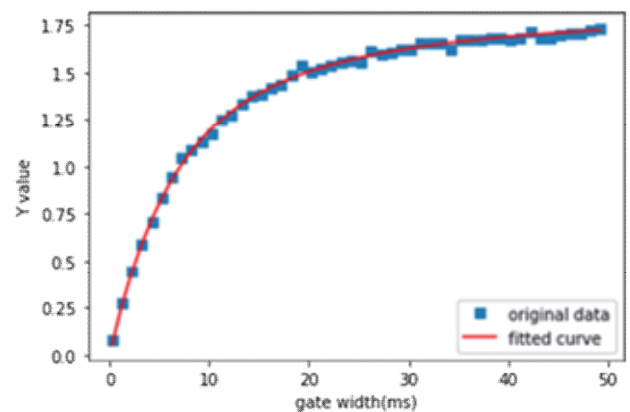


Fig 3: Example of present Feynman- $Y$  curve.

### REFERENCES:

[1] Kitamura, Y., Fukushima, M, J. Nucl. Sci. Technol., 51, 766 (2014).

# CO3-6 Reactor Physis Experiment in Graphite Moderation System for HTGR (II)

Y. Fukaya, S. Okita, K. Takahashi<sup>1</sup>, K. Nakajima<sup>1</sup>, A. Sakon<sup>1</sup>, T. Sano<sup>1</sup> and Y. Takahashi<sup>2</sup>

Sector of Fast Reactor and Advanced Reactor Research and Development, Japan Atomic Energy Agency

<sup>1</sup>Kindai University Atomic Energy Research Institute

<sup>2</sup>Institute for Integrated Radiation and Nuclear Science, Kyoto University

**INTRODUCTION:** To introduce noise analysis technique to High Temperature engineering Test Reactor (HTTR), noise measurement is performed based on B7/4”G2/8”p8EUNU+3/8”p38EU(3) core composed in the B-rack of Kyoto University Critical Assembly (KU-CA). In the previous experiment performed last year, the neutron source was set to out of core. In the present experiment, the neutron source of Cf was loaded into a fuel assembly.

**EXPERIMENTS:** The core configuration is shown in Fig.1. First, the fuel assembly with neutron source was loaded into the center of the core at T15 to mimic the power distribution in criticality. Second, that was loaded into the edge of the core at G15 to mimic the power distribution of the HTTR in subcriticality and neutron leak-age directly to the neutron detectors. In this case, the BF3 detector was moved from I15 to O21. In this report, the first case is called “criticality mimicked case”, and the second case is called “HTTR mimicked case”. The reactor noise driven by inherent neutron source was also measured and is called “inherent neutron source case.”

For these data, we apply Feynman- $\alpha$  method to observe sub-criticality. The control rods pattern and subcriticality is listed in Table 1.

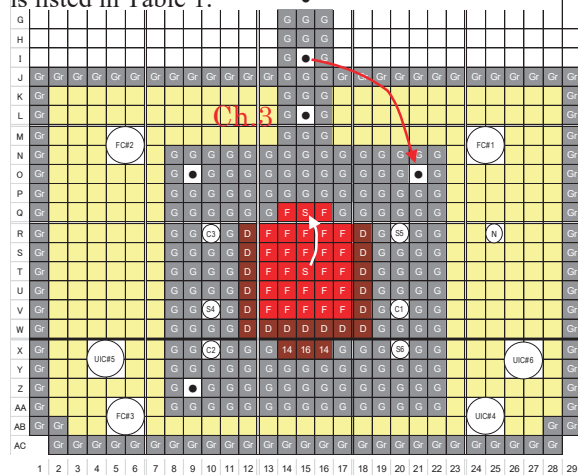


Fig. 1. Core configuration.

Table 1 Control rods pattern and subcriticality

Pattern	Control Rod Position						Center Core	Subcriticality [-%Δk/k]
	C1	C2	C3	S4	S5	S6		
A	U.L.	U.L.	L.L.	U.L.	U.L.	U.L.	U.L.	0.438
B	L.L.	U.L.	U.L.	U.L.	U.L.	U.L.	U.L.	0.857
C	L.L.	U.L.	L.L.	U.L.	U.L.	U.L.	U.L.	1.364
D	L.L.	L.L.	L.L.	U.L.	U.L.	U.L.	U.L.	1.848
E	L.L.	L.L.	L.L.	L.L.	L.L.	L.L.	U.L.	3.229
F	L.L.	L.L.	L.L.	L.L.	L.L.	L.L.	L.L.	4.882

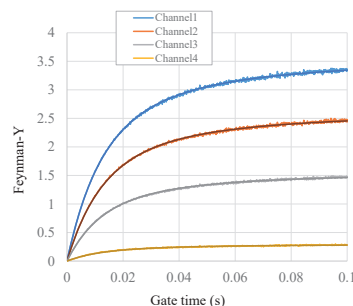


Fig. 2 Feynman-Y for inherent neutron source case with the control rod pattern of B.

**RESULTS:** To determine the prompt neutron decay constant, Feynman-Y is evaluated and the curve is fitted to an analytical formula by non-linear least square method as shown in Fig. 2. In general, the plotted Feynman-Y shows a good agreement with the analytical formula. The results are summarized in Tables 2, 3 and 4, respectively for the inherent neutron source case, criticality mimicked case, and HTTR mimicked case. Here, we focus on Ch.3 to observe directly detected neutron effect.

Comparing those result, the characteristics is found as follows:

- Generally, the inherent neutron source cases show a good agreement with the subcriticality measured by rod drop method listed in Table 1 without depending on the subcriticality. It is supposed that the neutron source distributes similar to the power distribution in criticality.
- With the external neutron source cases, that is criticality mimicked case and HTTR mimicked case, the subcriticality shows slight different with the shallow subcriticality control rod pattern.
- In the HTTR mimicked case, the difference is slightly larger than that in the criticality mimicked case. It is guessed that the error is caused by the directly detected neutron from the neutron source.

Table 2 Decay constant and subcriticality of inherent neutron source case

CR pattern	Channel	Decay constant (s <sup>-1</sup> )	Subcriticality (-%Δk/k)
C	Ch.3	167.8±0.9	1.250±0.011
D	Ch.3	239.4±1.8	2.105±0.021
E	Ch.3	343.6±4.9	3.349±0.059

Table 3 Decay constant and subcriticality of criticality mimicked case

CR pattern	Channel	Decay constant (s <sup>-1</sup> )	Subcriticality (-%Δk/k)
C	Ch.3	183.2±1.1	1.434±0.013
D	Ch.3	215.2±2.3	1.816±0.027
E	Ch.3	381.5±7.7	3.801±0.424

Table 4 Decay constant and subcriticality of HTTR mimicked case

CR pattern	Channel	Decay constant (s <sup>-1</sup> )	Subcriticality (-%Δk/k)
C	Ch.3	191.8±2.0	1.537±0.023
D	Ch.3	254.7±2.9	2.288±0.034
E	Ch.3	374.2±9.7	3.715±0.116

# CO3-7 Sample worth measurements of Lead and Bismuth in low-enriched uranium region at A-core of KUCA for ADS

M. Fukushima<sup>1</sup>, A. Oizumi<sup>1</sup>, M. Yamanaka<sup>2</sup> and C. H. Pyeon<sup>2</sup>

<sup>1</sup>Nuclear Science and Engineering Center, Japan Atomic Energy Agency

<sup>2</sup>Institute for integrated Radiation and Nuclear Science, Kyoto University

**INTRODUCTION:** The Japan Atomic Energy Agency (JAEA) has investigated neutronics of the accelerator-driven system (ADS) of a lead bismuth eutectic (LBE) cooled-tank-type core to transmute minor actinides discharged from nuclear power plants. For the design study of ADS, integral experimental data of nuclear characteristics of LBE is necessary to validate cross sections of lead (Pb) and bismuth (Bi). Previously, Pb and Bi samples experiments were performed in a high-enriched uranium (HEU) core [1]. In present study, a similar experiment was conducted in a variation of uranium core with a low-enriched uranium region.

**EXPERIMENTS:** The reference configuration had five test rods as shown in Figure 1. Figure 2 shows each test unit composed of two EU plates (1/16 inch×2), two Al plates (1/16 inch×2), a natural uranium plate (1.05 mm), two Al plates and two EU plates. The unit-averaged <sup>235</sup>U enrichment was about 17%. The test units were axially and radially surrounded by normal fuel units composed of two EU plates and a polyethylene plate.

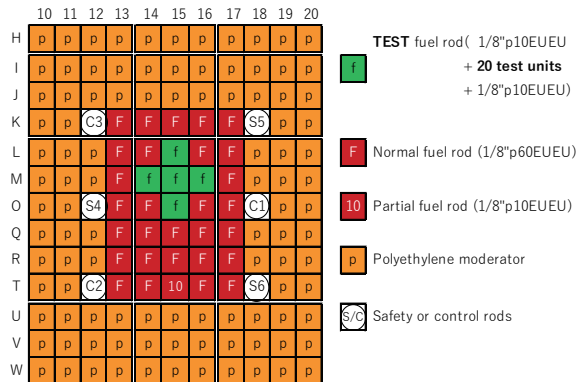


Figure 1. Reference configuration.

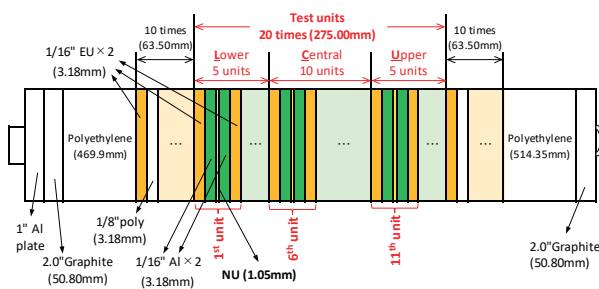


Figure 2. Schematic drawing of test fuel rod.

In the previous experiments for sample worth, solid Al plates were replaced with Pb (or Bi) plates, so aluminum cross sections should be considered as well as lead one (or bismuth) when verifying them. Instead, we used Al voided spacers with a low density that was about 1/10 that of solid Al plates to reduce the aluminum component. For the Pb sample worth, Pb plates instead of Al ones (See Figure 2) were installed in five test rods beforehand, and after then the Pb plates in the central 10 units were replaced with Al voided spacers. The Pb sample worth was estimated as difference excess reactivities before and after the replacement. The other patterns were summarized together with experimental results in Table 1.

Table 1 Experimental results.

Case	Pattern (U/C/B) <sup>*1</sup>	Excess reactivity (pcm)	Sample worth (pcm)
A	Pb/ Pb/Pb	280.3 ± 6.5	Pb sample (A-B)
B	Pb/ V <sup>*2</sup> /Pb	116.1 ± 2.1	164.2 ± 6.9
C	Bi/ Bi/Bi	228.8 ± 6.6	Bi sample (C-D)
D	Bi/ V <sup>*2</sup> /Bi	75.6 ± 0.9	153.2 ± 6.7
E	Al/ Al <sup>*3</sup> /Al	152.4 ± 5.6	Al sample (E-F)
F	Al/ V <sup>*2</sup> /Al	33.0 ± 5.6	119.4 ± 8.0

<sup>\*1</sup>(Upper 5 units / Central 10 units / Lower 5 units) of test regions.

<sup>\*2</sup>V indicates Al voided spacer. <sup>\*3</sup>Al indicates solid Al plate.

**RESULTS:** Numerical analyses were preliminary conducted with MCNP6.1 together with JENDL-4.0 (J40) and ENDF/B-VII.1 (B71). The sample worth was estimated as the difference of the effective multiplication factors between the sample-loaded and reference configurations, without considering the criticality bias. Figure 3 shows that the calculations agree with experiment for the Bi and Al sample worth. On the other hand, the calculations overestimate for the Pb sample worth. In FY 2020, the re-measurement is planned also in HEU core by the same method using Al voided spacers.

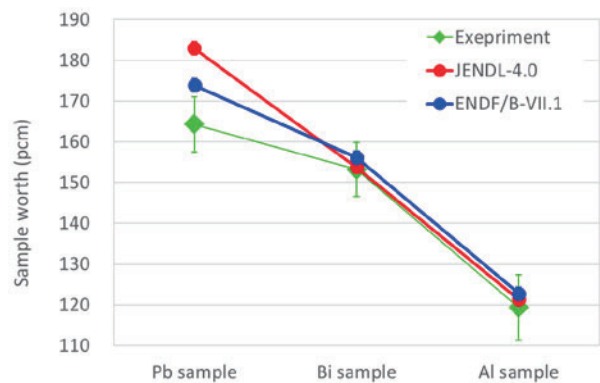


Figure 3. Results of sample worth.

**REFERENCES:**

[1] C. H. Pyeon, et al., J. Nucl. Sci. Technol., **53**, 602-612 (2016) and **55**, 1324-1335 (2018).

T. Misawa<sup>1</sup>, Y. Kitamura<sup>1</sup>, T. Takahashi<sup>1</sup> and A. Yasui<sup>2</sup>

<sup>1</sup>Inst. Integrated Radiation and Nucl. Sci., Kyoto Univ.  
<sup>2</sup>Graduate school of Energy Science, Kyoto Univ.

**INTRODUCTION:** Subcriticality monitoring system has to be used to detect criticality approach for each step of debris removal in Fukushima Daiichi nuclear power plant. For this purpose, International Research Institute for nuclear Decommissioning (IRID) is developing criticality control techniques for fuel debris removal based on neutron noise analysis using Feynman-alpha method. A prototype of the sub-criticality monitoring system was tested to verify applicability on various sub-criticality measurement conditions.

For this measurement, a small neutron detector based on a SiC with boron coated film is one of the candidates at Fukushima because of its toughness against radiation exposure and low detection efficiency for gamma-ray. We are also developing a data transfer system from this SiC neutron detector to data acquisition system which is placed at outside of a reactor vessel by a specially designed optical fiber with high resistance against radiation. In this research, we used this new data transfer system which will be connected to a small neutron detector to measure subcriticality.

**EXPERIMENTS:** Experiment was carried out at KUCA solid moderated core, B-core, as shown in Fig.1 whose main fuel assembly was 2/8”p23EUEU with relatively hard neutron spectrum. This core was aimed to simulate widely spread fuel debris. The fuel coupon plates were sandwiched with polyethylene plates and assemblies were surrounded by polyethylene reflector to simulate water and some part of the core was assembled with graphite region to simulate less water region which might be appeared during fuel debris digging process. This core was in subcritical state whose k-eff was approximately 0.89 and in steady state with Cf-252 neutron source inserted in a fuel assembly. Data transfer system is illustrated in Fig.2. Boron-lined neutron detector was inserted in a periphery fuel region whose neutron detection analog signal was transfer pre-amplifier and then a data sender system by a co-axial cable. In the data sender system, analog signal was changed to optical digital signal and it was transferred to the data receiver system located at outside of the reactor room by a thin and long quartz optical fiber cable. Then digital data was changed to analog data in the data receiver system and finally neutron detection time whose time bin was 1 micro-second was transferred to PC by USB cable and stored in PC.

**DATA ANALYSIS:** Neutron detection time stamp data stored in PC were analyzed by the neutron noise analysis methods, Feynman-alpha method (shown in Fig.3) and

Rossi-alpha method.

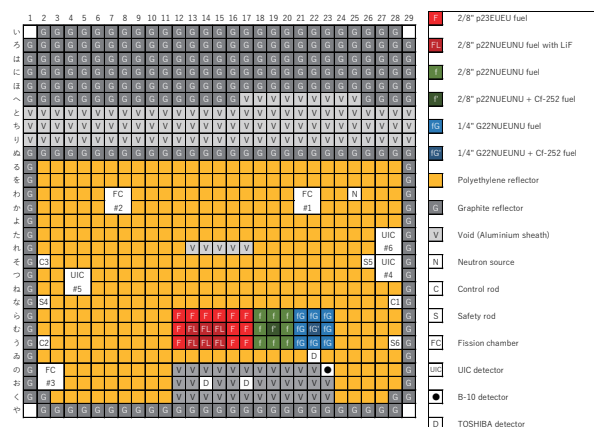


Fig.1 Core configuration of B-core.

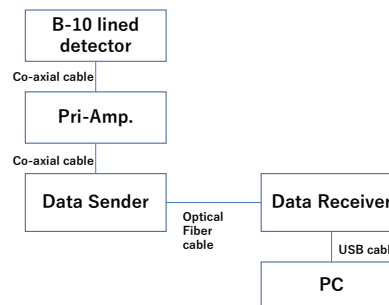


Fig.2 Data transfer system

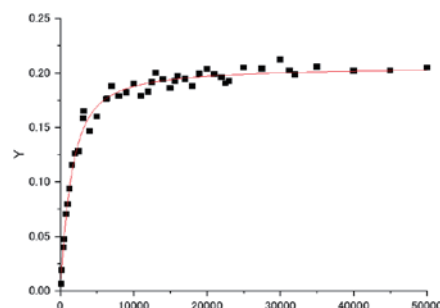


Fig.3 Example of Feynman-alpha result

**RESULTS:** As shown in Fig. 3, Y-values can be fitted by the theoretical formula (red line) and prompt neutron decay constant (alpha value) can be obtained by the least square fitting method. By Feynman-alpha and Rossi-alpha methods, alpha value was 1110+/- 44 (1/s) and 1250+/-24 (1/s), respectively, and we are now comparing those results with calculated ones by a computer code. We are planning to use this data transfer system combined with a SiC neutron detector next year.

Y. Yamane, S. Araki, Y. Kitamura<sup>1</sup>, T. Misawa<sup>1</sup>

Japan Atomic Energy Agency

<sup>1</sup>Institute for Integrated Radiation and Nuclear Science,  
Kyoto University

**INTRODUCTION:** The estimation of reactivity of an amount of unknown fissile material is one of important issues in the field of criticality safety.

JAEA has been theoretically developing a method to estimate the reactivity and composition of fissile isotope from neutron count rate alone[1-2]. The method is based on a newly developed equation of power in quasi-steady state after prompt jump/drop of power due to reactivity and/or neutron source change[3].

The purpose of the experiment is to obtain the experimental data for the verification and validation of the developed method. This time, a fixed intensity neutron source was used under shallow subcritical conditions, and an improved method which utilize the equation of power as it is, not its integral, was applied to the measured neutron count rate data.

**EXPERIMENTS:** A subcritical core was made by removing fuel elements from the basic critical core configuration known as 3/8" p36EU of A-core. The Am-Be was used as the external neutron source.

<sup>3</sup>He detectors were used. Figure 1 shows the core configuration and the position of Am-Be.

For the first several hundred seconds, as shown in Fig.2, the system was kept under steady state. Then the removing of Am-Be started. It takes several minutes but an air duct was used to rapidly terminate the effect of neutron injection to the core from Am-Be. After that, neutron count rate decreased and the measurement terminated after one or several thousand seconds. Another measurement was done under steady state for several thousand seconds in order to take data for Feynman- $\alpha$  method.

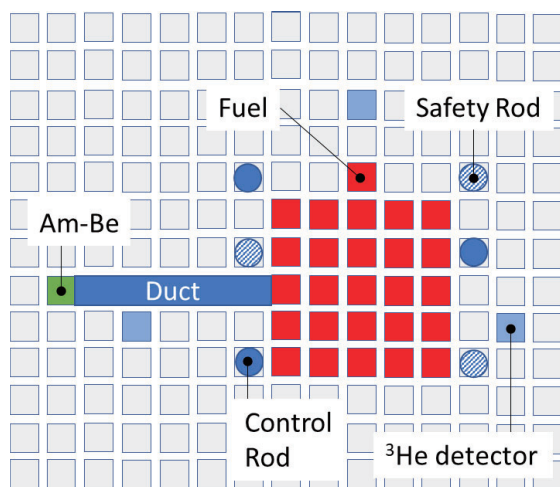


Fig. 1. Configuration of fuels and devices in A-core.

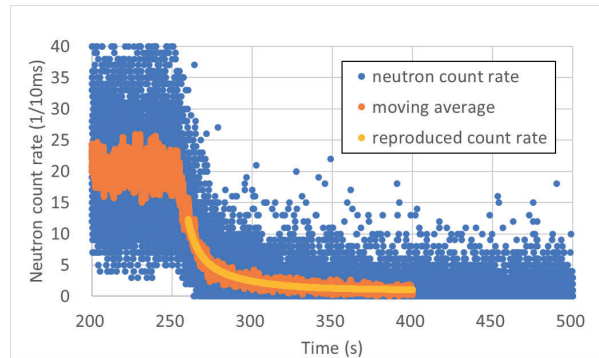


Fig. 2. Neutron count rate data. Blue circle shows neutron counts per 0.01s and orange line shows a profile of averaged neutron counts. Yellow line shows a reproduced count rate.

**RESULTS:** A preliminarily estimated value obtained by applying the new method to the neutron count rate data was plotted against data by Feynman- $\alpha$  method in Fig. 3, and the range of C/E was between 0.8 and 1.8. The reason for large difference may be that the neutron from slowly moving Am-Be kept the power of the core high for a while after the start of removing and changed the profile of neutron count rate from one without such effect. It is expected that more detailed analysis will make the reason clear.

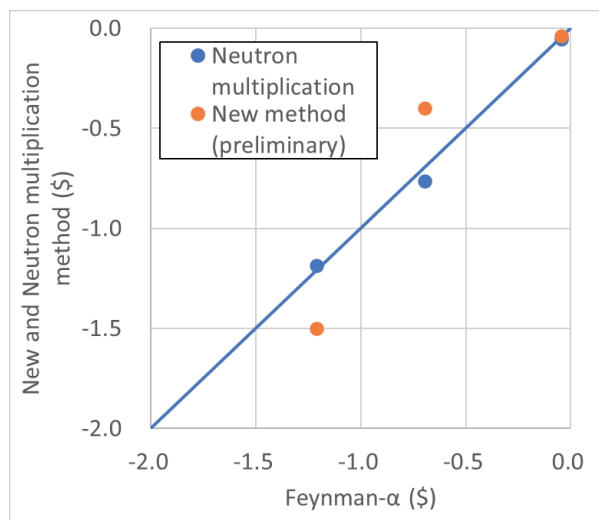


Fig 3. The reactivity estimated by applying new and neutron multiplication methods are plotted against that by Feynman- $\alpha$  method.

**REFERENCES:**

- [1] Y. Yamane, Proc. 2017 AESJ Spring meeting, 1F04, (2017) [in Japanese].
- [2] Y. Yamane, S. Araki, Y. Kitamura, T. Misawa, Proc. 2019 AESJ Spring meeting, 2J02, (2019) [in Japanese].
- [3] Y. Yamane, J. Nucl. Sci. Technol. <https://doi.org/10.1080/00223131.2020.1736682> (2020).

## CO3-10 Measurement of fundamental characteristics of nuclear reactor at KUCA (V)

Y. Kitamura<sup>1</sup>, T. Misawa<sup>1</sup>, X. Xiao<sup>2</sup> and Y. Hayashi<sup>3</sup>

<sup>1</sup>*Institute for Integrated Radiation and Nuclear Science, Kyoto University*

<sup>2</sup>*Department of Fundamental Energy Science, Graduate School of Energy Science, Kyoto University*

<sup>3</sup>*Toshiba Energy Systems & Solutions Corporation*

**INTRODUCTION:** We are developing a new signal transmitting/receiving devices. The reactor noise methods can measure the subcriticality through determination of the prompt neutron decay constant. Owing to a great amount of efforts devoted by many researchers, they are now regarded to be one of the most established methods. However, these methods still have one serious problem; the dead time effect that deteriorates the information from the neutron detector and disables the conventional theoretical formula. In 2014, Kitamura and Fukushima hence derived theoretical formulae of two major methods, i.e., Feynman- and Rossi-alpha ones by rigorously considering the dead time effect[1]. However, unfortunately, it was found that their formulae are too complicated to practically apply. Hence, in the present study, another technique for overcoming the dead time effect and its experimental investigation performed at the KUCA are reported.

**DEVICES:** In the Feynman-alpha method, neutron detection signals from the neutron detector arising within a certain length of the time interval, i.e., the gate width, are counted. By using thus obtained neutron counts, a correlation index  $Y$  is calculated to quantify the temporal fluctuations in neutron population in the subcritical multiplying system. The neutron counts with respect to various gate widths are further obtained to calculate the  $Y$  values as a function of the gate width, i.e., the Feynman-Y curve. This curve is fitted by the theoretical formula of the Feynman-alpha method to infer the prompt neutron decay constant. However, under high counting-rate conditions, the  $Y$  values with respect to shorter gate widths take negative values as shown in Fig. 1. Owing to this fact, the prompt neutron decay constant inferred under such conditions is biased.

In Fig. 2, a couple of neutron detection signals (red and blue dashed lines) overlapping with each other are shown. In the conventional technique, these signals are regarded to be one signal. On the other hand, in the present technique, before counting the neutron detection signals, the overlapped signals (yellow dots) are resolved. To realize such an analysis, in the present technique, a row signal wave-form recording system is introduced.

**EXPERIMENTALS:** The devices we are developing were examined at the B core of KUCA. The core configuration is given in Fig. 2. The signals from B-10 detector

were read by a pre-amplifier and then fed into the transmitting device. These signals were transmitted to the receiving device through the optical fiber. The time-stamp data were recorded by a PC.

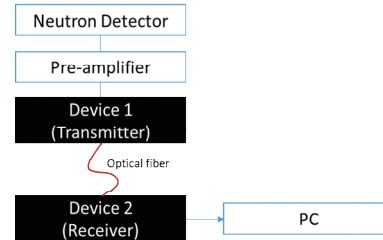
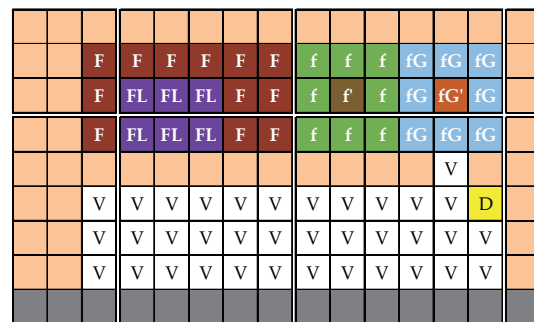


Fig. 1: Example of conventional Feynman-Y curve.



[F]: 2/8"p23EUEU fuel  
 [FL]: [F] including LiF  
 [f]: 2/8"p22NUEUNU fuel  
 [f']: [f] with Cf-252  
 [fG]: 1/4"G22NUENNU fuel  
 [fG']: [fG] with Cf-252  
 [D]: B-10 neutron detector  
 [V]: Void sheath

Fig. 2: Core configuration of B-core.

## CO3-11 Measurement of Neutronics Characteristics for Th loaded core at KUCA (II)

T. Sano, K. Nakajima<sup>1</sup>, J. Hori<sup>2</sup>, Y. Takahashi<sup>2</sup>, H. Yashima<sup>2</sup>, and H. Unesaki<sup>2</sup>

Atomic Energy Research Institute, Kindai University

<sup>1</sup>Graduate School of Science and Engineering, Kindai University

<sup>2</sup>Institute for Integrated Radiation and Nuclear Science, Kyoto University

**INTRODUCTION:** In order to perform integral evaluation of the <sup>232</sup>Th capture cross section, critical experiments with Th loaded various cores at KUCA has been carried out [1]. In those critical cores, the H/<sup>235</sup>U nuclide ratio were about 70 to 315 and the <sup>232</sup>Th/<sup>235</sup>U nuclide ratio were about 12.7 to 19.0. In this study, from the viewpoint of expanding critical experimental data, a new experiment was conducted by a Th fuel loaded core with 51 of H/<sup>235</sup>U and 19.0 of <sup>232</sup>Th/<sup>235</sup>U ratio at KUCA.

**EXPERIMENTS:** The new critical core consisted of two type fuel elements. One was Th loaded fuel element, and the other was driver fuel element shown in figure 1. A unit cell of Th loaded fuel element had 2 enriched uranium (EU) plates with 1/16" thickness, 1 Th plate with 1/8" thickness and 1 polyethylene plates with 1/8" thickness. The Th loaded fuel element consisted of 27 unit cells. A unit cell of driver fuel elements consisted of the 1 EU plate and the 2 polyethylene plates. The driver fuel element had of 49 unit cells.

Figure 2 shows the core configuration of the critical experiment. There were the 37 Th loaded fuel elements (F) and the 32 driver fuel elements (D). Table 1 shows the critical data of the core.

**RESULTS:** First of experiments, the neutronics characteristics of the Th loaded core was measured to check on the parameters are fallen within the KUCA regulations. Table 2 shows the measured neutronics characteristics. The all characteristics are satisfied with the KUCA regulations.

In order to observe an effective multiplication factor ( $k_{eff}$ ) of the core, the excess reactivity worth was measured by the positive reactor period method. As the seven-times-measured results, the evaluated excess reactivity worth was  $0.0826 \pm 0.0034$  (%dk/k) and the  $k_{eff}$  was  $1.00083 \pm 0.00003$  [2]. The calculated  $k_{eff}$  by MVP3.0[3] with JELDL-4.0[4] was  $1.00488 \pm 0.00002$  and C/E value was 1.0040 shown in Table 3.

### ACKNOWLEDGEMENT:

A part of the present study was supported by CHUBU Electric Power Co., Inc.

### REFERENCES:

- [1] T. Sano *et al.*, Proc on PHYSOR2020, Cambridge, UK, Mar.29<sup>th</sup> – April 2<sup>nd</sup>, (2020).
- [2] T. Sano *et al.*, Abstract of AESJ Spring meeting, 1I08, (2020).
- [3] Y. Nagaya *et al.*, JAERI1348, JAEA, (2005).
- [4] K. Shibata *et al.*, J. Nucl. Sci. Technol., 39(11), (2002).

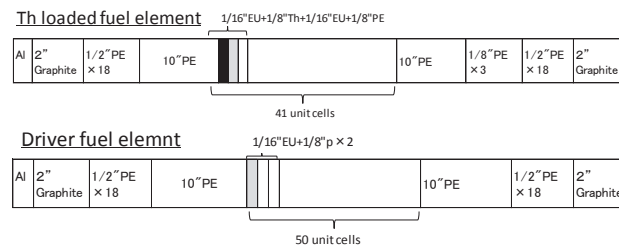
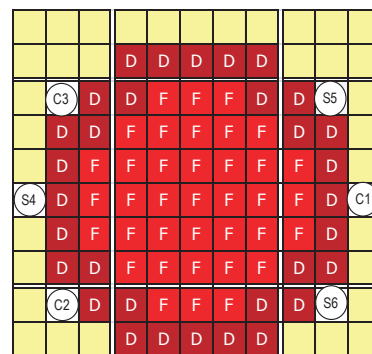


Fig. 1 Configuration of fuel element.



F: Th loaded fuel element, D: Driver Fuel element, C: Control Rod, S: Safety Rod

Fig. 2 Core configuration.

Table 1. Critical data of the Th loaded core.

Run No.		9855-1
No. of loaded EU plates		4634
No. of loaded Th plates		1517
Control Rod position (mm)	C1	723.14
	C2	1201.14
	C3	1201.37
	S4, S5, S6	1200
Core temperature (°C)		14.9

Table 2. Measured neutronics characteristics of the Th loaded core.

Neutronics Characteristics	Measured (%dk/k)	KUCA Regulation
Excess reactivity (%dk/k)	0.082	< 0.35 (%dk/k)
Rod worth (%dk/k)	C1 rod	Max. worth : < 1/3 of total worth
	C2 rod	
	C3 rod	
	Total*	(0.319+0.397+0.390)*2 = 2.212
Center core worth (%k/k)	2.329	> 1 (%dk/k)

\*S4, S5 and S6 rod worth are assumed same value as C1, C2 and C3 rods by symmetric geometry.

Table 3. Measured and calculated  $k_{eff}$ .

Measured	$1.00083 \pm 0.00003$
Calculated	$1.00488 \pm 0.00002$
C/E	$1.0040 \pm 0.003$ (%)

## CO4-1 Characterization of Additive in Lubricant using Small-Angle X-ray Scattering

Y. Oba, M. Hino<sup>1</sup>, R. Motokawa, N. Adachi<sup>2</sup>, Y. Todaka<sup>2</sup>, R. Inoue<sup>1</sup>, and M. Sugiyama<sup>1</sup>

Materials Sciences Research Center, Japan Atomic Energy Agency

<sup>1</sup>Institute for Integrated Radiation and Nuclear Science, Kyoto University

<sup>2</sup>Department of Mechanical Engineering, Graduate School of Engineering, Toyohashi University of Technology

**INTRODUCTION:** Lubricants usually contain a variety of additives to improve lubrication properties. In the lubricants, the additives form nanostructures such as micelles, which play a key role in lubrication properties. Small-angle scattering (SAS) is useful to characterize such nanostructures in solvent. However, SAS has been scarcely used in the field of tribology [1].

Therefore, we performed small-angle X-ray scattering (SAXS) measurements of the additives in the lubricants to determine proper experimental conditions and to obtain fundamental information needed for nanostructural analysis.

**EXPERIMENTS:** SAXS measurements were performed using the in-house SAXS instrument with Mo  $K\alpha$  radiation. Scattering patterns were obtained using a two-dimensional detector (PILATUS 100k) equipped with a 1000  $\mu\text{m}$ -thick silicon sensor. The path of X-ray between the entrance slit and up to the detector including the sample area was in vacuum to eliminate background scattering from air and vacuum windows. Oleic acid (OA) and oleyl acid phosphate (OLAP) were chosen as the additives. 1 mass% oleyl acid phosphate and 5 mass% oleic acid were dispersed in poly- $\alpha$ -olefin (PAO), respectively. The samples were sealed in sample cells made by stainless steel body, X-ray windows of cover glasses, and Viton O-rings. Two samples-to-detector distances (SDD), 0.4 and 1.8 m, were used to cover wide  $q$  range, where  $q$  is the magnitude of the scattering vector. The measurement times are 1 hour and 5 hours for 0.4 m and 1.8 m conditions, respectively.

**RESULTS:** Fig. 1 shows the SAXS profiles of 5 mass% OA in PAO, 1 mass% OLAP in PAO, and pure PAO. The scattering of an empty cell was subtracted as background. A peak is observed at around  $q = 4.5 \text{ nm}^{-1}$  in all the samples including pure PAO. This reflects the nanostructure in pure PAO. The profiles of the 5 mass% OA in PAO are almost similar to those of pure PAO.

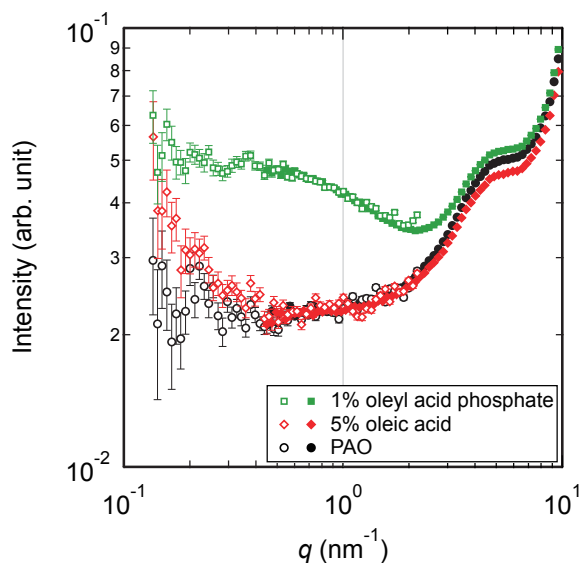


Fig. 1. SAXS profiles of 5 mass% OA in PAO, 1 mass% OLAP in PAO, and pure PAO. Open and filled symbols indicate the profiles obtained using SDD = 1.8 and 0.4 m, respectively.

Therefore, the scattering contrast of OA in PAO is probably too small to analyze. In contrast, 1 mass% OLAP in PAO shows a significant increase in the scattering intensity at  $q$  lower than about  $2.5 \text{ nm}^{-1}$ . This increase is the scattering of OLAP. The features of the scattering profiles are similar to the scattering profiles of tri- $n$ -butyl phosphate in organic solvent [2]. This suggests that OLAP forms aggregate in PAO. In summary, we successfully observed the nanostructure of OLAP in PAO. For OA in PAO, denser sample is required to obtain reasonable scattering intensity.

**ACKNOWLEDGMENTS:** A part of this work was supported by JST "Collaborative Research Based on Industrial Demand" Grand Number JPMJSK1511, Japan.

### REFERENCES:

- [1] M. J. Covitch *et al.*, *Adv. Chem. Eng. Sci.*, **5** (2015) 134-151.
- [2] R. Motokawa *et al.*, *J. Phys. Chem. B*, **116** (2012) 1319-1327.

## CO4-2 Synthesis of alloy nanoparticles in water solution by two steps reduction and one time $\gamma$ -ray irradiation

F. Hori, Y. Uchimura, T. Yamada<sup>1</sup>, T. Matsui<sup>1</sup>, N. Taguchi<sup>2</sup>, S. Tanaka<sup>2</sup> and Q. Xu<sup>3</sup>

Dept. of Engineering, Osaka Prefecture University

<sup>1</sup>Center for Advanced Education of Entrepreneurship and Innovation, Osaka Prefecture University

<sup>2</sup>AIST, Kansai Center

<sup>3</sup>Institute for Integrated Radiation and Nuclear Science, Kyoto University

**INTRODUCTION:** In general, it is known that metal nanoparticles (NPs) have some specific properties, which are not appeared in bulk materials such as catalytic activities, magnetic properties, electric conductivity and light absorption. These properties depend on its size, shape, structure, chemical composition and so on. They have many possibilities to applied for various industrial fields. However, it is not easy to fabricate multi elemental alloy NPs with controlling their size, shape and structure. Generally, many kinds of metal NPs commercially are synthesized by using chemical reaction method, which is not necessarily in water solution. Recent years, some reports show that it is possible to fabricate some metal NPs under irradiation reduction fields such as ultrasonic, solution plasma, electron beam, ion beam and gamma-ray [1]. We have been trying to synthesize various kinds of metal nanoparticles with size and shape controlled by gamma-ray irradiation reduction method. On the other hand, metal nanoparticles with high electronic conductivity is expected for the fields of printed electronics technologies as a metal nanoink. Cu is the high electronic conductivity and one of the most abundant resources on earth. However, the fabrication of Cu nanoparticle has a difficulty because its oxidation property. So far, we have successfully synthesized pure Cu nanoparticles in water by gamma-ray reduction method, but it was not stable. In this study, we have tried to synthesize Cu-Au alloy nanoparticles by two-step reduction with one gamma-ray irradiation.

### EXPERIMENTS:

Aqueous solution with a given concentration of copper complex ( $(\text{CH}_3\text{COO})_2\text{Cu}\cdot\text{H}_2\text{O}$ ) with an additive of sodium dodecyl sulfate (SDS) and 8.5 vol% ethylene glycol was prepared. The solution was argon gas purged and sealed into polystyrene vessels. They were irradiated at about 300 K with 1.17 and 1.33 MeV gamma-rays from  $^{60}\text{Co}$  radio active source at 4gamma irradiation facility in KURRI, Kyoto University. The total dose was fixed to 10 kGy with the dose rate of 1.0 kGy/h. After irradiation, a solution of 1.0 mM gold complex ( $\text{NaAuCl}_4\cdot 2\text{H}_2\text{O}$ ) was added with different ratios of Cu:Au=1:1, 4:1 and 9:1 in a nitrogen atmosphere. After irradiation, the samples were measured for UV-vis absorption spectra. The shapes and the

structures for all colloidal products were observed by TEM (JEM-2000FX and FEI-Titan) and energy dispersive X-ray spectrometry (EDS). X-ray Photoelectron Spectroscopy (XPS) measurement at KEK-PF BL-27 and X-ray diffraction have also performed.

### RESULTS:

Fig. 1 shows the light absorption spectra of each colloidal sample. After adding of the gold complex solutions, characteristic surface plasmonic absorption peaks of Cu and Au are observed. This result shows that gold ions are reduced in a Cu colloid fabricated by gamma-ray irradiation. Fig. 2 shows the XRD profiles for all samples. In this figure, it is confirmed that the formation of pure Cu, CuO, Au, Cu-Au compound and their solid solution. By analyzing of XPS results, it was found that reduced Cu ions have metallic combination in a particles. XRD result shows that after long period only in case of Cu:Au=9:1 pure Cu particles remains stable, but in another samples Cu and Cu alloys disappeared and only Au nanoparticles were survived.

### REFERENCES:

[1] N.Taguchi *et al.*, Rad. Phys. Chem., **78** (2009) 1049-1053.

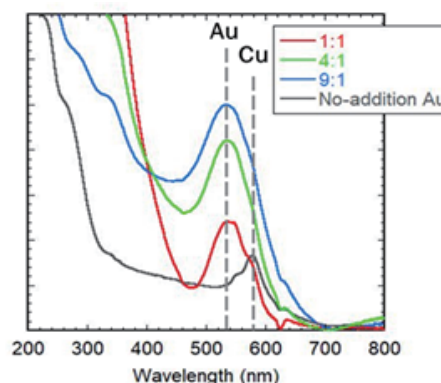


Fig.1. UV-vis spectra of gamma-ray irradiated samples.

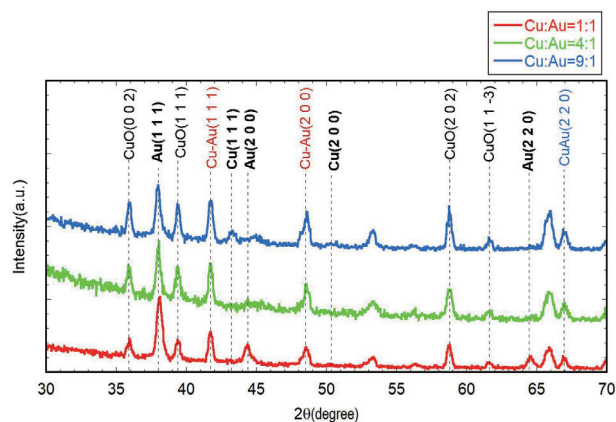


Fig. 2. XRD profiles of synthesized Au and Cu NPs by gamma-ray irradiation.

### CO4-3 Defects structure and characterization of electron irradiated intermetallic alloys

F. Hori, N. Ogawa, A. Takano, K. Sugita, T. Yamada, K. Ohsawa<sup>1</sup>, Q. Xu<sup>2</sup> and N. Abe<sup>2</sup>

*Dept. of Quantum & Radiation Eng., Osaka Pref. Univ.*

<sup>1</sup>*Res. Inst. of Appl. Mech., Kyushu University*

<sup>2</sup>*KURNS*

**INTRODUCTION:** In general, it is well known that intermetallic compounds has good properties such as specific strength to weight ratio, oxidation resistance and strength in elevated temperature. However, some of them arises degradation of fatigue strength caused by hydrogen embrittlement. The nature of their processes is not cleared yet. On the other hand, hydrogen is nowadays receiving a lot of attention for various kinds of materials research. It is important to clear the interaction between hydrogen and metallic materials for example hydrogen embrittlement, hydride formation and hydrogen induced transformation in hydrogen storage material. So far, we have been investigated the interaction between hydrogen atom and vacancies in B2 ordered intermetallic compounds. In that research, we found radiation induced hydrogen absorption by vacancies in B2 type of Fe-Al and Fe-Rh alloys. However, this effect is not confirmed for other type of intermetallic compounds. In this study, therefore, we have studied the interaction between hydrogen atom and vacancies in various type of intermetallic alloys, especially ZrCuAl intermetallic compound alloy.

**EXPERIMENTS:** Zr50%Cu40%Al10% alloy was prepared by arc melting method in argon gas atmosphere. Sliced samples with the thickness of 0.5 mm were annealed at 1073 K for 3 h. These specimens were irradiated with 8 MeV electron with water cooling system to the fluence of  $1 \times 10^{18}$  /cm<sup>2</sup> at KURRI, Kyoto University. Irradiation was carried out at about 330 K controlled. Cathodic charged hydrogen implantation have performed for before and after electron irradiated samples in a potassium hydroxide solution with a current of  $2.621 \times 10^3$  A/cm<sup>2</sup>. All samples were measured by X-ray diffraction and positron annihilation Doppler broadening measurements. Thermal desorption spectroscopy (TDS) measurement have done for

hydrogen implanted alloy samples annealing up to 600K with heating rate of 1 K/sec.

**RESULTS:** Figure 1 shows the XRD spectra of ZrCuAl alloy before irradiation, after electron irradiation and hydrogen charged after irradiation. In this alloy, irradiation induced phase transition and hydrogen induced new phase was not observed. Figure 2 shows the hydrogen desorption behavior from cathodic charged ZrCuAl alloys with and without electron irradiation. This figure clearly shows that hydrogen desorption behavior changes by electron irradiation. That is the desorption peak around 120 C disappeared and broad peak around 300–500 C appears instead. From these results, it found that metal hydride is not formed but hydrogen trapping by electron irradiation induced vacancies takes place.

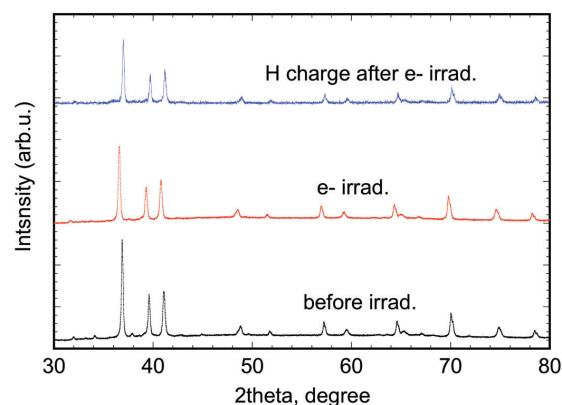


Fig. 1. XRD profiles of ZrCuAl alloy before irradiation, after electron irradiation and hydrogen charged after irradiation.

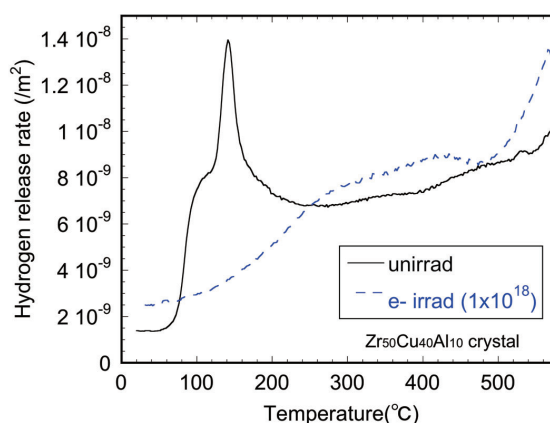


Fig. 2. TDS spectra of hydrogen desorption behavior for hydrogen charged ZrCuAl alloys with and without electron irradiation.

## CO4-4 Magnetic Scattering Contribution in Iron Characterized by Neutron Diffraction

Y. Oba, K. Mori<sup>1</sup>, M. Hino<sup>1</sup> and R. Okumura<sup>1</sup>

Materials Sciences Research Center, Japan Atomic Energy Agency

<sup>1</sup>Institute for Integrated Radiation and Nuclear Science, Kyoto University

**INTRODUCTION:** Magnetic scattering contribution is one of the most unique features of neutron diffraction and thus widely used for the investigation of magnetic structures. However, it is scarcely used in the research and development of practical ferromagnetic materials, such as permanent magnets and soft magnetic materials. Since the magnetic scattering analysis can provide the information about the directions of magnetic moments, it would be useful to understand magnetization process, which is a key to achieve higher permeability in the soft magnetic materials [1]. Therefore, we carried out the neutron diffraction experiments of the soft magnetic materials to confirm that the magnetic scattering contribution can be observed in the magnetization process.

**EXPERIMENTS:** An iron rod (99.9%) with the diameter of 12.7 mm was selected as a typical soft magnetic material. The neutron diffraction experiments were performed using the Versatile compact neutron diffractometer (VCND) at the B-3 beam port of the Kyoto University Research Reactor (KUR) [2,3]. An electromagnet was placed on a sample goniometer to apply a magnetic field to the sample (Fig. 1). The maximum field is about 300 Oe.

**RESULTS:** Fig. 2 shows the diffraction patterns of the iron rod and background. The iron rod shows clear Bragg peaks at 31° and 44° corresponding to (110) and (200) planes, respectively. Small peaks at 29°, 42°, and 50° come from the background caused by the electromagnet.

The diffraction pattern with a magnetic field is also shown in Fig. 2. The magnetic field was applied perpen-

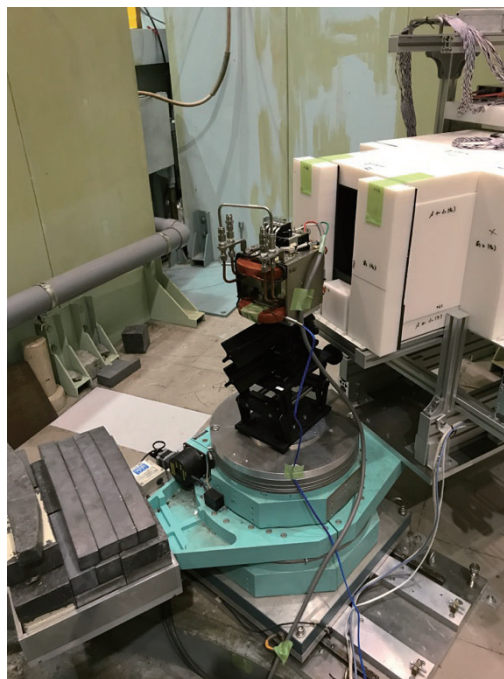


Fig. 1. Photograph of electromagnet installed at VCND. A magnetic field is vertically applied.

dicular to the scattering vector. In this condition, the magnetic scattering contribution must increase compared to a demagnetized state. The results indicate that the diffraction intensity with a magnetic field is higher than that without a magnetic field at the Bragg peaks, whereas the background intensity is not changed. This confirms that the magnetic scattering contribution can be observed in iron.

### REFERENCES:

- [1] M. Birsan *et al.*, Phys. Rev. B, **53** (1996) 6412-6417.
- [2] K. Mori *et al.*, KURNS Prog. Rep. 2018, (2019) 128.
- [3] K. Mori *et al.*, JPS Conf. Ser., (submitted).

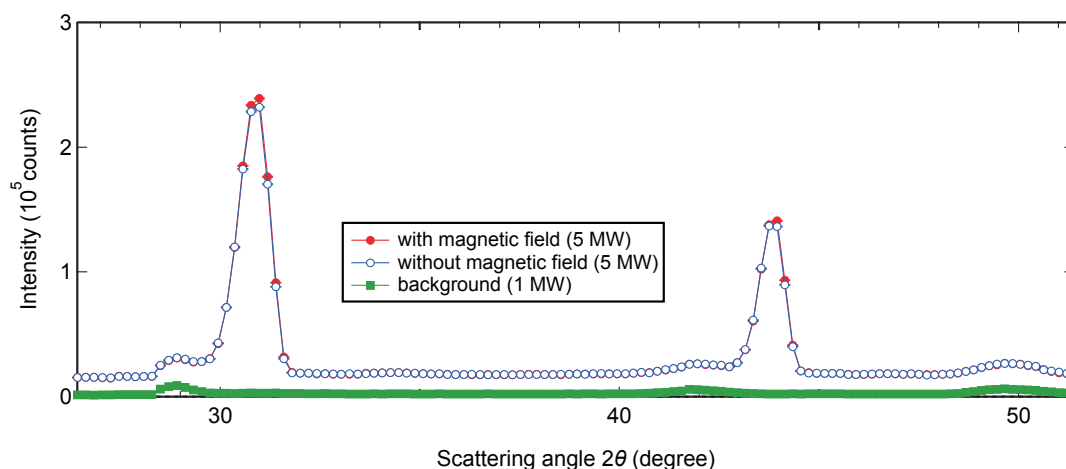


Fig. 2. Neutron diffraction patterns of iron and background. Filled and open circles denote the diffraction patterns of iron with and without a magnetic field, respectively. Filled squares is the diffraction patterns of background.

## CO4-5 What Exists in a 2-nm-sized Molecular Capsule Assembled in Water?

Y.-Y. Zhan<sup>1</sup>, N. Sato, K. Morishima, M. Sugiyama and S. Hiraoka<sup>1</sup>

*Institute for Integrated Radiation and Nuclear Science,  
Kyoto University*

<sup>1</sup>*Department of Basic Science, The University of Tokyo*

**INTRODUCTION:** Molecular capsules and cages provide a confined nano-space in which sensing, stabilization, activation, reaction, and catalysis can be realized based on the selective encapsulation of target molecules in their cavity. Previously, we developed cube-shaped molecular capsules (nanocubes), which are assembled from six gear-shaped amphiphiles (GSAs) in water.<sup>[1]</sup> One of the nanocubes, **BM**, shows high thermal<sup>[1-3]</sup> and kinetic<sup>[4]</sup> stabilities, though the GSAs are not connected by strong chemical bonds but only mesh each other. The **BM** nanocube has a 1-nm-sized hydrophobic cavity, in which various neutral and anionic species are encapsulated.<sup>[1,3,5]</sup> The thermodynamic parameters for the encapsulation of anions in the nanocube were previously determined by ITC measurements, and the encapsulation is enthalpically favorable but entropically unfavorable. However, to correctly interpret the thermodynamic parameters, it should be clarified what exist(s) in the cavity of the nanocube before the encapsulation. Considering that the **BM** GSA is a dicationic molecule with Cl<sup>-</sup> as counter anions, water molecules and/or Cl<sup>-</sup> anion(s) would be trapped in the nanocube. In this research, SAXS measurements of the **BM** nanocube with and without NaCl were carried out, which enabled us to discuss what exist in the cavity of the nanocube.

**EXPERIMENTS:** SAXS profiles were measured with a laboratory SAXS instrument (Rigaku NANOPIX) installed at Institute for Integrated Radiation and Nuclear Science, Kyoto University. X-ray wavelength was 1.54 Å and the typical sample-to-detector distance was 350 and 95 mm. A sample of the nanocube was prepared by dissolving solid sample of **BM** GSA in Milli-Q water. The concentration of the nanocube was determined by UV spectroscopy before the SAXS measurements of the nanocube in pure water and in 100 mM NaCl aqueous solution.

**RESULTS:** The SAXS profiles and the Guinier plots for the **BM** nanocube in pure water and in 100 mM NaCl solution are shown in Figure 1. In our previous study of the SAXS measurements, two prominent peaks were observed for the nanocubes, which suggests that a discrete structure is formed in water and that the discussion on the precise structure of the nanocube is possible based on the position and the intensity of the peaks. It was found that a similar SAXS profile was observed irrespective of whether NaCl (100 mM) is added or not but that the radius of gyration ( $R_g$ ) of the nanocube determined by the Guinier plot is largely affected by the salt.  $R_g$  of the nanocube in 100 mM NaCl is  $7.3 \pm 0.3$  Å, while that in

pure water is  $9.6 \pm 0.3$  Å. As the peak positions of the SAXS profiles of the two are almost same, the change in the  $R_g$  values with and without NaCl would arise from the difference in the environment of the cavity of the nanocube not from change in the size of the nanocube. Indeed, the simulation of the SAXS profiles by changing the size or the shape of the nanocube caused the shift of the prominent peaks, and the SAXS profile of the nanocube in 100 mM aq. NaCl could not be well reproduced by simulation. These results strongly suggest that Cl<sup>-</sup> anion(s) should be encapsulated in the nanocube in 100 mM aq. NaCl. In other words, the cavity of the nanocube in pure water should be filled with water molecules. Therefore, the encapsulation occurring in the **BM** nanocube can be described as the exchange of water molecules filled in the cavity with the guest molecule(s), so the release of unstabilized water molecules in the nanocube contributes to the encapsulation of anions.

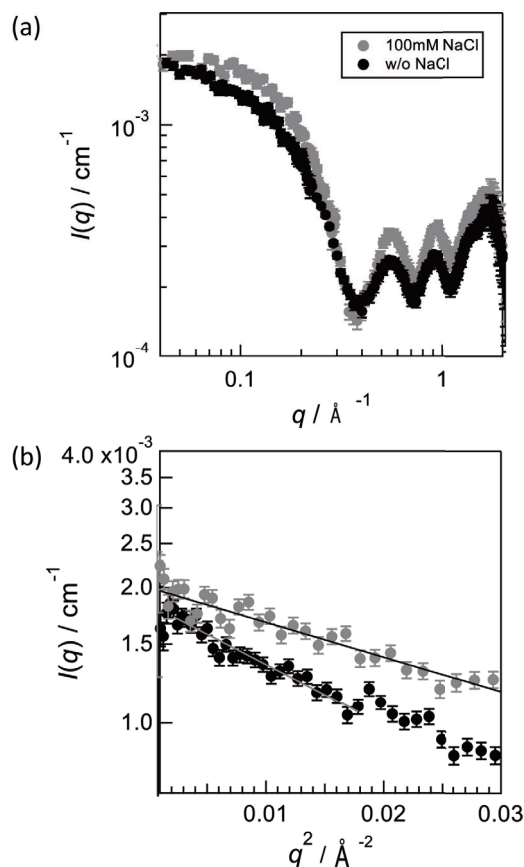


Fig. 1. (a) SAXS profiles of a solution of the **BM** nanocube in water with and without NaCl (100 mM). (b) The Guinier plots for the SAXS data.

### REFERENCES:

- [1] Y.-Y. Zhan *et al.*, *Commun. Chem.*, **1** (2018) 14.
- [2] Y.-Y. Zhan *et al.*, *Chem. Eur. J.*, **24** (2019) 9130–9135.
- [3] Y.-Y. Zhan *et al.*, *Nature Commun.*, **9** (2018) 4530.
- [4] Y.-Y. Zhan *et al.*, *Nature Commun.*, **10** (2019) 1414.
- [5] Y.-Y. Zhan *et al.*, *Commun. Chem.*, **2** (2019) 107.

I. Mukouda and Q. Xu<sup>1</sup>

*Hiroshima International University*

<sup>1</sup>*Institute for Integrated Radiation and Nuclear Science, Kyoto University*

**INTRODUCTION:** It is accumulated an attention that a damage structure in neutron irradiated metals differs if the temperature is varied during irradiation [1]. Especially effect of lower temperature irradiation on the development of damage structure in metals which are irradiated subsequently at higher temperature was reported to be remarkable because the point defects nucleate at lower temperature more frequently during an irradiation. Recently the temperature controlled irradiation devices were developed at KUR [2]. It becomes possible to irradiate continuously at two stage of temperature. In the present work, effects on damage formation in neutron-irradiated copper for the temperature variation were examined for an irradiation at low fluence regime.

**EXPERIMENTS:** Copper disks of 3mm in diameter were prepared with 99.999% nominal purity specimen. Before an irradiation, they were annealed for 5 hours at 1273 K in vacuum of  $10^{-5}$  Pa. Specimens were irradiated by fission neutrons in a temperature controlled irradiation device in KUR-SSS. In the previous temperature varying irradiation, specimens were irradiated at first at 473K and 573K. After a radiation cooling, they were observed by electron microscopy. A TEM observation was carried out using  $g = (002)$  reflection with  $(g, 5g)$  condition for the specimens of  $(110)$  configuration. Voids were observed in a bright field image by taking a slightly under focussed image. A triangular image was taken as stacking fault tetrahedra (SFT) and diffused dot image was tentatively taken to be an interstitial cluster.

Present temperature varying irradiation, specimens were irradiated at 473K-6hrs/573K-40hrs, 473K-23 hrs/573K-23 hrs and 473K-6 hrs/573K-20 hrs at 1MW. TEM observation are carried out recently.

**RESULTS:** In 473K-10hrs/573K-10hrs irradiation at 5MW, the number density of voids and SFT was smaller than those of constant temperature irradiation at 573K. Especially the decrease of number density of voids was significant [3]. shows dislocations in the specimen. Dislocations were not decorated by interstitial clusters. The number density of SFT was smaller than the value in copper which were irradiated at constant temperature of 573 K. Only one void was observed in specimens as in this picture, which means the formation of voids was suppressed significantly by the present temperature elevation irradiation.

Neutron-irradiated copper at 573K for 10 hours at 5MW, the dislocation structure show no decorated interstitial clusters around dislocation. Interstitial clusters, which

were accumulated along dislocation lines, were unified to grow to dislocations. This makes development of complicated structure of dislocations as reported by Mukouda and Shimomura [4].

The suppression of void formation in temperature-varied irradiation suggests that the nucleation of voids during a constant temperature irradiation at 573K in copper occurs during the period of dislocation decoration by interstitial clusters.

In 473K-6hrs/573K-40hrs irradiation at 1MW, the number density of voids and SFT was significant smaller than those of constant temperature irradiation at 573K as shown in Fig. 1. Only one void were observed. TEM observation of other irradiation condition specimens are progress at the present.

### REFERENCES:

- [1] N. Yoshida, Q. Xu, H. Watanabe, Y. Miyamoto and T. Muroga, *J. Nucl. Mater.*, 212-215 (1994) 471.
- [2] T. Yoshiie, *Annual Reports of KUR* (1998).
- [3] I. Mukouda and Q. Xu, *KURNS progress report 2018*, Co4-7.
- [4] I. Mukouda and Y. Shimomura, *Material Science & Engineering A309-310* (2001) 190-197.

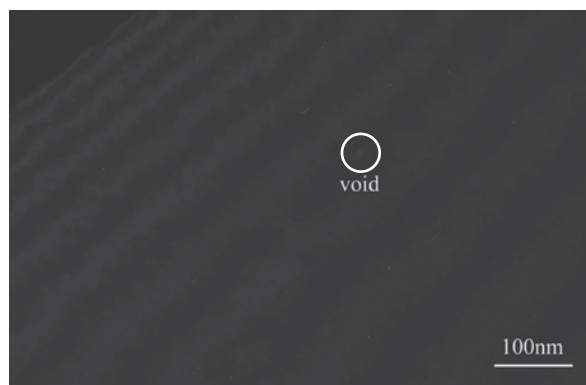


Fig. 1. Damages observed in neutron-irradiated copper with temperature varying schedule. The irradiation was carried out at first at 473K for 6 hours and subsequently at 573 K for 40 hours at 1MW.

Y. Iwashita<sup>1</sup>, M. Abe<sup>1</sup>, T. Yako<sup>1</sup>, T. Kurihara<sup>2</sup>, M. Fukuda<sup>2</sup>,  
M. Sato<sup>2</sup>, T. Sugimura<sup>2</sup>, Y. Iinuma<sup>3</sup>, Y. Fuwa<sup>4</sup>,  
Y. Kuriyama<sup>3</sup> and K. Takamiya<sup>3</sup>

<sup>1</sup>Institute for Chemical Research, Kyoto University

<sup>2</sup>Accelerator Laboratory, KEK

<sup>3</sup>Institute for Integrated Radiation and Nuclear Science,  
Kyoto University

<sup>4</sup>J-PARC Center, JAEA

**INTRODUCTION:** Permanent magnets are used as material of beam optical elements. While rare earth magnets, such as NeFeB and SmCo, are known to have radiation demagnetization [1], there is not enough information for ferrite magnets, which are economical but have less remanent field strength. In order to verify the resistivity of ferrite magnets, we carried out a trial experiment on radiation demagnetization of ferrite magnets irradiated by neutrons at Kyoto University Research Reactor (KUR).

**EXPERIMENTS:** We acquired cylindrical anisotropic ferrite magnets with 5 mm diameter and 2 mm length that have easy-axis parallel to the cylinder axis. They are popular off-the-shelf Y30H (Strontium Ferrite magnets). Since they seemed to have common non-uniformity on the easy-axis and they were randomly magnetized, they were re-magnetized to have better magnetic uniformity. We measured their magnetic field at both end surfaces with a Tesla meter (SENIS 3MH3) using a magnet fixture jig prepared for this experiment. The jig has a 0.5 mm thick plastic plate between the Hall probe and the magnet end surface to avoid a direct contact between them. Since the Hall probe measurement is sensitive to the positioning error of magnets, another measurement method was developed. This rotates the small magnet in a coil and the amplitude of the induced voltage is taken. This method is less sensitive to the positioning error.

The irradiation times were 46 hours at 1 MW operation and 6 hours at 5 MW operation (HYD), and 4 weeks (Long Term). In these two irradiation conditions, estimated values of thermal neutron fluence on the samples are  $5.7 \times 10^{18}$  [n/cm<sup>2</sup>] and  $8.6 \times 10^{18}$  [n/cm<sup>2</sup>], respectively. A permanent magnet samples packed in aluminum sheets was placed into a capsule together and sent to the reactor. After the residual radioactivity of the magnet and capsule decayed sufficiently, we took out the magnet samples from the capsule and measured the magnetic field. We compared the magnetic field strength before and after the irradiations.

**RESULTS:** Fig. 1 shows the ratios of the magnetic field strength before and after the irradiation. The error bars show the standard deviations of measured data for each magnet.

The broken vertical green line in Fig. 1 denotes neutron

dose at which radiation demagnetization becomes significant for NeFeB magnets [1]. Ferrite magnets were found to be more resistant to the radiation than NeFeB magnets. According to the data taken so far, the characteristic radiation demagnetization dose is estimated about  $1.4 \times 10^{20}$  [n/cm<sup>2</sup>]. Because of the regression function form, the data points at less radiations have almost no effect on the fitting result. The magnetization will be degraded to half at dose of about  $1 \times 10^{20}$  [n/cm<sup>2</sup>].

**PERSPECTIVES:** The radiation hardness level of ferrite magnets close to those for SmCo magnets is an important information for communities handling radiations. The ferrite magnets would be widely used in such applications.

More irradiation dose with improved magnetic field measurement procedure clarified the demagnetization as a function of the dose level. Measurements on other magnets such as NdFeB and SmCo magnets with the same procedure is planned for a systematic understanding on the radiation demagnetization on practical magnet materials.

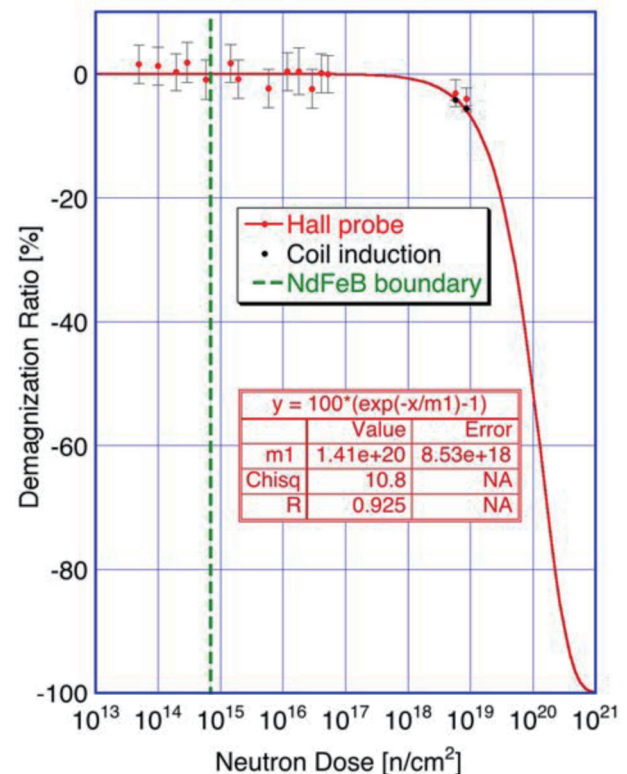


Fig. 1: Ratio of radiation demagnetization of ferrite permanent magnet.

**REFERENCES:**

[1] X. -M. Marechal, T. Bizen, Y. Asano, H. Kitamura, Proceedings of EPAC, Edinburgh, Scotland, 2006.

## CO4-8 Elucidation of the Mechanism of the Screw-sense Induction of Polymer Backbone Based on the Small Angle X-ray Scattering and Dynamic Light Scattering Measurements

Y. Nagata<sup>1</sup>, M. Sugimoto<sup>2</sup>, M. Sugiyama<sup>3</sup>, R. Inoue<sup>3</sup>, N. Sato<sup>3</sup>, and K. Morishima<sup>3</sup>

<sup>1</sup> Institute for Chemical Reaction Design and Discovery, Hokkaido University

<sup>2</sup> Graduate School of Engineering, Kyoto University

<sup>3</sup> Institute for Integrated Radiation and Nuclear Science, Kyoto University

**INTRODUCTION:** Increasing attention has focused on the structural control of helical polymers owing to their potential applications for asymmetric catalysts, chiral stationary phase, and chiroptical materials. Recently, we found that single-handed helical poly(quinoxaline-2,3-diyl)s (PQXs) bearing chiral side chains exhibit a solvent-dependent helix inversion,<sup>1-3</sup> which can serve as effective scaffold for chirality-switchable materials.<sup>4-7</sup> To elucidate the mechanism of the helix inversion of PQXs, we have investigated the detailed structures of a PQX (100mer) with right- or left-handed structures in tetrahydrofuran-*d*<sub>8</sub> (THF-*d*<sub>8</sub>) or a mixed solvent of 1,1,2-trichloroethane-*d*<sub>3</sub> (1,1,2-TCE-*d*<sub>3</sub>) and THF-*d*<sub>8</sub> (4/1, v/v) by using small-angle neutron scattering (SANS) experiments, in conjunction with theoretical calculations.<sup>8</sup> The obtained structures of the PQX suggested that the right-handed structure in THF-*d*<sub>8</sub> is well solvated, while the left-handed structure in 1,1,2-TCE-*d*<sub>3</sub>/THF-*d*<sub>8</sub> (4/1, v/v) is less solvated.

Our recent interest has focused on the impact of the dynamics of the side chains on the screw-sense induction. So far, we have carried out quasielastic neutron scattering (QENS) measurements to elucidate the impact of the molecular dynamics on the solvent-dependent helix inversion of the PQX at BL-02 DNA in J-PARC. In this study, we have carried out dynamic light scattering (DLS) measurements for the detailed analysis of the results of the QENS measurements.

**EXPERIMENTS:** A PQX bearing (*R*)-2-octyloxymethyl side chains (100mer) was prepared according to our previous paper. The light scattering measurements were carried out with a 22-mW He-Ne laser, an Avalanche Photo Diode (APD, ALV, Germany) mounted on static/dynamic compact goniometer, ALV/LSE-5003 electronics, and ALV-5000 Correlator (ALV-Laser Vertriebsgesellschaft GmbH, Langen, Germany). The measurements were performed at 313 K and CONTIN analysis was used to obtain the probability of decay rate at each  $Q$ .

**RESULTS:** The PQX was dissolved in THF-*d*<sub>8</sub> or a mixed solvent of 1,1,2-trichloroethane-*d*<sub>3</sub> (1,1,2-TCE-*d*<sub>3</sub>) and THF-*d*<sub>8</sub> (4/1, v/v), respectively, to carry out DLS measurements (Fig 1). In the both cases, the decay constant  $\Gamma$  and the square of the wave vector  $q^2$  showed linear relationship, affording the diffusion constants in these solvents. We are now working on the analysis of the

QENS measurements by using the results of the DLS measurements.

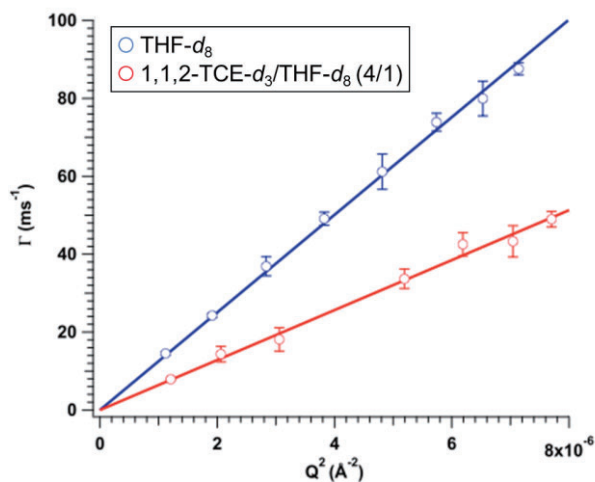


Fig. 1 Correlation between the decay constant  $\Gamma$  and the square of the wave vector  $q^2$ . The measurements were carried out using solutions of the PQX in THF-*d*<sub>8</sub> (blue) or a mixed solvent of 1,1,2-trichloroethane-*d*<sub>3</sub> (1,1,2-TCE-*d*<sub>3</sub>) and THF-*d*<sub>8</sub> (4/1, v/v, red).

### REFERENCES:

- (1) Yamada, T.; Nagata, Y.; Sugimoto, M. *Chem. Commun.* **2010**, *46*, 4914-4916.
- (2) Nagata, Y.; Yamada, T.; Adachi, T.; Akai, Y.; Yamamoto, T.; Sugimoto, M. *J. Am. Chem. Soc.* **2013**, *135*, 10104-10113.
- (3) Nagata, Y.; Nishikawa, T.; Sugimoto, M. *J. Am. Chem. Soc.* **2015**, *137*, 4070-4073.
- (4) Nagata, Y.; Nishikawa, T.; Sugimoto, M. *Chem. Commun.* **2012**, *48*, 11193-11195.
- (5) Nagata, Y.; Takagi, K.; Sugimoto, M. *J. Am. Chem. Soc.* **2014**, *136*, 9858-9861.
- (6) Nagata, Y.; Uno, M.; Sugimoto, M. *Angew. Chem. Int. Ed.* **2016**, *55*, 7126-7130.
- (7) Nishikawa, T.; Nagata, Y.; Sugimoto, M. *ACS Macro Lett.* **2017**, *6*, 431-435.
- (8) Nagata, Y.; Nishikawa, T.; Sugimoto, M.; Sato, S.; Sugiyama, M.; Porcar, L.; Martel, A.; Inoue, R.; Sato, N. *J. Am. Chem. Soc.* **2018**, *140*, 2722-2726.

K. Iwase and K. Mori<sup>1</sup>

Department of Materials Science and Engineering, Ibaraki University

<sup>1</sup>Institute for Integrated Radiation and Nuclear Science, Kyoto University

**INTRODUCTION:** Biomineralization, the process through which living organisms form mineralized tissues such as shell, bone, pearl, eggshell, exoskeleton, usually takes place at ambient temperature and pressure. The formed biominerals, nanocomposites made of inorganic and organic substances,[1,2] are renowned for their mechanical properties[3]. For example, the shell of *Strombus gigas* is formed of 99% of volume inorganic phase calcium carbonate with the aragonite structure and 1% of organic phase. The nacre in this shell is 3000 times tougher than single crystals of the pure mineral and has a “crossed lamellar microarchitecture”[4,5]. Calcium carbonate has three polymorphs: aragonite, calcite, and vaterite. Calcite is the thermodynamically most stable phase of calcium carbonate at ambient conditions, whereas aragonite and vaterite are less stable. The calcite phase is rhombohedral with space group  $R\bar{3}c$ , the aragonite phase is orthorhombic with the  $Pnma$  space group, and the vaterite phase has the  $P6_3/mmc$  space group.

In this study, we investigated the inner, and outer layers of Abalone shell (AWABI) by neutron diffraction

**EXPERIMENTS:** NPD data were collected by using the step-scan mode of a diffractometer (B-3) with 1.0294 Å wavelength. The powdered sample was sieved to a particle size of < 20 μm for the NPD measurements. The Abalone shell was measured as non-powder sample.

**RESULTS:** Fig. 1 shows neutron diffraction profiles of synthesized aragonite, synthesized calcite and Abalone shell (AWABI). The shell has two layers. The inner layer and outer layer are aragonite structure and calcite structure, respectively. The peak broadening was observed in aragonite and calcite of the Abalone shell.

Fig. 2 shows the Rietveld refinement of the Abalone shell. The shell consists of 82 mass % aragonite and 18 mass % calcite. The refined lattice parameters of aragonite phase of the Abalone shell were  $a = 0.5667(8)$  nm,  $b = 0.4962(6)$  nm and  $c = 0.791(1)$  nm, respectively. On the other hand, the refined lattice parameters of synthesized aragonite were  $a = 0.5736(4)$  nm,  $b = 0.4961(3)$  nm and  $c = 0.7960(5)$  nm. The aragonite phase of the Abalone shell expanded anisotropically along  $a$  and  $c$  axes from the synthesized aragonite. The calcite phase of the Abalone shell indicated lattice parameters  $a = 0.490(1)$  nm and  $c = 1.712(8)$  nm, which is smaller than that of the synthesized calcite,  $a = 0.4988(3)$  nm and  $c = 1.705(1)$  nm.

The lattice parameters of the Abalone shell are different from the synthesized sample. The Abalone shell has the anisotropic lattice strain both aragonite and calcite phases.

The mechanical properties of Abalone shell is superior to single crystals of the pure mineral [4,5], which may be relate to the anisotropic lattice expansion.

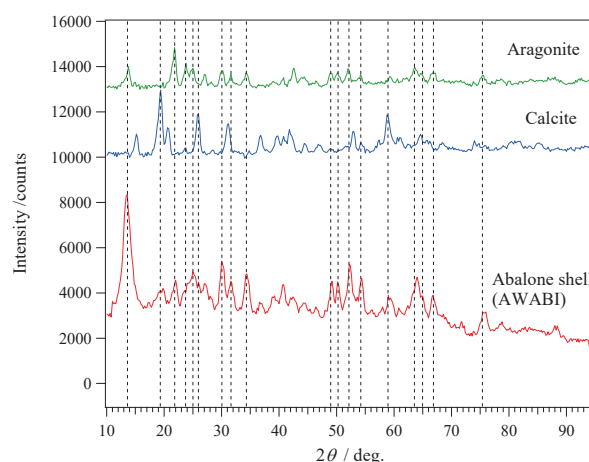


Fig. 1 Neutron diffraction profiles of synthesized aragonite, synthesized calcite and Abalone shell.

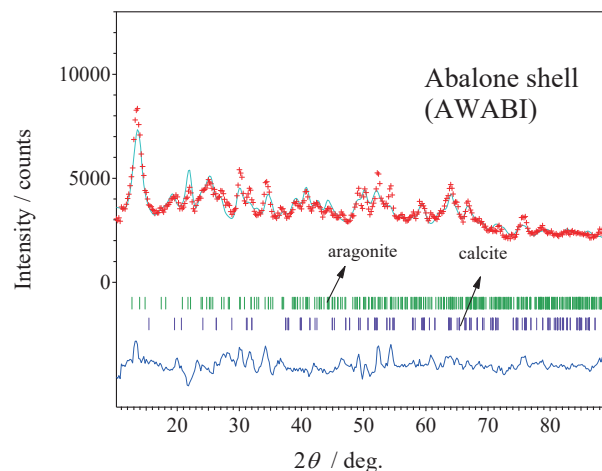


Fig. 2. Rietveld refinement pattern of Abalone shell.

#### REFERENCES:

- [1] Y. Dauphin, *Curr. Opin. Colloid Interface Sci.*, **7** (2002) 133-138.
- [2] Y. Dauphin, *et al.*, *J. Struct. Biol.*, **142** (2003) 72-280.
- [3] A. P. Jackson, *et al.*, *Proc. R. Soc. London, B* **234** (1988) 415-440.
- [4] S. Kamat, *et al.*, *Nature* **405** (2000) 1036-1040.
- [5] B. L. Smith, *et al.*, *Nature* **399** (1999) 761-763.

Y. Fujita, M. Seki, Y. Namekawa, K. Nishikata, K. Kato, N. Sayato, K. Tsuchiya, T. Sano<sup>1</sup>, Y. Fujihara<sup>2</sup>, J. Hori<sup>2</sup>, H. Yoshinaga<sup>2</sup>, J. Zhang<sup>2</sup>, T. Suzuki<sup>3</sup> and H. Suematsu<sup>3</sup>

Department of JMTR, Japan Atomic Energy Agency

<sup>1</sup> Atomic Energy Research Institute, Kindai University

<sup>2</sup> Institute for Integrated Radiation and Nuclear Science, Kyoto University

<sup>3</sup> Graduate School of Engineering, Nagaoka University of Technology

**INTRODUCTION:** The research and development (R&D) has been carried out for the production of Molybdenum-99 (<sup>99</sup>Mo) by the neutron activation method ((n,  $\gamma$ ) method) from viewpoints of limited availability of high-enriched uranium, no-proliferation and nuclear security, and disposal of nuclear fissile materials. It is essential to improve the properties of Alumina (Al<sub>2</sub>O<sub>3</sub>) used widely as Mo adsorbent for the <sup>99</sup>Mo/<sup>99m</sup>Tc generator.

In last year's study, four types of Al<sub>2</sub>O<sub>3</sub> specimens were prepared and their properties were evaluated by batch adsorption (Static adsorption) which immersed Al<sub>2</sub>O<sub>3</sub> specimens in the sodium molybdate solution (Mo solution). In this study, Mo was adsorbed by column adsorption (Dynamic adsorption) which packed Al<sub>2</sub>O<sub>3</sub> specimens in a tube and flown Mo solution in that. Then the elution test of Tc-99m was carried out.

**EXPERIMENTS:** The MoO<sub>3</sub> pellets were fabricated by the cold pressing and sintering method. Density of MoO<sub>3</sub> pellets was about 60%T.D. The MoO<sub>3</sub> pellet pieces (about 1.5g) were irradiated in the Pn-2 of the KUR for 20min. After the irradiation, the irradiated MoO<sub>3</sub> pellet pieces were dis-solved with 6M-NaOH solution. Then, the Mo adsorption tests of the Al<sub>2</sub>O<sub>3</sub> specimens were carried out with the Mo solution (10mg-Mo/mL, pH4) at RT. A column was prepared by packing 1g of each Al<sub>2</sub>O<sub>3</sub> specimens into a PFA tube (I.D. 1.59mm). <sup>99</sup>Mo was adsorbed by flowing in the column a Mo solution (0.3~0.4mL/min) using a peristaltic pump. After this process, the saline was flowed through in this column about every 24h and the <sup>99m</sup>Tc was eluted from each Al<sub>2</sub>O<sub>3</sub> specimens. The activities of <sup>99</sup>Mo and <sup>99m</sup>Tc in the solution were measured by the  $\gamma$ -ray spectrometer.

**RESULTS:** Table 1 shows the comparison results of <sup>99</sup>Mo adsorption capacity by each Al<sub>2</sub>O<sub>3</sub> specimen in dynamic adsorption and static adsorption. In dynamic adsorption, the Mo adsorption capacity was decreased as compared with that by the static adsorption. It seems that packing the Al<sub>2</sub>O<sub>3</sub> specimens into an elongated tube improved the washing efficiency and removed Mo weakly adsorbed on the Al<sub>2</sub>O<sub>3</sub> specimens, remaining in the column.

Table 2 shows the elution rate of <sup>99m</sup>Tc from the Al<sub>2</sub>O<sub>3</sub> specimens, the pH of the <sup>99m</sup>Tc eluate and the <sup>99</sup>Mo/<sup>99m</sup>Tc

ratio, which is an indicator of the <sup>99</sup>Mo contamination rate in the <sup>99m</sup>Tc eluate, on the first milking. As a result, the elution rate of <sup>99m</sup>Tc was over 100% at 1.5mL of milking in dynamic adsorption, while the elution rate was around 56-87% in static adsorption. It is thought that the elution efficiency was improved by filling Al<sub>2</sub>O<sub>3</sub> specimens into a long and thin tube, whereby the contact between saline and Al<sub>2</sub>O<sub>3</sub> specimens became uniform. The pH of the eluted <sup>99m</sup>Tc solution didn't depend on the method of adsorbing Mo, and satisfied the standard value of pH 4.5-7.0. This suggests that Al<sub>2</sub>O<sub>3</sub> specimens was sufficiently cleaned by either method. The <sup>99</sup>Mo/<sup>99m</sup>Tc ratio was greatly reduced in dynamic adsorption compared to that by static adsorption. Therefore, the <sup>99</sup>Mo/<sup>99m</sup>Tc ratio is greatly affected by the method of adsorbing Mo, which means the column shape and the linear flow rate during elution may affect that.

In the future, the effects of column diameter and linear flow rate on <sup>99m</sup>Tc elution and <sup>99</sup>Mo desorption will be investigated.

Table 1 Results of <sup>99</sup>Mo adsorption capacity of Al<sub>2</sub>O<sub>3</sub> specimens

Items	<sup>99</sup> Mo adsorption capacity (mg/g-Al <sub>2</sub> O <sub>3</sub> )	
	Dynamic	Static
Specimen-1 (D-201-300)	51.9	57.4
	48.7	55.4
Specimen-2 (V-V-300)	63.8	88.8
	27.0	39.0
Specimen-3 (V-B-300)	104.2	56.8
	56.8	50.6
Specimen-4 (Medical)	105.4	4.77
	79.5	4.50
Specimen-3 (V-B-300)	110.0	5.21
	68.4	4.69
Specimen-4 (Medical)	108.0	4.48
	86.6	4.41

Table 2 <sup>99m</sup>Tc elution rates from Al<sub>2</sub>O<sub>3</sub> specimens and the pH, the <sup>99</sup>Mo contamination of <sup>99m</sup>Tc solution in 1<sup>st</sup> milking

Items		<sup>99m</sup> Tc elution rates at 1.5mL in Milking (%)	pH of <sup>99m</sup> Tc solution*	<sup>99</sup> Mo contamination at 1.5mL in Milking
				[ <sup>99</sup> Mo/ <sup>99m</sup> Tc (%)]
Specimen-1 (D-201-300)	Dynamic	104.2	4.86	0.080
	Static	56.8	5.06	0.58
Specimen-2 (V-V-300)	Dynamic	105.4	4.77	0.500
	Static	79.5	4.50	3.46
Specimen-3 (V-B-300)	Dynamic	110.0	5.21	0.132
	Static	68.4	4.69	2.69
Specimen-4 (Medical)	Dynamic	108.0	4.48	1.108
	Static	86.6	4.41	8.77

\* in 4.5mL (Dynamic), in 9.0mL (Static)

### REFERENCES:

- [1] Y. Suzuki *et al.*, Transactions of the Materials Research Society of Japan, **43** (2018) 75-8.

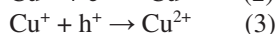
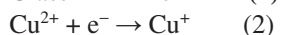
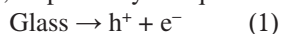
Y. Takada, R. Hashikawa, Y. Nishi, A. Kinomura<sup>1</sup>, T. Saito<sup>1</sup>, A. Okada<sup>2</sup>, T. Wakasugi<sup>2</sup>, K. Kadono<sup>2</sup>

Graduate School of Science and Technology,  
Kyoto Institute of Technology

<sup>1</sup>Institute for Integrated Radiation and Nuclear Science,  
Kyoto University

<sup>2</sup>Faculty of Materials Science and Engineering,  
Kyoto Institute of Technology.

**INTRODUCTION:** Radiophotoluminescence (RPL) is a luminescence phenomenon in a material induced by exposure to high-energy radiation. Silver-activated phosphate glasses are well known as a material exhibiting the RPL phenomenon, and these glasses are applied for a personal dosimeter [1]. However, only a few materials have been found to have a prominent RPL other than the silver-activated phosphate glasses. Thus, extensive exploration is performed to obtain materials having high performance RPL behavior. We have reported that in aluminoborosilicate glasses doped with an extremely low content of copper, intense photoluminescence is induced by the exposure of the glasses to X-ray and  $\gamma$ -ray irradiation [2]. The mechanism of the RPL phenomenon for the Cu-doped glass is considered to be as follows [2]: Copper in the glass mainly exists as divalent  $\text{Cu}^{2+}$  or monovalent  $\text{Cu}^+$  ions. The former,  $\text{Cu}^{2+}$  ion, has no luminescence while the latter,  $\text{Cu}^+$  ion, has a bright one around 500 nm by the excitation at 240 nm. When the glass doped with copper is exposed to high-energy radiation, electron and hole pairs are generated in the glass as expressed by (1) and a part of them are captured by  $\text{Cu}^{2+}$  and  $\text{Cu}^+$  ions, respectively as equations, (2) and (3).



When the electron capture process (2) is more predominant than the hole capture process (3), the concentration of the luminescence species,  $\text{Cu}^+$ , increases and as a result, the luminescence will increase.

We have investigated the RPL behaviors of copper in other glass systems. Here, we report the photoluminescence behaviors of Cu-doped silica glass that was prepared through the immersion of a porous silica glass in a  $\text{Cu}(\text{NO}_3)_2$  aqueous solution using the glass as a starting material [3].

**EXPERIMENTS:** The porous silica glass used as a starting material was prepared from a phase-separated borosilicate glass with a composition,  $9.0\text{Na}_2\text{O} \cdot 26.6\text{B}_2\text{O}_3 \cdot 64.4\text{SiO}_2$ . The porous silica glass was immersed in 0.0005 to 0.005 M  $\text{Cu}(\text{NO}_3)_2$  aqueous solution to dope copper into the porous silica glass. The Cu-doped porous silica glass was sintered at 900°C for 2 hours, and cut and optically polished to 1 mm thickness. The Cu-doped silica glass (abbreviated as Cu-SG, hereafter)

was exposed to  $\gamma$ -ray or X-ray radiations. The  $\gamma$ -ray irradiation experiments were performed with  $^{60}\text{Co}$   $\gamma$ -ray at the Co-60 Gamma-ray Irradiation Facility at Institute for Integrated Radiation and Nuclear Science, Kyoto University. The irradiation dose was represented as absorbed dose for water. The X-ray irradiation was performed using an X-ray source with a Rh target.

**RESULTS:** Figure 1 shows the photoluminescence spectra of the 0.0005 M-Cu-SG silica glass (prepared by the immersion in 0.0005 M  $\text{Cu}(\text{NO}_3)_2$  solution) measured before and after the  $\gamma$ -ray irradiation with the intensity of approximately 800 Gy and the appearance of the glass under the UV-radiation. The spectra and the appearance of the 0.005 mol% Cu-doped aluminoborosilicate glass (abbreviated as Cu-ABS25) was also shown for comparison. Both spectra after the irradiation are normalized with the intensity of the spectra before the irradiation, respectively. The photoluminescence intensity for the Cu-SG increased approximately two times by the irradiation (see the solid line arrow) while that for the Cu-ABS25 increased four times (dotted line arrow). The spectrum of the Cu-SG shifted to the longer wavelength direction after the irradiation and the color of the luminescence varied from blue to yellow. This is due to the difference in the coordination environment of the  $\text{Cu}^+$  generated by the electron capture from that of the  $\text{Cu}^+$  existing before the irradiation as the glass prepared.

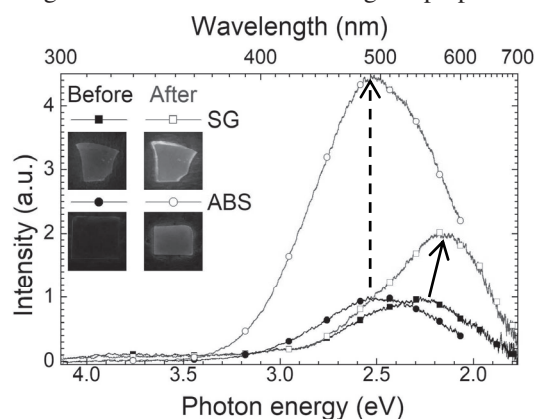


Fig. 1. Emission spectra of Cu-doped glasses (Cu-SG and Cu-ABS). The spectra were normalized with the peak intensities of the spectra before irradiation.

The intensity of photoluminescence after the irradiation was proportionally increased with the absorbed dose. The ratio of the intensities after and before the irradiation decreased with the concentration of copper incorporated into the glass.

#### REFERENCES:

- [1] R. Yokota, *et al.*, *J. Phys. Soc. Jpn.*, **23** (1966) 1038-1048.
- [2] H. Hashikawa, *et al.*, *J. Am. Cer. Soc.*, **102**(4) (2019) 1642-1651.
- [3] D. Chen, *et al.*, *Appl. Phys. Lett.*, **86** (2005) 231908.

## CO4-12 Study of resonant frequency change with irradiation dose of piezoelectric PZT element

M. Kobayashi, T. Miyachi, S. Takechi<sup>1</sup>, Y. Morita<sup>1</sup>, A. Umehara<sup>2</sup>, Reo Kunimatsu<sup>2</sup> and Ryo Sasaki<sup>2</sup>

*Planetary Exploration Research Center, Chiba Institute of Technology*

<sup>1</sup>*Graduate School of Engineering, Osaka City University*

<sup>2</sup>*Department of Engineering, Osaka City University*

**INTRODUCTION:** In the previous years, we have found that when irradiating high intensity heavy ions to a piezoelectric element (400 MeV/n Xe beam at HIMAC of the National Institute of Radiological Sciences [1][2]), its resonance frequency and anti-resonance frequency are shifted and also the impedance at the resonance frequency and anti-resonance frequency are changed by beam irradiation and then the electromechanical coupling coefficients of those piezoelectric elements were decreased.

There are two types of radiation damage to general materials, due to ionizing and non-ionizing dose effects (or displacement damage). Since the piezoelectric element is a crystalline material, it is considered that the crystal is damaged by the beam irradiation and thus the characteristic parameter such as the resonance frequency has changed. However, detailed mechanism such as its mechanism is not known.

Therefore, in this study, we investigated the response of the piezoelectricity against energetic electron beam irradiation which has dominantly ionizing effect (less non-ionizing effect) to compare with the previous results.

**EXPERIMENTS AND RESULTS:** In this year, we had two experiment campaigns for electron beam irradiation to piezoelectric PZT elements in KURRI-LINAC.

(1) *The first experiment on May 27 to 31 in 2019:* In the experiments up to the previous year, we found that the decrease in piezoelectricity due to electron irradiation was smaller than that due to xenon irradiation. Therefore, we devised an experiment setup to improve the quality of the experiment in order to have more quantitative discussion. The setup of irradiation target holder and positioning mechanism has been improved for more precise positioning against the electron beam because results were sometimes varied even if the beam condition was the same. As the results, the change of the electromechanical coupling coefficients of irradiated PZT targets against the current of electron beam became less variable.

We have monitored the temperature on the surface of the target piezoelectric elements which were cooled by forced air cooling during electron irradiation to the elements because the piezoelectricity can be lost or reduced by heat when the temperature becomes close to its Curie point. We estimated the internal temperature of the target piezoelectric elements with a thermal analysis taking into account of the forced air cooling and noticed that the internal temperature can be higher than the surface one. We performed how the piezoelectricity is reduced by temperature by using a thermostatic chamber and obtained a function of "piezoelectricity loss" of the piezoelectric element as temperature.

(2) *The second experiment on January 27 to 31 in 2020:* We performed the second electron irradiation experiment so that the internal temperature may not become over the point at which the piezoelectricity begins to be reduced, by monitoring the surface temperature of the target ones.

As the results, we could measure the net reduction in piezoelectricity due to electron beam irradiation. An experiment was conducted in which one specimen was irradiated with an electron beam for 15 hours or more, which we had never done previously because it was difficult to ensure the reproducibility of the experiment before this experiment.

We confirmed that the electromechanical coupling coefficient changes in the experiment of electron beam intensity, which is considered to be the effect of radiation only. For more better measurement, we used the other cable to connect the target piezoelectric with the measurement devices of impedance analyzer to exclude the effect of the capacitance of the cable and then we found that the measurement results vary depending on the cable attached to measure the piezoelectricity of the piezoelectric element. We will improve the situation in the future.

In this experiment campaign, we measured gamma rays emitted from radio-activated target piezoelectric material. That radioactivity may be produced by neutrons created by energetic electron. In order to determine the net effect of electron irradiation, we will evaluate the effect of radiation damage by neutron by analyzing the gamma ray spectra that we obtained in the experiments.

**SUMMARY AND FUTURE PROSPECTS:** In the experiments up to the previous year, we had difficulty to ensure reproducibility such as the alignment of the target with respect to the electron beam, but we were able to establish an experimental setup for high-precision measurement. As a result, we were able to specify a certain temperature point distinguish only the effects of radiation irradiation to piezoelectricity decrease. There is a problem with the cable for measurement, but we will solve the problem for experiments in the next experiment campaign for more further accurate measurements.

### REFERENCES:

- [1] M. Kobayashi *et al.*, Japanese Journal of Applied Physics 53, 066602 (2014).
- [2] M. Kobayashi *et al.*, Japanese Journal of Applied Physics 52, 126604 (2013).

## CO4-13 Formation of radiation defects on tungsten and their influence on effect of hydrogen isotope retention

K. Tokunaga, M. Matsuyama<sup>1</sup>, M. Hasegawa,  
K. Nakamura and Q. Xu<sup>2</sup>

*Research Institute for Applied Mechanics, Khushu University*

<sup>1</sup>*Hydrogen Isotope Research Center, University of Toyama*

<sup>2</sup>*Institute for Integrated Radiation and Nuclear Science, Kyoto University*

**INTRODUCTION:** It is of a great importance to clarify phenomena of implantation, retention, diffusion and permeation of tritium (T) on surface of the armor materials of the first wall/blanket and the divertor on fusion device from a viewpoint of precise control of fuel particles, reduction of tritium inventory and safe waste management of materials contaminated with tritium. Refractory metals such as tungsten (W) is potential candidate for the armor of the first wall and the divertor plate of the fusion reactor because of its low erosion yield and good thermal properties. The armor material will be subjected to heavy thermal loads in the steady state or transient mode combined with high energy neutron irradiation that will cause serious material degradation. In addition, high energy runaway electrons would bombard the armor materials along the equatorial plane in fusion device. It is considered that these cause radiation damage and enhance tritium retention. In the present works, T exposure experiments have been carried out on W samples which were irradiated by high energy electrons to investigate effects of high energy electrons irradiation on microstructure and tritium retention of W. In this fiscal year, pure W and recrystallized W were irradiated by high energy electron beam. Before and after that, positron annihilation experiment was carried out to identify the radiation defect. In addition, EBSD (Electron Back Scatter Diffraction Patterns) analyses has been carried out on the specimens before and after the electrons irradiation. Tritium exposure experiments have been carried out using a tritium (T) exposure device.

**EXPERIMENTS:** W samples used were ITER specification W (ALMT-grade) (SR-W) and its recrystallized W (RC-W). The SR-W was fabricated via a powder metallurgical route including cold isostatic pressing, sintering, hot rolling, and heat treating to relieve the residual stresses. Some of the machined SR specimens were subjected to a full recrystallization treatment at 2000 °C for 1 hr in vacuum. Sizes of the specimens were 10 mm x 10 mm x 1mm (10 mm x 10 mm : ND-TD). The surface of the both samples were polished to be mirrored. High energy electrons irradiation has been carried out using LINAC in Institute for Integrated Radiation and Nuclear Science, Kyoto University. An peak energy of electron irradiated was 8 MeV and DPA was  $5.8 \times 10^{-3}$ . Temperature during the irradiation was measured by thermocou-

ples which was contacted with a backside of the W samples. Before and after that, positron annihilation experiment was carried out to identify the radiation defect. In addition, EBSD (Electron Back Scatter Diffraction Patterns) analyses has been carried out on the specimens before and after the electrons irradiation. T exposure experiments have been carried out using a T exposure device in University of Toyama. Pressure of the T gas was 1.3 kPa and T exposure was kept for 4 h. T concentration in the gas was about 5 %. Temperatures of pre-heating and T exposures were 100 °C and 100 °C. After the exposure to T gas, T amount retained in surface layers of the sample was evaluated by  $\beta$ -ray-induced X-ray spectrometry (BIXS) and imaging plate (IP) measurements.

**RESULTS:** As shown in Fig. 1, mean lifetime from RC-W is smaller than that from SR-W. After the e irradiation, mean lifetime of both increases.  $\tau_1$  and  $\tau_2$  from the SR-W is bigger than that from RC-W. In addition,  $I_2$  from RC-W is bigger than that from SR-W. Because  $\tau_2$  of RC-W after the e irradiation is 266.1 ps, defects are considered to aggregate by temperature increase due to the irradiation.

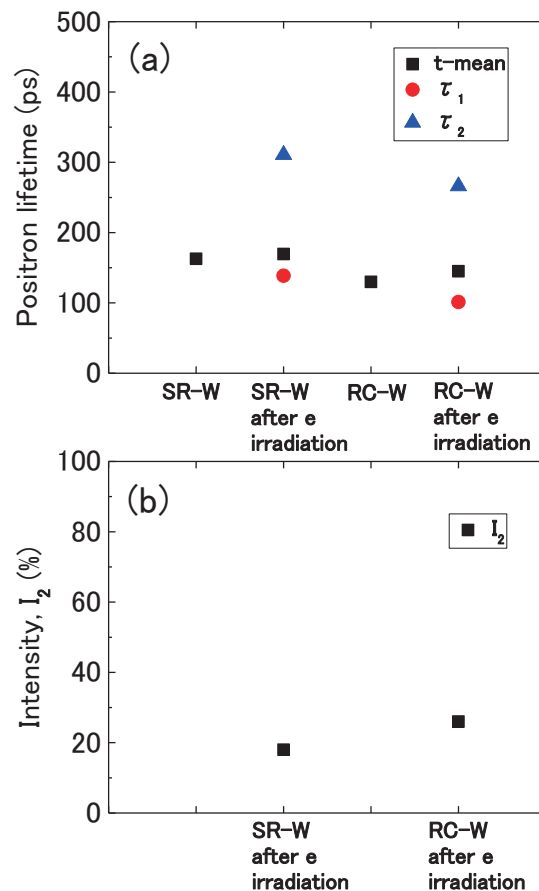


Fig. 1. Positron life time(a) and intensity of  $I_2$  (b).

K. Katayama, K. Kubo, K. Tsukahara, A. Ipponsugi, M. Oya, T. Takeishi<sup>1</sup>, S. Fukada, and Y. Inuma<sup>2</sup>

Department of Advanced Energy Engineering Science,  
Kyushu University

<sup>1</sup>Faculty of Engineering, Kyushu University

<sup>2</sup>Institute for Integrated Radiation and Nuclear  
Science, Kyoto University

**INTRODUCTION:** FLiNaBe, which is a mixed molten salt of  $\text{LiF}+\text{NaF}+\text{BeF}_2$ , is a promising liquid blanket material for a fusion reactor [1]. Tritium is produced in FLiNaBe by the nuclear reaction between neutrons and Li in the blanket. In the self-cooling system where the tritium breeding material itself transport heat to the heat exchanger, FLiNaBe plays two important roles of tritium transport and heat transport. Since FLiNaBe have a low solubility for hydrogen isotopes, the generated tritium tends to release from FLiNaBe. This property means that tritium can be easily recovered from FLiNaBe but also a part of tritium is lost to the outside of cooling tubes by the permeation on the way to the tritium recovery system. In order to control tritium safely and to design tritium recovery system, it is necessary to understand the fundamental behavior of tritium generated inside FLiNaBe by nuclear reaction. In this study, the solid state sample of FLiNaBe was irradiated by thermal neutrons at Kyoto University Research Reactor, and tritium release behavior from the free surface of FLiNaBe by heating was observed in Kyushu University.

**EXPERIMENTS:** In the powders of LiF, NaF and  $\text{BeF}_2$  were mixed in a Ni crucible under Ar atmosphere. The Ni crucible was put in the stainless-steel heating pot and repeatedly heated to 500 °C with Ar purging to remove impurity water vapor. The heating was repeated to homogenize the FLiNaBe. The prepared sample of FLiNaBe was packed into polyethylene bag with Ar gas and it was installed into a capsule. The thermal neutrons irradiation was performed by at pneumatic tube 2 (Pn-2) in Kyoto University Research Reactor with the fluence of at Pneumatic Tube 2 (Pn-2) of the  $1.7 \times 10^{15} \text{ cm}^{-2}$ .

Tritium release experiment was carried out in Kyushu University. The schematic illustration of experimental apparatus is shown in Fig.1 The irradiated sample was put in a Mo crucible and it was installed in the stainless-steel reaction tube. The sample was heated to 600 °C with Ar purge. The chemical form of tritium released from the sample was expected to be TF and HT ( $\text{T}_2$ ) and HTO ( $\text{T}_2\text{O}$ ). In this experiment, since HT and  $\text{T}_2$ , HTO and  $\text{T}_2\text{O}$  cannot be distinguished, here these are represented as HT and HTO, respectively. HTO was collected in a cold trap, which was a spiral copper tube immersed in ethanol with dry ice. TF was collected in a first water bubbler, and HT were collected in a second water bubbler after conversion to HTO by a CuO bed. The water of

each bubbler was sampled periodically to observe the changes with time in release rates of TF and HT. After the experiment was finished, the temperature was increased to room temperature and cumulative HTO in the cold trap was purged by Ar and it was collected in a new water bubbler.

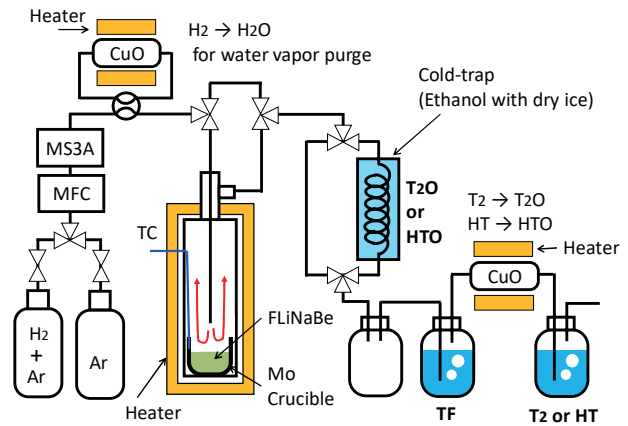


Fig.1. The schematic of experimental apparatus.

**RESULTS:** Fig.1 shows cumulative HT and TF released from neutron irradiated FLiNaBe in the initial heating to 600 °C. As shown in Fig.1, most tritium was released as HT. After cooling the temperature below the melting point, the heating at 700 °C was performed again. As a result, the release rate of TF gradually increased, and the rates of TF and HT reached the same degree. Initially tritium would be presence as TF in FLiNaBe but after melting TF was considered to react with Mo on the crucible and Fe on the reaction tube and converted to  $\text{T}_2$ . It can be said that as the fluoridation on the metal surface progressed, the reduction reaction of TF decreased, and the release rate of TF increased. This result suggests the possibility of redox control of TF by Mo. The release ratio of each chemical form was approximately TF: HT: HTO = 30:64:6. The majority of tritium was released as HT (or  $\text{T}_2$ ). This result indicates that corrosion of metals by TF occurred in tritium release process. In the next experiment, the effect of  $\text{H}_2$  purge on the suppression of corrosion will be investigated.

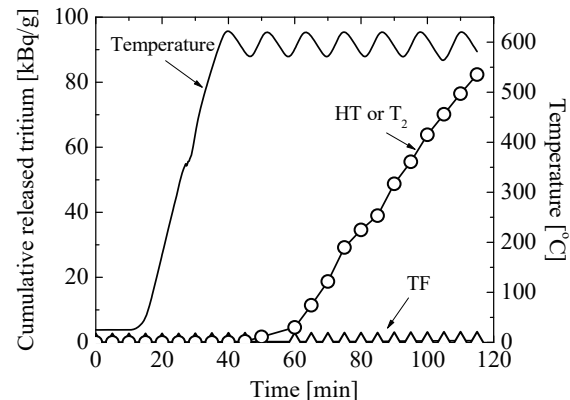


Fig.2. HT,  $\text{T}_2$  and TF release from irradiated FLiNaBe.

# CO4-15 Positron Age-Momentum Correlation Measurements of $\gamma$ -rays Irradited Polystyrene

H. Tsuchida<sup>1,2</sup>, S. Konishi<sup>2</sup>, Q. Xu<sup>3</sup>

<sup>1</sup>Quantum Science and Engineering Center, Kyoto University

<sup>2</sup>Department of Nuclear Engineering, Kyoto University

<sup>3</sup>Institute of Integrated Radiation and Nuclear Science, Kyoto University

**INTRODUCTION:** Studies on the irradiation-induced damage in polymers are of technical importance for developing radiation-resistance materials. In this work, we investigate microstructure changes of free volume in polystyrene induced by  $\gamma$ -rays irradiation at high dose. The free volume affects materials properties. The resultant damage was analyzed by the age-momentum correlation (AMOC) positron annihilation technique. The AMOC is a correlated measurement of the positron lifetime (positron age) and the momentum of the annihilating positron-electron pair. We study the radiation-induced damage near free volume of polystyrene via the annihilation processes of ortho-positronium (o-Ps).

**EXPERIMENTS:** The experiments were performed at the Co-60  $\gamma$ -rays irradiation facility of KURNS. Polystyrene was used as a target specimen. The specimens with a thickness of 2-mm were irradiated with Co-60  $\gamma$ -rays with energies of 1.17 and 1.33 MeV at various doses of 30, 200, 300 and 400 kGy. The irradiation experiments were performed at room temperature. The dose rate was 10 kGy/h. In the specimens after irradiation, we analyzed the resultant damage using  $\beta^+ - \gamma$  based AMOC measurement system with Ge-68 positron source.

**RESULTS:** Based on the observed AMOC spectrum, we obtained variation of S parameter as a function of positron age ( $t$ ), where S corresponds to the positron annihilation Doppler Broadening, which is defined as the ratio of the counts in the central position of the annihilation photopeak to the total counts in the peak. Figure 1 shows typical results. In this figure, S parameter at time region  $t = 0-3$  ns corresponds to annihilation of free positrons or para-positronium (p-Ps). S at  $t > 3$  ns corresponds to the pick-off annihilation of o-Ps formed in the free volume of polystyrene. The behavior strongly depends on the radiation dose, and the S parameter significantly decreases with increasing dose.

The S parameter of o-Ps is attributed to interactions of o-Ps with low-momentum electrons near free volume. We defined an average value of S parameter at time region  $3 \text{ ns} < t < 7 \text{ ns}$  as the S parameter for o-Ps pick-off annihilation. Figure 2 shows its dose dependence. One can see that the S parameter decreases with increasing  $\gamma$ -rays radiation dose. In this case, the measured lifetime of o-Ps annihilation ( $\tau_3 = 2.03 \text{ ns}$ ) remains unchanged after irradiation. We found that radiation damage near free volume

increases linearly with dose, and there is a clear correlation between the S parameter and  $\gamma$ -rays radiation dose.

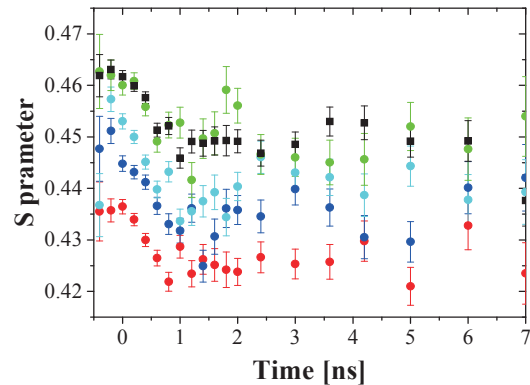


Fig. 1. Time dependent S-parameter of the o-Ps pick-off annihilation for before irradiation (■) and after Co-60  $\gamma$ -rays irradiation at different dose: 30 kGy (●), 200 kGy (●), 300 kGy (●), and 400 kGy (●).

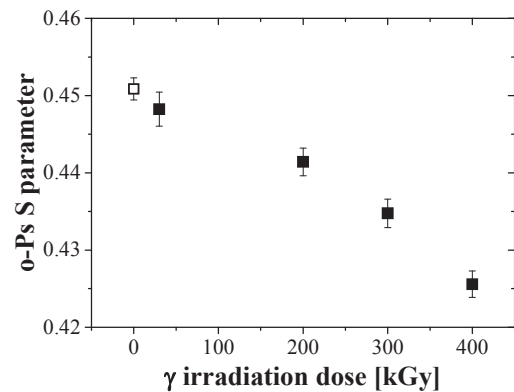


Fig. 2 Variation of S parameter for the o-Ps pick-off annihilation as a function of dose. The symbols denote data observed for before (□) and irradiated specimens (■).

J. Yanagisawa, R. Tsukamoto<sup>1</sup>, K. Ishihara, Q. Xu<sup>2</sup>, A. Yabuuchi<sup>2</sup>, K. Takamiya<sup>2</sup> and A. Kinomura<sup>2</sup>

*School of Engineering, The University of Shiga Prefecture*

<sup>1</sup>*Graduate School of Engineering, The University of Shiga Prefecture*

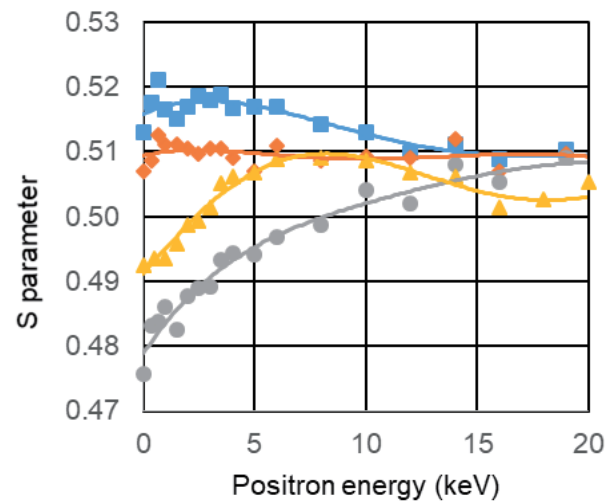
<sup>2</sup>*Institute for Integrated Radiation and Nuclear Science, Kyoto University*

**INTRODUCTION:** We have reported that the formation of swelled nano-porous structures can be formed on Ge surfaces by Ga, Au or Si ion irradiations at the energy of 100-200 keV, but no such structures were observed by 15-30 keV ion irradiations [1]. We have also observed the formation of nano structures on the 25-60 keV Ar<sup>+</sup>-irradiated areas of the Ge (110) surfaces, and the measurements of S parameters from the Doppler broadening of annihilation gamma-rays as a function of incident positron energy by the KUR slow positron beam system were performed [2]. The increases of the S parameters were observed for the ion-irradiated surfaces by the 25-50 keV Ar<sup>+</sup> with the ion fluences of 1-5 x 10<sup>16</sup> cm<sup>-2</sup>, showing the formation of atomic vacancies and/or voids on the ion-irradiated surfaces. On the other hand, we have found that nano-scale bumps on both Si and SiO<sub>2</sub> surfaces were formed by Ga<sup>+</sup> irradiation at an energy of 0.5 or 4 keV. In the present study, such Ga<sup>+</sup> irradiation was performed on Ge (110) surfaces and the S parameter was measured.

**EXPERIMENTS:** Ga<sup>+</sup> ion irradiation on the Ge (110) chip surfaces (each size of 1.5 x 1.5 cm<sup>2</sup>) was performed using a needle type liquid-metal ion source at the acceleration voltage of 0.5 or 4 kV with the ion fluence of 1 x

10<sup>14</sup> or 10<sup>15</sup> cm<sup>-2</sup>. S parameters were measured using the KUR slow positron beam system.

**RESULTS and DISCUSSION:** Figure 1 shows the three-dimensional atomic force microscope (AFM) images of the Ga<sup>+</sup>-irradiated surfaces. Figure 2 shows the S parameters as a function of positron energy for the corresponding samples as shown in Fig. 1. It is found that the behavior of the S parameter for the 0.5 keV, 1 x 10<sup>14</sup> cm<sup>-2</sup> Ar<sup>+</sup> irradiated surface was almost the same as that for the un-irradiated surface, although the values were unnaturally different each other. This can be supported from the similar AFM images, as shown in Figs. 1(a) and 1(d), although the density of the bumps was different. For the larger Ar<sup>+</sup> fluence and irradiation energy, however, the surface morphology was drastically changed, as shown in Figs. 1(b) and 1(c). This might be relevant to the drastic increase in the S parameters for them.



■ 0.5 keV, 1x10<sup>15</sup> cm<sup>-2</sup>, ◆ 4 keV, 1x10<sup>15</sup> cm<sup>-2</sup>  
▲ un-irradiated, ● 0.5 keV, 1x10<sup>14</sup> cm<sup>-2</sup>

Fig. 2. S parameters for low-energy Ga<sup>+</sup>-irradiated and un-irradiated Ge(110) surfaces as a function of positron energy.

**CONCLUSION:** Effect of the low-energy Ga ion irradiation on Ge (110) surfaces was studied using S parameters of the slow positron beam measurements. It is found that Ga<sup>+</sup> irradiation at lower energy (such as 0.5 keV) and lower fluence (1 x 10<sup>14</sup> cm<sup>-2</sup>) makes almost no effect on the formation of atomic vacancies and/or voids on the Ge surfaces.

#### REFERENCES:

- [1] J. Yanagisawa, K. Takarabe, K. Ogushi, K. Gamo and Y. Akasaka, *J. Phys.: Condens. Matter* **19** (2007) 445002 (10pp).
- [2] J. Yanagisawa, Q. Xu, A. Yabuuchi, K. Takamiya, and A. Kinomura, *KURNS Progress Report 2018* (Kyoto University), CO4-9 (30037).

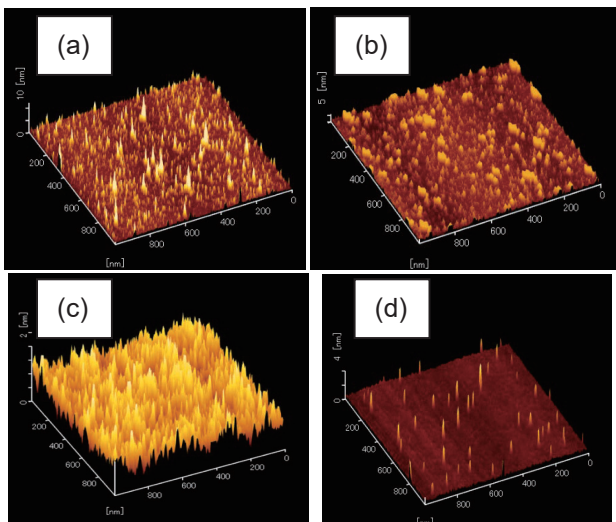


Fig. 1. AFM images of Ga<sup>+</sup>-irradiated (using ion energy and fluence of (a) 0.5 keV and 1x10<sup>14</sup> cm<sup>-2</sup>, (b) 0.5 keV and 1x10<sup>15</sup> cm<sup>-2</sup>, (c) 4 keV, 1x10<sup>15</sup> cm<sup>-2</sup>, respectively,) and (d) un-irradiated Ge(110) surfaces.

## CO4-17 Evaluation of Structural Vacancies in Icosahedral Cluster Solids using Positron Annihilation

J. Takahashi<sup>2</sup>, R. Nakajima<sup>3</sup>, K. Kitahara<sup>1</sup>, A. Yabuuchi<sup>3</sup>, N. Oshima<sup>4</sup>, I. Kanazawa<sup>2</sup>, A. Kinomura<sup>3</sup>, K. Kimura<sup>1</sup>

<sup>1</sup>*Department of Advanced Materials Science, The University of Tokyo*

<sup>2</sup>*Department of Physics, Tokyo Gakugei University*

<sup>3</sup>*Institute for Integrated Radiation and Nuclear Science, Kyoto University*

<sup>4</sup>*National Institute of Advanced Industrial Science and Technology (AIST)*

### INTRODUCTION:

The thermodynamically stable Al-based icosahedral quasicrystals, which contain transition metals, have the anomalous electrical-conductivities, such as semiconductor-like properties [1]. However, there is no evidence for a gap as in semiconductors, and the structure is highly ordered, although it is not periodic. Mayon et al.[2] proposed a possible explanation for the unusual transport properties of Al-based quasicrystals in terms of hopping processes between wave functions mainly localized inside icosahedral clusters. Kimura et al.[3] have discussed the importance of vacant centers of the icosahedral clusters in the anomalous transport properties and stabilities of Al-based quasicrystals. They have shown that 12-atoms Al icosahedra with a vacant center have a covalent bonding nature, while 13-atoms with a center atom have a metallic bonding nature. Kirihara et al.[4] performed an electron density distribution analysis for 1/1 AlReSi approximant crystal and 1/0 AlReSi approximant crystal by the MEM/Rietveld method, which induced metallic-covalent bonding conversion in Al-based quasicrystals and approximant crystals. Positron annihilation method is powerful one for detecting structural vacancies of icosahedral quasicrystals[5]. Recently Kimura and coworkers [6] have done positron annihilation measurements of the positron lifetime, coincidence Doppler broadening(CDB), and depth profiling by slow positron beams for 1/1 AlReSi approximant crystals. They showed that 1/1 AlReSi approximant crystal has structural vacancies in the order of  $10^{-3}$ , which are identified to be center sites of the first shell of icosahedral clusters, and then found that the structural vacancy density of metallic 1/1 AlReSi with less Re is lower than that of non-metallic AlReSi with more Re. These results accelerate further investigation of the relationship between structure, bonding nature, and electrical properties for 1/1 AlReSi approximant crystals with different Re concentrations, leading to better understanding of physics behind quasicrystals and approximant crystals in terms of the proposed metallic-covalent bonding conversion which occurs according to the occupation and vacancy of the center sites of the Al icosahedral clusters. Tamura et al.[7] have measured the electrical-conductivities of AlPdRu quasicrystals, 2/1 AlPdRu approximant crystal, and 1/0 AlPdRu approximant crystal. They found very interesting results. That is, quasicrystal AlPdRu and 2/1 AlPdRu approximant crystal have non-metallic properties, while 1/0 AlPdRu approx-

imant crystal have metallic properties. It is of significance to investigate AlPdRu quasicrystal and, AlPdRu approximant crystals, from the standpoint of structural vacancy density. In this study, we have measured the Doppler broadening of quasicrystal AlPdRu, 2/1 approximant crystal AlPdRu, and 1/0 approximant crystal AlPdRu by the slow positron beam, and also measured coincidence Doppler broadening(CDB) of 2/1 approximant crystal AlPdRu and 1/0 approximant crystal AlPdRu.

### EXPERIMENTS and RESULTS:

By using the slow positron beam, we have estimated the change in S-parameter with positron-incident energies in 2/1 approximant crystal AlPdRu, and 1/0 approximant crystal AlPdRu. In the case of 1/0 approximant crystal, S-parameter increases from  $\sim 0$  to  $\sim 1$  keV. While, in the case of 2/1 approximant crystal AlPdRu, S-parameter increases remarkably from  $\sim 0$  to  $\sim 0.5$  keV. This means that the density of structural vacancies in 2/1 approximant crystal AlPdRu might be higher than that of 1/0 approximant crystal AlPdRu. These results are consistent with those of positron lifetimes of approximant crystals 2/1 AlPdRu and approximant crystals 1/0 AlPdRu by slow positron beams (unpublished data). Furthermore, the present results seem to be reasonable from the standpoint of the metallic-covalent bonding conversion which occurs according to the occupation and vacancy of the center sites of the Al icosahedral clusters. Unfortunately, we could not prepare the sample of AlPdRu quasicrystals. In order to investigate the relationship between structure, bonding nature, and electrical properties, in Al-based quasicrystals, positron annihilation measurements of AlPdRu quasicrystals have been required.

We have done the coincidence Doppler broadening spectra of 2/1 approximant crystal AlPdRu and 1/0 approximant crystal AlPdRu. To identify the positron trapping sites in 2/1 approximant crystal AlPdRu and 1/0 approximant crystal AlPdRu, the core electron momentum distribution of samples were measured by the coincidence Doppler broadening spectra. Experimental results suggest strongly that the trapping sites of 2/1 approximant crystal AlPdRu and 1/0 approximant crystal AlPdRu seem to be similar.

### REFERENCES:

- [1] K. Kimura and S. Takeuchi in Quasicrystals: The State of the Art, 2<sup>nd</sup> ed., D.P. Divincenzo and P.J. Steinhart eds., World Scientific, Singapore (1999) pp.325-309.
- [2] D. Mayou *et al.*, Phys. Rev. Lett. **70** (1993) 3915.
- [3] K. Kimura *et al.*, J. Solid State Chem. **133** (1997) 302.
- [4] K. Kirihara *et al.*, Phys. Rev. Lett. **85** (2000) 3468.
- [5] I. Kanazawa *et al.*, Phys. Rev. Lett. **79** (1997) 2269.
- [6] K. Yamada *et al.*, Philog. Mag. **98** (2018) 107.
- [7] R. Tamura *et al.*, J. Phys:Condens. Matter **11** (1999) 10343.

## CO4-18 Absorption Coefficient of Amino Acid in the Sub-THz region using CTR

T. Takahashi

*Institute for Integrated Radiation and Nuclear Science,  
Kyoto University*

**INTRODUCTION:** Coherent radiation emitted from a short bunch of relativistic electrons is useful as a bright light source in the THz-wave and millimeter wave regions for the spectroscopic purpose. Coherent transition radiation (CTR), which is emitted from a boundary between two media, is one of such a coherent light source. CTR is usually utilized as a non-polarized light source, because the electric vector of transition radiation (TR) emitted from a metallic screen is axially symmetric with respect to the trajectory of an electron beam. In this wavelength range, it is difficult to generate the circularly polarized light because of the property of the optical device. In my previous reports [1] the circularly polarized CTR using a pair of wire-grid radiators with the different polarization has been developed with a new idea. The significant point of my new technique is the use of linearly polarized CTR with the wire-grid radiator. With this technique the polarization degree is able to be controlled precisely. Circularly polarized light has been useful in the circular dichroism spectroscopy. Before using the light, spectra of some kinds of amino acid have been measured using linearly polarized CTR [2]. In this report absorption coefficients of them are compared.

**EXPERIMENTAL PROCEDURES:** The experiment was performed at the coherent radiation beamline [3] at the L-band linac of the Research Reactor Institute, Kyoto University. The energy, the width of the macro pulse, and the repetition rate of the electron beam were 42 MeV, 47 ns, and 60 Hz, respectively. The average current of the electron beam was 2.3  $\mu$ A.

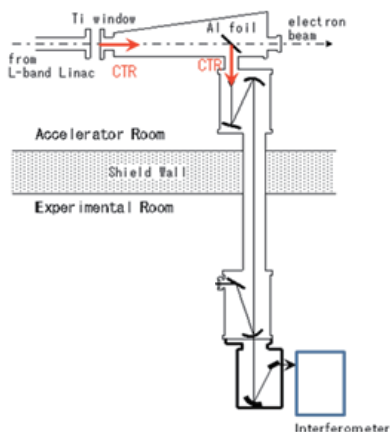


Fig.1 The schematic diagram of the experiment.

The spectrum of CTR was measured by a Martin-Puplett type interferometer and a liquid-helium-cooled Si bolometer. The schematic diagram of the experiment was shown in Fig.1. Figure 2 is the photograph of the spectrometer and the detector.

**RESULTS:** The thickness of these samples was 2 mm. Calculated absorption coefficient of  $\alpha$ -Alanine, Phenylalanine, and Tryptophan, are shown in Figs. 3. Difference between L and D forms has been observed. In order to investigate this discrepancy, it is necessary to measure using the circularly polarized light.

### REFERENCES:

- [1] T. Takahashi, *et al.*, KURRI-PR 2015 CO4-7.
- [2] T. Takahashi, *et al.*, KURRI-PR 2016 CO4-8.
- [3] T. Takahashi *et al.*, Rev. Sci. Instrum. **69** (1998) 3770.



Fig.2 The photograph around the spectrometer.

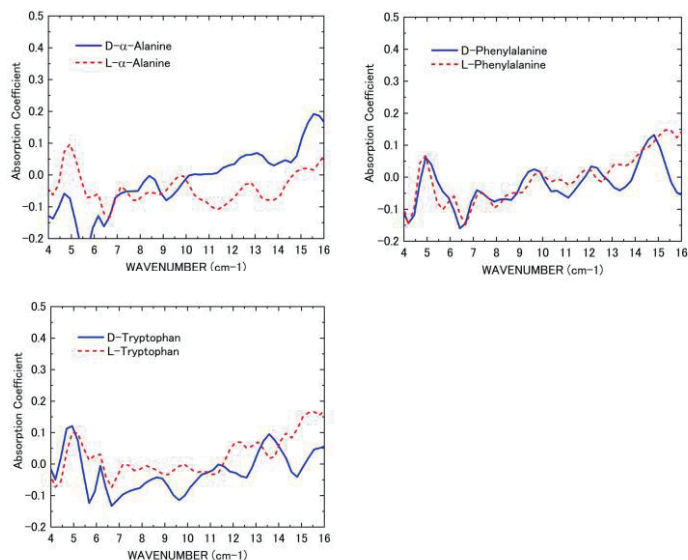


Fig.3 Absorption Coefficient of some kinds of amino acid.

## CO4-19 Vacancy migration behavior in CoCrFeMnNi high entropy alloys and their subsystems

K. Sugita, M. Mizuno, A. Yabuuchi<sup>1</sup>, A. Kinomura<sup>1</sup> and H. Araki  
Graduate School of Engineering, Osaka University  
<sup>1</sup>Institute for Integrated Radiation and Nuclear Science, Kyoto University

**INTRODUCTION:** Alloy design has traditionally been done by selecting the base material and adding the appropriate elements to achieve the desired properties. In the last decade, a new type of multicomponent alloy called "high entropy alloys" containing equiatomic / near-equiatomic ratios of constituent elements was proposed by Yeh et al [1-3]. These alloys often exhibit simple solid solution structures at high temperatures due to the high constituent entropy of random solid solution mixtures. High entropy alloys have been reported to have promising properties for practical use, such as high strength, high fracture toughness, excellent oxidation resistance and corrosion resistance combined with ductility. A major factor in these properties is thought to be the kinetics of "sluggish diffusion". Therefore, the diffusion kinetics of high entropy alloys has been actively studied by diffusion logarithms and tracer diffusion methods, as the atomic diffusion in a multiprincipal element matrix has also been of interest. In this work, we contribute to a debate about hypothetical sluggish diffusion phenomena in high entropy alloys by investigating the vacancy migration behavior in CoCrFeMnNi high entropy alloys and their subsystems during the isochronal annealing after electron-irradiation.

**EXPERIMENTS:** Vacuum induction melted ingots of CoCrFeMnNi, CoCrFe<sub>0.25</sub>MnNi, CoCrFeNi and CrFeNi alloys were purchased from Koujundo chemical laboratory (Japan). The ingots were homogenized at 1373K for 24 h in silica tubes under Ar atmosphere, and were then machined into 10 × 10 × 0.5 mm plate pieces by electric discharge machining. The alloy ingots were cut into square plate specimens with dimensions of 10 × 10 × 0.5 mm<sup>3</sup>. The specimens were subjected to strain relief annealing at 1373K for 10 h and then rapidly cooled to prevent secondary phase precipitation and to stabilize single-phase FCC structures. The specimens in water flow were exposed to 8 MeV electron beam irradiation for 3 h in KURNS-LINAC. The irradiation damage was evaluated at (1.3 - 1.8) × 10<sup>-4</sup> dpa. In order to investigate the thermal stability of vacancies, the electron irradiated specimens were subjected to the subsequent isochronal annealing at 373-673 K for 1 h.

Positron lifetime measurements were carried out by using a digital oscilloscope system with photomultiplier tubes mounted with BaF<sub>2</sub> scintillators, having a time resolution (FWHM) of 180 ps. The positron lifetime measurements require data acquisition for approximately 15 hours with

a Na-22 positron source of 0.5 MBq activity in order to acquire 3 million counts in the positron lifetime spectrum. The measured spectra were analyzed using the programs RESOLUTION and POSITRONFIT Extended.

**RESULTS:** The mean positron lifetime after isochronal annealing of the electron irradiated samples is shown in Fig.1. The positron lifetime spectra of as-irradiated samples show a clear separation into two exponential components of positrons with a long lifetime of 185-195 ps. This indicates that a part of positrons is trapped by monovacancies or relatively small vacancy clusters introduced by during the electron irradiation. After the subsequent isochronal annealing, the mean positron lifetime is found to decrease sharply around 473K. This can be attributed to the decrease in vacancy concentrations triggered by the free vacancy-migration. It demonstrates the vacancy migration enthalpy in the CoCrFeMnNi high entropy alloy is very similar to that in the CrFeNi alloy. These results indicate that the "sluggish diffusion" hypothesis is not supported in CoCrFeMnNi high entropy alloys and their subsystems at least in view of vacancy migration behavior.

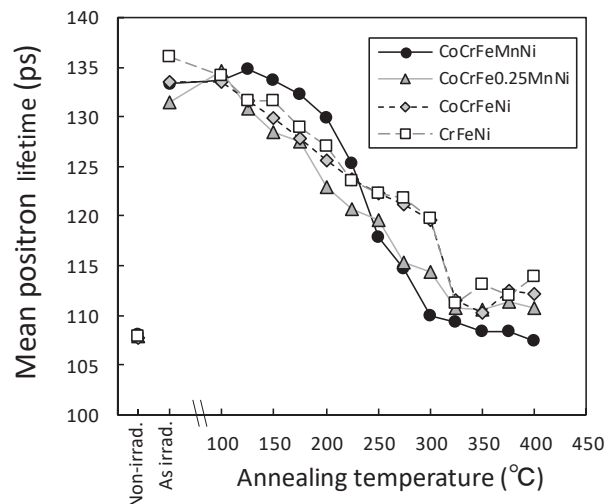


Fig. 1 Mean positron lifetime in the electron-irradiated CoCrFeMnNi, CoCrFe<sub>0.25</sub>MnNi, CoCrFeNi and CrFeNi alloys after isochronal annealing.

### REFERENCES:

- [1] C. Y. Hsu, J. W. Yeh, S. K. Chen and T. T. Shun, *Metall. Mater. Trans.*, **35A**(2004), 1465.
- [2] J. W. Yeh, S. K. Chen, S. J. Lin, J. Y. Gan, T. S. Chin, T. T. Shun, C. H. Tsau and S. Y. Chang, *Adv. Eng. Mater.*, **6** (2004). 299.
- [3] J. W. Yeh, *Ann. Chim. Sci. Mat.*, **31** (2006), 633.

## CO4-20 Observation of Gamma-ray Induced Current on Coaxial Cable for Analog Data Transfer

Y. Gotoh, Y. Okuno<sup>1</sup>, N. Sato<sup>2</sup>, M. Imaizumi<sup>3</sup>,  
T. Kobayashi<sup>4</sup>, M. Akiyoshi<sup>5</sup>, and T. Okamoto<sup>6</sup>

Graduate School of Engineering, Kyoto University

<sup>1</sup>Nuclear Science and Engineering Center, Japan Atomic Energy Agency

<sup>2</sup>Institute for Integrated Radiation and Nuclear Science, Kyoto University

<sup>3</sup>Research and Development Directorate, Japan Aerospace Exploration Agency

<sup>4</sup>Center for Advanced Photonics, RIKEN

<sup>5</sup>Radiation Research Center, Osaka Prefecture University

<sup>6</sup>National Institute of Technology, Kisarazu College

**INTRODUCTION:** In nuclear decommissioning of Fukushima Daiichi Nuclear Power Plant, observation of the inside of the primary containment vessel (PCV) is one of the key issues. For this purpose, many sensors including image sensor and radiation sensor have been under development [1, 2]. The data transfer from these devices put into the PCV should be made by cable, because radio wave cannot propagate out. The cable is also exposed to the radiation field, and therefore some currents would be induced by radiation. Such currents may cause an error in the sensor output. Therefore, it is important to know how large current would be induced at the cable, and to suppress the generation of the current. For this purpose, we have observed the current induced at a coaxial cable by gamma-ray irradiation.

**EXPERIMENTS:** The gamma-ray irradiation was performed at Co-60 gamma-ray irradiation facility at Institute for Integrated Radiation and Nuclear Science, Kyoto University. The coaxial cable examined in this study was 1.5D-QEV. A 15 m-long 1.5D-QEV cable was wound with a diameter of 20 cm. One end of the cable was connected to a coaxial cable of RG58A/U, which had been lain for taking the signal out of the irradiation room. The measurements of the current were performed with a compact pico-ammeter. Another end of the cable was terminated with a silicon diode installed in stainless steel can equipped with the connector of the coaxial cable. Use of the silicon diode was because it has similar structure with the solar cells, but it generates photocurrent only a little. For comparison, measurements were done with the cable with the end open. For both cases, the outer shield was grounded. Measurements were also made without grounding the outer shield of the cable. The cable was set at the position with different distance from the gamma-ray source. It was not easy to estimate the dose of irradiation to the cable accurately, the results were arranged with the dose rate at the center of the wound cable; the practical dose rate would be lower than this value.

**RESULTS:** Figure 1 shows the results of the observed currents as a function of the dose rate at the center of the wound cable. The data in Fig. 1 were acquired with the

grounded cable. When the one end of the cable was open, approximately -40 pA was observed at the position where the dose rate of irradiation was 200 Gy/h. When the end was terminated by a silicon diode, the current increased to about -110 pA at the same position. If the difference of these results was attributed to the generation of photocurrent of the diode including radiation excited one, the current should be shift towards positive. The reason for the difference has not yet been clarified. The slope at the lower dose rate region is steeper than that at the higher dose rate, and this would be attributed to the fact that the actual dose rate was lower than that at the center of the wound cable.

When the outer shield of the cable was not grounded, the observed currents showed positive value in most cases. It was also shown that the observed current had a gradual change. These phenomena would be due to the charging of the cable. The present study showed the fact that grounding the outer shield of the cable is important not only for the cancelling the electric noise but also for suppressing the radiation effects.

**ACKNOWLEDGEMENTS:** The present study was supported by “Development of Dosimeter in Harsh Core Radiation Environment”, through the Center of World Intelligence Project for Nuclear S&T and Human Resource Development by Japan Atomic Energy Agency.

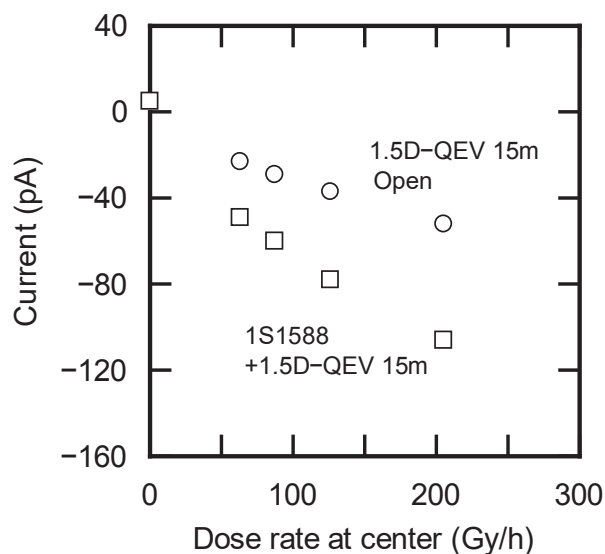


Fig. 1. Observed currents of the 1.5D-QEV cables under the gamma-ray irradiation.

### REFERENCES:

- [1] Y. Gotoh *et al.*, IEEE Trans. ED **67** (2020) 1660-1665.
- [2] T. Okamoto *et al.*, “Development of Dosimeter in Harsh Core Radiation Environment”, Workshop on Multicomponent Compounds and Solar Cells, Tokyo, November 30 – December 1, 2018.

## CO4-21 Correlation between Damage Accumulation by Neutron Irradiation and Hydrogen isotope Retention for Plasma Facing Materials

Y. Oya, M. Nakata, A. Koike, S. Yamazaki, T. Wada, M. Zhao<sup>1</sup>, F. Sun<sup>2</sup>, Q. Xu<sup>3</sup>, Y. Iinuma<sup>3</sup> and R. Okumura<sup>3</sup>

Graduate School of Integrated Science and Technology, Shizuoka University

<sup>1</sup>Graduate School of Science and Technology, Shizuoka University

<sup>2</sup>Faculty of Science, Shizuoka University

<sup>3</sup>Institute for Integrated Radiation and Nuclear Science, Kyoto University

**INTRODUCTION:** Due to the higher melting point and lower sputtering yield, tungsten (W) is considered as a candidate for plasma facing materials (PFMs) in the future fusion reactors. During the operation, W will be exposed to 14 MeV neutrons produced by D-T fusion reaction. The damages introduced by 14 MeV neutrons are considered to enhance hydrogen isotope retention compared to that for undamaged W. For the development of the effective fuel recycling and the safety operation, it is necessary to clarify the correlation between hydrogen isotope retention and damage level in W produced by neutron irradiation. In this study, irradiation damages were introduced by neutron and damage level was controlled by irradiation time, and the D retention behaviors were evaluated by thermal desorption spectroscopy (TDS). To evaluate the damage level by neutron irradiation, positron annihilation spectroscopy (PAS) was also performed.

**EXPERIMENTS:** A disk-type polycrystalline W (6 mm<sup>φ</sup>×0.5 mm<sup>l</sup>) purchased from A.L.M.T. Co. Ltd. was used. To remove impurities and damages introduced during the polishing processes, the samples were heat-treated at 1173 K under ultrahigh vacuum (< 10<sup>-6</sup> Pa). Thereafter, the samples were damaged with damage concentrations up to 4.6×10<sup>-6</sup> – 4.6×10<sup>-5</sup> dpa (displacement per atom) by the fission neutron irradiations under 323 K in Kyoto University Research Reactor Institute (KUR). After the damage irradiation, the 1.0 keV deuterium ion (D<sub>2</sub><sup>+</sup>) implantation was performed on the W sample at Shizuoka University. The D ion fluence was set to be 1.0 × 10<sup>22</sup> D<sup>+</sup> m<sup>-2</sup> with the ion flux of 1.0 × 10<sup>18</sup> D<sup>+</sup> m<sup>-2</sup> s<sup>-1</sup>. The D desorption behavior was evaluated by TDS at the temperature up to 1173 K with the heating rate of 0.5 K s<sup>-1</sup>.

**RESULTS AND DISCUSSION:** Fig. 1 shows D<sub>2</sub> TDS spectra for neutron damaged W samples and undamaged W sample. Positron lifetime of these samples are shown in Fig. 2. The D<sub>2</sub> TDS spectra were assumed to consist of four major D desorption stages located at 400 K, 550 K, 650 K and 850 K, respectively. Based on our previous studies, the D desorption stages were corresponded to the desorption of D adsorbed on the sample surface or trapped by dislocation loops, vacancies, vacancy clusters and voids, respectively [1]. In the neutron irradiated sam-

ple, D was adsorbed on the surface and/or trapped by dislocation loops and vacancies more than undamaged sample. Almost no D retention by vacancy clusters or voids were observed. These results were consistent with PAS results that long lifetime components which are considered as the existence of vacancy clusters or voids were not observed. In our previous report [1, 2, 3], the damages would suppress D diffusion according to the result of HIDT simulation. It was considered that the D diffusion was limited more for the sample irradiated up to damage level of 4.6×10<sup>-5</sup> dpa than that of 4.6×10<sup>-6</sup> dpa sample caused by the increase of vacancies by neutron irradiation. It was concluded D retention trapped by vacancies was increased with increasing the damage level.

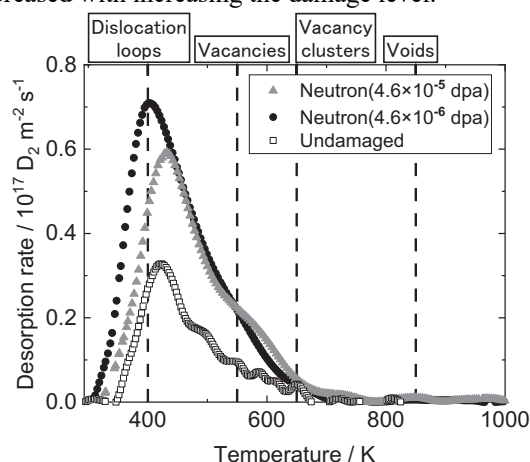


Fig. 1. D<sub>2</sub> spectra for neutron irradiated W and undamaged W.

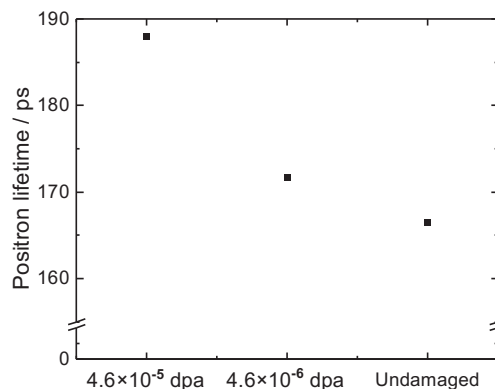


Fig. 2. Comparison of positron lifetime for neutron irradiated W and undamaged W.

### REFERENCES:

- [1] H. Fujita, K. Yuyama, X. Li, *et al*: Phys. Scr. **T167** (2016) 014068.
- [2] M. Nakata, K. Azuma, A. Togari, *et al*: Fusion Engineering and Design, **Volume 146, Part B**(2019) 2096-2099.
- [3] M. Nakata, A. Togari, F. Sun, *et al*: Fusion Science and Technology, Submitted.

A. Kawaguchi and Y. Morimoto

*Institute for Integrated Radiation and Nuclear Science,  
Kyoto University*

#### INTRODUCTION:

We have been investigating dynamical and interacted structures between iodine (polyiodide ions,  $I_n^{m-}$ ,  $m$ ,  $n$ : integer,  $n > 1$ ) and polymers.[1] While polyiodide ions (and their counter-ions, ex.  $K^+$  ion which presented within  $I_2$ -KI(aq)) are prepared as solutes in aqueous solution, they can be diffused into various polymeric matrix without softening nor melting. Such structures and procedures are expected to introduce novel functionality and wide applications to modify polymeric materials with easy operation at R.T.[2]

Or, ionic diffusion of polyiodide ions and their counter ions from aqueous solution of polyiodides ("1st iodine doping") can advance not only into hydrophilic polymers, such as polyamide-6 (PA6) or polyvinyl-alcohol (PVA), but also into hydrophobic polymers, such as polyethylene (PE) or polyethylene-terephthalate (PET); polyiodide ions in the aqueous solutions can easily diffuse even into *hydrophobic* matrices without melting.[3] Or, within some hydrophilic matrix, modification of structure (orientation of polymer chain, intercalated structure,,) can be also observed.

Furthermore, posterior ionic diffusion on the previous presence of polyiodides ("secondary doping") can also advances for both hydrophilic polymers and hydrophobic ones as ionic exchange process with the counter-ion previously introduced in "1st iodine doping". As phenomena, iodine-doped polymers can be regarded as "pseudo solvents" for ionic diffusion.[4,5] Inner precipitation of inorganic fillers can introduce hybrid composites without melting nor softening process for matrix and, occasionally, can be applied for electroless plating on hydrophobic surface with aqueous solution. Such unexpected behaviors of polymeric structures in existence of iodine (polyiodide ions) may be suggesting contradictive effects: activated diffusive environments (softening, plasticization, disordering in matrix,) vs. ordered structure (crystallization of crystalline polymer, precipitation of inorganic fillers, modified orientation of matrix).

On the other hand, structure of polyiodide ions can be also modified vaguely; they are able to change molecular structure and charge distribution not only in one molecule but between the polyiodide ions, cooperatively and interactively. Therefore, interactive dynamics and structure between polymers and iodine should be explained by extraordinary (also comprehensive and fundamental) schemes specified for polymeric structure and polyiodide ions.

#### DISCUSSION:

In the previously reported application utilizing "iodine doping" and following "secondary doping", the results mean activation of ionic diffusion in inner space of pol-

ymers. Characteristic and dynamic structure of the polyiodide ions show (almost general) affinity to both hydrophilic polymers and hydrophobic ones.

At first, we have to consider diffusion process of polyiodide ions into inner space of polymers, both for hydrophilic matrix and hydrophobic one while the polyiodide ions (and counter-ions) are solutes in aqueous solutions. Even though diameter of iodine atom is c.a. 4Å, they can be spontaneously diffused in polymeric matrix at room temperature; especially in some hydrophilic polymers (PA6, PVA,,), their diffusion is rapid and deep into the matrix. On the other hand, while iodine exist as mono-iodide ion ( $I^-$ ) or tri-iodide ion ( $I_3^-$ ) in each aqueous solution for "(1st) iodine doping" process, polyiodide ions doped and coordinated within polymers occasionally exist as  $I_3^-$  or tetra-iodide ion,  $I_5^-$ . It means that iodine elementally exists as polyiodide *ions* which have ionic charge and that counter ions ( $K^+$ ,  $Na^+$ ,  $NH_4^+$ , ,, ) also exist simultaneously; they do not exist as "not-charged" molecules, such as methanol.

Secondly, polyiodide ions which are doped and exist at inner space of polymeric matrix is *not* ones as molecules in the aqueous solutions prepared on "iodine doping"; even if  $I_3^-$  molecules exist in deep region of the matrices, they are *not* the similar molecules solved as the solutes in the solution for "iodine doping". Or, it should be remarked that  $I_5^-$  which is occasionally observed in coordination with polymeric matrix is very minor components in each aqueous solutions on "iodine doping";  $I_5^-$  molecules are not diffused from the solutions but *in situ* rearranged at inner space of matrix. It is not diffusion of unchanged molecules but diffusion of the molecules modified through diffusion. Since polyiodide ions can easily change their molecular structure and charge distribution, they can be diffuse as different structure from solute in the aqueous solutions and as efficient form for diffusion and binding. And it does not matter whether the coordinated form or molecular structure is different from the solutes in the doping solution or not. [to be continued]

**ACKNOWLEDGMENTS:** These results are researched with Dr. Gotoh (Shinshu Univ.) and his staff and are partially funded by NEDO.[6]

#### REFERENCES:

- [1] A. Kawaguchi, *Polymer*, **35**, 3797-3798 (1994).
- [2] patent. JPN-5444559 (2014).
- [3] A. Kawaguchi, *et.al.*, *KURRI Prog.Rep.*2015, 79-79. (2016).
- [4] A. Kawaguchi *et.al.*, *SPring-8 User Exp. Rep.* **5** (2000A), 354-354 (2000).
- [5] A.Kawaguchi, *Polym.Prep.Jpn.*, **62**,5116-5117 (2013).
- [6] "Projects for Practical Use from Innovation" sponsored by NEDO (2007-2009).

H. Ohashi, R. Takaku and T. Saito<sup>1</sup>

Faculty of Symbiotic Systems Science, Fukushima University

<sup>1</sup>Institute for Integrated Radiation and Nuclear Science, Kyoto University

**INTRODUCTION:** Pollucite which is one of cesium aluminosilicate compounds has attracted attention as a final storage material of <sup>137</sup>Cs. Pollucite is able to be synthesized by hydro-thermal method in low temperature below 300°C [1]. Pollucite has various properties that favor the immobilization of Cs ions.

However, the damage to the aluminosilicate framework by radiation decay is concerned because it contains <sup>137</sup>Cs. It has been reported that the effect of  $\beta$ -ray emission and nuclide conversion by  $\beta$ -decay of <sup>137</sup>Cs on aluminosilicate framework is minor [2, 3]. On the other hand, there are few reports of effects by gamma rays on pollucite framework. Therefore, we examined the effect of gamma radiation on the aluminosilicate framework of Pollucite. Pollucite samples were synthesized to investigate the effect of gamma irradiation.

**EXPERIMENTS:** The solution was prepared at the Al concentration of 50 mmol L<sup>-1</sup> and the composition ratio of Cs<sub>5</sub> Al<sub>1</sub> Si<sub>2</sub> O<sub>6</sub> Na<sub>10</sub> Cl<sub>11.2</sub> K<sub>2</sub> Ca<sub>0.2</sub> (OH)<sub>2.2</sub> (H<sub>2</sub>O)<sub>220</sub>, and placed in a Teflon inner cylinder pressure container. Pollucite was synthesized by hydrothermal method, holding the container at 180°C for 72 hours. The resulting precipitate was washed. Thereafter, each solid was collected by filtration and dried at 110°C for 16 hours or more.

The powder sample was divided into four, three of which were gamma-irradiated at 1, 10, and 100 kGy. Characterization was performed by XRD. The 7 days leaching test by PCT-A method [4] was carried out to evaluate the change of Cs retention performance by framework damage. The normalized release rate,  $NR_{Cs}$  [g m<sup>-2</sup> d<sup>-1</sup>], was calculated by equation (1).

$$NR_{Cs} = \frac{C_{Cs}}{f_{Cs} \frac{SA}{V} t} \quad (1)$$

Where  $C_{Cs}$  [g L<sup>-1</sup>] was the concentration of Cs in the solution,  $f_{Cs}$  was the weight ratio of the Cs in the sample before leaching,  $SA$  [m<sup>2</sup>] was the sample surface area,  $V$  [L] was the volume of the leaching liquid, and  $t$  [day] was the test duration.

**RESULTS:** Figure 1 shows the XRD patterns of Pollucite sample before and after gamma irradiation, and the diffraction peak of Pollucite was indicated by the Miller index. All the patterns showed that they contained

only single-phase pollucite. None of gamma irradiation sample did not shifted diffraction peaks compared to before irradiation one. This indicated that there was no change in the crystal structure of Pollucite.

Table 1 shows the various parameters obtained by the leaching test according to the PCT-A method, and the normalized release rate ( $NR_{Cs}$ ). In previous reports [5], the  $NR_{Cs}$  of Pollucite was around 10<sup>-5</sup> to 10<sup>-6</sup> [g m<sup>-2</sup> d<sup>-1</sup>], and was similar to the all samples after gamma irradiation at this study. This indicated  $NR_{Cs}$  was not increased by gamma irradiation.

From the above results, it was considered that the effect of gamma irradiation on the aluminosilicate framework of pollucite was not mostly observed until 100 kGy.

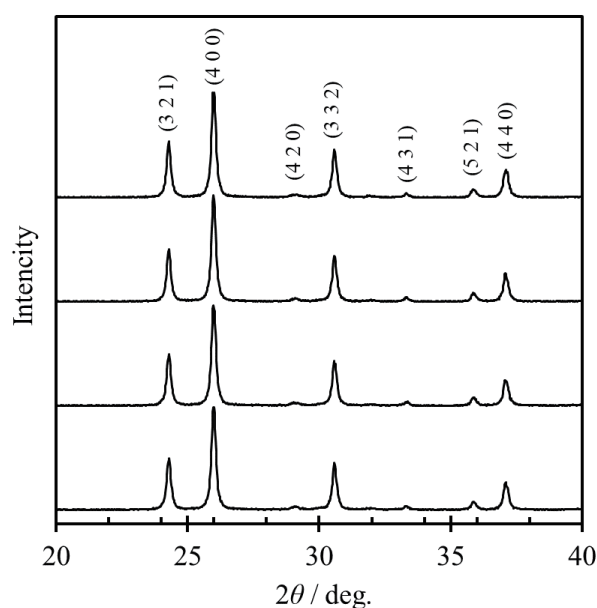


Fig.1. XRD patterns of (a) without irradiated, (b) 1 kGy, (c) 10 kGy, and (d) 100 kGy irradiated sample.

Table 1. Leaching test parameters in this study.

Dose [kGy]	$f_{Cs}$	$SA V^{-1}$ [m <sup>2</sup> L <sup>-1</sup> ]	$NR_{Cs}$
without-irr.	0.35	134	$1.5 \times 10^{-4}$
1	0.35	141	$1.5 \times 10^{-4}$
10	0.35	141	$1.2 \times 10^{-4}$
100	0.35	141	$1.3 \times 10^{-4}$

#### REFERENCES:

- [1] Y. Yokomori *et al.*, *Sci. Rep.*, **4** (2014) 4195.
- [2] J. Fortner *et al.*, Argonne National Laboratory, Argonne, Illinois 60439 (2001).
- [3] N. J. Hess *et al.*, *J. Nucl. Mater.*, **281** (2000) 22-33.
- [4] ASTM C 1285-02 (2008).
- [5] Z. Jing *et al.*, *J. Hazard. Mater.*, **306** (2016) 220-229.

## CO4-24 Effects of Buffers and Salts on Nanostructure of Soybean Proteins as Revealed by SAXS

N. Sato, R. Urade, A. Okuda, K. Morishima, R. Inoue,  
and M. Sugiyama

*Institute for Integrated Radiation and Nuclear Science,  
Kyoto University*

**INTRODUCTION:** It has long been known that soybeans contain abundant proteins. They consist of more than 30% of dry matters of their seed. Thus, soybeans have been eaten as nutritious natural food, not only as unprocessed beans but also as soybean food products such as *tofu* and *tofu* skin (*yuba*). *Tofu* is a kind of hydrogels composed of soybean proteins, and accordingly its property and quality are subject to coagulation behavior of soybean proteins. Aside from traditional soybean food products like *tofu*, soy protein isolate (SPI) have been industrially produced and provided to the commercial market in recent years for improving physical property of various food products by adding them to those foods. Soybean proteins are also used for making mimic meat products for vegetarians and vegans. World-wide increase in health consciousness leads to growing importance of soybean protein usage. From these reasons, soybean proteins are one of key substances in the field of food science.

In order to obtain high-quality soybean food products or SPI-containing foods, it is necessary to deeply understand the structure of soybean proteins at the molecular level. In particular, structural changes induced by the various conditions such as temperature change, salt addition and coagulant addition are of great significance to elucidate the relationship between the structure of proteins and the physical property of foods containing soybean proteins. For structural analysis on opaque, disorder and condensed soft matters such as gels, colloids, and rubber, small-angle X-ray and neutron scattering (SAXS, SANS) has been proved to be a useful technique, and it is also expected to be effective for structural analysis of foods, which has similar features to above soft matters. Therefore we have been studying the nanostructure of wheat and soybean proteins by SAXS and SANS. The behavior of isolated and aggregated protein molecules in aqueous solutions and hydrates has been investigated by taking advantage of SAXS and SANS.

In this study, we conducted a SAXS analysis on two major soybean proteins,  $\beta$ -conglycinin and glycinin, which have been conventionally referred to as 7S and 11S, respectively, according to their sedimentation coefficients determined by analytical ultracentrifugation. Difference of nanostructure of 7S and 11S in pure water and buffer solutions was examined by SAXS. Effects of NaCl addition was also investigated.

**EXPERIMENTS:** Soybean proteins 7S and 11S were extracted from hexane-defatted powder of soybean cultivar "Enrei" under a reducing condition with 2-mercaptoethanol. Isoelectric precipitation was applied

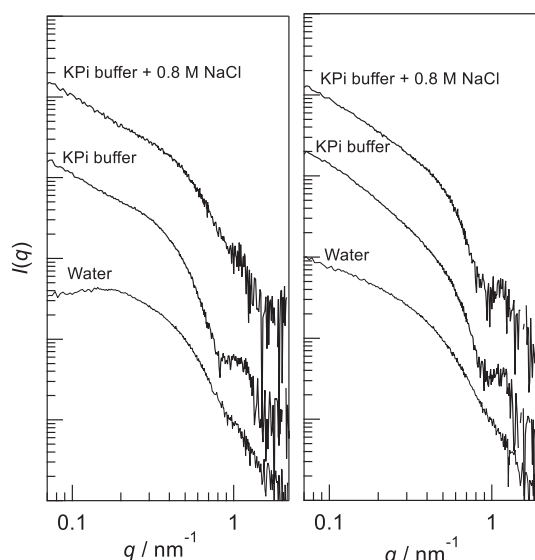


**Fig. 1** SAXS profiles for 7S (left) and 11S (right) in 0.5% pure water and KPi buffer solutions.

to isolation of each protein. By adjusting pH of the extract solutions, 11S and 7S was precipitated at pH 5.8 and pH 4.5, respectively. SAXS measurements were performed with a laboratory SAXS instrument (NANOPIX, Rigaku) installed at Institute for Integrated Radiation and Nuclear Science, Kyoto University. Each protein dissolved in pure water or 35-mM potassium phosphate (KPi) buffer solutions at pH 7.5 in presence of 0 or 0.8 M NaCl was put into aluminum cells and set for SAXS measurements. The wavelength of X-ray was 1.54 Å, the sample-to-detector distance was 1300 mm and the available  $q$ -range was 0.08 – 2.2 nm<sup>-1</sup>. Model calculation of SAXS profiles from crystal structure was done with a software, CRY SOL [1].

**RESULTS:** Fig. 1 shows SAXS profiles measured for 0.5% 7S and 11S solutions at 25°C. A small peak appeared around 1.2 nm<sup>-1</sup> in KPi buffer solutions, which is an indication of trimerring structure consisting of three subunits. In pure water, however, this peak was not recognizable, suggesting that the subunits cannot form trimer ring structure and exist as monomers in pure water. When 0.8 M NaCl was added to the KPi solution of 7S, the peak at 1.2 nm<sup>-1</sup> became weaker and the shoulder at 0.4 nm<sup>-1</sup> shifted to higher- $q$ . However, such changes were not observed for 11S. These profiles agree with the model calculation results for crystal structure of monomer, trimer and hexamer. Therefore it was demonstrated that monomeric subunits in pure water are assembled into hexamers in KPi buffer solutions by stacking two ring trimers, and dissociated into trimers at higher ionic strength conditions only for 7S.

### REFERENCES:

[1] D.I. Svergun *et al.*, *J. Appl. Cryst.*, **28** (1995) 768.

K. Wakamoto, T. Otsuka, K. Nakahara, A. Yabuuchi<sup>1</sup> and A. Kinomura<sup>1</sup>

Power Device R&D Department, ROHM Co., Ltd.

<sup>1</sup>Institute for Integrated Radiation and Nuclear Science, Kyoto University

**INTRODUCTION:** Sintered silver has attracted much attention as a die-attach material for the power electronics, owing to its high heat dissipation capability [1]. On the other hand, the coefficient of thermal expansion (CTE) inevitably does not match each other of the materials used in a power system. Thus the heat-cycle oriented mechanical stresses deteriorate die-attach materials, and therefore the mechanical properties of sintered silver impinge on the reliability of electricity systems.

However, nobody can predict how long sintered silver sustains, because the material is porous and its mechanical properties heavily depends how porous it is. Accordingly, the research is highly demanded to measure the porosity.

The porosity rate ( $p$ ) of sintered silver is reported by some papers [2-3], where  $p$  is measured by using cross sectional scanning electron microscopy (SEM). These studies focus only estimates the  $\mu\text{m}$ -order pores of sintered silver materials, not nm-order pores such as crystalline defects. Positron lifetime measurement method has advantages for this purpose. To this end, therefore, the authors used a conventional positron annihilation lifetime spectrometer in Kyoto University to estimate the nm-order pore sizes embedded in sintered silver with various  $p$ 's by measuring the positron lifetime of the material.

**EXPERIMENTS:** The fabrication process of sintered silver films is described as follows. Paste including silver nm-particles was stencil printed on a metal plate, and the containing organic solvent was dried at 140°C for 1 h. These dried films were sintered at 300 °C for 10 min with uniaxial press via a carbon buffer sheet with 0.5 – 120 MPa pressure. The film shape was 5 mm square and 50- $\mu\text{m}$  thick. Positron annihilation lifetime spectroscopy was performed to evaluate bulk lifetimes of the samples by using a <sup>22</sup>Na source sealed with 12.5  $\mu\text{m}$  Kapton foils. The thickness of the samples was approximately 50  $\mu\text{m}$ . Four sample plates were stacked and measured together to stop all the positrons from the source inside the sample. The measure samples are summarized in Table I.

**Table I** Summary of the measured specimens.

Sample	Sintering temp. (°C)	Pressure (MPa)	Sample size
A	300	120	5mm square and 200- $\mu\text{m}$ thick
B		80	
C		30	
D		0.5	

The spectrometer consists of two scintillation gamma-ray detectors with BF<sub>2</sub> crystals and a spectrometer based on

digital circuits. Total counts for each measurement were approximately 10<sup>6</sup> counts.

**RESULTS:** The data from the 1st sample set to investigate pressure dependence was analyzed as follows. Measured lifetime spectra were decomposed into three components as shown in Fig. 1. The lifetimes and intensities of the first and third components changed depending on formation pressure, while the second lifetime and intensity were almost constant except for the lowest pressure sample. In fig. 1(a), average lifetimes calculated from lifetime and intensity values were plotted as well. The average lifetimes were almost constant for all the samples. The lifetime values obtained from a literature for bulk Ag and monovacancy in Ag were indicated with broken lines in fig. 1(a). The second and third lifetime components can be attributed to monovacancies and vacancy clusters. It is necessary to further investigate the origin of each lifetime components to know the behavior of nanometer-sized voids (vacancies) that cannot be detected in secondary electron microscopy.

**SUMMARY:** Porosity of sintered Ag plates was characterized as a function of formation pressure by conventional positron annihilation lifetime spectroscopy. The third lifetimes corresponding to vacancy clusters changed depending on formation pressure, while the average lifetime was almost constant.

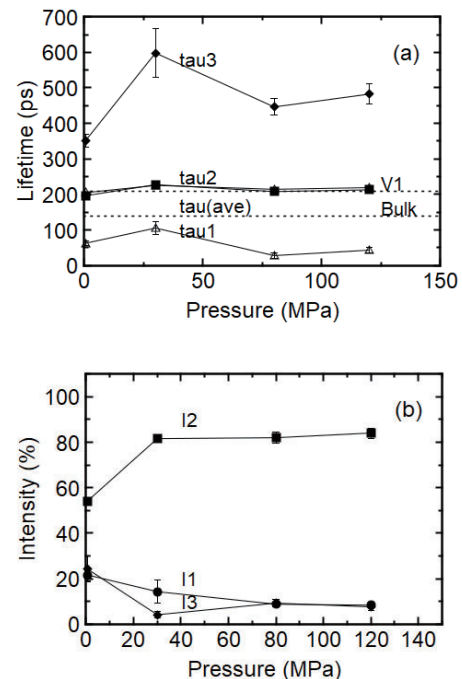


Fig. 1 Lifetimes and their intensities of the samples.

**REFERENCES:**

- [1] KIM S. SIOW, Journal of ELECTRONIC MATERIALS., **43** (2014) 947-961.
- [2] T. Yousseff *et al.*, Microelectronics Reliability., **55** (2015) 1997-2002.
- [3] M. Takesue *et al.*, Proc. PCIM., (2018) 148.

## CO4-26 Differences in the Recovery Behavior of Electron-Irradiation-Induced Vacancies in Metals with Different Purities

A. Yabuuchi, M. Tanaka, and A. Kinomura

*Institute for Integrated Radiation and Nuclear Science,  
Kyoto University*

**INTRODUCTION:** Since tungsten (W) is expected as a plasma-facing material for fusion reactors, many studies on vacancy-type defects in W are carried out using positron annihilation spectroscopy. Based on several first-principles calculations, the positron lifetime of monovacancy in W is expected to be 193–200 ps. On the other hand, defects having positron lifetimes of 165–180 ps have been observed in electron-irradiated W. In this study, the annealing behaviors of electron-irradiation-induced vacancies in two kinds of W samples with different purities were observed by using a positron annihilation lifetime spectroscopy in order to understand the cause of the difference between the calculated and experimental values. In addition, positron lifetimes in vacancy-impurity complexes consisting of several possible impurity atoms were also calculated and compared with experimental values.

**EXPERIMENTS:** Well annealed W samples having purities of 99.999% (5N) or 99.9% (3N) were irradiated with 8-MeV-electrons to a total dose of  $5 \times 10^{19} \text{ e}^-/\text{cm}^2$ . The sample temperature was kept at about 373 K during the irradiation. The irradiated samples were isochronally annealed at 50 K steps with a duration of 15 min. After each annealing, positron annihilation lifetime measurements were performed at room temperature. The acquired positron annihilation lifetime spectra were decomposed into two components. The longer lifetime component was recognized as the component derived from the irradiation-induced vacancies.

**RESULTS:** Figure 1 shows the changes in the longer positron lifetimes and their intensities of both samples during isochronal annealing [1]. The positron lifetimes of both as-irradiated samples ( $\sim 170$  ps) are about 25 ps shorter than the calculated positron lifetime of isolated monovacancy (195 ps). This implies that the vacancies introduced into W by electron-irradiation does not exist as isolated monovacancies, but rather exist as vacancy-impurity complexes. The positron lifetime calculations revealed that the positron lifetime becomes shortened from 195 ps to  $\sim 170$  ps when a monovacancy binds with interstitial-type impurity atoms such as carbon, oxygen, and nitrogen. It was also found that the positron lifetime of vacancy-hydrogen complex becomes only shortened to 185 ps, whereas it becomes shortened to  $\sim 170$  ps when two hydrogen atoms are bound to a monovacancy.

### REFERENCE:

[1] M. Tanaka, A. Yabuuchi, and A. Kinomura, AIP Conf. Proc., **2182** (2019) 050014-1–050014-4.

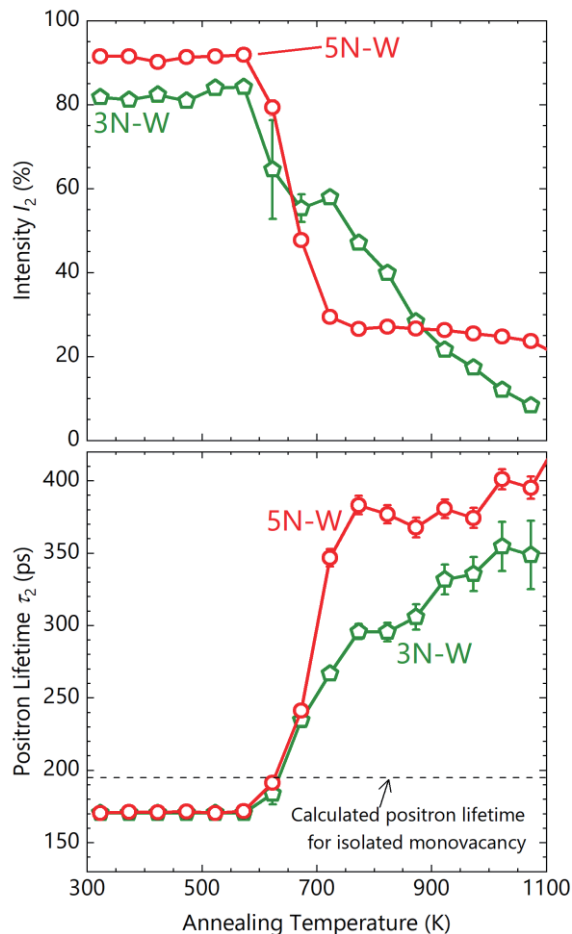


Fig. 1. Defect-related positron lifetimes  $\tau_2$  and their intensities  $I_2$  for 5N- (open circles) and 3N-W (open pentagons) samples as a function of annealing temperature. Calculated positron lifetime for isolated monovacancy (195 ps) is also depicted as a dashed line.

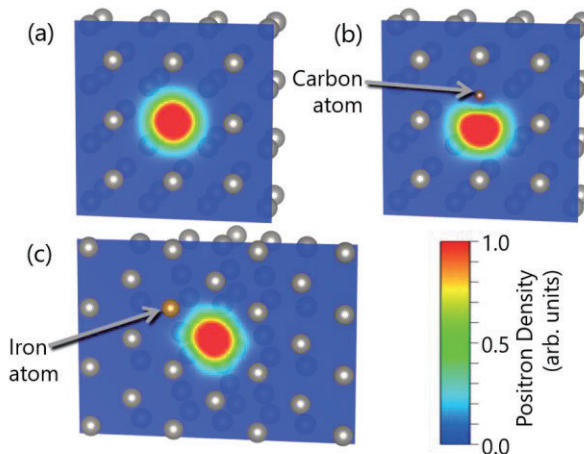


Fig. 2. Calculated positron density distributions at (a) isolated monovacancy, (b) vacancy-carbon complex, and (c) vacancy-iron complex. The atomic positions are also depicted as spheres.

## CO4-27 Differences in the Development of Vacancy-Type Defects During Annealing with Different Irradiated Ion Species

A. Yabuuchi, M. Tanaka, and A. Kinomura

*Institute for Integrated Radiation and Nuclear Science,  
Kyoto University*

**INTRODUCTION:** Since tungsten (W) is expected to use as a plasma-facing material for fusion reactors, the effects of hydrogen (H) and/or helium (He) ion irradiation into W have been well studied. Recently, several studies are carried out to reduce the heat load on W wall by injecting neon (Ne) or argon (Ar) gas into the fusion plasma. Positron annihilation spectroscopy is a useful tool for characterizing vacancy-type defects in materials. Thus, several positron-based studies of defects in  $H^+$ - or  $He^+$ -irradiated W have been reported. However, few studies have investigated the defects in  $Ne^+$ - and/or  $Ar^+$ -irradiated W by using positrons. Irradiating heavier ions than  $H^+$  and/or  $He^+$  may cause more serious damage to W. In this study,  $He^+$ - and  $Ne^+$ -irradiated W samples were prepared and investigated the differences in the developmental process of irradiation-induced defects during annealing by using a slow positron beam.

**EXPERIMENTS:** The well annealed W samples were irradiated with  $He^+$  or  $Ne^+$  ions with an energy of 50 keV. The irradiated and unirradiated samples were probed by a slow positron beam to acquire the Doppler broadening of the annihilation radiation (DBAR) spectra. The DBAR spectra were characterized by an  $S$ -parameter which represents the proportion of annihilation events with a small Doppler shift, and a  $W$ -parameter which represents the proportion of annihilation events with a large Doppler shift. In addition,  $R$ -parameters were also derived from the  $S$ - and  $W$ -parameters [1]. The  $S$ - and  $W$ -parameters depend on both defect species (defect size) and defect concentration, while the  $R$ -parameter does not depend on the defect concentration but only on the defect species.

**RESULTS:** Figure 1 shows the annealing temperature dependence of  $S$ -parameters for both irradiated samples. The increased  $S$ -parameters of as-irradiated both samples are finally reduced to the almost unirradiated-state by annealing at 900°C. Judging from the changes in  $S$ -parameters, superficially, the irradiation-induced defects appear to have been recovered in both samples. However, the changes in  $R$ -parameters shown in Fig. 2 indicate that the developmental processes of irradiation-induced defects in both samples are different during annealing. Figure 2 shows that defect species in the  $He^+$ -irradiated W finally become the same as those in the unirradiated W (*i.e.*, the irradiation-induced vacancies are fully recovered). In contrast, the changes in  $S$ -,  $W$ -, and  $R$ -parameters during annealing indicate that irradiation-induced vacancies aggregate and grow into larger vacancy clusters in  $Ne^+$ -irradiated W [2].

### REFERENCES:

- [1] S. Mantl and W. Triftshäuser, Phys. Rev. Lett., **34** (1975) 1554–1557.  
[2] A. Yabuuchi, M. Tanaka, and A. Kinomura, J. Nucl. Mater. **531** (2020) 152018-1–152018-5.

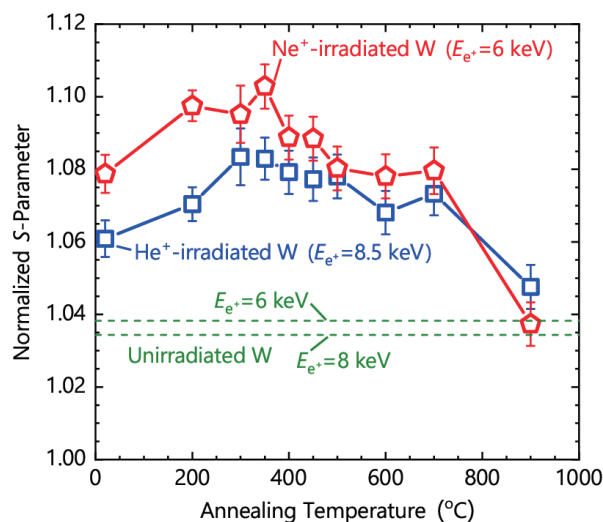


Fig. 1.  $S$ -parameters as a function of annealing temperature obtained from  $He^+$ - and  $Ne^+$ -irradiated tungsten. All the  $S$ -parameters are normalized to that obtained from unirradiated tungsten probed with positron energy of 20 keV. The  $He^+$ - and  $Ne^+$ -irradiated tungsten were probed with positron energies of 8.5 keV and 6 keV, respectively.  $S$ -parameters obtained from the unirradiated tungsten probed with positron energies of 6 keV and 8 keV are also depicted as dashed lines.

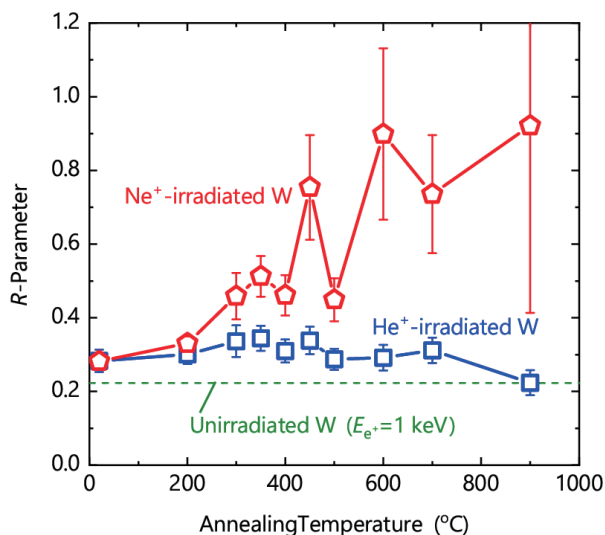


Fig. 2.  $R$ -parameters as a function of annealing temperature obtained from  $He^+$ - and  $Ne^+$ -irradiated tungsten. All the  $R$ -parameters are derived from the normalized  $S$ - and  $W$ -parameters. The  $R$ -parameter obtained from unirradiated tungsten probed with positron energy of 1 keV, corresponding to positron annihilation at the surface, is also depicted as a dashed line.

## CO4-28 Defect Characterization of Ion-Irradiated $\text{GdBa}_2\text{Cu}_3\text{O}_{7-\delta}$ Superconducting Tapes Probed by a Slow Positron Beam

T. Ozaki, H. Sakane<sup>1</sup>, T. Kashiwabara, A. Yabuuchi<sup>2</sup> and A. Kinomura<sup>2</sup>

School of Science and Technology, Kwansei Gakuin University

<sup>1</sup>SHI-ATEX Co., Ltd.

<sup>2</sup>Institute for Integrated Radiation and Nuclear Science, Kyoto University

**INTRODUCTION:** Superconducting materials, such as  $\text{GdBa}_2\text{Cu}_3\text{O}_{7-\delta}$  (GdBCO) investigated in this work, are known to improve a high magnetic field resistance by forming lattice defects using ion-irradiation techniques. The Doppler broadening of annihilation radiation (DBAR) spectra become sharpened by annihilating positrons at vacancy-type defects, which enables us to characterize the concentration and/or size of vacancy-type defects [1]. In this work, tape-shaped GdBCO films irradiated with 2-MeV- $\text{Au}^{2+}$  or 10-MeV- $\text{Au}^{4+}$  ions were probed by a slow positron beam.

**EXPERIMENTS:** The GdBCO(500 nm)/ $\text{CeO}_2$ (150 nm)/ $\text{Y}_2\text{O}_3$ (150 nm)/Ni/Cu/SUS samples were irradiated with 2-MeV- $\text{Au}^{2+}$  ( $4 \times 10^{12} \text{ Au}^{2+}/\text{cm}^2$ ) or 10-MeV- $\text{Au}^{4+}$  ( $6 \times 10^{12} \text{ Au}^{4+}/\text{cm}^2$ ) ions. The 2 MeV and 10 MeV ions stop in the GdBCO film and penetrate the GdBCO film, respectively. The unirradiated and irradiated samples were probed by the KUR slow positron beam and the DBAR spectra were acquired. The sharpness of the DBAR spectra is evaluated by a value called the S parameter, which becomes generally lower when positrons annihilate in a perfect lattice, and higher when positrons are trapped into vacancies [1].

**RESULTS:** Figure 1 shows S parameters for the unirradiated sample as a function of incident positron energy. The S parameters in the energy region of 5–12 keV correspond to positron annihilation in the GdBCO film. Figures 2 and 3 show S parameters for the 2-MeV- $\text{Au}^{2+}$ - and 10-MeV- $\text{Au}^{4+}$ -irradiated samples. Contrary to our initial expectation, both irradiated samples show a reduction in S parameters compared to the unirradiated one. This reduction in S parameters implies that the unirradiated sample already contained vacancy clusters larger than irradiation-induced vacancies. When a large number of relatively small vacancies are formed by ion irradiation, most positrons are trapped at the irradiation-induced vacancies rather than the pre-existing vacancy clusters. Positrons annihilated in small vacancies bring smaller S parameters than positrons annihilated in vacancy clusters, and thus the reduction in S parameters was considered to be caused by ion irradiation.

### REFERENCE:

[1] R. W. Siegel, Ann. Rev. Mater. Sci., 10 (1980) 393–425.

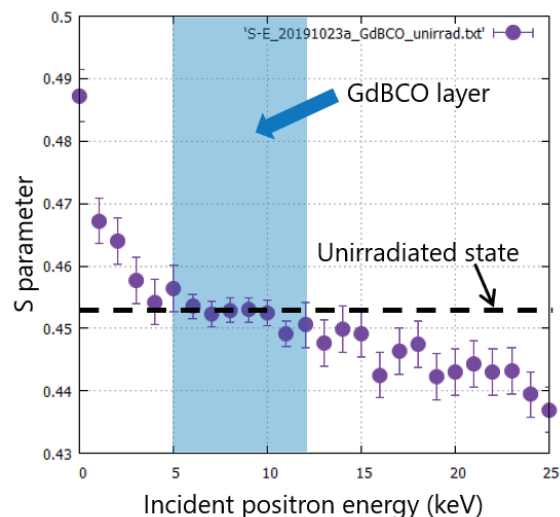


Fig. 1. S parameters for unirradiated GdBCO tape.

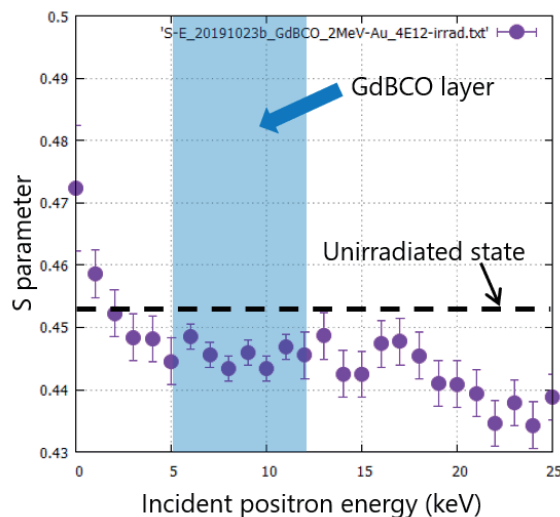


Fig. 2. S parameters for 2-MeV- $\text{Au}^{2+}$ -irradiated GdBCO tape with a total dose of  $4 \times 10^{12} \text{ Au}^{2+}/\text{cm}^2$ .

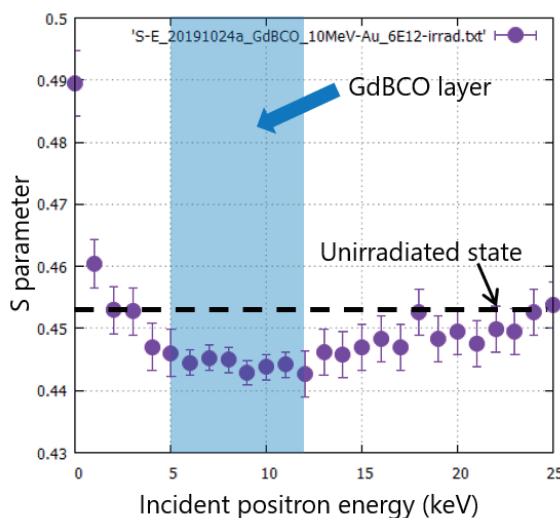


Fig. 3. S parameters for 10-MeV- $\text{Au}^{4+}$ -irradiated GdBCO tape with a total dose of  $6 \times 10^{12} \text{ Au}^{4+}/\text{cm}^2$ .

M. Ishikawa, E. Yatsuka, R. Imazawa, T. Ushiki, H. Murakami and T. Hatae

*National Institutes for Quantum and Radiological Science and Technology*

**INTRODUCTION:** International Thermonuclear Experimental Reactor (ITER) [1] is being built in France by international cooperation. This study focuses on neutron irradiation effects on optical elements and piezo-actuators used in ITER. Expected 1 MeV Silicon equivalent fluence is  $10^{12}$ - $10^{15}$  n/c m<sup>2</sup> depending on locations of components. In order to investigate the effect of such high fluence on the actual components in a short time, neutron irradiation was performed using the slant exposure tube and the pneumatic tubes of the KUR. Although there are similar studies in Europe [2], they don't cover all the components necessary for ITER plasma diagnostic systems developed by Japan. This report mainly presents effect of neutron irradiation on optical components for Edge Thomson scattering (ETS) system. We conducted a neutron irradiation test on radiation-resistant glasses that are guaranteed to withstand gamma irradiation of 10 MGy. In addition, the tests for other systems such as the Poloidal Polarimeter and Infrared Thermography systems are briefly described.

**EXPERIMENTS:** Three kinds of radiation resistant glasses (BK7G18, LF5G19 and SF6G05) with anti-reflection coatings, products of Schott in Germany, were irradiated with neutrons. By using one of these glasses together with fused silica, chromatic aberration of the collection optics the ETS is compensated [3]. The glass samples in this study have diameter of 25 mm and thickness of 5 mm. These glasses were irradiated at the bottom of slant exposure tube for maximum 20 hours at 1-MW reactor output power. Fast and total neutron fluences were  $6 \times 10^{15}$  cm<sup>-2</sup> and  $6 \times 10^{16}$  cm<sup>-2</sup>, respectively, considering neutron spectra at slant exposure tube. Spectral transmissions of glasses before and after irradiation were measured with spectrophotometer (Hitachi U-2910) and compared.

**RESULTS:** Figure 1 shows photographs of radiation hard glasses (a) BK7G18, (b) LF5G19 and (c) SF6G05, respectively, before and after irradiation. The values in figure denotes fast neutron fluence onto each sample. Degradations on light transmission of BK7G18 and LF5G19 were clearly observed with visual inspection. Figure 2 shows the spectral transmissions of (a) BK7G18, (b) LF5G19 and (c) SF6G05, respectively. In the ETS, light within spectral range of 590-1070 nm is analyzed for electron temperature and density measurements in ITER. Before irradiation, LF5G19 had the highest spectral transmission in the range of 590-1070 nm. It was clarified that SF6G05 is the most insensitive to neutron irradiation in that spectral range. In contrast to the samples with thickness of 5 mm were tested, ETS is expected to be designed to use thicker (20-50 mm) radiation hard glass. That is, in reality, it is considered that the influence of the degradation of transmission will be

more remarkable. Regarding SF6G05, drop of transmission around 800 nm (in total 4.3%) is mostly caused by reflections on surfaces (3.8%) rather than internal absorption (0.5%). If the antireflection coating is optimized, the initial transmittance may be improved to the same level as that of other types of glass. At present, SF6G05 seems promising as a glass for chromatic aberration compensation of ETS signal light under the neutron environment of ITER.

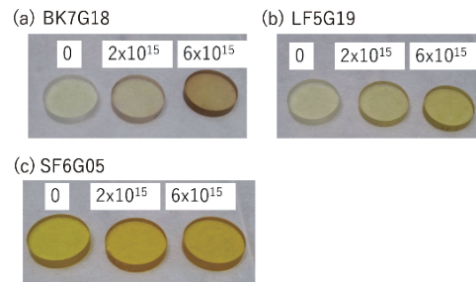


Fig. 1: Photographs of radiation hard glasses before and after irradiation.

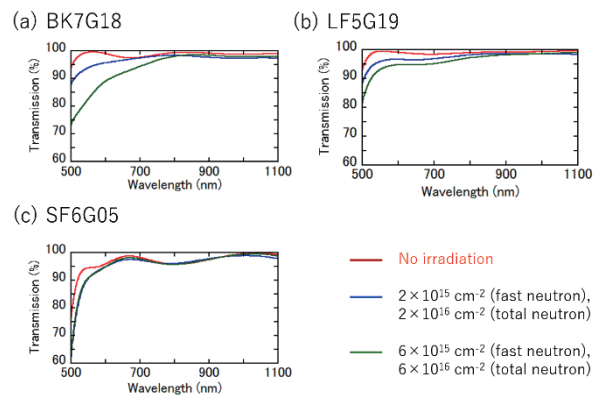


Fig. 2: Spectral transmissions of radiation hard glasses before and after irradiation.

#### ON GOING INVESTIGATIONS AND PROSPECTS:

Poloidal Polarimeter will be installed in ITER for measuring plasma current profile and use piezo actuators in radiological environment for adjusting laser beam position. Irradiation test of the piezo actuator was started from 2019. Target neutron fluence for the test is  $9 \times 10^{15}$  cm<sup>-2</sup>. Functional tests after neutron irradiation are planned on 2020.

Infrared Thermography system will use coating mirror and lens in radiological environment. Irradiation tests of several candidate materials for mirror and lens were started from 2019. In 2020, the irradiation tests will be continued to investigate threshold value of total dose for keeping their optical performance.

#### REFERENCES:

- [1] B. Bigot, *Fusion Eng. Des.*, **146**, 124 (2019).
- [2] M. Decreton *et al.*, *J. Nucl. Mat.*, **329** Part A, 125 (2004).
- [3] E. Yatsuka *et al.*, *Fusion Eng. Des.*, **136**, 1068 (2018).

O. Ishizuka, S. Sekimoto<sup>1</sup>, R. Okumura<sup>1</sup>, H. Yoshinaga<sup>1</sup>,  
Y. Inuma<sup>1</sup> and T. Fujii<sup>2</sup>  
*Geological Survey of Japan, AIsandT*

<sup>1</sup>*Institute for Integrated Radiation and Nuclear Science,  
Kyoto University*

<sup>2</sup>*Graduate School of Engineering, Osaka University*

**INTRODUCTION:** Submarine volcanic rocks are known to give ages different from their true eruption ages in some cases. This is due to the existence of excess  $^{40}\text{Ar}$  in the rapidly quenched glass or Ar loss and K remobilization caused by reaction with seawater or hydrothermal fluids. Stepwise-heating analysis in  $^{40}\text{Ar}/^{39}\text{Ar}$  dating is particularly useful for dating submarine volcanics.

Robust tectonic reconstruction of the evolving Philippine Sea Plate for the period immediately before and after subduction initiation at ~52 Ma to form the Izu-Bonin-Mariana (IBM) arc is prerequisite to understand cause of subduction initiation (SI) and test competing hypotheses for SI such as spontaneous or induced nucleation. Understanding of nature and origin of overriding and subducting plates is especially important because plate density is a key parameter controlling SI based on numerical modeling (e.g., Leng and Gurnis 2015). There is increasing evidence that multiple geological events related to changing stress fields took place in and around Philippine Sea plate about the time of SI ~52 Ma (Ishizuka et al., 2011). For our understanding of the early IBM arc system to increase, it is important to understand the pattern and tempo of these geological events, particularly the duration and extent of seafloor spreading in the proto arc associated with SI, and its temporal relationship with spreading in the West Philippine Basin (WPB).

The YK19-07S cruise aimed to investigate origin and age of formation of ocean basins in and around the Daito Ridge group. Especially ocean basins which potentially existed in the period of SI to form the IBM arc were the major targets of this cruise, because ocean crust of these basins might be part of overriding plate when subduction of Pacific plate initiated to form IBM arc. Since gravitational instability between the neighboring plates is supposed to be a critical factor for subduction initiation, it is important to understand characteristics (age, origin, crustal structure) of overriding plate to test hypotheses of subduction initiation. Recovery and characterization of igneous crust of these basins will provide crucial information about the possible basement of the IBM arc and critical constraints to evaluate models for subduction initiation along the Pacific margin. Recent cruises in the Philippine Sea basins recovered basalts from ocean crust along the major tectonic lines such as the Oki-Daito Escarpment and Mindanao Fracture Zone of the West Philippine Basin. These samples were dated by  $^{40}\text{Ar}/^{39}\text{Ar}$  dating method to obtain age of formation of the basins.

**EXPERIMENTS:** Samples were wrapped in an aluminum foil packet and the packets were piled up in a pure aluminum (99.5% Al) irradiation capsule (9 mm diameter and 30 mm long). The irradiation capsule was partitioned into 3 compartments to minimize the horizontal flux variation across the capsule.

For the experiments described here, around 5 mg of sample was analysed. Only minimum acid leaching was applied to the glass samples, i.e., ultrasonic cleaning with 3M HCl for 10 minutes at room temperature. After this acid treatment, the glass chips were examined under binocular microscope before packed for irradiation.

**RESULTS:**  $^{40}\text{Ar}/^{39}\text{Ar}$  dating of fresh basalt glasses from YK19-07 cruise returned variable results, with some “disturbed” age spectrum (Fig. 1). This spectrum is characterised by some steps with irregularly older ages among those with relatively constant ages of around 58 Ma. These older steps, however, show consistent Ca/K ratios with other steps. This strongly implies that these steps are not associated with particular minerals or melt inclusion, but possibly represent degassing from bubbles or “gas pockets” which partially preserve mantle-derived Ar. Konrad et al. (2019) reported similar spectrum from stepwise heating analysis of pyroxene crystals.

Presence of Ar inherited from mantle is a critical problem in dating glass samples. We still need more examples of high-precision dating experiments to understand behavior of mantle-derived Ar and its effect on age spectrum.

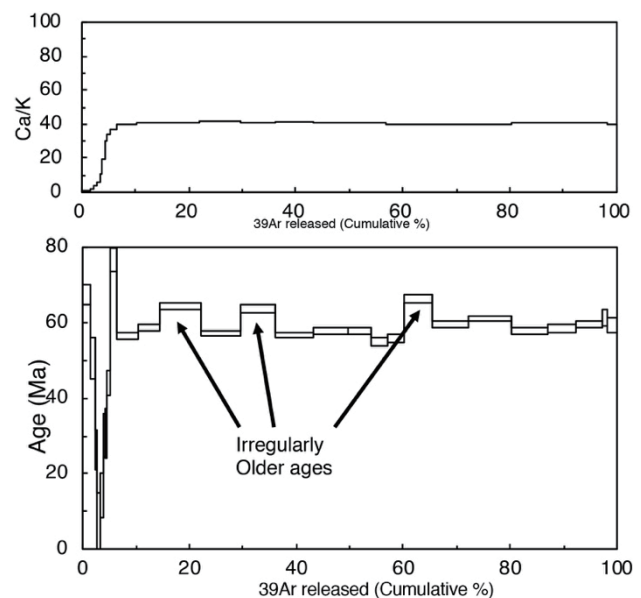


Fig. 1 Age spectrum for the basalt glass from the northernmost West Philippine Basin recovered by submersible Shinkai 6500.

**REFERENCES:**

[1] O. Ishizuka *et al.*, *Earth Planet. Sci. Lett.*, **306** (2011) 229-240.

# CO5-2 Long Term Observation of Element Concentrations in the Atmospheric Aerosols at Sakai, Osaka, 1995-2017

N. Ito, A. Mizohata, Y. Imura<sup>1</sup> and H. Yoshinaga<sup>1</sup>

Radiation Research Center, Osaka Prefecture University,  
<sup>1</sup> Institute for Integrated Radiation and Nuclear Science,  
 Kyoto University

Atmospheric aerosols are the fine and coarse particles suspended in the air and are emitted or produced from natural and artificial sources. To investigate the pollution of atmosphere, we have been collecting atmospheric aerosols using particle collector with size separator (Andersen sampler) at Osaka Prefectural University in Sakai City, Osaka since 1994. In this paper we show the some results of long term observations on the element (Cl, V, Cr, Mn, Fe, Zn, As, Br, Sb) which have shown decrease trend. In these element, Antimony (Sb) showed the most remarkable decreasing tendency.

The collection sampler, Andersen Sampler, has 9 stages on which particle are collected with size ranges (> 11 μm, 7.0-11.0 μm, 4.7-7.0 μm, 3.3-4.7 μm, 2.1-3.3 μm, 1.1-2.1 μm, 0.65-1.1 μm, 0.43-0.65 μm, <0.43 μm). By this sampler, atmospheric aerosol was collected on a

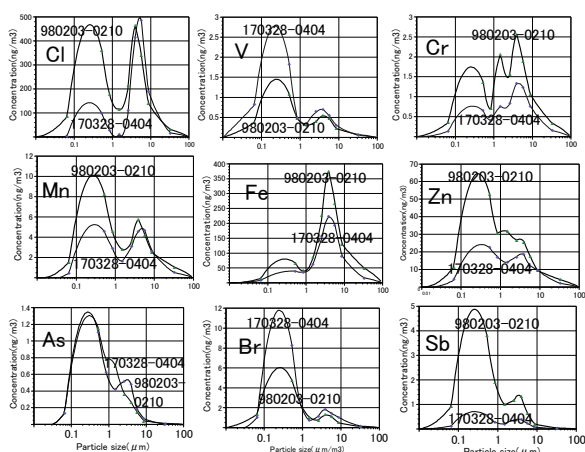


Fig.1. Concentration continuous distributions versus particle size. The concentrations were observed in 980203-0210 and 170328-0404 at Sakai.

polyethylene sheet with the collection period of one week. Samples collected on the some part of the sampling period were analyzed for the elements by neutron activation analysis using reactors, Rikkyo University, Japan Atomic Energy Agency, and Kyoto University Research Institute for Nuclear Atomic Energy.

To investigate the concentration tendency for 20 year, we show the size distribution of concentrations in Cl, V, Cr, Mn, Fe, Zn, As, Br, Sb on the two observation periods of 1998 (980203-0210) and 2017 (170328-0404) in Fig. 1. Compared for two periods, the elements that decreased concentration in 2017 for fine particles (<2.1 μm) were Cl, Cr, Mn, Zn, and Sb. Concentration change was small for Fe and As. The elements that increased the concentration were V, Br.

The tendency of the concentration change for the fine particles was examined for all observation periods (Fig. 2). Among the analyzed elements, Sb contained in the fine particles (<2.1 μm) showed the most remarkable decrease tendency. The concentration was 0.005 (μg / m<sup>3</sup>) at the beginning of the observation (around 1995), but decreased to 0.001 (μg / m<sup>3</sup>) in 2017 after 22 years. The slope (a) when approximated by a straight line (ax + b) was  $-0.25 \pm 0.03$  (ng / m<sup>3</sup> / year), and the relative increase rate (a / b) was  $-4.5 \pm 0.6$  (% / year). Other elements of fine particles were also approximated by ax + b. The estimated range of the increase rate obtained by the range as  $a \pm 2\sigma a$  indicating the trend suggest the remarkable decreasing trend for Cl, Cr, Mn, Zn, As, Br, Sb on these elements have the range of increase as  $a \pm 2\sigma a < 0$ . Regarding Cr, the tendency of decrease was observed, but the decrease rate was lower than that of other elements. Since fine particles of Cl, Zn, Br, and Sb are included in particles emitted from waste incineration facilities, the reduction of these elements suggests that the effects from waste incineration facilities have been reduced.

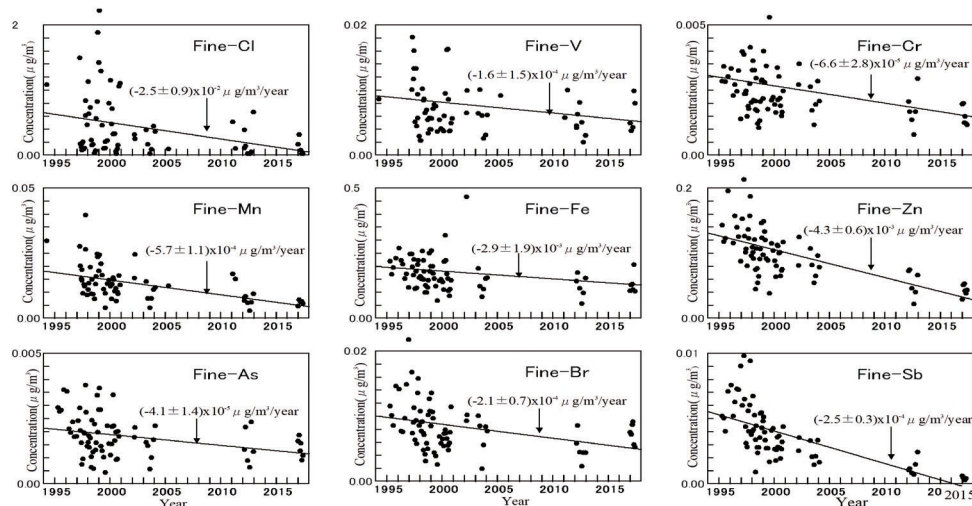


Fig.2. Concentration change in Cl, V, Cr, Mn, Fe, Zn, As, Br and Sb in fine atmospheric aerosols observed at Sakai, 1995-2017. Trends of concentration were estimated by fitting the concentration change with line(ax+b).

N. Hirano, H. Sumino<sup>1</sup> and S. Sekimoto<sup>2</sup>

*Center for Northeast Asian Studies, Tohoku University*

<sup>1</sup> *Graduate School of Arts and Sciences, University of Tokyo*

<sup>2</sup> *Institute for Integrated Radiation and Nuclear Science, Kyoto University*

**INTRODUCTION:** On the western part of the Pacific Plate, most seamounts formed during the Cretaceous pe-riod in the so-called West Pacific Seamount Province (WPSP). The eustatic sea level and global average tem-perature, increasing seafloor spreading rate, and volumi-nous volcanic activities occurred during the mid-Cretaceous period. Many of seamount chains, how-ever, cannot be explained by the classical hotspot and mantle plume hypothesis as well as the Hawaii-Emperor Seamount Chain could be done. Many of seamount and knoll had left their dating behind the volcanic evolutions on the western Pacific Plate. Moreover, the lithospheric flexure-induced volcanoes (petit-spots) are recently de-scribed at the outer-rises of Japan Trench prior to the subduction of northwestern and the western Pacific Plate [1]. Nobody has found such intra-plate volcanoes pre-ceded by the petit-spot volcanic activities since younger WPSP hotspots during Late Cretaceous on the western Pacific Plate. Similar volcanoes have been reported at subduction zones worldwide (e.g., the Japan, Tonga, Chile, and Java trenches) [1][2][3][4][5]. We, therefore, conduct to determine the eruption ages of volcano using Ar-Ar dating to understand the evolution of pacific Plate during Cretaceous to present.

**EXPERIMENTS:** The research cruise using R/V Yokosuka equipped with the submersible SHINKAI 6500, was conducted around the Marcus Island on May 2010 in order to know the detail history during the formation of the Marcus Island (Fig. 1). Radiometric Ar-Ar dating is commonly used to determine the ages of submarine lavas obtained during the submersible dives, because the traditional K-Ar dating is impossible to remove the alteration part of rocks [6]. After the rock-samples, crushed to 100-500  $\mu\text{m}$  grains, they were irradiated by neutrons in a reactor to produce  $^{39}\text{Ar}$  from  $^{39}\text{K}$  during a few hours. During the irradiation, samples were packed with EB-1 biotite flux monitors [7],  $\text{K}_2\text{SO}_4$  and  $\text{CaF}_2$  as correcting factors in an aluminum capsule. Then, radiogenic  $^{40}\text{Ar}$ , daughter nuclide of radioactive  $^{40}\text{K}$  and parent,  $^{39}\text{Ar}$  instead of  $^{40}\text{K}$ , were simultaneously analyzed using a mass-spectrometer with an extraction technique of mul-ti-step heating of approximately every 50 to 100  $^{\circ}\text{C}$  be-tween 500 to 1500  $^{\circ}\text{C}$ .

**RESULTS:** We obtained an estimated eruption age of no more than 3 Ma base on several dating methods of Ar-Ar and others. The NW Pacific petit-spots and this newly described WPSP petit-spot were all erupted from locations in the zone of concave flexure on the outer rise of the lithosphere, prior to its subduction at a trench.

The WPSP eruption site is >1100 km from the Ogasawara Trench and 800 km from the Mariana Trench. These relatively large distances from the trench axes could possibly be explained by the wider outer rise in this subduction system, where the distance to the crest of the outer rise at the Mariana Trench is greater than in other subduction systems [8].

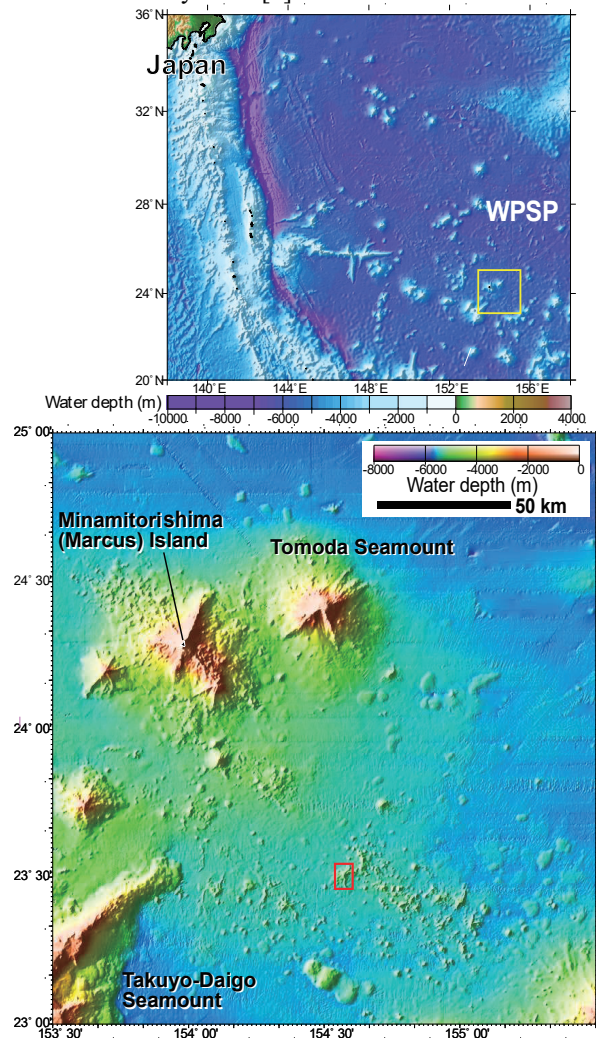


Fig. 1. Bathymetric map of the study area. Yellow box on the upper figure indicate the area of map shown in lower figure. The red square on lower figure indicates the area discovered the young volcano.

#### REFERENCES:

- [1] N. Hirano *et al.*, *Science*, **313** (2006) 1426-1428.
- [2] N. Hirano *et al.*, *Basin Res.*, **20** (2008) 543-553.
- [3] N. Hirano *et al.*, *Geochem. J.*, **47** (2013) 249-257.
- [4] R. Taneja *et al.*, *Gondwana Res.*, **28** (2014) 391-406.
- [5] N. Hirano *et al.*, *Marine Geol.*, **373** (2016) 39-48.
- [6] I. McDougall and T. M. Harrison, in *Geochronology and Thermochronology by the  $^{40}\text{Ar}/^{39}\text{Ar}$  Method*, (Oxford, New York, 1988).
- [7] N. Iwata, Ph.D. Thesis, Tokyo Univ. (1998).
- [8] N. Hirano *et al.*, *Deep-Sea Re. I*, **154** 103142 (2019).

## CO5-4 Recrystallization of an amorphous Si layer by H<sup>+</sup> ion beam and electron beam irradiation

J. Nakata, T. Iha, Y. Hoshino, A. Yabuuchi<sup>1</sup> and A. Kinomura<sup>1</sup>

Department of Math-Phys, Kanagawa University

<sup>1</sup>Institute for Integrated Radiation and Nuclear Science, Kyoto University

**INTRODUCTION:** IBIEC (ion beam induced epitaxial crystallization) phenomena have been widely studied for about forty years, especially by using MeV ion beam irradiation<sup>1-3</sup> The author proposed mechanism of IBIEC, consisting of formation of vacant spaces in the amorphous Si (a-Si) layer after vacancy-interstitial recombination in the crystalline Si (c-Si) substrate. The finally remained vacancies after recombination produced at the a-c interface were supplied to the amorphous layer and became vacant spaces in it. These resulted in the vibrational motion of Si atoms wider and more freely, eventually epitaxial recrystallization occurred at lower temperature than that in normal heat treatment. Electron-hole pairs creation also occurred effectively due to MeV ion irradiation. When they are recombined, emitted radiation energy also enhanced the vacancy or interstitial migration, eventually recrystallization rate was greatly enhanced.<sup>4</sup> However, the role of inelastic electronic scattering in the IBIEC process has not been necessarily and directly proved. Thus, we tried to make sure the effect of electronic scattering in the IBIEC process. We compared the IBIEC rate by H<sup>+</sup> ion beam with the EBIEC (Electron Induced Epitaxial Crystallization) rate by e-beam.

**EXPERIMENTS:** 190 keV Si<sup>+</sup> ions were implanted at 50~60°C with doses of 5, 10, 20, 50, 100×10<sup>14</sup>/cm<sup>2</sup> for 10 μA beam current, to form damaged and a-Si layers in the c-Si substrates. Then, 1) IBIEC, 2) EBIEC, 3) furnace annealing were undergone to these above obtained damaged and amorphized substrates. The H<sup>+</sup>-IBIEC was conducted at 150 keV with 2×10<sup>16</sup> cm<sup>2</sup> doses for ~3 μA continuous beam current at 400°C for 23 hours. 2) The EBIEC was conducted at 7.2 MeV with 4.07×10<sup>19</sup>/cm<sup>2</sup> doses for ~70 μA pulsed electron beam at 400°C for 46 hours. 3) thermal annealing for the as-amorphized sample was conducted at 400°C for 23 hours in vacuum chamber, and for 46 hours in the gold-furnace during Ar ambient flowing. The thicknesses of a-Si layers of these three samples were measured by the Rutherford Backscattering method with 2 MeV Li<sup>2+</sup> ions, SSB detector being settled at 120° angle to the Li<sup>2+</sup> beam direction.

**RESULTS:** Figure 1 and 2 show respectively the RBS spectra after IBIEC (mark○ in Fig. 1) and EBIEC (mark○ in Fig. 2) to the amorphized samples with 2.0×10<sup>15</sup>/cm<sup>2</sup> Si doses. We also show in these figures for the as-implanted and annealed samples at 400°C for 23 hours (mark▲ in Fig. 1) and at 400°C for 46 hours (mark▼ in Fig. 2). As clearly seen in Fig. 1, IBIEC at 400°C sample (mark○) was crystallized sharply, compared with that (mark▲) of the 400°C-annealing one in vacuum for 23 hours.

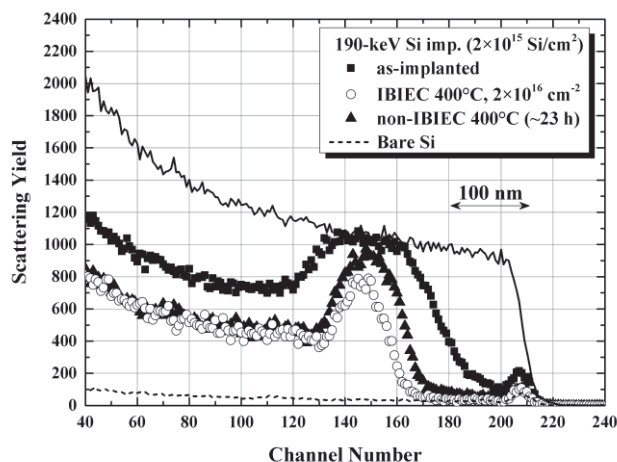


Fig. 1. RBS spectra for the IBIEC sample

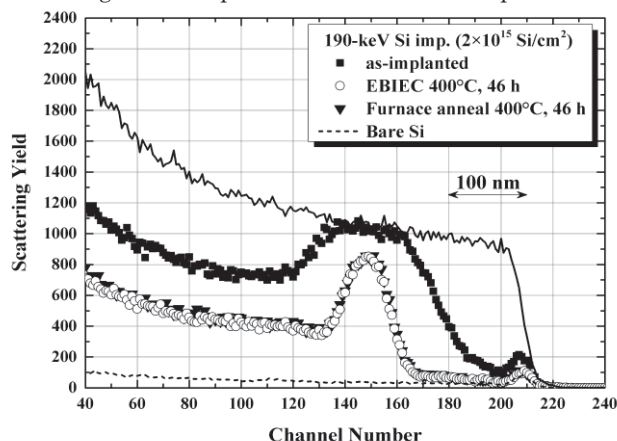


Fig. 2. RBS spectra for the EBIEC sample

As also clearly seen in Fig. 2, EBIEC sample at 400°C (mark○) was not entirely crystallized at all, compared with that (mark▼) for the furnace-annealed one in Ar ambient at 400°C for 46 hours.

**DISCUSSIONS:** In calculation, displaced Si atom density is almost the same for both 150-keV H<sup>+</sup> ion for 2×10<sup>16</sup> cm<sup>2</sup> and 7.2-MeV electron for 4.07×10<sup>19</sup>/cm<sup>2</sup> doses at around the a-c interface region. Furthermore, considering the total doses of H<sup>+</sup> ions and electrons, total inelastic electronic deposited energy density in EBIEC is about only 8 times higher than that in IBIEC in spite of the 2000 times higher doses in EBIEC. Consequently, it seems that the IBIEC rate is mainly determined by the elastic energy deposition and it cannot be decisively concluded that the electronic deposited energy density enhances the crystallization rate. It should be noted that IBIEC rate generally decreases as the irradiation dose rate increases. Thus, we should thoroughly compare the dose rate of EBIEC by **pulsed** electron beam with the dose rate of IBIEC by **continuous** H<sup>+</sup> ion beam.

### REFERENCES:

- 1) J. Nakata and K. Kajiyama: Appl.Phys.Lett., **40**(8) (1982) 686-688.
- 2) J. Nakata and K. Kajiyama: Jpn. J. Appl. Phys., **21** (1982) 211-216.
- 3) J. Nakata: Phys. Rev., **B43** (1991) 14643-14668.
- 4) J. Nakata: J. Appl. Phys., **79** (1996) 682-698.

## CO5-5 Study on Elemental Concentration in the Atmospheric Particulate Matter by INAA

N. Hagura<sup>1,2</sup>, Y. Okada<sup>2</sup>, H. Matsuura<sup>1,2</sup>, T. Uchiyama<sup>2</sup>

<sup>1</sup> Nuclear Safety Engineering, Tokyo City University

<sup>2</sup> Atomic Energy Research Laboratory, Tokyo City University

**INTRODUCTION:** The Atomic Energy Research Laboratory of Tokyo City University (TCU-AERL) has operated the research reactor "Musashi Institute of Technology Research Reactor (MITRR)" from 1963 to 1989, and has performed various neutron experimental research that is including instrumental neutron activation analysis (INAA). In 2003, it officially decided to decommission the research reactor, and it is currently in the decommissioning stage. At present, all the fuel has been carried out, and it is in the phase of storing and managing radioactive compounds.

Since 2002, sampling of airborne particulate matter have been performed on our facility. Even before that, research on the measurement of radioactivity in the environment has been conducted mainly by Dr. Honda, deceased in 2014, and the concentration distribution of Be-7 and Pb-210 and chemical form in deposition have been analyzed [1]. These studies mainly focused on the behaviors of yellow sand that came to the Japanese archipelago.

After the accident in Fukushima in March 2011, studies on the dynamics of radioactive cesium have been conducted. Especially, focusing on the difference between the rapid decay of radioactive cesium concentration after the accident and the gradual decay after several months, we have been investigating the relationship between the different chemical forms [2, 3].

The sampled filters have been accumulated in the laboratory and are ready to be analyzed again. This fiscal year, we aimed to detect the elements other than cesium by neutron activation analysis, targeting the samples from February to July in 2011.

**EXPERIMENTS:** We use a high volume air sampler (Shibata Scientific Technology LTD., HV-1000F, filter: ADVANTEC, QR-100 (collection efficiency: 99.99% for 0.3  $\mu\text{m}$  particles)) with an inhalation flow rate of 700 L  $\text{min}^{-1}$ . Samples are collected approximately every week. The radioactivity of the filter that has collected dust is measured by a high-purity germanium semiconductor detector (ORTEC, GMX-15190-P, wide range energy type, relative counting efficiency: 20.1%, FWHM: 1.22keV at 122keV, 1.9keV at 1.33MeV, wave height discriminator: SEIKO EG&G, MCA-7700), and a part of the filter was stored for neutron activation analysis.

Irradiation was performed at the research reactor KUR at the Institute for Integrated Radiation and Nuclear Science, Kyoto University, between the October and January with four machine times in FY2019. The irradiation conditions are shown in Table 1. The measurement of radioactivity of short half-life nuclides was carried out using the HP-Ge semiconductor detector of the hot laboratory of

KUR. And long and medium-lived nuclides, after cooling for one or two weeks, transported to the TCU-AERL, and was measured by a HP-Ge semiconductor detector. Jlk-1 was used as a comparative standard substance.

**RESULTS:** Figure 1 shows the time-series distribution of elements for each sample. Figure 2 shows the correlation coefficients of these 10 nuclides. As expected, we obtained reasonable results of relatively high concentrations of Na, Al, Ca, and Fe. Regarding the correlation coefficient, it was shown that Al and Ca are relatively strongly correlated with other elements.

In the future, we plan to proceed with the analysis of a large number of samples in combination with the PIXE analysis method using the tandem accelerator at our facility (TCU-Tandem) [4], because it is impractical to analyze all samples by the INAA method.

Table 1. Irradiation conditions.

Irradiation			Operating power	Thermal neutron flux
date	time	position		
2019/10/1	30 sec	Pn-3	1 MW	$4.7 \times 10^{12} \text{ n/cm}^2/\text{sec}$
2019/10/23	60 min	Pn-2		$5.5 \times 10^{12} \text{ n/cm}^2/\text{sec}$
2019/12/3	30 sec	Pn-3		$4.7 \times 10^{12} \text{ n/cm}^2/\text{sec}$
2020/1/15	60 min	Pn-2		$5.5 \times 10^{12} \text{ n/cm}^2/\text{sec}$

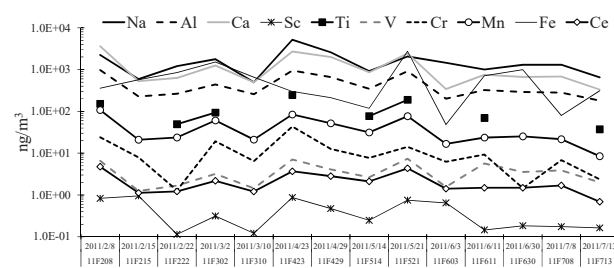


Fig. 1. Transition of element concentration for each sample from February to July in 2011

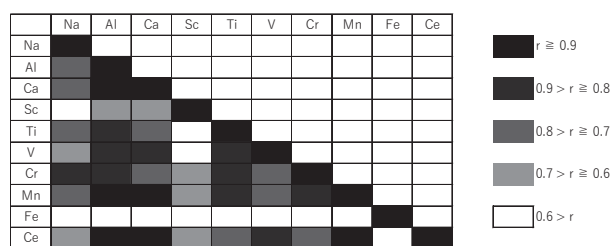


Fig. 2. Distribution chart of correlation coefficient between elements

### REFERENCES:

- [1] K. Hirose, *et al.*, Atmospheric Environment, 38 (38), pp. 6601-6608 (2004).
- [2] K. Nakamachi, *et al.*, Bunseki Kagaku, 64 (8) pp. 589-594 (2015).
- [3] N. Hagura, *et al.*, Bunseki Kagaku, 66 (3), pp. 201-204 (2017).
- [4] N. Hagura, *et al.*, Transactions of the Atomic Energy Society of Japan, 17 (3-4), pp. 111-117 (2018).

## CO5-6 Neutron activation analysis for sediments, phytoplankton, lake water of Lake Akagi Onuma

Y. Okada, T. Uchiyama, N. Kumagai<sup>1</sup>, N. Hagura<sup>2</sup>,  
H. Matsuura<sup>2</sup> and Y. Iinuma<sup>3</sup>

Atomic Energy Research Laboratory, Tokyo City University

<sup>1</sup>Cooperative major in Nuclear Energy, Tokyo City University

<sup>2</sup>Department of Nuclear Safety Engineering, Tokyo City University

<sup>3</sup>Institute for Integrated Radiation and Nuclear Science, Kyoto University

**INTRODUCTION:** Contamination of radioactive Cs of Lake Akagi Onuma in Gunma Prefecture was observed due to the accident at Fukushima Daiichi Nuclear Power Station. Recently, the levels of radioactive Cs in wakasagi that live there have been slowly decreasing with the decrease of that of the lake water. In order to clarify the cause of the gradual collapse, we have been investigating the inhabiting organisms and their surrounding areas for 8 years (1, 2).

This study will be conducted as part of investigating the contribution of sediments to lake water. In this research, we investigated lake sediments, phytoplankton, and trace elements in lake water.

**EXPERIMENTS:** The sediment sample was processed as in the 2018 report. 22 sediment samples from 10 to 570 mm deep collected in 2015, dried phytoplankton, and freeze-dried lake water collected at depths 0, 8 and 15 m in 2018 (wet weight approx. 500 g) was used for the analysis. These samples were double-packed in a clean polyethylene bag. 31 samples (about 50 mg) and comparative standards (JLK1-1, NIES8) were irradiated with a thermal neutron flux of  $4.68 \times 10^{12}$  n/cm<sup>2</sup> for a short time (30 seconds). Neutron flux  $5.5 \times 10^{12}$  n/cm<sup>2</sup> s<sup>-1</sup> for 2 s,  $1 \times 10^{12}$  n/cm<sup>2</sup> s<sup>-1</sup> for long time (3600 s) for KUR s<sup>-1</sup>. To monitor neutron flux, approximately 9 mg of aluminum wire containing 1.5% Sb and approximately 11 mg of Fe wire were doubly packed in a clean polyethylene bag and the sample and comparative standard were irradiated together.

The irradiated samples were measured by conventional  $\gamma$ -ray spectrometry using a coaxial Ge detector. Analysis of  $\gamma$ -ray spectrometry were at Gamma Studio (SEIKO EG&G Co.,LTD).

**RESULTS:** Using neutron activation analysis, 30 elements in sediment, 19 elements in phytoplankton, and 17 elements in lake water were quantified. Fig. 1 shows the stable Cs concentration in each sediment. The stable Cs concentration changes in the range of 2  $\mu\text{g/g}$  to 5  $\mu\text{g/g}$  at a depth of 10 mm to 570 mm. Among the 19 elements of phytoplankton, it was found that Mg, Mn, Si, Sb and Cs have similar concentrations to those of sediments. Fig. 2 shows a comparison of sediment and phytoplankton samples with Mg, Mn, Si, Rb, Sb and Cs concentrations.

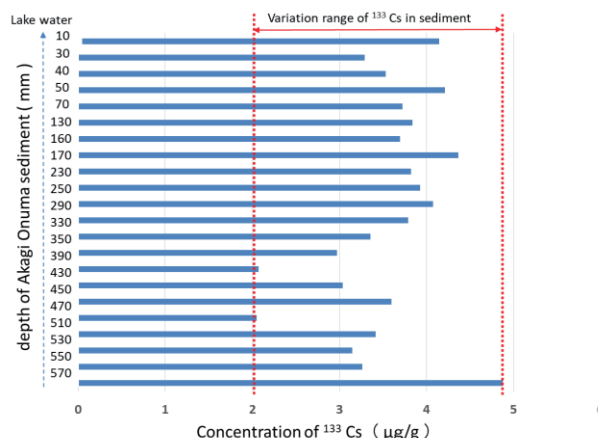


Fig.1 Concentration of <sup>133</sup>Cs for each depth of Akagi Onuma sediment

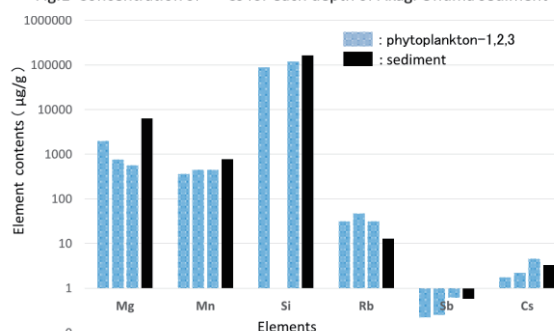


Fig.2 Mg, Mn, Si, Sb, Cs contained in phytoplankton and sediment

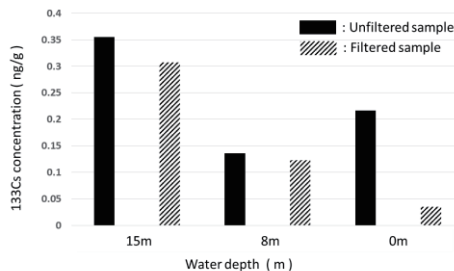


Fig.3 <sup>133</sup>Cs(stable Cs) concentration in the lake water of Akagi Onuma (2018 August)

Fig. 3 shows stable cesium quantification results collected in lake water in August 2018. Stable Cs quantification values for unfiltered and filtered lake water are shown at depths of 15 m, 8 m, and 0 m, respectively. The stable cesium concentration was highest at 15 m. This was the same trend as the radioactive cesium concentration in August. Comparing stable cesium with and without filtration, both 15 m and 8 m showed similar values. From this result, it is considered that stable cesium exists in a dissolved state. At 0m, stable cesium was found to be low with filtration and in suspension collected by 0.45 $\mu\text{m}$  filter.

### REFERENCES:

- [1]K.Suzuki *et al.*, Science of the Total Environment, **622-623** (2018)1153-1164.
- [2] M.Mori *et al.*, Science of the Total Environment, **575** (2017)1247-125.

## CO5-7 Formation age of Precambrian metamorphic rocks and thermal history

H. Hyodo<sup>1</sup>, K. Sato<sup>1,2,3</sup>, H. Kumagai<sup>3</sup> and K. Takamiya<sup>4</sup>

<sup>1</sup> Institute of Frontier Science and Technology,  
Okayama University of Science

<sup>2</sup> Department of Applied Chemistry and Biochemistry,  
National Institute of Technology, Fukushima College

<sup>3</sup> Submarine Resources Research Center, Japan Agency  
for Marine-Earth Science and Technology

<sup>4</sup> Institute for Integrated Radiation and Nuclear Science,  
Kyoto University

**INTRODUCTION:** Acasta gneiss is known as a part of the oldest crust (ca. 4.0 Ga) by U-Pb zircon SHRIMP dating [1]. The thermal history of the rock seems to be complicated [2] because it shows much younger age (1.9 Ga) in apatite U-Pb method [3].

K-Ar system is more susceptible to external disturbance compared to U-Pb system, and wide range of closure temperature. To elucidate the thermal history, hornblende and biotite samples of Acasta gneiss were dated by <sup>40</sup>Ar/<sup>39</sup>Ar method.

**EXPERIMENTS:** Experimental procedure is the same as described as previous studies on single grain datings. Rock samples were crushed and sieved in #25-100 mesh. After ultrasonic cleaning in distilled water, single mineral grains were handpicked. The mineral grains were irradiated in the KUR for 24 hours at 1 MW. The total neutron flux was monitored by 3gr hornblende age standard [4], [5], which was irradiated in the same sample holder. In the same batch, CaSi<sub>2</sub> and KAlSi<sub>3</sub>O<sub>8</sub> salts were used for interfering isotope correction. A typical J-value was  $(5.390 \pm 0.068) \times 10^{-3}$ . In stepwise heating experiment, the minerals were heated under defocused argon ion laser beam, and temperature of sub-millimeter grains was measured using infrared thermometer whose spatial resolution is 0.3 mm in diameter with a precision of 5 degrees. In order to achieve a precise temperature control, feedback system between temperature monitoring and laser power control were adopted. Extracted argon isotopes were measured using the custom made mass spectrometer with mass resolution of approximately 400 to separate <sup>39</sup>Ar peak from neighboring hydrocarbon peak [5].

**RESULTS:** One of <sup>40</sup>Ar/<sup>39</sup>Ar age spectra of biotite grains were illustrated in Fig. 1. The plateau age 1.935 Ga is consistent with 1.964 Ga of the hornblende and the U/Pb age of apatite of the Acasta gneiss, considering a prolonged thermal history.

The area known to have a metamorphic history caused by

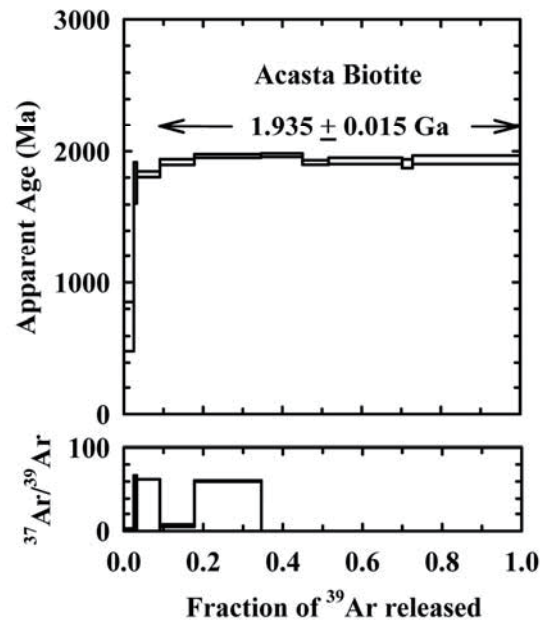


Fig. 1. <sup>40</sup>Ar/<sup>39</sup>Ar age spectra of a biotite grain from Acasta gneiss. The <sup>37</sup>Ar/<sup>39</sup>Ar error seems to be large, but little effect on the age spectra with a well-defined plateau.

Wopmay orogen around 2.0 Ga. On the other hand, zircons from the area typically show 4.0 Ga. The age gap seem to represent the difference in closure temperature of minerals.

Closure temperature depends on the grain size and cooling rate of the orogen. If we apply typical closure temperatures of hornblende and zircon, The Acasta area was heated to at least above 500°C and below 900°C, and the zircon preserved the formation age, but the hornblende was reset by the Wopmay metamorphism.

### REFERENCES:

- [1] S.A. Bowring and I.S. Williams, *Contributions to Mineralogy and Petrology*, **134** (1999) 3–16.
- [2] T. Iizuka *et al.* *Precambrian Research* **153** (2007) 179–208.
- [3] Y. Sano, *et al.*, *Geochimica Cosmochimica Acta* **63** (1999) 899–905.
- [4] J.C. Roddick, *Geochim. Cosmochim. Acta* **47** (1983) 887–898.
- [5] H. Hyodo, *Gondwana Research* **14** (2008) 609–616.

## CO5-8 A Study on Evaluation of Redox Condition of Tokyo Bay using Redox Sensitive Elements as an Indicator by Means of Instrumental Neutron Activation Analysis

M. Matsuo<sup>1</sup>, K. Shozugawa<sup>1</sup>, Y. Guan<sup>1</sup>, M. Komori<sup>1,2</sup>, R. Okumura<sup>3</sup>, Y. Inuma<sup>3</sup> and K. Takamiya<sup>3</sup>

<sup>1</sup>Graduate School of Arts and Sciences, The University of Tokyo

<sup>2</sup>Yokohama Environmental Science Research Institute

<sup>3</sup>Institute for Integrated Radiation and Nuclear Science, Kyoto University

**INTRODUCTION:** Hypoxia is water mass that is deficient in dissolved oxygen (DO), often occurs in closed water areas such as the inner bay [1]. In dredged trenches of Tokyo Bay severe hypoxia has been observed in annual summer seasons. The purpose of this study is to clarify the relationship between hypoxia and the sediment environment of dredged trench by chemical analysis of sediments in the vertical direction, assuming that the effect of past hypoxia could be preserved as a difference in concentrations and/or chemical states of elements in the sediments.

To estimate the sedimentary environment related to redox conditions, various elements have been used. For example, Fe and Mn are used because their various chemical states on Eh-pH diagrams have become clear [2]. And U is used for the evaluation of weak reductive conditions because the redox potential of U(VI)/U(IV) is between Mn(IV)/Mn(II) and S(VI)/S(-II) [3]. In this study, concentrations of Fe, Mn, U, Th, and Ce in the sediments were analyzed by instrumental neutron activation analysis (INAA).

**EXPERIMENTS:** We sampled sediment cores from the dredged trench and non-dredged seabed off Makuhari, Chiba Prefecture in August 2019. All cores were cut in the vertical direction at 2 cm intervals in the laboratory. Then, the samples were desalted by centrifugation with pure water washing three times and dried at 105 °C.

Approximately 30 mg of sediments were packed in double polyethylene film bags to perform INAA. All samples were irradiated with neutrons at the pneumatic tube, Kyoto University Research Reactor. Three types of gamma-ray measurement were carried out corresponding to half-lives of elements. For analysis of Mn, samples were irradiated for 10 seconds at 1 MW, and then gamma-ray was measured for 600 seconds by Ge detector after 600 seconds cooling. Regarding U, samples were irradiated for 20 minutes at 1 MW, and then gamma-ray was measured for 1400 seconds after 3-4 days cooling. Regarding Fe, Th and Ce, samples were irradiated for 20 minutes at 1 MW, and the measuring time of gamma-ray was for 10000 seconds after 2-3 weeks cooling.

**RESULTS:** The concentration of Mn was lower in dredged trench than that in non-dredged seabed, suggesting that the dredged trench was in more reductive condition (Fig. 1). On the other hand, there was no significant difference for Fe. It is well-known that the concentrations

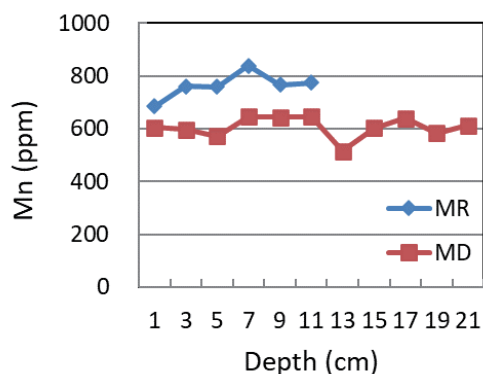


Fig. 1. Depth profile of Mn concentration in the sediments collected from dredged trench (MD) and non-dredged seabed (MR) off Makuhari.

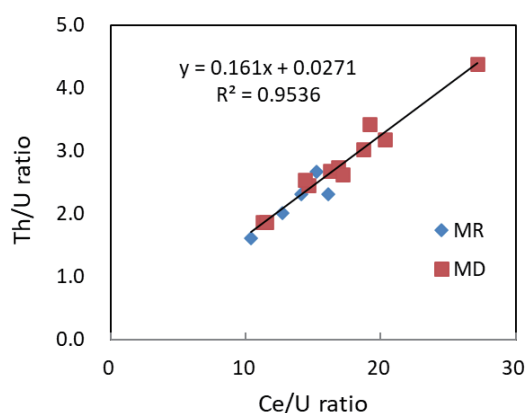


Fig. 2. Th/U-Ce/U plots in the sediments collected from dredged trench (MD) and non-dredged seabed (MR) off Makuhari.

of both Fe and Mn in sediments increase when condition of seawater is oxidative. However, we note that Mn precipitates under more oxidative conditions. Therefore, it is estimated that the oxidation-reduction potential in the dredged trench remained to the extent that Fe precipitation occurred but no Mn precipitation occurred.

In addition, we plotted the relation between Th/U and Ce/U ratios (Fig. 2). The values of Th/U and Ce/U ratios at each site existed on a same line. This fact indicates that the sediments cannot be the mixture of two or more sources which have different Th/U and Ce/U ratios. However, this figure shows that MD samples are in more oxidative condition. Also, comparing the MD sample ratios with the values of 2017-year sample shows that the dredged trench in this year is more oxidative. This fact indicates that the anoxic state is gradually recovering.

### REFERENCES:

- [1] R.J. Diaz *et al.*, *Science*, **321** (2008), 926-929.
- [2] D.G. Brookins, in *Eh-pH diagrams for geochemistry* (Springer-Verlag, 1988).
- [3] D.R. Turner, M. Whitfield and A.G. Dickson, *Geochim. Cosmochim. Acta*, **45** (1981), 855-881.

M. Yanaga, K. Ogawa<sup>1</sup>, T. Nagakura<sup>1</sup>, H. Yoshinaga<sup>2</sup>, R. Okumura<sup>2</sup> and Y. Iinuma<sup>2</sup>

Center for Radioscience Education and Research,  
Faculty of Science, Shizuoka University

<sup>1</sup>Department of Chemistry, Faculty of Science, Shizuoka University

<sup>2</sup>Institute for Integrated Radiation and Nuclear Science, Kyoto University

**INTRODUCTION:** The Fukushima Daiichi Power Plant accident caused a large amount of radioactive materials released in to the atmosphere[1-3]. Radioactive cesium is especially a problem because of its long half-life. Paddy field soil was also contaminated with radioactive cesium. However, simple removal of contaminated soil would create a vast quantity of radioactive waste. Therefore, separating radioactive cesium from the soil is necessary to prevent damage by rumors and to minimize the quantity of radioactive waste.

Previously, we reported that the absorption of radioactive cesium from artificially contaminated soil into rice plants increased by adding a stable isotope to irrigation water and that the possibility that the cesium atoms added were replaced with radioactive cesium atoms in soil [4, 5]. However, addition of excess amount of stable cesium caused an obstacle to growth of rice plant [6]. Therefore, in this study, we conducted hydroponic culture of white radish sprouts and analyzed trace elements contained in leaves and stems to investigate the behavior of cesium added to the culture solution and the competitive relationship between alkali metals.

**EXPERIMENTS: Materials and Method** Cultivation of white radish sprouts was carried out by adding alkali metal ions, such as potassium ions, rubidium ions and/or cesium ions, to a diluted solution of a commercially obtained culture solution, HYPONeX® (HYPONeX JAPAN CORP.,LTD.).

**INAA** The samples in polyethylene capsules were irradiated in Pn-3 for 90 seconds and in Pn-2 for 4 hours, for short and long irradiation, respectively. As comparative standards, the certified NIST Standard Reference Material 1577b Bovine Liver as well as elemental standard for Cs was used. The  $\gamma$ -ray spectroscopic measurements with an HPGe detector were performed repeatedly for the short-irradiated samples: the first measurements for 120 – 900 seconds after decay time of 5 - 15 minutes and the second one for 250 - 1200 seconds after 60 - 150 minutes. The long-irradiated samples were measured for 1 - 24 hours after an adequate cooling time (15 - 60 days).

**RESULTS:** In order to examine the change in the concentration of cesium ions contained in the leaves, white radish sprouts were cultivated by adding  $3.0 \times 10^{-5}$  mol of

cesium ions to the culture solution. When only cesium ions were added to the culture medium, the cesium concentration in the leaves increased with the growth of the white radish sprouts, indicating that cesium ions were absorbed and accumulated in the leaves. Furthermore, as shown in Fig. 1, when grown in a mixed solution with rubidium ions, the cesium concentration in leaves increased. Increasing the concentration of rubidium ions in culture medium increased the cesium concentration in the leaves. This suggests that rubidium ions promoted absorption of cesium ions by plants. However, when the cesium ion concentration in the culture solution was tripled, the leaves discolored and growth disorders were observed. On the other hand, when cesium and potassium ions were added in culture medium, cesium concentration in leaves decreased as the potassium ion concentration in medium increased. This suggests that the presence of potassium ions suppress absorption of cesium ions in plants.

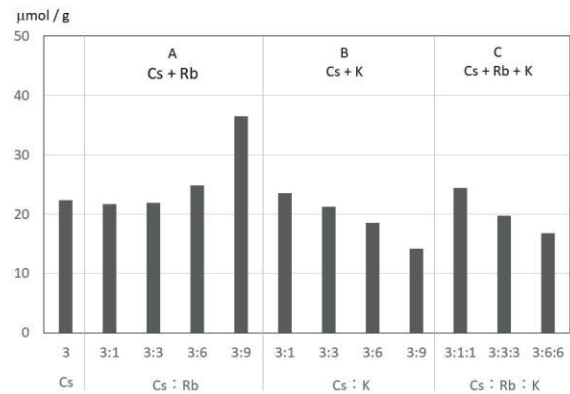


Fig. 1. Cesium ion concentration in leaves of white radish sprouts grown in culture solutions with various alkali metal in concentrations. The amount of cesium ion added to the culture solution was constant and was  $3.0 \times 10^{-5}$  mol.

#### REFERENCES:

- [1] S. Endo *et al.*, J. Environ. Radioact., 111 (2012) 18-27.
- [2] M. Yanaga and Y. Oya, Radiation Safety Management, 12 (2013) 16-21.
- [3] M. Yanaga *et al.*, Radiation Safety Management, 12 (2013) 37-42.
- [4] M. Yanaga *et al.*, NMCC ANNUAL REPORT, 22 (2015) 185-190.
- [5] M. Yanaga *et al.*, NMCC ANNUAL REPORT, 23 (2016) 172-179.
- [6] M. Yanaga *et al.*, KURNS Progress Report 2018 (2019) CO5-10.

R. Okazaki and S. Sekimoto<sup>1</sup>

*Department of Earth and Planetary Sciences, Kyushu University*

<sup>1</sup>*Institute for Integrated Radiation and Nuclear Science, Kyoto University*

**INTRODUCTION:** The major goal of this study is to determine the minor element compositions and Ar-Ar ages for submillimeter-sized extraterrestrial materials. We have been continually working to achieve this objective since 2013 (project #: 25066, PI: S.S.). In the Ar-Ar dating, concentrations of the parent (<sup>40</sup>K) and daughter (<sup>40</sup>Ar) nuclides are determined simultaneously. In order to obtain precise ages, it is important to adjust the irradiation condition, such as irradiation duration, neutron flux and neutron energy.

In the last year's proposal, we have investigated two irradiation conditions by using the hydraulic conveyor and the long-term irradiation plug. We have measured noble gases in JG-1 and orthoclase samples irradiated by the Hydro and Long-term irradiations. Based on the <sup>39</sup>Ar/<sup>40</sup>Ar ratio determined for the Hydro and Long-term orthoclase samples, we found that the neutron flux parameter (J-value) for the Long-term irradiation is about half of that for the Hydro irradiation. Especially for NAA, it is important to evaluate the difference in the neutron energy spectrum between the two irradiation conditions. In this year's proposal, we conducted NAA for the standard minerals and a meteorite sample (Allende) that was already measured for NAA previously by using the Hydro irradiation.

**EXPERIMENTS:** Several hundred milligram samples were prepared from the Allende CV chondrite (Provided by Smithsonian museum [1]) and our standard minerals (JB-1 [2], JP-1 [3], DTS-2b [4], orthoclase [5], sanidine, and wollastonite). Each of the samples was placed in a conical dimple (φ1, depth ~ 0.5 mm) of a sapphire disk (φ5.5, 1.5 mm thick), and covered with a sapphire disk (φ5.5, 0.3 mm thick). Each of the sapphire container was wrapped with pure aluminum foil. These Al-wrapped containers were stacked and sealed in the capsules for the Long-term irradiation. Condition of the Long-term irradiation as 122 hours under 1MW-operation + 18 h under 5MW-operation.

**RESULTS and DISCUSSION:** After irradiation, the samples were moved to non-irradiated glass container with similar dimension from the sapphire one in order to reduce the radioactivity from the sapphire containers and Al foil. For the selected samples (Allende, JP-1, and DTS-2b), gamma ray measurements of radioactive nuclides were performed. The results are now analyzed to examine if the gamma ray spectrum of the Long-term irradiated Allende sample is essentially identical to the previous result of the Hydro irradiation. Based on the spectrum of the Long-term irradiated Allende sample,

minor element concentrations in DTS-2b and JP-1 will also be calculated and compared with the compositions reported [3, 4].

After the gamma ray measurements, some of the irradiated samples were moved to Kyushu Univ. to measure noble gas isotopes. Noble gas analyses for these samples will be done this summer in order to evaluate the presence of interference isotopes produced by the low energy neutrons.

#### REFERENCES:

- [1] E. Jarosewich *et al.*, Smithsonian Contributions to the Earth Sciences **27** (1987) 1-49.
- [2] A. Ando *et al.*, Geochemical Journal **5** (1971) 151-164.
- [3] <https://gbank.gsj.jp/geostandards/igneous.html>
- [4] I. Raczek *et al.*, Geostandards Newsletter, **25** (2001) 77-86.
- [5] S. Weiss, Mineralien Magazin Lapis. **16** (1991) 13-14.

## CO5-11 Determination of Abundance of Rare Metal Elements in Seafloor Hydrothermal Ore Deposits by INAA Techniques-6: Evaluation of analytical accuracy

J. Ishibashi, T. Miyamoto, Y. Tada<sup>1</sup>, Y. Sekiya<sup>1</sup>, K. Yonezu<sup>1</sup>, R. Okumura<sup>2</sup>, Y. Iinuma<sup>2</sup> and K. Takamiya<sup>2</sup>

*Department of Earth and Planetary Sciences, Faculty of Science, Kyushu University*

<sup>1</sup>*Department of Earth Resources Engineering, Faculty of Engineering, Kyushu University*

<sup>2</sup>*Institute for Integrated Radiation and Nuclear Science, Kyoto University*

**INTRODUCTION:** Instrumental neutron activation analysis (INAA) has several advantages for geochemical tools to provide useful information for mineral exploration. For example, INAA enables highly sensitive multi-element analysis without geochemical pretreatment. We have conducted preliminary studies using mineralized samples collected from active seafloor hydrothermal fields, with a view to confirm and extend the range of application of this technique. Here, we report evaluation for analytical accuracy of INAA techniques.

**EXPERIMENTS:** We conducted a series of analysis of four materials (DS-1, CCU-1d, WMS-1a, and CH-4) from "Certified Reference Materials" which are provided by Natural Resource Canada in following three runs. In Run#1, samples were irradiated at Pn-3 (thermal neutron flux =  $4.6 \times 10^{12}$  n/cm<sup>2</sup>/sec at 1 MW operation) for 0.5 minute, and the gamma ray activity was measured for 2-5 minutes after adequate cooling time (<5 hours). In Run#2, samples were irradiated at Pn-2 (thermal neutron flux =  $5.5 \times 10^{12}$  n/cm<sup>2</sup>/sec at 1 MW operation) for 15 minutes, and the gamma ray activity was measured for 15 minutes after adequate cooling time (~25 hours). In Run#3, samples were irradiated at Pn-2 (thermal neutron flux =  $5.5 \times 10^{12}$  n/cm<sup>2</sup>/sec at 1 MW operation) for 30 minutes, and the gamma ray activity was measured for 15 minutes after adequate cooling time (~30 hours).

**RESULTS:** Gamma ray intensities per 1Bq of As-76 or Mn-56 of each irradiated Certified Reference Material were calculated assuming that the elemental contents are identical to the reported values. Then, they were compared with gamma ray intensities of an artificial standard material (a piece of plastic filter loaded with known amount of As or Mn) which was irradiated in the same capsule. Their ratios (Reference/artificial standard) were plotted along the energy (keV) of the calculated gamma rays in Fig. 1.

The obtained ratios were basically within the range of  $1.0 \pm 0.1$ , which assures good analytical accuracies. However, some of them deviated from the ideal ratio. For example, CCU-1d (Cu-rich sulfide) and WMS-1a (Fe-rich sulfide includes 1% of Cu) showed rather poor accuracy (actually, the obtained ratios for WMS-1a were around 2.0 during Run#2). Since the deviation was more obvious in the gamma ray peaks in low energy, interference by Cu-66 would be responsible. Moreover, we have recognized that

Cu-rich sulfides cause other samples in the same capsule to intensify activations of some nuclides in the case of long-time irradiation, as reported in the last year. It is important to minimize irradiation time for analysis of mineralized sulfides to obtain good accuracy.

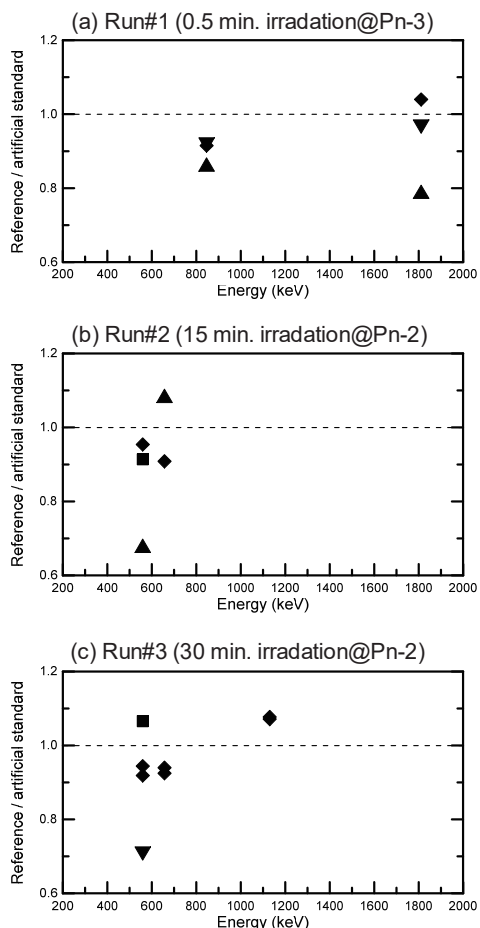


Fig. 1. Ratios of As-76 or Mn-56 gamma ray intensities of four materials (◆:DS-1, ▲:CCU-1d, ▼:WMS-1a, ■:CH-4) from the Certified Reference Materials to those of an artificial standard material irradiated in the same capsule.

N. Hasebe, M. Hamada<sup>2</sup>, K. Miura<sup>1</sup>, U. Uyangaa<sup>1</sup>, R. Januar<sup>1</sup>, Yudai Igarashi<sup>1</sup>, K. Oohashi<sup>2</sup>, Y. Minomo<sup>2</sup> and Y. Iinuma<sup>3</sup>

*Institute of Nature and Environmental Technology, Kanazawa University*

<sup>1</sup>*Graduate School of Natural Science and Technology, Kanazawa University*

<sup>2</sup>*Graduate School of Science and Technology for Innovation, Yamaguchi University*

<sup>3</sup>*Institute for Integrated Radiation and Nuclear Science, Kyoto University*

**INTRODUCTION:** Luminescence dating observes the natural accumulated radiation damage caused by radioisotopes such as U and Th as the form of glow after stimulation by heating or lightening. In this study, quartz vein distributed in Noto peninsula was collected and analysed by thermoluminescence (TL) and optical stimulated luminescence (OSL) methods. These quartz veins are found in the area where a small gold mine is located. There is a possibility that both of quartz vein and gold deposit is related and resulted from the thermal fluid circulation during the late stage of volcanic activity in the area.

**EXPERIMENTS:** A block of quartz vein with the size of ~15 cm in diameter was collected. This block was broken in the dark room and central small part was analysed. First, to examine the luminescence color, quartz was irradiated at gamma-ray irradiation facility at KUR to give a known dose of ~4 kGy. However, the luminescence emission was very dim and unable to identify the color. Remaining sample was measured by conventional OSL and TL methods. Annual dose is estimated from the U, Th, Sr, and K concentrations measured by LA-ICP-MS or X-ray fluorescence measurement (Ito et al., 2009, Stokes et al., 2003).

**RESULTS:** The OSL shows slowly decaying signal and suggests the small contribution of fast component. OSL signal is not very strong, and 14 measured aliquots show dispersed results (Fig. 1). Majority of samples showed equivalent dose less than 10 Gy. On the other hand, TL signal is strong. It is beyond the upper limit of artificial dose given by the in-house x-ray source, and could be estimated as around 3000 Gy (Fig. 2). Due to instrumental restrictions, it is not clear this value is close to the saturation or not. Therefore, this estimate could be the minimum value. The big difference between OSL and TL data may reflect the sample storage condition. Because quartz is transparent mineral, the inner samples may also be affected by the light and have lost the signal for OSL. Based on the TL results and annual dose, the estimated ages is older than 4.2 Ma. Considering that main volcanic activity was in the Miocene related to Japan Sea opening, this quartz vein might be formed during or just after the main volcanic activity.

## REFERENCES:

Ito, K., Hasebe, N., Sumita, R., Arai, S., Yamamoto, M., Kashiwaya, K., Ganzawa, Y., 2009. LA-ICP-MS analysis of pressed powder pellets to luminescence geochronology. *Chemical Geology* 262, 131-137.

Stokes, S., Ingram, S., Aitken, M.J., Sirocko, F., Anderson, R., Leuschner, D., 2003. Alternative chronologies for Late Quaternary (Last Interglacial-Holocene) deep sea sediments via optical dating of silt-sized quartz. *Quaternary Science Rev.* 22, 925-941.

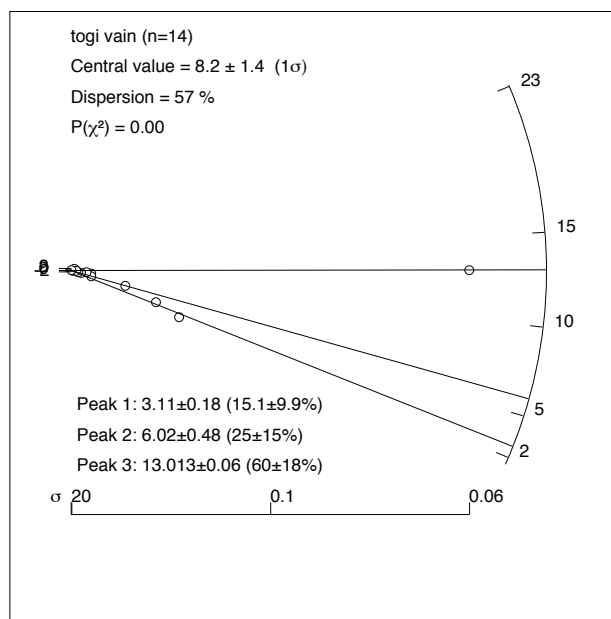


Fig. 1. Radial plot of fourteen OSL data (Gy).

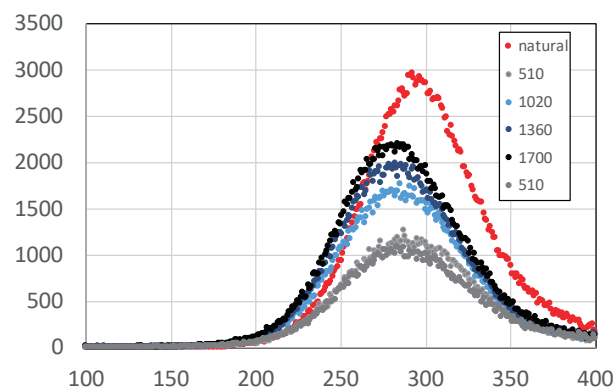


Fig. 2. Example of TL profile. Numerical numbers in the legend represent a given dose (Gy).

N. Shirai, S. Sekimoto<sup>1</sup>, M. Ebihara<sup>2</sup>

*Department of Chemistry, Tokyo Metropolitan University*

<sup>1</sup>*Institute for Integrated Radiation and Nuclear Science, Kyoto University*

<sup>2</sup>*Department of Earth Sciences, Waseda University*

**INTRODUCTION:** Howardite, eucrite and diogenite (HED meteorites) are the largest group of achondrite which are thought to have been derived from asteroid Vesta. Recently, the Dawn mission confirmed that the Vesta's surface is mineralogically and chemically similar to HED meteorites [1]. Depletions of siderophile elements in HED meteorites suggest that HED meteorites are products of differentiation [2]. Therefore, HED meteorites are important to elucidate the core formation of Vesta. Eucrites are mostly composed of pyroxene and plagioclase. As almost all eucrites are brecciated, it is difficult to bring out their primitive chemical compositions. Some eucrites (e.g., ALH 76005) were reported to contain foreign meteoritic components [e.g., 3]. From these materials, siderophile elements abundances for eucrites may have been modified. A few unbrecciated eucrites also have been found. As siderophile elements abundances for these unbrecciated eucrites were not affected by the incorporation of foreign materials, its chemical compositions give us the important information about the differentiation processes of Vesta. We determined elemental abundances for Northwest Africa (NWA) 10962, which was classified into unbrecciated eucrites [4] by using INAA and aimed to chemically characterize this meteorite in comparison with those for other eucrites.

**EXPERIMENTS:** A chip of NWA 10962 weighing 1.4 g was carefully ground in an agate mortars in order to obtain the representative chemical composition. This powder sample was firstly irradiated for 10 s at the pn-3 of the Institute for Integrated Radiation and Nuclear Science, Kyoto University with thermal and fast neutron fluxes of  $4.6 \times 10^{12}$  and  $9.6 \times 10^{11} \text{ cm}^{-2}\text{s}^{-1}$ , respectively. After irradiation, sample was immediately measured for gamma-ray emissions. After 24 hours, the same sample was irradiated for 3 h at the pn-2 of the Institute for Integrated Radiation and Nuclear Science, Kyoto University, with thermal and fast neutron fluxes of  $5.6 \times 10^{12}$  and  $1.2 \times 10^{12} \text{ cm}^{-2}\text{s}^{-1}$ , respectively. The sample was measured three times for gamma-rays after different cooling intervals over a one-month period. JB-1 and the Smithsonian Institution Allende meteorite sample were used as the standard reference material.

**RESULTS AND DISCUSSIONS:** Twenty elements could be determined by using INAA. Major elements abundances of NWA 10962 are similar to those of the common Main-group eucrites. However, it is noticed that trace element abundances of NWA 10962 are slightly different from those of the common Main-group eucrites. La abundances are plotted against Hf abundances for

eucrites in Fig. 1. On this plot, eucrites are classified into the three subgroups; cumulate eucrites, basaltic eucrites and residual eucrites [5]. As clearly confirmed in Fig. 1, NWA 10962 belongs to residual eucrites. In terms of rare earth elements (REEs) abundances, NWA 10962 is different from the common eucrites. NWA 10962 is slightly depleted in light REEs. Its REE pattern exhibits a pronounced positive Eu anomaly, which bears some resemblance to cumulate eucrites and residual eucrites. Thus, NWA 10962 is classified as residual eucrites.

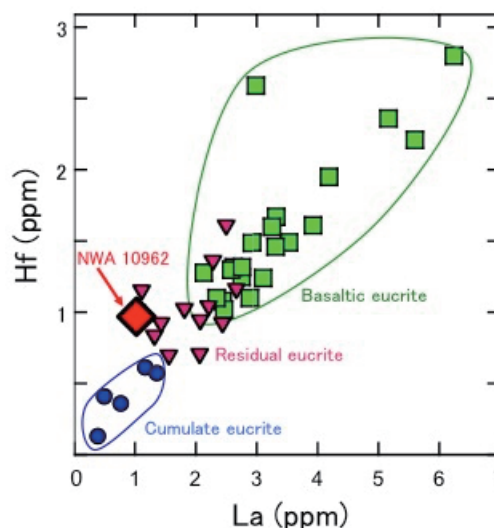


Fig. 1. La vs. Hf for eucrites.

Based on petrology [4], it was reported that NWA 10962 contain about 1% of FeNi metal. It is examined whether this FeNi metal endogenously produced or not based on its elemental abundances. To extract FeNi metal, the irradiated sample was leached with 6M HCl in an ultrasonic bath for 10 min. The obtained solution was measured by gamma-ray emissions. For this solution, Fe and Co could be determined, while Ir and Ni could not be detected. Nickel/Co and Ir/Co ratios of NWA 10962 are different from those of iron meteorites and FeNi metal for chondrites. These elemental ratios of NWA 10962 are lower than those of FeNi metal of Camel Donga, which was considered to be produced by reduction of FeO and FeS [6]. Thus, FeNi metal of NWA 10962 is not foreign meteoritic components and it is concluded that NWA 10962 is suitable for discussing about differentiation of asteroid Vesta.

#### REFERENCES:

- [1] M. C. De Sanctis *et al.*, *Science*, **336** (2012) 697-700.
- [2] K. Righter and M. J. Drake, *Meteorit. Planet. Sci.*, **32** (1997) 929-944.
- [3] N. Shirai *et al.*, *Earth Planet. Sci. Lett.*, **437** (2016) 57-65.
- [4] A. Bouvier *et al.*, *Meteorit. Planet. Sci.*, **52** (2017) 2411.
- [5] A. Yamaguchi *et al.*, *Geochim. Cosmochim. Acta*, **73** (2009) 7162-7182.
- [6] H. Palme *et al.*, *Meteoritics*, **23**, 49-57 (1988).

Y. Oura and Md. S. Reza

*Graduate School of Science, Tokyo Metropolitan University*

**INTRODUCTION:** Environmental pollution is an important issue for our healthy life. Determination of elemental composition is one of the ways for an environmental examination. For example, shellfish are commonly used for an assessment of ocean environment. In this case soft tissues in shellfish (e.g. mussels) are mainly analyzed for elemental concentration, whereas, shells seem not to be analyzed. Thus, we tried to determine elemental concentrations in shell if they are effective in assessing the coastal/lake environment. In this work, Japanese basket clam (scientific name: *corbicula japonica*) living in brackish-water lake was selected because it is easily available, and it has an easily handled size. For atmospheric environment, attention has been focused on the effects of very small particles called PM2.5 on human health in recent year. Elemental composition of particulates plays an important role for estimation of their origins. We have collected PM2.5 particulates at Hachioji, Tokyo and determination of elemental concentration in PM2.5 particulate was continued from last year.

## EXPERIMENTS:

### Shells

Japanese basket clam (Yamato Shijimi) yielded at Jyusan Lake in Aomori prefecture were got from a supermarket. After discarding soft tissues, clamshells were cleaned properly by ultrapure water using an ultrasonic water bath. Then they were made powder after drying. Ten different parts of clamshell (one clam contains two parts) from 5 individuals were subjected to analysis. About 180 mg of each sample was irradiated together with reference materials (GSJ JCp-1, JCT-1, and JB-1a) for 30 seconds and 4 hours at KUR (1 MW operation). After irradiation gamma-rays were measured by HPGe detector.

### PM2.5

PM2.5 particulates have been collected on a Nucleopore polycarbonate filter of 0.2  $\mu\text{m}$  of pore size for three weekdays every week at a rooftop of a building in Minami-Osawa campus of Tokyo Metropolitan University. Polycarbonate filters on which PM2.5 was collected were cut in half, then one half was subjected to analysis. Filter sample in clean polyethylene bag was irradiated together with reference materials (NIST 1648, NIST 1632c, NIES No.8, and GSJ JB-1a) for 5 minutes at KUR (1 MW operation) and 1 hour at KUR (5 MW operation). After irradiation, gamma-rays were measured by Ge detector.

## RESULTS:

### Shells

Thirteen elements (Na, Cl, Ca, Sc, Cr, Mn, Fe, Co, Zn, Br, Sr, Zr, and Ba) were detected under the analytical conditions in this study. The main element was Ca, whose concentrations (ca. 38 %) were almost same as those in JCp-1 (coral) and JCT-1 (giant clam). Sodium concentrations (ca. 4100 mg/kg), which were the second highest concentration among determined elements in this work, were also similar to those in JCp-1 and JCT-1.

Elemental concentrations of two parts of clamshell of an individual were consistent within their uncertainties for most elements with exception of Cr and Fe. Iron concentrations of one pair and Cr concentrations of three pairs of five pairs were inconsistent.

Fluctuations of concentrations among five individuals were small for most elements. Relative standard deviations were smaller than 7 % for Ca, Na, and Sr, which are the three main elements in this work. For Mn, Cr, and Fe, one individual has high Mn concentration (about 4 times higher than others) and another individual has extremely high Fe and Cr concentrations (about 15 times and 5 times higher, respectively). Ca, Sr, and Ba belong to alkaline-earth metals. Concentration ratios of Sr/Ca were relatively consistent among five individuals, whereas, Ba/Ca and Ba/Sr were varied. Their maximum ratio values were about two times higher than minimum ratio values.

### PM2.5

Mass concentrations of PM2.5 particulates collected in 2019 ranged from 3 to 36  $\mu\text{g m}^{-3}$ , and their median of 11  $\mu\text{g m}^{-3}$  was the same as the median in 2018, when the collection period was different from one in 2019. Determined elemental concentrations in PM2.5 particulates collected in 2019 are compared to those in 2018 in Fig.1. The median values of elemental concentrations in 2018 and 2019 are similar in general like the mass concentrations. Atmospheric environment around our university seems not to be different yearly between in 2018 and 2019 on the average.

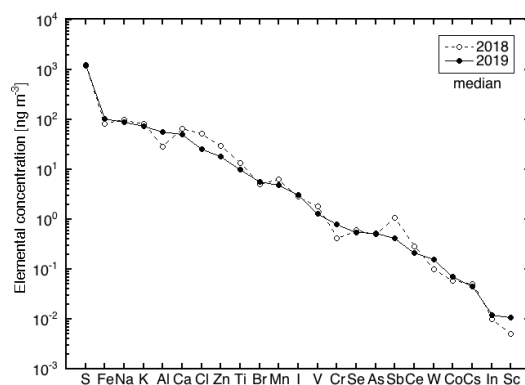


Fig.1. Median values of elemental concentrations in PM2.5 collected in 2018 and 2019. Elements are arranged in order of increase of their median in 2019.

M. Ebihara, Y. Hidaka, T. Fujimura, M. Kamata, S. Koshimizu, N. Shirai<sup>1</sup> and S. Sekimoto<sup>2</sup>

*Department of Earth Science, Waseda University*

<sup>1</sup>*Department of Chemistry, Tokyo Metropolitan Univ.*

<sup>2</sup>*KURNS, Kyoto University*

**INTRODUCTION:** CB and CH chondrites are metal rich chondrite groups [1, 2] and their oxygen isotopic compositions show a close relationship to CR chondrites [3]. Recently, the petrogenesis of CB chondrites came to be considered as the condensation from impact-induced vapor plume [4, 5]. According to the similarity of oxygen isotopic composition between CB and CH chondrites, the parent bodies of these chondrites might exist close to each other. Then, how impact processes affected the origin and the evolution of CH chondrites? What was the difference between CB and CH chondrites? These questions are quite interesting. Impact-induced vaporization causes volatility loss of elements, so chemical compositions and isotopic compositions must become powerful tool to discuss these issues.

Bulk chemical compositions of CB and CH chondrites have been scarcely reported and have been poorly discussed. Here, we report the preliminary results of our bulk chemical analyses for CB and CH chondrites, MacAlpine Hills (MAC) 02675 (CB<sub>b</sub>), Asuka 881020 (CH), Asuka 881541 (CH), Patuxent Range (PAT) 91546 (CH) and Pecora Escarpment (PCA) 91467 (CH).

**EXPERIMENTS:** Bulk chemical compositions of 1 CB<sub>b</sub> chondrite (MAC 02675) and 4 CH chondrites (Asuka 881020, Asuka 881541, PAT 91546 and PCA 91467) have been determined by INAA and ICP-MS in this study. A chip sample weighing 130-440 mg of each meteorite was crushed into small chips and fine grains. Small fractions weighing ~40 mg of each meteorite were used for INAA.

**RESULTS:** The Mg-, CI-normalized and Ni-, CI-normalized chemical compositions of CB<sub>b</sub> and CH chondrites obtained by INAA are shown in Fig. 1. The elements are sorted in decreasing of volatility [6]. In Fig. 1a, refractory lithophile element (Al, Ca, and Sc) abundances in CB<sub>b</sub> chondrite (CI x ~1.5) are significantly higher than those of CH chondrites (CI x ~1). The Cr/Mg and Mn/Mg ratios in CB<sub>b</sub> chondrite (2.6 and 0.28 x CI) are clearly higher and lower than those of CH chondrites (1.1 and 0.45 x CI). The range of Na/Mg ratios are nearly identical between CB<sub>b</sub> (0.20-0.32 x CI) and CH (0.18-0.34 x CI) chondrites.

In Fig. 1b, refractory siderophile element (Os, Ir, Ni, Co) abundance patterns are identical between CB<sub>b</sub> and CH chondrites, but as volatility increases, CB<sub>b</sub> and CH chondrites show different chemical compositional char-

acteristics. The principal differences are shown in Mn and Cr abundances. The Mn/Ni and Cr/Ni ratios are significantly lower in CB<sub>b</sub> chondrite (0.022 and 0.21 x CI, respectively) than those of CH chondrites (0.23 and 0.56 x CI).

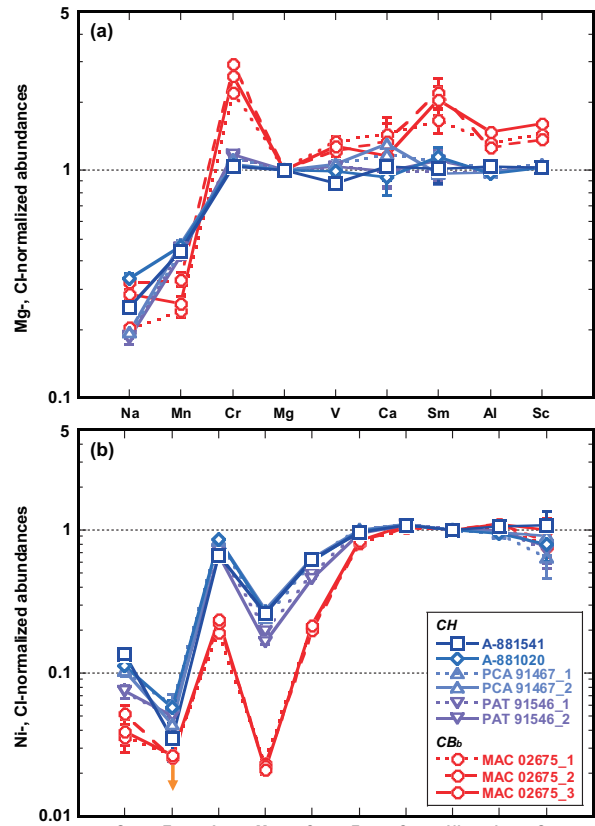


Fig. 1. Bulk chemical compositions of CB<sub>b</sub> and CH chondrites obtained by INAA. Fig. 1a shows Mg- and CI-normalized lithophile element abundance patterns. Fig. 1b shows Ni- and CI-normalized siderophile and chalcophile element abundance patterns. CI chondrite data used for normalization are from [7].

#### REFERENCES:

- [1] A. Bischoff *et al.* *Geochim. Cosmochim. Acta*, **57** (1993) 2631-2648.
- [2] M. K. Weisberg *et al.* *Meteoritics & Planet. Sci.*, **36** (2001) 401-418.
- [3] A. N. Krot, *Meteoritics & Planet. Sci.*, **37** (2002) 1451-1490.
- [4] A. V. Fedkin *et al.* *Geochim. Cosmochim. Acta*, **164** (2015) 236-261.
- [5] M. Weyrauch *et al.* *Geochim. Cosmochim. Acta*, **246** (2019) 123-137.
- [6] B. Fegley, in *The Chemistry of Life's Origins*, edited by J. M. Greenberg *et al.* (Kluwer, Dordrecht, 1993) 75-147.
- [7] E. Anders and N. Grevesse, *Geochim. Cosmochim. Acta*, **53** (1989) 197-214.

## CO5-16 Determination of Cl, Br and I contents in geochemical reference samples by radiochemical neutron activation analysis - revisited

M. Ebihara, S. Sekimoto<sup>1</sup> and N. Shirai<sup>2</sup>

*Department of Earth Science, Waseda University*

<sup>1</sup>*KURNS, Kyoto University*

<sup>2</sup>*Department of Chemistry, Tokyo Metropolitan Univ.*

**INTRODUCTION:** We have been determining three halogen contents in geochemical and cosmochemical samples by using radiochemical neutron activation analysis (RNAA). (Here, halogens denote chlorine, bromine and iodine). To verify the reliability of analytical data for rock samples, geochemical reference samples are to be routinely analyzed together with unknown samples. For such a verification, it is essential that reliable data are available for some (at least one) reference sample for target elements (here, halogens). Because it was not the case for halogens, we have been repeatedly analyzed several geochemical reference samples to contribute for making the situation better and establish reliable data base for halogens in selected geochemical reference samples. To continue to approach to our goal, we have analyzed five geochemical reference samples prepared by Geological Survey of Japan (JR-3) and United States Geological Survey (SBC-1, DTS-2a, AGV-2 and GSP-2) and encountered an unexpected problem in evaluating our halogen data., which is described in this report

**EXPERIMENTS:** About 100-200 mg of each powder samples was weighed, inserted into a clean, small plastic vial, which was then sealed in a clean polyethylene bag. For quantification of halogens, chemical standard solutions of halogens were prepared by dissolving appropriate amounts of potassium halides (KCl, KBr and KI) in pure water. In addition, a KOH solution was prepared to adjust the alkalinity in iodine solutions. An appropriate amount of each halogen solution was dropped onto a paper disk (17 mm  $\phi$ ), weighed, dried under a heat lamp and doubly sealed into polyethylene bags. An extreme care was taken when preparing the iodine reference sample, for which two set of samples (one with KOH and another without

KOH) were prepared. Two geochemical reference samples, together with a set of three (or four) reference samples, were irradiated for 10 min with a thermal neutron flux of  $3.3 \times 10^{12} \text{cm}^{-2} \text{s}^{-1}$  at Kyoto University Research Reactor of KURNS.

**RESULTS:** The Analytical results of the three halogens for the five geochemical reference samples are summarized in Table 1. The data obtained in this experiment are compared with our previous data published [1, 2]. For AGV-2 and GSP-2, additional literature values [3] also are shown. Our Cl data are consistent with our old data, being within 10%. The literature data of [3] are somewhat higher than ours but the difference may be permissible. The degree of agreement between our data (old and new) and among the three sets seems to become worse for Br and much worse for I. For Br, a systematic difference can be seen between our present data and previous data; the present data are 40% to 8% lower than the old data. In contrast, the literature data of [3] are 3 to 5 times higher than those of our literature values [1, 2]. For I, the large/small relation is different from that for Br; our present data are 19% to 87% smaller than the previous values, but larger than the literature values of [3]. Between our present data and our old data of [2] or [3], much smaller disagreement can be noticed for [2] than for [3], although statistics are poor. At this stage, a conclusive explanation for the disagreement of Br and I data between our present and past experiments. has not been attained yet. However, considering any conceivable possibility, we have just come up with a reasonable explanation. Once the reactor becomes usable, we will conduct the experiment to identify the source for yielding unsystematic as well as systematic inconsistencies.

### REFERENCES:

- [1] S. Sekimoto and M. Ebihara, *Geostand, Geoanal. Res.*, **41** (2017) 213-219.
- [2] S. Sekimoto and M. Ebihara, *Anal. Chem.*, **85** (2013) 6336-6341.
- [3] T. He, Z. Hu, W. Zhang, H. Chen, Y. Liu, Z. Wang and S. Hu, *Anal. Chem.*, **91** (2019) 8109-8114.

Table 1. Analytical results (in  $\mu\text{g/g}$ ) of halogens in geochemical reference samples\*

	Cl	Br	I
SBC-1	22.5 (24.9)	0.325 (0.355)	0.670 (5.07)
DTS-2b	10.5 (10.7)	0.098 (0.093)	0.119 (0.789)
AGV-2	75.9 (72.8; 84.0)	0.075 (0.101; 0.27)	0.034 (0.197; 0.013)
GSP-2	349 (363; 389)	0.068 (0.117; 0.57)	<DL (0.075; 0.013)
JR-3	126 (134)	0.450 (0.577)	0.390 (0.482)

\* Our present data are followed by previous values [2] (and literature values [3] for AGV-2 and GDP-2) in parentheses.

H. Sumino, J. Ren, A. Takenouchi, M. Koike, R. Okumura<sup>1</sup>, Y. Iinuma<sup>1</sup>, H. Yoshinaga<sup>1</sup> and S. Sekimoto<sup>1</sup>

*University of Tokyo*

<sup>1</sup> *Institute for Integrated Radiation and Nuclear Science, Kyoto University*

**INTRODUCTION:** Mantle wedge - the triangular shaped piece of mantle that lies above subducted plate (slab) and below the overriding plate - is essential for transporting water into mantle at subduction zone. The oceanic plate is hydrated before subducting, and then dehydrates at subduction zone to supply water to the mantle wedge. However, the details of hydration and dehydration processes remain debated. A major question is the exact depth where water is released, because water would notably change the chemical and physical properties of rocks and play an important role in volcanism and seismicity at subduction zones.

The heavy halogens (Cl, Br, I) are highly soluble in fluids, and hard to enter minerals during partial melting of peridotite (the major type of rock in the mantle) [1]. Furthermore, their ratios, especially I/Cl ratios vary up to several orders of magnitude among different reservoirs in subduction zones (e.g. mantle, subducting slab, sediments, and sedimentary pore fluids – water trapped in pore space in sediments), making them good tracers for fluid sources in subduction systems [2,3].

In this study, we analyzed the halogens in rock samples of an ancient slab-wedge mantle boundary [4] and observed the spatial distribution of halogen compositions, in order to constrain how the fluids from subducted plate modified the mantle wedge and how volatiles moved in subduction zones.

**SAMPLES AND BACKGROUND:** The Sanbagawa belt, which lies on the south of Median Tectonic Line, is composed of various kinds of metamorphic rocks which experienced subduction to deep in the Earth. It is proposed that Shiraga metaserpentinites (hydrated and deformed peridotites) in the Sanbagawa belt are originated from wedge mantle. Further, a previous study shows that the eastern boundary of Shiraga metaserpentinite preserved primary information about the ancient slab-wedge mantle interface [4]. In contrast, various types of schists represent altered slab materials that surrounding serpentinite body.

**EXPERIMENTS:** Samples were neutron irradiated in KUR to convert halogens (<sup>37</sup>Cl, <sup>79</sup>Br, <sup>127</sup>I) to noble gas proxies (<sup>38</sup>Ar, <sup>80</sup>Kr, <sup>128</sup>Xe). The extraction (crushing and heating) and measurement of these noble gas proxies were analyzed with a mass spectrometer at the University of Tokyo [5]. The crushing method releases halogen-derive noble gases from fluid inclusions, which are thought to partially preserve the information of the origi-

nal fluid that reacted with rocks. While the data obtained with heating of residual powder after crushing mainly represents the composition of halogens in solid phase, i.e. crystal lattice of minerals.

**RESULTS:** The halogen data of crush extraction show markedly higher I/Cl ( $1.5 \times 10^{-4} - 3 \times 10^{-3}$ ) comparing with normal upper mantle ( $4 \times 10^{-5}$ ), seawater ( $\sim 10^{-6}$ ), oceanic crust ( $\sim 10^{-6} - 10^{-7}$ ), or other reservoirs in subduction system. This is similar to the mantle wedge peridotites that come from  $\sim 100$  km depth [2], which are considered to originate from sedimentary pore fluids at seafloor.

It is notable that “Si-rich serpentinite”, samples near the slab wedge mantle boundary have evidently higher I/Cl than others. Within the serpentinite body, I/Cl tend to decrease with the distance from the boundary, which means that the original fluid with high I/Cl may come through/from the slab wedge mantle interface, then diffused upward into the mantle wedge and was gradually diluted by normal mantle with low I/Cl. In addition, this trend is not continuous at the slab wedge mantle boundary, implying the original fluid not necessarily came directly from the adjacent slab materials.

**CONCLUSIONS:** The halogens composition of Shiraga serpentinite body shows similar elemental ratios with that from deeper mantle wedge peridotites, which are considered to originate from the same source as sedimentary pore fluids. Based on the spatial distribution of I/Cl, the original fluid could come through slab wedge mantle interface, and then transfer upward into the mantle wedge.

#### REFERENCES:

- [1] D. M. Pyle & T. A. Mather. *Chem. Geol.*, **263** (2009) 110-121.
- [2] H. Sumino *et al.*, *Earth Planet. Sci. Lett.*, **294** (2010) 163-172.
- [3] M. A. Kendrick *et al.*, *Earth Planet. Sci. Lett.*, **365** (2013) 86-96.
- [4] H. Kawahara *et al.*, *Lithos*, **254-255** (2016) 53-66.
- [5] N. Ebisawa *et al.*, *J. Mass Spectrom. Soc. Jpn.*, **52** (2004) 219-229.

## CO5-18 Fission track age and thermal history of clay deposit of the Tsuchihashi Mine

H. Ohira and Y. Sampei

Department of Earth Science, Shimane University

**INTRODUCTION:** Fission track (FT) dating was carried out to estimate ages of hydrothermal alteration to form clay deposit of the Mitsuishi mining area at Bizen City, Okayama prefecture. Several clay deposits are located near the ring fault of eastern margin of the Wake Caldera, implying that hydrothermal fluid circulation along the ring fault contributed to form the deposit of this area [1]. The Tsuchihashi mine is typical mine operating underground quarry, yields high grade clayey rocks used for raw materials of refractories and ceramics. Several zones (such as pyrophyllite, sericite and silica rock) develop in response to conditions of hydrothermal alteration [2]. Samples were collected from above zones and U-Pb dating was also applied to estimate eruption age of host pyroclastic rocks.

**EXPERIMENTS:** Sample was crashed, sieved and heavy minerals were concentrated using conventional method of heavy liquid and magnetic separator. Minerals were mounted in PFA Teflon, and polished to reveal a complete internal surface, and etched in NaOH-KOH eutectic melt at 225°C [3] for 12-15 hours. Samples were irradiated at pneumatic tube of graphite facility (Tc-pn) of Kyoto University Reactor (KUR). After irradiation, external detectors (mica) were etched in 46% HF at 25°C for 6-7 minutes (for mineral mounts) and for 20-50min (for NIST-SRM612 glass). FT density was measured at 1000× magnification with a dry objective. U-Pb dating was carried out in cooperation with Dr. Hisatoshi ITO of Central Research Institute of Electric Power Industry (CRIEPI). Dating was performed using a Thermo Fisher Scientific ELEMENT XR magnetic sector-field ICP-MS coupled to a New Wave Research UP-213 Nd-YAG laser at CRIEPI [4].

**RESULTS:** FT ages obtained are 72.4±2.5Ma and 72.6±2.6Ma (silica rock zone), 75.9±2.7Ma (pyrophyllite zone) and 77.9±3.4Ma (sericite zone). These FT ages are relatively compatible with previously reported K-Ar ages for clay veins (78.1Ma, 74.0Ma, 73.0Ma) and clayey rocks (80.0Ma, 78.8Ma, 77.8Ma) [5]. Newly obtained U-Pb ages are 78.0±1.5Ma (silica rock zone) and 77.3±1.8Ma (sericite zone). These ages are slightly younger than previously reported age (82.4±0.6M [2]).

Ages versus closure temperature plot are shown in Fig. 1. U-Pb ages probably correspond to stage of eruption of host pyroclastic rocks or magmatic activity causing caldera structure, considering with its high closure temperature (800 °C < [6]). The variation of U-Pb ages (77-82Ma) should be examined in more detail. Previously reported K-Ar age (73-80Ma, [5]) probably correspond to a period of culmination of hydrothermal activity which formed several clay zones after caldera formation. Considering relatively lower closure temperature of FT methods (230°C<), FT ages (73-78Ma) probably indicate a period when sample cooled below 240°C during attenuation of hydrothermal alteration. The youngest FT age from silica rock zone (72.4-72.6Ma) show a period of latest stage of hydrothermal activity, which was probably sustained for a certain period (several Ma) after eruption of host pyroclastic rocks or caldera formation.

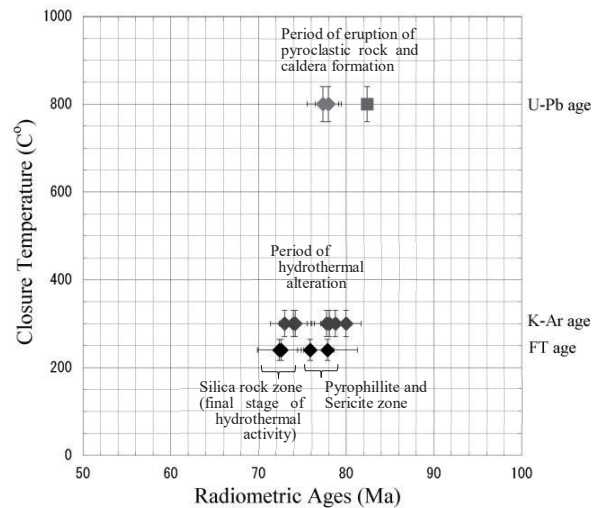


Fig.1 Closure temperature vs. Age plot.

- [1] ISHIHARA S. and IMAOKA T., 1999, Resource Geology, 49, 157-162.
- [2] Sato D., Yamamoto T. and Takagi T., 2016, Geology of the Banshu-Ako district. Quadrangle Series, 1:50000, Geological Survey of Japan, AIST, 68p (in Japanese with English abstract).
- [3] Gleadow A.J.W. *et al.*, 1976, Earth and Planetary Science Letter, 33, 273-276.
- [4] Ito H. *et al.*, 2017, Quaternary Geochronology 40, 12-22.
- [5] Hongu H., Kitagawa R. and Nishido H., 2000, Clay Science (Nendo Kagaku) 40, 46-53.
- [6] Cherniak, D.J. and Watson, E.B., 2000, Chemical Geology, 172, 5.

N. Iwata, S. Sekimoto<sup>1</sup>, R. Okazaki<sup>2</sup> and Y. N. Miura<sup>3</sup>

*Faculty of Science, Yamagata University*

<sup>1</sup>*Institute for Integrated Radiation and Nuclear Science, Kyoto University*

<sup>2</sup>*Department of Earth and Planetary Sciences, Kyushu University*

<sup>3</sup>*Earthquake Research Institute, University of Tokyo*

**INTRODUCTION:** Radiometric dating is useful tool for unveiling formation and evolution process of planetary material.  $^{40}\text{Ar}$ - $^{39}\text{Ar}$  method is invaluable to date the timing of heating events on planetesimal and asteroid (e.g. Swindle et al. (2014) [1]). Especially,  $^{40}\text{Ar}$ - $^{39}\text{Ar}$  dating method with laser heating technique is suitable for small amount sample (e.g. Kelley, 1995 [2] and Hyodo, 2008 [3]).

For example, tiny material returned from asteroid 25143 Itokawa is dated using laser heating  $^{40}\text{Ar}$ - $^{39}\text{Ar}$  dating method by Park et al. (2015) [4] and Jourdan et al. (2017) [5]. Park et al. (2015) reported an age of  $1.3 \pm 0.3$  Ga. Jourdan et al. (2017) reported an age of  $2.3 \pm 0.1$  Ga. These ages indicate the timing of catastrophic events which were occurred on Itokawa's precursor body. Combining the  $^{40}\text{Ar}$ - $^{39}\text{Ar}$  ages and other chronological data, Terada et al. (2018) [6] overviewed the time evolution of the Itokawa asteroid. Similar investigation, the integration of multichronological data is proposed to the material that recovered from asteroid 162173 Ryugu and other extraterrestrial materials.  $^{40}\text{Ar}$ - $^{39}\text{Ar}$  dating will play an important role within the investigations.

To implement of dating of extraterrestrial material by  $^{40}\text{Ar}$ - $^{39}\text{Ar}$  method, we will develop a system which includes gas extraction and gas purification line in KURNS (Fig. 1). A continuous Nd-YAG laser (~60 W) extract gas from neutron irradiated sample. The extracted gas is purified and encapsulated into metal gas trap. The purified gas in the metal gas trap is transported to laboratories of noble gas analysis (e.g. Kyushu University) and argon isotope of the gas is analyzed using noble gas mass spectrometer. Further, we have a plan to connect a quadrupole mass spectrometer to this system in the future, in order to perform on-lined laser heating  $^{40}\text{Ar}$ - $^{39}\text{Ar}$  dating.

**EXPERIMENTS:** Dr. R. Okazaki of Kyushu University designed the system. The gas extraction part consists of a sample chamber. The gas purification part consists of a Sorb-AC getter pump. Ti-Zr getter will be added as needed. Connecting port is used for jointing gas purification part and gas trap tree and/or the quadrupole mass spectrometer as needed. Whole of the parts are evacuated by two oil rotary pumps and two turbo molecular pumps to ultra-high vacuum condition.

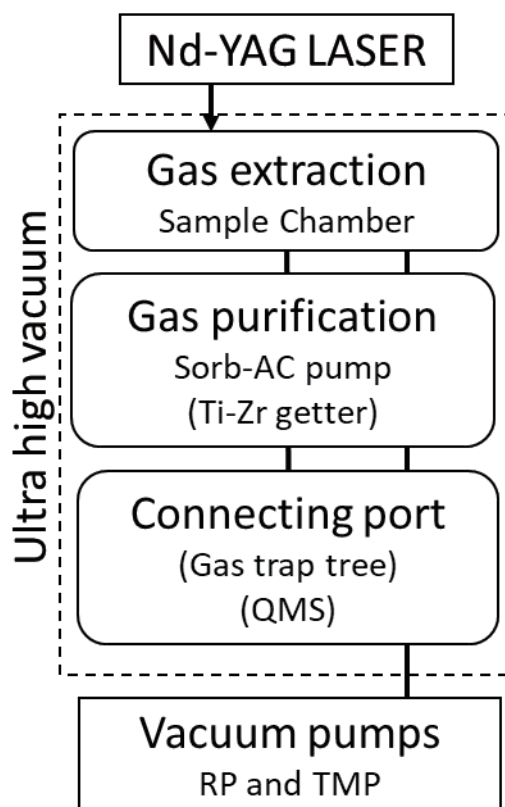


Fig. 1. Outline of gas extraction and purification line in KURNS. Components in parentheses are optional.

**RESULTS:** We started assembling of the laser-heating gas extraction and purification system in KURNS in 2019. The design work and configuration of the system is almost completed. Unfortunately, the constructing work was interrupted by influence of epidemic prevention of COVID-19. We are going to continue setting the system up during 2020.

#### REFERENCES:

- [1] T. D. Swindle *et al.*, in *Advances in  $^{40}\text{Ar}/^{39}\text{Ar}$  Dating: from Archaeology to Planetary Sciences*, edited by Jourdan, Mark, Verati (Geol. Soc., London, Spec. Pub. **378**, 2014) 333-347.
- [2] S. P. Kelley, in *Microprobe techniques in the earth sciences*, edited by Potts, Bowles, Reed, Cave (Chapman & Hall, London, 1995) 327-358.
- [3] H. Hyodo., *Gondwana Res.* **14** (2008) 609-616.
- [4] J. Park *et al.*, *Meteorit. and Planet. Sci.*, **50** (2015) 2087-2098.
- [5] F. Jourdan *et al.*, *Geology*, **45** (2017) 819-822.
- [6] K. Terada *et al.*, *Sci. Rep.*, **8** (2018) #11806.

S. Sekimoto, Y. Homura<sup>a</sup>, V.D. Ho<sup>1</sup>, M. Inagaki, N. Shirai<sup>2</sup>, T. Ohtsuki

*Institute for Integrated Radiation and Nuclear Science,  
Kyoto University*

<sup>1</sup>*Nuclear Research Institute, Vietnam Atomic Energy Institute*

<sup>2</sup>*Department of Chemistry, Tokyo Metropolitan University*

<sup>a</sup>*Present address: Novaltis Farma*

**INTRODUCTION:** Geochemists are often interested in the abundance of halogen elements in geochemical materials such as crustal rocks, mantle materials, and meteorite samples, because halogens play an important role in investigating the petrogenesis of such materials and assist in tracing their origins and/or precursor materials [1-3]. In our previous work, radiochemical neutron activation analysis (RNAA) was refined to accurately determine even trace amounts of halogens (chlorine, bromine, and iodine) in sedimentary rock reference samples [4]. Subsequently, U.S. Geological Survey (USGS) geochemical reference materials were subjected to RNAA, and the data obtained were compared with literature data [5]. The two kinds of carbonate reference materials investigated here, JCp-1 (Coral) and JCt-1 (Giant Clam), are prepared by the Geological Survey of Japan/National Institute of Advanced Industrial Science and Technology (GSJ/AIST), and the concentrations of many major and a few trace elements in these materials have been determined [6-8]. Data about the halogen contents in these materials is expected to significantly contribute to a better understanding of the chemistry of seawater and the marine environment, since halogens (especially iodine) are known to be extremely useful in investigating the geochemical circulation of terrestrial materials [9]. However, to our knowledge, there is not much data on the halogen contents of these carbonate materials.

The present study aims to use RNAA and instrumental NAA (INAA) to determine trace amounts of three halogens in JCp-1 and JCt-1, together with other elements. Based on the halogen data, the differences between the two carbonate reference materials is investigated. The INAA values obtained in the present study are compared with literature values, and the consistency between our data and the data from known literature is evaluated.

**EXPERIMENTS:** The procedure of RNAA used in this work has been reported previously.[4] For INAA studies, about 50 mg of JCp-1 and JCt-1, together with a similar amount of two kinds of USGS basalt reference materials for quantification, BCR-2 and BHVO-2, was irradiated for 4 h using KUR to measure the relatively long-lived nuclides (with half-lives > 24 h; <sup>46</sup>Sc, <sup>59</sup>Fe, <sup>60</sup>Co, <sup>85</sup>Sr, <sup>134</sup>Cs, <sup>140</sup>La, <sup>141</sup>Ce, <sup>152</sup>Eu, <sup>181</sup>Hf, and <sup>182</sup>Ta, and <sup>239</sup>Np) produced by the (n,γ) reaction in each material. As for <sup>239</sup>Np, the (n,γ) reaction is followed by γ decay. Addi-

tionally, the nuclides <sup>24</sup>Na, <sup>28</sup>Al, and <sup>49</sup>Ca in these materials were also measured by irradiating the samples for 10 s. Since the Mn content in the two carbonate materials of interest in this study (JCp-1 and JCt-1) is known to be very low relative to that in geochemical materials, irradiation for 20 min was required for the measurement of <sup>56</sup>Mn. For determination of the Mn content, a chemical standard solution of Mn was utilized. An appropriate amount of Mn solution (100 mg kg<sup>-1</sup>, typically) was dropped onto a filter paper, which was then dried under an infrared lamp. The filter paper was then doubly sealed in polyethylene bags, and after irradiation, the outer bags were exchanged for new (non-irradiated) ones.

**RESULTS:** The contents of Cl, Br, and I in JCp-1 and JCt-1 were determined by RNAA and is shown in Table 1. Uncertainties refer to counting statistics (1σ) from gamma-ray spectrometry just after the radiochemical purification, as well as from those in the reactivation process. Information values for Cl have been reported as determined by spectrophotometry (584 and 95 mg kg<sup>-1</sup> in JCp-1 and JCt-1, respectively) [8], which are in good agreement with the RNAA values from the present study, with uncertainties of 3σ. The estimates for the Br and I contents for these two carbonate materials are reported here for the first time. There is a scarcity of reliable and accurate halogen data for these materials. It is envisioned that the halogen data reported using RNAA will contribute to a compilation of such data for a database of GSJ/AIST reference materials.

**Table 1** Cl, Br, and I contents in JCp-1 & JCt-1, as estimated by RNAA

Sample	Cl(mg kg <sup>-1</sup> )	Br(mg kg <sup>-1</sup> )	I (mg kg <sup>-1</sup> )
JCp-1	620 ± 27	3.22 ± 0.10	6.14 ± 0.15
JCt-1	103 ± 8	0.301 ± 0.011	0.031 ± 0.005

#### REFERENCES:

- [1] MA Kndrick *et al.*, *Geochim. Cosmochim. Acta* **235** (2018) 285-304.
- [2] L. Hughes *et al.*, *Geochim. Cosmochim. Acta* **243** (2018) 1-23.
- [3] DE Harlov *et al.*, *The Role of Halogens in Terrestrial and Extraterrestrial Geochemical Processes* Springer Geochemistry, Gewerbestrasse, Switzerland (2018)
- [4] S. Sekimoto *et al.*, *Anal. Chem.* **85** (2013) 6336-6341.
- [5] S. Sekimoto *et al.*, *Geostand. Geoanal. Res.* **41** (2017) 213-219.
- [6] S. Aizawa, *J. Radioanal. Nucl. Chem.* **278** (2008) 349-352.
- [7] M. Inoue *et al.*, *Geostand. Geoanal. Res.* **28** (2004) 411-416.
- [8] T. Okai *et al.*, *Chikyuu Kagaku* **38** (2004) 281-286.
- [9] B. Deruelle *et al.*, *Earth Planet. Sci. Lett.* **108** (1992) 217-227.

## CO5-21 Long term analysis of Cs isotopic ratio by thermal ionization mass spectrometry

Y. Shibahara, S. Fukutani and T. Kubota

*Institute for Integrated Radiation and Nuclear Science,  
Kyoto University*

**INTRODUCTION:** The applicability of the mass spectrometry has been studied for the analysis of radionuclide related to the nuclear incident such as the Fukushima Dai-ichi Nuclear Power plant accident. In the recent studies of our group, a thermal ionization mass spectrometer (TIMS) was applied for the analysis of Cs isotopic composition [1], and it was discussed that the analytical results of Cs isotopic composition obtained within the latest 2 financial years from April 2017 to March 2019 [2]. In this study, we discussed the additive agent used in the analysis of Cs isotopic composition by TIMS and the analytical results of Cs obtained within the latest 3 financial years from April 2017 to March 2020.

**EXPERIMENTS:** From the environmental sample obtained in Fukushima prefecture, Cs was recovered according to the recovery scheme discussed at the previous studies [3-5]. The concentration of  $^{137}\text{Cs}$  of this sample corrected on Mar 11, 2011 was about  $2.6 \times 10^{-10}$  g/g. The Cs isotopic composition was analyzed by TIMS as the isotopic ratios of  $^{134}\text{Cs}/^{137}\text{Cs}$  and  $^{135}\text{Cs}/^{137}\text{Cs}$ .

A thermal ionization mass spectrometer (TRITON-T1, Thermo Fisher Scientific) was used for the analysis of Cs isotopic composition. The Cs sample was loaded onto a rhenium filament of a single filament system with a TaO activator or a glucose activator same as the previous study [2]. Because of the loading amount of Cs (*ca.*  $1 \times 10^{-12}$  g), the mass spectrometry was conducted with a secondary electron multiplier detector and the peak jump method [2-5]. For the discussion of the additive agent used to the ionization of Cs, about  $1 \times 10^{-12}$  g of the stable Cs (namely  $^{133}\text{Cs}$ ) was loaded onto a rhenium filament. TaO or glucose (or diluted them) was used as the additive agent.

**RESULTS:** Figure 1 shows the mass spectrum of Cs recovered from the environmental sample (observed at Oct 2019), and shows the peaks corresponding to  $^{133}\text{Cs}$ ,  $^{134}\text{Cs}$ ,  $^{135}\text{Cs}$  and  $^{137}\text{Cs}$ . It was observed that the ionization of Cs was affected by the kind of the additive agent, while that was not affected the dilution of additive agents with the dilution rate among 1 to 10.

The analytical result of  $^{135}\text{Cs}/^{137}\text{Cs}$  ratio obtained within latest 3 years was shown in Fig. 2. The averaged value of  $0.365 \pm 0.003$  was obtained, and this value shows the good agreement with the previous study [2] ( $0.365 \pm 0.004$ ). From the time profiles of  $^{135}\text{Cs}/^{137}\text{Cs}$  and  $^{134}\text{Cs}/^{137}\text{Cs}$ , the half-lives of  $^{134}\text{Cs}$  and  $^{137}\text{Cs}$  were evaluated as  $T_{1/2(\text{Cs-134})} = 2.07 \pm 0.03$  y and  $T_{1/2(\text{Cs-137})} = 30.2 \pm 2.2$  y respectively. These values also show the good agreement with the previous study [2] ( $2.08 \pm 0.02$  y for  $^{134}\text{Cs}$  and  $30.2 \pm 2.2$  for  $^{137}\text{Cs}$ ) and the literature data [6] ( $2.07$  y for  $^{134}\text{Cs}$  and  $30.2$  y for  $^{137}\text{Cs}$ ).

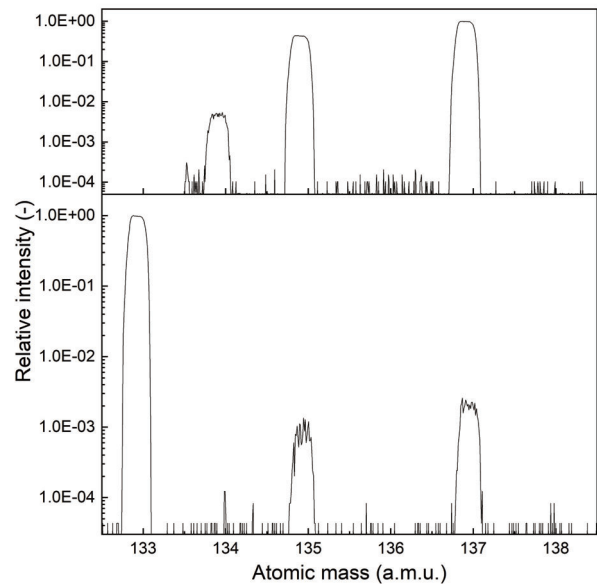


Fig. 1. Mass spectra of Cs recovered from environmental sample obtained at Fukushima prefecture observed at Oct 2019.

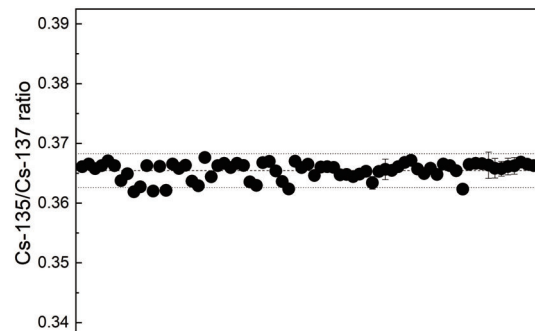


Fig. 2. Results of Cs isotopic ratio analysis obtained within latest 3 years corrected on March 11, 2011.

### REFERENCES:

- [1] Y. Shibahara *et al.*, KURRI progress report 2017, 157.
- [2] Y. Shibahara *et al.*, KURRI progress report 2018, 103
- [3] Y. Shibahara *et al.*, *J. Nucl. Sci. Technol.* 2014, 51, 575-579.
- [4] Y. Shibahara *et al.*, *Radiological issues for Fukushima's revitalized future.* Springer. 2016. 33-46.
- [5] Y. Shibahara *et al.*, *J. Nucl. Sci. Technol.* 2017, 54, 158-166.
- [6] R.B. Firestone *et al.*, *Table of Isotopes*, John Wiley and Sons, New York, 1998.

T. Inamura, S. Fukutani<sup>1</sup> and K. Takamiya<sup>1</sup>

*Archaeological Institute of Kashihara, Nara Prefecture*  
<sup>1</sup>*Institute for Integrated Radiation and Nuclear Science,*  
*Kyoto University*

**INTRODUCTION:** Parameters of the rice yield at the Yayoi period have been investigated on the basis of nitrogen supply, paddy structure etc. One of the important parameters to estimate the yield is the submerged condition of the paddy fields. However, the submerged condition has not been clear yet. It was found that the elemental composition of Cd and As of brown rice is good index of the submerged condition by elemental analysis using ICP-MS for modern rice seeds in the previous work [1]. However, the detected rice seeds which is cultural assets must be analyzed by a nondestructive method. We have tried to analyze the concentration of Cd and As of the detected rice seed by NAA (neutron activation analysis) using pneumatic irradiation system and normal Ge-detectors, and succeeded to determine the amount of As. On the other hand, the amount of Cd could not be estimated. The seeds buried in the ground contain high amounts of mineral elements compared to fresh seeds, and the mineral components such as iron and sodium disturb the determination of Cd by large Compton-background in gamma-ray measurements. In order to decrease the Compton continuum in gamma-ray measurement, determination of Cd using a Ge-detector combined with Compton suppression system had been tried in the previous work [2]. But the photo peak of Cd isotopes; <sup>107</sup>Cd ( $t_{1/2} = 6.5$  h), <sup>111m</sup>Cd ( $t_{1/2} = 48.5$  m) and <sup>115</sup>Cd ( $t_{1/2} = 53.5$  h), was not detected. In the present work, we irradiated rice samples using hydraulic irradiation system of KUR to detect the photo peaks of <sup>109</sup>Cd which has longer half-life of 462 d.

**EXPERIMENTS:** The buried rice seeds (Fig. 1) and chaffs irradiated in the present work were excavated at the Daifuku remains in Nara. The main elemental components of the samples were analyzed by EDX (Energy Dispersive X-ray spectrometry) before neutron irradiation. It was found that high amount of iron which produces

long half-lived isotopes, <sup>59</sup>Fe ( $t_{1/2} = 44.5$  d), is contained in the rice samples. Several grams of the samples double-sealed with polyethylene bag and aluminum foil was encapsulated in an aluminum capsule. Neutron irradiation for the samples was performed using the hydraulic neutron irradiation system for 70 hours under 1 MW operation of KUR. After the irradiation, sample stands for three months to decrease activities of short-lived nuclides such as <sup>56</sup>Mn, <sup>24</sup>Na and also long-lived ones such as <sup>59</sup>Fe, <sup>46</sup>Sc ( $t_{1/2} = 83.8$ d) produced by the neutron irradiation. The gamma-ray spectra of irradiated samples were measured by a Ge-detector to check the degree of disturbance caused by long-lived nuclides in the sample.



Fig. 1 The rice seeds sample excavated at the Daifuku remain.

**RESULTS:** The activity of <sup>59</sup>Fe decrease to about fourth compared with that at the end of irradiation. However, it was not low enough to detect photo peaks of <sup>109</sup>Cd clearly. The result suggests longer cooling time is required to decrease the activity of <sup>59</sup>Fe and detect photo peaks of <sup>109</sup>Cd. In the near future, the gamma-ray measurement will be carried out under the condition of low activities of <sup>59</sup>Fe and other products.

**REFERENCES:**

- [1] T. Inamura *et al.*, KURRI Progress Report 2017 (2018) 208-208.
- [2] T. Inamura *et al.*, KURRI Progress Report 2018 (2019) 189-189.

Y. Ogata, H. Minowa<sup>1</sup>, S. Kojima<sup>2</sup>, Y. Kato<sup>3</sup> and K. Takamiya<sup>4</sup>

Nagoya University

<sup>1</sup>The Jikei University School of Medicine

<sup>2</sup>Aichi Medical University

<sup>3</sup>Hitachi, Ltd.

<sup>4</sup>Institute for Integrated Radiation and Nuclear Science, Kyoto University

**INTRODUCTION:** Conventional analysis methods of radiostrontium in seawater are complicated and time-consuming using a lot of deleterious substances. We are developing rapid and safe methods<sup>[1,2]</sup>. In the new method, strontium is collected on a filter with methods using ion exchange resin or Sr adsorbent, and is measured by a liquid scintillation counter using plastic scintillator. In this experiment, we tried to analyse behavior of Ba and Na through the procedure. First of all, <sup>24</sup>Na was measured with modified sum-peak method developed by Ogata<sup>[3, 4]</sup>, also <sup>46</sup>Sc was measured to verify the method. After them, we analyse the behavior of Ba.

**EXPERIMENTS:** <sup>24</sup>Na produced by KUCA reactor was set on a p-type HPGe detector, GEM-35190S (ortec). The gamma spectrum from 0 to 4 MeV was converted to 8192 ch digital data with an ADC (Multi-port II, Canberra). The spectra were analysed using Gamma Explorer® software (Million Technologies). The source was placed on the axis of the detector at S-D distances (i.e., the distances from the surface of the end cap of the detector to the source), which were varied from 0 cm to 10 cm. The measurement time was set to collect more than 10,000 counts under the sum-peak area. Two peak counts, 1369 keV and 2754 keV, the sum peak counts and the total counts were collected. Also, <sup>46</sup>Sc produced by KUCA reactor was measured as the same way above. The peak, 889 keV and 1121 keV, the sum peak and the total counts were analysed. The angular correlation of the two peaks used here is 1.1184<sup>[5]</sup>.

The behavior of Ba is trying to analysis. Radiobarium produced by KUCA reactor was add to seawater sample. Chemical separation procedure, using ion exchange or Sr adsorbent, was performed and radiobarium in each fraction was analysed.

**RESULTS:** Fig. 1 shows the results of the sum-peak method and the modified sum-peak method applied to <sup>24</sup>Na analysis. The abscissa is the count rate of 1389 keV peak and the ordinate is the estimated activity. The activities calculated with the sum-peak method and the modified sum-peak method were 2.83 kBq and 3.25 kBq, respectively. The activities were somewhat different from the activity calculated using efficiency at SDD 10 cm, 3.18 kBq, where the sum peak effect was negligible. However, no reliable figure of the angular correlation of the two peaks was available. Therefore, the results cannot be verified. Contrary, the results of <sup>46</sup>Sc are shown in Fig. 2. The calculated

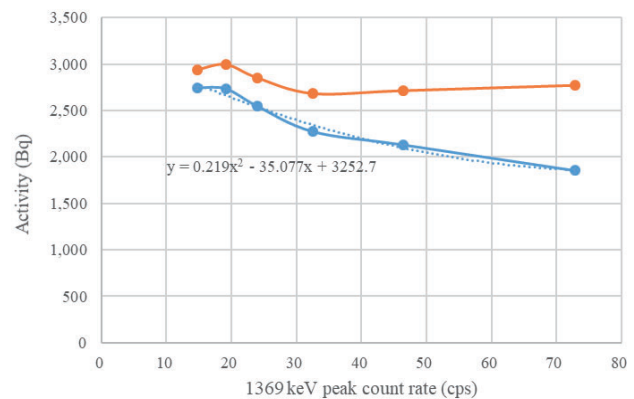


Fig. 1 <sup>24</sup>Na analysis with the sum-peak methods.

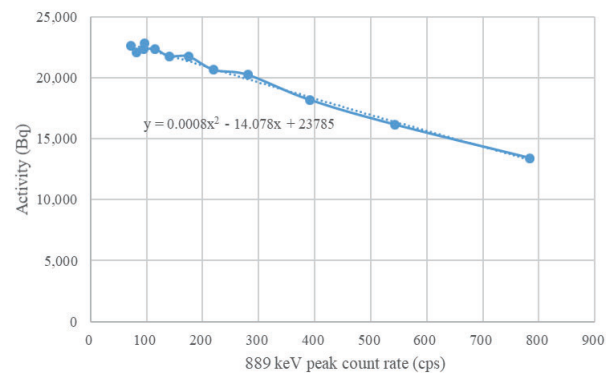


Fig. 2 <sup>46</sup>Sc analysis with the sum-peak methods.

activity by the modified sum-peak method were 26.6 kBq, and the figure was a little bit smaller than the activity calculated from the data obtained at SDD 10 cm, 28.7 kBq. The reason is now in investigation.

About the behavior of Ba, the limited results showed that Ba was remain in the filter for both procedures. Therefore, just after the reactor accident, <sup>140</sup>Ba was collected on the filter. But the half-life of <sup>140</sup>Ba is only 12.8 d, so that tree months after, the activity was less than two thousandth. Therefore, the effect would be limited. And the increase of the count brings conservative results. Moreover, the <sup>140</sup>Ba concentration will be estimated from the results by gamma spectroscopy by HPGe.

More detailed analysis will be performed hereafter.

[1] K. Yuka *et al.*, Proc. 19<sup>th</sup> Workshop on Environ. Radi-oact. KEK Proc. 2018-7, (2018).

[2] K. Yuka *et al.*, Proc. 33<sup>th</sup> Workshop on Environ. Radi-ation Uses. KEK Proc. 2019-4, (2019).

[3] Y. Ogata *et al.*, Nucl. Inst. Meth. Phys. Res. A. **775** (2015).

[4] Y. Ogata *et al.*, Appl. Radia. Isot., **109** (2016).

[5] G. Bertolini *et al.*, Nuovo Cimento, **3** (1956).

J.H. Moon, H.R. Lee, Y. Inuma<sup>1</sup>, H. Yoshinaga<sup>1</sup>, R. Okumura<sup>1</sup>, S. Fukutani<sup>1</sup> and K. Takamiya<sup>1</sup>

*Neutron & RI Utilization Research Division, Korea Atomic Energy Research Institute, South Korea*  
<sup>1</sup>*Institute for Integrated Radiation and Nuclear Science, Kyoto University*

**INTRODUCTION:** Air quality in urban areas is one of the most important environmental issues and air particulates consisting of various elements from both artificial and natural origins is an indicator of an air quality. Especially, toxic elements in fine air particulates can be accumulated in the lungs by inhalation and incur serious harmful effects to human health. In this study, instrumental neutron activation analysis (INAA) was applied for the determination of the trace elements in air particulate samples collected from two different sampling sites in South Korea.

**EXPERIMENTS:** PM10 and PM2.5 air particulate samples were collected by using high volume samplers (HiVol 3000, Ecotech, Austria) and quartz filter (8 x 10 inches) in Seoul and Daejeon during the spring season, 2019. Sixty-eight analytical samples (17 samples for PM10 and PM2.5 at Seoul and Daejeon) with size of 15 x 223 mm were prepared and NAA facilities at KUR were employed for INAA, because of shut-down of HANARO research reactor in Korea. The prepared samples were irradiated using the PN3 irradiation hole for 2 minutes to detect short-lived nuclides at 1 MW and for 50 minutes to detect medium/long-lived nuclides at 5 MW, respectively. Thermal neutron flux was measured by using Al wire for short irradiation and Fe wire for long irradiation. After proper decay according to target nuclides, gamma-rays emitted from the irradiated samples were measured by using gamma-ray spectrometer with a high purity Ge detector. Elemental contents were determined by activation formula based on absolute quantification method [1, 2]. Four blank filters were analyzed under the same analytical condition with particulate samples.



Fig. 1. A photo of PM10 and PM2.5 samplers in Daejeon.

**RESULTS:** Twenty-four elements like Al, Ba, Br, Ce, Co, Cr, Dy, Eu, Fe, Hf, K, La, Mg, Mo, Mn, Na, Sb, Sc, Sm, Tb, Th, U, Yb, Zn, were detected and quantified from blank filter samples. Among them, Al content is not confident, due to the fast neutron reaction of Si (main matrix of filter media). As, Au, Cl, I, In, Se, V and W were additionally determined in the air particulate samples. Eventually, thirty-two elements can be determined from the actual samples by INAA. The concentrations (ng/m<sup>3</sup>) of ten toxic elements such as As, Ba, Br, Cl, Cr, Fe, Mn, Sb, V and Zn of 32 elements were calculated with air flow volume and by the subtraction of elemental contents in blank filter, and their average concentrations were evaluated for 17 samples. The results are shown in Table 1. As expected, most of elemental concentrations in Seoul samples were higher than those in Daejeon samples, except for Cl. Fe shows the highest concentration level (0.81 ~ 2.19 µg/m<sup>3</sup>) among ten toxic elements, and As, Sb and V have a similar concentration level (2 ~ 10 ng/m<sup>3</sup>). These results will be used for various purposes such as epidemiological studies, source identification and apportionment [3].

Table 1. Concentration results for 10 toxic elements

Element	Seoul PM10	Seoul PM2.5	Daejeon PM10	Daejeon PM2.5
As	5.15±3.50	4.78±3.13	6.38±6.22	4.80±3.42
Ba	68.6±31.4	42.9±26.3	19.8±7.50	17.2±6.77
Br	18.9±22.0	19.7±24.3	17.1±5.66	15.4±5.59
Cl	352±194	334±204	916±595	515±275
Cr	10.5±4.91	8.68±4.03	6.39±2.16	5.62±1.40
Fe	2190±1370	1650±1120	1140±606	809±514
Mn	43.9±27.5	39.8±27.3	32.5±14.6	28.0±13.1
Sb	9.03±7.71	6.95±7.22	3.14±1.67	2.72±1.42
V	8.27±5.54	8.43±6.14	5.84±3.42	5.60±3.24
Zn	115±72.1	103±63.9	88.5±47.0	71.5±36.2

### REFERENCES:

- [1] D. De Soete, R. Gijbels, J. Hoste, Neutron Activation Analysis, Wiley-Interscience, New York (1972).
- [2] R.R. Greenberg, P. Bode, E.A. De Nadai Fernandes, Neutron activation analysis: a primary method of measurement, Spectrochim. Acta Part B 66 (2011) 193–241.
- [3] J. M. Lim, J. H. Lee, J. H. Moon, Y. S. Chung, K. H. Kim, Source apportionment of PM10 at a small industrial area using Positive Matrix Factorization, Atmospheric Research 95 (2010) 88–100.

## CO6-1 Effect of inter-protein interaction on SAXS profile in concentrated MurD solution

H. Nakagawa, T. Saio<sup>1,2</sup>, M. Sugiyama<sup>3</sup>, R. Inoue<sup>3</sup>

Materials Science Research Center, Japan Atomic Energy Agency

<sup>1</sup>Graduate School of Chemical Sciences and Engineering, Hokkaido University

<sup>2</sup>Department of Chemistry, Faculty of Science, Hokkaido University

<sup>3</sup>Institute for Integrated Radiation and Nuclear Science, Kyoto University

**INTRODUCTION:** In structural biology, precise determination of three-dimensional structures of proteins has been focused, and the structures with an atom-ic-resolution have given solid platforms to understand their biological functions. Recently, the idea of structural biology has extended beyond the static structural information with atomic resolution, in order to cover dynam-ical structures at different levels of space and time reso-lution. Neutron Spin Echo (NSE) is good methods to study the domain motions of a protein, where a relatively high concentrated protein solution, a few tens mg/ml, is often used [1]. In the high concentration, an effect of the inter-protein interaction on the NSE spectra as well as a small-angle scattering. In this study, the effect of the in-ter-protein interaction on Small angle X-ray scattering (SAXS) profiles were examined using MurD protein, which is a typical multi-domain protein (Fig.1) [2] and is good model to study the domain motion by NSE.

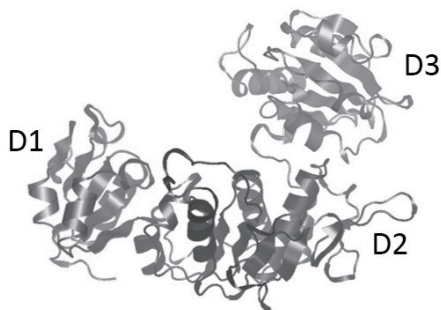


Fig. 1. Multi-domain protein, MurD, which are composed of three domains, D1, D2 and D3.

**EXPERIMENTS:** MurD were expressed in E. coli strain BL21 (DE3). SAXS were measured for MurD in apo state at the concentration of 5.0, 39.4 and 78.1 mg/ml. The buffer conditions were 20 mM Tris-HCl at pH=7.2.

**RESULTS:** SAXS profiles of MurD were successfully obtained for Apo state at various concentrations. Figure 2 shows the SAXS profiles. The inter-protein interaction effects were not observed in the SAXS profile at 5.0 mg/ml. At the lower Q region, at the higher protein concentrations, the intensity of SAXS decreased as a protein concentration increases. This should come from the inter-protein interaction. On the other hand, in the Q region

above  $0.08 \text{ \AA}^{-1}$ , all SAXS profiles almost coincided with each other. So, the higher concentration could not affect the conformation of a MurD protein molecule. These results suggest that the concentration effect on NSE spectra needs to be considered in the lower Q region than  $Q = 0.08 \text{ \AA}^{-1}$ . And at the higher Q region, NSE spectra can be analyzed without considering the concentration effect.

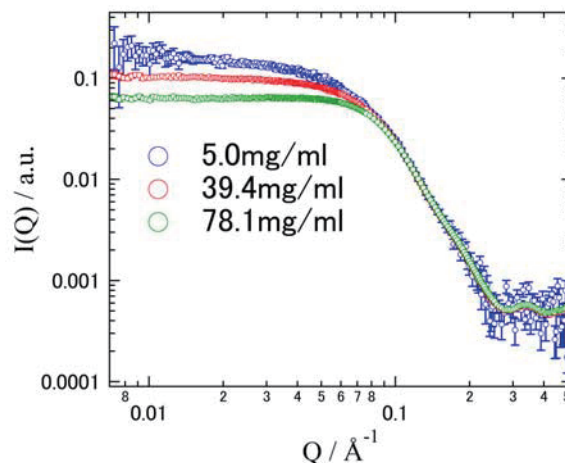


Fig. 2. SAXS profiles in MurD at several concentrations.

### REFERENCES:

- [1] R. Inoue *et al.*, Biophys. J. **99** (2010) 2309-2317.
- [2] T. Saio *et al.*, Sci. Rep., **5** (2015) 16685.

E. Hibino, K. Morishima<sup>1</sup>, A. Okuda<sup>1</sup>, R. Inoue<sup>1</sup>, M. Sugiyama<sup>1</sup>, and M. Nishimura

Molecular Neuroscience Research Center, Shiga University of Medical Science

<sup>1</sup>Institute for Integrated Radiation and Nuclear Science, Kyoto University

**INTRODUCTION:** The number of patients with Alzheimer's disease (AD) is increasing in Japan and AD is serious social issue. However, any effective AD-modifying drug is still undeveloped. The pathogenic processes of AD are considered to be triggered by accumulation of amyloid- $\beta$  protein (A $\beta$ ) in brain. Previously, we have identified a secretory protein named interleukin-like epithelial-mesenchymal transition inducer (ILEI, also known as FAM3 superfamily member C (FAM3C)) as a negative regulator of A $\beta$  production by a novel activity<sup>1</sup>. ILEI is secreted from cell to bind to the extracellular region of Presenilin-1, a component of the  $\gamma$ -secretase complex. The interaction of ILEI with Presenilin-1 enhances nonspecific degradation of A $\beta$  precursor protein. ILEI was also reported ILEI C185A showed dysfunction of tumor growth, and metastasis<sup>2</sup>. However, the relationship of A $\beta$  production inhibitory activity and tumor growth and metastasis activity are still to be clarified.

The objective of this study is to elucidate structure-function relationship that leads to develop a therapeutic drug for AD. We especially analyzed basic structural characteristics of wild-type and C185A mutant of ILEI and established experiment system.

**EXPERIMENTS:** Human wild-type ILEI and C185A mutant (residues 55-227) with hexahistidine tag were over-expressed in Rosetta-gamiB (DE3) pLysS strain and purified by Ni-NTA resin and size exclusion chromatography (SEC). CBB-stained SDS-PAGE gels on non-redox condition showed a single band.

For the MALDI-TOF/MS measurements, the purified proteins were directly transferred onto the 96 spotted polished steel target plate. After completely air drying, the plate was loaded to the Microflex LT (Bruker Daltonics, Bremen, Germany). The spectra were generated in linear positive ion mode.

For the structural characteristics, small-angle X-ray scattering (SAXS) measurements of the purified proteins at the concentrations of 1.0 mg/mL were performed with NANOPIX (Rigaku Corporation, Japan) at room temperature. The sample-to-detector distance and wavelength of X-ray used for present work was 650 mm and 1.542 Å, respectively. The scattering vector  $q$  covered from 0.02 to 0.3 Å<sup>-1</sup>.

**RESULTS:** We previously measured 2D-NMR spectra of wild-type and C185A <sup>15</sup>N-ILEI. It was observed the positions of around 20 peaks were changing (data not shown). To confirm whether the differences are caused by

overall conformational change or not, we firstly analyzed overall structural characteristics by MALDI-TOF/MS, analytical ultracentrifuge (AUC) and SAXS.

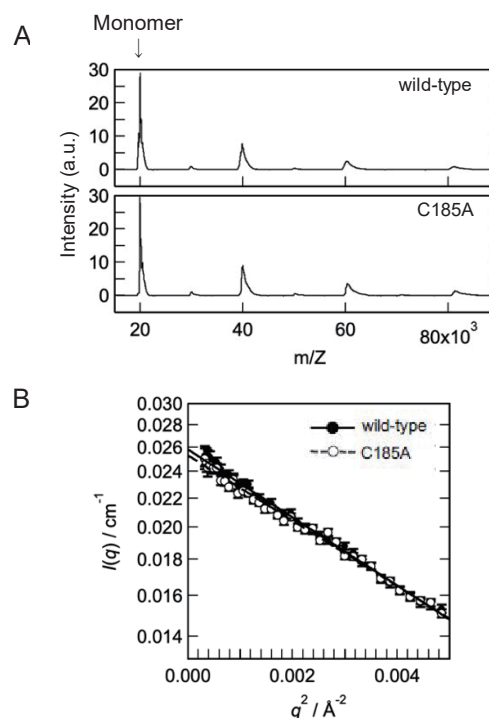


Fig. 1. (A) MALDI-TOF/MS measurements of wild-type and C185A mutant of ILEI indicated molecular weights of monomer and multimers.

(B) Guinier plots obtained from the scattering curves in SAXS experiments.

The molecular weight of wild-type ILEI is around 20.0 kDa. The MALDI-TOF/MS measurements indicated that no difference of abundance ratio of monomer and multimer between wild-type and C185A mutant (Fig. 1A). The AUC experiments also supported the similar results (data not shown).

Furthermore, to confirm overall structural differences between wild-type and C185A mutant, SAXS experiments were conducted. From the Guinier analyzes of SAXS profiles of wild-type and C185A mutant of ILEI, no significant structural difference was observed between them (Fig. 1B). Namely, C185A mutation did not affect to overall structure of ILEI.

Through these integrative experimental approaches, it is expected that the NMR spectral change due to C185A mutation is caused by the local structural change.

We have already had dysfunctional mutants for A $\beta$  production inhibitory activity. We apply these analytical methods to these mutants for elucidation activity center of ILEI.

## REFERENCES:

- [1] H. Hasegawa *et al.*, *Nat. Commun.*, 5:3917 (2014)
- [2] M. Kral *et al.*, *FEBS J.*, **284** 3484–3505 (2017)

H. Yagi<sup>1</sup>, Y. Yunoki<sup>1,2</sup>, K. Morishima<sup>3</sup>, A. Matsumoto<sup>4</sup>, N. Sato<sup>3</sup>, L. Porcar<sup>5</sup>, A. Martel<sup>5</sup>, R. Inoue<sup>3</sup>, H. Kono<sup>4</sup>, M. Sugiyama<sup>3</sup> and K. Kato<sup>1,2</sup>

<sup>1</sup>Graduate School of Pharmaceutical Sciences, Nagoya City University

<sup>2</sup>Exploratory Research Center on Life and Living Systems, National Institutes of Natural Sciences

<sup>3</sup>Institute for Integrated Radiation and Nuclear Science, Kyoto University

<sup>4</sup>National Institutes for Quantum and Radiological Science and Technology

<sup>5</sup>Institut Laue-Langevin

**INTRODUCTION:** The molecular machinery of the cyanobacterial circadian clock comprises three proteins: KaiA, KaiB, and KaiC. Through interactions among the three Kai proteins, the phosphorylation states of KaiC generate circadian oscillations *in vitro* in the presence of adenosine triphosphate (ATP). We especially focused on the KaiA-KaiB-KaiC ternary complex (ABC complex), which is considered to play the key role of the negative feedback loop of circadian rhythm. Recently, the cryo-electron microscopy (EM) structure of the ABC complex has been reported. However, the N-domains of KaiA subunits were poorly resolved due to their missing electron density maps. This observation probably reflected a high flexibility of linker between N- and C-domains. The whole structure of ABC complex has remained to be elucidated. Herein, for characterization of the overall structure of ABC complex, we conducted integrative techniques using small-angle X-ray scattering (SAXS), inverse contrast-matching small-angle neutron scattering (iCM-SANS), and native analytical ultracentrifugation (AUC) in conjunction with computer simulations.

**EXPERIMENTS:** The expression and purification of clock proteins, KaiA, KaiB and KaiC were performed according to methods previously described [1]. X-rays from a high-brilliance point-focused X-ray generator (MicroMAX-007HF, Rigaku, Tokyo, Japan) were focused with a confocal mirror (OptiSAXS) and collimated with a confocal multilayer mirror and two pinholes collimation system with the lower parasitic scattering, "ClearPinhole". The scattered X-rays were detected with a two-dimensional semiconductor detector (HyPix-6000, Rigaku, Tokyo, Japan). The sample-to-detector distance and wavelength of X-ray used for present work was 1320 mm and 1.542 Å, respectively. For removal of unfavorable aggregates from the sample solution, the laboratory-based SEC-SAXS System (LA-SSS) was employed to measure the SAXS profile in the  $Q$  range (0.01 Å<sup>-1</sup>–0.2 Å<sup>-1</sup>). The SANS experiments were performed using the D22 instrument installed at the Institut Laue-Langevin (ILL), Grenoble, France. The sample-to-detector distance and wavelength of neutron used

for present work was 5600 mm and 6.0 Å, respectively. SEC-SANS system was also utilized for present work.

**RESULTS:** The AUC data confirmed that KaiA, KaiB, and KaiC formed a 12:6:6 complex under the excess amount of KaiA.

With the aid of La-SSS, we succeeded to obtain mono-disperse ABC complex SAXS data. To obtain the structural information of subunits in the ABC complex in more detail, we also utilized the SEC-iCM-SANS. In this study, we prepared the ABC complex consisting of the 75% deuterated KaiB and KaiC subunits and the non-deuterated KaiA subunits. The solvent D<sub>2</sub>O ratio at the contrast matching point was determined to eliminate scattering originating from the 75% deuterated KaiC subunits. As a result, we could exclusively observe the SANS profile from KaiA subunits in the complex.

Under the assumption of six-fold symmetry of arrangement of the 12 KaiA N-domain connected with EM structure of ABC complex, we made 20 million distinct structural models of the ABC complex. The SAXS and SANS scattering profiles were calculated for each model and compared with the experimental data. As shown in Fig. 1, the whole structure of ABC complex as well as the structural arrangement of the KaiA-N-domains in the complex was resolved.

In summary, we succeeded to solve the ABC complex structure using SEC-SAXS and SEC-SANS in conjunction with computer simulation. Present result should provide the insights into the working mechanisms of the circadian clock comprised of Kai proteins.

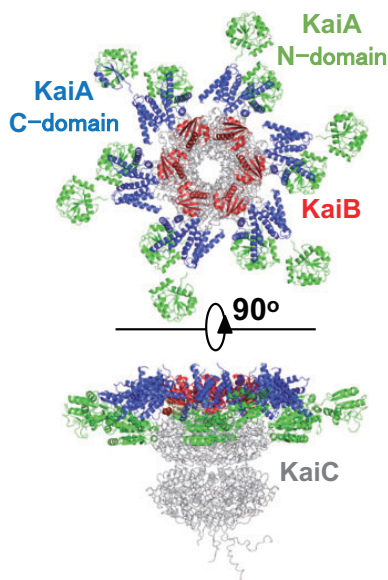


Fig. 1. Structural model of KaiA-KaiB-KaiC complex based on the scattering data. N- and C-domains of KaiA, KaiB and KaiC are shown in green, blue, red and gray, respectively.

**REFERENCES:**

[1] M. Sugiyama *et al.*, *Si. Rep.*, **6:35567** | (2016).

## CO6-4 Interaction between Mint3 and FIH-1 involved in hypoxia stress responses

R. Maeda, S. Nagatoishi<sup>1</sup>, K. Tsumoto<sup>1</sup>, K. Morishima<sup>2</sup>,  
R. Inoue<sup>2</sup>, M. Sugiyama<sup>2</sup> and M. Hoshino

Graduate School of Pharmaceutical Sciences, Kyoto  
University

<sup>1</sup>Institute of Medical Science, the University of Tokyo

<sup>2</sup>Institute for Integrated Radiation and Nuclear Science,  
Kyoto University

**INTRODUCTION:** Oxygen is essential for many organisms to produce ATP efficiently from nutrients in food. Under the normal oxidative conditions, nutrients are metabolized through glycolytic pathway, tricarboxylic acid cycle and electron transport system. Temporal or local drop of oxygen level induces cells to change the metabolic pathway, which is known as hypoxia stress responses. The responses are mainly triggered by hypoxia inducible factors (HIFs) that activate transcription of a group of genes.

Under the normal oxygen conditions, transcriptional activities of HIFs in the cells are inhibited by the factor inhibiting HIF-1 (FIH-1). On the other hand, several cells including tumor cells and macrophages, metabolize nutrients exclusively by nonoxidative glycolytic pathway even under the normal oxygen levels. Munc-18 interacting protein 3 (Mint3) is recently found to activate the hypoxia responses by binding and inhibiting the activity of FIH-1 in these cells [1]. Although the N-terminal 214 residues are found to be necessary for the interaction with FIH-1 to inhibit its activity, little is known about inhibitory mechanisms.

We attempted to elucidate the molecular mechanism of the interaction between Mint3 and FIH-1 by a various physicochemical methods, including small-angle X-ray scattering, analytical ultracentrifugation, and solution-state NMR.

**EXPERIMENTS:** High-expression systems for the N-terminal fragment proteins of Mint3 (Mint3(1–214) and Mint3(1–117)) and full-length FIH-1 were constructed by *E. coli* BL21 strains. The proteins were expressed in bacteria grown in LB-broth and <sup>15</sup>N-enriched M9 minimal medium to produce unlabeled and <sup>15</sup>N-labeled proteins, respectively.

NMR experiments were performed on a Bruker Avance 600 spectrometer equipped with a triple-resonance probe. A typical <sup>1</sup>H-<sup>15</sup>N HSQC experiments were performed at protein concentration of 50  $\mu$ M. The solvent conditions used were 20 mM sodium acetate (pH 7.3), and 10% D<sub>2</sub>O. The chemical shift value was referenced to DSS.

**RESULTS:** We measured <sup>1</sup>H-<sup>15</sup>N HSQC spectra of Mint3(1–214) and Mint3(1–117) proteins under the physiological conditions (pH 7.3). In both proteins, the chemical shift dispersion along the <sup>1</sup>H axis was small and most peaks were appeared within the range between 8.5 and 7.5 ppm, suggesting that the proteins were intrinsically disordered. This was also supported by the observation that the peak intensities were markedly decreased at higher temperature, probably rapid exchange of amide hydrogen with water molecules due to the lost of intramolecular hydrogen bonds.

Next, we measured the <sup>1</sup>H-<sup>15</sup>N HSQC spectra of Mint3(1–214) and Mint3(1–117) in the presence of a various amount of unlabeled FIH-1. In both proteins, the intensities for several peaks were markedly decreased in a concentration-dependent manner, suggesting the involvement of specific binding of these residues. It should be mentioned that the same results were obtained both in Mint3(1–214) and Mint3(1–117), suggesting that the specific binding site for FIH-1 is present in a smaller fragment protein Mint3(1–117) (Fig. 1).

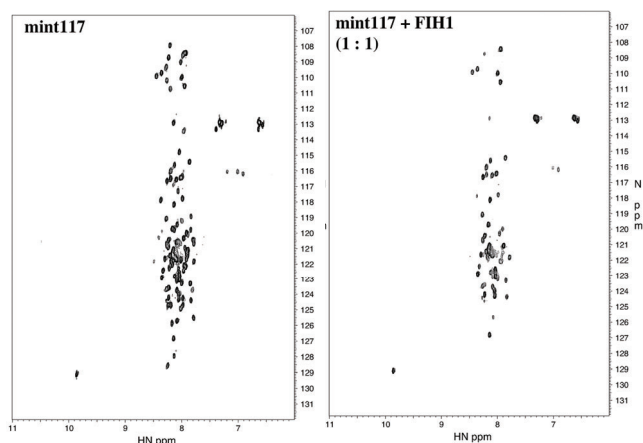


**Fig. 1.** <sup>1</sup>H-<sup>15</sup>N HSQC spectra of Mint3(1–117) in the absence (left) and presence (right) of unlabeled FIH-1.

In order to elucidate the binding site at residue-level, we are now analyzing several 3D-triple resonance experiments, including 3D-HNCACB and 3D-hNcoaNh, to assign the resonance peaks. We are also attempting to analyze global change in the molecular shape of Mint3(1–214) / Mint3(1–117) and FIH-1 by small-angle X-ray scattering.

### REFERENCES:

[1] Sakamoto *et al.*, (2014) *Mol Cell Biol.*, **34** (1) 30–42.

M. Yagi-Utsumi, R. Inoue<sup>1</sup>, M. Sugiyama<sup>1</sup> and K. Kato

*Exploratory Research Center for Life and Living Systems (ExCELLS) and Institute for Molecular Science (IMS), National Institutes of Natural Sciences*

<sup>1</sup>*Institute for Integrated Radiation and Nuclear Science, Kyoto University*

**INTRODUCTION:** Euryarchaeal genomes encode proteasome-assembling chaperone homologs, PbaA and PbaB, although archaeal proteasome formation is a chaperone-independent process. Homotetrameric PbaB functions as a proteasome activator, while PbaA forms a homopentamer that does not interact with the proteasome [1, 2]. Notably, PbaA forms a complex with PF0014, an archaeal protein without functional annotation. In this study, based on our previous research on PbaA crystal structure, we performed an integrative analysis of the supramolecular structure of the PbaA/PF0014 complex using native mass spectrometry, solution scattering, high-speed atomic force microscopy (HS-AFM), and cryo electron microscopy (cryo-EM).

**EXPERIMENTS:** For the purification of the PbaA/PF0014 complex, both recombinant proteins, PbaA (400  $\mu$ M monomer) and PF0014 (400  $\mu$ M monomer), were mixed at a 1:1 molar ratio and then dialyzed for 12 h against 50 mM Tris-HCl buffer (pH 8.0) containing 200 mM NaCl and 2 mM DTT.

SEC-SAXS measurements of the PbaA/PF0014 complex were obtained using UPLC ACQUITY (Waters) integrated with a SAXS set-up. In each measurement, 50  $\mu$ L of 6 mg/ml proteins was loaded onto a Superdex 200 Increase 10/300 GL (GE Healthcare) pre-equilibrated with 50 mM Tris-HCl buffer (pH 8.0) containing 150 mM NaCl at a flow rate of 0.5 ml/min. During the elution of proteins, the flow rate was reduced to 0.10 ml/min. X-ray scattering and UV spectra were collected every 10 s.

For iCM-SANS experiments, a complex of 3 mg/ml of non-deuterated PbaA/75%-deuterated PF0014 as well as a complex of 75%-deuterated PbaA/75%-deuterated PF0014 was dissolved in 99.8% D<sub>2</sub>O (ISOTECH) containing 50 mM Tris-HCl (pH 8.0) and 150 mM NaCl to reduce the incoherent scattering and obtain high-quality statistical data in the higher q-range. SANS experiments were performed using Quokka installed at the Australian Centre for Neutron Scattering (ANSTO, Sydney, Australia).

**RESULTS:** The results indicated that this highly thermostable complex constitutes ten PbaA and ten PF0014 molecules, which are assembled into a dumbbell-shaped structure. SEC-SAXS showed the PbaA-PF0014 complex exhibits an estimated radius of gyration ( $R_g$ ) of 54.6 Å and maximum dimension ( $D_{max}$ ) of 165 Å (Fig. 1).

iCM-SANS, cryo-EM, and HS-AFM showed that two PbaA homopentameric rings correspond to the dumbbell plates, with their N-termini located outside of the plates and C-terminal segments left mobile. Furthermore, mutant PbaA lacking the mobile C-terminal segment retained the ability to form a complex with PF0014, allowing 3D modeling of the complex. The complex shows a five-column tholos-like architecture, in which each column comprises homodimeric PF0014, harboring a central cavity, which can potentially accommodate biomacromolecules including proteins. Our findings provide insight into the functional roles of Pba family proteins, offering a novel framework for designing functional protein cages [3].

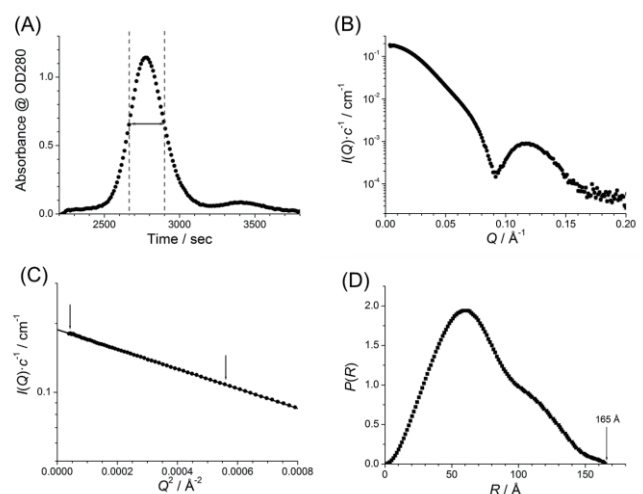


Fig. 1. (A) The SEC chart of the PbaA/PF0014 complex. We selected a region of full width at half maximum of the main peak from  $t = 2664$  to  $t = 2900$  s, indicated by red lines, for averaging the SAXS profile. (B) Averaged scattering profile. (C) Guinier plot indicating the range for the least square fitting by arrows and (D) distance distribution function,  $P(r)$ , of the averaged SAXS profile.

#### REFERENCES:

- [1] A. Sikdar *et al.*, *Biochem. Biophys. Res. Commun.*, **453** (2014) 493-497.
- [2] M. Yagi-Utsumi *et al.*, *Protein. Eng. Des. Sel.*, **31** (2018) 29-36.
- [3] M. Yagi-Utsumi, *et al.*, *Sci. Rep.*, **10**, (2020) 1540.

N. Yamamoto, E. Chatani<sup>1</sup>, T. Akai<sup>1</sup>, R. Inoue<sup>2</sup> and M. Sugiyama<sup>2</sup>

School of Medicine, Jichi Medical University

<sup>1</sup>Graduate School of Science, Kobe University

<sup>2</sup>Institute for Integrated Radiation and Nuclear Science, Kyoto University

**INTRODUCTION:** Amyloid fibrils are protein aggregates with  $\beta$ -sheet rich structure, which are associated with numerous amyloidoses and neurodegenerative diseases. Amyloid fibrils are typically formed through a nucleation-dependent mechanism. While a one-step nucleation is the simplest scheme, various oligomers have been identified in early stages, suggesting the presence of meta-stable nucleation intermediates [1].

In our previous work, we found that nucleation intermediates were formed in the early phases of amyloid fibril formation of an insulin-derived peptide, insulin B chain [2]. In addition, we found that fibrinogen, one of dominant plasma proteins, inhibits the formation of amyloid fibrils of insulin B chain by interacting with nucleation intermediates [3]. In this study, we elucidated structural properties of the nucleation intermediate by using small-angle X-ray scattering (SAXS) and analyzed change in SAXS profile after the addition of fibrinogen to elucidate the interaction manner of fibrinogen with the nucleation intermediate.

**EXPERIMENTS:** B chain was prepared from human insulin as described in a previous work [2]. The stock insulin B chain was diluted with 50 mM Tris-HCl buffer at a concentration of 1.4 mg/ml and was then put in a 1-mm path-length quartz cell. For the measurement of the B-chain nucleation intermediate, the sample was pre-incubated under quiescent conditions for 2 h at 25 °C. For the measurement of the complex with fibrinogen, a concentrated fibrinogen solution was added to the nucleation intermediate at the final concentration of 3.5 mg/ml approximately 5 min before the SAXS measurement. For the measurement of fibrinogen, a 3.5 mg/ml solution in 50 mM Tris-HCl buffer was used. SAXS profiles were measured at 25 °C with NANOPIX equipped with HyPix-6000 (Rigaku Corporation, Japan) with an exposure time of 30 min. A Cu K- $\alpha$  line (MicroMAX-007HF) was used as a beam source. The camera length was 1.33 m and the range of the scattering vector  $q$  was from 0.006 to 0.23  $\text{\AA}^{-1}$ .

**RESULTS:** Figure 1 shows the SAXS profile of the B-chain nucleation intermediate, fibrinogen, and the complex of the nucleation intermediate with fibrinogen. The slope of the log-log plot of the scattering profile of the nucleation intermediate was close to -1, suggesting a rod-like structure. As a result of the analysis of a cross-section plot for a cylindrical structure, it was suggested that the bottom radius is approximately 3 nm. It was also suggested that

the length was approximately 270 nm based on Broersma's relationship [4] with a diffusion coefficient determined by DLS measurement. The rod-like structure was maintained even after the addition of fibrinogen, and the slope of the log-log plot kept close to -1. When the base radius and length of the complex were calculated in the same manner as for the nucleation intermediate, they were estimated to be 6 nm and 290 nm, respectively [5].

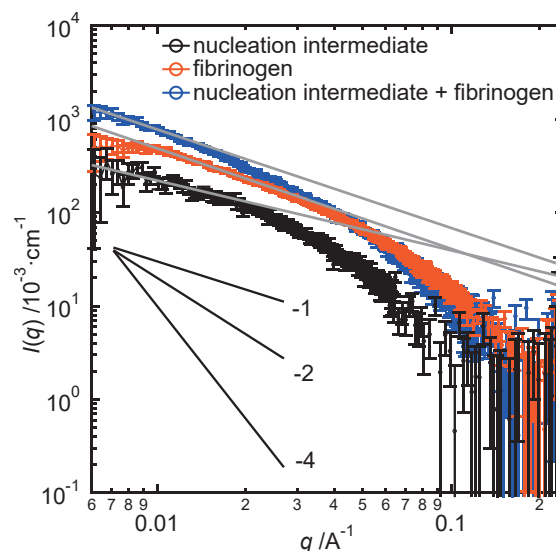


Fig. 1. One-dimensional SAXS profiles of the nucleation intermediate of insulin B chain (black), fibrinogen (orange) and the complex of the nucleation intermediate and fibrinogen (blue). Gray lines represent the slope of the profiles and the black slopes of -1, -2, or -4 indicate guides for the eyes.

The radius of fibrinogen was approximately 2.5 nm, and the increase in the radius by the fibrinogen binding could be explained reasonably when a single layer of fibrinogen molecules was assumed to surround the surface of the prefibrillar intermediates. It was thus suggested that fibrinogen binds to the surface of the nucleation intermediate so as to cover the surface of the nucleation intermediate, which would be the molecular basis of the inhibitory mechanism of B-chain amyloid fibril formation by fibrinogen. This structural insight of the B-chain nucleation intermediate complexed with fibrinogen will provide insights into general principles of functions of proteins that serve as chaperones or chaperone-like proteins involved in amyloid-related diseases.

#### REFERENCES:

- [1] E. Chatani and N. Yamamoto, *Biophys. Rev.*, **10** (2018) 527-534.
- [2] N. Yamamoto *et al.*, *Sci. Rep.*, **8** (2018) 62.
- [3] T. Akai, Master's Thesis, Kobe Univ. (2017).
- [4] S. J. Broersma, *Chem. Phys.*, **32** (1960) 1632-1635.
- [5] N. Yamamoto *et al.*, *Biochemistry*, **58** (2019) 2769-2781.

H. Terato, T. Saito<sup>1</sup>, Y. Sakurai<sup>1</sup>, T. Hanafusa, M. Isobe, S. Ihara<sup>2</sup> and Y. Tokuyama<sup>3</sup>

*Advanced Science Research Center, Okayama University  
<sup>1</sup>Institute for Integrated Radiation and Nuclear Science,  
 Kyoto University*

*<sup>2</sup>Graduate School of Engineering, Saga University*

*<sup>3</sup>Analytical Research Center for Experimental Sciences,  
 Saga University*

**INTRODUCTION:** Radiation biological effects are arrived via DNA damaging by ionizing radiation, because DNA brings the genetic information. We have a lot of knowledge about radiation DNA damage. But the most of them were derived from gamma- and X-rays' studies with less information of other radiation qualities. Therefore, we have studied for the DNA damage with heavy ion beams, previously [1, 2]. These studies indicated that the DNA damage with heavy ion beams were unique, indicating that a lot of clustered DNA damage were generated including DNA double strand break (DSB), clustered base lesions, and these mixtures. Clustered DNA damage is a complex damage containing multiple lesions in the local region of DNA. This damage strongly inhibits DNA polymerization with high efficiently stopping of DNA polymerase moving on DNA. Also, clustered DNA damage shows less repairable, because there is no scaffold for DNA repair enzyme attaching. Here, we analyze the DNA damage with neutrons from nuclear power plant to unveil the molecular mechanism of neutron biological effect. The neutron beam is also high LET radiation as same as heavy ion beam. Therefore, we will find some interesting character of DNA damage with neutron like heavy ion beam. In the previous study period, we found the relatively higher yields of DNA damage with the neutron beams than gamma-rays. In this year, we estimated the cell viability for the neutron beams for the biological effect of this radiation.

**EXPERIMENTS:** Cultured cells of Chinese hamster ovary (CHO) AA8 strain were irradiated with neutron beams in the Kyoto University Reactor. The cells were cultivated with the conventional method. The logarithmic growing cells were recovered by trypsinization, and set into a polypropylene tube for irradiation. The irradiation time was up to three hours with sampling in every 30 minutes. The estimated dose rate of neutron was 1Gy h<sup>-1</sup>. After irradiation, the cells were immediately dissolved again with the cultured medium and reseeded into fresh medium. The cells were cultivated for 10 days for growing the colony. The colony was fixed with ethanol and stained with methylene blue. The colony number was counted for estimation of the irradiated cell viability.

**RESULTS:** The result for cell viability indicated that neutron showed stronger cell damage ability than gamma-rays (Fig. 1). The surviving curve indicates that D<sub>37</sub> of the neutron seems to be around 1 Gy. The dosimetry of the neutrons indicates that a half of dose of the reactor neutrons is derived from the contaminated gamma-rays (data not shown). Gamma-rays usually show that the D<sub>37</sub> is around 4 Gy. This result suggests that the neutron has greater efficiency for the biological effect. We already have the result indicating that the neutron showed relatively higher efficiency to generate the DNA damage than gamma-rays. Thus, the severe biological effect with neutron beam seems to be derived from the higher yield of DNA damage.

In this yearly study, we obtained the relatively higher biological effect of the neutron. But, we need further study for elucidation of molecular mechanism of neutron biological effect. The first one is generalization of neutron effect. We are proceeding another neutron project at Kinki University Reactor (KUR). KUR generates weaker power neutron than the Kyoto University reactor. Comparing of the results with these two reactors will show a generalization of neutron efficiency. The second is analysis of DNA damage species with neutron beam. The future analyzing plan will contain the oxidative pyrimidine analysis such as 5-hydrooxycytosine. Also, the DSB will be analyzed by using of the mutant cell strains without homologous recombination (HR) and non-homologous end joining (NHEJ). Using of these mutants leads the initial yields of DSB without DNA repair process.

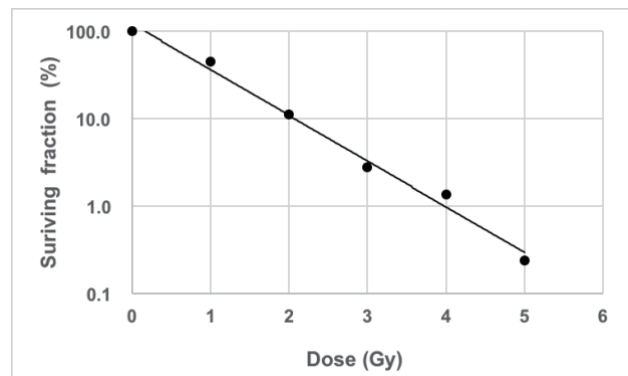


Fig. 1. Surviving fraction of the cells irradiated with the reactor neutrons.

#### REFERENCES:

- [1] H. Terato *et al.*, *J. Radiat. Res.*, **49** (2008) 133-146.
- [2] Y. Tokuyama *et al.*, *J. Radiat. Res.*, **56** (2015) 446-455.

## CO6-8 Radiation-induced clustered DNA damage estimated by homo-FRET analysis

K. Akamatsu, N. Shikazono and T. Saito<sup>1</sup>

*Institute of Quantum Life Science, National Institutes for Quantum and Radiological Science and Technology (QST)*

<sup>1</sup>KURNS

### INTRODUCTION:

DNA lesions induced by ionizing radiation and chemicals can cause mutation and carcinogenesis. In particular, “clustered damage” site, that is a DNA region with multiple lesions within one or two helical turns, is believed to hardly be repaired. This damage is considered to be induced, *e.g.*, around high-LET ionizing radiation tracks. In fact, evidence is found in the direct observation AFM (atomic force microscopy) and a simulation [1]. However, detail of the damage is not known. We have already developed a method for estimating degree of localization of abasic sites (APs) in DNA using Förster resonance energy transfer occurred between different fluorescence probes (“hetero-FRET” using Alexa350 and Alexa488) [2]. The results showed that <sup>12</sup>C<sup>5+</sup> beam produced close APs within a track: the apparent distance calculated was approximately 17 base pairs [3]. This finding indicates that direct radiation effect of <sup>12</sup>C<sup>5+</sup> beam near the Bragg peak produces clustered DNA damage. We have recently applied the method to DNA in a cell-mimetic radical scavenging condition. However, there are some problems of the complex protocol and of the sensitivity due to the low extinction coefficient of Alexa350. We have, therefore, developed “homo-FRET” occurred between two or more Alexa488 molecules. We will obtain magnitude of FRET also from “fluorescence anisotropy” of homo-FRET between Alexa488 molecules. The new protocol using homo-FRET [4] enables us to estimate DNA damage localization without any enzymes and improves sensitivity to detect a clustered damage.

### EXPERIMENTS:

#### ●Sample preparation and irradiation

The plasmid DNA digested by Sma I was used (linear form). The DNA was dissolved to be ~10 mg/mL in 0.2 M Tris-HCl buffer (pH 7.5) which is a cell-mimetic condition in relation to radical scavenging capacity. Eight microliters of the DNA solution was transferred to a glass plate (10 mmφ) under 100 % RH at r.t., and was irradiated with heavy ion beams, <sup>20</sup>Ne<sup>8+</sup> (LET: ~500 keV/μm), <sup>40</sup>Ar<sup>13+</sup> (LET: ~1800 keV/μm) at TIARA (QST), and <sup>60</sup>Co γ-rays (LET: ~0.3 keV/μm; KURNS) as a standard radiation source.

#### ●Preparation of fluorophore-labeled irradiated DNA and the FRET observation

The damaged sample DNA (10 μL in water) and 10 μL of 100 mM Tris-HCl (pH 7.5) were mixed in a microtube. Two microliters of Alexa488/DMSO was added to the DNA solution and was incubated for 24 h at 35°C. The fluorophore-labeled DNA was purified by etha-

nol-precipitation followed by ultrafiltration. The fluorescence anisotropy was measured at 525 nm (ex. 470 nm).

The anisotropy,  $\langle r \rangle$ , is defined as follows:

$$\langle r \rangle = (I_{VV} - G I_{VH}) / (I_{VV} + 2G I_{VH}),$$

where  $I_{VV}$  is the fluorescence intensity when the excitation and emission polarizers are both vertically oriented.  $I_{VH}$  is one when the excitation/emission polarizers are vertically/horizontally oriented.  $G$  is the grating factor defined as  $I_{HV}/I_{HH}$ .

### RESULTS AND DISCUSSION:

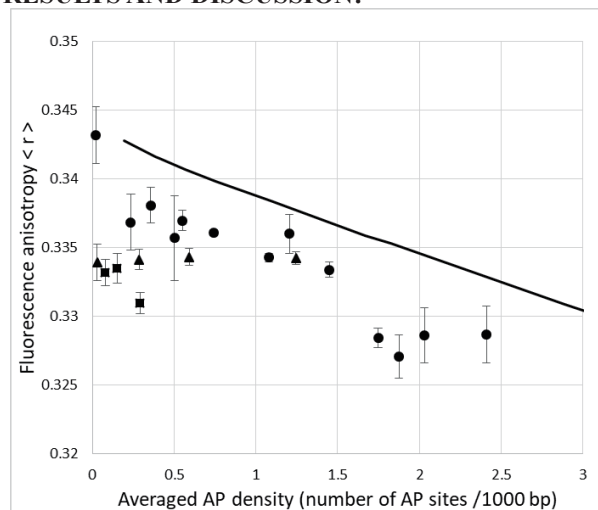


Fig. 1. Relationship between AP averaged density and fluorescence anisotropy for <sup>60</sup>Co γ-rays (●), Ne (▲), and Ar (■). The solid line indicates a theoretical curve when APs are randomly distributed.

In general, fluorescence anisotropy decreases with increasing FRET [5]. As shown in Fig.1, we found that the relationship differed significantly among the radiations tested. AP clustering even by the γ-rays seems to be more likely to occur than random distribution. Although the ion beams appeared to produce clustered AP more than the case of the γ-rays, the difference was not so significant that we expected from the results for the direct radiation effects using dry DNA samples [3]. Under cell-mimetic condition, most APs induced by the ion beams could exist as isolated lesions. Production of clustered APs by “indirect effect” (*e.g.*, by ·OH) may hardly occur due to recombination between radicals.

### REFERENCES:

- [1] Y. Matsuya, *et al.*, *Int.J.Mol. Sci.* 20, 1701.
- [2] K. Akamatsu, N. Shikazono, *Anal. Biochem.*, **433** (2013) 171-180.
- [3] K. Akamatsu, N. Shikazono, and T. Saito, *Radiat. Res.*, **183** (2015) 105-113.
- [4] K. Akamatsu, N. Shikazono, *Anal. Biochem.*, **536** (2017) 78-89.
- [5] L. W. Runnels, and S. F. Scarlata, *Biophys. J.* **69** (1995) 1569.

M. Kurosawa<sup>1</sup>, M. Fujiwara<sup>1</sup>, N. Takahashi<sup>1,2</sup>,  
M. Tamura<sup>1</sup>, Y. Kosuge<sup>2</sup>, N. Abe<sup>3</sup>, T. Kubota<sup>3</sup>, and T.  
Takahashi<sup>3</sup>

<sup>1</sup>Research Center for Nuclear Physics, Osaka University

<sup>2</sup>Kyoto Medical Technology Co.

<sup>3</sup>Institute for Integrated Radiation and Nuclear Science,  
Kyoto University

## INTRODUCTION:

In the  $^{18}\text{F}$  production, we use natural neon gas as a target in the gas recycling flow system. The  $^{18}\text{F}$ -FDG pharmaceuticals are obtained by blowing small bubbles of irradiated neon gas in the glucose aqueous solution. In the  $^{99\text{m}}\text{Tc}$  production, we use natural  $\text{MoO}_3$ . In both the methods, we can produce  $^{99\text{m}}\text{Tc}$  isotopes for the SPECT inspections and  $^{18}\text{F}$  isotopes for the PET inspections using the photoreaction on natural  $\text{MoO}_3$  and Ne targets. We are going to polish up the usages of these two methods in view of practical aspect.

## $^{18}\text{F}$ EXPERIMENT AND RESULTS

An electron beam from the linear accelerator facility at Institute for Integrated Radiation and Nuclear Science of Kyoto University (KURNS-LINAC) for producing RI from photoreactions. A 40 MeV electron beams with an intensity of 3-9  $\mu\text{A}$  is used to bombard a platinum target with a thickness of 4 mm to generate bremsstrahlung photons for producing  $^{18}\text{F}$  via the photoreaction on natural Ne gas.

The Ne gas circulation system has been developed for the present experiment. The irradiation time of bremsstrahlung photons was one hour. We expect that produced  $^{18}\text{F}$  isotopes circulate with Ne gas, and that the monovalent  $-\text{OH}$  in glucose will be easily replaced by  $^{18}\text{F}$  arrested in the liquid, resulting  $^{18}\text{F}$ -FDG. The first purpose of the experiment was to examine this principle. Instead of glucose, we used a sodium hydroxide (NaOH) aqueous solution to trap  $^{18}\text{F}$ . This seemed to be successful in  $^{18}\text{F}$  collection.

However, when we used glucose instead of NaOH, the  $^{18}\text{F}$  collection efficiency drastically decreased. The clear reason is still unknown. The reasons may come from 1) the intrinsic easiness of the chemical replacement reaction for the glucose and NaOH.

## $^{99\text{m}}\text{Tc}$ EXPERIMENT AND RESULTS

It had been reported that the high-rate production of  $^{99\text{m}}\text{Tc}$  radioisotopes is realized by irradiating the bremsstrahlung photons on natural  $\text{MoO}_3$  target [1,2]. We tried

to develop the new method for extracting  $^{99\text{m}}\text{Tc}$  using nano-particles.

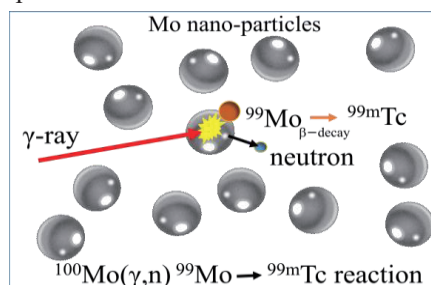


Figure 1: Photoreaction produces  $^{99}\text{Mo}$  in nano- $\text{MoO}_3$  powder which has a porous assembly of many  $\text{MoO}_3$ .  $^{99\text{m}}\text{Tc}$  radioisotopes decayed from  $^{99}\text{Mo}$  are washed out using saline.

Figure 1 shows the schematics scheme for producing  $^{99\text{m}}\text{Tc}$  via the  $^{100}\text{Mo}(\gamma, n)^{99}\text{Mo}$  reaction. We notice that the size of the nano-particles is very small and the most of the  $^{99}\text{Mo}$  produced by the photo-nuclear reaction can escape to the surface. Therefore, the produced  $^{99\text{m}}\text{Tc}$  is easily separated from the  $\text{nat}\text{MoO}_3$ . If we pour the isotonic sodium chloride solution (saline) into nano- $\text{MoO}_3$  powder,  $^{99\text{m}}\text{Tc}$  is readily soluble in saline even at the inside of nano-particles.

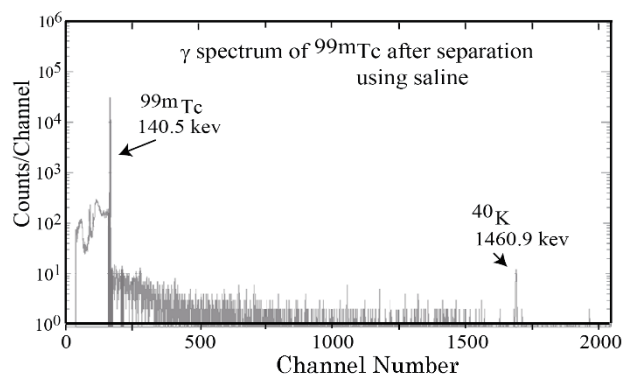


Figure 2:  $\gamma$ -ray spectrum measured with a Ge-detector after  $^{99\text{m}}\text{Tc}$  separation using saline. Two prominent  $\gamma$ -ray peaks at 140.5 keV from  $^{99\text{m}}\text{Tc}$  and at 1460.9 keV from  $^{40}\text{K}$  as background are measured. The event yields lower than 140.5 keV are due to X-ray background from Pb shields and due to the Compton scattering of 140.5 keV  $\gamma$ -ray.

Figure 2 shows a  $\gamma$ -ray spectrum measured for the saline leaked out from the target vessel of  $\text{MoO}_3$  nano-powder. Although we observe the backgrounds due to the X-rays from Pb-shields and due to the 1460.9 keV  $\gamma$ -ray from  $^{40}\text{K}$ , it is clear that the saline leaked out from the target vessel includes only  $^{99\text{m}}\text{Tc}$  (see the 140.5 keV peak).

## REFERENCES:

- [1] T. Takeda *et al.*,  $^{99\text{m}}\text{Tc}$  production via the  $(\gamma, n)$  reaction on natural Mo, *Journal of Radioanalytical and Nuclear Chemistry* (2018) 318: 811-821.
- [2] N. Takahashi, Patent Number 2014/05790.

## CO6-10 Small Angle X-ray Scattering Measurements on Insulin B chain; a Time-Resolved Measurement to Monitor the Amyloid Fibril Formation via Prefibrillar Intermediates

N. Yamamoto, R. Inoue<sup>1</sup>, K. Morishima<sup>1</sup>, E. Chatani<sup>2</sup>, and M. Sugiyama<sup>1</sup>

School of Medicine, Jichi Medical University

<sup>1</sup>Institute for Integrated Radiation and Nuclear Science, Kyoto University

<sup>2</sup>Graduate School of Science, Kobe University

**INTRODUCTION:** Amyloid fibrils are abnormal protein aggregates associated with a numerous number of diseases called amyloidoses such as Alzheimer's disease. Amyloid fibrils generally possess fibrous morphology and  $\beta$ -sheet-rich structure, and the formation of amyloid fibrils typically follows a nucleation-dependent polymerization mechanism. It has been believed that the fibril formation occurs by one-step reaction from fibril nuclei. However, a variety of oligomers have been identified in early stages of fibrillation. Such oligomeric species attract attention as a key molecule in the nucleation process as well as molecular species responsible for cytotoxicity [1].

We recently found that prefibrillar intermediates were formed in the early phases of amyloid fibril formation of an insulin-derived peptide (insulin B chain) [2]. Especially, it was confirmed that two kinds of prefibrillar intermediates, i.e. the first prefibrillar intermediate and the subsequently-occurring second prefibrillar intermediate were formed. The structural detail of prefibrillar intermediates was elucidated using time-resolved small-angle X-ray scattering (SAXS) at the concentration of 1.4 mg/ml [3]. The analysis of the time-resolved measurement suggested elongation of the rod-like structure as the number of the second prefibrillar intermediate increased.

In this study, we also performed time-resolved SAXS experiment at the B chain concentration of 2.8 mg/ml to understand more detail about the elongation mechanism of the prefibrillar intermediates toward the fibril formation.

**EXPERIMENTS:** For the purification of B chain from human insulin, we followed the purification method of B chain described in literature [4]. The stock insulin B chain, which was dissolved in 10 mM NaOH, was diluted with 50 mM Tris-HCl buffer at a concentration of 2.8 mg/ml. The sample solution was then put in a 1-mm path-length quartz cell. SAXS profile was obtained at 25 °C with NANOPIX equipped with HyPix-6000 (Rigaku Corporation, Japan). A Cu K- $\alpha$  line (Micro-MAX-007HF) was used as a beam source, which was further focused and collimated with a confocal multilayer mirror (OptiSAXS). The camera length was set to 1.33 m

and the range of the scattering vector  $q$  was from 0.05 to 2.35 nm<sup>-1</sup>. X-ray scattering data were collected with an exposure time of 30 min.

**RESULTS:** Fig. 1 shows time-resolved SAXS profiles of insulin B chain at the concentration of 2.8 mg/ml. It was demonstrated that the slope of the plot in the double-logarithmic scale was close to -1, indicating that the intermediates possess rod-like structures. A preliminary analysis of the cross-section plot, in which the intensity was plotted against  $q^2$ , was also performed to calculate the radius of the rod-like structure. As a result, it was demonstrated that the first prefibrillar intermediate was already formed even in the dead time of the measurement. It indicates that the increase in the concentration accelerated the formation of the first prefibrillar intermediate. Combined with a result of time-resolved dynamic light scattering measurement, it was also revealed that further elongation of the second prefibrillar intermediate occurred. This behavior supports our proposed idea that the formation of the amyloid fibril occurs via the second prefibrillar intermediate.

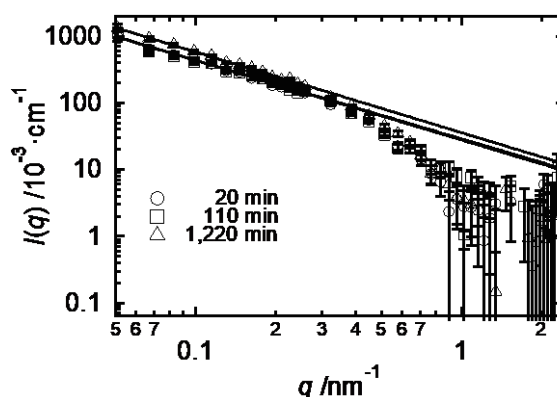


Fig. 1. Representative one-dimensional SAXS profiles of insulin B chain monitored at 20, 110, and 1,220 minutes. The lines indicate slopes obtained by curve fit.

### REFERENCES:

- [1] E. Chatani and N. Yamamoto, *Biophys. Rev.*, **10** (2018) 527-534.
- [2] N. Yamamoto *et al.*, *Sci. Rep.*, **8** (2018) 62.
- [3] N. Yamamoto *et al.*, *KURNS PROGRESS REPORT 2018, CO6-7* (2018).
- [4] N. Yamamoto *et al.*, *Biochemistry*, **58** (2019) 2769-2781.

## CO6-11      **Generation of radioresistant *Escherichia coli* by adaptive evolution using gamma rays as selection pressure II**

T. Saito

*Institute for Integrated Radiation and Nuclear Science,  
Kyoto University*

**INTRODUCTION:** In nature, organisms have evolved diversely by adapting themselves to various environmental conditions. Some organisms have been found to survive in environments that can be easily perceived as extremely severe. Elucidating the adaptive mechanisms of organisms to severe environmental conditions can provide meaningful information regarding evolution and diversity overall. Some bacteria, known as radioresistant bacteria, demonstrate extreme resistance to ionizing radiations [1]. The extreme resistance mechanism of these bacteria to ionizing radiation is an interesting area of research from the standpoint of adaptive mechanisms employed by organisms in nature. In order to elucidate the mechanisms of radioresistance in these organisms, it is important to investigate their biological defense mechanisms against external stresses at the molecular level. However, studies conducted on radioresistant organisms existing in nature are likely to encounter many challenges due to limited knowledge of their genetic and biochemical properties. Therefore, in this study, the generation of radioresistant cells of *Escherichia coli* was attempted by experimenting on their ability to undergo adaptive evolution when exposed to gamma rays. The following operations were repeated in this experiment: gamma-ray irradiation of *E. coli* cells whose genetic and biochemical properties are sufficiently known, growth of the surviving cells, and irradiation of the grown cells. Furthermore, the gene expression status in evolved *E. coli* was analyzed and compared with that of wild type *E. coli*.

**EXPERIMENTS: Evaluation of the sensitivity of *E. coli* cells to gamma irradiation:** *E. coli* K-12 cells were grown to the early log phase in LB medium at 37°C at 200 rpm. One milliliter of the culture was centrifuged at 4000 × *g* at 20°C for 10 min. The supernatant was discarded and the pellet was suspended in 1 mL of PBS (–). The cell suspension was irradiated with gamma rays at a dose rate of 22 Gy/min at 20 ± 3°C. Gamma irradiation was carried out at the Co-60 Gamma-ray Irradiation Facility of the Institute for Integrated Radiation and Nuclear Science, Kyoto University. The gamma-irradiated cell suspension was diluted appropriately with PBS (–), plated on LB agar, and incubated at 37°C for 12 hr. After incubation, the colonies were counted, colony forming units were determined, and survival rates were calculated.

**Selection with gamma rays:** *E. coli* K-12 clone cells

obtained by single colony pick-up were cultured to the early log phase in LB medium at 37°C at 200 rpm. The cell suspension was prepared as described above and irradiated with the 1% survival dose of gamma rays at a dose rate of 22 Gy/min at 20 ± 3°C. One milliliter of the gamma-irradiated cell suspension was inoculated in 100 mL of LB medium and cultured at 37°C at 200 rpm till the cells reached their early stationary phase. The glycerol stock was prepared and stored at –80°C. This procedure was repeated after culturing the glycerol stock cells to the early log phase.

**Analysis of gene expression status:** Total RNA was extracted from *E. coli* cells using RNAiso Plus (Takara), and further purified using NucleoSpin RNA Clean-up XS (Macherey-Nagel). The quality of the resulting total RNA was evaluated and confirmed with the Agilent 2200 TapeStation (Agilent). rRNA was removed from total RNA using Ribo-Zero Magnetic Kit (Gram-Negative Bacteria) (Illumina). The sequence library was prepared from the resulting RNA using TruSeq Stranded mRNA Sample Prep Kit (Illumina). The quality of the sequence library was evaluated and confirmed with the Agilent 2100 Bioanalyzer (Agilent). Sequence analysis was performed with NovaSeq 6000 (Illumina) and using NovaSeq 6000 S4 Reagent Kit (Illumina) and NovaSeq Xp 4-Lane Kit (Illumina). The gene expression levels were analyzed using Genedata Profiler Genome (Genedata) and STAR [2]. All procedures were done according to manufacturer's instructions.

**RESULTS:** The 1% survival dose to gamma rays of the wild type *E. coli* clone without selection was 240 Gy, whereas that of the *E. coli* population obtained after 20 selection cycles was 1900 Gy; the resistance of *E. coli* to gamma rays was increased 7.9-fold in this adaptive evolution experiment. The expression levels of 164 genes in the evolved *E. coli* were statistically significantly different from those in the wild-type *E. coli*. Among those genes, the expression level of 27 genes increased 2-fold or more, and the expression level of 23 genes decreased 0.5-fold or less. These results suggest that the radioresistance of the radioresistant *E. coli* obtained in this adaptive evolution experiment is attributed in part to these genetic changes. In the future, it is necessary to analyze in detail how these changes in gene expression are involved in the radioresistance of *E. coli*.

### REFERENCES:

- [1] T. Saito, *Viva Origino*, **30** (2007) 85–92.
- [2] A. Dobin *et al.*, *Bioinformatics*, **29** (2013) 15–21.

## CO6-12 Structural study for the nucleosome containing histone variant H2A.B

R. Hirano<sup>1</sup>, Y. Arimura<sup>1</sup>, T. Kujirai<sup>1</sup>, A. Okuda<sup>2</sup>, K. Morishima<sup>2</sup>, R. Inoue<sup>2</sup>, M. Sugiyama<sup>2</sup>, M. Koyama<sup>1</sup>, and H. Kurumizaka<sup>1</sup>

*Institute for Quantitative Biosciences, The University of Tokyo*

<sup>1</sup>*Department of Biological Sciences, The University of Tokyo*

<sup>2</sup>*Institute for Integrated Radiation and Nuclear Science (KURNS), Kyoto University*

### INTRODUCTION:

In eukaryotic cells, the genomic DNA is bound to histone proteins, and forms the chromatin structure [1]. The fundamental unit of the chromatin is the nucleosome, in which about 150-base-pairs of DNA are wrapped around the histone octamer containing two molecules of each four core histone (H2A, H2B, H3, and H4). The nucleosome generally prevents transcription factors from binding the genomic DNA. A group of the transcription factors, called pioneer transcription factors, are known to be able to bind their target DNA motifs in the nucleosome. The binding of pioneer transcription factors to the nucleosomes is reportedly influenced by histone variants, but the detail has not been understood. In this study, we focused on a histone H2A variant, H2A.B, as a representative for accessible nucleosome formation allowing transcription factor binding, and analyzed the solution structure of the nucleosome containing H2A.B by Small-Angle X-ray Scattering (SAXS).

### EXPERIMENTS:

Canonical H2A, H2A.B, and H2A<sup>H2A.B(103-115)</sup> nucleosomes were prepared by the salt dialysis method with recombinant histones and DNA, as described previously [2]. The reconstituted nucleosomes were purified by non-denaturing gel electrophoresis. SAXS analyses of these nucleosomes were performed with a NANOPIX instrument (RIGAKU) at the Institute of Radiation and Nuclear Science, Kyoto University [3]. In order to cover the wide  $q$ -range, we analyzed these nucleosomes with two sample-to-detector distance (1,330 mm for  $0.007 \text{ \AA}^{-1}$  to  $0.03 \text{ \AA}^{-1}$ , and 300 mm for  $0.03 \text{ \AA}^{-1}$  to  $0.8 \text{ \AA}^{-1}$ ) and then combined these data. We also performed the standard procedures of transmission correction, buffer solution of these nucleosomes scattering subtraction, and conversion to an absolute scale with water scattering.

### RESULTS:

We measured the SAXS curves of H2A, H2A.B, and H2A<sup>H2A.B(103-115)</sup> nucleosomes, and calculated the values of the radius of gyration ( $R_g$ ). We found that the  $R_g$  value of the H2A.B nucleosome was significantly larger than that of the canonical H2A nucleosome. This suggested that the H2A.B nucleosome is not compact as H2A nucleosome (Fig. 1). Interestingly, the  $R_g$  value of the

H2A<sup>H2A.B(103-115)</sup> nucleosome was also significantly larger than that of the canonical nucleosome. Therefore, the C-terminal region of H2A.B may play a role in forming apparently large conformation in solution (Fig. 2).

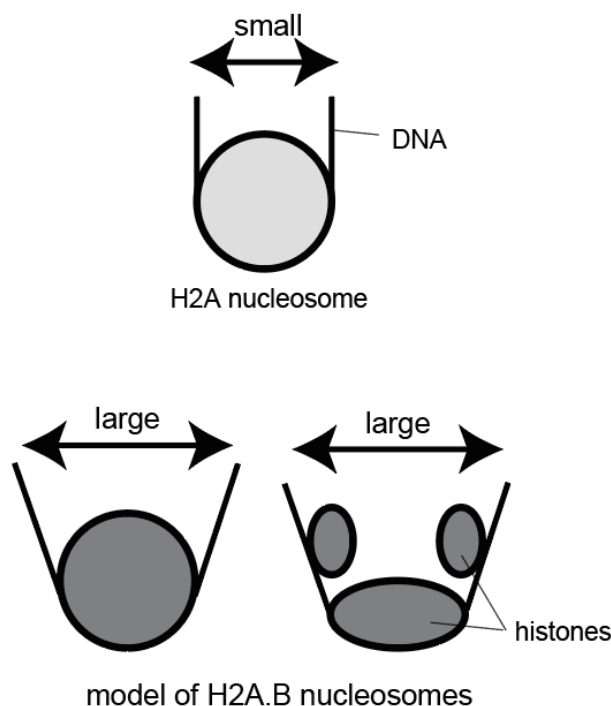


**Fig.1** The schematic representations of the conceivable relationship between the  $R_g$  value and the nucleosome structure in SAXS analysis.

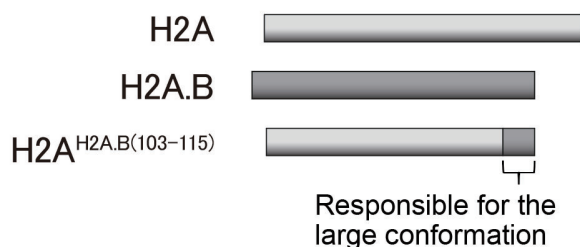


**Fig.2** Schematic representations of H2A, H2A.B, and H2A<sup>H2A.B(103-115)</sup>.

### REFERENCES:

- [1] M. Koyama and H. Kurumizaka, *J. Biochem.* **163** (2018) 85-95.
- [2] T. Kujirai *et al.*, *Methods Mol. Biol.* **1832** (2018) 3-20.
- [3] P. Bernadó *et al.*, *Biochim. Biophys. Acta. Gen. Subj.* **1862** (2018) 253-274.

## CO6-13 Effect of High-Intensity Pulsed Coherent Radiation on the Stability of the Gene

Y. Tanaka, S. Okuda and T. Takahashi<sup>1</sup>

Graduate School of Engineering, Osaka Prefecture University

<sup>1</sup>Institute for Integrated Radiation and Nuclear Science, Kyoto University

**INTRODUCTION:** The coherent transition radiation (CTR) from electron bunches of a linear accelerator (linac) has continuous spectra from a submillimeter to millimeter wavelength range corresponding to the terahertz (THz) frequency range. It is a picosecond pulsed light and hence, has extremely high peak-intensities compared with the other THz light sources. The light source system using the CTR from the electron beams of the 45 MeV L-band electron linac was established at Kyoto University Research Reactor Institute (KURRI) [1-3]. This CTR light source developed has been applied to absorption spectroscopy. Recently, the possibility of any nonlinear effects was found in the measurement of the absorption spectroscopy at KURRI.

However, biological effects of the radiation are unclear. The main purpose of the present work is the investigation of the biological effects of the high-intensity pulsed CTR using a gene of fruit fly, *Drosophila melanogaster*.

**EXPERIMENTAL METHOD:** The electron linac at KURRI was used in the experiments. In most experiments the beam energy, macropulse length and the repetition rate are 42 MeV, 47 ns and 60 Hz, respectively. The experimental configurations for the absorption spectroscopy are schematically described in our previous report [4] and the details of the methods for the measurements are described in ref. 2 and 3.

The detection method of effect on the stability of the gene was performed using the *mwh* (*multiple wing hair*) gene of *Drosophila melanogaster* as described in ref. 5. If the CTR have any effect on the gene, the mutation frequency rate will increase or decrease. The frequency is calculated as the small spot or large spot rates. The irradiation experiment was performed by packing the larvae in a container with glass, plastic cylinder and sponge, then the larvae were put in the path of the CTR, while the non-irradiated control larvae were put near the irradiated sample outside the path. Duration of irradiation was 2, 4 and 6 hrs. After irradiation the larvae were transferred into new culture vials.

### RESULTS AND DISCUSSION:

As shown in Fig.1, by irradiation of CTR for 2 and 4 hours, the small spot rate apparently increased compared with the non-irradiated control groups, while the large spot rate decreased compared with the non-irradiated control groups, however, this phenomenon seems to be within the variation because the large spot number was very scarce. By irradiation of CTR for 6 hours, both of small spot rate and large spot rate were similar with the non-irradiated control groups. Thus, irradiation of CTR for 2 and 4 hours could cause mutation or deletion of the wild-type *mwh* gene, or chromosomal disjunction.

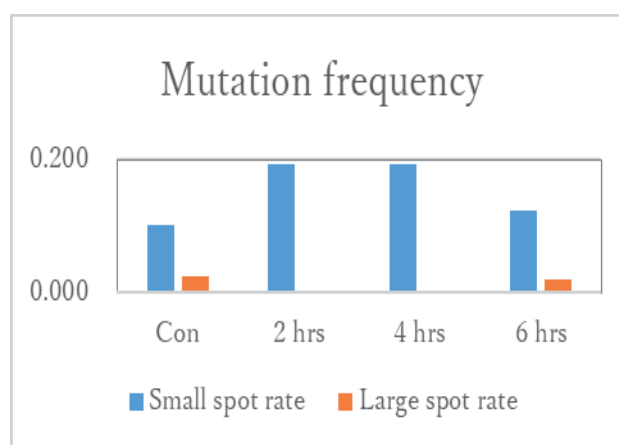


Fig. 1. Change of spot frequency by CTR (Terahertz wavelength). Spot frequency was calculated by small of large spot No./wing No.

### REFERENCES:

- [1] T. Takahashi *et al.*, Rev. Sci. Instrum., **69** (1998) 3770.
- [2] S. Okuda and T. Takahashi, Infrared Phys. Technol., **51** (2008) 410.
- [3] S. Okuda and T. Takahashi, J. Jpn. Soc. Infrared Science & Technology 25 (2016) 49 (in Japanese).
- [4] S. Okuda Y.Tanaka and T. Takahashi, KUR Progress Report 2018, (2019) CO6-17.
- [5] Y.Tanaka *et al.*, Eastern Medicine, 28 (2012) 21-35.

## CO6-14 Structural analysis of multi-domain protein as studied by complementary use of molecular dynamics simulation and small-angle X-ray scattering

R. Inoue, A. Okuda, M. Shimizu, K. Morishima, N. Sato, R. Urade, and M. Sugiyama

*Institute for Integrated Radiation and Nuclear Science, Kyoto University.*

### INTRODUCTION:

Under physiological condition, it is well recognized that most of proteins including multi-domain proteins are not fixed to certain configurations but rather dynamically fluctuating due to their internal dynamics [1]. The internal dynamics of protein are considered to be deeply related to the development of their functions, hence characterization of internal dynamics such as time constant and spatial scales are essential for revealing the mechanism of their intrinsic functions. The advantage of small-angle X-ray scattering (SAXS) measurement is that it can study the structure of protein under near physiological condition: solution state, hence the possible dynamics in it is essentially observable from this technique. Recently, molecular dynamics simulation (MD simulation) enables to identify the internal dynamics of protein. Therefore, the complementary use of SAXS and MD simulation would offer the better opportunity for identifying the possible internal dynamics of protein. As a first step of work, we firstly performed structural analysis of four-domain protein through the complementary use of SAXS and MD simulation.

### EXPERIMENTS:

The preparation and purification of four-domain protein should be referred to our future paper [2]. SAXS measurement was performed with NANOPIX (Rigaku Corporation, Japan). X-rays from a high-brilliance point-focused X-ray generator (MicroMAX-007HF, Rigaku, Tokyo, Japan) were focused with a confocal mirror (OptiSAXS) and collimated with a confocal multilayer mirror and two pinholes collimation system with the lower parasitic scattering, "ClearPinhole". The scattered X-rays were detected with a two-dimensional semiconductor detector (HyPix-6000, Rigaku, Tokyo, Japan). The sample-to-detector distance and wavelength of X-ray used for present work was 1320 mm and 1.542 Å, respectively. For removal of unfavorable aggregates from the sample solution, the laboratory-based SEC-SAXS System (LA-SSS) was employed to measure the SAXS profile in the  $Q$  range ( $0.01 \text{ \AA}^{-1}$ – $0.2 \text{ \AA}^{-1}$ ) [3]. As for MD simulation, we performed both all-atom and coarse-grained MD simulation. All the measurement and calculations were performed at 25 °C.

**RESULTS:** Figure 1 shows the SAXS of four-domain protein. Firstly, we compared the SAXS profile calculated from the snapshot of All-atom MD simulation to experimentally observed SAXS profile. The calculated SAXS profile could not reproduce the SAXS profile

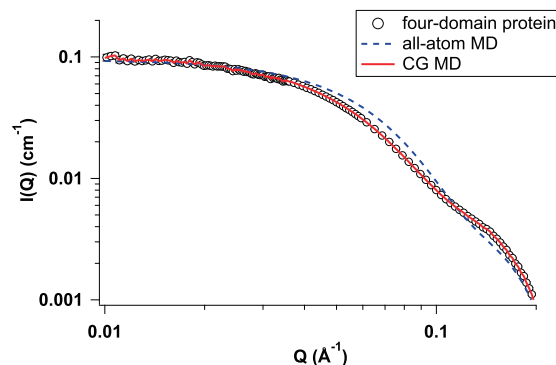


Fig. 1. SAXS profile of four-domain protein (circle). The dotted and continuous lines correspond to the calculated SAXS profile from the snapshot from all-atom MD and CG MD simulation, respectively.

adequately. We also calculated the SAXS profiles from several snapshots from all-atom MD simulation, however all the extracted snapshots could not reproduce the SAXS profile especially at the  $Q$  region lower than  $0.10 \text{ \AA}^{-1}$ . It is expected that present all-atom MD simulation could not sample the possible configurations of four-domain protein within MD simulation time. Performing the longer time all-atom MD simulation is one of the solutions for improving the sample efficiency, however it will also increase the computational cost as well. In order to overcome such situation, we also performed coarse-grained MD (CG-MD) simulation. The advantage of CG-MD simulation is the increase of sampling efficiency due to coarse-graining an amino acid residue as a sphere. A snapshot was extracted from the trajectory of CG-MD simulation and the corresponding SAXS was calculated based on it. The calculated SAXS profile from CG-MD simulation is also included in Fig. 1. Compared to the result of calculation with all-atom MD simulation, the CG-MD derived SAXS profile could reproduce the SAXS results nicely, implying the high sampling efficiency with CG-MD calculation.

At present, we are trying to analyze the trajectory from CG-MD calculation to figure out the internal dynamics of this four-domain protein. It is expected that the complementary use of MD simulation and SAXS measurements will contribute to identify the functionally relevant internal dynamics of multi-domain protein.

### REFERENCES:

- [1] J. A. McCammon, and S. C. Harvey, Dynamics of Proteins and Nucleic Acids., (Cambridge University Press, 1987).
- [2] A. Okuda *et al.*, *in preparation*.
- [3] R. Inoue *et al.*, *Sci. Rep.*, **9** 12610 (2019).

M. Yohda, M. Nakamura, K. Morishima<sup>1</sup>, R. Inoue<sup>1</sup>, M. Sugiyama<sup>1</sup>

Department of Biotechnology and Life Science, Tokyo University of Agriculture and Technology  
<sup>1</sup>Institute for Integrated Radiation and Nuclear Science, Kyoto University

**INTRODUCTION:** Small heat shock protein (sHsp) is a ubiquitous molecular chaperone with a relatively small molecular weight. The characteristic feature of sHsp is the  $\alpha$ -crystallin domain, which is named after the  $\alpha$ -crystallin in vertebrate lenses. Among mammalian sHsps, HspB1, also known as Hsp27, is the most ubiquitous one. Previously, we reported the structure and function of HspB1 from Chinese hamster (*Cricetulus griseus*) ovary cells (CgHspB1). SEC-MALS and SAXS analyses suggested the 16mer structure of CgHspB1 [1]. However, there exist several contradicting reports on the oligomeric structures of HspB1[2, 3]. HspB1 may take various oligomeric conformations. In this study, we analyzed the oligomeric structure of CgHspB1 by analytical ultracentrifuge (AUC). In addition, we examined the effect of the deletion of the C-terminal region and the N-terminal region.

**EXPERIMENTS:** CgHspB1 variants (WT, Wild type; S15D, phosphorylation mimic mutant; DelN, N-terminal deletion mutant; DelC, C-terminal deletion mutant) were expressed in *E. coli* and purified by anion exchange chromatography and size-exclusion chromatography. To suppress nonspecific hydrophobic interaction, size exclusion chromatography was carried out using a buffer containing 20% ethylene glycol. The oligomeric conformation of CgHspB1 variants were investigated by size exclusion chromatography on HPLC (SEC), electron microscopy, and analytical ultracentrifugation (AUC).

**RESULTS:** We speculated that the previous observations of various oligomeric conformations should be due to the nonspecific interaction by the hydrophobic surface of sHsp. Thus, we purified CgHspB1 variants by gel filtration chromatography using the buffer containing 20% ethylene glycol (Fig. 1). The purified WT and S15D exist as large oligomers and dissociate to small oligomers at the elevated temperature in SEC. DelN appeared as small oligomers without any temperature-dependent change. Curiously, DelN was digested into two fragments by protease. DelC appeared as various conformations. Then, WT and S15D were examined by AUC using a buffer containing 20% ethylene glycol. At 4°C, WT appeared as a single peak of 18mer (Fig. 2). The sedimentation coefficient increased as the elevation of temperature. At 40°C, it seemed to form 30mer. The conformation change is reversible. It changed to the original conformation by lowering the temperature. In addition, small oligomers of about 6mer and 12mer were also observed. Almost the same results were observed in S15D.

Based on these observations, we propose the following conformational change model. The structural unit of CgHspB1 is 6mer. In the inactivated condition, it assembles to 18mer. At the elevated temperature, they dissociate and reassemble to the activated conformations of 24mer or 30mer. They return to 18mer by lowering the temperatures. The N-terminal region is responsible for the assembly of 6mers, and the role of the C-terminal region is the stabilization of oligomeric structures.

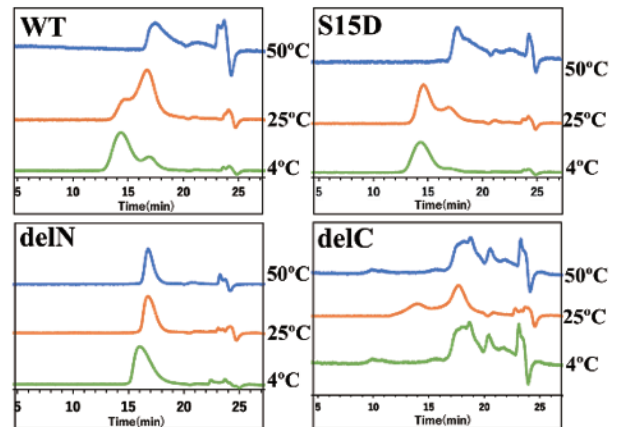


Fig.1 SEC analyses of CgHspB1 variants

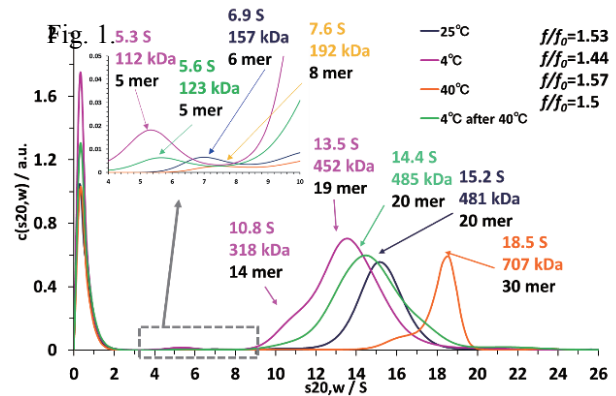


Fig. 2 AUC analyses of CgHspB1 WT

#### REFERENCES:

- [1] E. Sha *et al.*, FEBS Open Bio., **9** (2019) 1826-1834.
- [2] J. Behlke *et al.*, FEBS Lett., **288** (1991) 119-122.
- [3] B. Lelj-Garolla *et al.*, J. Mol. Biol., **345** (2005) 631-642.

K. Ono<sup>1</sup>, T. Aihara<sup>1</sup>, H. Tanaka<sup>2</sup>, Y. Tamari<sup>2</sup>, T. Watanabe<sup>2</sup>, S. Suzuki<sup>2</sup>, S. Masunaga<sup>2</sup>

<sup>1</sup>Kansai BNCT Medical Center, Osaka Medical College

<sup>2</sup>Institute for Integrated Radiation and Nuclear Science,, Kyoto University

**INTRODUCTION:** Tumor tissue consists of tumor cells and stroma, especially the vasculature that supplies the cells with oxygen and nutrients. The antitumor effect in BNCT is almost specific to cells accumulating boron compounds. In this study, we compare the effect of this tumor cell-specific BNCT with the effect of X-rays that has no tumor cell specificity, and quantitatively elucidate the effect of damage caused in the vascular system on the overall antitumor effect. This is the purpose of this research.

In fiscal 2019, prior to research on tumors, we conducted an experiment to confirm the effect of BNCR on normal tissue cells. This article reports the experimental results.

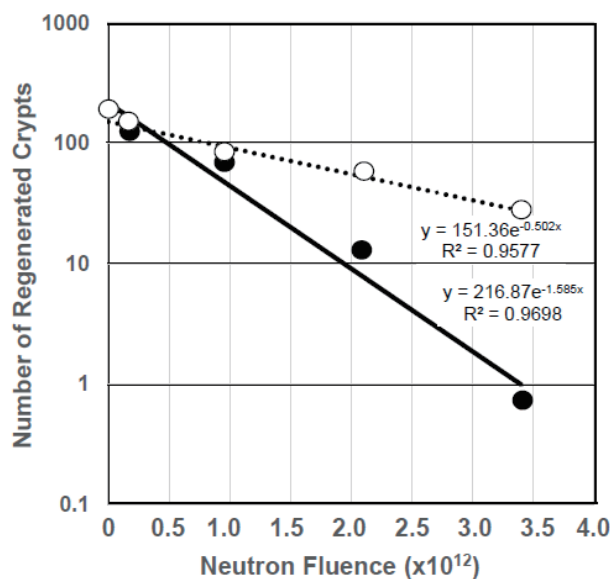
**EXPERIMENTS: Mice and Irradiation of X-rays or neutron.** 8-week-old C3H/He mice were prepared. The abdomen was irradiated with 10 Gy of photons 12 hours prior to the BPA-neutron irradiation. The rest of the abdomen was shielded with a lead plate. Two and half hours before neutron irradiation, <sup>10</sup>B-BPA in the form of a fructose complex (300 mg/kg body weight in terms of BPA) was subcutaneously administered to the mouse. The blood boron concentration at the time of irradiation was 15.2 ppm. The irradiation dose to the mouse was changed by changing the distance from the neutron beam exit hole in four steps, so that a single irradiation (30 minutes) gave four different doses. The control group of neutron irradiation alone was similarly irradiated. The highest neutron flux was  $1.88 \times 10^9 / \text{cm}^2 \text{s}$ . The flux was determined by the amount of activity induced in the gold foil.

**Evaluation of radiation responsiveness using regeneration of intestinal crypt cells.** Three and half days after neutron irradiation, a 10 cm long intestine was excised from the same predetermined site in the jejunum, and 3 specimens were cut out. After fixing with 10% formalin, histopathology microslide with HE staining was prepared, and the number of crypts in which regeneration was observed on the inner circumference of the intestinal wall was counted under a microscope.

**Radiation sensitivity analysis.** The relationship between the number of crypts in which regeneration was recognized and the neutron fluence was plotted in a semilogarithmic plot, and the slopes of the curves of the neutron alone group and the BPA-neutron group were compared. Since the doses of neutrons themselves and the amount of gamma rays accompanying them are equal at the same irradiation position, the difference in the slope is derived

from the neutron reaction with BPA boron. The neutron fluence  $\phi_0$  similar to the dose  $D_0$  was obtained, and the difference in  $\phi_0$  was converted into the dose due to the reaction of BPA boron and neutrons, and the  $D_0$  at the boron-neutron reaction dose of BPA was obtained. Here, it was assumed that the concentration of boron in the crypt cells was equal to the concentration of boron in blood.

**RESULTS and DISCUSSION:** The results are shown in the figure. As can be seen in the figure, the  $\phi_0$  of the BPA-neutron irradiation group (closed circle), that is, the neutron fluence required to reduce the number of crypts by  $e^{-1}$ , is  $0.925 \times 10^{12} / \text{cm}^2$ . The  $D_0$  calculated from this fluence value and the boron concentration of 15.2 ppm was 1.04 Gy. Data on such intestinal crypt susceptibility have not been reported yet, but are unexpectedly large. Incidentally, the  $D_0$  of gamma rays is about 1.3 Gy. It is very interesting to see how the values obtained this time agree with the estimated value by N/C ratio of the cell (Ono's equation). However, this requires to know boron concentration in the crypt cell, and it is a future research topic. I believe that the high-precision  $\alpha$ -autoradiography developed by Ono and Tanaka will be useful for that purpose.



Closed circle: BPA+Neutron, Open circle: Neutron alone

### REFERENCES:

- [1] Eric J. Hall & Amato J. Giaccia, in Radiobiology for the Radiologist, 7<sup>th</sup> ed., 2012 by LIPPINCOTT WILLIAMS & WILKINS, a WOLTERS KLUWER.
- [2] K. Ono, *et al.*, Journal of Radiation Research, Vol. 60, No. 1, 2019, pp. 29–36.
- [3] K. Ono, *et al.*, Applied Radiation and Isotope Vol. 161, 2020, 109159.

U. Matsushima, N. Kubota, D. Ito<sup>1</sup>, Y. Saito<sup>1</sup> and H. Shono<sup>1</sup>

Faculty of Agriculture, Iwate University

<sup>1</sup>Institute for Integrated Radiation and Nuclear Science, Kyoto University

**INTRODUCTION:** Graft-incompatibility is known to increase hydraulic resistance at the grafted joint. Large hydraulic resistance at the grafted joint due to graft-incompatibility is expected to produce sweet tomato fruits by limiting water uptake. However, Such graft-incompatibility may cause plant death [1]. It is important to know how much water uptake can be limited by graft-incompatibility. We observed water uptake in alternate grafting of tomato and eggplant by using neutron imaging and deuterium oxide (D<sub>2</sub>O) as tracer.

**MATERIALS and METHODS:** 4 kinds of grafted samples, including tomato grafted onto eggplant rootstock (T/E) and tomato rootstock (T/T), and eggplant grafted onto tomato rootstock (E/T) and eggplant rootstock (E/E) were prepared. Tomato (TO) and eggplant (EO) without grafts were prepared as control plants. The tomato and eggplant seedlings were grafted on the 23th of August 2019, after 29 and 30 days from sowing, respectively. Control samples were selected from the seedlings that were sown at the same time with seedlings for grafted plants. Four days after grafting, the samples were transplanted into glass tubes filled with glass beads in order to deliver quick D<sub>2</sub>O supply. We performed neutron imaging at the E2 hole of Kyoto University Reactor (KUR) from the 3rd to the 5th of September. After removing water from the glass tube using a syringe, D<sub>2</sub>O was injected into the glass tube. Immediately after the injection, interval neutron imaging was started. The exposure and interval times were 300 s and 360 s, respectively.

**RESULTS:** The neutron cross section of D<sub>2</sub>O is much lower than that of water. On another note, chemical characteristics of D<sub>2</sub>O is similar to water. Therefore, plant can uptake D<sub>2</sub>O through the root system. In the presence of D<sub>2</sub>O, neutron attenuation first decreased from the shoot part near the roots then toward the upper shoot part. The plant neutron image became brighter by increasing the D<sub>2</sub>O content in it. Therefore, increasing the D<sub>2</sub>O content in plant shoots can cause changes in neutron attenuation, which can be calculating by neutron imaging. The amount of change in the neutron attenuation coefficient is calculated as the difference in initial attenuation coefficient ( $\mu$ ) and that of at a certain time point ( $\mu'$ ). Changes in the neutron transmission coefficient is calculated using following equation:

$$\mu - \mu' = \frac{1}{x} \ln \frac{I'}{I}$$

The distance of neutron transmission  $x$  is equal to plant shoot diameter in this case. The initial neutron intensity  $I$  and that of at the certain time point  $I'$  are pixel value of those of the neutron images, respectively.

As a region of interest (ROI), we observed changes in the neutron attenuation coefficient with a plant shoot length of 5 mm near the roots. However, Plant transpiration indicated by D<sub>2</sub>O uptake is highly influenced by plant size. Therefore, the changes in the neutron attenuation coefficient were compared by per dry mass ( $M_{dry}$ ) of the samples. Figure 1 shows the history of the amount of the change in the neutron attenuation coefficient,  $(\mu - \mu')/M_{dry}$ . Significance

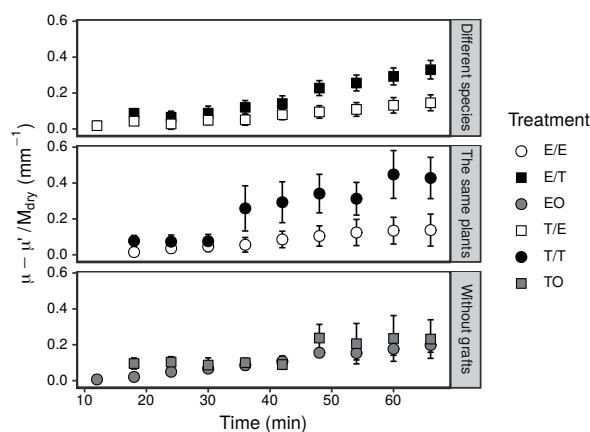


**Fig. 1.** History of the amount of change in the neutron attenuation coefficient,  $(\mu - \mu')/M_{dry}$ . Rows in matrix of the graphs were divided by 3 groups, namely grafted with different species, grafted with the same plants, and without grafts.

tests were performed using the Tukey HSD test ( $n = 3$ ). There was no significant difference between the six groups. The tomato and eggplant without grafts showed the same changes in neutron attenuation. The uptake of D<sub>2</sub>O might be similar among tomato and eggplant when without grafts. On another note, samples that were grafted with the same plants variedly changed. It means that the wounds produced by grafting strongly influenced sample growth for those that were grafted with the same plants (T/T and E/E). Interestingly, the eggplant grafted on the tomato rootstock (E/T) showed the second highest change in neutron attenuation. In previous studies, eggplant grafted on tomato rootstock produced larger roots [1]. The large tomato roots of the E/T sample supposedly contributed to the increased D<sub>2</sub>O uptake.

#### REFERENCES:

- [1] M. Oda *et al.*, J. Japan. Soc. Hort. Sci., **74**(6), 458-463 (2005).

S. Sekimoto, T. Ohtsuki

*Institute for Integrated Radiation and Nuclear Science,  
Kyoto University*

**INTRODUCTION:** A shortage in the supply of  $^{99}\text{Mo}$  resulting from the shutdown of reactors used for its production is a global problem. Because  $^{99}\text{Mo}$  is an indispensable source of  $^{99\text{m}}\text{Tc}$ , which is used in nuclear medicine to make diagnoses using techniques such as scintigraphy and single photon emission computed tomography (SPECT), a stable supply of  $^{99}\text{Mo}$  is vital. Therefore, production of  $^{99}\text{Mo}$  by using neutrons or protons generated in accelerators has been investigated [1–3]. To separate  $^{99\text{m}}\text{Tc}$  from  $^{99}\text{Mo}$  produced by an accelerator, methods based on sublimation, solvent extraction, and ion-exchange column chromatography have been examined and developed [2,4–6]. In addition, Gopalakrishna et al. have reported the preparation of  $^{99}\text{Mo}$  by the  $^{100}\text{Mo}(\gamma, n)$  reaction using bremsstrahlung photons [6], followed by conventional solvent extraction using methyl ethyl ketone (MEK) and zirconium (Zr) molybdate gel to separate  $^{99\text{m}}\text{Tc}$ . According to the regulations of the Japanese pharmacopeia, the extraction using organic materials and the gel method using heavy metal elements such as Zr are not approved for the  $^{99\text{m}}\text{Tc}$ -separation methods. Additionally, it is also difficult and impractical to use the sublimation method, which requires complicated and/or large scale devices for the mass-production of pure  $^{99\text{m}}\text{Tc}$ . Recently, Kaken Inc. developed a new method, known as the “technetium master milker” (TcMM). This technique can produce highly pure  $^{99\text{m}}\text{Tc}$  at a maximum activity of  $1.85 \times 10^{13}$  Bq (500 Ci) per batch from  $^{99}\text{Mo}$  of low specific activity [7]. We carried out the production of  $^{99}\text{Mo}$  by the  $^{100}\text{Mo}(\gamma, n)$  reaction using bremsstrahlung photons generated in an electron linear accelerator (LINAC), a technique that has not been investigated significantly in Japan. The amounts of  $^{99}\text{Mo}$  produced at several electron energies ( $E_e$ ) were examined. To separate  $^{99\text{m}}\text{Tc}$  from the irradiated target, in this work, the TcMM was applied to the  $^{99}\text{Mo}$  produced by LINAC, and the subsequent yield of  $^{99\text{m}}\text{Tc}$  was evaluated.

**EXPERIMENTS:** The TcMM applied to the irradiated  $^{99}\text{Mo}$  pellets was essentially the same as that reported by Tatenuma et al. [7]

**RESULTS:** The results of the TcMM applied to the  $^{99}\text{Mo}$  pellets irradiated with bremsstrahlung photons are shown in Table 1. The activities of  $^{99}\text{Mo}$  and  $^{99\text{m}}\text{Tc}$  in the  $^{99}\text{Mo}$  solution prepared in the first step of the TcMM and the solution obtained from the final step of TcMM, and the chemical yield of  $^{99\text{m}}\text{Tc}$  are presented in Table 1. The table header ‘Run No.’ 10-1 and 15-1 indicate the results for the solutions containing dissolved  $^{99}\text{Mo}$  pellets irradiated with bremsstrahlung photons of  $E_e$ 's of 25 and 30 MeV, respectively. In contrast, ‘Run No.’ 10-2 and 15-2 are the results for the solution where transient equilibrium has been reached between  $^{99}\text{Mo}$  and  $^{99\text{m}}\text{Tc}$  after the initial milking of  $^{99\text{m}}\text{Tc}$  in the 10-1 and 15-1 solutions. The chemical yield of  $^{99\text{m}}\text{Tc}$  ranged between 83 to 99% over the four runs of the TcMM. In particular, the activity of  $^{99}\text{Mo}$  in the solution collected by the TcMM was low, being below the detection limit of  $\gamma$ -ray spectrometry. This can also be confirmed by examining the  $\gamma$ -ray spectra of the  $^{99}\text{Mo}$  solution before the TcMM and the solution collected by the TcMM. Those spectra were reported in ref. [8].

#### REFERENCES:

- [1] Y. Nagai *et al.*, J. Phys. Soc. Jpn., **82** (2013) 064201.
- [2] Y. Nagai *et al.*, J. Phys. Soc. Jpn., **83** (2014) 08320.
- [3] K. Nakai *et al.*, Proc. Jpn. Acad. Ser. **B 90** (2014) 413–421.
- [4] M. Kawabata *et al.*, J. Phys. Soc. Jpn., **84** (2015) 023201.
- [5] K. Mang'era *et al.*, J. Radioanal. Nucl. Chem., **305** (2015) 79-85.
- [6] A. Gopalakrishna *et al.*, J. Radioanal. Nucl. Chem., **308** (2016) 431-438.
- [7] K. Tatenuma *et al.*, Radioisotopes **63** (2014) 501-513.
- [8] S. Sekimoto *et al.*, J. Radioanal. Nucl. Chem., **311** (2017) 1361-1366.

Table 1. Yield of  $^{99\text{m}}\text{Tc}$  from bremsstrahlung photon-irradiated  $^{99}\text{Mo}$  by TcMM process.  
(<sup>a</sup> Second crop, <sup>b</sup> End of bombardment, <sup>c</sup> Detection limit)

Run No.	Weight of $^{99}\text{Mo}$ & $E_e$	Elapsed time from EOB <sup>b</sup> (h)	Activity in $^{99}\text{Mo}$ solution (Bq)		Activity in solution collected by TcMM process (Bq)		Yield of $^{99\text{m}}\text{Tc}$ (%)
			$^{99}\text{Mo}$	$^{99\text{m}}\text{Tc}$	$^{99}\text{Mo}$	$^{99\text{m}}\text{Tc}$	
10-1	0.97 g,	213.2	4.91E+04	5.40E+04	<DL <sup>c</sup>	5.05E+04	93.5
10-2 <sup>a</sup>	25 MeV	237.3	3.74E+04	3.98E+04	<DL <sup>c</sup>	3.33E+04	83.7
15-1	0.96 g,	215.3	1.15E+05	1.26E+05	<DL <sup>c</sup>	1.19E+05	94.2
15-2 <sup>a</sup>	30 MeV	239.2	5.20E+04	8.48E+04	<DL <sup>c</sup>	8.33E+04	98.3

## CO6-19 N-Acetylneuraminic acid functioned as the scavenger for reactive oxygen species generated by the gamma-ray irradiation

N. Fujii<sup>1</sup>, S. Kishimoto<sup>1</sup> and T. Takata<sup>2</sup>

<sup>1</sup> Radioisotope Research Center, Teikyo University

<sup>2</sup> Institute for Integrated Radiation and Nuclear Science, Kyoto University

### INTRODUCTION:

N-Acetylneuraminic acid (Neu5Ac) is a sialic acid, which occurs in mammals, certain mollusks, and some microorganisms, and is found a capping sugar in the oligosaccharide chains of glycoproteins and glycolipids [1]. Most studies on glycanic Neu5Ac have focused primarily on cell protection, fertilization, immunology, inflammation and tumors [2-4]. Free Neu5Ac molecules is oxidized by H<sub>2</sub>O<sub>2</sub> to provide its decarboxy product, 4-(acetylamino)-2,4-dideoxy-D-glycero-D-galacto-octonic acid (ADOA) [5]. Therefore, monomeric Neu5Ac is the potent defense molecule against oxidative damage.

Ionizing radiation decomposes water and generates free radicals and reactive oxygen species. Then we expected the monomeric Neu5Ac might be scavenged the reactive oxygen species generated the ionizing radiation. In this study, we developed the method to quantitate the potential scavenging reaction of Neu5Ac for gamma-ray irradiation. In order to test our methods, we irradiated Neu5Ac solution with gamma-ray, then quantitated product (ADOA) by liquid chromatography–tandem mass spectrometry (LC-MS/MS) using by our developed method.

### EXPERIMENTS:

**Material** Nu5Ac was dissolved in water, and the pH of the solution was adjusted to 7.0 with sodium hydroxide.

**Gamma-irradiation** Gamma-irradiation was carried out at the Co-60 Gamma-ray Irradiation Facility of the Kyoto University Institute for Integrated Radiation and Nuclear Science. Nu5Ac aqueous solution were irradiated with gamma ray at a dose rate of 943 Gy/h.

**Quantitation of ADOA** The quantitative analysis of ADOA was used by LC-MS/MS. The high performance liquid chromatography was used a U3000HPLC system (Thermo Fisher scientific). The column was CAPCELL CORE PC (OSAKA SODA, 2.7 μm, 2.1 mm I.D.×100 mm). A sample were eluted with a flow rate of 0.2 mL/min and an isocratic mode with mobile phase (75% acetonitrile, 25% water, 10 mM ammonium formate, pH 3.5). The mass spectrometer was used Q Exactive (Thermo Fisher scientific). ADOA was measured by parallel reaction monitoring (PRM) in the positive ion mode, using transitions m/z 282.11 → m/z 186.07

### RESULTS:

To quantitatively investigate the amount of ADOA,

PRM method was set the optimal for commercial standard. Then, the method was used for Neu5Ac aqueous solution after gamma-ray irradiation.

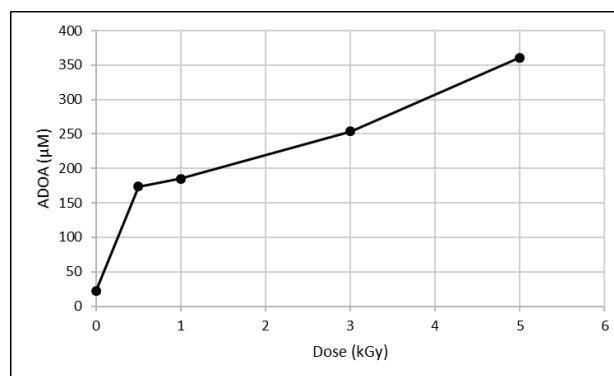


Fig. 1. Production of ADOA from Neu5Ac by irradiation with gamma-ray

Fig. 1 show the production of ADOA from 100mM Neu5Ac aqueous solution irradiated with gamma-ray at doses of 0, 0.5, 1, 3 and 5 kGy. As the radiation dose was increased, the production of ADOA increased. The 1 kGy gamma-ray irradiation for 100 mM Neu5Ac solution increased the ADOA amount to 184 μM (Fig. 1), suggested the yields of ADOA from Nu5Ac was 0.184 %. On the other hand, in 10 mM Neu5Ac solution, the yields of ADOA from 1kGy gamma-ray irradiation was 1.34 % (data not shown). The lower concentration of substrate, the higher yields of ADOA, suggested that gamma-ray promotes reaction from Neu5Ac to ADOA via formation of reactive oxygen species (H<sub>2</sub>O<sub>2</sub>) in solvent (indirect action).

Those results suggested monomeric Neu5Ac as scavenger for reactive oxygen species generated by the gamma-ray irradiation.

### REFERENCES:

- [1] R. Schauer R., *Zoology*, **107** (2004) 49-64
- [2] T. Angata *et al.*, *Chem. Rev.* **102** (2002) 439-469
- [3] R. P. Crocker, *Curr. Opin. Struct. Biol.* **12** (2002) 609-615
- [4] K. Takayama *et al.*, *Proc. Natl. Acad. Sci. USA* **93** (1996) 10662-10667
- [5] R. Iijima *et al.*, *FEBS Lett.* **561** (2004) 163-166

## CO6-20 Preliminary analysis of structural composition of menaquinone-7 produced by *Bacillus subtilis natto*

T. Chatake, Y. Yanagisawa<sup>1</sup>, A. Okuda, K. Morishima, R. Inoue, M. Sugiyama

*Institute for Integrated Radiation and Nuclear Science, Kyoto University*

<sup>1</sup>*Faculty of Pharmaceutical Science, Chiba Institute of Science*

**INTRODUCTION:** Natto is a Japanese traditional fermented food, which is made of soybeans. It attracts a great attention from the point of view of nutrition, because it contains various kinds of physiologically active substances. In particular, menaquinone-7, which is a kind of vitamin K<sub>2</sub>, is abundantly contained in natto [1]. In Japan, young women intake 99% of menaquinone-7 from pulses including *natto*, and the pulse food is the main source of vitamin K (45.1%) for the *natto* eater of the young Japanese women [2]. Menaquinone-7 produced by *Bacillus subtilis natto* (*natto*-MK-7) has a remarkable physiochemical property. All types of vitamin K are water-insoluble compounds. Meanwhile, *natto*-MK-7 is a water-soluble macromolecular complex, of which molecular weight is estimated to be 80~100 kDa by size-exclusion chromatography [3,4]. This property has an advantage on application of food/medical uses: pharmaceutical preparation, supplements, and food manufacture. Previously, Ikeda and Doi reported that the complex is composed of ~3kDa glycopeptides named K-binding factor (KBF) [3]. Our recent study of highly purified *natto*-MK-7 indicated an additional component with the molecular weight of ~11 kDa [5]. However, the detail information about the structural components of *natto*-MK7 is still unknown. In the present study, mass spectroscopy of *natto*-MK7 has been succeeded. Here, our new finding is shown.

**EXPERIMENTS:** *Natto*-MK-7 was produced and purified as previously reported [5]. *Bacillus subtilis natto miyagino* was incubated in liquid medium containing 2% hipolypepton-S, 3% glycerol, and 0.5% methionine. After cultivation at 42 °C with shaking at 100 rpm for 7 days, liquid medium was concentrated before purification. The purification was carried out by fast protein liquid chromatography. Four times of weak anion-exchange chromatography using DEAE sepharose FF were carried out with a gradient from 0.3 M to 1.0 M NaCl in 20 mM Tris-HCl buffer (pH 7.6). The final step of the purification was size-exclusion chromatography using GE HiPrep 16/60 Sephacryl S-300HR in 20 mM Tris-HCl buffer (pH 7.6) and 0.1 M NaCl. Mass spectroscopy was measured by MALDI-TOF/MS (microflexLT).

**RESULTS:** As shown in Fig. 1, mass spectra of *natto*-MK-7 could be observed for the first time. Strong peaks with  $m/z < 600$  are derived from the matrix used for TOF/MS. Significant peaks could not be observed at  $m/z > 10,000$ , indicating that the whole structure of *natto*-

*to*-MK-7, of which molecular weight was presumed to be 80~100 kDa, was not observed. A peak with  $m/z = 656$  corresponds to menaquinone-7 (MW~650). Most significant peaks were around  $m/z = 1050$ , implying that KBF is smaller than 3kDa, of which value was estimate by SDS-PAGE. In addition, the plural number of the peaks suggests the variation of the amino acid sequences of KBF.

It is just the first data of mass spectroscopy of *natto*-MK-7. The further experiments are under planning.

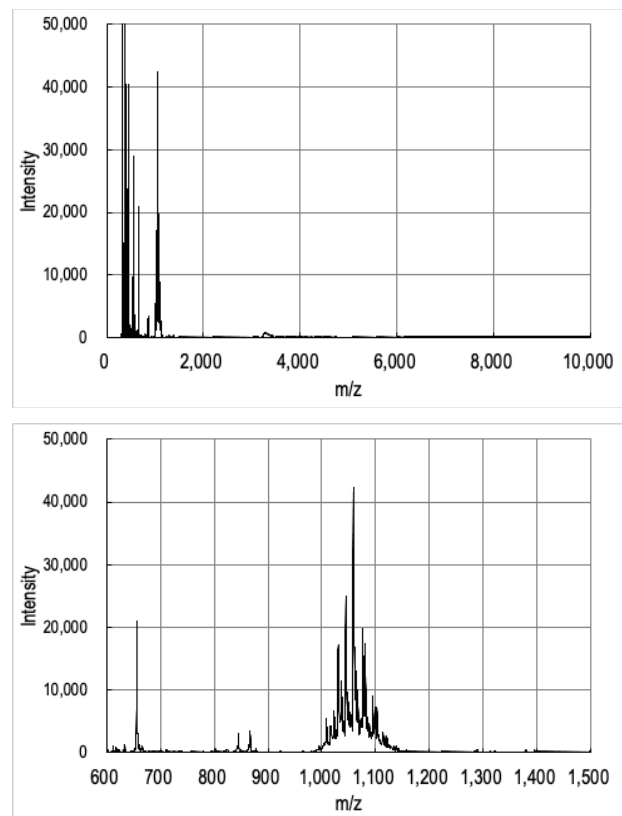


Fig. 1. The results of mass spectroscopy of *natto*-MK-7 in the ranges of 0~10,000 Da (upper) and 600~1,500 Da (lower).

### REFERENCES:

- [1] D.H. Bishop, K.P. Pandya, H.K. King, *Biochem. J.* **83**, 606-614 (1962).
- [2] M. Kamao *et al.*, *J. Nutr. Sci. Vitaminol (Tokyo)* **53**, 464-470 (2007).
- [3] H. Ikeda, Y. Doi, *Eur. J. Biochem.* **192**, 219-224 (1990).
- [4] Y. Yanagisawa, H. Sumi, *J. Food Biochem.* **29**, 267-277 (2005).
- [5] T. Chatake *et al.*, Y. Yanagisawa, R. Inoue, M. Sugiyama, T. Matsuo, S. Fujiwara, *J. Food Biochem.* e12630(6) 1-7 (2018).

## CO6-21 Measurement of Absorption Spectra of a Human Calcified Aorta Tissue in the Sub-Terahertz Region, which Depended on the Thickness (III)

N. Miyoshi and T. Takahashi<sup>1</sup>

Department of Molecular Chemistry, Kyoto Institute of Technology

<sup>1</sup>Institute for Integrated Radiation and Nuclear Science, Kyoto University

**INTRODUCTION:** The LINAC (Electron linear accelerator) technology in the millimeter- and terahertz-waves had been unique and had been used as a coherent synchrotron light source in the Institute for Integrated Radiation and Nuclear Science of Kyoto university (KURNS) to observe the transmittance spectra of a human calcified aorta tissue as a collaborate study. The absorption spectra in the sub-terahertz region had been not so clear for the raw tumor tissue although Ashworth-PC. *et al.* [1] had reported for the excised human breast cancer by a terahertz pulsed spectroscopy observed at 320 GHz, which was estimated a longer relaxation time component of the induced electricity for water molecules [2-3] in the raw tumor tissue for three years at the linear analysis.

We had started to measure of new biological sample of a calcified human aorta dried tissue sampling from the pathological autopsy in the last year. Furthermore, the getting spectral information was estimated with the SEM-EDX elements images of the calcified aorta tissue with a biological meaning in this year. It was reported the relation of the biological information between both of the element images and sub-THz spectral components in this report.

**EXPERIMENTS: (1) Instrument of Near-field in Terahertz Region:** The photograph of the instrument was shown in Fig. 1. Mark-A: Pre-probe Wiston cone; 50-10mm diameter, Length=60mm; the irradiate diameter=0.775mm; Mark-B: The concentrate light probe (diameter=3mm). The instrument was developed by Dr. T. Takahashi [4] for the transmittance measurements.

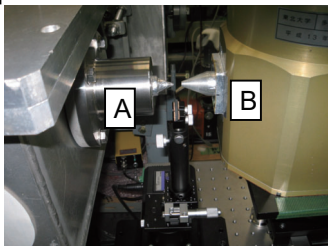


Fig. 1. The near field area of sample holder position.

**(2) Measurement of the Thickness of Sample:**

The thickness on the three points was measured by a laser

spot type (CL-P030, Keyence, Osaka, Japan).

**RESULTS and DISCUSSION: (1)** The thickness of samples on the three points were measured as shown in Fig. 2. A (calcified deposition) =0.0929, B (cholesterol deposition) =0.837, C (protein deposition) =0.379 mm, respectively.

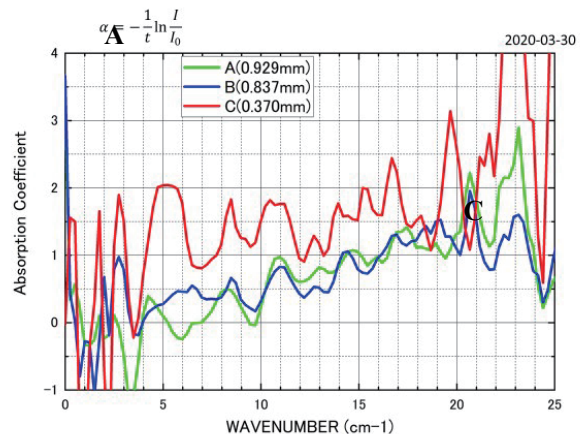


Fig. 2. The absorption spectra at 3 points (A: calcified point), the (B: cholesterol deposition, C: protein deposition) of a human aorta blood vessel wall, respectively.

**(2)** The absorption spectra of the sample tissue for each points A, B and C were measured according the different thickness points as shown in Fig. 2, which might be changing the refraction to dependent on the thickness values. It was different from the last reported spectra a little.

In the results, the absorbance of the dried tissue at 248 and 522 GHz were observed in the calcified area (included of CaPO<sub>4</sub> components from the data of SEM-EDX analysis of calcified aorta tissue), and the absorption peaks of 330, 620 GHz were observed in the cholesterol adhesion area. In the both areas, it was observed the absorption peaks at 500 and 659 GHz also.

In this report, it can report of more detail analysis combined with the thickness information data of the dried tissue by an laser measurement technology.

### REFERENCES:

- [1] Phillip C. Ashworth *et al.*, Optics Express, **17** (2009) 12444-12454.
- [2] Toshiko Fukasawa, *et al.*, Phys. Rev. Lett., **95** (2005) 197802.
- [3] Hiroyuki Yada, *et al.*, Chem. Phys. Lett., **464** (2007) 166-170.
- [4] T. Takahashi, *et al.*, J. Phys.: Conf. Ser. **359** (2012) 012016-1-4.

T. Watanabe, H. Tanaka, T. Takata, Y. Sakurai and M. Suzuki

*Integrated Radiation and Nuclear Science, Kyoto University*

**INTRODUCTION:** Boron neutron capture therapy (BNCT) is a two-step binary therapy. First, the patient is injected with a tumor-localizing drug containing boron-10 ( $^{10}\text{B}$ ), which has a high propensity to capture thermal neutrons. In the second step, the patient is irradiated with epithermal neutrons. After capture reaction, high-energy alpha particles and  $^7\text{Li}$  particles are emitted with short pathlength (less than  $10\mu\text{m}$ ). When a boron drug is concentrated in the tumor tissue, BNCT becomes cellular-based tumor selective radiation therapy [1].

Preclinical and clinical data show that radiotherapy sensitizes refractory tumors to immune checkpoint inhibitors, which has been proven to be effective in cancer treatment. In the past, radiotherapy was thought to be just local treatment. Now radiotherapy has an additional role: an enhancer of immunotherapy. Radiotherapy is now called “game changer” in this view point in immunotherapy [2].

So far no one knows how “immunologically active” BNCT is combining with immunotherapy and how host immune responses occur after BNCT in the tumor tissue and the surrounding normal tissues. Considering that BNCT is cellular-level particle therapy, the aim of this project is to identify novel immune reactions after BNCT compared to after conventional radiotherapy and other cancer therapies.

#### EXPERIMENTS:

Mice and cell lines: Luciferase-expressing B16F10 melanoma cells (B16-Luc), which were transduced with Luciferase gene in pLV5IN-EF1apuro vector, was purchased from National Institutes of Biomedical Innovation, Health and Nutrition, JCRB cell Bank (Osaka, Japan). B16-Luc was maintained in DMEM (Nacal Tesque, Inc., Kyoto, Japan) with 10% fetal bovine serum and penicillin/streptomycin (100 U/mL). SCC-VII, a squamous cell carcinoma cell line derived from C3H/He mice (Department of Radiology, Kyoto University), was maintained in Eagle's minimum essential medium (Nacal Tesque, Inc., Kyoto, Japan) supplemented with 12.5% fetal bovine serum and penicillin/streptomycin (100 U/mL). The cells were cultured at  $37^\circ\text{C}$  with 5%  $\text{CO}_2$ . All of the animal experiments were approved by the Animal Research Committee of Kyoto University and were performed in accordance with the institutional laboratory animal handling guidelines and the guidelines governing animal care in Japan. Mice were purchased from CLEA Japan (Tokyo, Japan). Syngeneic B16-F10 (2x10<sup>5</sup>) or SCC-VII (2x10<sup>5</sup>) were subcutaneously inoculated with Matrigel (Corning Inc., NY, USA) into the right hind legs of six-week-old C57Bl/6 or C3H/He mice, respectively.

Treatment: L-BPA and fructose were dissolved in distilled water at a molar ratio of 1:1.5, and then a 1.15 M ratio of 1 N NaOH was added. The mixture was stirred until L-BPA had completely dissolved, and the pH value was titrated to 7.6 with 1 N HCl. The solution was filtered through a  $0.22\mu\text{m}$  syringe filter for sterilization (Merck Millipore, Massachusetts, USA). The final concentration was set to 30 mg/mL.

Tumor volumes were calculated using the formula  $\pi/6 \times \text{Length} \times \text{Width} \times \text{Height}$ . Treatments were started when the tumor reached a volume of 100-150 mm<sup>3</sup> in the B16-Luc model and 150-220 mm<sup>3</sup> in the SCC-VII model. For BNCT group, 500 mg/kg of BPA was subcutaneously injected into mice into the nuchal sites. Tumor was irradiated by thermal and epi-thermal neutron (5MW, Institutes for Integrated Radiation and Nuclear Science, Kyoto University) 45 min after BPA injection for 15 min. For in vivo depletion of CD8+ T cells, CD8+ cell-depleting antibody was injected intraperitoneally (i.p.) just before BNCT treatment, and was maintained by weekly injections thereafter. For BNCT + immunotherapy combination group, aPD1 antibody was administered i.p. just after BNCT treatment (Day 0) and once per week thereafter until Day 41 (7 weeks).

Statistical analysis: Statistical analyses were performed with GraphPad Prism software version 7 (GraphPad Software Inc.). A *P*-value of less than 0.05 was considered significant. One-way ANOVA and Tukey's multiple comparison test were used to compare multiple groups. Kaplan-Meier analysis was used when comparing survival data.

#### RESULTS:

Mean irradiated physical dose was 9.42 Gy (Thermal neutron: 0.482 Gy, epi-thermal: 0.051 Gy, fast neutron: 0.357 Gy, gamma-ray: 0.491 Gy, boron dose: 0.268 Gy/ $^{10}\text{B}$  1ppm, estimated boron concentration: 30 ppm).

In both B16-Luc and SCC-VII groups, CD8 depletion results in tumor regrowth 7 days after BNCT, while tumor continues to decrease in volume for at least 14 days in BNCT group. The combination of aPD1 antibody with BNCT shows significant better anti-tumor effect in both tumor models ( $p < 0.05$ ).

#### REFERENCES:

- [1] R.F. Barth *et al.*, *Radiat Oncol.*, **7** (2012) 146-166.
- [2] S. Demaria *et al.*, *Trends Cancer.*, **2** (2016) 286-294.

## CO7-2 Boron nitride ( $^{10}\text{B}$ ) a prospective material for boron neutron capture therapy

Manjo Kaur<sup>1</sup>, Paviter Singh, Kulwinder Singh, Usha Singh Gaharwar<sup>1</sup>, Ramovatar Meena<sup>2</sup>, Manjeet Kumar<sup>2</sup>, Fumiko Nakagawa<sup>3</sup>, Shangze Wu<sup>3</sup>, Minoru Suzuki<sup>4</sup>, Hiroyuki Nakamura<sup>3</sup>, Akshay Kulmar

*Advanced Functional Materials Laboratory, Department of Nanotechnology, Sri Guru Granth Sahib World University, Punjab, India*

<sup>1</sup>*Nanotoxicology Laboratory, School of Environmental Sciences, Jawaharlal Nehru University, New Delhi, India*

<sup>2</sup>*Department of Electrical Engineering, Incheon National University, South Korea*

<sup>3</sup>*Laboratory for Chemistry and Life Science, Institute of Innovative Research, Tokyo Institute of Technology, Yokohama, Japan*

<sup>4</sup>*Institute for Integrated and Nuclear Science, Kyoto University*

**INTRODUCTION:** Boron Neutron Capture Therapy (BNCT) is an expecting cancer therapy for the treatment of harsh and un-operatable malignant tumors. The efficiency of boron agent depends highly on tumor selectivity, sufficient amount of boron agent in tumor site, non-toxicity, tumour/normal tissues ratio (>3) and absorption of thermal neutrons by boron. Among a variety of bioceramics, boron nitride (BN) have remarkable properties that can be used as investigations for diagnostic purposes and drug delivery. In this study,  $^{10}\text{B}$  was prepared using simple and cost effective solvothermal method to get the product with highest purity. BNCT studies were performed at Kyoto University Research Reactor Institute (KURRI).

**EXPERIMENTS:** Boric acid ( $^{10}\text{B}$  enriched with 99 atom%  $^{10}\text{B}$  isotopic purity) and ammonia solution were used as boron source and nitrogen respectively to synthesize  $^{10}\text{B}$  by solvothermal method. Details of experimental procedure and characterization are described in the literature.[1]

**RESULTS:** The structure is layered with B-N layers stacked over each other having very high surface area with electronegative atoms which makes this material highly dispersible in water. TEM images also shows that the particles are in 15–25 nm range interacting with each other.

MTT assay using HeLa, MCF-7, and HEK-293 cell lines was carried out. The results showed relatively less changes with lower concentration (150 and 300  $\mu\text{g}/\text{mL}$ ) of  $^{10}\text{B}$  nanostructures, however up to 40 percent cytotoxicity rate was observed at higher concentration (1200  $\mu\text{g}/\text{mL}$ ). These results indicate that these nanostructures are not cytotoxic for tested cell lines at the concentration of up to 1 mg/mL and can be used for biomedical application at safe concentration below the studied doses.

Intracellular boron concentration was detected and results confirm the presence of boron inside cells. Boron content of cells treated with 25 ppm and 100 ppm concentration was 0.57 ppm and 1.9 ppm respectively. These results indicate concentration dependent uptake of boron in HeLa cells and ability to enter in intracellular environment.

BNCT study of  $^{10}\text{B}$  was studied in comparison to L-BPA. Fig. 1(a) shows the schematic representation of 96-well plate irradiation. HeLa cells treated with  $^{10}\text{B}$  shows almost similar dose-dependent cell killing effects as L-BPA at neutron fluence range of  $3.6\text{--}6.3 \times 10^{12}/\text{cm}^2$  (Fig.1(b)). Thermal neutron fluence of  $\sim 6.3 \times 10^{12}/\text{cm}^2$  resulted in almost 50% cell death of  $^{10}\text{B}$  treated cells.

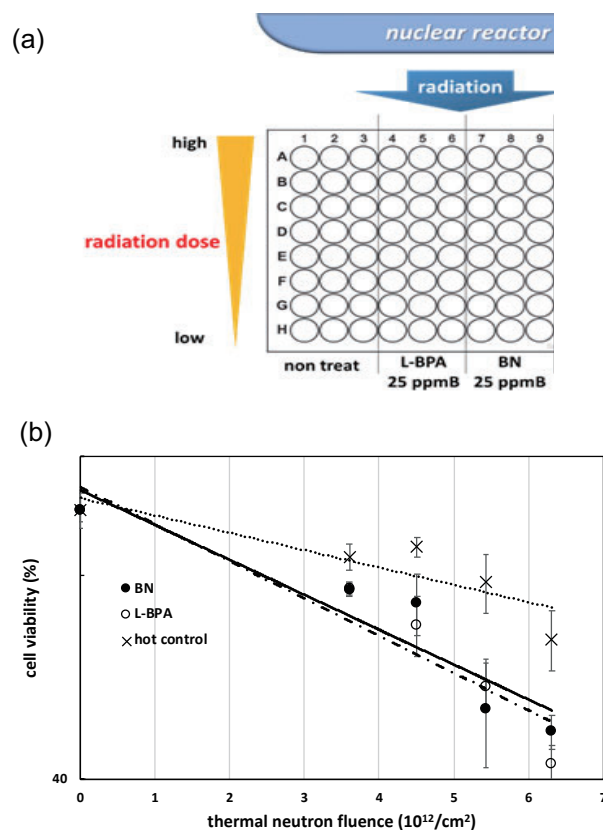


Fig. 1. (a) Schematic representation of irradiation to 96 well plate. (b) BNCT effect of  $^{10}\text{B}$  enriched BN on HeLa cell lines in comparison to L-BPA.

**CONCLUSION:** The aim of present work was to synthesize  $^{10}\text{B}$  enriched nanostructured boron nitride from boric acid and ammonia solution. BN was synthesized by solvothermal method at  $650\text{ }^\circ\text{C}$  for 24 hours. The decomposition of ammonia solution produces hydrogen which is responsible for BN formation even at relatively low temperature. BNCT studies of boron nitride were performed using thermal neutron source on HeLa cells in comparison to L-BPA. The thermal neutron fluence of  $\sim 6.3 \times 10^{12}/\text{cm}^2$  resulted in almost 50% cell killing of BN treated HeLa cells. These results show that  $^{10}\text{B}$  enriched BN can be used as a potential candidate for BNCT.

### REFERENCES:

[1] A. Kumar *et al.*, *Materials Lett.*, **259** (2020) 126832.

# CO7-3 A Fundamental Investigation on Contents of Important Elements for Activation in Various Concrete

K. Kimura, T. Takata<sup>1</sup>, Y. Sakurai<sup>1</sup>, H. Tanaka<sup>1</sup>, and K. Takamiya<sup>1</sup>

Fujita Corporation

<sup>1</sup>Institute for Integrated Radiation and Nuclear Science, Kyoto University

**INTRODUCTION:** One of the typical materials for radiation shield is concrete at the points of its flexibility, sufficient supply, and inexpensiveness. On the other hands, once radiation facilities with shielding concrete start to operation, the concrete are affected by the radiation ray from the operating radiation source in the facilities and activated. Various types of low activation concrete[1]-[3], which are typically white cement based concrete, are the one of the ways to solve the problem. Especially, boron neutron capture therapy (BNCT) should be effective facilities to apply the low activation concrete.

**METHODS:** Various types of concrete samples were crushed to certain size (typically under 0.7mm or less), and were packed for 0.1 to 0.3 g with special treatment for the irradiation in KUR. After the irradiation with 10 to 60 minutes and with the certain cooling period, these samples were measured by Ge detector one by one. The quantity of the target elements, which were selected by former investigations as Co, Cs, Sc, Fe and Eu[1]-[3], in each sample were estimated by the comparison of the known standard material in the same package for the irradiation.

**RESULTS:** Figure 1 shows the correlation of the sample preparation procedures (typical and additional with disc mill) for measured contents of elements and introduces each result by two preparation methods is similar. Metal disc mill was used for crushing the samples additional to typical procedure samples, in order to reduce the grain size down to a few tenth micrometer. Figures 2 and 3 show the distribution of Eu, Co, and Cs contents in while cement based concrete (39 samples) and ordinary concrete (52 samples).

**CONCLUSION:** More than 200 concrete samples were prepared for estimating the contents of Eu, Co, and Cs, including investigation of preparation of the samples. These data would contribute the establishment of material data for shielding materials.

## REFERENCES:

- [1] K. Kimura, *et al.*, Proceedings of 8th International Conference on Radiation Shielding, vol. 1, pp.35-42, ANS inc, Arlington, USA, 1994.
- [2] M. Kinno, *et al.*, ANS Radiation Protection & Shielding Conference, pp.673-678, Spokane, USA, 2002.
- [3] K. Kimura, *et al.*, Proc. of Int. Conf. on Nuclear Engineering (ICONE16), Florida, USA, May 11-15, (2008) 4848.

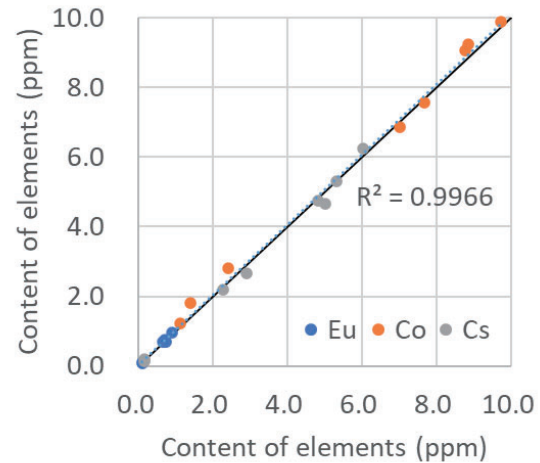


Fig. 1. Correlation of different preparations of sample.

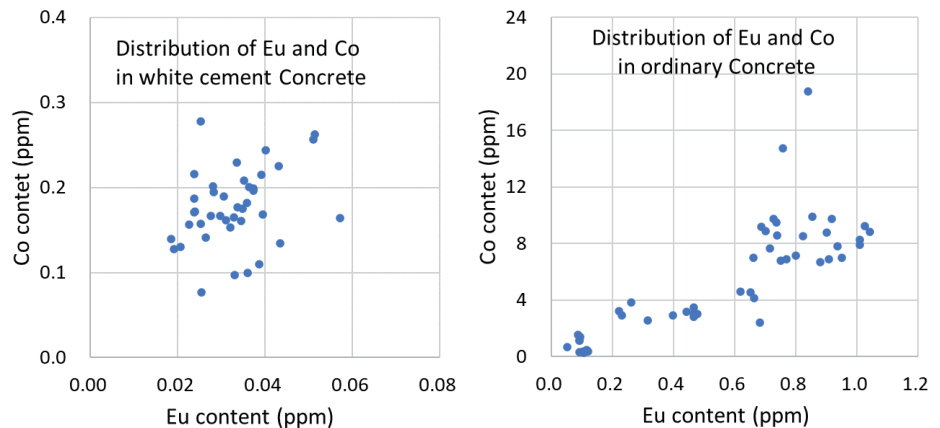


Fig. 2. Distribution of Eu and Co in various concrete.

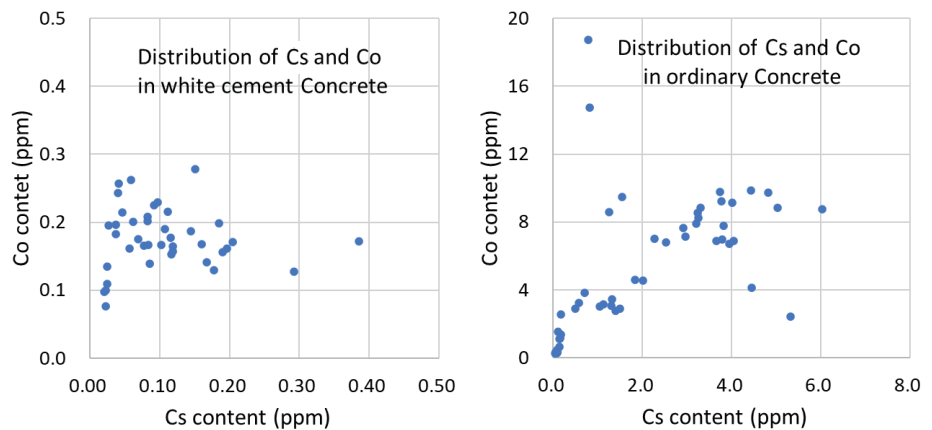


Fig. 3. Distribution of Cs and Co in various concrete.

## Evaluation of the abscopal effect observed by mouse head irradiation following thermal neutron irradiation

Y. Kinashi and T. Takata

*Institute for Integrated Radiation and Nuclear Science  
Kyoto University*

**INTRODUCTION:** The effect of metastasis of lymph nodes such as lymph nodes in areas that are not irradiated sites in radiation therapy of malignant lymphoma is reported in 1953 and is called abscopal effect. Abscopal is a Latin meaning of "far away" ab and the ancient Greek "target" scopal, a phenomenon that collectively refers to the indirect effects of radiation on sites that are not the sites of the irradiation. It is reported about the abscopal effect in radiotherapy that immune response is activated by partial radiation [1]. The influence on immune organization of the mouse at the time of the head irradiation is not well known. The purpose of this study is to evaluate the relative biological effectiveness in the severe combined immunodeficiency (SCID), so-called SCID mice, those are having well-known high radiation sensitivity comparing with C3H/He mice having normal radiation sensitivity.

**EXPERIMENTS:** CB17/Icr-Prkdc<sup>scid</sup>/CrICrIj (SCID mice) were obtained from Charles River Inc. As a comparison experiment for the SCID mice, C3H/He mice were obtained from Japan Animal Inc.

Neutron irradiation was performed as follows. The Heavy Water Facility of the Kyoto University Research Reactor (KUR) was used. Mice were restrained in a plastic box on a radiation board. Neutron fluence was measured by radio-activation of gold foil and gamma-ray doses by TLD. Mice were restrained in a plastic box on an acrylic plate. In order to irradiate the head of the mouse, the mice head was left radially to the irradiation area of the plate. Gold and TLD placed on the head and abdomen, respectively. The mice were fixed on tape and the acrylic plate and mice were covered with a plastic bag to prevent the escape. After irradiation, the splenic cell suspension was adjusted and incubated. At 48 hour, 72 hours after irradiation, apoptotic induction of the cells was examined by Cell Death Detection ELISA (Roche).

**RESULTS:** As shown in Table 1, the apoptotic change of radiation dose. The apoptotic induction of the splenocytes of SCID mice was larger than that of C3H mice at 48 hours and 72 hours after irradiation. The difference of the apoptosis of the splenic cells between SCID mice and C3H mice was larger at the 72 hours than 48 hours after the neutron radiation.

**Table1.** Apoptotic induction of the splenocytes at 48 and 72 hours after neutron irradiation\*

Radiation dose	SCID		C3H	
	48 h. after radiation	72 h. after radiation	48 h. after radiation	72 h. after radiation
control	1.1 ± 0.1	1.1 ± 0.1	1.1 ± 0.1	1.0 ± 0.1
0.5Gy	1.5 ± 0.1	1.8 ± 0.2	1.1 ± 0.1	1.1 ± 0.1
1.0Gy	2.1 ± 0.2	2.5 ± 0.2	1.5 ± 0.1	1.1 ± 0.1

\*Each data shows the enrichment factor at neutron radiation dose. Each data shows the mean value ± SD.

### DISCUSSION

Previously we reported the RBE values for SCID mice of the LD50 by radiation oral death assay and gamma H2AX foci number of the lymphocytes. The RBE values calculated from radiation oral death assay and gamma H2AX foci number of the lymphocytes were 1.6 for SCID mice and 2.0 for C3H mice [2]. The SCID mice show extreme sensitivity to ionizing radiation, because cells lack functional DNA-dependent protein kinase. In this study, our results suggest that the abscopal effect for SCID mice were larger than C3H mice. The difference of the apoptosis of the splenic cells between SCID mice and C3H mice was larger on the time dependent. That is to say, the hyper radiation sensitivity was observed in the abscopal effect after the neutron irradiation.

### REFERENCES:

- [1] K Reynders *et al.*, Cancer Treatment Reviews, 41(2015)503-510.
- [2] Y Kinashi *et al.*, ICRR 15<sup>th</sup> abstract book (2015).

## CO7-5 The feasibility study of Eu:LiCAF neutron detector for an accelerator-based BNCT

T. Nakamura, Y. Matsui, A. Yamaguchi, D. Nio, K. Sakasai, H. Nakashima, R. Okumura<sup>1</sup> and K. Takamiya<sup>1</sup>

Japan Atomic Energy Agency

<sup>1</sup> Institute for Integrated Radiation and Nuclear Science, Kyoto University

**INTRODUCTION:** The stability of neutron flux at an accelerator-based BNCT facility is relatively worse than that at a reactor-based one. Therefore, it is necessary to measure the neutron flux precisely in real-time to optimize the patient's exposure dose for the accelerator-based BNCT. However, the neutron flux is so intense (about  $10^9$ (n/cm<sup>2</sup>/s)) that the real-time measurement has not been realized yet. Hence we tried to measure the neutron flux with a small detector using a Eu:LiCAF scintillator [1] on the tip of optical fibers, as shown Fig.1. We reported that this detector has the linearity to the neutron flux to  $10^9$ (n/cm<sup>2</sup>/s) in our previous article [2]. In this



Fig. 1 Detector coupled with the optical fiber.

experiment, we tried to check the linearity for neutron flux up to  $10^{11}$ (n/cm<sup>2</sup>/s) using the KUR-SLY, and to check it can be used not only exposure dose monitor but also beam monitor.

\*\*\*\*\*

**EXPERIMENTS:** The experiments were performed at the KUR-SLY where the maximum neutron flux of about  $10^{12}$ (n/cm<sup>2</sup>/s) is available at the bottom when the reactor power is 1MW [3]. Figure 2 shows the experimental set-up for the measurement, where the photon counting unit C8855 and 994 is able to count up to 1 Mcps. The optical output from the Eu:LiCAF scintillator through the optical fibers was properly converted to an electric signal and counted with the counting units. Prior to the measurement, the detector was put into the plastic bottle, where Figure 3 shows the situation, and loaded to 47 cm from the bottom of the KUR-SLY. At this position, the maximum neutron flux is about  $1.8 \times 10^{10}$ (n/cm<sup>2</sup>/s). First experiment was carried out from the starting-up to 1 MW-arrival of the reactor. Next, after arrived at 1MW, we changed the detector position in the KUR-SLY, to measure counting of different neutron fluxes using the

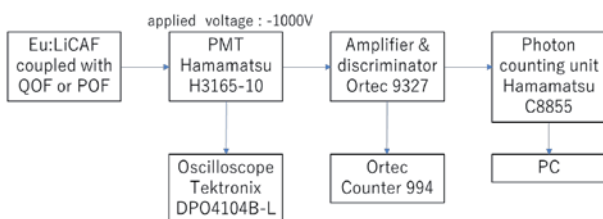


Fig. 2 Experimental setup.

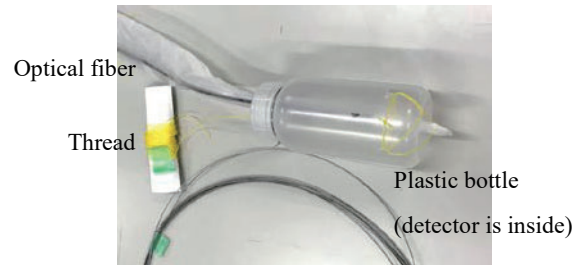


Fig. 3 Situation about the putting into the plastic bottle.

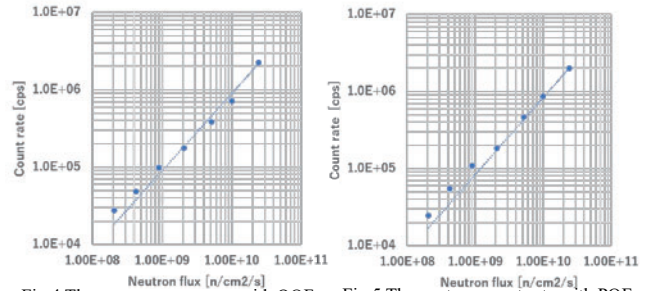


Fig.4 The neutron count rate with QOF

Fig.5 The neutron count rate with POF

detector coupled with the quartz optical fiber (QOF) or the plastic optical fiber (POF).

\*\*\*\*\*  
**RESULTS:** The count rate using the detector coupled with QOF was varied according to reactor power during the reactor power rises to 1MW from starting-up. Figure 4, 5 show the neutron count rate using QOF and POF respectively with the detector. The results indicate the detector coupled with QOF or POF have approximately linearity to the neutron flux up to  $2 \times 10^{10}$  (n/cm<sup>2</sup>/s).

\*\*\*\*\*

**CONCLUSIONS:** We developed detector which is small detector using a Eu:LiCAF scintillator on the tip of optical fibers, and confirmed that the detector coupled with QOF has the same performance as the detector coupled with POF. The detector can measure neutron flux of  $10^8$  to  $2 \times 10^{10}$  (n/cm<sup>2</sup>/s), therefore it can be used not only exposure dose monitor but also beam monitor for accelerator-based BNCT facility.

It is confirmed that QOF is more radiation-resistant than POF [4]. We are planning to conduct experiments to confirm the detector coupled with QOF have enough radiation-resistance for practical use in the future.  
 \*\*\*\*\*

### REFERENCES:

- [1] N. Kawaguchi., Doctor Thesis, Tohoku University, <http://hdl.handle.net/10097/56580>
- [2] KURRI PROGRESS REPORT 2017 CO7-2
- [3] KUR-SLY <http://www.rri.kyoto-u.ac.jp/JRS/>
- [4] T. Nakamura, K. Sakasai, H. Nakashima, K. Takamiya, H. Kumada, 2016. Characteristics of Radiation-Resistant Real-Time Neutron Monitor for Accelerator-Based BNCT. JOURNAL OF RADIATION PROTECTION AND RESEARCH. 41, No.2. 105-109. DOI: <https://doi.org/10.14407/jrpr.2016.41.2.105>

## CO7-6 Enhancement of the cancer cell-killing effects of boron neutron capture therapy by overexpression of *LAT1* in human cancer cells

K. Ohnishi, M. Misawa<sup>2</sup>, N. Sikano<sup>1</sup> and M. Suzuki<sup>3</sup>

*Departments of Biology, <sup>1</sup>Radiological Science, Ibaraki Prefectural University of Health Sciences*

*<sup>2</sup>National Institute of Advanced Industrial Science and Technology*

*<sup>3</sup>Institute for Integrated Radiation and Nuclear Science, Kyoto University*

**INTRODUCTION:** Outcome from BNCT largely depends on amount of intracellular accumulation of boron compound. L-type amino-acid transporter 1 (LAT1) [1], through which boronophenylalanine (BPA) is transported into cells, is frequently expressed in various types of tumor cells including glioblastoma but not in normal cells [2]. We transfected *pCMV/LATI-GFP* plasmids into a glioblastoma cell line, T98G, and selected several clones and confirmed that those clones stably overexpress LAT1 in cell membrane with confocal laser microscopic observation and western blot analysis. In this study, we measured the sensitivity to the neutron and gamma-ray fluences generated by KUR in T98G/K1 and T98G/K4 clones that uptake <sup>14</sup>C-BPA 2.5 and 5.0 times, respectively, larger than T98G/KC2 control clone.

**EXPERIMENTS:** T98G/K1, T98G/K4, T98G/KC2 and transiently *pCMV/LATI-GFP*-lipofected T98G/KC2 cells (treated with Lipofectamine 2000 overnight) were treated with medium containing <sup>10</sup>BPA (0, 5 or 20 ppm) for 3 hours. The cells were trypsinized and the cell suspensions in 1.5-ml cryo-tubes were irradiated with the fluences (0.4 or 0.8 Gy in total doses of neutrons and  $\gamma$ -rays) from KUR. The irradiated cells were plated on three replicate dishes for colony formation assay. The cells were fixed

with ethanol and stained with crystal violet after cell culture for 10-14 days.

**RESULTS:** T98G/K4 cells showed slightly enhanced sensitivity to the fluences compared with T98G/K1, T98G/KC2 and the lipofected T98G/KC2 cells in the case of 5 ppm <sup>10</sup>BSA treatment. There is no significant difference in the sensitivity between T98G/K1 and T98G/KC2 cells as well as transiently lipofected T98G/KC2 cells. In the case of 20 ppm <sup>10</sup>BSA treatment, T98G/K4 and the lipofected T98G/KC2 cells showed largely enhanced sensitivity to the fluences compared with T98G/KC2 cells (ER=1.5). T98G/K1 cells showed slightly enhanced sensitivity (ER=1.2). The sensitivity of the cells to the fluences was correlated with the expression level of LAT1 of the cells. Figures of results are now in preparation for publication in journal.

**CONCLUSION:** This study showed that overexpression of LAT1 in cancer cells causes enhanced anticancer effects of BNCT and BNCT combined with gene therapy is beneficial for tumors bearing low LAT1 expression.

### REFERENCES:

- [1] Y. Kanai *et al.*, J. Biol. Chem., **273** (1998) 23629-23632.
- [2] K. Kaira *et al.*, Br. J. Cancer, **107** (2012) 632-638.

## CO7-7 Clinical Outcome of BNCT for Advanced or Recurrent Head and Neck Cancer

N. Kamitani<sup>1</sup>, Y. Tanaka<sup>2</sup>, Y. Fukuda<sup>3</sup>, M. Suzuki<sup>4</sup>, Y. Sakurai<sup>4</sup>, J. Hiratsuka<sup>1</sup>

<sup>1</sup>Department of Radiology Oncology, <sup>2</sup>Department of Dermatology, <sup>3</sup>Department of Otolaryngology, Kawasaki Medical School, <sup>4</sup>Institute for Integrated Radiation and Nuclear Science, Kyoto University

**Introduction:** We report outcome of BNCT for AHNC (advanced head and neck cancer) and RHNC (recurrent head and neck cancer). The principal endpoints specified in this study were progression-free and overall survival consequences.

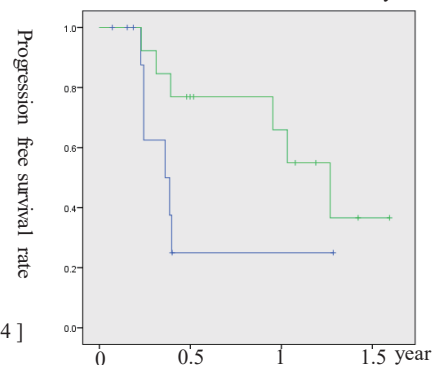
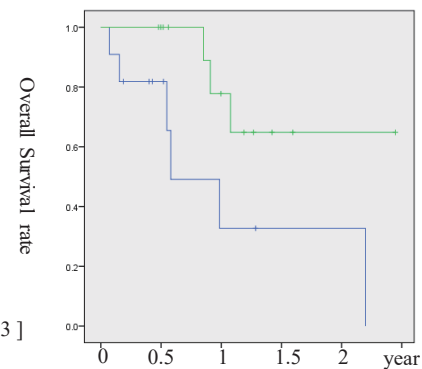
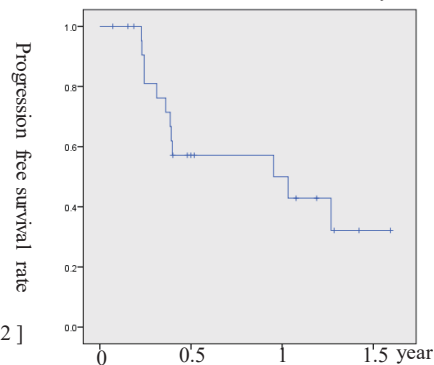
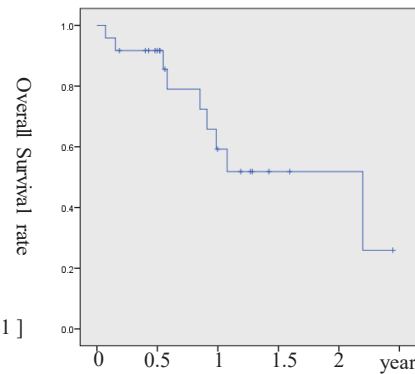
**Methods:** 24 patients (25 cases) were included in this study and received BNCT between Aug. 2017 and Feb. 2019. One patient was received BNCT twice, because of tumor progression after first BNCT. Characteristics of the patients are detailed in Table1. FBPA-PET was under-gone in all cases to determine the indication for BNCT, and the median T/B ratio was 3.2 (range 2.5-8). 13 patients had received systemic therapy (ST), such as nivolumab, cetuximab or TS-1, and the therapy had been continued for 6 months after BNCT. Overall survival (OS) time was measured from the date of BNCT until confirmed death or the date of the last follow-up examination.

**Results:** Median follow-up of surviving cases was 8.7 months (range 0.9-29.8). At the time of analysis, 15 patients (62.5 %) were alive, and 9 patients (37.5%) out of them were alive with no evidence of disease. The local recurrence was occurred in 12 patients, and a median time to recurrence was 4.8 months (range 2.7-15.4). Nine patients died during an observation period, and eight of them died of disease progression. 1year OS and progression free survival (PFS) rate was 50.0% (Fig 2.) and 59.2% (Fig 1.), retrospectively. 1year OS rate of ST group and non-ST group was 77.8% (median time 12.5 months) and 32.7% (median time 6.3 months) respectively ( $p=0.039$ ) (Fig.3). 1year PFS rate of ST group and non-ST group was 65.9 % (median time 11.6 months) and 25.0 % (median time 3.6 months) respectively ( $p=0.075$ ) (Fig.4). There were no associations between the number of T/B ratio and OS rate, either PFS rate. An addition of ST to BNCT did not increase any adverse effects.

**Conclusion:** BNCT is effective in the treatment of locally recurred head and neck cancer.

[ Table 1 ]

[ Table 1 ]		Number of patients
Sex	Male / Female	10 / 14
Age	Median(range)	53 (34-78) years
Histology	SCC/ Non-SCC	18 / 6



## CO7-8 Establishment of a novel mutation breeding using Boron Neutron Capture Reaction (BNCR)

M. Kirihata, S. Segami<sup>1</sup>, Y. Hattori, Y. Kinashi<sup>2</sup>

Research Center of BNCT, Osaka Prefecture University

<sup>1</sup>Research Institute of Environment, Agriculture and Fisheries, Osaka Prefecture

<sup>2</sup>Institute for Integrated Radiation and Nuclear Science, Kyoto University

**INTRODUCTION:** Boron Neutron Capture Reaction (BNCR) is based on the nuclear reaction of <sup>10</sup>B atom with thermal/epithermal neutron already applied to cancer treatment (BNCT) [1, 2]. As a new utilization method of BNCR, the purpose of this study is to establish a novel mutation breeding using BNCR.

This method uses the principle of inducing mutation by an alpha particle and <sup>7</sup>Li recoil nuclei high linear energy transfer and short range when irradiated with neutrons (low energy thermal neutrons (< 0.5 eV) can be absorbed the <sup>10</sup>B atoms, leading to generating high linear energy transfer alpha particles (~ 150 keV/μm) and <sup>7</sup>Li nuclei (~ 175 keV/μm) that are produced by BNCR of <sup>10</sup>B selectively taken into the meristematic cell with thermal neutron. This principle is different from both chemical mutagens, such as EMS and MNU, and physical mutagens, such as gamma rays and ion beams, used for mutation breeding so far. In other words, the mutagenic effect depends on chemical and physical factors, such as <sup>10</sup>B concentration, thermal neutron intensity, and irradiation time.

The germination rate is used as one of the traits to verify the effect of mutagenesis [3]. The immersed into BPA but not irradiated with neutrons seeds were germinated normally at different concentrations (0, 10, 100, 200 ppm) of BPA in the range of from 70% to 100%. This time, it was confirmed that the germination rate was affected a thermal neutron fluence-dependent or a BPA concentration-dependent manner by causing BNCR.

**EXPERIMENTS:** The experimental material used *Oryza sativa* L. cv. Nipponbare. The dry seeds were immersed into different concentrations (0, 10, 100, 200 ppm) of <sup>10</sup>B-enriched *p*-boronophenylalanine (BPA) [4] for 16 h. Some concentrations were also tried with hulled rice. The samples were washed with water and re-dried at room temperature. The seeds in 2-mL tubes were irradiated with thermal neutron for 90 minutes in the Kyoto University Research Reactor (KUR). To provide four different levels of neutron fluence, the tubes were set to four columns microtube rack at the time of irradiation. After the irradiation treatment, the seeds were cultured in petri-dishes with continual moistening of filter paper at 25°C under a photoperiod of 16 h light and 8h dark, it was investigated the germination rate.

**RESULTS:** The typical thermal neutron fluence were 1.1x10<sup>13</sup> cm<sup>2</sup>, 8.1x10<sup>12</sup> cm<sup>2</sup>, 6.0x10<sup>12</sup> cm<sup>2</sup>, 4.2x10<sup>12</sup> cm<sup>2</sup>, at the time of irradiation. The germination rate not de-

creased with both thermal neutron fluence and BPA concentrations (Table 1, 2). That is, the meristematic cell in the seeds were not damaged enough to initiate cell division in the range of the present experimental conditions. Besides, using hulled rice, the samples were fragile due to re-drying. The hulled rice was not suitable for this method. We are set to confirm conditions for making a strong effect by making the fructose complex higher BPA concentrations and extending the immersion time. By investigating inhibition of germination and reduction in survival of the samples, we will consider the suitable conditions as a mutagenesis method.

Table 1. The relationship between thermal neutron fluence and germination rate.

Thermal neutron fluence	Concentrations of BPA (ppm)	No. of seeds	No. of seeds germinated	germination rate (%)
high ▼ low	0	37	31	84
		35	32	91
		38	28	74
		40	29	73
high ▼ low	10	38	30	79
		35	27	77
		37	27	73
		33	26	79
high ▼ low	100	35	26	74
		40	31	78
		36	29	81
		36	31	86
high ▼ low	200	35	26	74
		35	27	77
		35	26	74
		36	30	83

Table 2. The relationship between BPA concentrations and germination rate.

Concentrations of BPA (ppm)	No. of seeds	No. of seeds germinated	germination rate (%)	germination index
0	150	120	80	100
10	143	110	77	96
100	147	117	80	99
200	141	109	77	97

### REFERENCES:

- [1] H. A. Soloway *et al.*, Chem. Rev., **98** (1998), 1515-1562.
- [2] B. Farhood, *et al.*, Rep. Pract. Oncol. Radiother. **23** (2018), 462-473.
- [3] Tanaka A. *et al.*, Int. J. Radiat. Biol., **72**, (1997), 121-127.
- [4] H. R. Snyder, *et al.*, J. Am. Chem. Soc. **80** (1958), 835-838.

N. Kondo<sup>1</sup>, T. Kinouchi<sup>1</sup>, M. Natsumeda<sup>2</sup>, Y. Sakurai<sup>1</sup>, T. Takata<sup>1</sup> and M. Suzuki<sup>1</sup>

<sup>1</sup> Institute for Integrated Radiation and Nuclear Science, Kyoto University (KURNS)

<sup>2</sup>Department of Neurosurgery, Brain Research Institute, Niigata University

**INTRODUCTION:** BNCT have been applied to recurrent malignant glioma and even after standard therapy (surgery, chemo-radiation therapy) because of the selective damage to the tumor. Especially, glioblastoma (GBM) is the most miserable cancer, whose patient survival is 14.6 months and remarkably resistant to chemo-radiation and immuno- therapy. With BNCT, we achieved better local control and survival benefit in malignant glioma using thermal neutrons produced by the reactor in Kyoto University. However, the recurrence is inevitable after BNCT. Reasons for recurrence after BNCT have not been fully elucidated, but they may reflect tumor characteristics. In fact, we've found cerebrospinal fluid dissemination, frequent cause of death, after BNCT occurs more frequently in the small cell subtype of IDH1R132H mutation-negative glioblastoma [1]. On the other hand, exosomes, extracellular vesicles with diameter of between 50 nm to 150 nm used for communication tools between cells, are receiving a lot of attention because containing microRNAs, lipids and proteins are possible biomarker for various diseases. In this study, we investigate the exosomes from glioma cells after BNCT.

#### EXPERIMENTS:

**Cell culture:** U87 MG glioma cells were cultured with exosome-free fetal bovine serum (FBS) at 10 % final concentration in Dulbecco's Modified Eagle's Medium (DMEM) at 37 °C in 5 % CO<sub>2</sub> incubator for two days. Cells were divided into four groups, control, Boronophenylalanine (BPA) alone, thermal neutron irradiation alone, and BNCT. BPA was added to the medium at 25 ppm the day before irradiation. One group consisted of more than 3×10<sup>6</sup> cells.

**Thermal neutron irradiation:** After trypsin treatment, cell suspensions were divided in Eppendorf tubes at 1×10<sup>6</sup> cells/mL with exosome-free FBS at 10 % final concentration in DMEM with or without 25 ppm BPA and irradiated with thermal neutrons at D<sub>2</sub>O facility for one hour.

After irradiation, cells were centrifuged to change the medium, then dissociated into 10cm dishes with exosome-free FBS at 10 % final concentration in DMEM (1×10<sup>6</sup> cells / dish).

**Exosome isolation:** 48 hours after irradiation, cell culture medium (CCM) of each group was collected and centrifuged to remove the cell debris at 2000 rpm for 20 min at 4 °C. The supernatant was removed without disturbing the pellet and filtered through 0.22 μm filters (Merck Millipore) to remove contaminating remaining microvesicles, and cell debris and kept in – 80 °C deep freezer.

After thawing, the CCM was concentrated to 500 μL with Centrifugal Filter (Amicon Ultra-15, 100 kDa) devices at 4 °C. Following this, 500 μL of CCM was overlaid on qEV size exclusion columns (IZon) and exosome containing fractions were collected. Exosome fractions were pooled and concentrated in Amcon Ultra-0.5 10 kDa molecular weight centrifugal filter units to a final volume of 50 μL. Purified exosomes were then store at – 80 °C until use.

**Tunable resistive pulse sensing:** The size distribution profile and concentration of exosomes were analysed with tunable resistive pulse sensing (TRPS) (qNano, IZon Science Ltd). Carboxylated polystyrene beads (70 nm) were used to calibrate the concentration and size.

#### RESULTS:

The exosomes size distribution and concentration of each group was assessed by TRPS. Exosome size from all groups have the typical range of between 50 to 150 nm in diameter (Fig.1). Concentrations of exosomes of each group: control, BPA alone, thermal neutron irradiation alone, and BNCT, were 2.68 ×10<sup>9</sup>, 1.89×10<sup>8</sup>, 1.84×10<sup>9</sup>, 1.18×10<sup>8</sup>(/mL), respectively.

The contents of exosomes are to be analyzed by proteomics.

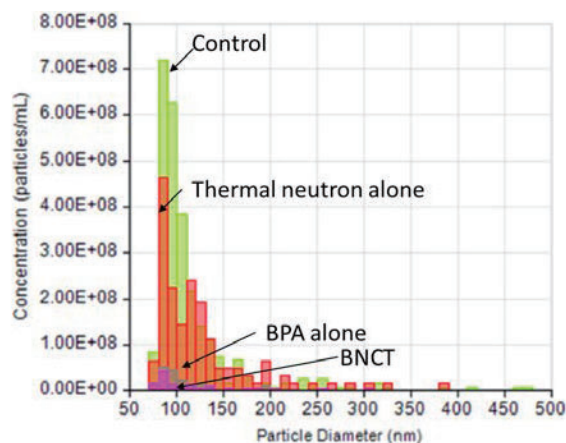


Fig. 1: TRPS analysis of exosomes confirming the size range of 50-150 nm in diameter. (Arrows indicate each group.)

#### REFERENCES:

[1] Kondo N, *et al*, 2017, J Neurooncol. 2017;133: 107-118. doi: 10.1007/s11060-017-2408-x

## CO7-10 iPS cells - derived neuronal cell death and inflammation by thermal neutron irradiation

N. Kondo<sup>1</sup>, H. Fukusumi<sup>2</sup>, Y. Sakurai<sup>1</sup>, T. Takata<sup>1</sup>, Y. Kanemura<sup>2</sup> and M. Suzuki<sup>1</sup>

<sup>1</sup> *Institute for Integrated Radiation and Nuclear Science, Kyoto University (KURNS)*

<sup>2</sup> *Department of Biomedical Research and Innovation Research, National Hospital Organization Osaka National Hospital*

**INTRODUCTION:** Biological effect of thermal neutron irradiation on neuron is unknown. Thermal neutron is used for clinical treatment for Boron Neutron Capture Therapy (BNCT). To avoid radiation brain necrosis after BNCT, we investigate the pathway of cell death and inflammation induced by BNCT using human induced pluripotent stem cells (iPSCs)-derived neuronal cells.

### **EXPERIMENTS:**

Cell culture: We used human iPSC-derived Neural stem/progenitor cell (NSPC) lines [1]. We differentiated these iPSC derived NSPCs and seeded into laminin-coated 8 well chambers and T25 flasks. Cells were sealed and transferred from the Osaka national hospital to KURNS the day before irradiation kept at 24 °C in the box and cultured at 37 °C CO<sub>2</sub> incubator after transfer.

Thermal Neutron Irradiation: We irradiated thermal neutron irradiation to these cells with sealing for 30 minutes at room temperature by D<sub>2</sub>O facility.

Cell death assay: We stained the cells in 8 well chamber 24 hour after irradiation with Hoechst 33342, Annexin V-FITC and Propidium Iodide Solution following the manufacture's protocol (nacalai tesque, Japan) and captured them by the microscope [Keyence BZ9000].

Sampling for RNA isolation: We rinsed the cells in T25 flasks with PBS 24 hours after irradiation and lysed them with QIAzol following the manufacture's protocol (QIAGEN, Japan) and kept the cells at – 80 °C deep freezer.

**RESULTS:** We are still analyzing the results.

### **REFERENCES:**

[1] Fukusumi *et al.* (2018), Peer J, DOI 10.7717/peerj.4187

## CO7-11 Resistant Mechanism of Glioma Conferred by Tumor Microenvironment after BNCT

N. Kondo<sup>1</sup>, E. Hirata<sup>2</sup>, M. Natsumeda<sup>3</sup>, Y. Sakurai<sup>1</sup>, T. Takata<sup>1</sup>, and M. Suzuki<sup>1</sup>

<sup>1</sup> *Institute for Integrated Radiation and Nuclear Science, Kyoto University (KURNS)*

<sup>2</sup> *Division of Tumor Cell Biology and Bioimaging Cancer Research Institute of Kanazawa University*

<sup>3</sup> *Department of Neurosurgery, Brain Research Institute, Niigata University*

**INTRODUCTION:** BNCT have been applied to recurrent malignant glioma and even after standard therapy (surgery, chemo-radiation therapy) because of the selective damage to the tumor. Especially, glioblastoma (GBM) is the most miserable cancer, whose patient survival is 14.6 months and remarkably resistant to chemo-radiation and immuno-therapy. With BNCT, we achieved better local control and survival benefit in malignant glioma using thermal neutrons produced by the reactor in Kyoto University. However, the recurrence is inevitable after BNCT. Reasons for recurrence after BNCT have not been fully elucidated. In this study, we investigate the crosstalk between tumor microenvironment cells and tumors which survive after BNCT.

### **EXPERIMENTS:**

Cell culture: We used mouse G261 glioma cell line and human glioma GBM1 line. Cells were cultured at 37 °C in CO<sub>2</sub> incubator.

#### Xenograft model

Animals were anesthetized and immobilized in a small animal stereotactic device.  $2 \times 10^5$  cells were transplanted through a hole 2 mm to the right of the bregma, at a depth of 3 mm, at a rate of 1 micro L/min. G261 were transplanted to C57BL/6J mice and G261 were transplanted to Balb/cA-nude mice.

#### Boronophenylalanine (BPA) Treatment and Thermal

Neutron Irradiation: After 10 days from transplantation, 500mg/kg of BPA was administrated subcutaneously 1 hour before irradiation. We irradiated thermal neutron to these mice shielding body trunk with lithium fluoride for 15 minutes at room temperature by D<sub>2</sub>O facility with 5MW power.

Sampling for Immunohistochemistry: 48hours and 7 days after irradiation, mice were anesthetized and sacrificed after transcardiac perfusion of PBS and 4 % paraformaldehyde (PFA). The brain tissue was removed and fixed with 4% paraformaldehyde overnight, then transferred to 30 % sucrose in PBS. The tissue blocks were frozen at -80 °C.

**RESULTS:** We are still analyzing the results.

## CO7-12 Improvement of the method for analysis of micro boron distribution in tissues

M. Suzuki, H. Tanaka, Y. Tamari, T. Watanabe, S. Takeno<sup>1</sup>

*Institute for Integrated Radiation and Nuclear Science,  
Kyoto University*

<sup>1</sup>*Graduate School of Science, Kyoto University*

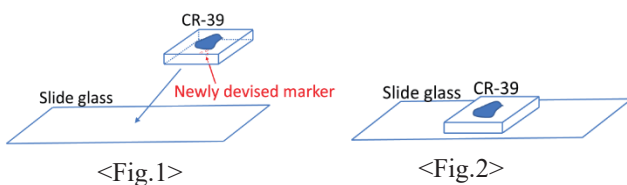
**INTRODUCTION:** In the process of ARG, we need to acquire tissue staining image and etched pit image separately and merge them using its markers. So precise marking system is the essential for precise analysis. But in the etching process, ordinary markers using ink are easily disappeared. To avoid disappearing the markers, we used scratch markers on the CR-39 since scratch remains after etching process [1].

However, in chemical etching process, scratch marker is also etched, and the marker become larger. Because the shape of the marker is deferent before and after etching, the preciseness of matching image is not good enough.

In this study, we devised new marking system, of which the marker deformation before and after etching is minimal by keeping the marker away from the etching solution. Here, we report the method of the newly devised marking system and the assessment the precision of it.

**EXPERIMENTS:** The process of ARG using newly devised marking system is shown as bellows.

1. Put the tissue section on the CR-39 and irradiate them with thermal neutron.
2. Put small marker using ball-point pen near the place to be analyzed, on the opposite side of tissue section. <Fig.1>
3. Put the CR-39 on the slide glass using epoxy adhesives, which has good chemical resistance. In this process, the marker should be inside between CR-39 and slide glass. <Fig.2>
4. Stain the tissue section and acquire both tissue image and corresponding marker image using optical microscope.
5. Remove the tissue section from the CR-39.
6. Etch the CR-39 chemically and acquire both the etched pit image and corresponding marker image.
7. Merge two images (acquired in process 4 and 6) using its markers.



In the experiment, we used CR-39 (BARYOTRAK) and acquired their images using microscope (Keyence BZ-9000). Automatic marker matching program was created and tested.

### Marker deformation before and after chemical etching

- We defined maximum deformation length (dL) between before and after etching marker as bellows.



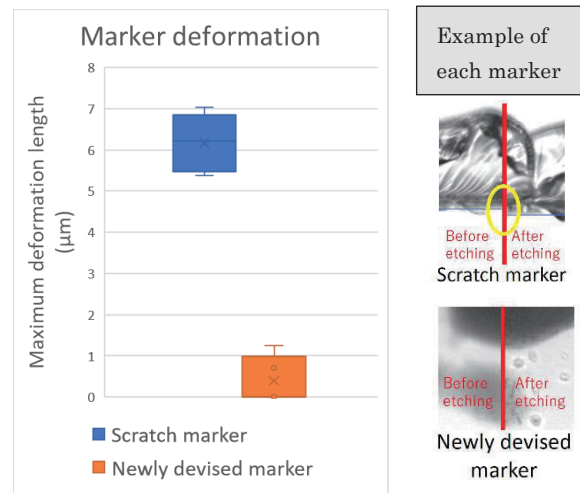
$$dL = \sqrt{dx^2 + dy^2}$$

dx: size difference of horizontal direction

dy: size difference of vertical direction

- The maximum deformation length means maximum potential error in matching images using the markers.
- Five samples are assessed.

**RESULTS:** The maximum deformation length of each marking method is shown as bellows. The average maximum deformation length is 6.17um and 0.39um for scratch marker and newly devised marker, respectively.



### REFERENCES:

1. H.Tanaka *et al. J. Radiat. Res.* **55**, (2014) 373–380

Y. Sakurai, H. Matsunaga<sup>1</sup>, T. Takata, H. Tanaka, M. Suzuki

*Institute for Integrated Radiation and Nuclear Science,  
Kyoto University*  
<sup>1</sup>*Graduate School of Engineering, Kyoto University*

**INTRODUCTION:** Whole organ irradiation in radiotherapy is effective on multiple tumors and minimal residual tumors, such as whole brain irradiation for brain metastasis, whole conserved-breast irradiation in conservative therapy for breast tumor, etc.. However, it cannot be realized for liver and lung tumors. It is because the tolerant dose of these organs is 20 to 40 Gy, which is smaller than the tumor control dose of 50 to 80 Gy. In BNCT, the ranges of the heavy charged particles due to the  $^{10}\text{B}(n,\alpha)^7\text{Li}$  reaction in the boron compound, which selectively accumulates in tumor cells, are too short to reach the adjacent normal cells. Therefore, BNCTs with the whole organ irradiation for liver and lung tumors can be realized as radiotherapy.

In BNCT clinical studies for liver and lung tumors at KUR, the equivalent doses for normal liver and/or lung have been estimated on the basis of boron concentration in blood, which is measurable by prompt gamma-ray analysis. But actually, the variation for the boron concentration in normal liver and/or lung is assumed to be larger among the patients with basal disease, such as cirrhosis, pulmonary fibrosis, pulmonary emphysema, etc..

The purpose of this research is the development of the real-time boron-concentration estimation system in liver and/or lung during BNCT, in order to improve the dose estimation accuracy for BNCTs with the whole-liver and/or whole-lung irradiation. In this system, the technique of prompt gamma-ray telescope is applied. A gamma-ray telescope system has been in use for liver tumor BNCT at Heavy Water Neutron Irradiation Facility of KUR (KUR-HWNIF) from 2005 [1]. The collimation system of this telescope was improved in 2017.

An experiment was performed to confirm the basic characteristics of this improved telescope system in 2019.

**METHODS:** Figure 1 shows the outline of the original gamma-ray telescope system. A 100 cm-long collimator is located in the hall through the irradiation-room ceiling wall. The first collimator is settled just before the detector, and the second collimator is settled at the bottom of the collimation system. In the improved system, both collimators are placed in the collimation system. The distance between these collimators is changeable.

The layout of the characterization experiment was almost similar to the layout in Fig. 1. Instead of a patient, a whole-body liquid phantom was placed. This phantom was the 1-cm-thick acrylic case filled with boric acid water. The boron concentration of the boric acid water was 25 ppm for boron-10. A higher-concentration spheri-

cal region of 5 cm in diameter was settled in the phantom. This region was modelled after a tumor part, and its boron concentration was 250 ppm. The standard epi-thermal neutron irradiation mode was used for this experiment. For the positions of the first and second collimators, the prompt gamma-rays due to  $^{10}\text{B}(n,\alpha)^7\text{Li}$  and  $^1\text{H}(n,\gamma)^2\text{D}$  reactions were counted by the high-purity germanium (HPGe) detector settled on the irradiation room ceiling.

**RESULTS:** Figure 2 shows the ratio of the prompt gamma-ray counts of boron-10 to hydrogen-1 for the collimator interval. In this case, the collimator position is settled to be highest, and the second collimator moves from the highest position to the lowest position. As the second collimator position is lower, the collimator interval is larger and the telescope FOV is smaller. As shown in Fig.2, the count ratio is smaller as the collimator interval is larger. This reason is considered to be the influence of the position of the higher-concentration region in the telescope FOV. It is thought that the higher-concentration region gradually goes out from the telescope FOV, according to the increase of the collimator interval.

**CONCLUSION:** The basic characteristics of the improved telescope system were experimentally confirmed. The further analyzation of the experimental data and the additional experiments are planned.

**ACKNOWLEDGEMENTS:** This study was supported by The Kyoto University Research Fund (Core Stage Back-up, in 2017).

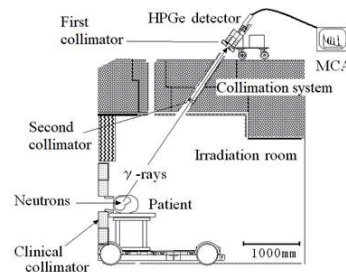


Fig. 1. Outline of the original gamma-ray telescope system installed at KUR-HWNIF.

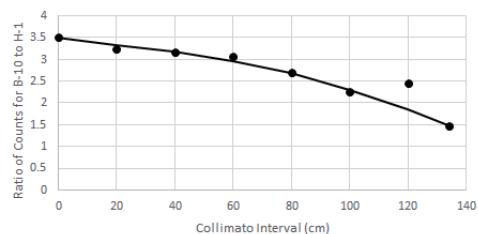


Fig. 2. Ratio of gamma-ray counts for B-10 to H-1.

#### REFERENCES:

- [1] Y. Sakurai *et al.*, *Appl. Radiat. Isot.* **61** (2004) 829-833.

## CO7-14 Establishment of protocol for neutron capture therapy for head and neck cancer

I. Ota, H. Uemura, A. Nishimura, T. Kimura<sup>1</sup>, S. Mi-kami, T. Yamanaka, M. Suzuki<sup>2</sup>, Y. Sakurai<sup>2</sup>, H. Tanaka<sup>2</sup>, N. Kondo<sup>2</sup>, T. Tamamoto<sup>1</sup>, M. Hasegawa<sup>1</sup> and T. Kitahara

*Department of Otolaryngology-Head & Neck Surgery,*

<sup>1</sup>*Department of Radiation Oncology, Nara Medical University*

<sup>2</sup>*Institute for Integrated Radiation and Nuclear Science, Kyoto University*

**INTRODUCTION:** Neutron capture therapy (BNCT) for head and neck tumors has been clinically studied since 2001, with the BNCT research group at Kyoto University Reactor Laboratory, which is a co-investigator, highly effective, with high safety. It is being established. Since November 2012, we implemented the therapy as a joint research with Kyoto University Reactor Laboratory, with the consent of the patients in 4 cases of refractory recurrent head and neck cancer. As a result, the response rate was a very high 100%. The tumor reduction effect in recurrent cases after radical irradiation, which could not be achieved by conventional treatment methods, strongly suggests the possibility of expanding the indications for BNCT for refractory carcinomas as well as for head and neck cancer cases. Here, we will perform BNCT for refractory and recurrent head and neck tumors and examine their efficacy and optimal protocol.

**EXPERIMENTS:** We will treat BNCT for refractory and recurrent head and neck tumors that meet the following criteria and examine their efficacy and optimal protocol.

### Inclusion Criteria

- (1) The patient with local recurrence of head and neck cancer who can not perform the standard therapy any more after radiotherapy.
- (2) The patient with local recurrence of head and neck cancer by the imaging diagnosis, such as CT, MRI and PET.
- (3) The patient with previous radiotherapy (total 40-75 Gy, 2Gy/fq) for the recurrent region.
- (4) The patient with the period of more than one month since the previous treatment.
- (5) The patient with recurrence lesion in the less than 6cm of depth from skin as GTV for BNCT.
- (6) The Patients who have PS less than 2 and are expected to survive more than 6 months after BNCT.
- (7) The patient with good condition of renal function: creatinine <1.2 mg/dl for male and <1.0 mg/dl for female.
- (8) The patient with the age between 20 and 80.
- (9) Written informed consent with one own will.

### Exclusion Criteria

- (1) The patient with active multiple primary cancers; synchronous or metachronous (within 5 years) double cancers .
- (2) The patient with metastatic lesion.
- (3) The patients with severe complications.
- (4)The patients with infection requiring systemic treatment.
- (5) The patient with severe adverse event (>Grade3, CTCAE v4.0) in the BNCT region.
- (6) The patient with cardiac pacemaker.
- (7) The patient judged to have difficulty in maintain posture during the protocol treatment.
- (8) The patient with WBC; < 3000/mm<sup>3</sup>, PLT; < 100000/mm<sup>3</sup>
- (9) The patient with recurrence lesion invasive to carotid artery and to skin.
- (10) Patients with phenylketonuria.

**RESULTS:** We enrolled one patient and undertook BNCT during this period as follows:

Patient #1: 46 y.o. female  
Recurrence of cancer of the external ear  
Histology: squamous cell carcinoma  
Effect: SD  
SAE: none; dermatitis, Grade 2

### CONCLUSION:

We will continue to accumulate the cases carefully to establish a safe and stable treatment of BNCT.

## CO7-15 Anti-tumor evaluation of Gadolinium Neutron Capture Therapy through comparison of tumor size using with polymeric nanocarriers

X. Hou<sup>1,2</sup>, C. Qin<sup>2</sup>, H. Yanagie<sup>1,3,4</sup>, M. Yanagawa<sup>5</sup>, Y. Sakurai<sup>3,4</sup>, K. Mouri<sup>3,4</sup>, Y. Ueda<sup>6</sup>, N. Dewi<sup>4</sup>, H. Cabral<sup>2</sup>, Y. Morishita<sup>7</sup>, T. Kanai<sup>8</sup>, S. Dowaki<sup>8</sup>, T. Nagasaki<sup>8</sup>, Y. Sakura<sup>9</sup>, H. Tanaka<sup>9</sup>, M. Suzuki<sup>9</sup>, S. Masunaga<sup>9</sup> and H. Takahashi<sup>1,2,3</sup>

<sup>1</sup>Dept of Nuclear Engineering & Management, School of Engineering, Univ of Tokyo, <sup>2</sup>Dept of Bioengineering, School of Engineering, Univ of Tokyo, <sup>3</sup>Cooperative Unit of Medicine & Engineering, Univ of Tokyo Hospital, <sup>4</sup>Niigata Univ of Pharmacy & Applied Life Sciences, <sup>5</sup>Obihiro Univ of Agriculture and Veterinary Medicine, <sup>6</sup>Kumatori Veterinary Hospital, <sup>7</sup>Dept of Human & Molecular Pathology, Graduate School of Medicine, The University of Tokyo, <sup>8</sup>Osaka City University Graduate School of Engineering, <sup>9</sup>Institute for Integrated Radiation and Nuclear Science, Kyoto University

### INTRODUCTION:

Neutron Capture Therapy(NCT) is a nonsurgical therapeutic modality for treating locally invasive malignant tumor. Basically, there are boron NCT and Gadolinium NCT. Considering the possibility of MRI-guided GdNCT because gadolinium compound is a kind of MRI contrast agent [1], we focused on GdNCT. However, clinical Gd-chelates lack high and selective accumulation in tumors for electing safe and potent GdNCT [2].

Recently, nanoscale drug becomes more and more popular because it can promote the accumulation of Gd agents in tumor through the enhanced effect of permeability and retention (EPR). Therefore, we built a series of nanocarriers to improve the accumulation in tumor and evaluated its antitumor effect through the comparison of tumor size.

### EXPERIMENTS:

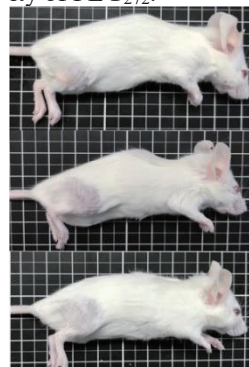
First of all, a series of nanocarriers based on poly(aspartic acid) (P(Asp)) were developed and they were modified with poly(ethylene glycol) (PEG) chains in order to have different molecular weight (Mw). And then, through the introduction of Gd-DOTA, PEG<sub>272</sub>(PEG<sub>272</sub>-P(Asp-Gd-DOTA)) and PEG<sub>454</sub>(PEG<sub>454</sub>-P(Asp-Gd-DOTA)) were made as the final products.

After 24h injection into colon 26 tumor-bearing mice with PEG<sub>272</sub> and PEG<sub>454</sub>, respectively, the tumor-bearing mice received neutron irradiation 60 minutes at Nuclear Reactor Facility of Kyoto Univ Institute for Integrated Radiation & Nuclear Science with average neutron fluence of  $2.0 \times 10^{12}$  n/cm<sup>2</sup>. Moreover, considering the influence of irradiation, we also set the mice injected same samples but without receiving irradiation as controls groups.

After almost one-month observation, the situation of all mice was recorded and the conclusion about antitumor effect was showed below according to the tumor size comparison photos.

### RESULTS:

From the photo of tumor size after one-month observation, we can easily know that compared with the control group, tumor growth was suppressed with the injection of samples and according to the comparison in the control group, the suppression worked not only through the irradiation, but the influence of samples. Especially in the PEG<sub>272</sub> group, the tumor almost disappeared after irradiation which indicated the excellent tumor suppression ability of PEG<sub>272</sub>.



With irradiation(Left)

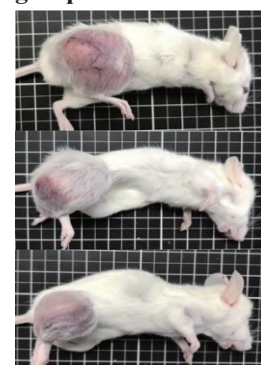


Without irradiation(Right)

PEG<sub>272</sub> group



With irradiation(Left)



Without irradiation(Right)

PEG<sub>454</sub> group



With irradiation(Left)



Without irradiation(Right)

Control group

Table1. Tumor growth suppression by GdNCT using PEG<sub>272</sub> / PEG<sub>454</sub>

### REFERENCES:

- [1] A. Narmani *et al.*, J. Drug Deliv. Sci. Technol., 2018, 44, 457-466.
- [2] H. Tokumitsu *et al.*, Pharm. Res., 1999, 16, 1830-1835.

## CO7-16 Accelerated deterioration assessment of SOF detector under high neutron flux environment

M. Ishikawa<sup>1,2</sup>, H. Handa<sup>2</sup>, K. Baba<sup>2</sup>, K. Takamiya<sup>3</sup> and Y. Sakurai<sup>3</sup>

<sup>1</sup>Faculty of Health Sciences, Hokkaido University

<sup>2</sup>Graduate School of Biomedical Science and Engineering, Hokkaido University

<sup>3</sup>Institute for Integrated Radiation and Nuclear Science, Kyoto University

**INTRODUCTION:** In the conventional BNCT, thermal neutron flux and thermal neutron fluence during treatment could not be measured in real time because gold wire activation was used to evaluate thermal neutron fluence. Therefore, we developed a detector (SOF detector; Scintillator with Optical Fiber Detector) with a plastic scintillator attached to the tip of the optical fiber, tried real-time measurement of thermal neutron flux in neutron capture therapy, and got good results. The long-term stability of the SOF detector and the wide measurement dynamic range (linearity of  $10^4$  to  $10^{10}$  n/cm<sup>2</sup>/s) have been confirmed in previous collaborative experiments. [1,2] However, signal degradation of SOF detector in long-term exposure was reported [3]. The signal degradation might not be a significant problem in case that calibration can be performed before use. However, signal degradation greatly affects measurement accuracy in case of long-term monitoring because calibration prior to use is difficult. In previous experiment performed at last academic year, we tried to identify the causative substance of signal deterioration of the material in the SOF probe, however, it was difficult to specify the caused material because the amount of signal deterioration was not sufficiently large at Heavy Water Neutron Irradiation Facility (HWNIF). Therefore, we conducted a deterioration characteristic assessment in a high flux environment.

**EXPERIMENTS:** The experimental geometry is shown in Fig. 1. The Slant exposure tube (SET) facility SET of KUR was used for irradiation. The SOF detector probes were arranged at about 50 cm above from the bottom of Slant hole where estimated thermal neutron flux was  $4.68 \times 10^{10}$  n/cm<sup>2</sup>/s with 5 MW operation. The combinations of neutron converter and reflectors contained in the irradiated probes are shown in Table 1. All probes used BC490 as a plastic scintillator, and Probes 1 and 2 were mixed with <sup>6</sup>LiF as a neutron converter. Moreover, BC642 (PTFE Reflector Tape) and BC620 (Reflector paint) were used as a reflective material.

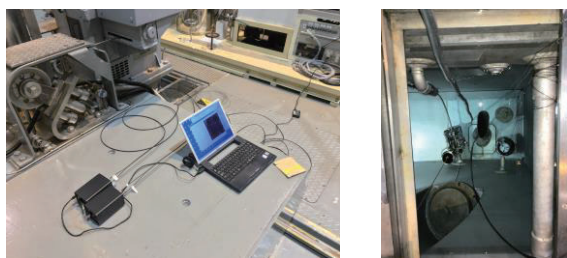
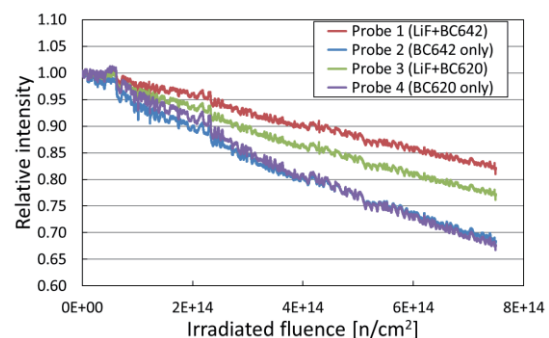


Fig. 1. Irradiation geometry for on-line assessment of deterioration characteristics at Slant exposure tube.

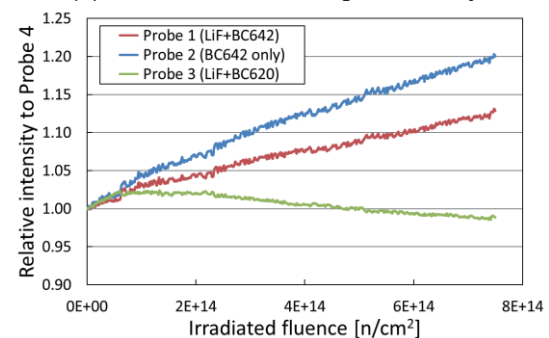
Table 1 Probe characteristics.

Probe	Neutron conv.	Reflector	Slope [%/n·cm <sup>-2</sup> ]
1	<sup>6</sup> LiF	BC642	$-2.38 \times 10^{-14}$
2	-	BC642	$-4.55 \times 10^{-14}$
3	<sup>6</sup> LiF	BC620	$-3.26 \times 10^{-14}$
4	-	BC620	$-4.53 \times 10^{-14}$

**RESULTS:** Figure 2 shows the relative change for each probe from the initial signal intensity at irradiation start. From Fig. 2, the signal intensity is greatly attenuated with the irradiation. The slope of signal deterioration assuming attenuated linearly was shown in Table 2. With respect to the thermal neutron dose of  $10^{14}$  n/cm<sup>2</sup>, it was confirmed that the probe mixed with the neutron converter showed ~3% attenuation, and the probe containing no neutron converter had 4.5% attenuation. Usually, neutron fluence of  $\sim 10^{13}$  n/cm<sup>2</sup> is irradiated in BNCT treatment, so it is estimated that signal deterioration during treatment is less than 0.5%. On the other hand, according to the report of Nakamura *et al.*, the deterioration of the plastic optical fiber is considered to be a major factor because the damage caused by irradiation was reduced by constructing SOF detector probe with a quartz optical fiber.[4] Our result that the signal deterioration was confirmed regardless of the presence or absence of the neutron converter is consistent with the report of Nakamura *et al.*



(a) Normalized at initial signal intensity.



(b) Normalized with probe #4.

Fig. 2. Irradiation geometry for on-line assessment of deterioration characteristics.

### REFERENCES:

- [1] M. Ishikawa *et al.*, Appl. Radiat. Isot., **61** (2004) 775-779.
- [2] M. Ishikawa *et al.*, Nucl. Instr. Meth., A **551** (2005) 448-457.
- [3] M. Komeda *et al.*, Appl. Radiat. Isot., **67** (2009) 254-257.
- [4] T. Nakamura *et al.*, J Radiat. Prot. Res. **41** (2016) 105-109.

Y. Seki<sup>1</sup>, T. Shinohara<sup>1</sup>, Y. Matsumoto<sup>2</sup>, M. Hino<sup>3</sup>, T. Oda<sup>3</sup>

<sup>1</sup>J-PARC Center, JAEA

<sup>2</sup>Comprehensive Research Organization for Science and Society

<sup>3</sup>Institute for Integrated Radiation and Nuclear Science, Kyoto University

**INTRODUCTION:** Neutron phase imaging using the Talbot-Lau interferometer is a method which causes neutron intensity contrast through the phase shift of the neutron wave and produces a visibility image reflecting smaller structures than spatial resolution of imaging system, which are normally detected by USANS method. Therefore, neutron phase imaging is recognized as a special technique not only giving neutron imaging a good sensitivity to a thin or weak neutron-absorbing object but also connecting real space observation and reciprocal space measurements.

We have been developing this imaging technique using pulsed neutrons at “RADEN” in J-PARC MLF [1, 2], and we have started experiments at CN-3 beam port in Kyoto University Reactor (KUR) from 2018, so as to confirm the feasibility applying neutron phase imaging to small/medium flux neutron source facilities. In the previous study, we have succeeded to obtain moire images at the CN-3 beam port by using a portable Talbot-Lau interferometry system, but the exposure time was very long and the resulting visibility was not high enough. In this work, we have prepared a new set of gratings optimized to the neutron spectra of the CN-3 port and introduced a new detector system using a sCMOS camera.

**EXPERIMENTS:** The Talbot-Lau interferometer consists of three gratings (G0, G1, and G2), and the design parameter of these gratings roughly depends on the central wavelength, where visibility becomes maximum, and the distances between gratings. The previous gratings are designed to suit the central wavelength of 5 Å to get good sensitivity against the phase shift, but this design parameter didn't make use of the neutron spectrum at CN-3 beam port. Hence, we have prepared a set of new gratings which is optimized to the CN-3 beam port having the central neutron wavelength of 2.7 Å. In addition, the size of grating was increased to 6 cm x 6 cm to increase the Field of View. The imaging detector was replaced to a system composed of a sCMOS camera (ORCA-Flash4.0 V3, Hamamatsu Corporation) and a <sup>6</sup>LiF/ZnS(Cu) scintillator with the thickness of 200 μm.

The phase imaging experiment was performed by means of “phase-stepping method” in which the G2 grating travels horizontally for a period of the grating with several steps more than 5. Then the intensity profile against the step number was analyzed at each position to produce three images: differential phase image, visibility image and absorption image.

**RESULTS:** At first, we have studied the performance of the new gratings. A moire image was obtained in an exposure time of only 10 sec, while more than 1 min was needed using the previous setup (Fig.1 left). The evaluated visibility was around 42%, which was two times higher than previous one, without severe inhomogeneity (Fig.1 right).

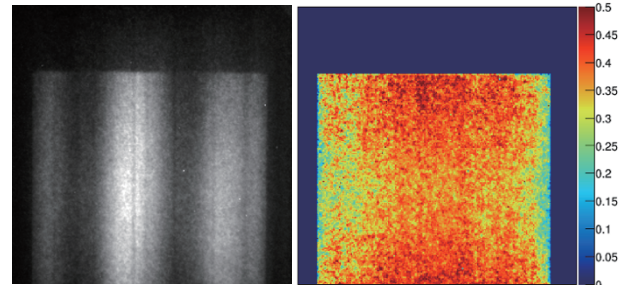


Fig. 1. Moire image obtained with new gratings and detector system (right) and evaluated visibility image by phase-stepping method (left).

Then, we have conducted visibility imaging experiments using this imaging system. Additively manufactured Inconel rods (10mm-φ and 70 mm-L), where one was as-made and the other was annealed, were used as samples. The exposure time for each step was 100 sec and the step number was 8. The obtained visibility images shown in Fig. 2 indicates different contrast between two samples. This result suggests that the micro structure of as-made sample was disappeared due to annealing, this means that the grain structure constructed by additive manufacturing process was homogenized by annealing. Thus, the neutron phase imaging can be applied to study inhomogeneity of microstructures in a metallic object.

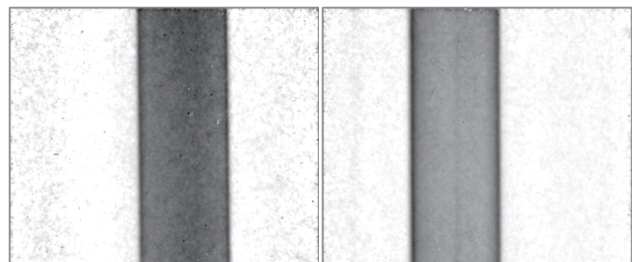


Fig. 2. Visibility images for Inconel sample. Right image is for as-made and left one is for annealed sample.

**ACKNOWLEDGEMENT:** This work was supported by JST ERATO Momose Quantum Beam Phase Imaging Project, Grant Number JPMJER1403. We would like to thank Dr. T. Samoto of Tohoku University for the fabrication of gratings used in this study.

**REFERENCES:**

- [1] T. Shinohara *et al.*, Rev. Sci. Instr., **91** (2020) 012007.  
 [2] Y. Seki *et al.*, EPL, **123** (2018) 12002.

## CO8-2 Study on the Visualization of Organic Matter between Metals to Contribute to the Advancement of the Industrial Products

K. Hirota, H. M. Shimizu<sup>1</sup>, M. Kitaguchi<sup>1</sup>, Y. Tsuchikawa<sup>1</sup>, N. Yamamoto<sup>1</sup>, A. Uritani<sup>2</sup>, K. Watanabe<sup>2</sup>, S. Yoshihashi<sup>2</sup>, A. Yamazaki<sup>2</sup>, D. Ito<sup>3</sup> and Y. Saito<sup>3</sup>

RCNP, Osaka University

<sup>1</sup>Graduate School of Science, Nagoya University

<sup>2</sup>Graduate School of Engineering, Nagoya University

<sup>3</sup>Institute for Integrated Radiation and Nuclear Science, Kyoto University

**INTRODUCTION:** Mechanical and industrial products such as automobiles and aircraft are progressing with higher performance and higher accuracy in Japan. One of the demands at the development site of these state-of-the-art products is a visualization of the state of organic materials (oil film, grease, electrolyte, etc.) existing between metals, which can not be seen directly by our eyes. In this research, we will explore the possibility of observing the dynamic state of the organic materials (shape, properties, thickness distribution) and its dynamic change mainly between automobile parts as an example.

At present Nagoya University is constructing an accelerator-driven small neutron source (NUANS) and neutron radiography ports [1]. We are planning an in-site measurement of the fuel cell during power generation. And we are also proceeding with the quantitative evaluation of the CCD output image. This year, we produced a neutron camera for radiography to be used at NUANS, so we evaluated its performance in KUR E2 port.

**EXPERIMENTS:** In fuel cell development, the elimination of water from the electrode during power generation is a very important issue. In order to visualize the movement of minute water in the transmission image, we constructed a new evaluation software. Images were acquired for the evaluation of the constructed software. A groove with a width of 1 mm is made on an aluminum plate, and neutrons are irradiated in the state of accumulating water to acquire the image. Next, the movement of the water was simulated by moving this plate. The results obtained are shown in Fig. 1. In this figure, the aluminum plate is moving upward at 10 mm/s. The water image can be seen only at the first and last places, and is almost invisible while moving. When the moving speed is set to 2 mm / s, the water images appear to be continuous. In this way, we can understand the relationship between water movement and visualization.

**FOCUS ADJUSTMENT:** Focusing work is very important to visualize a fine image, but in neutron transmission image measurement, this work usually confirms the focus position by taking multiple images and comparing them by human eyes. The focus position is depending on the person who works and the measurement conditions. To obtain the same result irrespective of the person who performed it, it was decided to evaluate the focus adjustment quantitatively. For focus adjustment, it is necessary to perform edge extraction on the acquired image. The image obtained by the CCD camera is subjected to a noise filter for removing the CCD element error and an FFT (Fast Fourier transform) filter for removing the neutron intensity distribution dependency, and then the second derivative of the space (Laplace calculation). Since the Laplacian filter is easily affected by noise, it is necessary to eliminate noise such as dot filtering using a noise filter. Focus adjustment by this edge extraction method was able to determine the focus position correctly. In addition, the neutron irradiation time required for this work is two digits shorter or more than that when it is identified by human eyes. It may be possible to build an autofocus function in the future.

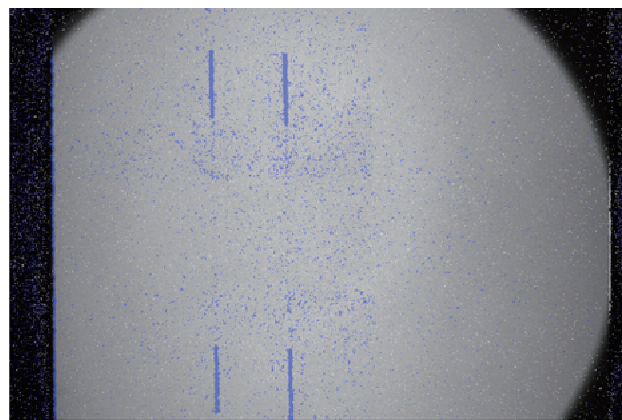


Fig. 1. Measurement of the water motion.

### REFERENCES:

- [1] K.Hirota, *et al.*, EPJ Web of Conf. **231**(2020)05002.

## CO8-3 Measurements of multiphase flow dynamics using neutron radiography

Y. Saito and D. Ito

*Institute for Integrated Radiation and Nuclear Science,  
Kyoto University*

**INTRODUCTION:** Neutron radiography (NRG) is a powerful tool for multiphase flow visualization as well as ordinary fluid dynamics. As one of the applications of NRG, gas-liquid two-phase flows in a metallic pipe have been clearly visualized by using NRG. However, the measurement accuracy of thin liquid film formed in such two-phase flows has not been fully evaluated. The liquid film thickness is one of the important parameters to investigate the two-phase flow behavior. In this work, our neutron imaging system has been modified to realize more sophisticated flow visualization and precise measurements of thin liquid film.

**DEVELOPMENT OF HIGH-SPEED NEUTRON IMAGING SYSTEM:** A high-speed neutron imaging system for flow visualization has been developed at the B-4 supermirror neutron guide facility [1] of the Institute for Integrated Radiation and Nuclear Science, Kyoto University. This imaging system consists of a neutron converter, a dark box with a single mirror, an ultrasensitive lens, an optical image intensifier and a high-speed camera. The high frame rate up to 10,000 frame/sec could be achieved using above-mentioned combination at the B-4 port [2]. The pixel resolution and frame rate can be adjusted by selecting the optics.

**VISUALIZATION OF SIMULATED THIN FILM:** Neutron imaging experiments were conducted at the E-2 port of the Kyoto University Research Reactor. In this port, the neutron flux is  $1 \times 10^5$  n/cm<sup>2</sup>s, and the beam size is 15 cm in diameter. CCD camera system was employed, and the static film thickness was estimated from the neutron transmission images. As a preliminary work, the liquid film formed in two-phase flows was simulated by the thin polyimide sheet and the thickness was varied from 75  $\mu$ m to 250  $\mu$ m. The polyimide has the macroscopic neutron cross-section of 1.3cm<sup>-1</sup>. The film sample and rotation stage are shown in Fig.1. The angle of the polyimide film was set at 0~75 degrees. The neutron transmission images of the polyimide film with the thickness of 250  $\mu$ m are shown in Fig.2. At smaller angle conditions, there is little change in the transmission. However, at the angle of 75 degrees, the neutron attenuation changes obviously. The mean value of the neutron transmission in the polyimide film area is plotted in Fig.3, and they are compared with the results of geometric calculation. Most of the results show good agreement, however, some measured results with the transmission values larger than 0.98 depart from the calculation results. It would be suggested that the estimation of very thin film should be a challenging problem in present neutron imaging technique. In the next step, the measure-

ment error in the film thickness shall be quantitatively estimated by improving the imaging system and processing method.



Fig. 1 Sample and rotation stage.

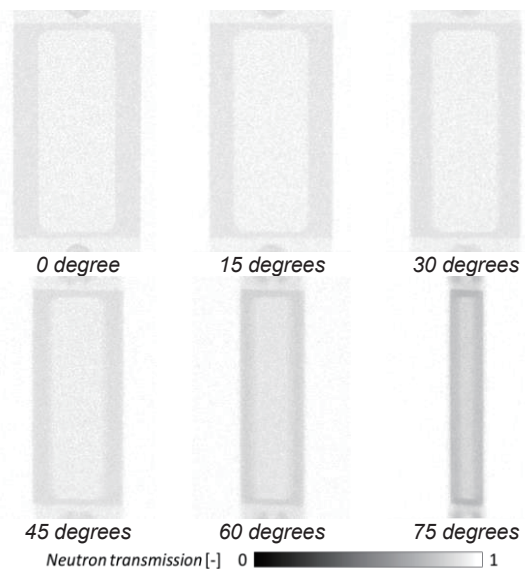


Fig. 2 Neutron transmission images of polyimide sheet ( $\delta = 250 \mu$ m).

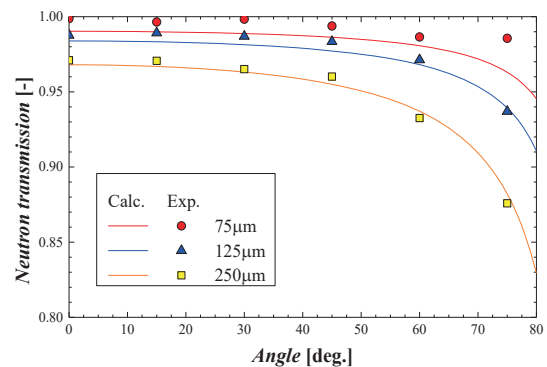


Fig. 3 Angle dependence of neutron transmission.

### REFERENCES:

- [1] Y. Saito, *et al.*, Nucl. Instr. Meth. Phys. Res., A, **651** (2011) 36-41.

K. Shimizu<sup>1</sup>, H. Toda<sup>2</sup>, K. Hirayama<sup>2</sup>, H. Fujihara<sup>2</sup>, D. Ito<sup>3</sup>, Y. Saito<sup>3</sup>

<sup>1</sup>Department of Physical Science and Materials Engineering, Iwate University

<sup>2</sup>Department of Mechanical Engineering, Faculty of Engineering, Kyushu University

<sup>3</sup>Institute for Integrated Radiation and Nuclear Science, Kyoto University

**INTRODUCTION:** It is widely recognized that hydrogen in metallic materials degrades the mechanical properties of the materials. Various hydrogen embrittlement mechanisms, such as HELP, HEDE and HESIV have been proposed to date [1], but there is still no comprehensive interpretation. However, for each mechanism, it is consistent that hydrogen trapping and the resulting localization of hydrogen to defects and microstructures are the dominant factors of hydrogen embrittlement [2]. To understand the hydrogen embrittlement, it is necessary to visualize the hydrogen distribution and to elucidate its evolutionary behavior over time. In this study, hydrogen in a metal was visualized by neutron radiography and tomography, and hydrogen accumulation under stress was assessed. Several palladium specimens with different hydrogen contents were prepared and a notch was introduced. It has been demonstrated that hydrogen content can be analyzed by neutron tomography, and the possibility of evaluating hydrogen accumulation under stress is discussed.

**EXPERIMENTS:** Palladium specimens with hydrogen contents of 0 at%, 10 at%, and 20 at% were prepared for neutron imaging. Hydrogen content was controlled by high temperature hydrogen exposure. Neutron radiography was performed on the KUR E-2 port [3]. The imaging system consists of a <sup>6</sup>LiF:ZnS visible light converter and a cooled CCD detector. The exposure time was set to 5 min at a thermal power of 1 MW in the research reactor. Neutron tomography was also performed at the KUR E-2 port. A rotating stage for tomographic observation was added to that of radiography. Neutron transmission images were obtained by rotating the specimen from 0 to 180° in 1° increments. Total 180 images were reconstructed in a 3D image using a convolutional back projection algorithm.

**RESULTS:** Fig. 1 shows tomographic cross-sectional images of the central part of specimens before and after tensile loading. Fig. 1(d) shows the profile of CT value obtained from the white lines in Fig. 1(a-c). The contrast between 0%H and 10%H at no load indicates that the difference in hydrogen content can be evaluated from image contrast as well as the transmission image. On the other hand, no hydrogen accumulation was observed when comparing before and after tensile loading at 10% H. The location of  $x = 3$  mm in Fig. 1(d) corresponds to the notch tip of specimen, but the change in hydrogen

content before and after loading could not be measured even in the line profile. This was true not only at the center of specimens shown in Fig. 1(a-c), but also near the surface. The notch opening displacement was measured to be about 510  $\mu\text{m}$ . The plastic zone size of the notch tip was calculated to be about 220  $\mu\text{m}$  by estimating the applied stress of the specimen from the opening displacement. It is inferred that the hydrogen accumulation is remarkable in this region. The measured tomographic image has a resolution of about 400  $\mu\text{m}$ . This suggests that hydrogen accumulation was not visualized in Fig. 1(c) and (d), because of accumulation region was smaller than 400  $\mu\text{m}$ . It is expected that short-time 3D imaging with a spatial resolution of 200  $\mu\text{m}$  is available by upgrading the imaging system. Using this system, 3D/4D analysis of hydrogen accumulation behavior will be revealed by neutron tomographic observation.

### REFERENCES:

- [1] I. M. Robertson *et al.*, Metall. Mater. Trans. A 46 (2015) 1085-1103.
- [2] Z. Zhang *et al.*, Acta. Mater. 113 (2016) 272–283.
- [3] Y. Saito *et al.*, J. Jpn. Soc. Precis. Eng. 79 (2013) 822–825.
- [4] K. Shimizu *et al.*, J. Japan Inst. Met. Mater. 83 (2019) 434–440.

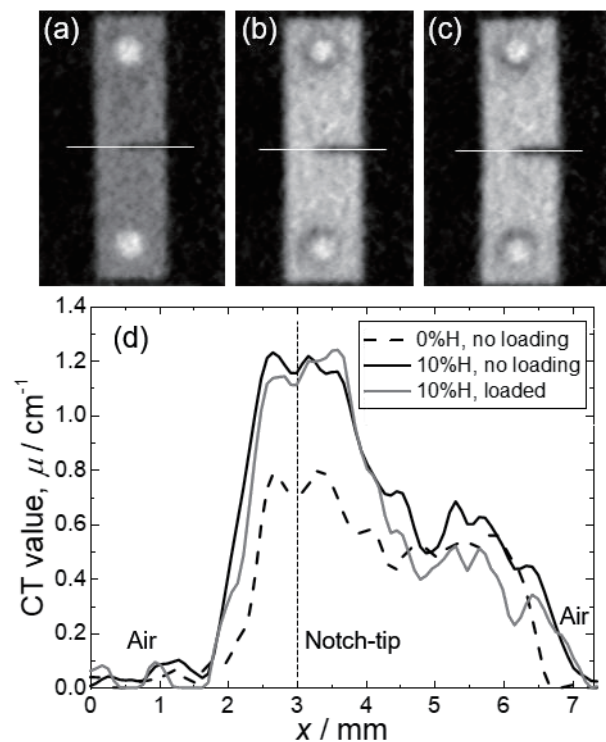


Fig. 1. Virtual cross-sections of the 3D neutron tomographic images; (a) palladium without hydrogen, (b) that with 10 % hydrogen, and (c) that with 10 % hydrogen after loading. (a) and (b) were observed without loading. (d) Line profiles obtained from the white solid lines in (a-c).

H. Asano, H. Murakawa, R. Moriyasu, S. Inoue, K. Sugimoto, D. Ito<sup>1</sup> and Y. Saito<sup>1</sup>

Department of Mechanical Engineering, Kobe University  
<sup>1</sup> Institute for Integrated Radiation and Nuclear Science, Kyoto University

**INTRODUCTION:** Microchannel compact heat exchangers are paid attention for the compactness and reduction in temperature difference between fluids. Since smaller diameter leads to larger pressure loss, micro channel heat exchanger has many parallel channels. Therefore, in the case that the heat exchanger is used for evaporator, refrigerant flow distribution often causes a deterioration in the heat transfer performance. In this study, boiling flow behaviors in a single layer microchannel heat exchanger had been visualized by neutron radiography, and void fraction distributions had been measured from the radiographs.

**EXPERIMENTS:** The tested heat exchanger was manufactured by diffusion bonding of thin stainless steel plates, and consists of single-layer refrigerant and heating medium parallel channels. The channel cross-section and flow arrangement are shown in Fig. 1 and 2, respectively. HFC-134a and FC3283 were used as the refrigerant and

the heating medium, respectively. The number of channels are 21 for the refrigerant and 20 for the heating medium. Each channel has semicircular cross-section. The heat exchanger was placed in vertical plane to form vertically upward boiling flows of the refrigerant. To avoid maldistribution of refrigerant flows, two kinds of divided ribs, such as perforated and offset types, as shown in Fig. 3 are used. Radiographs were recorded by a cooled CCD camera with the exposure time of 30 seconds and the pixel size of 88 μm/pixel.

**RESULTS:** Void fraction was measured for each pixel of visualized images, and the distributions for the test sections with the straight parallel channels, the perforated and offset type channels of refrigerant are shown in Fig. 4 (a) to (c), respectively. It can be clearly observed that the void fraction on the right side close to the heating medium inlet was higher than the left side due to the larger temperature difference. It was seemed that void fraction distribution became more homogeneous for the perforate rib. In this case, the inlet condition of refrigerant was a subcooled liquid. The onset of boiling might affect the flow distribution. For the perforated type, the holes through the ribs might help bubble nucleation and development of two-phase flows.

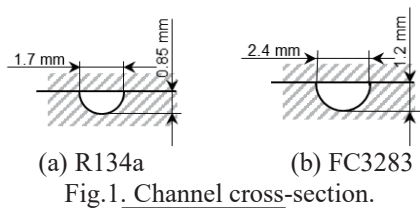


Fig. 1. Channel cross-section.

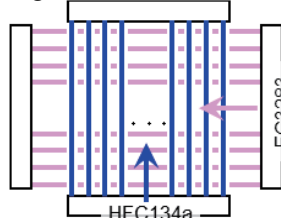
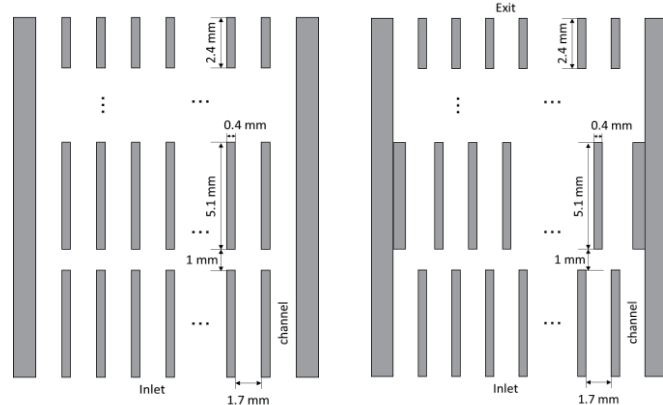
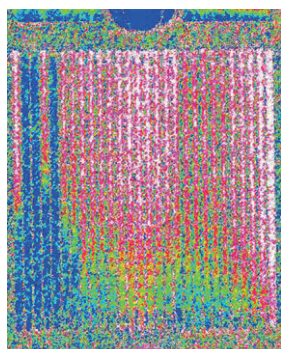


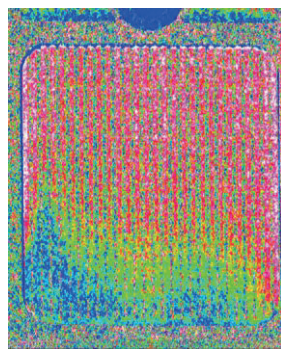
Fig. 2. Flow arrangement.



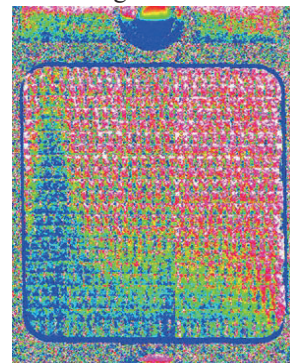
(a) Perforated type (b) Offset type  
 Fig. 3. Rib pattern in refrigerant channel.



(a) Straight parallel channels



(b) Perforate rib



(c) Offset rib

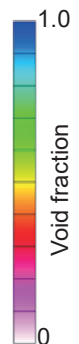


Fig. 4. Void fraction distributions (mass flux : 150 kg/(m<sup>2</sup>·s) for R134a, 920 kg/(m<sup>2</sup>·s) for FC3283, inlet temperature : 50 °C for FC3283) .

H. Murakawa, S. Torii, K. Mine, K. Sugimoto, H. Asano, D. Ito<sup>1</sup> and Y. Saito<sup>1</sup>

Graduate School of Engineering, Kobe University

<sup>1</sup>Institute for Integrated Radiation and Nuclear Science, Kyoto University

**INTRODUCTION:** Water management is a key topic of a polymer electrolyte fuel cell (PEFC). If condensed water exists in the gas diffusion layer (GDL) and the gas channel, it may depress the gas diffusion as flooding. Furthermore, loss in electric power generation in PEFCs is due to resistances such as ionic, activation, concentration, etc. Many of these resistances are related to the mass transport in the PEFC. To evaluate the resistances in a PEFC, electrochemical impedance spectroscopy (EIS) has been widely used [1]. However, the effect of water in the PEFC on the resistances has not been fully understood. Aim of this study is to clarify the effect of water in the PEFC on the resistances. Simultaneous measurements of the water distribution and the electrical impedance were carried out by using neutron radiography and EIS. Changes in water accumulation in the PEM and the GDL were compared with the resistances.

**EXPERIMENTS:** A small size PEFC having a single-serpentine gas-channel with cross-sectional area of  $1 \times 1 \text{ mm}^2$  was used for measuring two-dimensional water distribution and the electrochemical characteristics. Nafion® NR-212 was used as the PEM with a thickness of approximately  $90 \text{ }\mu\text{m}$  having catalyst layers on both the anode and cathode sides. The GDL was carbon paper (Toray Ind.) with thickness of  $190 \text{ }\mu\text{m}$  at the cathode side and  $280 \text{ }\mu\text{m}$  at the anode side. The porosity of the GDL was approximately 78%. Two-dimensional water distributions were obtained every 60 sec during the PEFC operation. The EIS measurements were simultaneously carried out with the neutron radiography for evaluating the PEM resistance and the reaction resistance,  $R_{CT}$  [ $\Omega$ ]. The hydrogen and air flow rates were 84 and 196 cc/min, respectively. The experiments were carried out at room temperature, while the temperature of the PEFC varied between  $25 - 30 \text{ }^\circ\text{C}$ .

**RESULTS:** Two-dimensional water distributions at current density  $i = 316$  and  $500 \text{ mA/cm}^2$  are compared in Fig. 1. Measurement area is between 4<sup>th</sup> and 6<sup>th</sup> channels, and the top channel in the figure is the upstream position. Liquid water accumulation during the PEFC operation can be confirmed as indicated by the gray-scale. The time represents the elapse time from the power generation. Amounts of water accumulation in the GDL under the lands and channels are different and a large amount of water existed under lands at the earlier results. It indicated that water accumulation is started under the lands. Then, liquid water reaches channel and are particularly concentrated on the land corners. Difference of the water

distributions at 9 and 15 min is not significant for  $i = 316 \text{ mA/cm}^2$ . Therefore, it can be confirmed that the water distributions are almost steady states after 9 min. On the other hand, water gradually accumulated in the channel for  $i = 500 \text{ mA/cm}^2$ . The water accumulation at downstream channel, *i.e.* 6<sup>th</sup> channel, is greater than that at 4<sup>th</sup> channel. This is because the relative humidity becomes higher at downstream position, and the water accumulation is easy to occur.

Fig. 2 represents change of the reaction resistance,  $R_{CT}$ .  $R_{CT}$  gradually decreases until 15 min at  $i = 316 \text{ mA/cm}^2$ . For  $i = 400 \text{ mA/cm}^2$ ,  $R_{CT}$  gradually decreases until 9 min, and it became almost constant after the time. Furthermore, it gradually increases after 2 min for  $i = 500 \text{ mA/cm}^2$ . As confirmed from the water distribution, the much water accumulation was confirmed in the channel. This prevent the water supply to the GDL resulting in increases of the concentration resistance. However, the effect was not significant although water accumulation was clearly confirmed in the channels at 15 min for  $i = 500 \text{ mA/cm}^2$ .

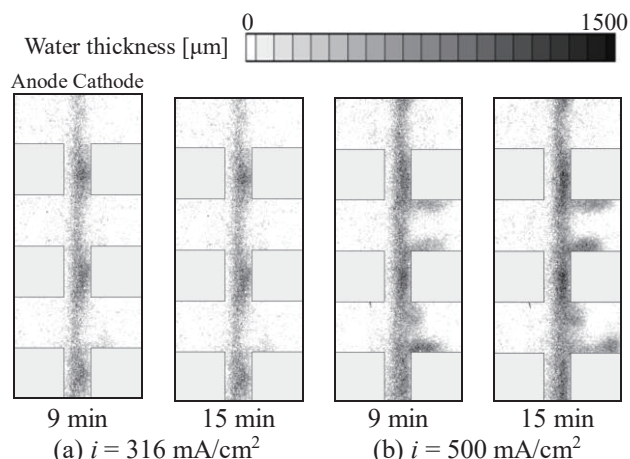


Fig. 1. Two-dimensional water distributions.

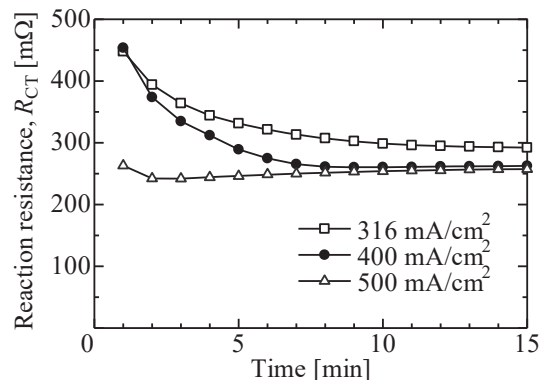


Fig. 2. Time-series of the reaction resistances.

### REFERENCES:

- [1] E. Antolini, *et al.*, J. Power Sources, **77** (1999) 136-142.

## CO8-7 Meltwater Behavior During the Defrosting Process by using Neutron Radiography

R. Matsumoto, T. Shiokawa<sup>1</sup>, Y. Nishiura<sup>1</sup>, T. Makihara<sup>1</sup>, D. Ito<sup>2</sup> and Y. Saito<sup>2</sup>

Faculty of Engineering Science, Kansai University  
<sup>1</sup>Graduate School of Science and Engineering, Kansai University  
<sup>2</sup>Institute for Integrated Radiation and Nuclear Science, Kyoto University

**INTRODUCTION:** The frost formation on heat exchanger causes serious problem to the heat transfer performance by thermal resistance between the cold surface and the humid ambient air. Defrosting is important to keep the heat transfer performance of the heat exchanger. The defrosting operations were carried out periodically by the reverse cycle on the air conditioning systems, or the electrical heating on the domestic refrigerators. The frost layer has a micro porous structure with ice crystals and air pores. The meltwater penetrates into the remaining frost layer by the capillary effect through the micro porous. In this study, the meltwater behavior on the aluminum plate-fin-tube heat exchanger was measured by using neutron radiography. The water deposition distribution on the heat exchanger was estimated quantitatively by neutron beam attenuation during the defrosting period.

**EXPERIMENTS:** Fig.1 shows the schematic view of the experimental apparatus. Cooled humid air adjusted to the flow rate 70 L/min was supplied to the test section. The test section consisted of styrofoam block duct with a cross section of 68 mm x 25 mm and the aluminum plate fin-tube heat exchanger. The heat exchanger consisted by 6 fins with 60 mm in height, 28 mm in width, 0.25 mm in thickness, and together with two tubes of an outer 8.5 mm. Fig.2 shows the aluminum heat exchanger used in this experiment. Fin pitch was 5 mm. On the frosting process, the heat exchanger was cooled by circulating the -25 °C fluorinert for 66 min. After the frost formation, the air flow was stopped, and the coolant flow was switched to 1°C coolant for defrosting. The water deposition on the heat exchanger was observed by CCD camera (Princeton Inst., 16-bit, 1024 × 1024 pixels) with image intensifier (Toshiba Electron Tubes & Dev., E5830NE-P4K). Exposure time is 0.15sec. The procedure of the image processing is referred to ref.[1].

**RESULTS:** Fig.3 shows the water deposition on the heat exchanger during the defrosting process. The main flow direction is right to left in Fig.3. Fig.3(a) shows the frost formation just before the defrosting. Frost was formed almost uniformly on the fin surface except the wake area of the tubes. In Fig.3(b) at 1min53sec from starting the defrost, frost near the tubes are melted and the meltwater penetrated into the remaining frost layer. In Fig.3(c) at 3min2sec, the frost melting spreads around the tubes, and the meltwater is hold in the remaining frost layer at the leading edge of fins. In Figs.3(d) and (e), meltwater flows down to the bottom of the heat exchanger due to the water saturation in frost layer. Finally, the meltwater is discharged from the bottom of the fin, and no melted water remains on the fin surface. This results suggested the smooth removal of the meltwater by the water penetration into the remaining frost layer.

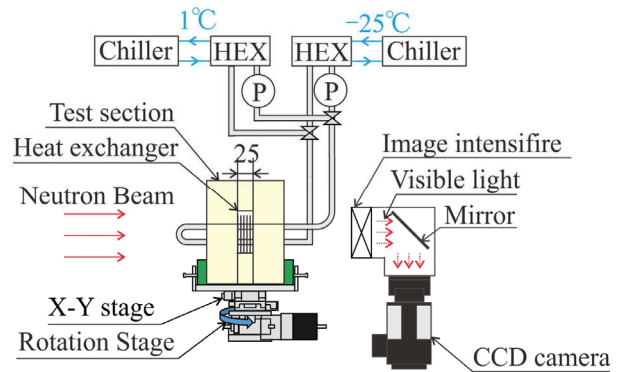


Fig.1. Schematic view of the experimental apparatus.

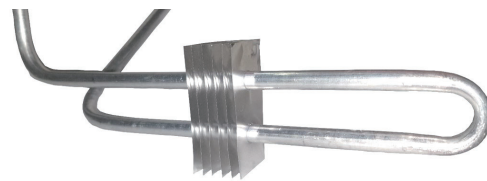


Fig. 2. Plate-fin tube heat exchanger.

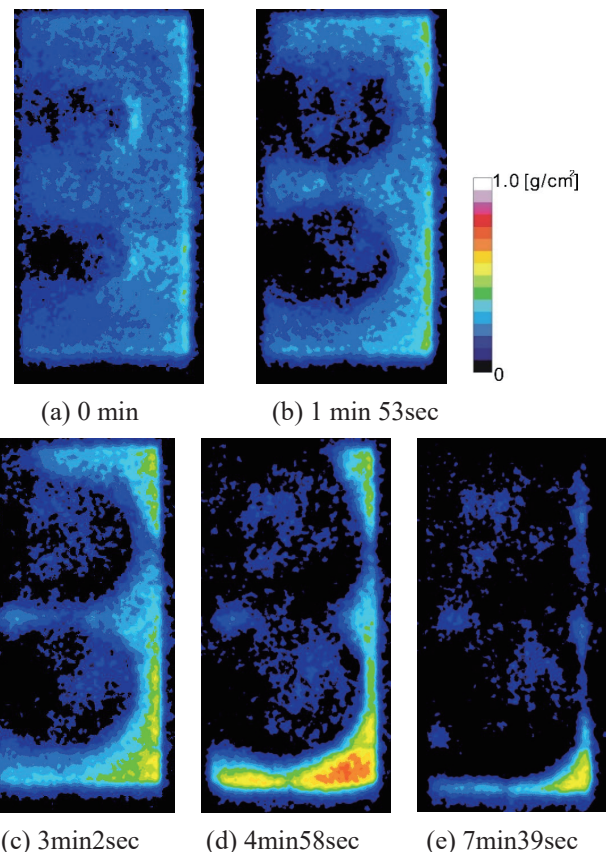


Fig.3. Meltwater behavior in defrosting process.

### REFERENCE:

[1] R. Matsumoto, *et al.*, Proceedings of the International Heat Transfer Conference IHTC-15, IHTC15-9144, Kyoto, pp. 3603-3615.

## CO8-8 Flow visualization of heavy oil in supercritical water using neutron radiography

T. Tsukada, M. Kubo, E. Shoji, N. Ito, T. Kaneko, S. Kodaira, S. Takami<sup>1</sup>, K. Sugimoto<sup>2</sup>, D. Ito<sup>3</sup>, Y. Saito<sup>3</sup>

*Dept. of Chemical Engineering, Tohoku University*

<sup>1</sup> *Dept. of Materials Science and Engineering, Nagoya University*

<sup>2</sup> *Dept. of Mechanical Engineering, Kobe University*

<sup>3</sup> *Institute for Integrated Radiation and Nuclear Science, Kyoto University*

**INTRODUCTION:** With an increase in the demand for petrochemical feedstock and middle distillate, utilization of heavy oil such as atmospheric or vacuum residue is also necessary. Since the heavy oil has high viscosity and its quality is low, desulfurization and upgrading processes are required to use the heavy oil effectively. In such a situation, upgrading process using supercritical water has been proposed and studied recently.

Understanding of flow behavior of heavy oil in reactors filled with supercritical water is important to improve the performance of upgrading process. However, the phenomena are too complicated to simulate numerically. Since, in experiment, the reactor is made of metal for operation at high pressure and high temperature, the visualization using visible light is not available. Thus, the numerical simulation and experimental flow visualization of heavy oil flow in supercritical water have not been conducted. In our previous study [1], we have visualized the heavy oil flow in a trickle bed reactor under N<sub>2</sub> atmosphere using neutron radiography, and indicated the potential of neutron radiography to investigate the flow behavior of heavy oil. Therefore, as a next step, the visualization of the heavy oil behavior in supercritical water by neutron radiography was carried out, continuing from last year.

**EXPERIMENTS:** In neutron radiography for the flow visualization of heavy oil in supercritical water, the Kyoto University Research Reactor (KUR) was utilized as neutron source. A series of neutron radiography experiments was conducted with a thermal neutron flux of  $8.5 \times 10^7$  n/(cm<sup>2</sup>·s).

The reactor consists of a 1/2-inch stainless steel tube filled with Al<sub>2</sub>O<sub>3</sub> particles with a diameter of 3 mm. The heavy oil, i.e., atmospheric residue (AR), was supplied to a reactor from above with the flow rates of 2.5 or 5.0 g/min. On the other hand, the water was supplied counter-currently with the flow rates ranged from 0.05 to 7.5 g/min. The reactor was heated to temperatures of 400°C and was operated at 25 MPa.

An image intensifier and a camera at the framerate of 30 fps were used to obtain radiography images of the unsteady flow behavior. An image processing to reduce noises and to calculate neutron attenuation was performed for the obtained radiography images.

**RESULTS:** The flow behavior of heavy oil in the reactor varied depending on the experimental conditions

were visualized using neutron radiography. Fig. 1 shows the time variation of flow behavior of heavy oil in supercritical water at the flow rates of heavy oil ( $\omega_o$ ) and water ( $\omega_w$ ) were 2.5 g/min and 0.05 g/min, respectively.

Fig. 2 shows the variations in the area-averaged neutron attenuation ( $\overline{\mu\rho d}$ ) over time, which were calculated over the 8 mm (40 pixels) × 40 mm (200 pixels) area shown in the inset of Fig. 2 under the four experimental conditions. The area-averaged neutron attenuation increased with time and reached a constant value under all the tested conditions. The time required to reach a constant attenuation became longer with increasing supercritical water flow rate, particularly at  $\omega_o = 2.5$  g/min. In addition, Case D shows the increase in the attenuation after 40 s due to the upward flow of heavy components of oil from the bottom of the reactor.

**CONCLUSION:** The results obtained by neutron radiography showed that the flow behavior of heavy oil in the packed bed reactor under supercritical water environment depends on the flow rates of heavy oil and supercritical water.

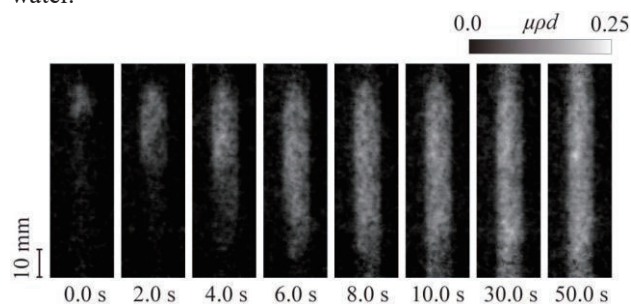


Fig. 1: Flow behavior of heavy oil in supercritical water when the flow rates of heavy oil and water were 2.5 g/min and 0.05 g/min, respectively.  $\mu$ ,  $\rho$ , and  $d$  are mass attenuation coefficient of thermal neutrons [m<sup>2</sup>/kg], density of heavy oil [kg/m<sup>3</sup>], and thickness along the neutron beam direction [m].

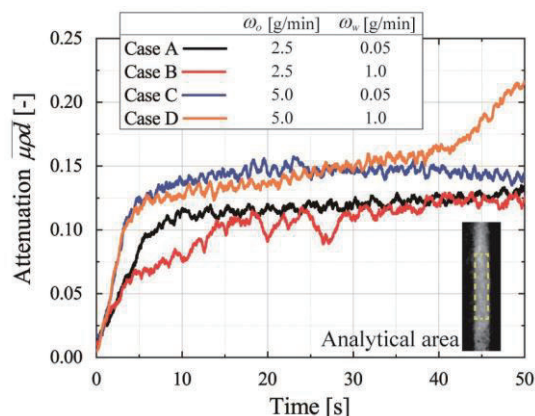


Fig. 2: Time variations of area-averaged neutron attenuation.

## REFERENCES:

[1] E. Shoji *et al.*, Chem. Eng. Sci., **196** (2019) 425-432.

## CO8-9 Analysis of moisture transfer in high-strength concrete embedded rebar exposed to fire

M. Kanematsu<sup>1</sup>, Y. Nishio<sup>1</sup>, A. Miyabe<sup>1</sup>, K. Kobayashi<sup>1</sup>, K. Ueno<sup>1</sup>, D. Ito<sup>2</sup>, Y. Saito<sup>2</sup>, T. Noguchi<sup>3</sup> and M. Tamura<sup>3</sup>

<sup>1</sup>Department of Architecture, Tokyo University of Science

<sup>2</sup>Institute for Integrated Radiation and Nuclear Science, Kyoto University

<sup>3</sup>Department of Architecture, The University of Tokyo

**INTRODUCTION:** RC structure is fireproof structure, but explosion phenomenon, so called spalling, might occur when subjected to fire especially at high-strength concrete. Thermal stress and water vapor pressure in concrete seems to be the main causes of spalling, therefore, to capture detailed moisture movement in concrete under fire is important to clarify the mechanism of spalling [1]. However, the detailed mechanism of spalling has not been fully understood. In this research, focusing on concrete made of different type of aggregate and on with or without embedded reinforcing bar, we applied neutron radiography (NR) to verify moisture transfer in concrete exposed to fire in order to understand the spalling phenomenon of high strength concrete. We also tried to obtain X-ray transmission images simultaneously.

**EXPERIMENTS:** Concrete specimens (70×100×30 mm<sup>3</sup>) with W / B of 18% were prepared. In some of them, a single rebar (D10, 120mm) with a thermocouple was embedded at 20mm from the bottom surface (Fig.1). The initial relative water content of concrete was about 90%. Graywacke from Ome or limestone from Sano was used for each sample as coarse aggregate. In this experiment, the specimens were heated at the bottom surface with a Bunsen burner. Temperatures in specimen were measured by thermocouples installed in the holes at the position of 10 and 20 mm from the heating surface or attached with rebar. NR was performed at TNRF in the B-4 port of KUR. The angle of view of CCD camera was 100 × 100 mm, and the spatial resolution was about 0.1 mm / pixel.

**RESULTS:** As shown in Fig. 2, 2 dimensional moisture movement in concrete can be successfully observed. This result shows that embedded rebar can suppress dryness at the backside of concrete, and be apt to condense water and form moisture clog near the heating surface. Comparing the difference in aggregate as shown in Fig.3, concrete of graywacke was apt to condense moisture amount at 10mm depth from the heating surface. However, the time spalling occurred didn't match the time when moisture condensation observed, therefore, further study is needed to clarify the relationship between spalling and moisture movement in concrete.

### REFERENCES:

[1] JCI, (2017). "Committee Reports:JCI-TC-154A"

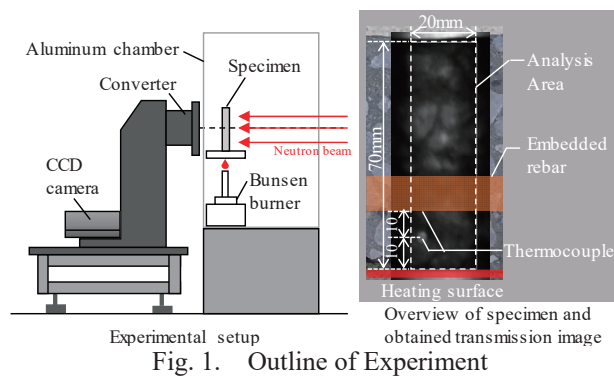


Fig. 1. Outline of Experiment

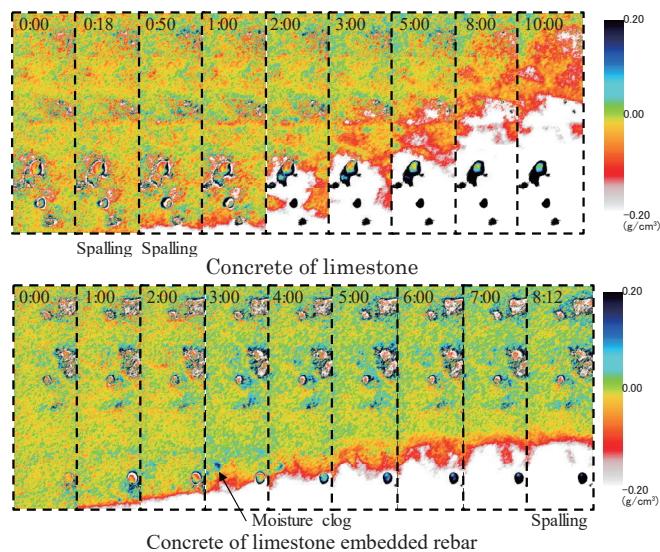


Fig. 2. Relationship between moisture distribution and heating time

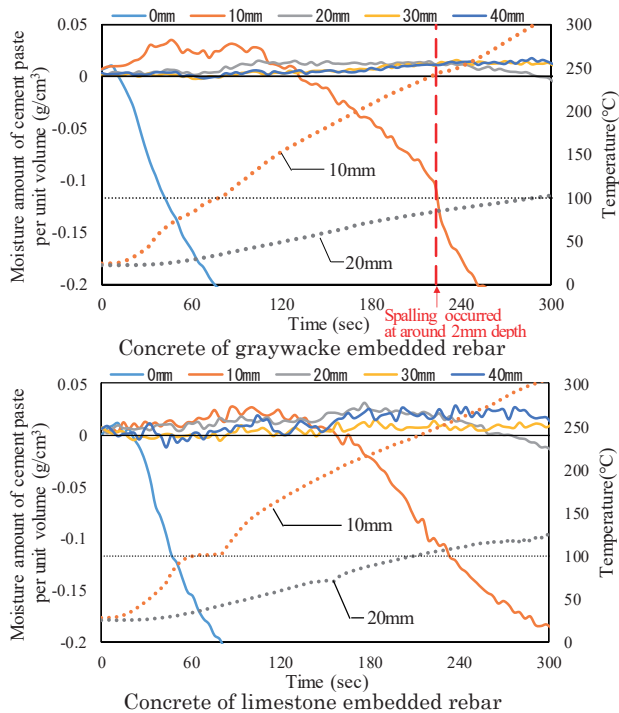


Fig. 3. Moisture and temperature profile evolution at different depths from the heating surface.

## CO8-10 Development of capillary-plate-based fluorescent plates for neutron radiography

T. Sakai<sup>1</sup>, K. Kurita<sup>1</sup>, H. Iikura<sup>1</sup>, D. Ito<sup>2</sup>, Y. Saito<sup>2</sup>

<sup>1</sup>Materials Sciences Research Center, Japan Atomic Energy Agency

<sup>2</sup>Institute for Integrated Radiation and Nuclear Science, Kyoto University

**INTRODUCTION:** Fluorescent plates are widely used for neutron radiography. In the case of the imaging devices, the spatial resolution of fluorescent plates conflicts with their detection efficiency. In general, a thicker phosphor layer increases the efficiency, but adversely affects the resolution because of blurring [1]. In this work, we developed a new approach to fabricate micro-structured fluorescent plates. The devices consist of capillary plates and fine phosphor grains [2]. Herein, we introduce the adding neutron sensitivity to the fine fluorescent plates for neutron imaging device.

**EXPERIMENTS:** The capillary plate is made from borosilicate glass. The specifications of the plates are as follows: plate thickness, 0.4 mm; diameter of each capillary, 25  $\mu\text{m}$ ; pitch of each hole, 31  $\mu\text{m}$ ; open area ratio, 59 %; diameter of effective area, 20 mm. The phosphor grains were sifted silver-activated zinc sulfide (ZnS:Ag) with a mean particle size of approximately 7  $\mu\text{m}$  [1, 2]. The plates are impregnated with <sup>10</sup>B-enriched orthoboric acid to add neutron detection sensitivity. The method of impregnation is shown in Fig. 1.

1) The plate is put on a petri dish.

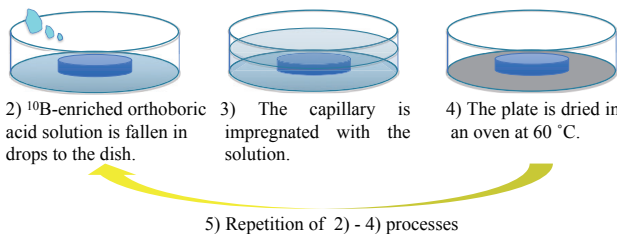
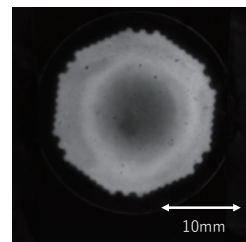


Fig. 1. Schematic of the orthoboric acid impregnation method.

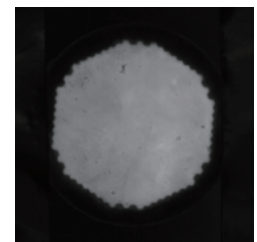
The neutron imaging experiments were performed at KUR E-2. The images were collected using a CCD camera, and the results are indicated in Fig. 2.

**RESULTS:** Neutron induced fluorescence is clearly observed, however the uniformity differs according to the drying time. Fig.2 (a) and (b) show that 1 hour drying times seems to be enough, but 20 minutes drying is not enough. The repetition times of impregnation increase neutron sensitivity as shown in Fig.2 (c) and (d).

We have developed the micro-structured fluorescent plates successfully. Impregnation with <sup>10</sup>B-enriched orthoboric acid is effective to add neutron sensitivity to the fluorescent plates. The fabricated fluorescent plates are expected to be useful in high-spatial-resolution imaging devices with good detection efficiency. The next step of the work is to increase the neutron detection efficiency. The metal coating inside the capillary walls is considered to be a promising method.



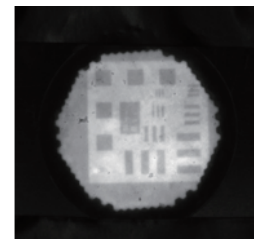
a) 20 minutes drying time



b) 1 hour drying time



c) Repetition is 8 times



d) Repetition is 16 times

Fig. 2. Results of fluorescent plates neutron imaging. Each plate was exposed to neutrons for 10 minutes. Image (a) drying time is 20 minutes, (b) drying time is 1 hour, respectively. Image (c) repetition of orthoboric acid lution is 8 times, (d) repetition is 16 times, respectively. In (c) and (d), the object is a line-pair indicator [3].

### REFERENCES:

- [1] T. Sakai *et al.*, Nucl. Instr. and Meth. Phys. Res. B 332 (2014) 1238.
- [2] T. Sakai *et al.*, JPS Conf. Proc. 11, 020005 (2016).
- [3] R. Yasuda *et al.*, Physics Procedia 43 (2013) pp.196-204.

# CO8-11 Visualization of a Microchannel Heat Exchanger under Non-uniformly Heated Condition

H. Sakai, H. Umekawa<sup>1</sup>, T. Ami<sup>1</sup>, Y. Saito<sup>2</sup> and D. Ito<sup>2</sup>

Graduate School of Science and Engineering, Kansai University

<sup>1</sup>Department of Mechanical Engineering, Kansai University

<sup>2</sup>Institute for Integrated radiation and Nuclear Science, Kyoto University

**INTRODUCTION:** Recently, microchannel heat exchangers have been widely adopted in air-conditioning units, instead of conventional fin-tube heat exchangers which composed of copper tubes and aluminum fins. Microchannel heat exchangers have a lot of advantages, i.e. large specific surface area increases the heat-transfer performance, the small diameter reduces the amount of refrigerant and prevents the flow separation, and aluminum body reduces the weight and contact thermal resistance with aluminum fin. However, microchannel heat exchangers are consisted from many parallel mini channels, thus the control of flowrate in each channel is quite difficult. Especially as the heat exchangers for air-conditioning unit, the flow path of refrigerant is normal to the path of air flow, thus the heat flux distribution becomes non-uniform. Under these heating conditions, the flow maldistribution and flow instability in parallel channels may occur, and it reduce the performance of heat exchangers.

Several papers have been reported on heat transfer performance of microchannel heat exchangers so far. However, those investigations mostly treated the micro channel heat exchanger as one equipment, and the report treated the flow condition in each channels has been quite limited.

The main purpose of this investigation is understanding the heat and flow characteristics in each micro channel. In this report visualization results of a microchannel heat exchanger under non-uniform heating by using neutron radiography are briefly introduced.

**EXPERIMENTS:** Experiments of the visualization were carried out using the B-4 beam line in KUR (1 MW). The experimental apparatus is shown in Fig.1. The working fluid used in this study is Methanol (99.5% purity), which has low viscosity similar with actual refrigerant (R32) and enough attenuation coefficient for visualization. The experimental apparatus is consisted of a reserve tank, pump, test section. Test section is an actual aluminum microchannel heat exchanger of air-conditioning unit, and it is heated by joule heating by using two nichrome foils attached to the plate surface with electrical insulation of Kapton film. These nichrome foil heaters can be heated separately and which can achieve the non-uniform heating condition.

**RESULTS:** Fig. 2 shows the visualization results of microchannel heat exchange under heating condition. These figures are results under same total heat input with different heat flux ratio in two film heaters. The left side of each figure corresponds to the lower heat flux side, and the maldistribution of flow is clearly observed as the difference of void fraction distribution. On the basis on these results the influence of the heat flux ratio on the void fraction distribution will be qualitatively estimated. Moreover, by using the dynamic image the stability of flow condition may be reported in future.

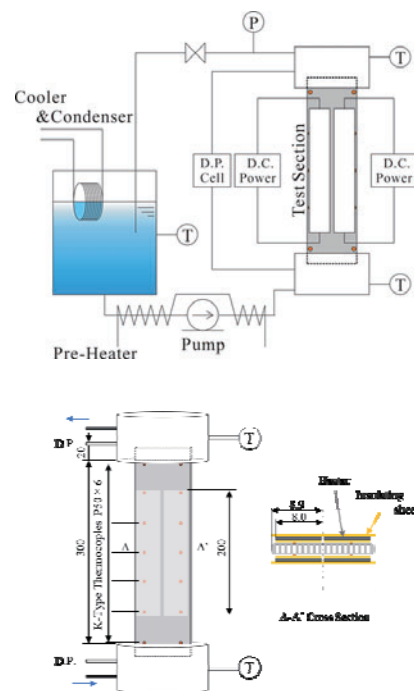


Fig. 1. Experimental apparatus.

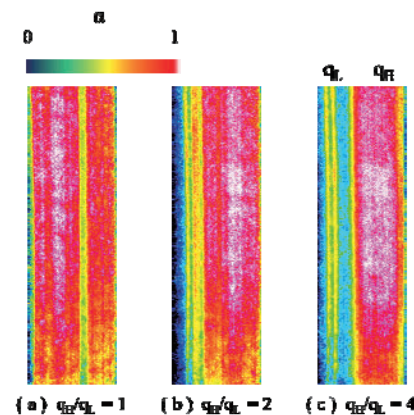


Fig. 2. Void fraction distribution. ( $q_{\text{average}} = 40 \text{ kW/m}^2$ ,  $G = 150 \text{ kg/m}^2\text{s}$ )

## CO8-12 Diffusion Measurements on NASICON-Type Structured Lithium Ion Conductors by Means of Neutron Radiography

S. Takai<sup>1</sup>, F. Song<sup>1</sup>, H. Chen<sup>1</sup>, K. Ota<sup>1</sup>, T. Yamamoto<sup>1</sup>,  
T. Yabutsuka<sup>1</sup>, T. Yao<sup>2</sup>, D. Ito<sup>3</sup> and Y. Saito<sup>3</sup>

<sup>1</sup>Graduate School of Energy Science, Kyoto University

<sup>2</sup>Kyoto University

<sup>3</sup>Institute for Integrated Radiation and Nuclear Science,  
Kyoto University

**INTRODUCTION:** Heterogenous doping effect, originally observed in halide solid state electrolytes, is proven to be favourable in oxide solid-state electrolytes by Onishi *et. al* [1]. Heterogenous doping is to disperse insulative particles in  $\text{Li}^+$  ion conductors and create space charge layers at the vicinity of the insulative particles, which eventually improves the overall ionic conductivity of solid-state electrolyte [2]. Such dispersion system is referred as composite solid-state electrolytes.

In this work, neutron radiography method is applied to study the diffusion characteristics of LATP-4wt% LLTO composite solid-state electrolyte. Such technique has been a standardised method developed by our group, which utilises the difference in cross-section between  $^7\text{Li}$  and  $^6\text{Li}$  in neutron beam, such that the diffusion profile of  $^6\text{Li}^+$  in  $^7\text{Li}$  solid-state electrolytes can be visualised. This method eventually allows calculation of diffusion coefficient  $D^*$  of  $^6\text{Li}^+$  [3-6].

**EXPERIMENTS:** Precursor of  $^7\text{Li}_{1.3}\text{Al}_{0.3}\text{Ti}_{1.7}(\text{PO}_4)_3$  and  $^7\text{Li}_{0.348}\text{La}_{0.55}\text{TiO}_3$  are synthesised by solid-state reaction method. By mixing the components in ratio of 96:4 and sintering, cubic pellets of  $^7\text{Li}$  LATP-LLTO composite are prepared.  $^6\text{LiNO}_3$  paste is applied to single side of the pellets, after which the pellets are annealed at different temperatures (300 °C, 400 °C and 500 °C) for 150 minutes to facilitate diffusion of  $^6\text{Li}$  in  $^7\text{Li}$  electrolytes. After cooling to room temperature, the pellets are subjected to direct neutron beam radiation at B4-port in KUR. The transmission neutron is converted to light signal by a converter plate, which is captured by a CCD camera.

**RESULTS:** The original radiography image and the intensity profiles are shown in Fig. 1. By Beer-Lambert's Law, the natural logarithm of  $I_N$  over  $I_0$  is proportional to  $c_N$ , where  $I_N$  and  $I_0$  are intensities of transmitted radiation with and without scattering,  $c_N$  is the light-scattering particle (in this case,  $^6\text{Li}^+$ ). This allows conversion of intensity profiles into diffusion profiles which are shown in Fig. 2. It is assumed that  $^6\text{Li}^+$  diffuses down the concentration gradient, and diffusivity of  $^6\text{Li}^+$  is indifferent to its concentration. By the semi-finite solution to the Fick's equation, the diffusivities of  $^6\text{Li}^+$  at different temperatures can be calculated, which are also shown in Fig. 2. It is evident that after annealing at 500 °C for 150 minutes, the  $^6\text{Li}^+$  is homogenised across the entire  $^7\text{Li}$  composite solid-state electrolyte.

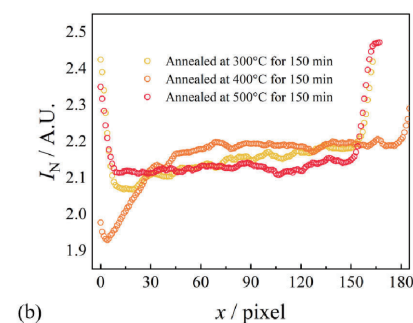
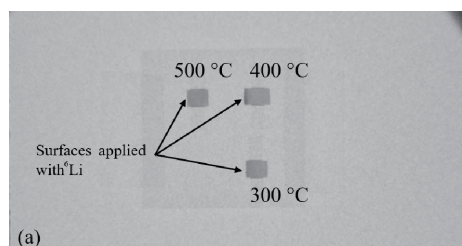


Fig. 1. (a) Original CCD camera photograph (radiography image) and (b) intensity profiles obtained by Image J.

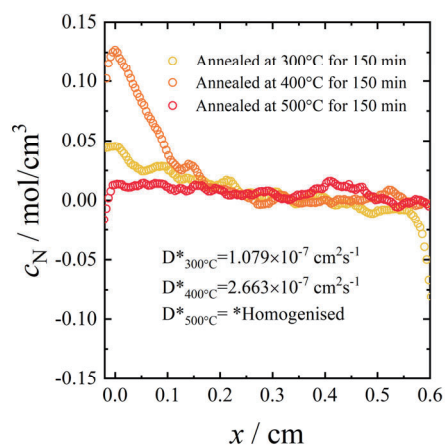


Fig. 2. Diffusion profiles and calculated diffusivity of  $^6\text{Li}^+$ .

### REFERENCES:

- [1] H. Onishi *et al.*, *Electrochemistry*, **84** (2016) 967.
- [2] C. C Liang. *J. Electrochemical Soc.*, **120** (1973) 1289.
- [3] S. Takai *et al.*, *Solid State Ionics.*, **256** (2014) 93.
- [4] S. Takai *et al.*, *Solid State Ionics.*, **176** (2005) 2227.
- [5] S. Takai *et al.*, *Solid State Ionics.*, **171** (2004) 107.
- [6] S. Takai, *et al.*, *Solid State Ionics.*, **123** (1999) 165.

## CO8-13 Study on the non-destructive nuclide assay for nuclear materials with a self-indication method

J. Hori<sup>1</sup>, T. Sano<sup>2</sup>, Y. Takahashi<sup>1</sup>, and H. Yashima<sup>1</sup>

<sup>1</sup>Institute for Integrated Radiation and Nuclear Science, Kyoto University

<sup>2</sup>Atomic Energy Research Institute, Kindai University

**INTRODUCTION:** For decommissioning of Fukushima Daiichi Nuclear Power Plants, the identification and quantification of the nuclear material in fuel debris are important issues for appropriate nuclear material management. However, it is considered that fuel debris contains unknown amounts of minor actinides, fission products and neutron absorbers except for nuclear materials. Therefore, it is difficult to apply a conventional non-destructive assay to fuel debris. Neutron Resonance Densitometry (NRD) is one of the candidate techniques of non-destructive nuclide assay applicable to quantity nuclear materials in fuel debris. Especially, a self-indication method [1] is considered as a suitable technique for the identification and quantification of nuclides in fuel debris.

In the self-indication method, an indicator consisting of the target nuclide is placed at the neutron beam downstream from a sample. The self-indicator is a transmission neutron detector that has high efficiency around the objective neutron resonance energies of the target nuclide, enabling us to quantify effectively the amount of resonance absorption of the target nuclide.

In this study, we considered the possibility of nuclear discrimination imaging using a stationary neutron source as an application of the self-indication method. By inserting the self-indicator filter into the beam line, the transmitted neutrons around the objective neutron resonance energies are decreased especially. Therefore, we expect to identify the neutron absorption due to the target nuclide resonance without using a time-of-flight (TOF) information.

**EXPERIMENTS:** The experiment was performed at the 46-MeV electron linear accelerator in Institute for Integral Radiation and Nuclear Science, Kyoto University. The linac was operated with a repetition rate of 50 Hz, a pulse width of 4  $\mu$ s, a peak current of about 0.5 A, and an electron energy of about 30 MeV. The pulsed neutron beam was collimated to 50 mm in diameter. Three foils of In, Ag and Ta were placed in the center of beam line at a distance of 12 m from the neutron source as shown in Fig. 1. A GEM detector (THIN-GEM, Bee Beans Technologies Co., Ltd.) was used as a neutron position sensitive detector. The detector can obtain the two-dimensional information of TOF for transmitted neutrons. A Cd sheet of 0.5 mm in thickness was inserted into the TOF neutron beam line to shield thermal neutrons. Runs with and without the sample (sample run and blank run) were carried out. Moreover, we performed the measurement with

the sample and additional In filter of 0.5 mm in thickness as a self-indicator (sample with filter run). Each measurement time was about 10 hours.

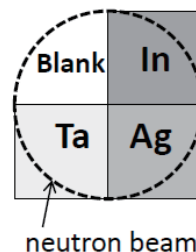


**Fig.1** Sample arrangement of In, Ag, Ta foils for the present neutron imaging experiment.

**RESULTS:** Figure 2 shows the transmission neutron radiographs of the test sample illustrated in Fig. 1. The spatial distribution of the transmitted neutron flux was obtained by gating on the TOF region corresponding to the 1.46-eV resonance of In. The region of In was clearly identified as shown in Fig. 2(a). On the other hands, the spatial distribution of the relative counting rate in the sample with filter run to that in the sample run was obtained as shown in Fig. 2(b). Though the contrast between In and other materials was inferior to that of the imaging gated on the resonance, the region of In can be identified. It is noted that the radiograph was obtained without using TOF information. It indicated that the self-indication method can be utilized to the nuclear discrimination imaging using a stationary neutron source.

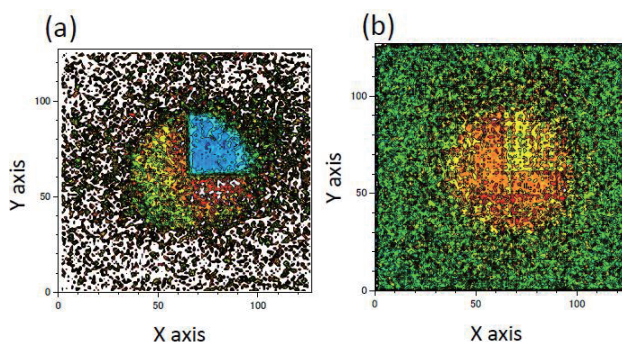


**Fig.2** Neutron radiographs obtained by (a) gating on the resonance region of In and (b) using the relative counting rate in the sample with filter run to that in the sample run.

Present study was supported by JSPS KAKENHI Grand Number JP17K07012.

### REFERENCES:

[1] J. Hori *et al.*, EPJ Web of Conferences, 146, 09042 (2017).

## CO8-14 The measurability of photofission reaction of uranium induced by bremsstrahlung photons

K.W. Chin, H. Sagara, J. Hori<sup>1</sup>, Y. Takahashi<sup>1</sup>

Tokyo Institute of Technology

<sup>1</sup>Institute for Integrated Radiation and Nuclear Science, Kyoto University

**INTRODUCTION:** Non-destructive assay technique for nuclear material is one of the most important technical issues in the field of safeguard. A non-destructive assay using photonuclear reaction has been considered as a promising one. Previous work suggested new method using a mono-energy Gaussian photon beam to measure the isotopic composition of nuclear fuel materials without relying on their self-generated neutron information [1]. However, producing a Gaussian photon beam requires costly laser Compton scattering instrument. Thus, this re-search aims to replace the source with a bremsstrahlung photon beam from an accelerator[2]. In this work, we tried to perform the feasibility study on the detection of prompt neutron produced by the photonuclear reaction in the uranium sample.

**EXPERIMENTS:** The experiment was performed at the KURNS-LINAC. A natural uranium sheet was used as a sample and placed in the center of beam line at a distance of about 12 m from the photon source. A platinum target was used as the photon source of bremsstrahlung. The linac was operated with a pulse repetition rate of 100 Hz. The energy of electron was optimized to 18 MeV based on the parameter survey in the range from 8 to 30 MeV. An organic liquid scintillator (BC-501A) with a high performance associated with the discrimination ability between neutron and gamma ray was used as a neutron detector. The detector was placed at a distance of 10 cm from the sample. The signals from the detector were taken in the pulse-shape discrimination system and the two-dimensional data of pulse height and rise time were obtained. We carried out six kinds of measurements. Three measurements were done with no sample and standard sources (Cf-252, Cs-137) without linac operation. The remaining measurements were done with linac operation in the following conditions of no sample without shields, a natural uranium sample with a neutron shield, and a natural uranium sample with neutron and gamma-ray shields. In the linac experiment, intense gamma flash and photo-neutron from the target is obstructive to the measurement of prompt neutron from the sample. Therefore, two polyethylene blocks and two lead blocks were used as shielding materials. Moreover, the electron beam current was reduced from 91  $\mu$ A to 2  $\mu$ A to inhibit the effect of gamma flash for every run.

**RESULTS:** Two-dimensional data of pulse height and rise time were shown in Fig. 1 for six measurements, respectively. It is noted that the horizontal axis is rising time whereas the vertical axis is pulse height. At first, we can identify the region of interest (ROI is shown as the dotted box) as neutron events by comparing the run of Cf-252

with that of Cs-137. However, a few gamma-ray events were unfortunately observed in the ROI and those should be taken account of background. The counting rate for each run in the ROI is shown in Table 1. We observed a significant difference between the run of no sample and that of uranium sample with neutron and gamma-ray shields. Further analysis and experiment were necessary in order to obtain conclusive evidence of the measurability of neutron caused by photoreaction.

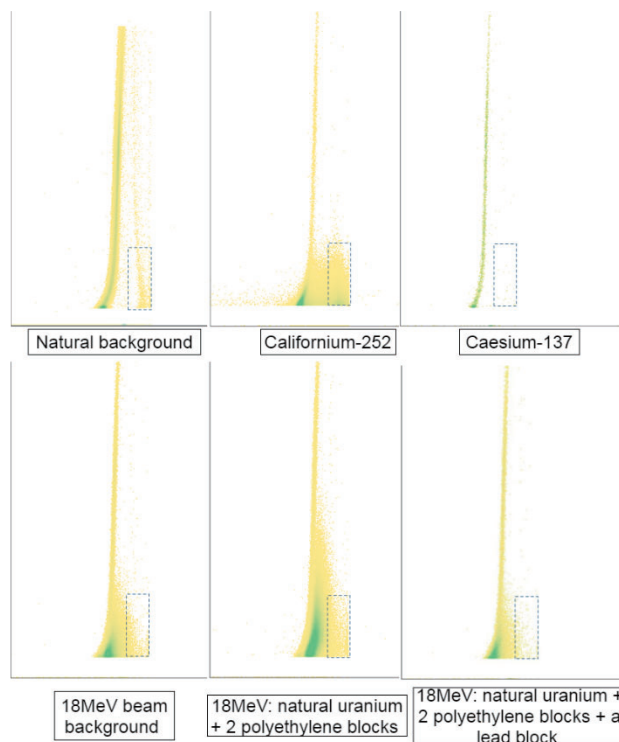


Fig. 1. Different cases of natural background, <sup>252</sup>Cf, <sup>137</sup>Cs, 18 MeV beam background and natural uranium.

Table 1. Statistical data of counting in ROI.

ROI Cases	Total count rate, cps	Total counts, N	Absolute error,	Relative error,
Natural BG	0.02158	1025	32.0	0.0312
BG <sub>beam-18MeV</sub>	0.2094	754	27.5	0.0364
<sup>252</sup> Cf	75.87	4570 6	213	0.0046
NU+PolyB	0.7754	2793	52.8	0.0189

### REFERENCES:

- [1] R. Kimura *et al.*, JNST, **53(12)**, (2017).
- [2] K.W. Chin *et al.*, AESJ, Univ. Ibaraki, (2019).

## CO8-15 Distribution of coolant inside a flat laminate vapor chamber in a vertical posture

K. Mizuta, Y. Saito<sup>1</sup> and D. Ito<sup>1</sup>

Faculty of Engineering, Kagoshima University

<sup>1</sup>Institute for Integrated Radiation and Nuclear Science, Kyoto University

**INTRODUCTION:** Recently, severity in the cooling electronic devices is increasing because of shrinking size of such devices. Poor ability of heat exhausting system leads to various problems such as low reliability and low working efficiency of semiconductor. Various types of vapor chambers are attracting attention than ever with a hope for solving such problems by higher heat spreading ability of vapor chambers. In the practical use of vapor chambers, postural effect on thermal performance of vapor chambers is very important, because the change in the thermal performance of vapor chamber with posture, if it occurs, may restrict the performance of the electronic devices. A flat laminate vapor chamber called FGHP (Fine Grid Heat Pipe) is one of the most promising candidates to solve such thermal problems, with the highest heat spreading ability concerning the overall heat transfer coefficient based on the area of heat source [1]. Our previous study shows that the effect of gravity on the coolant distribution of FGHP is negligible [2].

In this study, we investigated the gravitational effects on the coolant distribution in the FGHP by using neutron radiography at the Kyoto University Research Reactor (KUR) with higher input and smaller heat source than our previous work.

**EXPERIMENTS:** Experiment was conducted at the E-2 port of the KUR, where the thermal neutron flux at the sample position was about  $3 \times 10^5 \text{ cm}^2\text{s}$  at 5 MW operation. The size of the test sample of FGHP heat spreader was 65 mm square and 2 mm thick. The test sample was set vertically, which means that its bottom and top plate was placed parallel to the gravitational direction. Figure 1 shows the experimental setup. A ceramic heater of  $10 \times 10 \times 1.75 \text{ mm}^3$  was attached to the central part of the bottom plate as a heat source, and the top plate was cooled by plate-fin type aluminum heat sinks of  $70 \times 70 \text{ mm}^2$  under forced convection conditions. K-type thermocouples were utilized to measure both surface temperature of the heat spreader and the atmospheric temperature to estimate the thermal resistance. A CCD camera (BU-53LN, BITRAN Co. Ltd.) was utilized, which has  $4008 \times 2672$  pixels and  $^6\text{LiFZnS}$  (50  $\mu\text{m}$  thickness) was used as a scintillator screen. The spatial resolution was 9.0  $\mu\text{m}/\text{pixel}$  at the present system setup, however, the effective spatial resolution was about 50  $\mu\text{m}/\text{pixel}$  due to the scintillator screen characteristics. Neutron imaging of the sample was performed at the 1 MW operation mode of the KUR and the exposure time was 300 s. Neutron images of the sample were utilized to calculate liquid thickness in the FGHP. The effect of gravity on the coolant distribution was evaluated by the calculated liquid thickness in the wick area at different four positions.

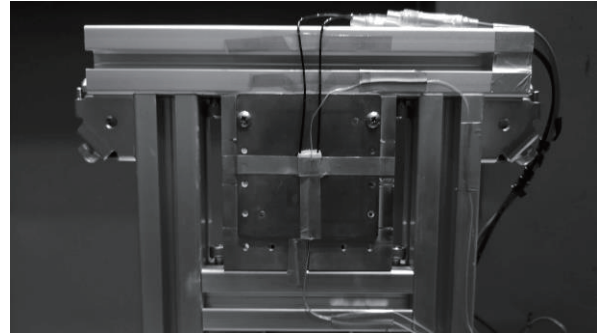


Fig. 1 Experimental setup.

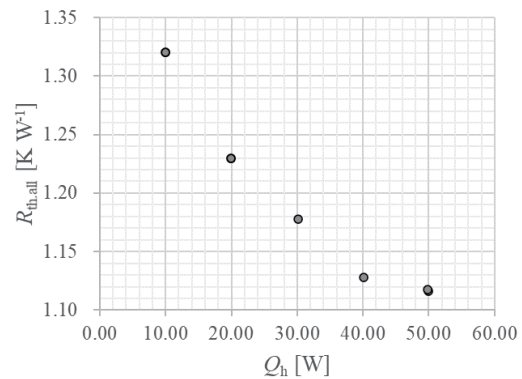


Fig. 2 Variation of total thermal resistance of the system with heat input ( $Q_h$ ).

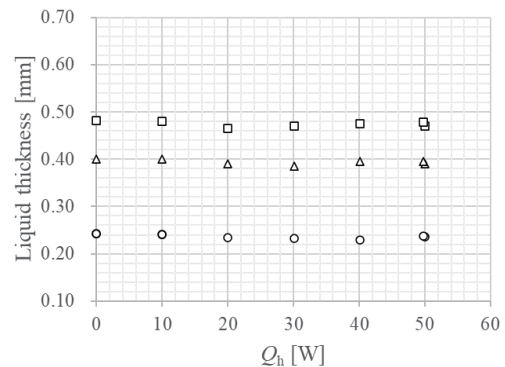


Fig. 3 Variation of liquid thickness with heat input. (○:top, □:bottom, △:horizontal average)

**RESULTS:** Figure 2 shows the variation of total thermal resistance of the system with heat input ( $Q_h$ ). As shown in Fig. 2, thermal resistance decreased with increasing heat input, as reported in the previous work [1]. Figure 3 shows that liquid thickness at various positions were almost constant regardless of heat input, which means that FGHP work properly with about 20 times higher heat flux than the previous work [2].

### REFERENCES:

- [1] Mizuta, K., *et al.*, Applied thermal management, **104** (2016) 461-471.
- [2] Mizuta, K., *et al.*, Physics Procedia, **69** (2015) 556-563.

## CO8-16 Demonstration experiments of an innovative method to detect nuclear material

M. Komeda, Y. Toh, Y. Kitamura<sup>1</sup>, T. Misawa<sup>1</sup> and K. Tanabe<sup>2</sup>

*Nuclear Science and Engineering Center, Japan Atomic Energy Agency*

<sup>1</sup>*Institute for Integrated Radiation and Nuclear Science, Kyoto University*

<sup>2</sup>*National Research Institute of Police Science*

**INTRODUCTION:** A compact and low-cost non-destructive assay system to detect hidden nuclear material is required in the fields of nuclear security. We have therefore developed an innovative nuclear material detection method by using a neutron source of Californium-252, which is capable to assemble such system [1]. In this method, a neutron source is rotated at a speed of thousands of rpm nearby the target. Meanwhile, it is possible to detect nuclear materials by confirming the de-formation of the time-distribution spectrum obtained by a neutron detector near the target. The machine to rotate the neutron source is less than 60 cm in width, depth, and height. The rated output of the motor is only 750W. We installed the machine at an experimental laboratory in the KUCA, and carried out demonstration experiments using a neutron source (5MBq of Cf-252) and uranium.

**EXPERIMENTS:** Figure 1 shows the overview of apparatuses used in the experiment. A neutron source was installed at the outer periphery of a disc of 32 cm diameter. The uranium sample that was surrounded with polyethylene moderator set between the rotation machine and neutron detectors. The neutron detector system consists of 6 He-3 proportional counters, which are wrapped with a cadmium plate and a boron rubber sheet in order to detect only fission neutrons effectively. The time distribution of neutron measurement was performed by a multi-channel scaler (MCS) that is synchronized with the disc rotation. A measurement time was 15 minutes for each experiment.

**RESULTS:** Figure 2 shows an example of experimental results of a natural uranium sample and a blank sample under the condition that the rotation speed is 4000 rpm. The polyethylene moderator was utilized in the measurements of both the uranium and blank samples. The neutron source was closest to the uranium sample approximately at 6300 micro-seconds in Figure 2. Since the neutron source, the uranium sample, the polyethylene moderator and the neutron detector system have a complicated geometry, the dips appear before and after the peak. When the uranium sample was used, data after 6300 micro-seconds (from 6300 to approximately 9000 micro-seconds) had higher counts compared to the blank sample. This is due to the delay effect of the interrogation neutrons (Cf-252 neutrons). The delay effect can be observed only when a sample contains a fissile material under a condition of high speed rotation of Cf-252. We could detect nuclear material for the first time by using

the present new method. Thus, we could verify the innovative nuclear material detection method through these experiments at KURNS. This study and experiment would make a large impact in the field of nuclear security. A further study would be required to confirm the effects in various conditions, such as positional dependence of nuclear material, and would be conducted in near future.

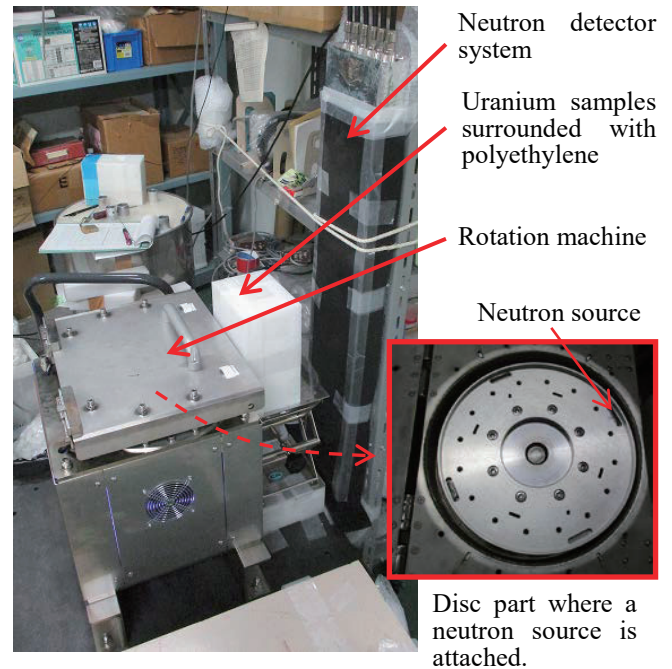


Fig. 1. Overview of experimental devices.

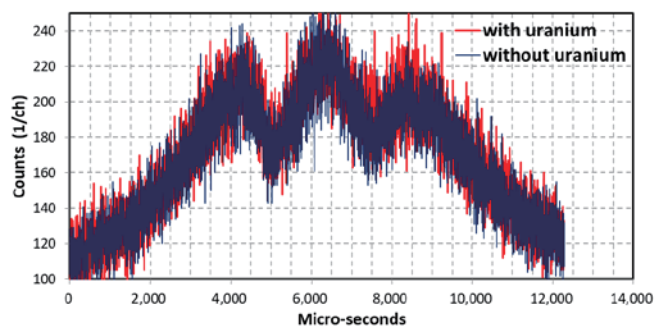


Fig. 2. Experimental examples of the uranium sample (red line) and blank sample (blue line). The measurement time was 15 minutes with the rotation speed of 4000 rpm.

### REFERENCES:

[1] M. Komeda, Y. Toh, *Annals of Nuclear Energy*, **135** (2020) 106993.

T. Sasaki, N. Sato<sup>1</sup>, A. Kirishima<sup>1</sup>, D. Akiyama<sup>1</sup>, T. Kobayashi, K. Takamiya<sup>2</sup>, S. Sekimoto<sup>2</sup>, Y. Kodama and Q. Zhao

Graduate School of Engineering, Kyoto University

<sup>1</sup> Institute of Multidisciplinary Research for Advanced Materials, Tohoku University

<sup>2</sup> Institute for Integrated Radiation and Nuclear Science, Kyoto University

**INTRODUCTION:** Under the high-temperature conditions in the reactor cores of the Fukushima Daiichi Nuclear Power Station (FDNPS) during the accident, UO<sub>2</sub>, zircaloy, and structural materials such as concrete are thought to be reacted [1]. Uranium and these elements in the fuel debris could take various chemical states depending on chemical conditions to which they were exposed. Therefore, the aging degradation of fuel components contacting with water would be investigated to evaluate the long-term stability. Several fission products (FPs) have been produced by short-time neutron irradiation of simulated debris, which was synthesized by heat treatment of MCCI debris under reducing and oxidizing conditions. The leaching ratio of elements such as Zr, Ru, I, and Ba would be a proportional relationship with that of uranium or Cs as a matrix or a major FP, respectively, under various solution conditions.

**EXPERIMENTS:** In the preparation of MCCI debris, U:Zr was assumed to be 5:1, as a typical combination of UO<sub>2</sub> fuel and oxidized zircaloy-clad. The mixing ratios of cement intended to be shortage and excess amount of Ca to U; 1:0.75, 1:1.75, and 1:6.75. The mixture was heated at 1200°C for 2 hours under a reducing (10% H<sub>2</sub>) and oxidizing (2% O<sub>2</sub>) atmosphere — called as #R and #O series. During furnace cooling, pure argon gas was kept flowing. After the cooling, the sample was investigated by XRD. The simulated MCCI debris sealed in a quartz ampoule was inserted into a polyethylene capsule and irradiated using Pn-2 of Kyoto University Reactor. The gamma-ray activity, which is considered as an initial inventory of each radionuclide in the solid sample, was measured using a Ge detector after cooling in order to allow for the decay of highly radioactive, short-lived nuclides.

**RESULTS:** Under reducing heat treatment conditions of H<sub>2</sub> gas, Ca and SiO<sub>2</sub> did not react with UO<sub>2</sub>, while Ca<sub>3</sub>SiO<sub>5</sub> was assigned (a component of cement). The presence of ZrO<sub>2</sub>, Ca zirconate was preferentially produced. Under oxidizing heat treatment conditions O<sub>2</sub> gas, dominant phase (w/o cement) was U<sub>3</sub>O<sub>8</sub>, and the solid solution was partly observed. The presence of less Ca to U (1:0.75), cubic-fluorite-type solid solutions formed, and in the presence of excess Ca, trigonal CaUO<sub>4</sub> (1.75), and Ca<sub>3</sub>UO<sub>6</sub> (1:6.75) were obtained. Excess Ca was produced Ca silicate

(Ca<sub>2</sub>SiO<sub>4</sub>) and Ca zirconate (CaZrO<sub>3</sub>) similar to #R. Thus, Ca reacted with U preferentially compared to Zr and Si, forming a Ca-rich uranate with increasing Ca:U ratio.

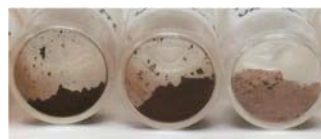


Fig. 1. Typical appearance of simulated MCCI debris prepared under reducing conditions.

Five FPs were mainly produced by thermal-neutron irradiation. Static leaching test was done by using 0.1 M NaClO<sub>4</sub> at pH 7. After 4 weeks shaking, the radioactivity or the molar concentration in filtrate were measured, and then the leaching ratio *R* [2] was evaluated.

The *R*<sub>Cs</sub> values higher than those of UO<sub>2</sub> and U<sub>3</sub>O<sub>8</sub>, suggesting an induced leaching due to Ca dissolution of MCCI debris or complexing U with CSH. Such speculation would be supported by *R*<sub>Cs</sub>. The same trend was observed in I and Ba systems. Trace I as I<sup>-</sup>, *R*<sub>I</sub> showed a similar trend as Cs.

Compared to U compounds w/o Ca, most of *R*<sub>M</sub> values of MCCI debris (at 1200°C) increased. Meanwhile, log*R*<sub>Ca</sub> of #R series showed quite high order range of 3–5, whereas the values of #O were relatively low. This result would be because of the different predominant species of Ca between #R and #O. About trace Ba as Ba<sup>2+</sup>, *R*<sub>Ba</sub> showed the same trend as *R*<sub>Ca</sub>. The *R*<sub>Ru</sub> of #R and #O were slightly lower than others (except Zr), which is consistent with previous reports of U(Zr)O<sub>2</sub>, although the chemical property is unknown. Most of *R*<sub>Zr</sub> values could not be determined due to the quite low activity below the detection limit, corresponding to 10<sup>-15</sup> M.

In conclusion, a mixture of cement components heated at 1200°C under H<sub>2</sub> and O<sub>2</sub> conditions formed UO<sub>2</sub> (unreacted) and calcium uranates, respectively. Under this specific condition, the excess Ca and Si could form CaZrO<sub>3</sub> and Ca<sub>2</sub>SiO<sub>4</sub> (and CaO), which cause to increase pH in the present batch-wise tests. Significant increase of *R*<sub>M</sub> was observed comparing with *R*<sub>M</sub> in the absence of cement components. It is thought to be due to 1) an increase of the surface area of powder samples by matrix Ca dissolution, or 2) formation of U-CSH.

Combination of spectroscopic methods will give a new insight into the chemical property of debris before and after leaching test.

#### REFERENCES:

- [1] T. Kitagaki *et al.*, J Nucl Mater., **486** (2017) 206-215.
- [2] T. Sasaki *et al.*, J. Nucl Sci Technol., **53** (2016) 303-311.

T. Kobayashi, T. Sasaki, T. Saito<sup>1</sup>, K. Takamiya<sup>1</sup>, S. Sekimoto<sup>1</sup>, M. Moniruzzaman, T. Fushimi, K. Haruki, and T. Suzuki

Graduate School of Engineering, Kyoto University  
<sup>1</sup> Institute for Integrated Radiation and Nuclear Science, Kyoto University

**INTRODUCTION:** Tetravalent zirconium, Zr(IV), is known to undergo extensive hydrolysis in aqueous solution and its solubility is limited by a sparingly soluble amorphous hydroxide solid phase, Zr(OH)<sub>4</sub>(am), in neutral to alkaline pH range. In the presence of suitable inorganic or organic ligands, Zr(IV) solubility is increased by the formation of soluble complexes. Enhanced Zr(IV) solubility is an issue in the environmental context of safe radioactive waste disposal, because the long half-life fission product <sup>93</sup>Zr (T<sub>1/2</sub>=1.53×10<sup>6</sup> y) in radioactive waste forms Zr(IV) and can migrate with groundwater under the disposal conditions. Although a very few inorganic or organic ligands can compete with the strong hydrolysis reactions that occur in neutral to alkaline solutions, we have found that several poly(hydroxy)carboxylic acids formed stable complexes with Zr(IV) in neutral to alkaline solutions[1]. In the present study, we investigated the solubility of Zr(IV) in the presence of three simple hydroxycarboxylic acids (hydroxyacetic (glycolic, O20) and 3-hydroxypropionic (O21) to clarify the role of the hydroxy groups in Zr complexation. The Zr(IV) solubility dependence on hydrogen ion concentrations (pH<sub>c</sub>) and hydroxycarboxylic acid concentrations ([L]<sub>tot</sub>) was examined to identify the dominant soluble species and to determine their formation constants.

**EXPERIMENTS:** Sample solutions were prepared by an undersaturation approach. An aliquot of Zr(OH)<sub>4</sub>(am) stock suspension was added to sample solutions at selected pH<sub>c</sub> and [L]<sub>tot</sub> (L = O20 and O21, see Fig. 1) values within the pH<sub>c</sub> range of 7 to 13 and [L]<sub>tot</sub> range of 10<sup>-4</sup> to 10<sup>-1</sup> M. Sample solutions in polypropylene tubes were kept in the Ar-filled glove box and in some cases manually shaken for a few minutes. After given aging periods, the pH<sub>c</sub> of the sample solutions was measured and a 0.5-mL aliquot of the supernatant was passed through an ultrafiltration membrane (3kDa, pore size ~ 2 nm). The filtrate was

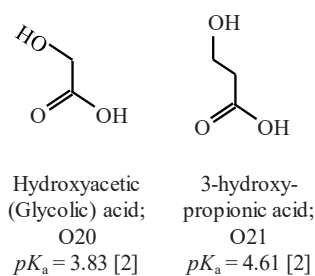


Fig. 1. Hydroxycarboxylic acids used in this study.

acidified with 0.1 M nitric acid prior to the concentration measurements by inductively coupled plasma mass spectrometry (ICP-MS). The detection limit of Zr(IV) solubility was approximately 10<sup>-8.5</sup> M.

**RESULTS:** Figure 2 shows the Zr(IV) solubility in the presence of 0.01 M and 0.1 M glycolic acid (O20) as a function of pH<sub>c</sub>, together with those in the absence of O20 [3,4]. The solubility in the presence of 0.1 M O20 equaled 10<sup>-7</sup> M throughout the whole pH<sub>c</sub> range, and the solubility was about one order of magnitude higher than that in the absence of O20. Zr(IV)-O20 complexes were considered to be the predominant Zr(IV) species in 0.1 M O20 solution. Assuming that the solid phase retained its Zr(OH)<sub>4</sub>(am) stoichiometry, the zero slope of the log [Zr] versus pH<sub>c</sub> plot indicated that the soluble Zr(IV)-O20 complex contained four OH groups in its chemical formula. Since the solubility increased monotonically with a slope of two at constant pH<sub>c</sub> levels, we assumed that Zr(OH)<sub>4</sub>(O20)<sub>2</sub><sup>2-</sup> was the major species in the solution.

On the other hand, the Zr(IV) solubility in the presence of 0.01 M and 0.1 M 3-hydroxypropionic acid (O21) showed no significant increase from those in the absence of O21. This result suggested that complexation by O21 was not strong enough to solubilize Zr(IV) under the present experimental conditions. Zr(IV) chelation featuring 5-membered rings with O20 might be more stable than that with 6-membered rings with O21.

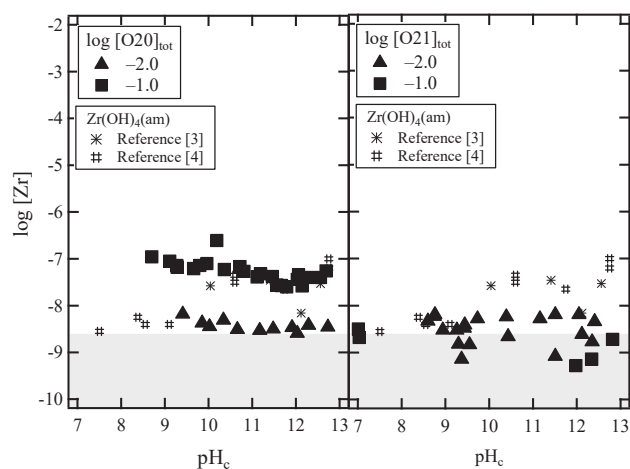


Fig. 2. Zr(IV) solubility in the presence of 0.01 M and 0.1 M O20 (left) and O21(right).

#### REFERENCES:

- [1] T. Kobayashi *et al.*, J. Chem. Thermodynamics, **138** (2019) 151-158.
- [2] R. M. Smith, NIST Critically Selected Stability Constants of Metal Complexes Database Version 5.0, Gaithersburg, USA (1998).
- [3] T. Sasaki *et al.*, Radiochim. Acta, **94** (2009) 489-494.
- [4] M. Altmaier *et al.*, Radiochim. Acta, **96** (2008) 541-550.

## CO9-3 Electrodeposition Behaviors of Uranium and Aluminum on Copper Cathode in LiCl-KCl Eutectic Melts

Y. Sakamura, T. Murakami, K. Uozumi, M. Iizuka and K. Takamiya<sup>1</sup>

Central Research Institute of Electric Power Industry  
<sup>1</sup>Institute for Integrated Radiation and Nuclear Science,  
Kyoto University

**INTRODUCTION:** Electrorefining in molten LiCl-KCl eutectic-based salts is the key separation process in the pyrochemical treatment of spent nuclear fuels [1,2]. It has been reported that Al cathode is suitable for collecting actinides in the form of intermetallic compounds with a high separation factor against rare-earth fission products [2]. Then, a chlorination process for the actinide-Al alloys using Cl<sub>2</sub> or HCl has been examined to separate volatile AlCl<sub>3</sub> from actinide chlorides [3,4]. A chemical reduction is subsequently conducted to obtain actinide metals [4].

We propose an electrorefining process to separate actinides from Al. Since U and Al simultaneously dissolve into LiCl-KCl eutectic melts during anodic dissolution of U-Al alloy [5], the separation between U and Al has to be conducted at cathode. The Al-Cu and U-Cu binary phase diagrams [6] suggest that Cu likely forms a stable alloy with Al but not with U. In the present study, electrodeposition behaviors of Al<sup>3+</sup> and U<sup>3+</sup> on Cu electrode in LiCl-KCl eutectic melts were investigated to evaluate the possibility of electrochemical separation between U and Al.

**EXPERIMENTS:** A LiCl-KCl eutectic melt was contained by a high-purity Al<sub>2</sub>O<sub>3</sub> crucible at ~723 K, where a working electrode of Cu wire (1 mm diameter), a counter electrode of glassy carbon rod (3 mm diameter), a Ag/AgCl reference electrode and a type-K thermocouple were placed. The Ag/AgCl electrode consisted of a Ag wire immersed in a LiCl-KCl eutectic salt mixture with 1.0 wt% AgCl, which was contained in a closed-end Pyrex tube. The concentration of U<sup>3+</sup> in the melt was increased by adding a prepared LiCl-KCl-UCl<sub>3</sub> salt whose U concentration was 11.4 wt% determined by ICP-AES analysis. KAlCl<sub>4</sub> (99.9% purity) obtained from APL Engineered Materials was used as a source of Al<sup>3+</sup> ions because AlCl<sub>3</sub> is highly volatile. All the experiments using chlorides were conducted in a high-purity Ar atmosphere glove box (H<sub>2</sub>O, O<sub>2</sub> < 1 ppm).

**RESULTS:** Figure 1 shows cyclic voltammograms (CVs) on Cu electrode in LiCl-KCl-UCl<sub>3</sub> and LiCl-KCl-KAlCl<sub>4</sub> melts. The CV in the LiCl-KCl-UCl<sub>3</sub> melt has a cathodic current peak at -1.46 V, which corresponds to the deposition of U metal. The sharp anodic current peak at -1.35 V is due to the dissolution of the deposited U metal. The redox potential of U<sup>3+</sup>/U is in agreement with that previously reported [7]. There is no other distinct current peak, indicating that Cu forms

hardly any alloys with U, which was verified in the temperature range 723-823 K.

The CV in the LiCl-KCl-KAlCl<sub>4</sub> melt has two distinct anodic peaks at -0.75 and -0.93 V, which are due to the dissolution of Al from Cu-Al alloy and Al metal, respectively. The cathodic peak at -0.90 V, corresponding to the anodic peak at -0.75 V, is due to the formation of Al-Cu alloy. The deposition of Al metal occurs at about -1.0 V [5]. The anodic peak at -0.65 V might be due to the Al dissolution from different Al-Cu alloys with less Al activity. The anodic current increasing at -0.40 V is due to the dissolution of Cu into the melt in the form of Cu<sup>+</sup> ions.

**CONCLUSIONS:** The results of electrochemical measurements show that the difference in deposition potential on Cu between Al and U is 0.58 V, suggesting that Al is expected to be highly separated from U by using Cu as the cathode. Al electrodeposition tests in LiCl-KCl melts containing both Al<sup>3+</sup> and U<sup>3+</sup> will be conducted in the near future. The formation rate of Al-Cu alloy should be examined in detail, which may be affected by the operation temperature. The separation technique between U and Al investigated in this study can be applied to the treatment of irradiated U-Al alloy fuels.

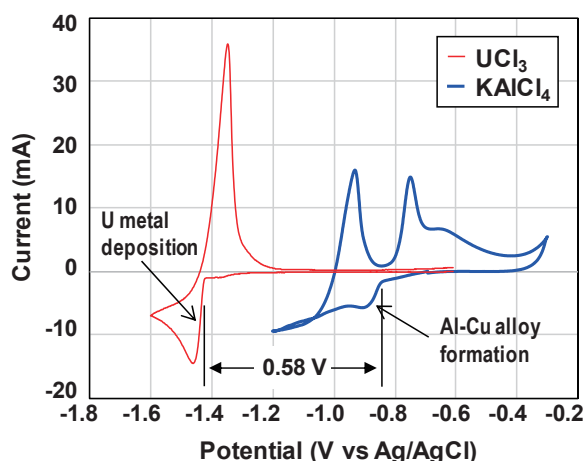


Fig. 1. Cyclic voltammograms obtained on Cu working electrode in LiCl-KCl-UCl<sub>3</sub> (0.16 mol% U) and LiCl-KCl-KAlCl<sub>4</sub> (0.099 mol% Al) melts at ~723 K. Scan rate 0.1 V/s.

### REFERENCES:

- [1] T. Murakami *et al.*, J. Nucl. Sci. Technol., **55** (2018) 1291.
- [2] P. Soucek *et al.*, J. Nucl. Mater., **526** (2019) 151743.
- [3] P. Soucek *et al.*, J. Nucl. Mater., **447** (2014) 38.
- [4] R. Meier *et al.*, J. Nucl. Mater., **498** (2018) 213.
- [5] Y. Sakamura *et al.*, KURRI Progress Report 2012, pp. 100.
- [6] T. B. Massalski, *Binary Alloy Phase Diagrams*, Vol. 1, American Society for Metals, Metals Park, OH, 1986.
- [7] Y. Sakamura *et al.*, J. Nucl. Mater., **502** (2018) 270.

## CO9-4 Structural Change of Borosilicate Glass by Boron Isotope Composition

T. Nagai, Y. Okamoto, D. Akiyama<sup>1</sup>, A. Uehara<sup>2</sup>, T. Fujii<sup>3</sup>, and S. Sekimoto<sup>4</sup>

Japan Atomic Energy Agency (JAEA)

<sup>1</sup>Institute of Multidisciplinary Research for Advanced Materials (IMRAM), Tohoku University

<sup>2</sup>National Institute of Quantum and Radiological Science and Technology (QST)

<sup>3</sup>Graduate school of Engineering, Osaka University

<sup>4</sup>Institute for Integrated Radiation and Nuclear Science, Kyoto University

**INTRODUCTION:** A high-level radioactive liquid waste from a reprocessing process for spent nuclear fuels is processed into a solidified waste made of a borosilicate glass. We estimated the Si-O bridging structure of neutron irradiated borosilicate glass by using Raman spectrometry, and confirmed that the Si-O non-bridging structure increased by the irradiation in our previous study [1]. The structural change by irradiation is regarded as the nuclear reaction  $^{10}\text{B}(n,\alpha)^7\text{Li}$  studied by S. Peugeot, et al [2], but the influence to a Si-O bridging structure by the boron isotope effect has not been clear.

In this study, to understand the influence of glass structural change by neutron irradiation and boron isotope composition, glass samples were made from enrichment boric acid reagents and neutron irradiation of those samples was carried out in Pn-2 of KUR. The structural change of glass sample after the irradiation will be investigated in 2020FY.

**EXPERIMENTS:** Three kinds of borosilicate glass of  $17\text{B}_2\text{O}_3\text{-}65\text{SiO}_2\text{-}17\text{Na}_2\text{O-CeO}_2\text{-Nd}_2\text{O}_3\text{-Y}_2\text{O}_3$  were prepared from raw material reagents of  $\text{SiO}_2$ ,  $\text{Na}_2\text{CO}_3$ ,  $\text{CeO}_2$ ,  $\text{Nd}_2\text{O}_3$ ,  $\text{Y}_2\text{O}_3$ , and natural boric acid of  $\text{H}_3\text{BO}_3$ , enrichment boric acid of  $\text{H}_3^{10}\text{BO}_3$  or  $\text{H}_3^{11}\text{BO}_3$ . These reagents were loaded in an alumina crucible and were melted at  $1,150^\circ\text{C}$  in an electric furnace. After the molten glass samples were solidified by cooling to room temperature, they were cut into thin plates. In this report, it is marked with  $^{10}\text{B}$ -glass, natural-B-glass and  $^{11}\text{B}$ -glass by kind of used isotopic boric acid reagents.

In Oct. of 2019, these thin plate samples were set in a polyethylene tube and were irradiated under the condition of 1,000 kW for 5, 10, and 20 min in the Pn-2 of KUR. After the radioactivity of the samples reduces to the background level, the Raman spectra of the samples will be measured by using a Raman spectrometer, NRS-3100 of JASCO in KUR.

Before neutron irradiation test of glass samples, the Si-O bridging structure difference by boron isotope composition compared by using a Raman spectrometry

**RESULTS:** The Raman spectrum of Si-O bridging structure of a silicate glass were in the wavenumber of  $850\text{-}1200\text{ cm}^{-1}$ , and the peak positions of Raman shifts were different from the number of non-bridging oxygen,

NBO, of the Si-O bridging structure [3]. The Raman shifts of borosilicate glass samples appear in similar wavenumber of  $850\text{-}1,200\text{ cm}^{-1}$ . The Raman peak of  $\text{Q}^4$  structure without NBO appeared in around  $1,150\text{ cm}^{-1}$ , and those of  $\text{Q}^3$ ,  $\text{Q}^2$ , and  $\text{Q}^1$  structures with the NBO number = 1, 2, and 3 were in 1,090, 1,000, and  $900\text{ cm}^{-1}$  respectively. The peaks of  $\text{Q}^2$  and  $\text{Q}^3$  structures can be subdivided into plural by the Si-O-X connecting state, and were divided into  $\text{Q}^{2(1)}$ ,  $\text{Q}^{2(2)}$ ,  $\text{Q}^{3(1)}$ , and  $\text{Q}^{3(2)}$ .

When the Raman shifts of  $^{10}\text{B}$ -glass and  $^{11}\text{B}$ -glass samples were compared, the difference was observed and the measured spectra were separated into six Gaussian waves as shown in Fig. 1. The Raman peaks of  $\text{Q}^1$ ,  $\text{Q}^{2(1)}$  and  $\text{Q}^{2(2)}$  structures of  $^{10}\text{B}$ -glass were higher than those of  $^{11}\text{B}$ -glass, and those of  $\text{Q}^{3(1)}$ ,  $\text{Q}^{3(2)}$  and  $\text{Q}^4$  structures of  $^{10}\text{B}$ -glass were lower than those of  $^{11}\text{B}$ -glass. It was presumed that Si-O non-bridging structure in the borosilicate glass increased with an increase of the  $^{10}\text{B}$  percentage.

The cause of the difference in Raman spectra by boron isotope composition of borosilicate glass is unclear in the present, and an additional investigation is necessary.

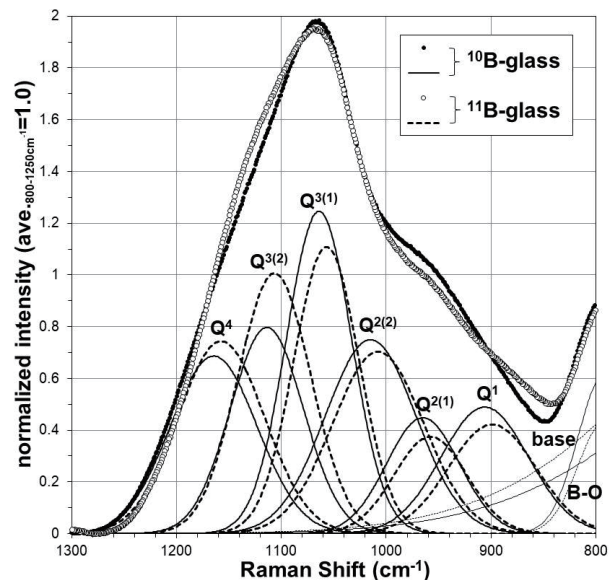


Fig. 1. Raman spectra and separated Gaussian waves. closed circles and fine lines are  $^{10}\text{B}$ -glass, and open circles and dotted lines are  $^{11}\text{B}$ -glass.

### REFERENCES:

- [1] T. Nagai, *et al*, 2018FY KURRI progress report, 30P10-7 (2019).
- [2] S. Peugeot, *et al*, Nucl. Inst. Methods in Phys. Res. B, **327** (2014) 22-28.
- [3] P. McMillan, Am. Mineralogist, **69** (1984) 622-644.

## CO9-5 Study on leaching behavior of carbon-14 from neutron irradiated stainless steel

R. Nakabayashi, S. Sekimoto<sup>1</sup>, T. Sasaki<sup>2</sup>, D. Sugiyama, T. Fujita

*Radiation Safety Research Center, Nuclear Technology Research Laboratory, Central Research Institute of Electric Power Industry (CRIEPI)*

<sup>1</sup>*Institute for Integrated Radiation and Nuclear Science, Kyoto University*

<sup>2</sup>*Graduate School of Engineering, Kyoto University*

**INTRODUCTION:** The speciation of <sup>14</sup>C released from low-level radioactive waste (irradiated stainless steel) is a key parameter in the safety assessment of the intermediate-depth disposal system in Japan. Most of the radionuclides released from the waste will sufficiently decay in the disposal facility owing to the multibarrier system. However, <sup>14</sup>C may not be retained in the multibarrier system until it sufficiently decays, depending on its chemical form. This indicates that it is necessary for the safety assessment to determine the chemical form of <sup>14</sup>C released from the waste under the disposal conditions (highly alkaline and low-oxygen conditions). To develop an understanding of the mechanism of release of <sup>14</sup>C from irradiated stainless steels, leaching experiments have been carried out using a non-irradiated stainless-steel powder in NaOH solutions (of approximately pH 12) under low-oxygen conditions [1, 2]. The results showed that the dominant chemical form of <sup>12</sup>C is a colloidal carbon. If the chemical form of <sup>14</sup>C released from the low-level waste under the disposal conditions is the colloidal carbons, most of the <sup>14</sup>C will be retained for sufficient time and decay in the disposal facility owing to the effect of the filtration property of the engineered barrier (i.e., bentonite). In the safety assessment, this can lead to a reduced dose derived from <sup>14</sup>C. It is essential to carefully determine the chemical forms and clarify why the colloidal carbons formed. In particular, there are few data for the <sup>14</sup>C species released from the irradiated stainless steel under the disposal condition. Therefore, the objective of this study is to identify the chemical form of <sup>14</sup>C released from the neutron irradiated stainless steel under the disposal conditions with the leaching experiments.

**EXPERIMENTS:** The type 316LN stainless-steel powder (particle size ranges from 20 to 53 μm, Lot No. F-1296, Sanyo Special Steel Co., Ltd., Japan) was used in this study. The powder was produced by a gas atomization process. The process essentially consists of the atomization of a stream of liquid metal by high-pressure gas jets and nitrogen is taken into the metal as an impurity. The nitrogen content of the powder is 0.134 wt%, which were taken from a mill test report (No. 1385180011) provided by the suppliers. The chemical depth profile of the stainless-steel powder was obtained by scanning Auger electron spectroscopy/microscopy. The oxide thickness was estimated to be approximately 4

nm for the powder from half the decay of the oxygen content. The oxide layer is mainly composed of iron, chromium and nickel, which is similar to the surface characteristic of irradiated stainless steel generated by the operation of nuclear power plants [3]. The atomized powder (4 g) was packed in a quartz ampoule with 8 mm in diameter and 60 mm in depth and sealed by heating the top part of the ampoule in vacuo. These sealed ampoules were wrapped with aluminum foil and inserted into an aluminum capsule. Capsules containing the atomized powder were irradiated for 10 hours at 1 MW in Hyd facility of Kyoto University Reactor (KUR). The total amount of irradiated sample is 48 g. The thermal neutron flux was  $1.63 \times 10^{13} \text{ n cm}^{-2} \text{ s}^{-1}$  and the thermal neutron capture cross section for the <sup>14</sup>N(n,p)<sup>14</sup>C reaction was  $1.81 \times 10^{-24} \text{ cm}^2$ .

**RESULTS:** In August of 2019, the samples were irradiated using Hyd facility of KUR. The samples irradiated for 10 hours are still cooled to allow for the decay of highly radioactive, short-lived nuclides. The <sup>14</sup>C inventory of irradiated sample was evaluated to be very low ( $\sim 2.5 \times 10^3 \text{ Bq g}^{-1}$ ). The corrosion rate of this sample has not yet been clear. However, the corrosion rate of the type 316L stainless-steel powder, which is very similar to chemical composition of the type 316LN stainless-steel powder, in alkaline condition is extremely low ( $\sim 1.5 \times 10^{-13} \text{ m y}^{-1}$ ), according to previous studies [4]. Based on the above, the amount of <sup>14</sup>C species released from the irradiated steel during the leaching experiment is expected to be quite low and conventional radioanalytical techniques for <sup>14</sup>C detection (e.g., liquid scintillation counting) cannot detect the <sup>14</sup>C species in the leaching experiment. Therefore, a high-sensitivity analysis is planned to be carried out using accelerator mass spectrometry (AMS). AMS has a much lower detection limit than radioanalytical techniques because AMS does not depend on the disintegration of the radionuclide [5]. We plan to transfer the cooled samples to CRIEPI in order to carry out long-term leaching experiments in NaOH solutions under low-oxygen conditions. After the leaching experiments, we also plan to quantify the chemical species of <sup>14</sup>C in liquid and gas phases using AES.

### REFERENCES:

- [1] R. Nakabayashi and T. Fujita, *MRS advances*, **2** (2017) 597-602.
- [2] R. Nakabayashi and T. Fujita, *Radiocarbon*, **60** (2018) 1691-1710.
- [3] D. Bradbury *et al.*, *Proceedings of International Joint Topical Meeting of the American Nuclear Society-Canadian Nuclear Association on the Decontamination of Nuclear Facilities*. (1982).
- [4] R. Nakabayashi and T. Fujita, *Migration 2019*, (2019) PA1-6.
- [5] B. Z. Cvetković *et al.*, *Radiocarbon*, **60** (2018) 1711-1727.

## CO9-6 Solvent extraction of selenium in the nitric acid solution with selected elements

T. Kawakami, Y. Yoneda, S. Ogawa, C. Kato, S. Fukutani<sup>1</sup>, T. Matsumura<sup>2</sup>, Y. Tsubata<sup>2</sup>, K. Morita<sup>2</sup>, A. Uehara<sup>3</sup>, and T. Fujii

Graduate School of Engineering, Osaka University  
<sup>1</sup>Institute for Integrated Radiation and Nuclear Science, Kyoto University

<sup>2</sup>Nuclear Science and Engineering Center, Japan Atomic Energy Agency

<sup>3</sup>National Institutes for Quantum and Radiological Science and Technology

**INTRODUCTION:** As a method to preserve high level waste from spent nuclear fuel, vitrification followed by geological deposition is considered. High level waste contains long-lived fission products (LLFP), with some that have a half-life of over 1,000,000 years. <sup>79</sup>Se is a LLFP with a half-life of 326,000 years and compared to other LLFP and minor actinides (MA), its toxicity appears earlier. Due to the half-life of <sup>79</sup>Se, it does not pose as an immediate risk, but considering geological deposition, it would be beneficial to separate and transmute Se before the disposal. Selenium is also a rare earth element, and is used for glass manufacturing and Li-Se batteries. The separation and conversion method to reduce the long-term toxicity of LLFP is considered in previous studies using novel extractants [1]. However, the solvent extraction behavior of Se is not well known with these extractants. In this study, we focused on the separation of Se and the solvent extraction characteristics in a nitric acid system using novel extractants proposed for the SELECT process to understand the behavior of Se in the separation process of MA. Furthermore, we used extractants that are known to extract Se separately [2], and test whether it is possible to achieve high distribution ratios with co-existence of other elements simulating the high-level radioactive waste solution.

**EXPERIMENTS:** For the organic phase, *N, N, N', N', N'', N''*-hexaocetyl nitrotriacetamide (HONTA), alkyl diamide amine (ADAAM), *N, N, N', N'*-tetradodecyl-diglycol amide (TDdDGA), *N*-phenyl ethylenediamine (*N*-PDA), *o*-phenylenediamine (*o*-PDA), and 4,5-dimethyl-1,2-phenylenediamine (DMePDA) were used as extractants and *n*-dodecane, 1-octanol and nitrobenzene were used as solvents. Tetravalent Se was dissolved in HNO<sub>3</sub> for the aqueous phase. For the simulation of high-level radioactive liquid waste, La was selected as a representative element of light lanthanides, Dy as a representative of heavy lanthanides, and Gd due to having an intermediate mass. In addition, Pd as a platinum group element in fission products, and Sr and Cs, which are elements with a large abundance in the liquid waste. The concentration of each element in the simulated solution are as follows: Se 1 mM, Pd 10 mM, Cs 15 mM, Sr 2.5 mM, Gd 1 mM, La 10 mM, Dy 1 mM. Both phases were stirred for 30 minutes to perform fore extraction, and then separated by centrifugation at 2000 rpm for 5 mins. Thereafter, HNO<sub>3</sub> was added to the separated

organic phase to perform back extraction. All experiments were carried out at 298 K. The Se concentration of the aqueous phase after both extractions were measured by Inductively Coupled Plasma-Atomic Emission Spectrometry (ICP-AES) and Inductively Coupled Plasma-Mass Spectrometry (ICP-MS), and the distribution ratios were determined.

**RESULTS:** The distribution ratio of Se between HNO<sub>3</sub> and the organic phases of HONTA, ADAAM and TDdDGA was well below 1. Using *o*-PDA as the extractant with octanol, and high concentration HNO<sub>3</sub> for back extraction had the highest distribution ratio ( $D = 3.6$ ). Using this condition, the distribution behavior of Se with multiple elements was observed (Fig 1). In the low nitric acid concentration, it was  $D > 10$  for Se, and the separation factor for each element exceeded 1000.

**CONCLUSION:** Se was not extracted by the novel extractants and remained in the residual solution. For the simple extraction of Se, it was effective to use *o*-PDA as the extractant, octanol as the solution, and concentrated nitric acid for back extraction. Se was effectively separated from other elements in the simulated solution at low HNO<sub>3</sub> concentration.

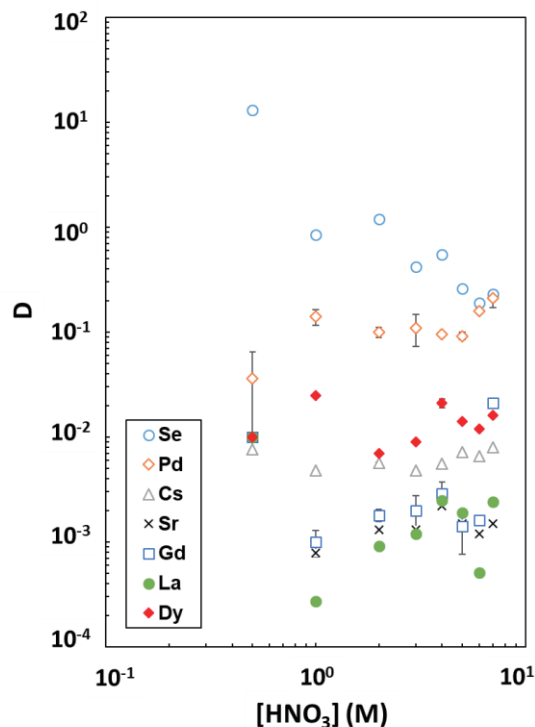


Fig. 1. Dependence of  $D$  on nitric acid concentration for selected elements using *o*-PDA.

### REFERENCES:

- [1] Y. Ban *et al.*, Solvent Extr. Ion Exch., **37** (2019) 27-37.
- [2] Y. Sasaki *et al.*, Solvent Extr. Res. Dev. Jpn., **24** (2017) 113-122.

## CO9-7 Effect of $\gamma$ -Ray Irradiation in $\text{HNO}_3$ on Adsorptivity of Long-Chain 6-Membered Cyclic Monoamide Resin

Y. Yoshimura<sup>1</sup>, R. Hamashiro<sup>1</sup>, M. Nogami<sup>1</sup>, and N. Sato<sup>2</sup>

<sup>1</sup>Faculty of Science and Engineering, Kindai University

<sup>2</sup>Institute for Integrated Radiation and Nuclear Science, Kyoto University

**INTRODUCTION:** It is of great importance to develop resins with selectivity to uranium(VI) species in nitric acid media. As a part of this purpose, we have been investigating the change in chemical structure and adsorptivity to metal ions of a cyclic monoamide resin. The manner of structure change in the resins has been found basically identical, namely, starting from the cleavage of the monoamide ring by the addition of oxygen atom originating from  $\text{HNO}_3$ , followed by the formation of chain monoamides by the continuous addition of oxygen. These compounds have multiple coordinative oxygen atoms, *e.g.*, carboxyl groups, but the change in the adsorptivity has been found different resulting probably from the number of atoms in the ring[1-3]. More recently, our attention has been paid to long-chain cyclic monoamides, and we have previously reported the results for the resin consisting of 1-(4-vinylbenzyl)piperidin-2-one (VBPP)[4]. It has a 6-membered cyclic piperidine ring with a spacer between the functional carbonyl group and the main polymer chain. In the present study, a newly synthesized long-chain cyclic monoamide resin consisting of 5-membered pyrrolidone ring (1-(4-vinylbenzyl)-pyrrolidone-2-one(VBPR)) was similarly investigated.

**EXPERIMENTS:** VBPR was synthesized by reacting 2-pyrrolidone with copolymer beads of chloromethylstyrene and divinylbenzene by following the literature[5].  $\gamma$ -Ray irradiation to VBPR was carried out using 6 M  $\text{HNO}_3$  similarly to the earlier study (max. 0.2 MGy)[1]. The irradiated VBPR was separated from the supernatant liquid and washed using distilled water to avoid further degradation by  $\text{HNO}_3$ . Adsorptivities of the irradiated VBPR to metal ions at equilibrium were obtained by a batch method. Samples of the conditioned resin (wet 0.15 g) and 3  $\text{cm}^3$  of 0.1 - 6 M  $\text{HNO}_3$  solutions containing 1 mM Re(VI) or Zr(IV), or tracer U(VI) were shaken at 298K in a thermostatic shaking bath for 24 h. After shaking, samples of the supernatant were taken and the concentrations of the metal ions were measured using ICP-OES for Re and Zr, and ICP-MS for U. Adsorptivities were evaluated by the distribution ratio,  $K_d$ .

**RESULTS:** Adsorptivities of VBPR irradiated in 0.1 M  $\text{HNO}_3$  at various dose to the examined metal ions are shown in Fig. 1. The  $K_d$  values for Re(VII) and Zr(IV) are found basically increased with increasing dose. For U(VI), the identical tendency is found for lower dose, and  $K_d$  values are found constant above 0.1 MGy. The  $K_d$  values for Re(VII) for VBPP were in an opposite manner

decreased with increasing dose[4], and the reason remains unclear.

It is known that the bond between methylene carbon and nitrogen atom of tertiary-amine-type anion exchange resins undergoes cleavage by heating or  $\gamma$ -ray irradiation, leading to decrease in adsorptivity to metal ions. The results in Fig. 1 indicate that the reaction of the route (I) in Fig. 2 is dominant and that the route (II) is negligible in the present irradiation experiments. In fact, very little water-soluble organic compounds were detected by NMR analysis.

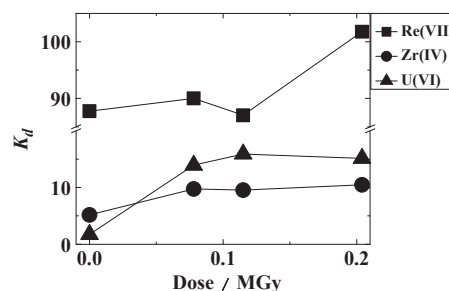


Fig. 1. Adsorptivity of VBPR irradiated in 6 M  $\text{HNO}_3$  at various dose to metal ions in  $\text{HNO}_3$

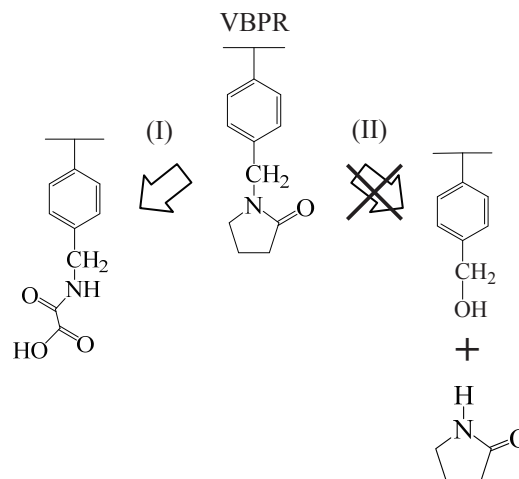


Fig.2. Expected major route of change in chemical structure of VBPR by  $\gamma$ -ray irradiation in  $\text{HNO}_3$

### REFERENCES:

- [1] N. Miyata *et al.*, KURRI Progress Report 2010 (2011) 258.
- [2] M. Nogami *et al.*, J. Radioanal. Nucl. Chem., **296** (2013) 423-427.
- [3] T. Nishida *et al.*, KURRI Progress Report 2013 (2014) 295.
- [4] M. Nogami *et al.*, KURRI Progress Report 2017 (2018) 197.
- [5] M. Nogami *et al.*, Prog. Nucl. Energy, **50** (2008) 462-465.

K. Takamiya, Y. Takeuchi, T. Takeuchi, S. Sekimoto, Y. Oki and T. Ohtsuki

*Institute for Integrated Radiation and Nuclear Science, Kyoto University*

**INTRODUCTION:** A large amount of radioactive materials containing fission products have been released from the Fukushima Daiichi Nuclear Power Plant after the Great East Japan Earthquake in 2011. Main forms of the radioactive materials are insoluble micro-particles [1] and soluble aerosol particles. The generation processes of these materials are important to understand the environmental condition of the reactors. Experimental approach to elucidate the generation process of the radioactive aerosols has been performed in our previous work [2-5]. It was found that there is an attachment process induced by electrostatic interaction between a fission product and surface of an aerosol particle. However, the electrostatic interaction could not be quantitatively clarified because fission products emitted from  $^{252}\text{Cf}$  source used in the previous work have recoil velocities which induces the attachment process by geometric collision. In the present work, the attachment behavior has been observed using aerosol generating apparatus combined with neutron irradiated  $\text{UO}_2$  as a source of fission products. Since fission products released from the irradiated  $\text{UO}_2$  by heating have no recoil velocity, observation of attachment behavior without geometric collisions becomes possible.

**EXPERIMENTS:** The experimental setup to generate and collect radioactive aerosols containing fission product is expressed in the previous report [6]. Powder of  $\text{UO}_2$  was encapsulated in a quartz tube under reduced pressure, and the quartz tube covered by a polyethylene tube was inserted into polyethylene capsule to irradiate neutrons using pneumatic transport system, Pn-2, of KUR. The amount of  $\text{UO}_2$  was 10 mg, and the neutron irradiation time is 30 min. A few mg of irradiated  $\text{UO}_2$  powder was extracted to another quartz tube placed in an electric furnace. Fission products produced in the irradiated  $\text{UO}_2$  powder was released by heating the furnace up to  $1000^\circ\text{C}$ . On the other hand, atomizer filled with 0.01 M sodium chloride solution generate solution aerosol. Both released fission products and solution aerosol particles were aspirated by a suction pump to be transported and mixed in a cylindrical chamber. The volume of chamber is changeable to interact fission products and aerosol particles for different durations. Radioactive aerosol particles were produced by attaching fission products to aerosol particles in the chamber, and the difference of interaction time causes the difference of effective surface area of aerosol particles to attach fission products. The produced radioactive aerosol particles were collected on a polycarbonate filter at downstream of the chamber. The amount of fission products which attaches to

aerosol particles were estimated by gamma-ray spectrometry for the filter using a Ge-detector. On the other hand, the amount of fission products released from the irradiated  $\text{UO}_2$  powder by heating was estimated by subtraction of gamma-ray spectra measured before and after heating the  $\text{UO}_2$  powder.

**RESULTS:** The attachment ratio of fission products to NaCl solution aerosol particles is shown in Figure 1 as a function of total effective surface area. Squares, triangles and circles show the attachment ratio of  $^{95}\text{Zr}$ ,  $^{103}\text{Ru}$  and  $^{131}\text{I}$ , respectively. Diamonds indicate the previous result for  $^{104}\text{Tc}$  observed by using  $^{252}\text{Cf}$  as a source of fission products. Attachment ratio of  $^{104}\text{Tc}$  is larger than those of other isotopes clearly because  $^{104}\text{Tc}$  could attach through both processes of electrostatic interaction and collision with recoil velocity. Three kinds of fission product observed in the present work show different attachment ratio each other that indicate the different degree of electrostatic interaction caused by the difference of chemical species.

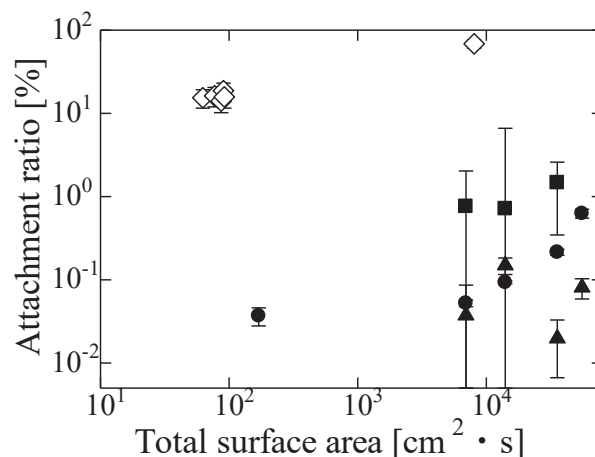


Fig. 1 Attachment ratio of fission products to sodium chloride solution aerosol particles as a function of the total surface area of the aerosol particles.

This work was supported by JSPS KAKENHI Grant Numbers JP24110005 and JP26286076.

### REFERENCES:

- [1] K. Adachi et al., Scientific Reports, **3** (2013) 2554.
- [2] K. Takamiya et al., J. Radioanal. Nucl. Chem. **307** (2016) 2227-2230.
- [3] K. Takamiya et al., J Radiat. Prot. Res. **41** (2016) 350-353.
- [4] K. Takamiya et al., KURRI Progress Report 2016 (2017) 45-45.
- [5] K. Takamiya et al., KURRI Progress Report 2017 (2018) 13-13.
- [6] K. Takamiya et al., KURNS Progress Report 2018 (2019) 95-95.

## CO9-9 Precipitation of alkaline earth elements toward the chemical study of Nobelium

S. Hayami, Y. Kasamatsu, K. Tonai, E. Watanabe, K. Takamiya<sup>1</sup> and A. Shinohara

Graduate School of Science, Osaka University  
<sup>1</sup>Institute for Integrated Radiation and Nuclear Science,  
Kyoto University

**INTRODUCTION:** Nobelium (No) with atomic number 102 is one of actinide elements. It is reported that stable oxidation state of No is +2 although those of the other heavy actinide elements are all +3. The chemical behavior of No is reported to be similar to that of group 2 elements in HCl [1]. However, it is difficult to investigate the chemical properties of No because of low production rates and short half-lives of the No nuclides. Therefore, it is important to conduct fundamental experiments of Group 2 elements for chemistry of No.

Previously we reported new experimental method in which the hydroxide complexation of the target elements can be studied from the coprecipitation behavior with samarium hydroxide [2]. So far, we have qualitatively investigated the coprecipitation behaviors of various elements, and we successfully applied the method to element 104, rutherfordium (Rf). Recently, coprecipitation experiments with group 2 elements that are comparative elements for No have been in progress. In this study, both coprecipitation and precipitation experiments were performed for Group 2 elements Ca, Sr, and Ba. In addition, in order to elucidate the new chemical properties of No, we focused on the reaction with sulfate ions, and conducted experiments on coprecipitation behavior of these elements with BaSO<sub>4</sub> using ammonium sulfate in addition to sulfate precipitation experiments.

**EXPERIMENTS:** <sup>85</sup>Sr and <sup>133</sup>Ba samples were prepared by irradiating protons on pellet samples of RbCl for 1 h and of CsCl for 10 h using the AVF cyclotron at RCNP. <sup>47</sup>Ca sample was prepared by irradiating thermal neutrons ( $3 \times 10^{13} \text{ cm}^{-2} \text{ s}^{-1}$ ) on a powder sample of CaO for 1 h using the reactor at KUR. They were separated from other majority of radioisotopes by cation-exchange and anion-exchange methods.

In the hydroxide coprecipitation experiment, 20  $\mu\text{L}$  (20  $\mu\text{g}$ ) of Sm standard solution (1 M HNO<sub>3</sub>) was added into the <sup>85</sup>Sr or <sup>133</sup>Ba solution. In case of the precipitation experiment, 20-1000  $\mu\text{g}$  of Sr or Ba chloride or 10 mg of <sup>47</sup>CaO in aqueous solution was added. After mixing it, 2 mL of basic solution was added to generate hydroxide precipitate. In the present experiment, we used dilute or concentrated NH<sub>3</sub> solution, or 0.1, 1, or 6 M NaOH solution as the basic solution to observe the dependence of the precipitation yield on the concentration of the basic solution.

In the sulfate coprecipitation experiment, 20  $\mu\text{L}$  (20  $\mu\text{g}$ ) of BaCl<sub>2</sub> solution was added to the <sup>85</sup>Sr or <sup>133</sup>Ba solution. In case of precipitation experiment, 20-1000  $\mu\text{g}$  of

Sr or Ba chloride solution was added. After mixing it, 2 mL of 0.01, 0.1, or 1.0 M (NH<sub>4</sub>)<sub>2</sub>SO<sub>4</sub> solution was added to generate sulfate precipitate. These solutions were stirred for 5 min at room temperature. The precipitates were collected with membrane filter by suction filtration. The precipitate and filtrate samples were then dried on heater at 100 degree C and were assayed by  $\gamma$ -ray measurements. The coprecipitation yields were determined from radioactivity of the  $\gamma$ -ray measurements.

**RESULTS:** The precipitation (ppt) and coprecipitation (co-ppt) yields were determined from the equation:  $A_{\text{ppt}} / (A_{\text{ppt}} + A_{\text{fil}})$ , where  $A$  represents the radioactivity, and ppt and fil indicate the precipitate and filtrate, respectively.

In the hydroxide precipitation and coprecipitation experiment, the yields of precipitation of Ca, Sr, and Ba were very low at low [OH<sup>-</sup>] and increased in high [OH<sup>-</sup>]. However, the yields of coprecipitation of Sr, and Ba were high at low [OH<sup>-</sup>] and almost zero at high [OH<sup>-</sup>]. These results might be due to the facts that for alkaline earth metal elements, formation of polynuclear precipitates and species were reported in macro scale. Coprecipitation behavior is considered to relate to the behavior in a mononuclear precipitate. Since the No can be dealt as single atoms, the data on coprecipitation behavior would be able to be used as comparative data to discuss the complex formation of No.

In the sulfate precipitation and coprecipitation experiments (Fig.1), it was found that the coprecipitation behavior of Sr and Ba was basically consistent with that in precipitation. Differences were also found in the coprecipitation yields among group 2 elements which are qualitatively consistent with their solubility products.

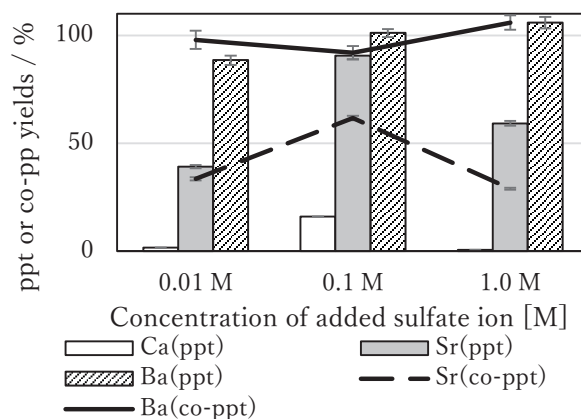


Fig. 1. The yields in sulfate precipitation and coprecipitation experiments.

### REFERENCES:

- [1] R. J. Silva *et al.*, *J. Inorg. Chem.*, **13**, 9, 2233-2237 (1974).
- [2] Y. Kasamatsu, *et al.*, *Appl. Radiat. Isot.* **118**, 105-116 (2016).

T. Iimoto, Y. Igarashi, J. Nakayama, R. Miura,  
K. Yamamoto and T. Takahashi<sup>1</sup>

*The University of Tokyo*

<sup>1</sup>*Institute for Integrated Radiation and Nuclear Science,  
Kyoto University*

**INTRODUCTION:** Important aspects of the study can be found in the following keywords, such as safety, security, hygiene and disaster prevention. Nuclear research reactor is one of representative facilities together with these keywords under their operation. It is effective to investigate the latest status on practical measures on these keywords in various facilities including nuclear research reactors, to compare each other among facilities, and to discuss more optimized ones for our positive safety management. Through this process, it is also essential to investigate the latest international and/or national regulations and the movement of revision of them. In addition, development of human resource and public literacy on nuclear science and technology is also within the scope of the research. The total discussion contents and their fruits are directly useful for all relating laboratories.

### RESEARCH APPROACH:

General research approach is as follows.

- Measures of safety management during operation or standstill status of the real facilities would be investigated. This information would be used for our research discussion on the positive and more optimized safety management.
- It would not be a single year research, but maybe two to three years research for one theme.
- Information source of facilities would not be only KUR, KUACA or the other facilities in Kyoto University, but also the Kinki university research nuclear reactor or the facility of National Institute of Fusion Science, etc. This research is an active joint-research with these relating facilities and positive researchers on safety management.
- One of the distinctive features of this research is to involve office staffs as cooperators as well as researchers and technical staffs. In The University of Tokyo, most of the members in Division for Environment, Health and Safety are office staffs who knows real situation of safety management in laboratories very well.

Concrete discussion target in FY of 2019 was determined as following two; “standardizing education system for safety managers and users in universities for application

of small amount of U and Th” and “radiation education and human resource development in secondary school from global viewpoint” through our member discussion.

### EDUCATION SYTEM IN UNIV. FOR SMALL AMOUNT U&Th APPLICATION:

Safety education system for managers and users of small amounts of U and Th has been discussed to standardize it in universities. Latest status of their education in several Japanese universities have been investigated and concluded the common and needed viewpoints. In addition, throughout this discussion, not only good practices and ideas for nuclear material safety management at the laboratory and laboratory levels, but also issues to be overcome under the current Japanese legal system were shared. The discussion fruits are started to be opened through technical journals, for example, the first article was published in the early 2020 as the reference [1].

### RADIATION EDUCATION AND HRD IN SECONDARY SCHOOL:

International Atomic Energy Agency (IAEA) RAS0065/0079 (2012-2021) Technical Cooperation Programme (TCP) relating secondary school education on nuclear science and technology (NS&T) in Asia and Pacific region became a trigger for us to organize Team JAPAN. This team consists of several Japanese experts to support the activities and develop several educational tools and modules with “WOW factor” using the STREAM (Science, Technology, Robotics, Engineering, Arts and Mathematics) education concept. So far, a hand-made Air-GM counter, a wide-view Peltier type cloud chamber, a handy radiation monitor for school application, motivation-up movies, etc, has been developed by us. Team JAPAN continues its activities with the cooperation with experts, teachers, and other stakeholders in the world. The discussion fruits are started to be opened through technical journals, for example, several articles were published as the reference [2][3][4].

### REFERENCES:

- [1] K. Yasuda, M. Yasuda, T.Iimoto *et.al.*, RADIOISOTOPES, **69** (2020) 55-65.
- [2] T. Iimoto *et.al.*, Journal of Radiation Emergency Medicine, **8** (2019)33-38.
- [3] K. Katengeza, T. Iimoto *et.al.*, Japanese Journal of Health Physics, **54** (2019) 206-211.
- [4] T. Toda, T. Iimoto *et.al.*, Radiation Protection Dosimetry, **184** (2019) 539-542.

M. Takagaki and S. Masunaga<sup>1</sup>

*Louis Pasteur Center for Medical Research*  
<sup>1</sup>*Institute for Integrated Radiation and Nuclear Science,*  
*Kyoto University*

In this report, we will report the ethnography of the returned residents of Iitate Village in the 9th year after the disaster in two parts. Part 1 is about the responsibility of science, which is the main subject of this research. In Part 2, I will briefly report on the criticism of science that can be intensely drawn from the story of villagers who lives in nature.

Former UNSCEA Commission on Radiation Effects Prof. Wolfgang Weiss stated the responsibility for science after the Fukushima nuclear accident as follows; “The most serious damage caused by Fukushima accident is that people lost trust for science and scientists. This certainly will influence long- term human history, and we cannot recover such situation so easily. We scientists are responsible to such situation.” (Prof. Wolfgang Weiss)

Clearly explaining the responsibility of science is difficult. Because it is an essential factor unavoidably embedded in the uncertainty of science. What is science to humanity? In particular, regarding the responsibility of science in nuclear accidents, it is important to structurally analyze various factors in addition to science and approach where responsibility lies. There are much factors involved such as politics, economy, energy and environment are numerous. There is always a danger in using the results of natural science as a technology in society. Technology is always absorbed by human society while maintaining a sympathetic relationship with safety, such as danger due to immaturity of technology and danger as the sum total due to interaction with other technologies. Nuclear power generation technology has been used for human welfare while balancing danger and safety issues at unrealizable levels.

Occasionally, in the human society, it is not uncommon for security to be neglected by paying attention to the return of capital based on the logic of investment. Once the basic science is put into practical use and used as a technology in society (politico-economic engine), the logic of capital, such as investment in technology and recovery and

recovery of wealth, will return the basic science to investment (positive feedback), and the position of science will be politico-economically jeopardized (Fig.1).

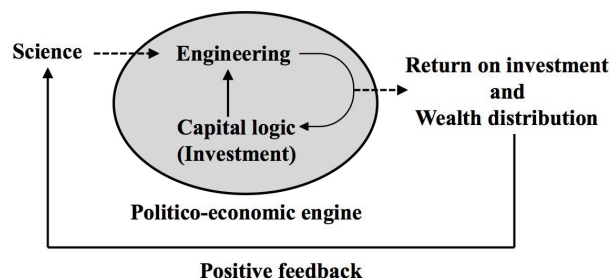


Fig.1 Politico-economic engine for technologizing the science.

Scientists should be discreet enough to apply their science findings to technology. If the principle of capital intervenes at this stage, science will possibly become a non-science, and it will become one of the engines absorbed by the capital principle as technology, and the location of risk will no longer be clear. Professor Hideki Yukawa, who was the first member of the Reactor Promotion Committee under the Nakasone administration, resigned in opposition to the promotion of nuclear technology, saying that safety could not be guaranteed. I don't know if his actions can be justified, but it could be considered as a waiver of scientists' responsibility. I have long argued for the need for regulatory anthropology, but few researchers have shown understanding. A cultural anthropology department that investigate the safety of nuclear science with the peace of mind that the public is convinced should be installed in a nuclear research institute.

Is it possible to regulate so that both scientific safety and psychological security can be achieved at the same time, or not? Such regulation science does not exist in much fields of our natural science, but rather in fields of medicine and drug safety. Approximately 10 years before the accident occurred, National Institute of Radiological Sciences (NIRS) tried to advance the field of regulatory science, but the Science and Technology Agency at that time showed little understanding. It means that the Science and Technology Agency was just for promoting nuclear power, so safety was just an excuse. I wonder if the gaps around it will be filled up a little with anthropology.

## CO10-3 Assessment of non-homogenous exposure of radiation workers in accelerator facility – situation in the small linac facility -

M. Kowatari and T. Kubota<sup>1</sup>

Center for Advanced Radiation Emergency Medicine,  
National Institutes for Quantum and Radiological Science and Technology

<sup>1</sup> Institute for Integrated Radiation and Nuclear Science, Kyoto University

**INTRODUCTION:** The reduced occupational dose limit for the lens of the eye has been adopted by the International Atomic Energy Agency [1], the European Union [2] and the United States [3]. Annual equivalent dose limit for the lens of the eye for occupational exposure in planned situations was reduced from 150 mSv to 20 mSv averaged over five consecutive years and 50 mSv in any single year. Comprehensive survey was made and the technical document for eye lens monitoring has been released from the IAEA [5].

The study focuses on how the inhomogeneous exposure of radiation workers due to radiation from activated apparatus of the accelerators can be assessed. The purpose of the study is to evaluate whether the additional monitoring of the eye lens dose is required for the radiation workers in the accelerator facility. The authors introduce a quantitative index, HI which expresses how much radiation workers are exposed non-homogeneously for their radiation work. HIs were defined as the ratio of the personal dose equivalent for the eye lens and the extremity monitoring to that for the whole-body monitoring.

**EXPERIMENTS:** We focused on the exposure situation of radiation workers who are engaged in the handling of the activated target in the linac facility. The HIs for this exposure situations were experimentally evaluated using a water-filled phantom with the Optically Stimulated Luminescence (OSL) dosimeters (nanoDot™, Nagase Landauer Ltd.) incorporated with a water-filled phantom. The phantom was placed in the workplace to mimic the respective work. Since inhomogeneous exposure will be expected in terms of extremities as well as the lens of the eye, OSL dosimeters were put on the fingers and palms of the physical phantom. The ambient dose equivalent rate of the vicinity of the target was measured to be

around 100  $\mu\text{Sv h}^{-1}$ . The physical phantom with the OSL dosimeters was set for 18 hours and the OSL dosimeters were read after the irradiation.

**RESULTS:** Table 1 was listed the comparison of the ratio of the eye lens dose or the extremity dose to the trunk dose measured on the physical phantom set close to the accelerator target for mimicking the target handling and adjustment. Table 1 also showed the results of the ratio of HIs analytically estimated in accordance with the inverse square law of the radiation emission. The theoretically estimated HIs can predict the measured HIs within factor two. However, the discrepancy between analytically estimated and measured HIs were found to be factor 5. This might be explained by the difference of the exact distance between the source and the hand (palm) and the influences of the shielding and the source shape of the target.

### REFERENCES:

- [1] International Atomic Energy Agency (IAEA). Radiation protection and safety of radiation sources: International Basic Safety Standards. General Safety Requirements Part 3.
- [2] European Union (EU). Basic safety standards for protection against the dangers arising from exposure to ionizing radiation. Council Directive 2013/59/EURATOM.
- [3] NCRP Commentary No. 26 - Guidance on Radiation Dose Limits for the Lens of the Eye (2016). ISBN 978-0-913392-17-1.
- [4] ORAMED: Optimization of Radiation Protection of Medical Staff, EURADOS Report 2012-02. ISBN 978-3-943701-01-2.
- [5] International Atomic Energy Agency (IAEA). implications for occupational radiation protection of the new dose limit for the lens of the eye. IAEA-TECDOC-1731. (2013), ISBN 978-92-0-115213-8.

**Table 1. Evaluated HIs from measurement using the physical phantom and the OSLs in the exposure situation which the adjustment of the target is simulated**

	HI <sup>eye</sup> or HI <sup>ext</sup>	Ratio analytically estimated from the inverse square law
Right eye lens dose vs Trunk dose $H_p(3)_{\text{eye}} / H_p(10)_{\text{trunk}}$	$3.09 \pm 0.09$	5.67
Left eye lens dose vs Trunk dose $H_p(3)_{\text{eye}} / H_p(10)_{\text{trunk}}$	$4.62 \pm 0.09$	6.93
Right finger dose vs Trunk dose $H_p(0.07)_{\text{ext}} / H_p(10)_{\text{trunk}}$	$23.2 \pm 0.63$	149
Left finger dose vs Trunk dose $H_p(0.07)_{\text{ext}} / H_p(10)_{\text{trunk}}$	$20.7 \pm 0.5$	149

## CO10-4 Investigation for validation of trace elements concentration in accelerator room concrete

G. Yoshida, K. Nishikawa, Y. Sakaki, Y. Morikawa<sup>1</sup>, M. Inagaki<sup>2</sup>, S. Sekimoto<sup>2</sup>, T. Miura, A. Toyoda, H. Matsumura and K. Masumoto

Radiation Science Center, KEK

<sup>1</sup>Accelerator Laboratory, KEK

<sup>2</sup>Institute for Integrated Radiation and Nuclear Science, Kyoto University

**INTRODUCTION:** We are working on the research for establishment of more reasonable decommissioning process of accelerator facilities with the aid of Japan Nuclear Regulation Authority. Especially, concrete materials used as shields and buildings occupy the most amount of weight in a facility, and significantly contribute to the cost of decommissioning. The generated radionuclides should be identified in advance and waste should be separated into activated and non-activated areas for efficiency and waste reduction, when decommissioning an accelerator facility.

However, the assessment of an activation concrete material is not easy. Currently, the destructive analysis by core boring is the only method of investigating that. From this background, we had developed a breakthrough method to estimate the activity of <sup>60</sup>Co and <sup>152</sup>Eu in activated concrete in the accelerator facility from the contact dose rate measurement with a survey meter [1,2]. This method strongly depends on the concentrations of cobalt and europium which is trace elements in a concrete. From the viewpoint of practical use, the variation of trace elements concentration in the concrete must be understood.

We also had developed the method for prediction the activity in the concrete material at future, by measuring the activities of <sup>24</sup>Na and <sup>56</sup>Mn immediately after the accelerator operation [3]. For this method, information of variation of natural sodium and manganese in concrete of accelerator facilities is indispensable.

In this study, we analyzed trace element concentrations in concrete samples of some accelerator facilities in Japan with neutron activation analysis which suitable for trace element analysis of ppm order, and compared the result.

**EXPERIMENTS:** Total 89 of core concrete samples collected from 8 facilities were prepared as irradiation samples. Each core sample were grounded to 100 μm mesh particle size by a ball mill. Two igneous rocks (JA-1, JG-3) were employed as references and prepared in the same way. For analysis of short-lived nuclides generated by neutron irradiation, 40 samples were irradiated at Pn-3 with 1 MW during 10 s, and measured with a Ge detector immediately after irradiation. All samples including the above 40 samples were irradiated at Pn-2 with 5 MW during 3000 s, and measured with a Ge detector after short lived nuclides were attenuated.

**RESULTS:** From the gamma-ray spectra of the samples, total 26 radionuclides generated by neutron capture reaction were identified. Although the analysis is in pro-

gress, variations of elemental concentration in concrete of the samples were determined as shown in Fig. 1. The concentration of cobalt and europium had been discussed in elsewhere [4]. We will discuss the other elements in the near future. Currently, we are working on a database of accelerator facility concrete measurements and plan to update it as needed.

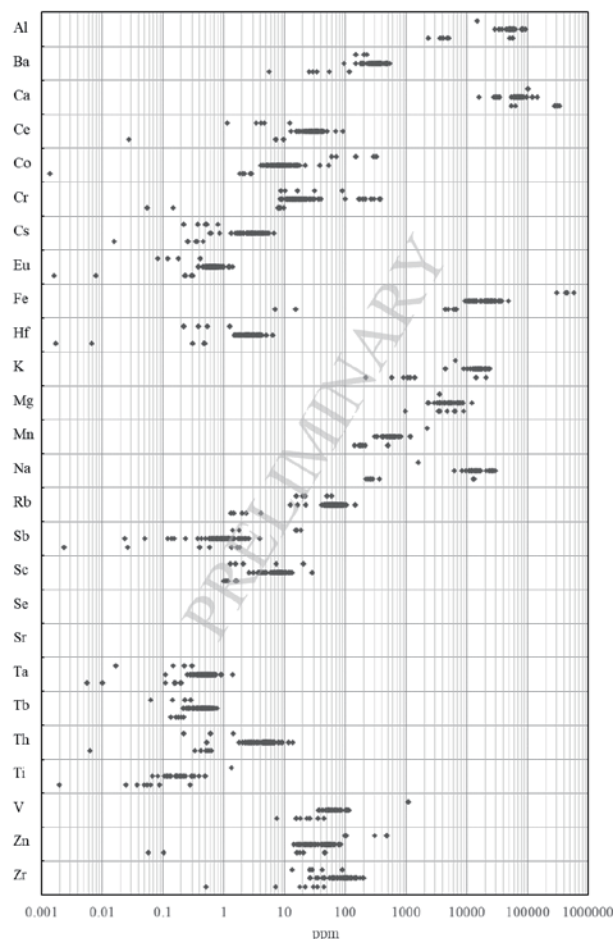


Fig. 1. Variation of elemental concentration in concrete samples of accelerator facilities determined by neutron activation analysis.

### REFERENCES:

- [1] H. Matsumura, A. Toyoda *et al.*, *J.Phys.Conf.Ser.*, **1046** (2018) 0120016.
- [2] H. Matsumura, G. Yoshida *et al.*, *Environmental Radiochemical analysis VI*, (2019) 135-147.
- [3] H. Matsumura, G. Yoshida *et al.*, *Radiation Protection*, in Press.
- [4] G. Yoshida, K. Nishikawa *et al.*, *J.Radioanal. Nucl.Chem.* in Press.

# CO10-5 Comparison of Chlorine Concentration in Each Municipal Solid Waste Fraction Measured by Neutron Activation Analysis and Bomb Calorimeter- Ion Chromatography

K. Oshita, S. Hayasaki, S. Fukutani<sup>1</sup> and M. Takaoka

Department of Environmental Engineering, Graduate School of Engineering, Kyoto University

<sup>1</sup>Institute for Integrated Radiation and Nuclear Science, Kyoto University

**INTRODUCTION:** In recent years, plastic contained in waste has become a serious problem worldwide. Specifically, from the viewpoint of hazardous substances, some plastics generate hydrogen chloride and organic chlorine compounds when they burn, so information on chlorine is necessary. Therefore, in this study, the chlorine in each fraction contained in the municipal solid waste (MSW) was analyzed by the bomb calorimeter - ion chromatographic method (B-IC) and the neutron activation analysis (NAA), and the results were discussed and compared.

**EXPERIMENTS:** The MSW sampled from the pit of the MSW incineration facility of municipality A was classified into 20 categories, dried at 100 °C, and then homogenized to 2 mm or less with a crusher. Chlorine measurement was carried out for 16 categories listed in the Table 1 in which sufficient amounts were obtained for measurement. First, NAA for chlorine was performed four times for each sample. Samples were irradiated for 5 min with a thermal neutron flux of  $2.0\text{--}2.4 \times 10^{13} \text{ cm}^{-2} \cdot \text{s}^{-1}$  at KURRI. <sup>38</sup>Cl ( $t_{1/2} = 37.18 \text{ min}$ ,  $E_{\gamma} = 1642, 2168 \text{ keV}$ ) were measured by using a Ge semiconductor detector for 60 sec. Chlorine conc. was also measured once by B-IC based on JIS K 7302-6 [1].

**RESULTS:** The chlorine concentrations measured by NAA and B-IC are shown in the Table 1. The difference in chlorine concentrations between the two methods was small except for used papers.

Regarding the kitchen wastes, the chlorine concentration of other kitchen wastes was smaller than that of the left untouched or uncooked foods. Except for the results of NAA for used papers, the chlorine concentration of disposable diapers was higher than that of other paper fractions. Especially for disposable diapers for infants, NAA result was about 13,000 mg/kg and B-IC result was about 18,000 mg/kg. It has been reported that it has not been disposed so long and that urine contains 8,600 mg/L of chlorine [2]. The high chlorine concentration in the disposable diaper is considered to be due to the adherence of chlorine derived from human. As the amount of disposable diaper waste increases with aging society, it is expected that the chlorine concentration in all papers will increase. The chlorine concentration of textiles, waste wood and grass were lower than that of the other categories. Plastics, except for PET bottles, generally had a high chlorine concentration. Although the composition of PET bottles does not contain chlorine, it is considered that chlorine was detected due to the adhesion of beverages and the like on the bottle. Wrapping plastics, other plastics, rubber and leather had a significantly high chlorine

concentration. In particular, wrapping plastics exceeded 300,000 mg/kg by either method. It is conceivable that the chlorine content of the plastic as a whole and of the MSW as a whole will change greatly depending on how much of the wrapping plastics accounts for.

The chlorine concentrations measured by the two methods were compared (Fig.1). The slope of the regression line was 0.873, the correlation coefficient was 0.997, and the p-value was  $1.5 \times 10^{-16}$ , indicating a correlation. The chlorine concentration measured by B-IC was smaller than that measured by NAA, neutron activation analysis, and it was considered that only combustible chlorine was measured by the former.

Table 1 Chlorine conc. in each fraction of MSW measured by NAA and B-IC.

Items	Sub-Items	NAA mg/kg	B-IC mg/kg
Kitchen wastes	Left untouched or uncooked foods	10,100	13,000
	Others kitchen wastes	8,210	6,120
Papers	Disposable diaper for adults	6,170	6,180
	Disposable diaper for infants	13,300	18,000
	Used papers (Newspaper, Magazine, etc.)	11,400	1,360
	Packing papers (Cardboard, Carton)	2,480	1,100
	Other papers	4,140	2,030
Textiles	Textiles	3,200	1,130
Waste wood and grass	Waste wood and grass	1,530	729
	Packing plastics	17,700	8,510
Plastics	PET bottles	1,690	913
	Plastic container for lunch pack	10,700	7,880
	Other plastics	60,800	63,000
	Wrapping plastics	339,000	300,000
Others	Rubber and leather	142,000	108,000
	Others (Combustibles)	8,090	13,000

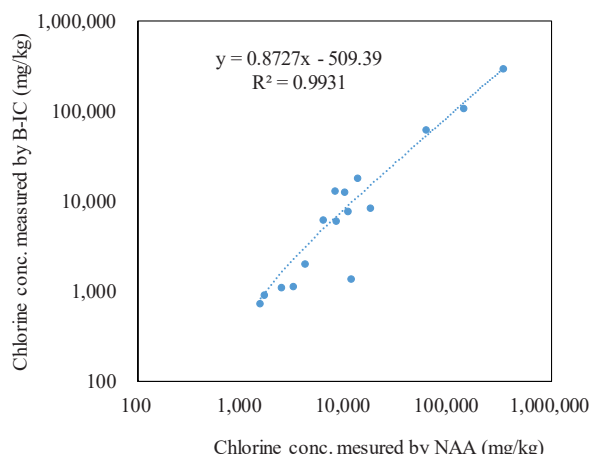


Fig.1. Relationship of chlorine conc. measured by between NAA and B-IC.

## REFERENCES:

- [1] JIS K 7302-6, Densified refuse derived fuel – Part 6 : Test method for total chlorine contents, 1999.
- [2] H. Nakanishi, Progress of night soil treatment techniques, *Japan journal of water pollution research*, Vol.14, No.11, pp.766-771, 1991.

K. Daiku<sup>1</sup>, M. Yoneda<sup>2</sup>, Y. Shimada<sup>2</sup>, R. Gomi<sup>2</sup>, S. Fukutani<sup>3</sup>, M. Ikegami<sup>3</sup>

<sup>1</sup>Department of Engineering, Kyoto University

<sup>2</sup>Graduate School of Engineering, Kyoto University

<sup>3</sup>Institute for Integrated Radiation and Nuclear Science, Kyoto University

**INTRODUCTION:** The radioactive Cs released by Tokyo Electric Fukushima Daiichi Nuclear Power Plant accident deposited on the widespread soil. Decontamination of the contaminated soil was carried out in residential area, but, when we consider disposal of contaminated soil on the occasion of final disposal, reduction of soil volume and Cs concentration by soil washing method may be necessary. So, elution of Cs from the soil needs to be care about, and the studies for its elution rate are often performed. This study clarified how problems of the liquid waste treatment can be improved by the ammonium ion soil washing method, how recycling rate of washed soil can be improved, and how Cs density of soil particle decreases quantitatively, by experiments using simulated pollution soil.

**EXPERIMENTS:** Two kinds of soil, Soil A and Soil B, from the experiment forest of Iwate University were used. Each soil was used without any treatment or with heat treatment. Heat treatment was 1 hour heating at 500°C in a muffle kiln. So, four types of soil were used, which were Soil A without treatment, Soil B without treatment, Soil A with heat treatment, and Soil B with heat treatment. Contaminated soil was created artificially by adding 25 g of water solution containing 0.030 mg of Cs and 0.10 mg of Sr to 10g of each soil. They were dried for two nights at 45°C, then, added 25g of pure water again, and dried again by the same condition. 10 g of each soil was put into 250cc PP bottle, 50g of pure water or  $\text{NH}_4\text{HCO}_3$  (0.56 mol/L) water solution was added to it, and shaken one hour. Then, 2.5cc solution was collected from each PP bottle, 1cc was used for metal element measurement by MP-AES and ICP-MS, and 1.5cc was used for  $\text{NH}_4^+$  concentration measurement. After sieving out about half weight of total amount of soil with appropriate size of sieve, sieved solution was applied for ammonia stripping for the search of effects of decreasing the concentration of  $\text{NH}_4^+$ . 2.5cc of solution was collected at scheduled some times, and used for measurement of elements and  $\text{NH}_4^+$ .

**RESULTS:** Comparing the quantity of Cs and Sr elution by  $\text{NH}_4^+$  before ammonia stripping with those by pure water, Sr elution by  $\text{NH}_4^+$  is 1/2-1/5 of that by pure water, but, Cs elution by  $\text{NH}_4^+$  is 70-300 times more of that by pure water. It means that residual rate of the Cs in soil by pure water elution was more than 98%, although, it was about 27.7-67.6% in the case of  $\text{NH}_4^+$  washing depending on soil type. It also means that the concentration of Cs in soil treated with  $\text{NH}_4^+$  washing can be decreased about half compared with that with pure water washing. Regarding the treatment of elution water by ammonia stripping where  $\text{NH}_4^+$  concentration decreased shown as Fig.1, clear

decrease was found in the case of following: all ions in soils with heat treatment; only Cs and K in soils without treatment shown as Fig.2. The concentration of just two monovalent ions in elution clearly decreased with elapsed time by the decrease of  $\text{NH}_4^+$  concentration. Although, all metal ions in elution of soils with heat treatment, which had less changeable electric charge sites, decreased with process of ammonia stripping, those of soils without treatment, which had more changeable electric charge sites, showed clear decrease of adsorption of just only monovalent K and Cs which has less adsorption strength than multivalent ions and less effect from decrease of changeable electric charge sites at 180min elapsed time of ammonia stripping. It probably means that pH decreased with the decrease of  $\text{NH}_4^+$  and cation exchange capacity by changeable electric charge sites where multivalent ions mainly adsorbed decreased. It is thought that competition adsorption theory with detail geological ion dynamics is necessary to understand the change of ion elution based on the existence ratio of various adsorption sites of each soil. The ratio is also changeable with pH changing with concentration of  $\text{NH}_4^+$  in the process of ammonia stripping.

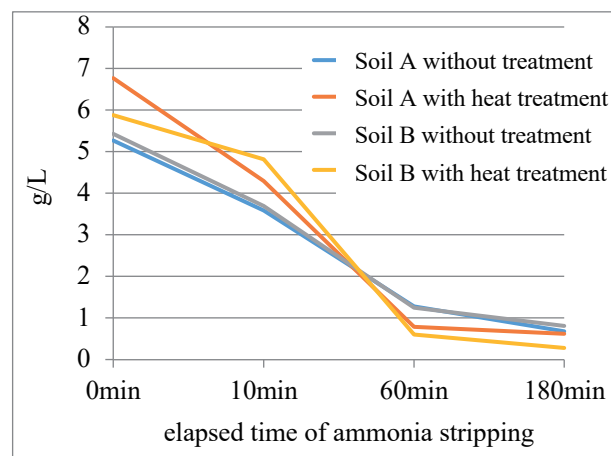


Fig. 1. Change of concentration of  $\text{NH}_4^+$  by ammonia stripping.

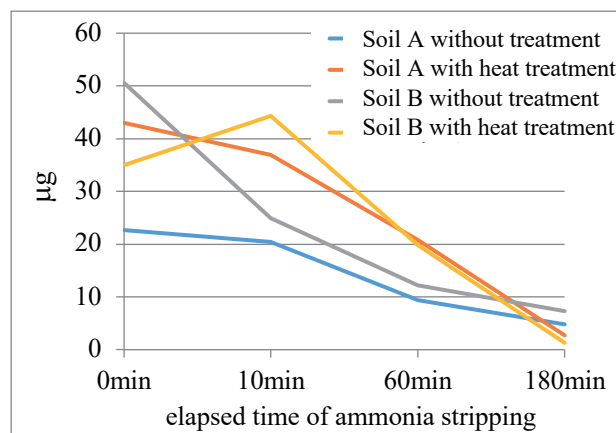


Fig. 2. Change of quantity of Cs in the solution by ammonia stripping.

## CO10-7 Measurement of Radioactivity-Based Particle Size of Radiation-Induced Aerosols using a Diffusion Battery System in Accelerator Facilities

Y. Oki

*Institute for Integrated Radiation and Nuclear Science,  
Kyoto University*

**INTRODUCTION:** Recently mA-class accelerators have been used for isotope production and medical use. In the medical application, high intensity beams are necessary to reduce irradiation time for patients. The nature of radioactive species in air of the accelerator rooms is very important from the viewpoint of radiation safety in the high intensity accelerators.

During machine operation the accelerator room is filled with radiation-induced aerosol particles in the size range of several nm to ca. 100 nm in addition to radioactive gases. The size for the radioactive particles was often measured using a wire screen technique in accelerator facilities. Convenient size measurement techniques are needed for radiation protection in accelerator facilities.

In this work, continuing from the previous years [1], a newly-assembled screen-type diffusion battery (SDB) system was applied to measure aerosol particle size in the accelerator room (target room) of an electron linear accelerator (LINAC) facility.

### EXPERIMENTS:

**Principle:** When very fine aerosol particles pass through wire screens, a part of the particles are deposited on the wire surface of the screens by their diffusion according to their particle size. The loss by the screens is expressed as a function of particle size, coarseness and number of screens, and flow rate of particles. The radioactivity-based size distribution of the aerosol particles can be calculated by measuring the penetration ratio ( $A/A_0$ ), where  $A_0$  and  $A$  are activity of the nuclide of the aerosol particles before and after penetrating screens, respectively.

**The measurement system:** The SDB system used in this work consists of an SDB line (Line A in Fig. 1) and a compensation line (Line B). Each line was connected to a ball valve and a mass flow controller (MFC) to change a flow rate independently. All valves and MFCs were controlled by a PC for automatic measurement of aerosol size distribution. In the SDB line, an air-tight wire screen cylinder containing a stack of three pieces of stainless steel screens (500 mesh).

**Irradiation:** The air-irradiation experiment was carried out in the 46-MeV electron LINAC of the Institute for Integrated Radiation and Nuclear Science, Kyoto University (KURNS). An irradiation chamber was placed

at a rear position of a platinum target. During the irradiation, aerosol-free air was introduced to the chamber from the experiment room next to the target room. The target was bombarded with a 30-MeV electron beam to produce bremsstrahlung. The bremsstrahlung ionizes air and produces the radiation-induced aerosol. The beam current was ca. 80  $\mu$ A.

### Measurement of activity-based aerosol size for the radiation-induced aerosol:

The irradiated air containing the aerosol was simultaneously introduced to the SDB line and the compensation line. The aerosol particles were collected at the rear position of the SDB cylinder on a polytetrafluoroethylene (PTFE) membrane filter at the flow rate in the range of 0 to 15 L/min. During the sampling, the flow rate of the compensation line was adjusted so that total flow rate of both lines was 15 L/min.

Principal radionuclides collected on the filter were positron emitters such as  $^{13}\text{N}$  and  $^{15}\text{O}$ . The 511-keV annihilation  $\gamma$ -ray of the filter was measured to determine the activity with a coincidence counting system using two BGO detectors. The irradiated air was sampled continuously from both the upstream and downstream positions of the SDB cylinder, and the penetration ratios were calculated.

**RESULTS:** The particle size of  $^{13}\text{N}$ -bearing aerosol particles was analyzed in this work. The PTFE filter is useful for accurate analysis of the particle size because the  $^{13}\text{N}$  particles can be collected without absorption of  $\text{NO}_x$  and nitric acid gases on PTFE. The  $^{13}\text{N}$  activity was determined by analyzing the decay curve of each filter. The curve of the penetration ratios ( $A/A_0$ ) obtained by changing air flow rate were fitted to a theoretical function [2] for lognormal distributions to obtain the geometric mean and geometric standard deviation of particle diameter. The preliminary result of the size was 60 nm in diameter.

### REFERENCES:

- [1] Y. Oki, *et al.*, KEK-Proceedings, **2018-7**, 265-269.
- [2] Y.S. Cheng and H.C. Yeh, *J. Aerosol Sci.*, **11** (1980) 313-320.

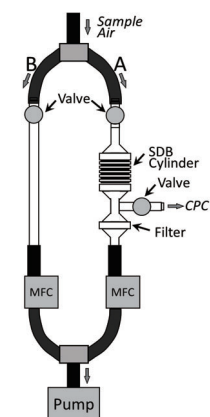


Fig. 1 The SDB system employed in this work

## CO10-8 Consideration of radon concentration measurement under natural fluctuation environment by a new monitor using two filter method

Y. Igarashi, Y. Wang<sup>1</sup>, J. Nakayama<sup>2</sup>, T. Misawa<sup>3</sup>, T. Takahashi<sup>3</sup> and T. Iimoto<sup>2</sup>

Graduate School of Frontier Science, The University of Tokyo

<sup>1</sup>Nuclear and Radiation Frontier Technology Research Center, China Institute for Radiation Protection

<sup>2</sup>Division for Environment, Health and safety, The University of Tokyo

<sup>3</sup>Institute for Integrated Radiation and Nuclear Science, Kyoto University

**INTRODUCTION:** This study focuses on improving a prototype monitor for accurately and versatily measuring the concentration of radon and its decay products in response to increasing international demand for monitors that measure both radon and its decay products under several conditions. We have already developed the prototype monitor based on the two-filter method. The measurement target of this method is  $\alpha$ -ray from  $^{218}\text{Po}$  generated from the decay of  $^{222}\text{Rn}$  as shown in Fig. 1.

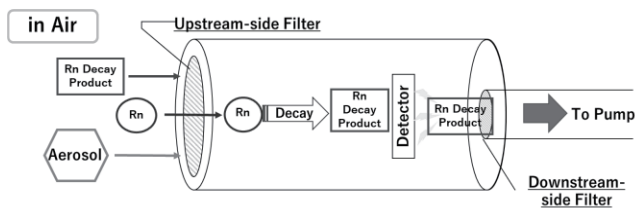


Fig. 1. Radon concentration measurement apparatus of 2filter method.

Through simple calibration tests and characteristic tests of the prototype monitor, we selected the suitable detector position for measurement and filters for up-stream side and down-stream side. From the results of these tests, we developed a new prototype monitor that can measure accurate radon concentration. The conversion factor from the counts of prototype monitor to the radon concentration was also obtained [1]. In order to evaluate the measurement ability of the new monitor, we measured radon concentration in the reactor room of KUCA where the fluctuation of radon concentration is close to that in the natural environment using the monitor.

**EXPERIMENTS:** To measure the radon concentration in KUCA reactor room, the new prototype monitor using two-filter method and a calibrated radon concentration monitor (RAD7) were installed in the room to compare with the results of these monitors. Experimental conditions of the prototype monitor were; detector: PIPS CAM300-17AM (40V), Upstream-side filter: No.4A+HE-40T, Downstream-side filter: GF/F, distance of detector-filter: 5mm, pump flow:  $10\text{L min}^{-1}$ . The measurement interval was set to 1 run:  $5\text{ min} \times 5\text{ times} = 25\text{ minutes}$ , and this run was repeated for 50 hours. All ventilation systems of the reactor room were stopped

because the radon concentration was not controlled. Therefore, the indoor condition in which the radon concentration will increase naturally was set.

**RESULTS and DISCUSSION:** Radon concentration ( $\text{Bqm}^{-3}$ ) measured by the calibrated radon concentration monitor and the number of counts (cpm) measured by the prototype monitor are shown in Fig.2. From the results in Fig.2, the radon concentration increased to about  $300\text{ Bq}$  in 50 hours with a tendency similar to the previous study [2]. The number of counts measured by the prototype monitor also increased to about 15 cpm in 50 hours. On the other hand, large fluctuations in both the concentration and the counts were observed after 45 hours. These behaviors were caused by unexpected changes in the measurement environment. Therefore, the conversion factor of relation the concentration and the count was calculated from the measurement result obtained from the start to 44 hours after. As a result, an average value of the conversion factor was  $17\text{ Bqm}^{-3} / \text{cpm}$ .

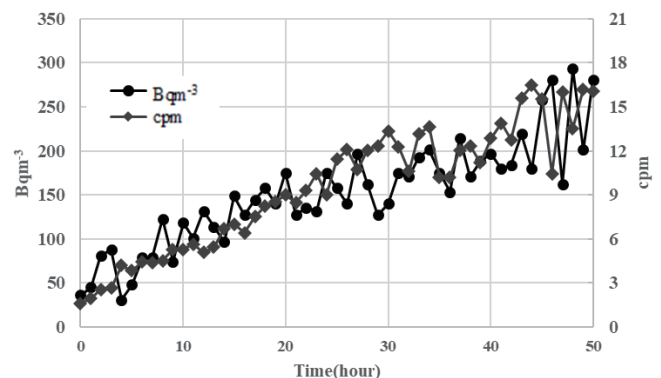


Fig. 2. Radon concentration ( $\text{Bqm}^{-3}$ ) of the RAD7 and number of counts (cpm) of the prototype monitor in KUCA reactor room.

From the above results, the radon concentration measurement for a long time can be performed stably under the environment that a radon concentration naturally increases. There are some problems that the unintended noise significantly affects the measurement results. Therefore, it is necessary to consider an operating method that can eliminate the noise for outdoor measurements. In the future, we will improve the prototype monitor to measure the deposition of particulate nuclides on the inner wall of the decay chamber and the effect of the aerosol for the radon decay products to investigate for the operational stability of the concentration measurement of radon decay products.

### REFERENCES:

- [1] Y. Igarashi *et al.*, Rad. Prot. Dosim., **184** (2019) 418-421.
- [2] KUR Aerosol Research Group, KURRI-TR-232 (1982).

## CO12-1 Isotope Dilution-Neutron Activation Analysis for Quantifying Hafnium

T. Takatsuka, K. Hirata, Y. Iinuma<sup>1</sup>, R. Okumura<sup>1</sup>,  
H. Yoshinaga, and K. Takamiya<sup>1</sup>

National Metrology Institute of Japan, National Institute  
of Advanced Industrial Science and Technology  
<sup>1</sup>Institute for Integrated Radiation and Nuclear Science,  
Kyoto University

**INTRODUCTION:** Hafnium (Hf) oxide is utilized as high-*k* dielectric films for semiconductor devices especially with fast and low-power operation. Additionally, the films are being introduced as ferroelectric material on ferroelectric transistors and memories. The device fabrication process should be precisely controlled for such dielectric films. We aimed to quantify Hf in Hf oxide films in weight unit by means of isotope dilution-neutron activation analysis (ID-NAA) [1].

**EXPERIMENTS:** Hf oxide films were deposited on 4-inch Si wafers by magnetron sputtering. The target thickness was set to 4 nm. The prepared wafers with the films were cut into 10 mm × 10 mm pieces for the measurements.

The procedure for ID-NAA has two sequences of an isotope dilution (ID) and a reverse-ID to ensure traceability to the SI units; the latter sequence was performed to determine the Hf concentration in a spike solution by referring to a Hf standard. The spike solution was prepared by dissolving <sup>174</sup>Hf-enriched Hf oxide (Oak Ridge) in a HNO<sub>3</sub> + HF aqueous solution, and by diluting to a proper concentration. For calibrating the amounts of Hf, a working standard solution was prepared by diluting NIST SRM 3122 gravimetrically. For the ID analysis, small amount of the spike solution was dropped onto each Hf oxide sample (HfO<sub>2</sub>+Sp), while the spike solution or standard solution was dropped separately onto each piece of cleaned filter paper (Sp or STD), as shown in Fig. 1. For the reverse-ID analysis, the spike and standard solutions were dropped onto one piece of filter paper (Sp+STD).

For validation, the Hf concentration of the spike solution was also determined by NAA with internal standards. Four concentration levels of working standard solutions were prepared; an internal standard solution of Sb from NIST SRM 3102, three Hf and Sb mixed standard solutions with different Hf concentrations for the calibration. For the quantification of the spike solution, the specimens were prepared using the spike solution before diluting since the diluted spike solution has little Hf-180 to be quantified. Weighed portion of the spike solution was dropped onto a filter paper followed by dropping the Sb standard. As for standards, aliquots of the working standard solutions of Hf and Sb mixture were weighed and dropped onto filter papers.

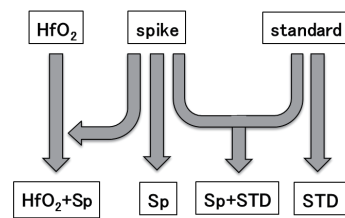


Fig. 1. Sample preparation for ID-NAA.

All the samples were sealed up separately in clean polyethylene bags, followed by being stacked in a polyethylene container for the neutron irradiation. The irradiation was performed for 4 hours with a  $5.5 \times 10^{12} \text{ cm}^{-2} \cdot \text{s}^{-1}$  thermal neutron fluence rate at Pn-2 in the Kyoto university research reactor (KUR). The gamma-ray activity of each sample was measured by a high-purity germanium detector (CANBERRA).

**RESULTS:** From the gamma-ray spectrum, the gamma-ray intensity ratio of <sup>175</sup>Hf to <sup>181</sup>Hf and <sup>181</sup>Hf to <sup>124</sup>Sb were calculated for ID and internal standard method, respectively. The Hf concentration in a spike solution was determined to be 6.63 mg/kg by reverse-ID. The amounts of Hf in the Hf oxide samples were calculated from the intensity ratios based on a formula reported in Ref. 1. Dividing the Hf amounts by measured sample surface areas, the area densities were calculated to be 3.64  $\mu\text{g} \cdot \text{cm}^{-2}$  and 3.63  $\mu\text{g} \cdot \text{cm}^{-2}$  for two measured samples. From the calibration curve by internal standard method in Fig. 2, the spike concentration was determined to be 108 mg/kg. For comparison, the determined spike concentrations were converted into the relative ones to the nominal concentrations since the nominal concentrations were different from each other. The resultant relative concentrations were 0.982 and 0.978 for reverse-ID and internal standard method, respectively. This agreement showed the reverse-ID procedure in ID-NAA was appropriate for the quantification.

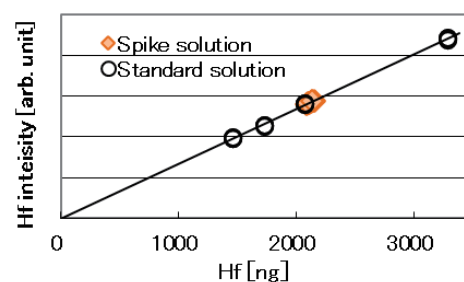


Fig. 2. Calibration curve for determining the spike concentration by the internal standard method.

### REFERENCES:

- [1] C. Yonezawa *et al.*, *Anal. Chem.*, **55** (1983) 2059-2062.

## CO12-2 Study on Superposition of Terahertz Coherent Radiation Using a Ring Resonator

N. Sei and T. Takahashi<sup>1</sup>

Research Institute for Measurement and Analytical Instrumentation, National Institute of Advanced Industrial Science and Technology

<sup>1</sup>Institute for Integrated Radiation and Nuclear Science, Kyoto University

**INTRODUCTION:** Research on nonlinear spectroscopy has been explored in the terahertz (THz) region where low-energy excitations and photoinduced phase transitions can be observed, and developments of broadband THz light sources with high peak power have been desired [1]. A short-pulse relativistic electron beam is suitable for generating coherent radiation in the THz region, and THz light sources and their applications have been developed in a lot of accelerator facilities [2]. As coherent Cherenkov radiation matched to a circular plane wave, which was demonstrated in our past joint research [3], a method for extracting high-power THz light from the relativistic electron beam by devising a principle of light emission has been mainly studied. Although the development of a new high-efficiency principle of light emission was important factor for realizing high-power THz light, this approach alone was not enough.

Therefore, we proposed that coherent radiation generated by a pulse train of electron bunches was confined in a ring resonator and superimposed with the same phase. We succeeded in observing THz light pulses extracted from a ring resonator in an L-band linac at Kyoto University Institute for Integrated Radiation and Nuclear Science (KURNS-LINAC).

**EXPERIMENTS:** The experiments were performed using an electron beam with the energy of 42 MeV and the macropulse duration of 47 ns. The repetition frequency of the macropulse of the electron beam was 30 Hz. Figure 1 shows a photograph of the ring resonator used in the experiments. A hollow aluminum cylindrical tube with an inner diameter of 17.5 mm was installed as a collimator upstream the ring resonator. The electron beam

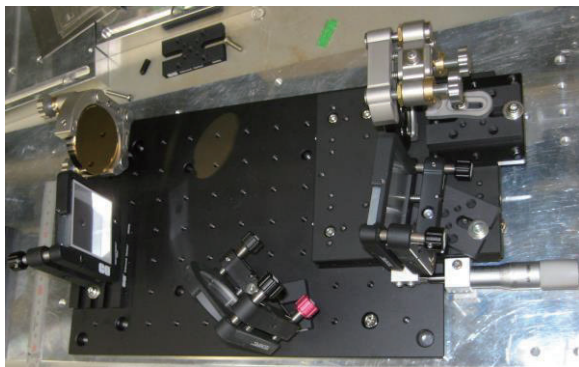


Fig. 1. Photograph of the ring resonator.

passing through the collimator injected to a hole with a diameter of 5 mm on an aluminum thin foil and generated coherent forward diffraction radiation in the ring resonator. Furthermore, the electron beam passed through an aluminum thin foil and generated coherent backward transition radiation. The current of the electron beam passed through another aluminum thin foil was approximately 60  $\mu$ A. These aluminum thin foils were also used as mirrors constituting the ring resonator. The two coherent radiations were confined in the ring resonator composed of four mirrors, which included two parabolic mirrors with the focal length of 508 mm. The length of the resonator was 922 mm, which was four times the interval of the electron bunches. A part of the resonant light was extracted from the resonator through the hole formed in the aluminum thin foil and transported to an experimental room. The transported resonant light was detected by a D-band diode detector (Millitech Inc., DXP-06), and the output power was measured by an oscilloscope with the frequency band less than 350 GHz.

**RESULTS:** Figure 2 shows a macropulse of the THz-light power measured by the D-band diode detector. Although the temporal resolution of the measured THz-light power was insufficient due to the low frequency band of the oscilloscope, it was found that the detector could identify coherent radiation generated by each electron bunch. By using an oscilloscope with a wider band, it will be possible to observe the micropulse waveform of the resonant THz light and to adjust the length of the resonator. We also plan to extract the THz light from the resonator using a thin film which hardly absorbs light in the THz region.

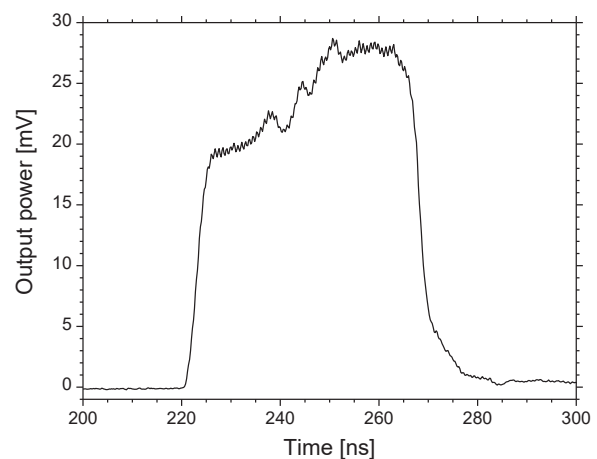


Fig. 2. THz-light power measured by the D-band diode detector.

### REFERENCES:

- [1] P. U. Jepsen *et al.*, *Laser Photonics Rev.*, **5** (2011) 124.
- [2] M. Gensch *et al.*, *Proc FEL2013, New York, 2013*, p. 474.
- [3] N. Sei and T. Takahashi, *Sci.Rep.*, **7** (2017) 17440.

S. Sato, K. Mori<sup>1</sup>, Y. Yoshino<sup>1</sup>, T. Seya, T. Otomo, H. Oshita, K. Okawa<sup>2</sup>, N. Hikida<sup>2</sup>, K. Ishizawa<sup>2</sup>, A. Yamaguchi<sup>3</sup>, M. Matsuura<sup>3</sup>

High Energy Accelerator Laboratory, KEK

<sup>1</sup> Institute for Integrated Radiation and Nuclear Science, Kyoto University

<sup>2</sup> Canon Electron Tubes & Devices Co., Ltd

<sup>3</sup> Clear-Pulse Co., Ltd

**INTRODUCTION:** Recently, the industrial use of neutrons has become widespread, and compact accelerator-driven neutron sources have been used to develop new materials. However, the development of neutron detectors that support these experimental facilities has been delayed.  $^3\text{He}$  gas detectors are the most reliable neutron detectors and are typically utilized as position-sensitive detectors (PSDs) [1, 2]. However, these detectors have low count rates and low position resolutions. Therefore, joint research has begun between Canon Electron Tubes & Devices Co., Ltd. (CETD), which manufactures PSDs, and the High Energy Accelerator Research Organization (KEK), which develops readout circuits for neutron detectors.

In this research, we are developing to increase the counting rate of a  $^3\text{He}$  gas position sensitive detector (PSD), and a maximum counting rate of 535 k cps has been obtained. We report the key technology of a pulse width method that has been verified of effectivity at KUR.

**EXPERIMENTS:** A pulse width measurement function is provided to diagnose whether a PSD can increase the count rate. This technology [3] has been developed for other detector systems. Figure 1 shows the pulse width measurement method. The pulse width is obtained by acquiring the pulse height from the pulse waveform. To determine the pulse width, the counting starts from the rising edge of the pulse and stops when it reaches half the height of the pulse. The function has been verified at the B3 beam port in KUR.

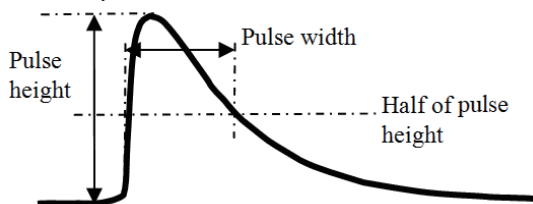
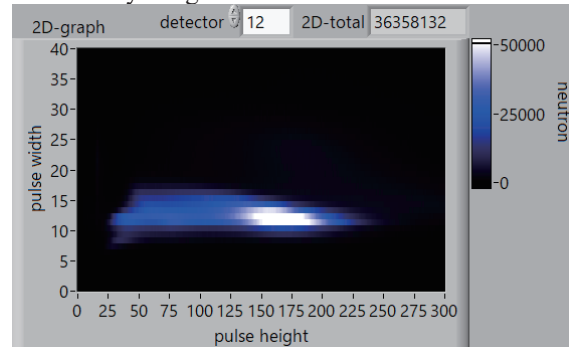


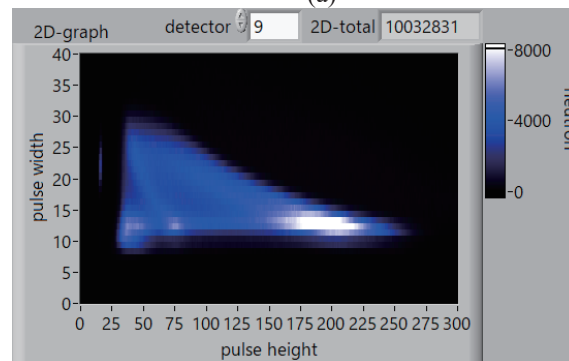
Fig. 1. Pulse-width measurement method

**RESULTS:** Figure 2 shows the pulse height versus width (PHW) graphs using the pulse width measurement function. The vertical axis is the pulse width (25 ns per channel), and the horizontal axis is the pulse height. Figure 2(a) shows that the entire signal gathers around 280 ns along the vertical axis, and it is a high-count-rate PSD (stopping gas: CF<sub>4</sub>,  $^3\text{He}$  gas pressure: 6 atm.). Figure 2(b) shows that the low pulse height signal extends to around

700 ns, and it is a low-count-rate PSD (stopping gas: CF<sub>4</sub>,  $^3\text{He}$  gas pressure: 20 atm.). The conditions are the same except that the gas pressure is different. As shown in these examples, the pulse width measurement function can identify a high-count-rate PSD.



(a)



(b)

Fig. 2. PHW graphs of (a) fast PSD and (b) slow PSD

Various techniques are necessary to increase the counting rate of the  $^3\text{He}$  neutron detector, and the pulse width method is an essential technique. KUR is the optimal neutron generator to verify this method.

#### REFERENCES:

- [1] S.Sato *et al.*, EPJ Web Conf, UCANS-8, <https://doi.org/10.1051/epjconf/202023105004>.
- [2] S. Satoh *et al.*, NIMA, **600**, 103–106 (2009), DOI 10.1016/j.nima.2008.11.054.
- [3] S. Satoh, Physica B, 551, 401–404 (2018), DOI 10.1016/j.physb.2018.03.011.

T. Miura, N. Yoshinaga<sup>1</sup>, Y. Iinuma<sup>1</sup> and S. Sekimoto<sup>1</sup>

National Metrology Institute of Japan, AIST

<sup>1</sup>Institute for Integrated Radiation and Nuclear Sciences  
Kyoto University

**INTRODUCTION:** National Metrology Institute of Japan (NMIJ) is responsible for developing certified reference materials and for establishing the traceability of SI (The International System of Units) on chemical metrology in Japan. To establish SI traceability, the primary method of measurements should be applied to the characterization of the certified reference materials. Recently, neutron activation analysis using comparator standard is recognized as a potential primary ratio method [1]. Despite the potential of neutron activation analysis as primary ratio method, the evaluation of the measurement uncertainty is required in any analysis. In general, there are three main components of uncertainty in neutron activation analysis, that is, sample preparation uncertainty, neutron flux homogeneity, and gamma ray measurement uncertainty. Usually, flux monitor is used to correct the neutron flux in-homogeneity. However, although the flux monitor can correct the neutron flux variation using the count rate of the known amount of the monitor nuclide, it does not reflect the neutron flux of the actual sample. The most practical method to eliminate neutron flux in-homogeneity and to improve gamma ray measurement uncertainty is an internal standard method [2, 3]. For the development of primary inorganic standard solution as national standard, the purity of starting material has to be determined. The high purity Ti metal was candidate starting material for preparation of titanium standard solution as national standard of Japan. The several trace analytical methods including neutron activation analysis, were used for purity determination of the high purity Ti metal. In this work, we presented that capability of instrumental neutron activation analysis for determination of Ar in high purity Ti metal.

**EXPERIMENTS:** The high purity Ti metal was purchased from Sumitomo Metal Mining Co. Ltd. The informative purity value of the Ti metal was 99.9 %. The ambient air in pre-cleaned 1 mL volume of PFA (Perfluoroalkoxy alkanes) vials were used as Ar calibration standard. The volume of PFA vials were calibrated by weighing mass of pure water prepared from Mill-Q Advance pure water system filled in each vial. The calibration of volume Mettler Toledo XP205 semi-micro balance was used for volume calibration. The calibrated PFA vials were heat sealed into Al coated polyethylene bags. One hundred mg of the Ti metal samples were used for Ar analysis. The neutron irradiations were performed by KUR (Kyoto University Research Reactor) Pn3 (thermal neutron flux:  $4.7 \times 10^{12} \text{ cm}^{-2}\text{s}^{-1}$ ) for 2 min.

The  $\gamma$  ray measurement system consisted of an ORTEC GEM 30-76-LB-C-HJ Ge detector and a multichannel analyzer SEIKO EG & G MCA 7. Because the short-lived radioactive nuclide  $^{20}\text{F}$  ( $t_{1/2}=11 \text{ s}$ ) was produced in PFA vial by neutron irradiation, the gamma ray measurement was started after 15 min.

**RESULTS:** The stable isotope  $^{40}\text{Ar}$  produce radioactive nuclide  $^{41}\text{Ar}$  by neutron irradiation. Usually, air contain 0.93 % of Ar. Hence, air in PFA vial can be used for calibration standard for Ar.

In this experiment, Ar in the high purity Ti metal sample could not be detected by instrumental neutron activation analysis. Therefore, the upper limit of Ar in the high purity Ti metal sample were estimated from the count rate of energy region of gamma rays emitted by  $^{41}\text{Ar}$  induced radioactive nuclide. The estimated upper limit of Ar were  $<4.0 \times 10^{-8} \text{ g/g}$ .

Table Analytical results of Ar in high purity Ti metal

Sample	Ar g/g
Ti-a	$< 4.6 \times 10^{-8}$
Ti-b	$< 3.0 \times 10^{-8}$
Ti-c	$< 2.6 \times 10^{-8}$
Ti-d	$< 3.5 \times 10^{-8}$
Ti-e	$< 4.1 \times 10^{-8}$
Ti-f	$< 4.0 \times 10^{-8}$

#### REFERENCES:

- [1] R.Greenberg, P. Bode, E. De Nardi Fernandes, Spectrochim. Acta B, 66 (2011) 193-241.
- [2] T. Miura, K.Chiba, T. Kuroiwa, T. Narukawa, A.Hioki, H. Matsue, Talanta, 82 (2010) 1143-1148.
- [3] T. Miura, R. Okumura, Y. Iinuma, S. Sekimoto, K. Takamiya, M. Ohata, A.Hioki, J. Radioanal. Nucl. Chem., 303(2105), 1417-1420.
- [4] NuDat 2, National Nuclear Data Center in Brookhaven National Laboratory, <https://www.nndc.bnl.gov/nudat2/index.jsp>

A. Yunoki, H. Yashima<sup>1</sup>, R. Okumura<sup>1</sup> and T. Yamada<sup>2</sup>

National Metrology Institute of Japan, National Institute of Industrial Science and Technology

<sup>1</sup>Institute for Integrated Radiation and Nuclear Science, Kyoto University

<sup>2</sup>Kindai University Atomic Energy Research Institute

**INTRODUCTION:** Equipment for continuous monitoring of radioactivity in gaseous effluents are widely used in nuclear power plants and other radiation facilities. A response of the equipment to radioactive gas is one of the most important characteristics. It is usually checked by using a sealed solid source, however, a test using radioactive gases is necessary when testing a newly developed equipment and calibrating an equipment for maintenance. In the test, the radioactive gas whose activity per unit volume is known is supplied to the equipment. Then, the response is obtained by dividing the indication of the equipment by the activity per unit volume. The activity per unit volume can be determined by using a set of proportional counters, however, this measurement is rather complexed and is not suitable for product tests. To solve this problem, the inner-through type ionization chamber, which is easier to handle, is used. The national metrology institute of Japan (NMIJ) determined the response of the inner-through type ionization chamber (Ohkura ionization chamber: type I-4096 01/06) by using a radioactive gas calibrated by the set of proportional counters.  $^{85}\text{Kr}$  has been used for testing the monitoring equipment [1-3]. On the other hands,  $^{133}\text{Xe}$  and  $^{41}\text{Ar}$  are useful for obtaining an energy dependence characteristic, however, they are not commercially available. Especially, a half-life of  $^{41}\text{Ar}$  is only 109.6 minutes, therefore, measurement needs to be finished in several hours after production. Therefore, self-production of a radioactive argon ( $^{41}\text{Ar}$ ) by irradiating thermal neutrons to the stable argon ( $^{40}\text{Ar}$ ) is necessary. Accordingly, we produced  $^{41}\text{Ar}$  gas in KUR-SLY and determined the response of the inner-through type ionization chamber by using the  $^{41}\text{Ar}$  whose activity per unit volume was determined by the set of proportional counters.

**SOURCE PREPARATION:** The source of  $^{41}\text{Ar}$  was prepared by the activating stable argon ( $^{40}\text{Ar}$ ) by irradiating thermal neutron. A research grade pure argon gas was poured to a small vessel of crystal glass whose volume was  $10\text{ cm}^3$ . A pressure of the gas was 300 hPa. The vessel was sealed with petroleum jelly. Then, the vessel was placed at the bottom of the KUR-SLY operating at 1 MW for approximately 60 seconds. The nominal flux of the thermal neutron was  $7.84 \times 10^{11} [\text{n}^{-1} \text{s}^{-1} \text{cm}^{-2}]$ . The  $^{41}\text{Ar}$  of 300 [kBq] was produced through  $^{40}\text{Ar}(\text{n}, \gamma)^{41}\text{Ar}$  reaction. The  $^{41}\text{Ar}$  was then transported to the Kindai University Atomic Energy Research Institute where a measurement system was temporally installed.

**MEASUREMENTS:** An activity of unit volume was

assessed by using a set of proportional counters connected in series. Conventional pulse counting electronics were connected to the counters. The  $^{41}\text{Ar}$  diluted by P-10 gas (nominally argon 90% and methane 10%) was flown through both the counters and the ionization chamber. The designs of the counters are the same except for their length. In order to eliminate distortion of counts near both ends of the counter, the net count rate was used which was obtained by subtracting a count rate obtained by a shorter counter from that obtained by a longer counter. The activity per unit volume [ $\text{Bq cm}^{-3}$ ] was obtained by dividing the net count rate by net volume of the counter. Temperature and pressure of the gas were monitored during measurement to adjust the results to the standard condition. For impurity assessment, an energy spectrum of gamma photon from the vessel containing the  $^{41}\text{Ar}$  was obtained by using a high-purity germanium detector.

**RESULTS:** Fig. 1 shows the pulse count rate as a function of a volume of proportional counter. An activity per unit volume is derived from an inclination of approximate straight line obtained by the least square method. The determined activity per unit volume was  $85.3\text{ Bq cm}^{-3}$ . The output of inner through ionization chamber flown by the  $^{41}\text{Ar}$  gas was 24.0 pA. Then, the response of  $0.281\text{ pA} (\text{Bq cm}^{-3})^{-1}$  was obtained. The result was adjusted to the standard condition ( $20^\circ\text{C}$ , 101.3 kPa). As the result of gamma photon spectrometry, an amount of impurity of the sample gas of  $^{41}\text{Ar}$  was negligible.

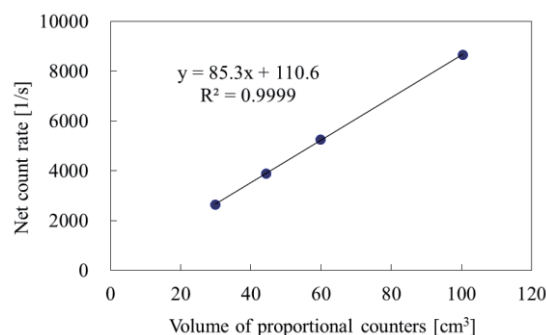


Fig. 1. Count rates as a function of a volume of proportional counters.

$^{41}\text{Ar}$  emits gamma photon of 1293.64 keV whose emission probability is 99.157 per 100 disintegration [4]. The measurement will be improved by considering the effect of the photon to the measurement.

#### REFERENCES:

- [1] A. Yunoki, *et. al.*, Applied Radiation and Isotopes, Vol. 68 (2010) pp.1340-1343.
- [2] M Unterweger, L Johansson, L Karam, M Rodrigues and A Yunoki, Metrologia 52 (2015) S156-S164.
- [3] A. Yunoki, *et. al.*, Applied Radiation and Isotopes, Vol. 134 (2018) pp.325-328.
- [4] DDEP, URL: [http://www.nucleide.org/DDEP\\_WG/DDEPdata.htm](http://www.nucleide.org/DDEP_WG/DDEPdata.htm).

## CO12-6 Development of neutron imager based on hole-type MPGD with glass capillary plate

F. Tokanai, T. Moriya, T. Sumiyoshi<sup>1</sup>, H. Kondo<sup>2</sup>, H. Sugiyama<sup>2</sup>, M. Hayashi<sup>2</sup>, T. Okada<sup>2</sup> and M. Hino<sup>3</sup>

Faculty of Science, Yamagata University

<sup>1</sup>Graduate School of Science, Tokyo Metropolitan University

<sup>2</sup>Electron Tube Division, Hamamatsu Photonics K. K.

<sup>3</sup>Institute for Integrated Radiation and Nuclear Science, Kyoto University

**INTRODUCTION:** Neutron imaging is useful for light elements in the sample such as hydrogen, lithium, boron, carbon, and nitrogen. Owing to their unique ability to probe inside samples, neutrons have been widely utilized for neutron radiography in various fields, including fundamental science, archaeology, and industry.

High position resolution with a moderate effective area is required in practical applications of neutron imaging. We have been developing a high-spatial-resolution neutron gas scintillation imager (n-GSI) with a capillary plate gas detector (CPGD) [1,2]. It consists of a converter layer of <sup>10</sup>B<sub>4</sub>C, a CPGD filled with a Ne (90%) + CF<sub>4</sub> (10%) gas mixture, a mirror, lens optics, an imaging intensifier unit, and a CMOS camera. A <sup>10</sup>B<sub>4</sub>C converter is directly mounted on the inlet surface of the CP. Charged particles ( $\alpha$ -rays and <sup>7</sup>Li nuclei) are generated by a nuclear reaction between incident neutrons and the <sup>10</sup>B. The charged particles ionize the gas molecules and then generate electrons in the gas. The scintillation light is emitted from the capillary holes upon gas excitation, simultaneously with electron multiplication. The scintillation light from each capillary is read out as the imaging signal through the optical mirror and lens system using an image intensified (II) CMOS camera.

Since the <sup>10</sup>B converter is directly mounted on the inlet surface of the CP, the track length of the charged particles is restricted to within the capillary. Thus, the spatial resolution of incident neutrons is expected to be close to the capillary diameter.

**EXPERIMENTS:** Fig. 1 shows the experimental setup. The light yield and imaging capability of the n-GSI were investigated using the cold neutron beam line CN-3 installed to the Kyoto University Reactor (KUR) [3]. The

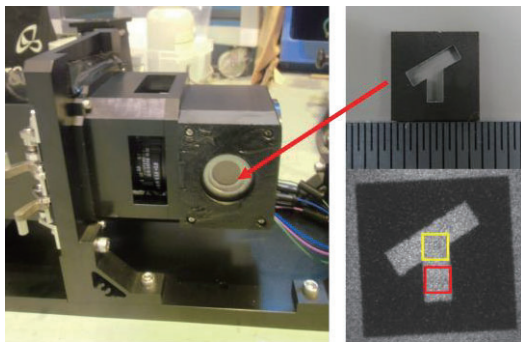


Fig. 1. Experimental setup of the n-GSI. The region of interest ROI-1 (yellow) and ROI-2 (red) are defined to investigate the light yield of the neutron transmission image.

neutron wavelength giving the maximum intensity and the total flux of the CN-3 guide tube were 2 Å and  $3.8 \times 10^6$  neutron cm<sup>-2</sup> s<sup>-1</sup>, respectively. The n-GSI system was placed 300 mm from the downstream exit of the neutron guide. The neutrons were irradiated into a sample.

**RESULTS:** The neutron transmission image of a character obtained with the n-GSI is shown in Fig. 1. The exposure time for image was 10 s. Fig. 2 shows the anode currents of the n-GSI as a function of the voltage across the CP electrode. The dependence of light yield on the voltage of  $\Delta V$  is shown in Fig. 3. The light yields are defined as the total counts in the ROI-1 and ROI-2, respectively. The light yield increases exponentially with the gap voltage across the CP. This result indicates that the n-GSI operates as a gas scintillation proportional counter.

### REFERENCES:

- [1] H. Kondo *et al.*, Plasma Fusion Res. **13** (2018) 2406018.
- [2] H. Kondo *et al.*, Nucl. Instrum. and Methods. A **958** (2020) 162804.
- [3] M. Hino *et al.*, Nucl. Instrum. and Methods. A **797** (2015) 265.

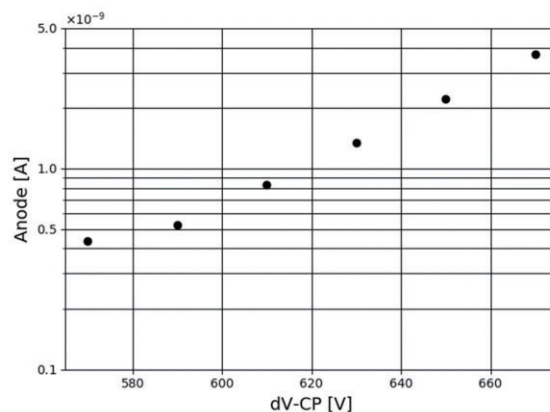


Fig. 2. n-GSI anode current as a function of the voltage across the CP electrode.

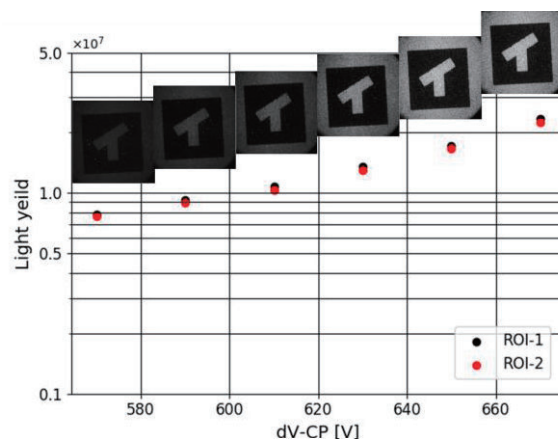


Fig. 3. Neutron transmission images and light yields as a function of the voltage across the CP electrode.

## CO12-7 Gamma ray measurement in the basement of the Kyoto University Research Reactor facility

K. Okada, A. Fushimi, Y. Murakami, S. Sekimoto<sup>1</sup>, T. Ohtsuki<sup>1</sup>, R. Okumura<sup>1</sup>

Center for Technology Innovation – Energy, Research and Development Group, Hitachi, Ltd.

<sup>1</sup> Institute for Integrated Radiation and Nuclear Science, Kyoto University

**INTRODUCTION:** Conventionally, fission chambers are adopted as in-core detectors for neutron flux monitoring. Part of the current value of the fission chamber during rated operation does not follow the instantaneous changes of the reactor power because decay gamma rays from reactor structure materials and delayed gamma rays from fission products have a time lag for response. However, it is difficult to separate neutron detection signals from gamma ray detection signals with a fission chamber in a high dose rate environment. Therefore, we are considering a method that monitors the neutrons only indirectly by measuring prompt gamma rays from the reactor core[1-2].

In the method, metal pieces are placed in a mixed field of neutrons and gamma rays. The prompt gamma rays emitted by the nuclear reaction between the neutrons and the metals are measured. At this time, other gamma rays around the reactor are interfering with measurements made with gamma ray spectrometers located under the reactor vessel. In this study, we used the Kyoto University Research Reactor (KUR) facility to measure the gamma ray energy distribution under the reactor vessel to evaluate the interference gamma ray components.

**EXPERIMENTS:** The measurement was carried out in the heat exchanger room in the basement of the KUR facility. Two gamma ray spectrometers were used, a high purity germanium semiconductor detector (HPGe) and an LaBr<sub>3</sub>(Ce) scintillation detector. Fig.1 shows the detector positions. Dose rate given in the figure was estimated in a previously done calculation[3]. The LaBr<sub>3</sub>(Ce) detector was covered with a Pb shield having a collimator opened in the reactor core direction to measure the prompt gamma rays emitted from the reactor core. In order to measure the decay gamma rays around the LaBr<sub>3</sub>(Ce) detector, the HPGe was covered with a shield having a collimator opened in the LaBr<sub>3</sub>(Ce) direction.

The energy spectrum of gamma rays obtained with the LaBr<sub>3</sub>(Ce) detector during 1 MW operation is shown in Fig.2. Total absorption peak of the 6130 keV gamma ray which was emitted by decay of N-16 in the primary cooling system pipe was seen. Both the single escape peak and double escape peak of the 6130 keV gamma ray were confirmed. In addition, total absorption peak of the 511 keV gamma ray which was emitted by decay of N-13 in the primary cooling system pipe were seen. The sum peak of the 511 keV gamma ray was confirmed. Three peaks were measured as other gamma rays. The energies of the gamma ray peaks were about 4600 keV (a), about 4100 keV (b) and about 3600 keV (c).

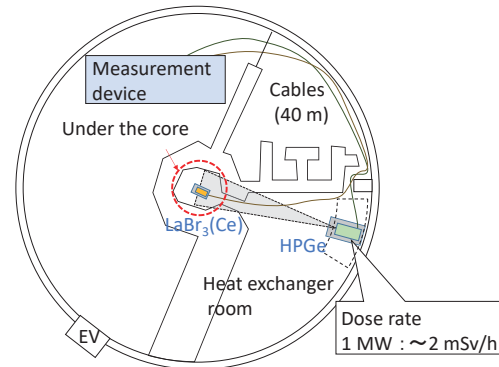


Fig. 1. Detector positions in the basement of the KUR facility.

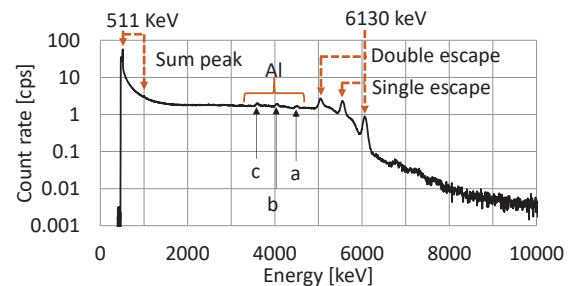


Fig. 2. Energy spectrum obtained with the LaBr<sub>3</sub>(Ce) detector.

**RESULTS:** The energy calibration between 1022 keV (the sum peak of 511 keV) and 5108 keV (the double escape peak of 6130 keV) was difficult because there was no standard source to emit high energy gamma rays. In addition, by taking into account that the energy resolution of the LaBr<sub>3</sub>(Ce) detector was too low to analyze nuclides in detail, we considered that these gamma rays were likely to be prompt gamma rays emitted from Al whose energies were 4733 keV, 4111 keV and 3465 keV[4]. Al was used as a material for a tank of the KUR. Therefore, we attribute these observed gamma rays to the Al tank.

This Al tank is equivalent to a reactor pressure vessel (RPV) or a channel box in commercial reactors. The RPV and channel box are made of stainless steel. Thus, in commercial reactors, prompt gamma rays originating from stainless steel and decay gamma rays from N-13 and N-16 interfere with measurement. In the evaluation of applicability, it is necessary to estimate the influence of the gamma rays originating from these reactor structures.

### REFERENCES:

- [1] K. Okada *et al.*, J. Nucl. Sci. Technol. **57**, 514-522(2020).
- [2] K. Okada *et al.*, KURNS progress report 2018 CO12-13 (2019).
- [3] K. Okada *et al.*, KURRI progress report 2012 CO3-3 (2013).
- [4] D L Anderson, *et al.*, (ed), Kluwer Academic Publishers, Handbook of prompt gamma activation analysis with neutron beams, 190-364 (2004).

## CO12-8 Neutron efficiency of a two-dimensional neutron detector with MPPC (Mpix)

H. Ohshita, H. Endo, T. Seya, Y. Yasu, M. Hino<sup>1</sup>, T. Oda<sup>1</sup>

*Institute of Materials Structure Science, KEK*

<sup>1</sup>*Institute of Integrated Radiation and Nuclear Science, Kyoto University*

**INTRODUCTION:** The village of neutron resonance spin echo spectrometers (VIN ROSE) [1] is built in BL06 at the Materials and Life Science Experimental Facility (MLF). Mechanisms involving slow dynamics such as diffusion and relaxation in samples are observed by VIN ROSE. VIN ROSE consists of two spectrometers; the Neutron Resonance Spin Echo (NRSE) spectrometer and Modulated Intensity by Zero Effort (MIEZE) spectrometer [2]. The MIEZE spectrometer measures a time beat signal depending on the operation conditions of two resonance spin flippers. As it is well known, the MIEZE signal is modulated when a polarized neutron interacts with the magnetic momentum of a sample. By spring 2020, we achieved the MIEZE frequency of 800 kHz. In order to observe the slow dynamics of a sample with high accuracy, a neutron detector with a suitable time resolution under 100 ns is required. Therefore, we are developing a neutron pixel detector called Mpix. Mpix is a medium-sized neutron detector and its active area is 320 mm×320 mm. The time resolution is under 100 ns and the value is limited by the repetition of the readout electronics. A <sup>6</sup>LiF/ZnS (Ag) scintillator with 0.25 mm thickness is used as a neutron converter. The detector also consists of 1024 Multi-Pixel Photon Counters (MPPCs) for photon counting [3]. Each MPPC is located by a 10 mm pitch, and consists of a 32×32 MPPC array. In order to measure the neutron efficiency, the neutron irradiation test was performed in CN3 [4] at the Kyoto University Reactor (KUR). This paper describes the experimental results of the neutron irradiation test.

**EXPERIMENTS and RESULTS:** Figure 1 shows the neutron irradiation tests to evaluate the detector performance of Mpix carried out from August 27 to August 29, 2019. The neutron efficiency of Mpix is introduced by comparing with the measurement data of a helium-3 proportional chamber (<sup>3</sup>He gas filled pressure: 993 kPa). A disk chopper is worked at 30 Hz to obtain the wavelength dependence of the neutron efficiency of Mpix. Neutrons from 1.5 Å to 4 Å, pass through the disk chopper. The helium-3 proportional chamber is set downstream at the distance of 1.221 m from the disk chopper. The detector is placed in a neutron shielding case which is made from a B<sub>4</sub>C resin. The size of the opening area of the neutron shielding case is 1 cm<sup>2</sup>. The neutron intensity in CN3 is derived from the measurement data of the helium-3 proportional chamber with the absorption correction of the SUS detector housing. Therefore, after the estimation of the absorption correction with Geant4 [5], a toolkit to provide the simulation of the passage of particles through matter, the measurement data is converted to the neutron intensity. As a result, the expected neutron intensity in the

neutron irradiation test is approximately 785.2±0.2 neutrons/s·cm<sup>2</sup>. Furthermore, the counting rate of Mpix was measured by replacing the helium-3 proportional chamber. The neutron efficiency  $\varepsilon$  is defined as follows,

$$\varepsilon = \frac{N_{\text{Mpix}}}{F_n}$$

Where  $N_{\text{Mpix}}$  is the counting rate of Mpix and  $F_n$  is the expected neutron intensity in CN3. The neutron efficiency of Mpix is shown in figure 2. From the result, we found that Mpix has a thermal neutron efficiency of approximately 21%. The neutron efficiency tends to increase linearly to 2 Å, and saturates beyond that value. This is caused by the contribution of the absorption in the detector housing and the neutron detection limitation with a <sup>6</sup>LiF/ZnS (Ag) scintillator of 0.25 mm thickness. In future, we plan to further evaluate the neutron efficiency by comparing the simulation results. This work has been carried out in part under the visiting Researcher's Program of the Institute for Integrated Radiation and Nuclear Science, Kyoto University.



Fig. 1 Overview of the experimental setup.

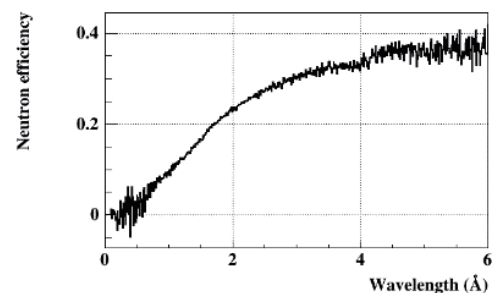


Fig. 2 Neutron efficiency of Mpix.

### REFERENCES:

- [1] M. Hino *et al.*, Physics Procedia, **42** (2013) 136-141.
- [2] T. Oda *et al.*, J. Phys. Soc. Conf. Proc., in press.
- [3] Web page of Hamamatsu Photonics K. K., <https://hamamatsu.com/jp/en/index.html>.
- [4] M. Hino *et al.*, Annu. Rep. Res. Reactor Inst. Kyoto Univ. **27** (1994) 196-204.
- [5] S. Agostinelli *et al.*, Nucl. Instr. and Meth. A **506** (2003) 250-303.

M. Seki, K. Ishikawa, T. Sano<sup>1</sup>, H. Nagata, K. Ohtsuka, T. Ohmori, H. Hanakawa, H. Ide, K. Tsuchiya, Y. Fujihara<sup>2</sup>, J. Zhang<sup>2</sup> and J. Hori<sup>2</sup>

Department of JMTR, Japan Atomic Energy Agency

<sup>1</sup>Atomic Energy Research Institute, Kindai University

<sup>2</sup>Institute for Integrated Radiation and Nuclear Science, Kyoto University

**INTRODUCTION:** The radioactive waste for decommission is usually solidified by alkaline cement fillers. However, hydrogen produced by reaction of aluminum (Al) with alkaline materials may damage the waste body. Therefore, it is necessary to establish the treatment technology of radioactive Al waste for safety management of the storage facility. Last year, the irradiated Al alloy was successfully separated into relative long half-life radionuclides and Al component by our group.

In this study, the solution pH dependence of the nuclide coprecipitated with aluminum hydroxide (Al(OH)<sub>3</sub>) was investigated for the purpose of recovering the Al component as Al(OH)<sub>3</sub>.

**EXPERIMENTS:** At first, the impurities included in an Al alloy separated it by filtration within cold examination. These solutions were analyzed of elementals by ICP-AES.

Secondly, the Al samples were irradiated in Pn-2 of KUR pneumatic transportation facility and cooled for 4 days. The irradiation condition and chemical composition of the sample are listed in Table 1 and Table 2, respectively. After the irradiation, sodium aluminate (Na[Al(OH)<sub>4</sub>]) was produced by dissolving the samples in NaOH solution with pH of 5 - 11. The insoluble impurities included in the sample were separated by filtration. This solution was neutralized by hydrochloric acid (HCl) to precipitate as Al(OH)<sub>3</sub>. The radioactivity of the impurities and Al(OH)<sub>3</sub> were measured by a germanium semiconductor detector so as to investigate chemical behavior of the radionuclides.

Table 1 Irradiation conditions of sample in Pn-2.

Items	Values
Thermal power	5 MW
Thermal neutron flux	$2.8 \times 10^{17} \text{ m}^{-2}\text{s}^{-1}$
Epithermal neutron flux	$1.1 \times 10^{16} \text{ m}^{-2}\text{s}^{-1}$
Fast neutron flux	$6.0 \times 10^{16} \text{ m}^{-2}\text{s}^{-1}$
Irradiation time	20 min.
Cooling time	4 days
Sample	0.25 g

Table 2 Chemical Compositions of sample.

	Si	Fe	Cu	Mn	Mg	Cr	Zn	Ti
rate [%]	0.61	0.42	0.28	0.02	0.99	0.24	0.01	0.04

**RESULTS:** Table 3 shows the results of Al recovery by ICP-AES. In pH = 7 and 9, the Al concentration of this solution was less than detection lower limit level.

In pH = 5 and 11, it was revealed that Al could be collected 85% or more as Al(OH)<sub>3</sub>. In addition, the NaCl was produced with Al(OH)<sub>3</sub> and included by Al(OH)<sub>3</sub>.

Secondly, a hot examination was conducted similarly. Al(OH)<sub>3</sub> was measured radioactivity by a germanium semiconductor detector after it was filtered and enough to be wash with ion exchanged water. As a result, Cr-51 and Na-24 coprecipitated with Al(OH)<sub>3</sub> were obtained. Cr-51 was produced by a reaction of (n,γ) which was impurities element of A6061. Na-24 was produced by Al-27 (n, α) Na-24.

Cr-51 was equal values under conditions of all. In Na-24, pH = 5 is maximum, because there was much produced NaCl and quantity of Na-24 Cl was included in Al(OH)<sub>3</sub> more than other conditions.

Table 3 The results of Al recovery by ICP-AES.

pH	① Meltability [mg]	② Quantity of a filtrate [mg]	①-② [mg]	③ Recovery [%]
5	100.0	0.40	99.60	99.6
7	100.0	<0.05*	99.95	100.0
9	100.0	<0.05*	99.95	100.0
11	100.0	13.70	86.30	86.3

\* The detection lower limit value

Table 4 The results of radioactivity measurement with the germanium semiconductor detector [Bq / Al-1g].

pH	5	7	9	11
Cr-51	$1.67 \times 10^1$	$1.82 \times 10^1$	$2.36 \times 10^1$	$2.20 \times 10^1$
Na-24	$2.11 \times 10^5$	$2.79 \times 10^4$	$1.85 \times 10^4$	$3.06 \times 10^4$

**CONCLUSION:** The radionuclide which coprecipitated with Al(OH)<sub>3</sub> were Cr-51 and Na-24Cl was included in the NaCl which was produced at the same time when Al(OH)<sub>3</sub> was produced.

In future, an experiment scale would be scale up the model and A more realistic processing condition is demanded.

#### REFERENCES:

- [1] Taichi Sato, Journal of the Mineralogical Society of Japan, 19(1), 1989, pp.21-41.
- [2] Gitzen, W.H. (ed.), Alumina as a ceramic material., American Ceramic Society, 1970.
- [3] M. Seki, *et al.*, KURNS Progress Report, p.257, 2018.

M. Aoki, N. Abe<sup>1</sup>, Y. Higashino, H. Ikeuchi<sup>2</sup>, K. Komukai<sup>2</sup>, D. Nagao, H. Natori<sup>3</sup>, Y. Seiya<sup>2</sup>, T. Takahashi<sup>1</sup>, T. Takahashi<sup>2</sup>, N. Teshima<sup>2</sup>, K. Yamamoto<sup>2</sup> and S. Yamashina

*School of Science, Osaka University*

<sup>1</sup>*Institute for Integrated Radiation and Nuclear Science, Kyoto University*

<sup>2</sup>*Faculty of Science, Osaka City University*

<sup>3</sup>*Institute of Materials Structure Science, KEK*

**INTRODUCTION:** Charged-lepton flavor violation (CLFV) process such as  $\mu \rightarrow e\gamma$ ,  $\mu$ -e conversion,  $\tau$ -CLFV decays are heavily suppressed in the standard model of particle physics (SM). However, in the most of the models beyond SM, it is considered to be occurred with a strength that can be reached in the coming experiments. DeeMe is one of experiments that aims to search for  $\mu$ -e conversion in nuclear field [1] at a level of  $10^{-13}$  of the branching ratio in the single event sensitivity. It uses high-power high-purity pulsed proton beam from J-PARC RCS. The detector of DeeMe should be operational after  $\mathcal{O}(\mu\text{s})$  from a burst of particles ( $100 \text{ GHz/mm}^2$ ) produced by the proton pulse. In order to solve the problem, a multi wire proportional chamber (MWPC) with high-voltage switching technique was successfully developed [2]. It is very important to improve the total performance of the MWPC before the start of the physics data taking at J-PARC MLF in order for better physics sensitivity.

**EXPERIMENTS:** Two experiments were performed in this fiscal year. In the 1<sup>st</sup> experiment, three MWPCs were sequentially placed so that the beam electrons from the KURNS electron LINAC hit through all three of them. The MWPC performance with three different gas mixtures were tested, where gas mixtures of Ar : i-C<sub>4</sub>H<sub>10</sub> : R-134a were 74:20:6, 70:20:10 and 65:20:15. At first, the burst electrons ( $10^7$  electrons/200-ns/360-mm<sup>2</sup>) with energy being 16 MeV were injected to the MWPCs at the timing when they were in the off-state. The MWPCs were turned to on-state right after each burst, and the amount of delayed false pulses induced on the read-out electrode strips were measured by using Fast-FADC system [3]. Less delayed false pulses were seen as the mixture of R-134a increases. Next, the burst electrons were turned off and the MWPC efficiencies were measured with low rate DC electrons at 16 MeV energy from the LINAC. The time averaged efficiencies are  $(94.2 \pm 0.6)\%$ ,  $(87.7 \pm 0.4)\%$  and  $(73.3 \pm 0.5)\%$  for 6%, 10% and 15% of R-134a fractions, respectively. Finally, the electron energy was increased to 30 MeV, and the position resolution of MWPC was measured. The quick off-line analysis shows that the position resolution is better than 1 mm (rms) including the multiple scattering effect, which is sufficient for the physics data taking in  $\mu$ -e conversion search.

In the 2<sup>nd</sup> measurement, a prototype MWPC was used with methylal-mixed gas instead of R-134a mixed gas since the goodness of the performance of the ion

absorption by methylal has been well known, and expected to outperform R-134a. The gas system was modified so that liquid methylal shall be mixed to the Ar and i-C<sub>4</sub>H<sub>10</sub> mixed gas with a precisely controlled mixture fraction. Figure 1 shows a correlation between delayed false pulse rate and a pulse height that produced by an electron hitting through the MWPC. The unit of the delayed false pulse rate is arbitrary. The red-filled circle labeled as 1510 V corresponds to the same configuration of the gas we obtained 73.3% of efficiency in the 1<sup>st</sup> measurement. The blue-triangle labeled as 1460 V provides two-times higher gas gain with two-times smaller delayed false pulse rate.

**RESULTS:** The positional resolution of MWPC measured with higher energy than that we used in the previous study shows better value, and it is sufficient for the purpose of DeeMe. A beam test with a prototype MWPC revealed that the delayed false pulse can be suppressed by using methylal-mixed Ar and i-C<sub>4</sub>H<sub>10</sub> gas while maintaining good gas gain. The final performance should be checked by using a production-version of MWPC in 2020.

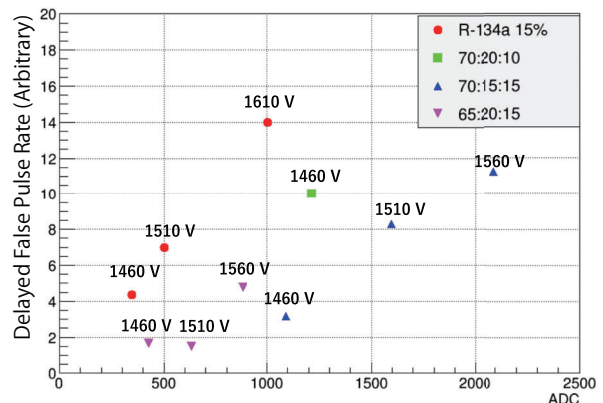


Fig. 1 Correlation between the delayed false pulse rate and signal gain. See text for more details.

### REFERENCES:

- [1] N. Teshima on behalf of the DeeMe Collaboration, "DeeMe experiment to search for muon to electron conversion at J-PARC MLF", in proceedings of NUFACT conference PoS (NuFact2017) 109 (2018).
- [2] H. Natori, *et al.*, "A fast high-voltage switching multi-wire proportional chamber", Prog. Theor. Exp. Phys. 2017(2) 023C01 (2017).
- [3] N.M. Truong, *et al.*, "Real-Time Lossless Compression of Waveforms Using an FPGA", IEEE Trans. Nucl. Sci. 65 2650 (2018).

## CO12-11 An attempt to produce carrier free tracer through photonuclear reaction and hot atom effect

T. Kubota, K. Takamiya, S. Fukutani and Y. Shibahara

*Institute for Integrated Radiation and Nuclear Science,  
Kyoto University*

**INTRODUCTION:** Photonuclear reactions can produce radioisotopes which are hardly produced through neutron irradiation. The production reaction and its rate depend on the energy of photons. Photons are usually generated through the irradiation of high-energy electrons to heavy metal. The KURNS-LINAC can accelerate electrons up to 46 MeV, hence in this limitation ( $\gamma, n$ ) reaction is dominant. The effective cross-section of this reaction is roughly 100 times as large as other reactions, such as ( $\gamma, 2n$ ), ( $\gamma, p$ ), and ( $\gamma, np$ ) reactions [1-2]. It is desirable that the ( $\gamma, n$ ) reaction is used to produce radioisotopes. In the case that radio isotopes are used for biological experiments as tracer, carrier free ones, whose specific activity and purity is high, are required in order to avoid chemical toxicity. However, carrier free isotopes cannot be produced through ( $\gamma, n$ ) reactions because products are basically the same element as target. In order to solve this difficulty, the production of carrier free isotopes was attempted by hot atom effect. As an example, Shibata et al. reported that a mixture of  $UO_2$  and NaCl was irradiated with neutrons and recoil fission products were trapped inside soluble NaCl and were separated from insoluble  $UO_2$  by adding water [3]. In this research radioisotopes were produced through photon irradiation to a mixture of oxides and salts.

**EXPERIMENTS:**  $Fe_3O_4$  and  $MoO_3$  were used as oxide and NaCl and KCl as salt, and the composition of a mixture is listed in Table 1. Each mixture was homogenized by grinding in a mortar and pestle and then was encapsulated in a quartz test tube under vacuum. The quartz test tube was irradiated with photons generated by the bombardment of 30 MeV electrons to platinum sheet of 2 mm thick at the KURNS-LINAC. The platinum sheet and quartz test tube were cooled by cooling water and blowing air, respectively. The irradiation time is listed in Table 1. After the decay of short half-life nuclides in irradiated materials, they were transported to the Tracer laboratory and subject to further treatment. The mixture was added with water to suspension solution, and this solution was transferred from the quartz tube to a polyethylene centrifugation tube. The quartz test tube was washed twice with water, and the washing solution was combined with the suspension solution. The centrifugation tubes were added with water to dissolve salt completely, shaken, and centrifuged to precipitate oxides. The aqueous phase was separated from the residue phase. The radioactivity of both phases was determined by  $\gamma$ -spectrometry and yielded the fraction of radionuclide produced from oxide phase to salt phase through a hot atom effect.

Table 1 Irradiation condition

Sample ID	#1	#2*	#3
$Fe_3O_4$	0.90 g	2.40 g	
$MoO_3$			0.14 g
NaCl	2.05 g		
KCl		27.31 g	0.91 g
Irradiation time	12 hr	6 hr	1 hr

\* An aliquot of the mixture was used for irradiation.

**RESULTS:** Irradiation of chloride provided Cl-34, which was dominant radioactivity immediately after irradiation and was, however, trivial matter due to its short half-life. On the other hand, irradiation of sodium provided long half-life Na-22, which was required to be removed, if necessary. The use of KCl was therefore desirable as binding salt. Table 2 shows the transfer fraction of Fe-52 and Mo-99 from the oxide phase to the salt phase, as carrier free tracer of iron and molybdenum, respectively. The value of Fe-52 was calculated from the radioactivity of Mn-52, and was lower than the detection limit, showing that no activated iron element was liberated from iron oxide crystal. The value of Mo-99 was 3%; however, during the water treatment the solution turned to blue purple, showing the dissolution of matrix  $MoO_3$  and no longer carrier free solution. In conclusion the production of carrier free tracer through photonuclear reaction and hot atom effect requires alternative methods.

Table 2 Transfer fraction by hot atom effect

Sample ID	#1	#2	#3
Mixture	$Fe_3O_4$ NaCl	$Fe_3O_4$ KCl	$MoO_3$ KCl
Tracer	Fe-52/Mn-52	Fe-52/Mn-52	Mo-99
Transfer fraction	~0 %	~0 %	3 %

### REFERENCES:

- [1] T. Kubota *et al.*, KURRI Progress Report 2014 (2015).
- [2] T. Kubota *et al.*, KURRI Progress Report 2017 (2018) 209.
- [3] S. Shibata *et al.*, Applied Radiation and Isotopes **60** (2004) 625–628.

R. Hazama, T. Yoshimoto, A. Rittirong, Y. Sakuma<sup>1</sup>, T. Fujii<sup>2</sup>, T. Fukutani<sup>3</sup>, Y. Shibahara<sup>3</sup>

Graduate School of Human Environment, Osaka Sangyo University

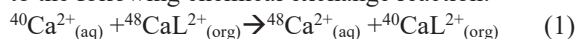
<sup>1</sup>Laboratory for Advanced Nuclear Energy, Tokyo Institute of Technology,

<sup>2</sup>Graduate School of Engineering, Osaka University

<sup>3</sup>Institute for Integrated Radiation and Nuclear Science, Kyoto University

**INTRODUCTION:** Chemical isotope separation for calcium has been studied in liquid-liquid extraction (LLE) with an appropriate crown-ether (CE) by utilizing a conventional batch (macroscopic) method [1] and a cutting edge micro-reactor/chip method [2]. Based on the measured reaction time between organic and aqueous solution seems fast (less than a minute) (Fig.1), a new test tube method has been pursued and its Ca mass balance between two phases was confirmed (Fig. 2) as with the case of batch and micro-reactor/chip methods.

**EXPERIMENTS:** Isotopic enrichment occurs according to the following chemical exchange reaction:



where L represents macrocyclic polyether(18-crown-6).

An aqueous solution (3M CaCl<sub>2</sub>) and organic solution (0.07M DC18C6 in chloroform) were stirred by a magnetic stirrer with changing a mixing time from 0 sec (no-mixing) to 60 min at room temperature and separated with a constant standing time of 30 min. The Ca concentration for both phases was measured by AAS in Fig. 1.

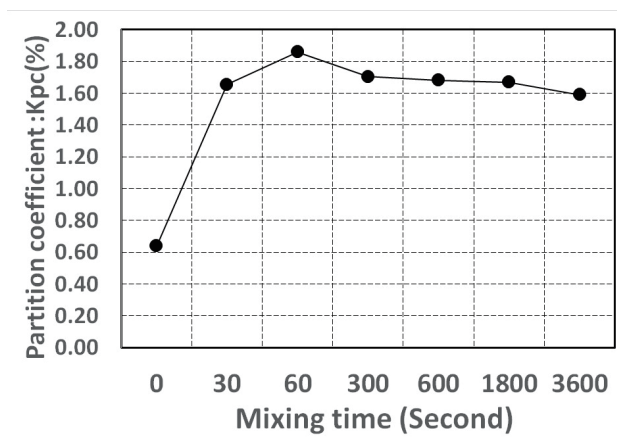


Fig 1. The partition coefficient (Kpc) (= (Ca concentration in organic phase) / (Ca concentration in aqueous phase)) was measured by changing the mixing time of 0 (no-mixing), 30 sec and 1, 5, 10, 30, 60 min: Preliminary.

A new test tube method was studied with the same two phases stirred by hand (only a second), separated by a centrifuge with 3 min, and iterated for fifteen times. The Ca concentration of both phases was measured by AAS and its Ca transfer between the two phases and no loss to the other medium was confirmed in Fig.2.

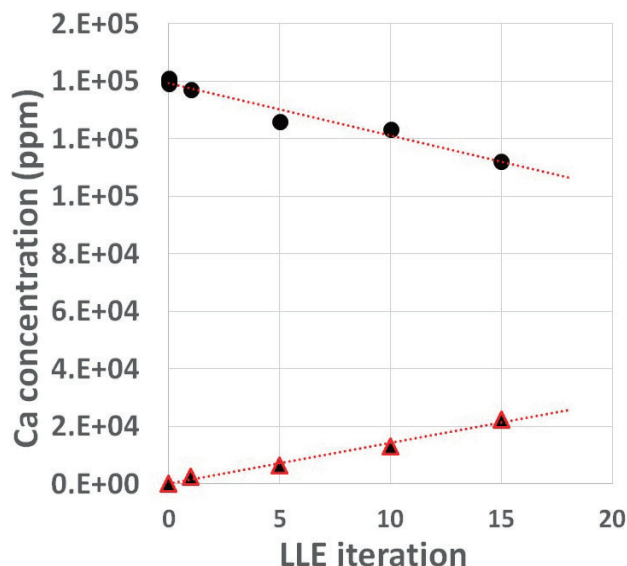


Fig 2. Ca concentration in aqueous phase (circle) and organic phase (triangle) for the process of LLE. Iteration is 15 times, zero is feed solution for CaCl<sub>2</sub> aqueous and crown-ether organic (CHCl<sub>3</sub>) phase: Preliminary.

**RESULTS:** It is noted that one process of this mixing/separation is only a few minutes and it takes less than an hour for the total of fifteen times multistage process. More than 3000 multistage enrichment process for ten times enrichment of Ca natural abundance can be achieved for a week and the scale-up for the mass production with an order of ton size is also promising due to this simple and easy handling procedure by utilizing the lab shaker and centrifugal separator in Fig. 3

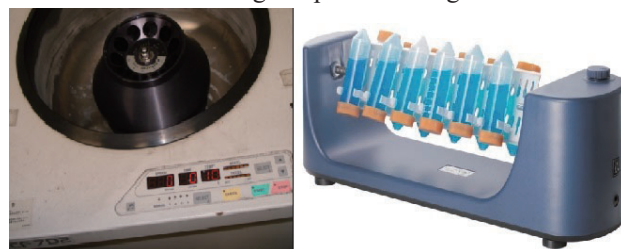


Fig 3. An example of lab shaker (Right) and centrifugal separator (Left).

**REFERENCES:**

- [1]R. Hazama *et al.*, KURRI Progress Report 2017, 104.  
[2]R. Hazama *et al.*, KURRI Progress Report 2018, 252.

# CO12-13 Radius of Gyration of Polymer for Viscosity Index Improver at Various Temperatures Evaluated by Small-Angle X-Ray Scattering

T. Hirayama, R. Takahashi<sup>1</sup>, Y. Takashima<sup>2</sup>, K. Tamura<sup>2</sup>, N. Sato<sup>3</sup>, M. Sugiyama<sup>3</sup>

Dept. of Mechanical Eng. and Science, Graduate School of Kyoto University

<sup>1</sup>Dept. of Mechanical Eng., Graduate School of Doshisha University

<sup>2</sup> Idemitsu Kosan Co., Ltd.

<sup>3</sup>Institute for Integrated Radiation and Nuclear Science, Kyoto University

<sup>4</sup>Japan Atomic Energy Agency

**INTRODUCTION:** Lubricating oils are necessary for friction reduction and high wear durability of sliding surfaces in machine components, and the development of the best oils is strongly required from industry. Viscosity index improver (VII) is a kind of additives for relieving the reduction of viscosity of lubricating oil due to temperature rise. Classical textbooks say that the VII molecules work with changing their equivalent radius in base oil in accordance with oil temperature. However, there are only few papers investigating the equivalent radius of VII molecules by small-angle X-ray scattering (SAXS) and/or small-angle neutron scattering (SANS)<sup>[1]</sup>, and there is still room for discussion of the behavior and working mechanism of VII molecules in oil. This study tried to investigate the radius of gyration of several kinds of VII polymers in base oil at various temperatures by SAXS, and the behavior of polymers was investigated and discussed.

**EXPERIMENT:** To investigate the radius of gyration of VII polymer, we used a SAXS instrument (NANOPIX, Rigaku) with a Cu-target X-ray source emitting X-ray with a wavelength of 1.54 Å, a characteristic line of Cu-Kα. The 1.2 mm-thick aluminum cell having optical windows made of 20-μm thermally-resistant engineering plastic film (Superio-UT, Mitsubishi chemical) was used for the measurement. The cell temperature increased to be 25, 40, 60, 80 and 100°C in turn, and the last measurement was carried out at 25°C again after cooling for checking if the VII molecule degenerated or not by heat. Poly(methyl acrylate) (PMA) type VII, as shown in Fig. 1, was prepared as a typical one used in engine oil in the study. Squalane was used as a model base oil, and the concentrations of PMA into squalane were 0.5, 1.0 and 2.0 mass%.

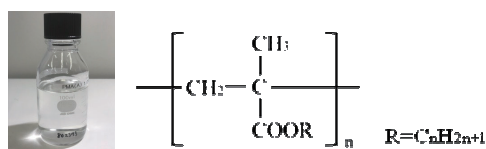


Fig. 1. Chemical structure of PMA type VII.

**RESULTS AND DISCUSSION:** The SAXS intensity profiles versus scattering vector  $q$  from squalane with 0.5 and 2.0 mass%-PMA type VII at each temperature were shown in Fig. 2, for example. The profiles were obtained by subtracting the intensity profiles from pure squalane at each temperature previously measured with the same liquid cell. The radius of gyration  $R_g$  estimated from the Guinier plot is shown in Fig. 3. We can see that the intensity profiles had little change even if the temperature changed, but the estimated  $R_g$  was gradually increased in accordance with the temperature rise even though the change of  $R_g$  was not so large. The trend of  $R_g$  change was similar with the  $R_g$  estimated by SANS and  $R_{\eta}$  estimated from the actual viscosity change. From the whole measurement, we succeeded to estimate the behaviour of PMA type VII against the temperature rise as shown in Fig. 4.

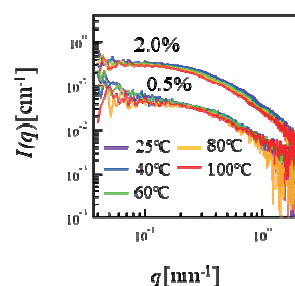


Fig. 2. SAXS profiles from squalane with 0.5 and 2.0 mass%- PMA type VII at various temperatures.

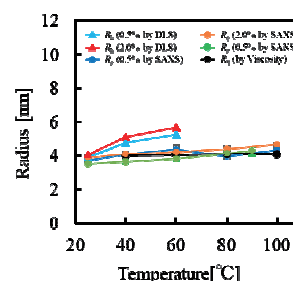


Fig. 3. Estimated  $R_g$  from Guinier plot of squalane with PMA type VII with various concentrations.

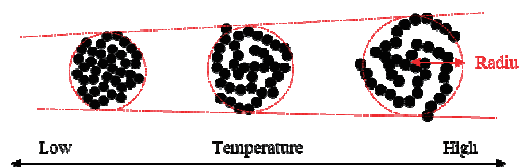


Fig. 4. Structure of PMA type VII with temperature change.

## REFERENCES:

- [1] M. J. Covitch, K. J. Trickett, How Polymers Behave as Viscosity Index Improvers in Lubricating Oils, Adv. Chem. Eng. Sci., 5 (2015) 134.

## CO12-14 Friction Reduction by the Combination Use of MoDTC and Organic Friction Modifier

T. Hirayama, N. Yamashita<sup>1</sup>, M. Hino<sup>2</sup>

Dept. of Mechanical Eng. and Science, Graduate School of Kyoto University

<sup>1</sup>Dept. of Mechanical Eng. and Science, Graduate School of Kyoto University

<sup>2</sup>Institute for Integrated Radiation and Nuclear Science, Kyoto University

**INTRODUCTION:** Engine oil is a blend of base oil such as mineral oil and synthetic oil with additives, and it contributes to saving fuel by reducing the friction loss of the engine. Therefore, among various additives, those having a friction reducing effect under boundary lubricated conditions are blended in the engine oil, of which molybdenum dithiocarbamate (MoDTC) is particularly effective. MoDTC is known to produce a boundary lubrication layer containing molybdenum disulfide (MoS<sub>2</sub>), which is effective for reducing friction. In addition, it is recently expected that a system using a combination organic friction modifier (OFM) that has no phosphorus in its molecule and MoDTC will alleviate environmental problems and obtain a sufficient friction reducing effect. The lubrication properties under boundary lubricated conditions are greatly influenced by the interfacial structure of the boundary lubrication layer formed by additives. Therefore, the interfacial structure formed by the combination use of MoDTC and OFM and its nanotribological properties were investigated in this study.

**EXPERIMENTS:** In this study, the oil in which MoDTC (0.3 mass%) and OFM is added to the base oil was used as the lubricating oil model. Hexadecane and palmitic acid (0.1 mass%) were used as models for the base oil and OFM. For neutron reflectometry (NR), deuterated palmitic acid, was used for the purpose of facilitating the analysis since a clear difference occurs in the reflectivity profile between hydrogen and deuterium.

We used the time-of-flight (TOF) type neutron reflectometer SOFIA installed at the J-PARC in Tokai, Ibaraki. In order to grasp the film thickness and density of the boundary lubrication layer formed on the Cu surface under each system added alone or in combination, experiments were conducted to obtain the reflectivity profile under each case.

**RESULTS:** First, we conducted the NR experiment to investigate the boundary layer structure formed by *d*-palmitic acid. When *d*-palmitic acid was added, the fringe interval became short; as a result of the analysis, it was found that an adsorption layer having a thickness of about 2.1 nm was formed on the copper surface immediately after the addition of *d*-palmitic acid. The SLD value of *d*-palmitic acid at the bulk state was  $6.7 \times 10^{-6} \text{ \AA}^{-2}$ , whereas the analysis value was  $2.1 \times 10^{-6} \text{ \AA}^{-2}$ .

From this, the density of the adsorption layer was approximately 30% with respect to the bulk density. From 0h to 2h, the fringe interval did not change; it indicated that the film thickness and the density of the adsorption layer by *d*-palmitic acid barely change with time.

For the combined system being used, measurements were carried out under the three cases described below. [Case 1]: Measurement was carried out for four hours after placing hexadecane+*d*-palmitic acid (0.1 mass%) + MoDTC (0.3 mass%) into the sample holder. [Case 2]: Measurement was carried out for two hours after hexadecane+*d*-palmitic acid (0.1 mass%) was placed in the sample holder. After the measurement, the sample holder was rinsed with hexadecane, and hexadecane+MoDTC (0.3 mass%) was added, and then the measurement was carried out for four hours. [Case 3]: Measurement was carried out for four hours after hexadecane+MoDTC (0.3 mass%) was placed in the sample holder. After the measurement, the sample holder was rinsed with hexadecane, and hexadecane+*d*-palmitic acid (0.1 mass%) was added, and then the measurement was carried out for two hours.

As a result of analysis of [Case 1], it was found that an adsorption layer with a thickness of about 2 nm and a density of approximately 30% with respect to the bulk density was formed immediately after *d*-palmitic acid was added. Although the film thickness did not change with time, the density increased to about 60% in four hours. When MoDTC is added first, film thickness and density cannot be detected since MoDTC was not deuterated. However, from the NR experiment of [Case 3], it can be seen that immediately after the addition of *d*-palmitic acid, an adsorption layer having the 2-nm film thickness and the approximately 30% density with respect to the bulk density is formed. While no change in film thickness with time was observed, the density increased from about 30% to about 45% in 2 hours. This result shows the same tendency with as [Case 1]. In addition, it is interesting to note that the nanotribological property measured by SiO<sub>2</sub> colloidal probe was better when we used MoDTC and palmitic acid in combination than that when we used only MoDTC or palmitic acid each. It indicated that the combination use of MoDTC and OFM is effective for friction reduction by forming thicker boundary lubrication layer.

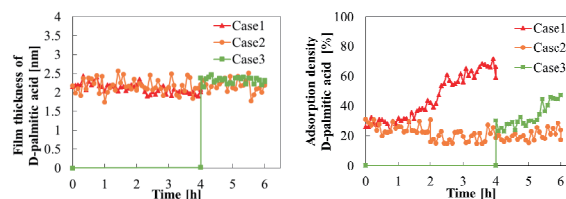


Fig. 1. Estimated film thickness and density of palmitic acid by neutron reflectometry for the three cases.

# CO12-15 Multi-element neutron activation analysis of selected Japanese food samples by neutron activation analysis

M. Fukushima, T. Maeda and Y. Inuma<sup>1</sup>

Faculty of Sciences and Engineering, Ishinomaki Senshu University

<sup>1</sup>Institute for Integrated Radiation and Nuclear Science, Kyoto University

**INTRODUCTION:** It is important to obtain multi element levels in food samples for nutritional purposes. For the analysis of multi elements in food samples, atomic absorption spectrometry (AAS) and induced coupled plasma spectrometry (ICP-AES) are widely used after pre-treatment of acid extraction or acid digestion. Though complete acid digestion is needed for obtaining total levels of elements in food samples, it is not easy by the presence of high concentrations of lipids, polysaccharides, etc. preventing acid digestion. For eliminating this problem, neutron activation analysis was used for multi elements analysis of Japanese food samples. Bioaccessible trace element levels in soft tissues of oysters were also estimated by using an AOAC method.

**EXPERIMENTAL:** Vegetables, fish, mushroom, seaweeds, and wild plants were collected from Ishinomaki farmers and fish markets mainly in 2017-2019. Samples were washed with tap water, separated edible parts, freeze dried, and pulverized for dried powder samples. NAA was done by three different conditions according to nuclides for the interest. 1) One portion of samples was irradiated for 1-1.5 min in TcPn site. After 3 minutes decay, gamma spectrum was measured for 10 minutes by Ge detector with CSS. Levels of Br, Ca, Cl, I, K, Mg, Mn, Na, and V were analyzed using <sup>80</sup>Br, <sup>49</sup>Ca, <sup>38</sup>Cl, <sup>128</sup>I, <sup>42</sup>K, <sup>27</sup>Mg, <sup>56</sup>Mn, <sup>24</sup>Na, and <sup>52</sup>V. 2) Another portion of samples was irradiated for 20 minutes, and gamma spectrum was measured for 20 minutes after 2-3 days decay for analyzing As using <sup>76</sup>As. 3) Another portion of samples was irradiated for 1 hour, and gamma spectrum was measured for 20 minutes after 1 month decay for analyzing Ag, Co, Cr, Cs, Fe, Rb, Sc, Se, and Zn using <sup>76</sup>As. 1 h in the Kyoto University Reactor, Japan. Gamma-ray spectra of the irradiated samples were recorded after one-month decay for 20-30 min using a Ge detector system. Levels of Ag, Co, Cr, Cs, Fe, Rb, Sc, Se, and Zn were obtained using <sup>110m</sup>Ag, <sup>60</sup>Co, <sup>51</sup>Cr, <sup>134</sup>Cs, <sup>59</sup>Fe, <sup>86</sup>Rb, <sup>46</sup>Sc, <sup>75</sup>Se, and <sup>65</sup>Zn, respectively. NAA method used was validated using NIST SRM 1570a Spinach Leaves, NIST SRM 1566b Oyster Tissue, NIST SRM 1575 Pine Needles, NIST SRM 1573a Tomato Leaves, and NIST SRM 1548a Typical Diet.

Bioaccessible trace element levels in food samples were estimated for several fish samples by using an AOAC method. Briefly, about 1 g of dried oyster soft tissue powders was incubated with  $\alpha$ -amylase, protease, and amyloglucosidase one after another. Water soluble dietary fiber was filtered from the undigested residue after adding ethanol, and both fractions were analyzed by INAA.

**RESULTS:** Ag was found only in dried sakuraebi and ami. I and V were found only in seaweeds. Several data obtained for fish samples are shown in Table 1.

**Table 1. Levels of elements in fish muscle (unit: mg/kg, dry weight)**

Fish sample	Cs	Fe	Se	Zn
Tuna red muscle	0.31	35.8	2.75	16.8
Tuna medium fatty muscle	0.20	22.4	2.11	13.5
Skipjack tuna without dark muscle	0.15	38.1	2.17	21.8
Skipjack tuna dark muscle	0.20	313.6	12.38	25.9
Salmon	0.45	11.4	2.32	11.7

From the results in Table 1, differences of Fe and Se levels between skipjack tuna muscle dark muscle and without dark muscle were remarkable.

Bioaccessible levels of Se in fish sample were obtained, and the ratios of bioaccessible Se to total Se were; 0.45, 0.39, 0.51, 0.56, and 0.46 for tuna red muscle, tuna medium fatty muscle, skipjack tuna without dark muscle, skipjack dark muscle, and salmon, respectively. It may be said that about half of total Se is bioaccessible level.

Wild plants analyzed were; shidoke, Ostrich Fern, alpine leek, fiveleaf aralia, Aralia sprout, udo, butterbur, bracken, mizu, urui, bonna, Japanese parsley, and bamboo shoots from 4 different collection areas. Several levels of elements in wild plants were interesting when compared to ones of vegetables. For example, Mn levels in 13 species, except shidoke, fiveleaf aralia, and Japanese parsley, were high, though Mn levels in 32 vegetables were under the detection limit. Mn levels were 244 - 3620 mg/kg, DW in brackens, 2910 mg/kg, DW in bonna, 1540 mg/kg, DW in udo. Also, several elemental levels showed difference between collection area, and showed in Fig.1. Fig. 1 shows difference between three shidoke collected from Yamagata Prefecture, Kahoku (Ishinomaki, Miyagi), and Kamaishi (Iwate Prefecture).

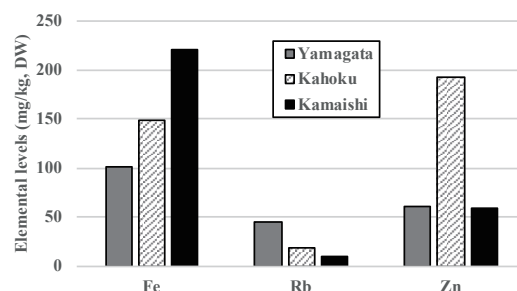


**Fig.1. Elemental levels of shidokes collected from three different areas.**

M.A. Soliman, K. Takamiya, T. Kubota, R. Okumura and T. Ohtsuki

*Institute for Integrated Radiation and Nuclear Science, Kyoto University*

**INTRODUCTION:** Flowing sample neutron activation analysis (FSNAA) is a subclass of NAA, which has been developed for analysis of water/liquid samples [1]. It involves continuous pumping a large volume of the sample, in a tube, between the irradiation site and the  $\gamma$ -ray detector [1]. Analysis of large volume of a sample improves the detection limits, while continues pumping allows better measurement of short-lived radionuclides. The set-up was previously investigated for analysis of synthetic and real samples using  $^{252}\text{Cf}$  as a neutron source [1, 2]. The purpose of the present work is to install FSNAA at the slant irradiation tube of KUR to take the benefit of its high flux.

**EXPERIMENTS:** Irradiation durability test was performing to select a suitable tubing material. Samples of polyethylene, TYGON, and Ethylene tetrafluoroethylene tubes were irradiated for different periods and then a simple bending test was performed [3].

The FSNAA set-up was constructed (Figure 1) using the selected tube. The tube was rolled around the HPGe detector to increase the counting time. The general procedures including: placing the sample in a sample tank, pumping it to the irradiation site, and then record a gamma-ray spectrum with HPGe. Finally the irradiated sample was stored in a storage tank. A run with de-ionized water was carried out for leakage test and to check the performance of the set-up components as well as for background measurements. FSNAA was tested for analysis of tap (from KURNS) and Kashii River waters samples based on relative method using multi-elements reference standard solution. The analyzed sample volume was  $\sim 1$  l and the flow-rate was 30 ml/min.

**RESULTS:** However, irradiation durability test showed that all tested tubes have acceptable radiation resistance, TYGON was used for constructing the system due to its low chlorine content and excellent bending flexibility.

Table 1 shows the analysis results of tap water and river water samples. Nine elements were detected and quantified, while Cl, Br, I, and  $^{18}\text{O}$  were detected but not quantified due to the lack of reference standard. Levels of the quantified elements in the tap water are below the WHO guidelines [4]. The detection limits obtained from this preliminary FSNAA study are satisfied in comparison to conventional NAA and other techniques. Under the current experimental conditions, the decay time (the traveling time between the irradiation site and HPGe) was  $\sim 3.5$  min. This relatively long decay time hinders the analysis of several elements (those with shorter half-lives

isotopes ex:  $^{20}\text{F}$ ,  $^{46\text{m}}\text{Sc}$ ,  $^{77\text{m}}\text{Se}$ ,  $^{107\text{m}}\text{Pb}$ ,...).

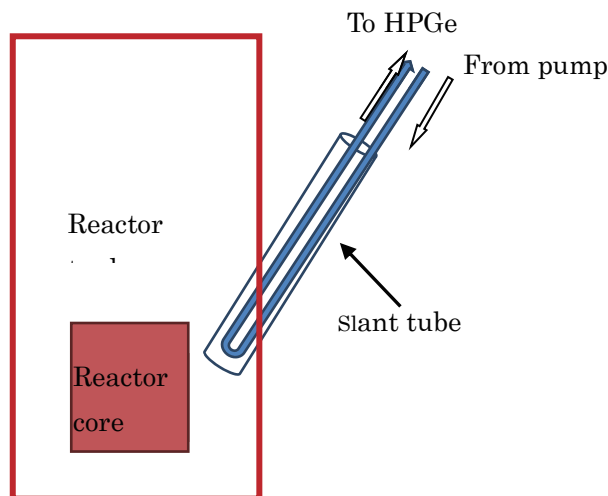


**Fig 1.** FSNAA setup installed in slant tube

Also, it adversely affects the detection limits of  $^{28}\text{Al}$ ,  $^{52}\text{V}$ , and  $^{66}\text{Cu}$  due to the decay of major fraction of their radioactivities before reaching the HPGe.

As a future plan, use of powerful pump will reduce the decay times; and hence it is expected to increase the number of measured elements and improves the detection limits for some elements like Al, V, and Cu. The capability of FSNAA to measuring  $^{18}\text{O}$  reveals its potential for determining past climate temperatures using, for example, water samples collected from ice cores.

**Table 1.** Analysis results of tap and river water samples

Element	Tap water		River water	
	$\mu\text{g/l} \pm \%$	DL	$\mu\text{g/l}$	DL
O ( $^{18}\text{O}$ )	D		D	
Na	$9700 \pm 2$	110	$8800 \pm 2$	105
Mg	$1300 \pm 5$	135	$3720 \pm 3$	200
Al	$25.5 \pm 6$	2.2	$240 \pm 1.3$	2.0
S	$8000 \pm 25$	7400	$10500 \pm 20$	6600
Cl	D		D	
K	$1350 \pm 23$	980	$1350 \pm 25$	1180
Ca	$10100 \pm 4$	280	$15900 \pm 2.5$	240
V	$0.40 \pm 14$	0.14	$0.37 \pm 15$	0.15
Mn	$1.7 \pm 30$	1.5	$132 \pm 2$	1.9
Cu	$28.0 \pm 35$	25	ND	
Br	D		D	
I	D		D	

D: detected only, DN: not detected

#### REFERENCES:

- [1] M. Soliman *et al.*, *J. Radioanal. Nucl. Chem.*, **295** (2013) 245-254.
- [2] M. Soliman *et al.*, *J. Radioanal. Nucl. Chem.*, **299** (2014) 89-93.
- [3] H. Kikunaga, *et al.*, KURRI Progress Report 2013, PR10-3, (2014).
- [4] Dinelli *et al.*, *L. Geochem. Explor.* 112 (2012) 54-75.

J. Kawarabayashi, H. Tagawa, Y. Ikeda, K. Mitsui and J. Hori<sup>1</sup>

*Department of nuclear safety engineering, Tokyo City University*

<sup>1</sup>*Institute for Integrated and Nuclear Science, Kyoto University*

**INTRODUCTION:** In order to support nuclear facility regulations in Japan for safe use, it is necessary to develop educational training course with broad knowledge associated with nuclear engineering. Nuclear facilities include reprocessing, nuclear fuel factories, research facilities, etc. in addition to nuclear power plants, it is important to teach not only the knowledge of radiation, reactor physics, but also the physics of nuclear material itself at each stage of the nuclear fuel cycle. The knowledge of physical and chemical properties of nuclear material is also needed for effective regulation. As a part of this human resource development, we propose an isotope ratio measurement training with uranium using pulsed neutron spectrometry as a candidate for the nuclear regulatory educational course to deepen the understanding of the nuclides in nuclear fuel cycle. Observation of the neutron resonance absorption phenomena of natural, enriched and depleted uranium will develop the understanding of the isotope itself and the properties of the nucleus of uranium. In this fiscal year, we conducted experiments to acquire neutron resonance absorption spectra of various samples including uranium in order to establish a procedure for practical training.

**EXPERIMENTS:** Natural Uranium oxide sample and some metal plates (Ag, Ta, etc.) were irradiated at KURRI-LINAC to record neutron transmission spectrum. A <sup>3</sup>He proportional counter followed by a multiple-stop time spectrometer (ORTEC EASY-MCS) was set just behind the sample at 13m experimental room and generated neutron detection signal. A signal from the accelerator was used as the start signal of the time spectrometer. The timing calibration between start signal and output signal of the <sup>3</sup>He proportional counter was performed with an oscilloscope by gamma-flash signal generated at the Ta target of the accelerator.

**RESULTS:** As shown in Fig.1, time spectrum with and without the natural uranium sample were obtained successfully with measurement of 20,000 sweeps and 21 m second range. The accelerometer was running in 50Hz Long mode, each spectrum was recorded within about 15 minutes. There were some resonance dips corresponding to <sup>238</sup>U while no dip of <sup>235</sup>U was observed. The cross section of resonance peak in <sup>235</sup>U is about one order lower than that of <sup>238</sup>U and the isotope ratio of <sup>235</sup>U to <sup>238</sup>U is about 0.71%, the dip intensity of <sup>235</sup>U would be three order lower than that of <sup>238</sup>U. The number of counted signal in one channel (i.e. 1 micro second) is in about as shown in Fig. 1, it would be necessary to record

least one order of magnitude more signals to detect the resonance absorption of <sup>235</sup>U in this experiment. In Fig. 2, a resonance dip of <sup>109</sup>Ag was observed in the time spectrum with the sample of silver plate. The energy of this dip was estimated to be 5.25eV derived from the source-detector distance of 13m and dip position of 0.317 msec. The first energy level of <sup>109</sup>Ag is 5.19eV<sup>[1]</sup>. There is a good agreement between the experimental result and literature values.

**CONCLUSION:** We proposed pulsed neutron spectrometry as a candidate for the nuclear regulatory educational course to deepen the understanding of the nuclides in nuclear fuel cycle. The experimental results require at least acquisition period of 150 minutes to observe <sup>235</sup>U in natural uranium sample.

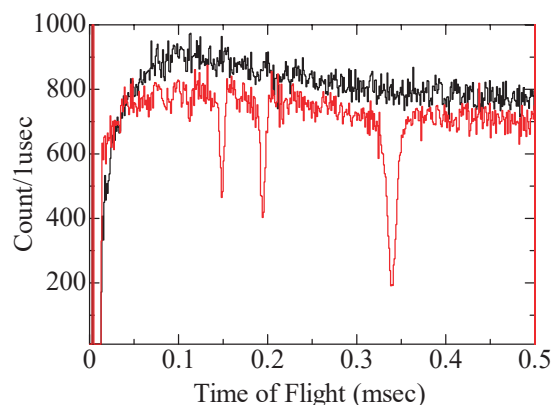


Fig. 1. Time spectrum of natural uranium sample (red). Black line is time spectrum of no sample. There are three dips corresponding to resonance absorption of <sup>238</sup>U.

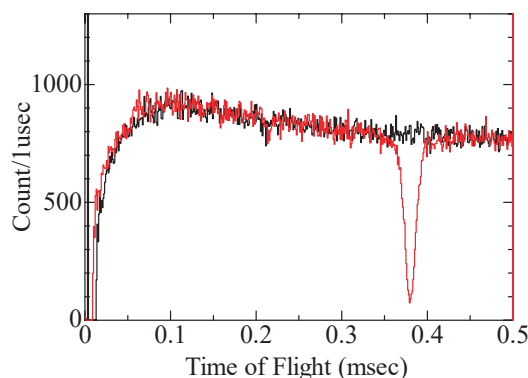


Fig. 2. Time spectrum of a silver plate sample (red). Black line is time spectrum of no sample. There is one dip at 0.317msec which is corresponded to resonance absorption of <sup>109</sup>Ag energy level of 5.25eV.

#### REFERENCES:

S. F. Mughabghab, Atlas of Neutron Resonances.

H. Masui, T. Murase, M. Cho, S. Wei<sup>1</sup>, C. Joseph<sup>1</sup> and K. Takamiya<sup>2</sup>

Laboratory of Spacecraft Environment Interaction Engineering, Kyushu Institute of Technology

<sup>1</sup>Nanyang Technological University

<sup>2</sup>Institute for Integrated Radiation and Nuclear Science, Kyoto University

**INTRODUCTION:** Commercial-Off-The-Shelf (COTS) Integrated Circuits (ICs) are mostly sensitive to irradiations (e.g., protons, heavy-ions, etc.) in space, leading to various Single-Event Effects (SEEs). Among different SEEs, Single-Event-Latchup (SEL) is probably the most critical because it is detrimental and often damages ICs[1, 2]. This paper reports a circuit implementation that serves to provide protection for COTS ICs from SEL. Kyushu Institute of Technology (Kyutech) and Nanyang Technological University (NTU) are conducting a joint research program in 1U CubeSats project of BIRDS-4. In BIRDS-4 project, LDAP(Latch-up Detection and Protection) developed by NTU as a part of the mission of BIRDS-4[3] were installed (Fig. 1). LDAP monitors the latch-up current occurred in a device and shutdowns the power line of the device. The on-ground hardware verification on the basis of <sup>252</sup>Cf was demonstrated that the circuit successfully cuts off the SEL current and subsequently resets the COTS IC. The reported circuit has been adopted in a 1U CubeSat that will be launched early 2020.

**EXPERIMENTS:** Figure 2 shows the circuit diagram. In this test, an AD converter was adopted as a sample, and SEL was induced in the AD converter. A package of the AD convertor was removed(=de-caped) for radiation from <sup>252</sup>Cf. The AD convertor was set in the vacuum chamber and its pressure was less than 30 Pa. <sup>252</sup>Cf source was mounted on XYZ stage and the position of <sup>252</sup>Cf was controlled from outside and was moved above the sample. We checked whether LDAP can detect the SEL and can cut the power line connected the AD convertor. To check the function of LDAP, the actual latch-up current was measured with a measuring instrument and the response of LDAP with a serial communication was monitored with PC1.

**RESULTS:** Figure 3 shows the current profile acquired with the measuring instrument. The current peak in the current profile shows the current increasing due to SEL. After the SEL, the current quickly recovered to the nominal current. This means that LDAP was able to detect the SEL in the AD convertor and to reset the power line of the AD convertor. In the same way, it was confirmed that the LDAP correctly worked with the serial communication. Since the LDAP function was confirmed, LDAP was installed on the mission board of the BIRDS-4 flight model. BIRDS-4 satellite will be launched in FY2020 and on-orbit demonstration will be planed.



Fig. 1. LDAP (Latch-up Detection and Protection).

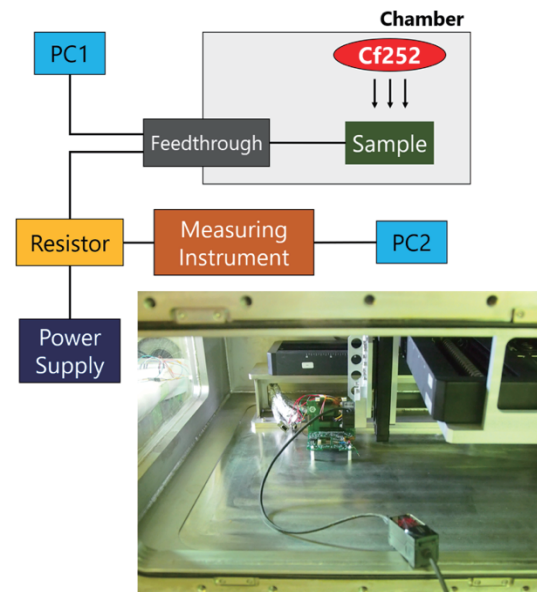


Fig. 2. Circuit diagram and phot of setup.

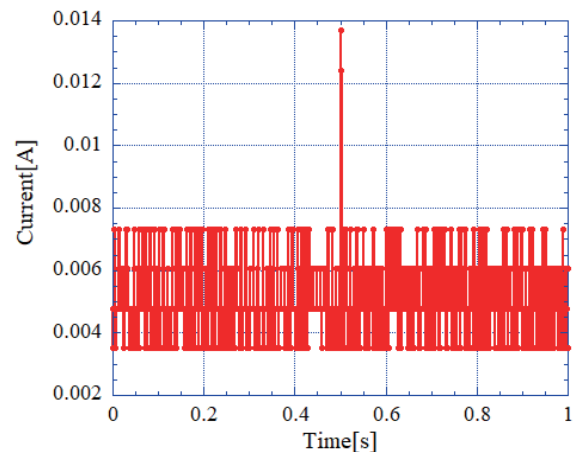


Fig. 3. Latch-up current detection and recovery.

**REFERENCES:**

[1] M. Cho *et al.*, “Test and Verification of Nanosatellite HORYU-II and Orbital Anomaly Investigation”, Aerospace Technology Japan, 12 17-24, 2013.  
 [2] Tomioka *et al.*, “Screening of nanosatellite microprocessors using californium single-event latch-up test results”, Acta Astronautica, 126, 334-341, 2016.  
 [3] <https://www.birds-project.com/>

**II. PUBLICATION LIST**  
**(APRIL 2019 – MARCH 2020)**

## 1. Slow Neutron Physics and Neutron Scattering

### Papers

Potential-Dependent Structure of the Ionic Layer at the Electrode Interface of an Ionic Liquid Probed Using Neutron Reflectometry

N. Nishi, J. Uchiyashiki, Y. Ikeda, S. Katakura, T. Oda, M. Hino and N. L. Yamada  
The Journal of Physical Chemistry C **123** (14) (2019) 9223- 9230.

Current status of the neutron resonance spin echo spectrometer on BL06 “VIN ROSE” at MLF, J-PARC

H. Endo, T. Oda, M. Hino and T. Hosobata  
Physica B: Condensed Matter **564** (2019) 91- 93.

Elliptic neutron-focusing supermirror for illuminating small samples in neutron reflectometry

T. Hosobata, N. L. Yamada, M. Hino, H. Yoshinaga, F. Nemoto, K. Hori, T. Kawai, Y. Yamagata, M. Takeda and S. Takeda  
Optics Express **19** (2019) 26807.

A study of TOF-MIEZE reflectometry for nanomagnetic dynamics

M. Hino, T. Oda, H. Endo, N. L. Yamada, H. Seto, H. Ohshita and Y. Kawabata  
Journal of Physics: Conference Series **1316** (2019).

Experimental test of <sup>3</sup>He neutron-spin filter in MIEZE spectrometer

H. Hayashida, M. Hino, H. Endo, T. Oku, T. Okudaira, K. Sakai and T. Oda.  
Journal of Physics: Conference Series **1316** (2019) 012013.

Focusing and imaging of cold neutrons with a permanent magnetic lens

J. T. Cremer, H. Filter, J. Klepp, P. Geltenbort, C. Dewhurst, T. Oda and R. H. Pantell.  
Review of Scientific Instruments **91**(1) (2020) 013704.

Structural and electrochemical features of (Li<sub>2</sub>S)<sub>x</sub>(SiS<sub>2</sub>)<sub>100-x</sub> superionic glasses

K. Mori, K. Iwase, Y. Oba, K. Ikeda, T. Otomo and T. Fukunaga  
Solid State Ionics **344** (2020) 115141.

### Proceedings

小角 X 線散乱法による DN-polymers の構造解析 /

SAXS study of the DN-polymers under different temperature and humidity atmosphere

T. Tominaga, R. Inoue, N. Sato and M. Sugiyama

Proceedings of the 54th KURNS Scientific Meeting Kumatori, Japan (Feb5-6, 2020) 19. (in Japanese)

X 線小角散乱法による潤滑油中の添加剤の解析 /

Structural analysis of lubricant additive using small-angle X-ray scattering

Y. Oba, M. Hino, N. Adachi, Y. Todaka, R. Inoue and M. Sugiyama

Proceedings of the 54th KURNS Scientific Meeting Kumatori, Japan (Feb.5-6, 2020) 20. (in Japanese)

核共鳴小角散乱による電子状態の微細構造観測手法の開発 /

Nuclear resonant small-angle scattering for investigation of microstructures in electronic states

S. Kitao, M. Kurokuzu, Y. Kobayashi, M. Seto, Y. Yoda and S. Kishimoto

Proceedings of the 54th KURNS Scientific Meeting Kumatori, Japan (Feb.5-6, 2020) 32. (in Japanese)

MPPC を使用した二次元中性子検出器 Mpix の性能評価 /

Performance evaluation of a two-dimensional neutron detector with MPPC (Mpix)

H. Ohshita, H. Endo, T. Seya, Y. Yasu, M. Hino and T. Oda

Proceedings of the 54th KURNS Scientific Meeting Kumatori, Japan (Feb.5-6, 2020) 40. (in Japanese)

中性子準弾性散乱測定を用いた溶媒依存性主鎖らせん反転を示す高分子の分子ダイナミクスの解明/

Elucidation of the molecular dynamics of the macromolecules exhibiting the solvent-depeibiting helix inversion by using quasielastic neutron scattering measurement

Y. Nagata, M. Sugimoto, M. Sugiyama, R. Inoe, N. Sato and K. Morishima

Proceedings of the 54th KURNS Scientific Meeting Kumatori, Japan (Feb.5-6, 2020) 43. (in Japanese)

X線小角散乱法および動的散乱法による潤滑油中粘度指数向上剤の構造解析/

Structural analyses of viscosity index improvers in lubricant oil by means of dynamic light scattering and small angle X-ray scattering

R. Takahashi, T. Hirayama, N. Sato, M. Sugiyama, Y. Takashima, T. Nakano and Y. Oba

Proceedings of the 54th KURNS Scientific Meeting Kumatori, Japan (Feb.5-6, 2020) 44. (in Japanese)

中性子とX線を利用した複合イメージング手法の高度化/

Development of hybrid imaging technique using neutrons and X-ray

D. Ito, R. Okumura, K. Ito and Y. Saito

Proceedings of the 54th KURNS Scientific Meeting Kumatori, Japan (Feb.5-6, 2020) 52. (in Japanese)

X線・中性子反射率法による潤滑界面の平均構造評価/

Investigation of lubrication interface by X-ray and neutron reflectometry

M. Hino, N. Adachi, Y. Todaka, Y. Oba, T. Hirayama, T. Oda, K. Oda, H. Endo and T. Hirayama

Proceedings of the 54th KURNS Scientific Meeting Kumatori, Japan (Feb.5-6, 2020) 55. (in Japanese)

実験手法と計算機手法の融合による溶液散乱法の最前線/

Mariage of computational and experimental techniques for solution small-angle scattering

R. Inoue, M. Sugiyama, N. Sato, K. Morishima, A. Okuda and R. Urade

Proceedings of the 54th KURNS Scientific Meeting Kumatori, Japan (Feb.5-6, 2020) 56. (in Japanese)

箱型自己集合体の水中における動的特性/

Dynamic property of a box-shaped self-assembly in water

N. Sato, Y. Y. Zhang, Q. Jiang, T. Kojima, K. Morishima, T. Koide, M. Tachikawa, M. Sugiyama and S. Hiraoka

Proceedings of the 54th KURNS Scientific Meeting Kumatori, Japan (Feb.5-6, 2020) 57. (in Japanese)

小角散乱と超遠心分析の協奏的解析(AUC-SAS)による弱会合性タンパク質複合体の構造解析/

Structural analysis of weakly bound protein complex with concerted use of small angle scattering and analytical ultracentrifugation (AUC-SAS)

Ken Morishima, Maho Yagi-Utsumi, Rintaro Inoue, Nobuhiro Sato, Aya Okuda, Reiko Urade, Koichi Kato, and Masaaki Sugiyama

Proceedings of the 54th KURNS Scientific Meeting Kumatori, Japan (Feb.5-6, 2020) 58. (in Japanese)

X線小角散乱による大豆タンパク質の構造解析/

Nanostructural analysis of soy bean proteins by small-angle X-ray scattering

N. Sato, R. Urade, A. Okuda, K. Morishima, R. Inoue and M. Sugiyama

Proceedings of the 54th KURNS Scientific Meeting Kumatori, Japan (Feb.5-6, 2020) 59. (in Japanese)

KUR-IBSを用いた多層膜中性子ミラー開発の現状/

Current status of multilayer neutron mirror development with KUR-IBS

M. Hino, T. Oda, F. Funama, H. Yoshinaga, Y. Kawabata, T. Hosobata, M. Takeda, S. Ikebe and Y. Yamagata, H. Endo and N. L. Yamada

Proceedings of the 54th KURNS Scientific Meeting Kumatori, Japan (Feb.5-6, 2020) 60. (in Japanese)

強相関f電子系金属間化合物の結晶・磁気構造の研究/

Magnetic and crystal structure analyses on strongly correlated f-electron systems

Chihiro Tabata

Proceedings of the 54th KURNS Scientific Meeting Kumatori, Japan (Feb.5-6, 2020) 64-65. (in Japanese)

## Reviews

100nm 未満の空間分解能を発揮する超微粒子原子核乳剤を用いた冷・超冷中性子検出器  
長縄直崇  
日本中性子科学会誌 波紋 **29(3)** (2019) 133-137. (in Japanese)

## 2. Nuclear Physics and Nuclear Data

### Papers

Neutron total cross section measurements of polyethylene using time-of-flight method at KURNS-LINAC  
J. Lee, J. Nishiyama, J. Hori, R. Kimura, T. Sako, A. Yamada and T. Sano  
Journal of Nuclear Science and Technology **57(1)** (2019) 1-8.

Measurements of Spallation Products Induced by Heavy Ions  
H. Yashima and T. Nakamura  
RADIOISOTOPES **68(8)** (2019) 567-573.

X-ray pumping of the  $^{229}\text{Th}$  nuclear clock isomer  
T. Masuda, A. Yoshimi, A. Fujieda, H. Fujimoto, H. Haba, H. Hara, T. Hiraki, H. Kaino, Y. Kasamatsu, S. Kitao, K. Konashi, Y. Miyamoto, K. Okai, S. Okubo, N. Sasao, M. Seto, T. Schumm, Y. Shigekawa, K. Suzuki, S. Stellmer, K. Tamasaku, S. Uetake, M. Watanabe, T. Watanabe, Y. Yasuda, A. Yamaguchi, Y. Yoda, T. Yokokita, M. Yoshimura and K. Yoshimura  
Nature **7773** (2019) 238-242.

Conceptual study on parasitic low-energy RI beam production with in-flight separator BigRIPS and the first stopping examination for high-energy RI beams in the parasitic gas cell  
T. Sonoda, I. Katayama, M. Wada, H. Iimura, V. Sonnenschein, S. Iimura, A. Takamine, M. Rosenbusch, T. M. Kojima, D. S. Ahn, N. Fukuda, T. Kubo, S. Nishimura, Y. Shimizu, H. Suzuki, H. Takeda, M. Tanigaki, H. Tomita, K. Yoshida and H. Ishiyama  
Progress of Theoretical and Experimental Physics **11** (2019) 113D02.

IMPROVEMENT OF GAMMA-RAY SUBTRACTION PROCEDURE FOR A CURRENT-MODE NEUTRON DETECTOR WITH A PAIR OF  $^6\text{Li}$ - AND  $^7\text{Li}$ -GLASS SCINTILLATORS  
T. Matsumoto, A. Masuda, H. Harano, J. Hori and T. Sano  
Radiation Protection Dosimetry ncz**266** (2019) 1-6.

Experimental study of multiplex energy recovery internal target ring  
H. Okita, A. Taniguchi, Y. Kuriyama, T. Uesugi, Y. Ishi, Y. Mori, M. Muto, Y. Ono, N. Ikeda, Y. Yonemura, A. Sato, M. Kinsho, Y. Miyake, M. Yoshimoto and K. Okabe  
Nuclear Instruments and Methods in Physics Research Section A: Accelerators, Spectrometers, Detectors and Associated Equipment **953** (2019) 162988.

### Proceedings

Measurement of Temperature-dependent Thermal Neutron Spectrum in  $\text{CaH}_2$  Moderator Material for Space Reactor  
J. Lee, T. Sano, J. Hori, T. Sako, R. Kimura, A. Yamada and J. Nishiyama  
International Conference on Nuclear Data for Science and Technology (ND2019) Beijing, China (May19-24, 2019).

Neutron Capture Cross Section Measurement of Minor Actinides in Fast Neutron Energy Region for Study on Nuclear Transmutation System  
T. Katabuchi, J. Hori, N. Iwamoto, O. Iwamoto, A. Kimura, S. Nakamura, Y. Shibahara, K. Terada, K. Tosaka, S. Endo, G. Rovira, Y. Kodama and H. Nakano  
Proceedings of the 2019 Symposium on Nuclear Data Fukuoka, Japan (Nov.28-29, 2019).

MCS Multi-group Cross Sections Generation for Fast Reactor Analysis  
T. D. C. Nguyen, H. Lee, X. Du, V. Dos, T. Q. Tran and D. Lee  
Proceedings of Reactor Physics Asia Conference 2019 (RPHA2019) Osaka, Japan (Dec.2-3, 2019) 2-5.

A Systematic Way to Determine Neutron Generation Size in Monte Carlo Simulation Accelerated by the CMFD  
T. D. C. Nguyen, H. Lee, X. Du, V. Dos, T. Q. Tran and D. Lee  
Proceedings of Reactor Physics Asia Conference 2019 (RPHA2019) Osaka, Japan (Dec.2-3, 2019) 6-9.

Validation of Activation Analysis Method on RWRVI of Kori Unit using MCCARD/ORIGEN2  
Y. I. Kim, S. H. Jang, D. H. Lee and H. J. Shim  
Proceedings of Reactor Physics Asia Conference 2019 (RPHA2019) Osaka, Japan (Dec.2-3, 2019) 10-13.

Uncertainty Quantification of Neutronics Characteristics in Thermal Systems using Random Sampling and Continuous Energy Monte-Carlo Methods  
H. Oike, R. Kondo, T. Endo and A. Yamamoto  
Proceedings of Reactor Physics Asia Conference 2019 (RPHA2019) Osaka, Japan (Dec.2-3, 2019) 14-17.

Peak Power Characteristics of Postulated Criticality in Fuel Debris  
Y. Yamane  
Proceedings of Reactor Physics Asia Conference 2019 (RPHA2019) Osaka, Japan (Dec.2-3, 2019) 31-33.

Development of Integral Kinetic Model with Delayed Neutrons Effect for Criticality Accident Analysis of Fukushima Daiichi NPP Fuel Debris  
H. Takezawa, D. Tuya and T. Obara  
Proceedings of Reactor Physics Asia Conference 2019 (RPHA2019) Osaka, Japan (Dec.2-3, 2019) 34-35.

Radiation Dose by Criticality Accidents of Fuel Debris in Water  
K. Fukuda, J. Nishiyama and T. Obara  
Proceedings of Reactor Physics Asia Conference 2019 (RPHA2019) Osaka, Japan (Dec.2-3, 2019) 36-39.

Development of Criticality Safety Evaluation Method Based on the Actual Dynamic Behavior of the Fuel Debris in Water  
T. Muramoto, J. Nishiyama and T. Obara  
Proceedings of Reactor Physics Asia Conference 2019 (RPHA2019) Osaka, Japan (Dec.2-3, 2019) 40-43.

Treatment of R-matrix Limited Formula in FRENDY  
K. Tada and S. Kunieda  
Proceedings of Reactor Physics Asia Conference 2019 (RPHA2019) Osaka, Japan (Dec.2-3, 2019) 229-232.

Validation of New Fission Yield by Analysis of Post-Irradiation Examination  
A. Iso, S. Takeda and T. Kitada  
Proceedings of Reactor Physics Asia Conference 2019 (RPHA2019) Osaka, Japan (Dec.2-3, 2019) 233-235.

Continuous Thermal Neutron Scattering Data Processing Capability in RMC Code  
L. Zheng, K. Wang and W. Wang  
Proceedings of Reactor Physics Asia Conference 2019 (RPHA2019) Osaka, Japan (Dec.2-3, 2019) 236-239.

Thermal neutron Scattering Data Generation Function in the nuclear Data Processing Code NECP-Atlas  
Y. Tang, T. Zu, S. Yi, J. Xu and L. Cao  
Proceedings of Reactor Physics Asia Conference 2019 (RPHA2019) Osaka, Japan (Dec.2-3, 2019) 240-243.

Quantification of Effectiveness of Integral Data Using Active Sub-Space in nuclear Data Testing  
D. Imazato and G. Chiba  
Proceedings of Reactor Physics Asia Conference 2019 (RPHA2019) Osaka, Japan (Dec.2-3, 2019) 244-247.

Estimated Criticality Lower-Limit Multiplication Factor Considering Neutronic Similarity and Uncertainties of Effective Multiplication Factor Using the Bootstrap Method (1) Theory  
T. Hayashi, F. Nishioka, T. Endo and A. Yamamoto  
Proceedings of Reactor Physics Asia Conference 2019 (RPHA2019) Osaka, Japan (Dec.2-3, 2019) 250-253.

Estimated Criticality Lower-Limit Multiplication Factor Considering Neutronic Similarity and Uncertainties of Effective Multiplication Factor Using the Bootstrap Method (2) Application  
F. Nishioka, T. Hayashi, T. Endo and A. Yamamoto  
Proceedings of Reactor Physics Asia Conference 2019 (RPHA2019) Osaka, Japan (Dec.2-3, 2019) 254-257.

- Covariance-Oriented Sample Transformation Method for Uncertainty Analysis  
Z. Sui, L. Cao and C. Wan  
Proceedings of Reactor Physics Asia Conference 2019 (RPHA2019) Osaka, Japan (Dec.2-3, 2019) 258-261.
- Effectiveness of Subcritical Measurement at Solid Moderated KUCA Core for Reducing nuclear Data-Induced Uncertainties in Other Light Water Reactor Analysis  
T. Endo and A. Yamamoto  
Proceedings of Reactor Physics Asia Conference 2019 (RPHA2019) Osaka, Japan (Dec.2-3, 2019) 262-265.
- Benchmark Study of Nuclear Processed Systems with NCA Data  
S. Wada, K. Yoshida and T. Sugita  
Proceedings of Reactor Physics Asia Conference 2019 (RPHA2019) Osaka, Japan (Dec.2-3, 2019) 266-269.
- Sensitivity Analysis for Generalized Response with RMC code  
G. Shi, C. Jia, Q. Cheng and K. Wang  
Proceedings of Reactor Physics Asia Conference 2019 (RPHA2019) Osaka, Japan (Dec.2-3, 2019) 270-273.
- Uncertainty Analysis of neutron Parameters for NESTOR  
H. Liao, Q. Li, Y. Yu and Y. Hu  
Proceedings of Reactor Physics Asia Conference 2019 (RPHA2019) Osaka, Japan (Dec.2-3, 2019) 274-277.
- Comparison of Methods of Generating Covariance Matrix of Fission Yield  
K. Honta and G. Chiba  
Proceedings of Reactor Physics Asia Conference 2019 (RPHA2019) Osaka, Japan (Dec.2-3, 2019) 278-281.
- Application of Surrogate Modeling with Singular Value Decomposition for Design Basis Accident Aiming Statistical Safety Analysis  
M. Matsushita, T. Endo and A. Yamamoto  
Proceedings of Reactor Physics Asia Conference 2019 (RPHA2019) Osaka, Japan (Dec.2-3, 2019) 282-285.
- Preliminary Performance Assessment of the GPU Acceleration Module in a Pinwise Core Thermal Hydraulics Code ESCOT  
K. M. Kim, N. Choi, J. Lee and H. G. Joo  
Proceedings of Reactor Physics Asia Conference 2019 (RPHA2019) Osaka, Japan (Dec.2-3, 2019) 288-291.
- BEAVRS Benchmark Analysis by a Whole Core Transport Code nTER  
H. Park and J. Y. Cho  
Proceedings of Reactor Physics Asia Conference 2019 (RPHA2019) Osaka, Japan (Dec.2-3, 2019) 292-295.
- Initial Assessment of Anderson Acceleration on Pinwise Coupled Neutronics/Thermal-Hydraulics Code nTER/ESCOT  
J. Lee, J. Y. Cho and H. G. Joo  
Proceedings of Reactor Physics Asia Conference 2019 (RPHA2019) Osaka, Japan (Dec.2-3, 2019) 296-299.
- Pin-By-Pin Multi-physics Analysis and Evaluation of the Critical Heat Flux (CHF) in a PWR Core  
J. Kim, K. S. Chaudri and Y. Kim  
Proceedings of Reactor Physics Asia Conference 2019 (RPHA2019) Osaka, Japan (Dec.2-3, 2019) 300-303.
- Functional Expansion Tallies in Monte Carlo High Fidelity LWR Analysis  
Bamidele Ebiwonjumi, Hyunsuk Lee, Peng Zhang and D. Lee  
Proceedings of Reactor Physics Asia Conference 2019 (RPHA2019) Osaka, Japan (Dec.2-3, 2019) 304-307.
- Hybrid Parallelism of Internal Coupling Method between Monte Carlo Code RMC and Sub-channel Thermal-Hydraulic Code CTF  
K. Li, S. Liu, J. Guo and K. Wang  
Proceedings of Reactor Physics Asia Conference 2019 (RPHA2019) Osaka, Japan (Dec.2-3, 2019) 308-311.
- NECP-X and CTF Solutions to VERA Benchmark  
B. Wang, Z. Liu and L. Cao  
Proceedings of Reactor Physics Asia Conference 2019 (RPHA2019) Osaka, Japan (Dec.2-3, 2019) 312-315.

CRITICAL EXPERIMENT OF THORIUM LOADED THERMAL CORES AT KUCA (1) A NEW CRITICAL EXPERIMENT OF THORIUM LOADED CORE WITH HARDER NEUTRON SPECTRUM IN KUCA

T. Sano, J. Hori, J. Lee, Y. Takahashi, K. Takahashi and H. Unesaki  
Physics of Reactor Conference 2020 (PHYSOR2020) Cambridge, UK (Mar. 2020).

CRITICAL EXPERIMENT OF THORIUM LOADED THERMAL CORES AT KUCA (2) CRITICALITY ANALYSIS OF THORIUM LOADED CORES IN KUCA

H. Unesaki, J. Hori, Y. Takahashi, J. Lee and T. Sano  
Physics of Reactor Conference 2020 (PHYSOR2020) Cambridge, UK (Mar. 2020).

Experimental Study on Neutron Correlation Analysis for a Subcritical System Driven by a Pulsed Spallation Neutron Source in KUCA

K. Nakajima, K. Takahashi, A. Sakon, S. Hohara, T. Sano, M. Yamanaka, C.H. Pyeon and K. Hashimoto  
Physics of Reactor Conference 2020 (PHYSOR2020) Cambridge, UK (Mar. 2020).

短寿命 RI を用いた核分光と核物性研究/

Nuclear spectroscopy and condensed matter physics using short-lived nuclei

Y. Ohkubo, A. Taniguchi, M. Tanigaki, M. Shibata, Y. Kojima, W. Sato, and S. Komatsuda  
Proceedings of the 54th KURNS Scientific Meeting Kumatori, Japan (Feb.5-6, 2020) 10-14. (in Japanese)

## Reviews

燃料デブリ核特性評価に関わる核データニースー中性子照射ガンマ線スペクトル測定一  
名内泰志

核データニュース **122** (2019) 54-66.

## 3. Reactor Physics and Reactor Engineering

### Papers

AN IMPROVED PRESSURE CALCULATION METHOD FOR SIMULATIONS OF GAS-LIQUID TWO-PHASE FLOWS ON UNSTRUCTURED MESHES

K. Ito, T. Kunugi, T. Ezure, M. Tanaka, D. Ito and Y. Saito  
Multiphase Science and Technology **31(2)** (2019) 109-131.

Benchmarks of Criticality in Solid-Moderated and Solid-Reflected Core in at Kyoto University Critical Assembly

M. Yamanaka and C. H. Pyeon  
Nuclear Science and Engineering **193** (2019) 404-416.

Experimental Analysis of Unique Combination-Number for the Third- and Fourth-order Neutron-Correlation Factors in the Zero Power Reactor Noise

T. Endo, A. Yamamoto, M. Yamanaka and C. H. Pyeon  
Journal of Nuclear Science and Technology **56(4)** (2019) 322-336.

Measurements of the  $^{243}\text{Am}$  Neutron Capture and Total Cross Sections with ANNRI at J-PARC

A. Kimura, S. Nakamura, K. Terada, T. Nakao, K. Mizuyama, N. Iwamoto, O. Iwamoto, H. Harada, T. Katabuchi, M. Igashira, T. Sano, Y. Takahashi, C. H. Pyeon, S. Fukutani, T. Fujii, T. Yagi, K. Takamiya and J. Hori  
Journal of Nuclear Science and Technology **56** (2019) 479-492.

Proton Beam Characteristics with Wavelength Shifting Fiber Detector at Kyoto University Critical Assembly

M. Yamanaka, K. W. Jang, S. H. Shin, C. H. Pyeon and B. Lee  
Japanese Journal of Applied Physics **58** (2019) 036002-1\_036002-6.

A Monte Carlo technique for sensitivity analysis of alpha-eigenvalue with the differential operator sampling method

T. Yamamoto and T. Sakamoto  
Annals of Nuclear Energy **127** (2019) 178-187.

Effect of Neutron Spectrum on Subcritical Multiplication Factor in Accelerator-Driven System

N. Aizawa, M. Yamanaka, T. Iwasaki and C. H. Pyeon  
Progress in Nuclear Energy **116** (2019) 158-167.

- Experiments on gas entrainment phenomena due to free surface vortex induced by flow passing beside stagnation region  
T. Ezure, K. Ito, M. Tanaka, H. Ohshima and Y. Kameyama  
Nuclear Engineering and Design **350(15)** 90-97.
- First Nuclear Transmutation of  $^{237}\text{Np}$  and  $^{241}\text{Am}$  by Accelerator-Driven System at Kyoto University Critical Assembly  
C. H. Pyeon, M. Yamanaka, A. Oizumi, M. Fukushima, G. Chiba, K. Watanabe, T. Endo, W. F. G. van Rooijen, K. Hashimoto, A. Sakon, N. Aizawa, Y. Kuriyama, T. Uesugi and Y. Ishi  
Journal of Nuclear Science and Technology **56(8)** (2019) 684-689.
- Integral Experiments on Critical Irradiation of  $^{237}\text{Np}$  and  $^{241}\text{Am}$  Foils at Kyoto University Critical Assembly  
C. H. Pyeon, M. Yamanaka, T. Sano and K. Takamiya  
Nuclear Science and Engineering **193(9)** (2019) 1023-1032.
- Calculation of the Cross and Auto Power Spectrum Densities for Low Neutron Counting from Pulse Mode Detectors  
A. Talamo, Y. Gohar, T. Yamamoto, M. Yamanaka and C. H. Pyeon  
Annals of Nuclear Energy **131** (2019) 138-147.
- Removal of Scale from Feed-water in Thermal Power Plant by Magnetic Separation  
-Analysis of Oxygenated Treatment Scale-  
M. Hiramatsu, J. Yamamoto, Y. Akiyama, F. Mishima, S. Nishijima, H. Okada, N. Hirota, T. Yamaji, H. Matsuura, S. Namba, T. Sekine, Y. Kobayashi and M. Seto  
Journal of Physics: Conference Series **1293(1)** (2019) 012079.
- Visualization of phase distribution in lead-bismuth eutectic during one-dimensional solidification process  
D. Ito, H. Sato, Y. Saito, J. D. Parker, T. Shinohara and T. Kai  
Journal of Visualization **22(5)** (2019) 889-895.
- An Impact of Inherent Neutron Source on Subcriticality Measurement in A Highly Enriched Uranium Core of Kyoto University Critical Assembly  
A. Sakon, T. Sano, S. Hohara, C. H. Pyeon and K. Hashimoto  
Journal of Nuclear Science and Technology **56** (2019) 935-944.
- Decomposition of neutron noise in a reactor into higher-order mode components and investigation of the space and frequency dependence  
T. Yamamoto and H. Sakamoto  
Progress in Nuclear Energy **117** (2019) 103098.
- Two-step Monte Carlo sensitivity analysis of alpha- and gamma-eigenvalues with the differential operator sampling method  
T. Yamamoto and H. Sakamoto  
Annals of Nuclear Energy **133** (2019) 100-109.
- Application of Linear Combination Method to Pulsed-Neutron Source Measurement at Kyoto University Critical Assembly  
R. Katano, M. Yamanaka and C. H. Pyeon  
Nuclear Science and Engineering **193** (2019) 1394-1402.
- Experimental study on local interfacial parameters in upward air-water bubbly flow in a vertical  $6 \times 6$  rod bundle  
X. Han, X. Shen, T. Yamamoto, K. Nakajima, H. Sun and T. Hibiki  
International Journal of Heat and Mass Transfer **444** (2019) 118696.
- Feasibility Study on Application of an Artificial Neural Network for Automatic Design of a Reactor Core at the Kyoto University Critical Assembly  
S. H. Kim, S. G. Shin, S. S. Han, M. H. Kim and C. H. Pyeon  
Progress in Nuclear Energy **119** (2020) 103183.
- Calculation of the Prompt Neutron Decay Constant of the KUCA Facility Configurations Driven by a Californium of Spallation External Neutron Sources  
A. Talamo, Y. Gohar, M. Yamanaka and C. H. Pyeon  
Journal of Nuclear Science and Technology **57** (2020) 145-156.

Estimation of Kinetics Parameters by Monte Carlo Fixed-Source Calculations for Accelerator-Driven System  
H. J. Shim, D. H. Kim, M. Yamanaka and C. H. Pyeon  
Journal of Nuclear Science and Technology **57(2)** (2020) 177-186.

Experimental Analyses of beff / L in Accelerator-Driven System at Kyoto University Critical Assembly  
M. Yamanaka, C. H. Pyeon, T. Endo, K. Watanabe, G. Chiba and W. F. G. van Rooijen  
Journal of Nuclear Science and Technology **57(2)** (2020) 205-215.

Measurement of Prompt Neutron Decay Constant with Spallation Neutrons at Kyoto University Critical Assembly using Linear Combination Method  
R. Katano, M. Yamanaka and C. H. Pyeon  
Journal of Nuclear Science and Technology **57** (2020) 169-176.

Nuclear Data-Induced Uncertainty Quantification of Prompt Neutron Decay Constant based on Perturbation Theory for ADS Experiments at KUCA  
T. Endo, K. Watanabe, G. Chiba, M. Yamanaka, W. F. G. van Rooijen and C. H. Pyeon  
Journal of Nuclear Science and Technology **57** (2020) 196-204.

Paralyzable and Non-Paralyzable Dead-Time Corrections for the Neutron Detectors of the KUCA Facility using External Neutron Sources  
A. Talamo, Y. Gohar, M. Yamanaka and C. H. Pyeon  
Journal of Nuclear Science and Technology **57** (2020) 157-168.

Real-Time Subcriticality Monitoring System based on A Highly Sensitive Optical Fiber Detector in An Accelerator-Driven System at the Kyoto University Critical Assembly  
K. Watanabe, T. Endo and M. Yamanaka and C. H. Pyeon  
Journal of Nuclear Science and Technology **57** (2020) 136-144.

Special Issue on Accelerator-Driven System Benchmarks at Kyoto University Critical Assembly  
C. H. Pyeon, A. Talamo and M. Fukushima  
Journal of Nuclear Science and Technology **57** (2020) 133-135.

Subcriticality Estimation by Extended Kalman Filter Technique in Transient Experiment with External Neutron Source at Kyoto University Critical Assembly  
M. Yamanaka, K. Watanabe and C. H. Pyeon  
European Physical Journal Plus **135** (2020) 256-256.

Data Assimilation Using Subcritical Measurement of Prompt Neutron Decay Constant  
T. Endo and A. Yamamoto  
Nuclear Science and Engineering Selected papers from the 2019 M&C Conference (2020) 1-16.

Measurement of A Very Large Negative Reactivity Inserted by Rapid Withdrawal of A Partial Fuel Loading in Kyoto University Critical Assembly  
A. Sakon, T. Sano, K. Takahashi, K. Nakajima, S. Hohara, C. H. Pyeon and K. Hashimoto  
Journal of Nuclear Science and Technology **57** (2020) 335-343.

## Proceedings

Parametric analysis of bubble and dissolved gas behavior in primary coolant system of sodium-cooled fast reactors  
K. Matsushita, K. Ito, T. Ezure and M. Tanaka  
27th International Conference on Nuclear Engineering: Nuclear Power Saves the World!, ICONE 2019 Ibaraki; Japan (May19-24, 2019).

Study on numerical simulation of void fraction profile in LBE two-phase flow  
K. Maeda, G. Ariyoshi, D. Ito, K. Ito and Y. Saito  
27th International Conference on Nuclear Engineering: Nuclear Power Saves the World!, ICONE 2019 Ibaraki; Japan (May19-24, 2019).

Study on evaluation method for entrained gas flow rate by free surface vortex  
K. Ito, D. Ito, Y. Saito, T. Ezure, K. Matsushita, M. Tanaka and Y. Imai  
18th International Topical Meeting on Nuclear Reactor Thermal Hydraulics, NURETH 2019 Portland, Oregon, USA (Aug.18-23, 2019) 6632-6642.

Two-phase flow structure in a particle bed packed in a confined channel  
D. Ito, T. Kurisaki, K. Ito, Y. Saito, Y. Imaizumi, K.-I. Matsuba and K. Kamiyama  
18th International Topical Meeting on Nuclear Reactor Thermal Hydraulics, NURETH 2019 Portland, Oregon, USA  
(Aug.18-23, 2019) 6430-6439.

Measurement of Gamma Rays from Radiative Capture of Uranium-238 and Decay of Short Lived Fission Products from Subcritical System  
Y. Nauchi, T. Sano, H. Unesaki, S. Sato, M. Suzuki and H. Ohta  
11th International Conference on Nuclear Criticality safety (ICNC2019) Paris, France (Sept.15-20, 2019).

Conversion from Prompt Neutron Decay Constant to Subcriticality Using Point Kinetics Parameters Based on Alpha- and keff-eigenfunctions  
Y. Nauchi, T. Sano, H. Unesaki, S. Sato, M. Suzuki and H. Ohta  
11th International Conference on Nuclear Criticality safety (ICNC2019) Paris, France (Sept.15-20, 2019).

Measurements of subcriticality in dollar units using time-domain decomposition based integral method  
A. Nonaka, T. Endo, A. Yamamoto, M. Yamanaka, T. Sano and C.H. Pyeon  
11th International Conference on Nuclear Criticality safety (ICNC2019) Paris, France (Sept.15-20, 2019).

水平管群内空気-水二相流の熱流動特性に及ぼすピッチ直径比の影響に関する研究/  
Effect of Pitch-to-Diameter Ratio on Heat Transfer and Flow Characteristics of Air-Water TwoPhase Flow in Horizontal Tube Bundle  
荒木 峯也, 村川 英樹, 杉本 勝美, 浅野 等, 伊藤 大介/  
K. Araki, H. Murakawa, K. Sugimoto, H. Asano and D. Ito  
第 24 回 動力・エネルギー技術シンポジウム[in Japanese] Tokyo, Japan (July20-21, 2019) E144.

Experimental Analyses of Spallation Neutrons By 100 MeV Protons and Lead—Bismuth Target at Kyoto University Criticality Assembly  
K. Morioka, M. Yamanaka, K. Sugiura and C.H. Pyeon  
Proceedings of Reactor Physics Asia Conference 2019 (RPHA2019) Osaka, Japan (Dec.2-3, 2019) 19-21.

Applicability of Extended Kalman Filter Technique to Reactivity Monitoring at Kyoto University Criticality Assembly  
M. Yamanaka and C. H. Pyeon  
Proceedings of Reactor Physics Asia Conference 2019 (RPHA2019) Osaka, Japan (Dec.2-3, 2019) 22-25.

Core Design of Accelerator Driven System with Reactivity Control Method using Thorium  
K. Nakamura, H. Saito, N. Aizawa and T. Iwasaki  
Proceedings of Reactor Physics Asia Conference 2019 (RPHA2019) Osaka, Japan (Dec.2-3, 2019) 26-29.

BEAVRS Benchmark Simulation by using NECP—Bamboo  
J. Yang, H. Wu and Y. Li  
Proceedings of Reactor Physics Asia Conference 2019 (RPHA2019) Osaka, Japan (Dec.2-3, 2019) 47-50.

Optimization and Verification of PWR Pin-by-pin Fuel Management Calculation Code NECP —Bamboo2.0  
S. Wang, L. Cao, Y. Li and W. Yang  
Proceedings of Reactor Physics Asia Conference 2019 (RPHA2019) Osaka, Japan (Dec.2-3, 2019) 51-54.

Application of cosKERNEL Code for NPP Shielding Calculation  
W. Song, Y. Sun, S. Li, X. Wang, H. Yu and Y. Chen  
Proceedings of Reactor Physics Asia Conference 2019 (RPHA2019) Osaka, Japan (Dec.2-3, 2019) 55-57.

GPU/CPU Concurrent Heterogeneous Parallel MOC Calculation with Asynchronous Communication Scheme  
L. Liang, P. Song, Q. Zhang, Z. Zhang and Q. Zhao  
Proceedings of Reactor Physics Asia Conference 2019 (RPHA2019) Osaka, Japan (Dec.2-3, 2019) 58-61.

Impact of Diffusion Coefficient and Correction Term on the Convergence of CMFD Acceleration for MOC  
Y. Oshima, T. Endo and A. Yamamoto  
Proceedings of Reactor Physics Asia Conference 2019 (RPHA2019) Osaka, Japan (Dec.2-3, 2019) 62-65.

Application of Improved Tone

X. Du, S. Choi, J. Choe, W. Lee and D. Lee

Proceedings of Reactor Physics Asia Conference 2019 (RPHA2019) Osaka, Japan (Dec.2-3, 2019) 66-69.

Application of the SuPer-Homogenization Method in Fast Reactor Analysis System SARAX

L. Wei, Y. Zheng, B. Xiao, L. Xu and H. Wu

Proceedings of Reactor Physics Asia Conference 2019 (RPHA2019) Osaka, Japan (Dec.2-3, 2019) 70-73.

Progress on Multi-physics Calculations of Nuclear Reactor Cores with the IGA Method

W.F.G. van Rooijen

Proceedings of Reactor Physics Asia Conference 2019 (RPHA2019) Osaka, Japan (Dec.2-3, 2019) 74-77.

Research on a Method for Self-Shielding Calculations Based on IGA-Method

M. Nezonet and W.F.G. van Rooijen

Proceedings of Reactor Physics Asia Conference 2019 (RPHA2019) Osaka, Japan (Dec.2-3, 2019) 78-81.

Study on Effective Cross Section of Pu Spot in MOX fuel

T. Kawano, S. Takeda, T. Kitada, Y. Ohoka, S. Matsuoka and H. Nagano

Proceedings of Reactor Physics Asia Conference 2019 (RPHA2019) Osaka, Japan (Dec.2-3, 2019) 82-85.

Modification of MOC for Considering Double Heterogeneity due to Pu Spots in MOX Fuel

A. Ogawa, H. Yamaguchi, S. Takeda, T. Kitada, Y. Ohoka, S. Matsuoka and H. Nagano

Proceedings of Reactor Physics Asia Conference 2019 (RPHA2019) Osaka, Japan (Dec.2-3, 2019) 86-89.

Homogenization Analysis of double-Heterogeneous Fuel and Bumable Poison

L. Lou, Y. Dong, C. Xiaoming, Y. Yingrui and P. Xingjie

Proceedings of Reactor Physics Asia Conference 2019 (RPHA2019) Osaka, Japan (Dec.2-3, 2019) 90-93.

Prediction Analysis of  $^{243}\text{Am}/^{235}\text{U}$  Solid Fission Rate Ration at KUCA solid Moderator Core

T. Sano, J. Hori and Y. Takahashi

Proceedings of Reactor Physics Asia Conference 2019 (RPHA2019) Osaka, Japan (Dec.2-3, 2019) 94-97.

Effect of neutron Absorber on Production of Plutonium238 for BWR Assembly

H. Ohuchi, S. Takeda and T. Kitada

Proceedings of Reactor Physics Asia Conference 2019 (RPHA2019) Osaka, Japan (Dec.2-3, 2019) 99-102.

Study on the Optimization of Assembly Design of Single-Pass Supercritical Water-Cooled Fast Reactor

L. Huang, Z. Liu and X. Wang

Proceedings of Reactor Physics Asia Conference 2019 (RPHA2019) Osaka, Japan (Dec.2-3, 2019) 103-107.

Application of Direct Simulation Method for neutron Space-Time Kinetics Based on RMC

J. Lijun, S. Xiaotong, G. Xiaoyu and W. Kan

Proceedings of Reactor Physics Asia Conference 2019 (RPHA2019) Osaka, Japan (Dec.2-3, 2019) 108-111.

Core Design of a Molten Salt Reactor with Chloride Fuel

M. Watanabe and W.F.G. van Rooijen

Proceedings of Reactor Physics Asia Conference 2019 (RPHA2019) Osaka, Japan (Dec.2-3, 2019) 112-115.

Monte Carlo Based Analysis for CANDLES Burning Reactor

H. H. Nguyen, J. Nishiyama and T. Obara

Proceedings of Reactor Physics Asia Conference 2019 (RPHA2019) Osaka, Japan (Dec.2-3, 2019) 116-118.

Verification of FRBurner Module of CBZ Code System Based on OECD/NEA Benchmark Report

J. Fan and G. Chiba

Proceedings of Reactor Physics Asia Conference 2019 (RPHA2019) Osaka, Japan (Dec.2-3, 2019) 127-130.

Development of a Steady-State Core Analysis Code System for VVER

L. Yu, G. Chen, J. Bao, L. Wei, Z. Liao and S. Zhang

Proceedings of Reactor Physics Asia Conference 2019 (RPHA2019) Osaka, Japan (Dec.2-3, 2019) 131-134.

BEAVRS Benchmark Evaluations with Studsvik CMS5 Code Package

T. Bahadir and M. Yamasaki

Proceedings of Reactor Physics Asia Conference 2019 (RPHA2019) Osaka, Japan (Dec.2-3, 2019) 135-138.

- An Improved Chebyshev Rational Approximation Method Base on Order Reduction of Krylov Subspace Method  
Y. Hu, Q. Luo, D. Yao, Y. Yu, H. Liao and B. Zhou  
Proceedings of Reactor Physics Asia Conference 2019 (RPHA2019) Osaka, Japan (Dec.2-3, 2019) 139-142.
- Improvement of Optimally-Weighted Predictor-Corrector Method for Nuclear Fuel Burnup Calculations  
J. Sasuga, G. Chiba, Y. Ohoka, K. Yamamoto and H. Nagano  
Proceedings of Reactor Physics Asia Conference 2019 (RPHA2019) Osaka, Japan (Dec.2-3, 2019) 143-146.
- Robustness of the GPS Functions in Pinwise Neutronics Analysis of PWRs  
H. Yu and Y. Kim  
Proceedings of Reactor Physics Asia Conference 2019 (RPHA2019) Osaka, Japan (Dec.2-3, 2019) 147-150.
- APEC-corrected NEM Analysis of the VERA Core  
S. Jang, K. Lee and Y. Kim  
Proceedings of Reactor Physics Asia Conference 2019 (RPHA2019) Osaka, Japan (Dec.2-3, 2019) 151-154.
- Discontinuity Factor ; A Discontinuity Condition for Angular Flux?  
A. Yamamoto and T. Endo  
Proceedings of Reactor Physics Asia Conference 2019 (RPHA2019) Osaka, Japan (Dec.2-3, 2019) 155-157.
- Calculation of Higher Eigen-modes of the Forward and Adjoint neutron Diffusion Equations Using IRAM Algorithm Based on Domain Decomposition  
W. Wu, Y. Yu, Q. Luo, D. Yao, Q. Li and X. Chai  
Proceedings of Reactor Physics Asia Conference 2019 (RPHA2019) Osaka, Japan (Dec.2-3, 2019) 158-161.
- Performance of the RSE (Resonance calculation using energy Spectral Expansion) Method for Heterogeneous Pin-cell Geometry  
R. Kondo, T. Endo, A. Yamamoto, S. Takeda, H. Koike, K. Yamaji and D. Sato  
Proceedings of Reactor Physics Asia Conference 2019 (RPHA2019) Osaka, Japan (Dec.2-3, 2019) 162-165.
- Application of Singular Value Decomposition and Low Rank Approximation for Compression of Macroscopic and Microscopic Cross Section Table for Core Calculations  
M. Yamamoto, T. Endo and A. Yamamoto  
Proceedings of Reactor Physics Asia Conference 2019 (RPHA2019) Osaka, Japan (Dec.2-3, 2019) 166-169.
- Compression of Multi-Physics SimUlation OutPut Data Using Principle Component Analysis  
A. Cherezov, J. Park, H. Kim, N. S. M. Ali and D. Lee  
Proceedings of Reactor Physics Asia Conference 2019 (RPHA2019) Osaka, Japan (Dec.2-3, 2019) 170-174.
- Refinement of Convolutional Neural Network for Neutronic Design Parameter Prediction of a Loading Pattern  
H. Jang, H. C. Shin and H. C. Lee  
Proceedings of Reactor Physics Asia Conference 2019 (RPHA2019) Osaka, Japan (Dec.2-3, 2019) 175-178.
- Experimental Validation for the Pin-wise Isotope Prediction Methodology  
M. Lee, T. Noh and M. H. Kim  
Proceedings of Reactor Physics Asia Conference 2019 (RPHA2019) Osaka, Japan (Dec.2-3, 2019) 179-182.
- The neutron Streaming Correction Method in the Homogenization of Pebble-bed HTGR Reflector  
Y. Wen, D. She, L. Shi and J. Zhao  
Proceedings of Reactor Physics Asia Conference 2019 (RPHA2019) Osaka, Japan (Dec.2-3, 2019) 183-186.
- Application of neutron Balance Analysis in Enhancing the Temperature Reactivity Feedback of Gas-cooled Fast Reactor  
C. Zhang, Y. Zheng and L. Wei  
Proceedings of Reactor Physics Asia Conference 2019 (RPHA2019) Osaka, Japan (Dec.2-3, 2019) 187-190.
- Innovative Design Concepts of Burnable Poison Rods for PWR  
A. Dandi and M. H. Kim  
Proceedings of Reactor Physics Asia Conference 2019 (RPHA2019) Osaka, Japan (Dec.2-3, 2019) 191-195.
- Research on Core Design of Pebble Bed Advanced High Temperature Reactor  
W. Lianjie, S. Wei, X. Bangyang, Z. Yang and Y. Rui  
Proceedings of Reactor Physics Asia Conference 2019 (RPHA2019) Osaka, Japan (Dec.2-3, 2019) 196-199.

C5G7-TD Benchmark Analysis using Multigrid Amplitude Function Method

K. Tsujita, T. Endo and A. Yamamoto

Proceedings of Reactor Physics Asia Conference 2019 (RPHA2019) Osaka, Japan (Dec.2-3, 2019) 201-204.

Fast (Floating Absorber for Safety at Transient) for the Improved Safety of MOX -loaded Sodium-cooled Fast Reactors

C. Kim and Y. Kim

Proceedings of Reactor Physics Asia Conference 2019 (RPHA2019) Osaka, Japan (Dec.2-3, 2019) 205-208.

A Comparative Study on the IQS (Improved Quasi-Static) and PCQS (Predictor Cor Mtor Qusai-Static) Methods

T. Oh, Y. Chung and Y. Kim

Proceedings of Reactor Physics Asia Conference 2019 (RPHA2019) Osaka, Japan (Dec.2-3, 2019) 209-212.

Point Kinetics Analysis for Source-jerk Experimentat AGN-201K

S. Lim, H. J. Shim and M. H. Kim

Proceedings of Reactor Physics Asia Conference 2019 (RPHA2019) Osaka, Japan (Dec.2-3, 2019) 213-215.

A Subcriticality Measurement of AGN –201K Reactor Using the Rossi-q Method

S. Moon, J. H. Kim, M. H. Kim and S. G. Hong

Proceedings of Reactor Physics Asia Conference 2019 (RPHA2019) Osaka, Japan (Dec.2-3, 2019) 217-220.

Experiment using a Random Selection Method for AGN-201K

J. H. Kim, S. H. Moon, S. G. Hong and M. H. Kim

Proceedings of Reactor Physics Asia Conference 2019 (RPHA2019) Osaka, Japan (Dec.2-3, 2019) 221-224.

Education on Reactor Physics and Fuel Cycle using Experimental Facilities of the Nuclear Industry

K. Yoshioka, T. Sugita, S. Wada, R. Kimura, Y. Yamashita, H. Kumanomido, T. Masuyama, M. Akiyama, H. Miyadera and K. Hiraiwa

Proceedings of Reactor Physics Asia Conference 2019 (RPHA2019) Osaka, Japan (Dec.2-3, 2019) 225-227.

Neutron Correlation Analysis for a Subcritical Reactor System Driven by a Pulsed Spallation Neutron Source in KUCA

K. Nakajima, A. Sakon, S. Hohara, K. Takahashi, M. Yamanaka, T. Sano, C.H. Pyeon and K. Hashimoto

Proceedings of Reactor Physics Asia Conference 2019 (RPHA2019) Osaka, Japan (Dec.2-3, 2019).

A Correlation Characteristics of Spurious Counts of Fission Counter Installed in Kyoto University Reactor for Reactor Operation

S.y. Hohara, A. Sakon, T. Sano, K. Nakajima, K. Takahashi and K. Hashimoto

Proceedings of Reactor Physics Asia Conference 2019 (RPHA2019) Osaka, Japan (Dec.2-3, 2019).

ポンプ内気泡挙動の数値解析と X 線イメージング /

Numerical simulation and X-ray imaging of entrapped gas bubble behavior in coolant pump

R. Xiong, K. Ito, D. Ito and Y. Saito

Proceedings of the 54th KURNS Scientific Meeting Kumatori, Japan (Feb.5-6, 2020) 33. (in Japanese)

球充填層内における気液二相流特性に対する配管径の影響 /

Effect of pipe diameter on gas-liquid two-phase flow characteristics in a spherical packed bed

A. Ishikuro, D. Ito, K. Ito and Y. Saito

Proceedings of the 54th KURNS Scientific Meeting Kumatori, Japan (Feb.5-6, 2020) 34. (in Japanese)

A two-phase flow database in a light-water-reactor-simulated rod bundle

X. Han, X. Shen, T. Yamamoto, K. Nakajima and T. Hibiki

Proceedings of the 54th KURNS Scientific Meeting Kumatori, Japan (Feb.5-6, 2020) 46. (in Japanese)

熱電変換 –基礎,応用,材料– /

Thermoelectrics -fundamental, applications and materials-

K. Kurosaki

Proceedings of the 54th KURNS Scientific Meeting Kumatori, Japan (Feb.5-6, 2020) 66-67. (in Japanese)

核破碎中性子源を用いた加速器駆動システムに関する基礎研究 /

Basic Basic research of accelerator-driven riven system with spallation neutrons

C. H. Pyeon, M. Yamanaka, K. Hashimoto, N. Aizawa, K. Watanabe, G. Chiba and and A. Oizumii

Proceedings of the 54th KURNS Scientific Meeting Kumatori, Japan (Feb.5-6, 2020) 68-70. (in Japanese)

Reactor Noise Analysis for a Graphite-moderated and -reflected core in KUCA  
A. sakon, K. nakajima, K. takahashi, S. hohara, T. sano, Y. fukaya and K. hashimoto  
PHYSOR 2020: Transition to a Scalable Nuclear Future Cambridge, United Kingdom (Mar., 2020).

#### 4. Material Science and Radiation Effects

##### Papers

Effect of Y<sub>2</sub>O<sub>3</sub> particles on the helium ion irradiation damage of W-2%Y<sub>2</sub>O<sub>3</sub> composite prepared by wet chemical method

Y. Gang, L.L. Ma, T.X. Yue, Z. Xiang, Q. Xu, Z.X. Yong, L.E. Yang, C.X. Zhong, C.J. Gui and W.Y. Cheng  
Materialia **6** (2019) 100268.

Microstructure and Its High Temperature Oxidation Behavior of W-Cr Alloys Prepared by Spark Plasma Sintering

Q.Q. Hou, K. Huang, L.M. Luo, X.Y. Tan, X. Zan, Q. Xu, X.Y. Zhu and Y.C. Wu  
Materialia **6** (2019) 100332.

固体電解質を用いた起電力法による高温溶融塩の熱力学量の測定/

Measurement of Thermodynamic Properties in Molten Salts by EMF Method Using a Solid Electrolyte

関本 英弘/ H. Sekimoto

溶融塩および高温化学/ Molten Salts **62(2)** (2019) 68-74. (in Japanese)

A first-principles theoretical study on the potential thermoelectric properties of MgH<sub>2</sub> and CaH<sub>2</sub>

Y. Wang, Y. Ohishi, K. Kurosaki and H. Muta

Materials Research Express **6(5)** (2019) 055510.

Nanostructured bulk Si for thermoelectrics synthesized by surface diffusion/sintering doping

S-a Tanusilp, N. Sadayori and K. Kurosaki

RSC Advances **9(27)** (2019) 15496-15501.

Release Kinetics of Tritium Generation in Neutron Irradiated Biphasic Li<sub>2</sub>TiO<sub>3</sub>-Li<sub>4</sub>SiO<sub>4</sub> Ceramic Breeder

Q.L. Zhou, A. Togari, M. Nakata, M.Z. Zhao, F. Sun, Q. Xu, Y. Oya

Journal of Nuclear Materials **522** (2019) 286-293.

Thermal Stability of Microstructures and Mechanical Properties in a Fe-Based Fe-Cr-Mn-Cu-Mo Multi-Component Alloy

Z.H. Zhong, Q. Xu, K. Mori and M. Tokitani

Philosophical Magazine **99** (2019) 1515-1527.

混合アニオン層状化合物 Sr<sub>2</sub>CrFeAsO<sub>3-δ</sub> の子磁気相図/Electronic and Magnetic Phase Diagram of Mixed Anion Layered Compound Sr<sub>2</sub>CrFeAsO<sub>3-δ</sub>

山口道太郎, 藤岡弘孝, 大塚貴史, 瀬戸誠, 北尾真司, 的場正憲, 神原陽一/

M. Yamaguchi, H. Fujioka, T. Otsuka, M. Seto, S. Kitao, M. Matoba and Y. Kamihara

日本磁気学会論文特集号/Transaction of the Magnetics Society of Japan Special Issues **3(1)** (2019) 28-33.  
(in Japanese)

Fabrication and Thermoelectric Property of Bi<sub>0.88</sub>Sb<sub>0.12</sub>/InSb Eutectic Alloy by Melt Spinning and Spark Plasma Sintering

N.M. Natashah, Y. Ohishi, K. Kurosaki and H. Muta

MATERIALS TRANSACTIONS **60(6)** (2019) 1072-1077/.

Light emission from treated surfaces of poly (ethylene terephthalate)

H. Nakamura, T. Kamata, N. Sato and K. Mori

Review of Scientific Instruments **90(6)** (2019) 063104.

Si-Based Materials for Thermoelectric Applications

S-a Tanusilp and K. Kurosaki

Materials **12** (2019) 1943.

Density and viscosity of liquid ZrO<sub>2</sub> measured by aerodynamic levitation technique

T. Kondo, H. Muta, K. Kurosaki, F. Kargl, A. Yamaji, M. Furuya and Y. Ohishi

Heliyon **7** (2019) e02049.

Crystal structure and hydrogen absorption-desorption property of  $\text{La}_5\text{Co}_{19}$

K. Iwase, T. Ueno and K. Mori

International Journal of Hydrogen Energy **44(41)** (2019) 23172-23178.

Direct observation of interlayer molecular translational motion in a smectic phase and determination of the layer order parameter

M. Saito, J. Yamamoto, R. Masuda, M. Kurokuzu, Y. Onodera, Y. Yoda and M. Seto

Physical Review Research **1** (2019) 012008.

First-principles calculation study of  $\text{Mg}_2\text{XH}_2$  (X=Fe, Ru) on thermoelectric properties

Y. Wang, Y. Ohishi, K. Kurosaki and H. Muta

Materials Research Express **8** (2019) 085536.

Magnetic Field Induced Triple-q Magnetic Order in Trillium Lattice Antiferromagnet  $\text{EuPtSi}$  Studied by Resonant X-ray Scattering

C. Tabata, T. Matsumura, H. Nakao, S. Michimura, M. Kakihana, T. Inami, K. Kaneko, M. Hedo, T. Nakama and Y. Ōnuki

Journal of the Physical Society of Japan **88(9)** (2019) 093704.

Newly developed Laboratory-based Size exclusion chromatography Small-angle x-ray scattering System (La-SSS)

R. Inoue, T. Nakagawa, K. Morishima, N. Sato, A. Okuda, R. Urade, R. Yogo, S. Yanaka, M. Yagi-Utsumi, K. Kato, K. Omoto, K. Ito and M. Sugiyama

Scientific Reports **9(1)** (2019) 12610.

Time response of poly (ethylene naphthalate) light emission to charged particles

H. Nakamura and K. Mori

Physica Scripta **94(10)** (2019) 105302.

$^{125}\text{Te}$ -Mössbauer study of  $\text{Fe}_{1.1}\text{Te}$  and  $\text{FeTe}_{0.5}\text{Se}_{0.5}$  superconductor

S. Kitao, M. Kurokuzu, Y. Kobayashi and M. Seto

Hyperfine Interactions **240(1)** (2019) 112.

Development of a measurement system enabling the reconstruction of  $\gamma$ -ray time spectra by simultaneous recording of energy and time information

H. Tajima, S. Kitao, R. Masuda, Y. Kobayashi, T. Masuda, K. Yoshimura and M. Seto

Japanese Journal of Applied Physics **58(10)** (2019) 108001.

The First Observation of Pure Nuclear Bragg Reflection from Natural Iron  $\alpha\text{-Fe}_2\text{O}_3$  by Synchrotron Mössbauer Diffraction

S. Nakamura, T. Mitsui, Y. Kobayashi and S. Shimomura

Journal of the Physical Society of Japan **88(10)** (2019) 103702.

A new and practical Se(IV) removal method using  $\text{Fe}^{3+}$  type cation exchange resin

D. Kawamoto, Y. Yamanishi, H. Ohashi, K. Yonezu, T. Honma, T. Sugiyama, Y. Kobayashi, Y. Okaue, A. Miyazaki and T. Yokoyama

Journal of Hazardous Materials **378** (2019) 120593.

Thermophysical and mechanical properties of CrB and FeB

Y. Ohishi, M. Sugizaki, Y. Sun, H. Muta and K. Kurosaki

Journal of Nuclear Science and Technology **56(9-10)** (2019) 859-865.

Design of S-S bond containing maleimide-conjugated closo-dodecaborate (SSMID): identification of unique modification sites on albumin and investigation of intracellular uptake

S. Ishii, S. Sato, H. Asami, T. Hasegawa, J. Y. Kohno and H. Nakamura

Organic & Biomolecular Chemistry **17** (2019) 5496-5499.

Dynamic motion and freezing of polaronic local structures in a colossal-magnetoresistive perovskitemanganite  $\text{La}_{0.7}\text{Ca}_{0.3}\text{MnO}_3$  detected with radioactive nuclei

W. Sato, S. Komatsuda, H. Shimizu, R. Moriichi, S. Abe, S. Watanabe, S. Komatsu, T. Terai, S. Kawata and Y. Ohkubo

Physical Review **B100** (2019) 184111.

Mössbauer Spectroscopy Study of  $K_xFe_{2-y}Se_2$  under Pressure

Y. Yamamoto, T. Mitsui, S. Kitao, M. Seto, N. Mizobata, T. Ozaki, H. Yamaoka and J. Mizuki  
*Journal of the Physical Society of Japan* **12** (2019) 124703.

Positive Weiss Temperature in Layered Antiferromagnetic FeNiN for High-Performance Permanent Magnets ACS  
S. Goto, H. Kura, H. Yanagihara, E. Kita, M. Tsujikawa, R. Sasaki, M. Shirai, Y. Kobayashi, T. Honda and K. Ono  
*Applied Nano Materials* **2(11)** (2019) 6909-6917.

Positron annihilation study on the phase transition of thermally aged Fe-Cr binary alloys at 748K

R. Kasada and K. Sato

*Philosophical Magazine Letters* **99(10)** (2019) 360-371.

Thermal and mechanical properties of  $U_3Si$  and  $USi_3$

A. Mohamad, W. Silpawilawan, H. Muta, K. Kurosaki and Y. Ohishi

*Annals of Nuclear Energy* **133** (2019) 186-193.

Effect of Annealing on the Microstructure Behavior of D<sup>+</sup>-Irradiated W-2vol.%TiC Composite Prepared by Wet-Chemical Method

Y.X. Zhang, X.Y. Tan, X. Zan, L.M. Luo, Y. Xu, Q. Xu, K. Tokunaga, X.Y. Zhu and Y.C. Wu

*Fusion Engineering and Design* **148** (2019) 111321.

Effect of Interaction between H and He on Micro-Defects in Fe9Cr Alloy Investigated by Slow Positron Beam

L. Li, S.X. Jin, P. Zhang, D.D. Wang, X.Z. Cao, L.P. Guo, Q. Xu, J. Li, T.M. Zhang, L.B. Li, B.Y. Wang

*Journal of Nuclear Materials* **526** (2019) 15174.

Microscopic molecular translational dynamics in cholesteric and cholesteric blue phases

M. Saito, J. Yamamoto, R. Masuda, M. Kurokuzu, Y. Yoda and M. Seto

*Hyperfine Interactions* **241(1)** (2019) 14.

Microstructural Evolution in W-1%TiC Alloy Irradiated He ions at High Temperatures

Q. Xu, H.Y. Chen, L.M. Luo, M. Miyamoto, M. Tokitani and Y.C. Wu

*Tungsten* **1** (2019) 229-235.

Microstructure Evolution of the W-TiC Composite Conducted by Dual-Effects from Thermal Shock and He-Ion Irradiation

Y.F. Zhou, X.Y. Tan, L.M. Luo, Y. Xu, X. Zan, Q. Xu, K. Tokunaga, X.Y. Zhu and Y.C. Wu

*Tungsten* **1** (2019) 213-219.

Negative ionic states of tin in the oxide superconductor  $Sr_{3-x}SnO$  revealed by Mössbauer spectroscopy

A. Ikeda, S. Koibuchi, S. Kitao, M. Oudah, S. Yonezawa, M. Seto and Y. Maeno

*Physical Review B* **100(24)** (2019) 245145.

Neutron Transmission Spectrum of Liquid Lead Bismuth Eutectic

Y. Oba, D. Ito, Y. Saito, Y. Onodera, J. D. Parker, T. Shinohara and K. Oikawa

*Materials Research Proceedings* **15** (2019) 160-164.

Origin of the mixed alkali effect in silicate glass

Y. Onodera, Y. Takimoto, H. Hijiya, T. Taniguchi, S. Urata, S. Inaba, S. Fujita, I. Obayashi, Y. Hiraoka and S. Kohara

*NPG Asia Materials* **11(1)** (2019) 75.

Simulation for the correlation of positron annihilation rate with charge density near defects in iron

L. Xiaoshuang, L. Xiangyu, W. Baoyi, L. Eryang, J. Shuoxue, Z. Yujie, Z. Te, C. Xingzhong, C. Guodong and Q. Xu

*Nuclear Instruments and Methods in Physics Research Section B: Beam Interactions with Materials and Atoms* **461** (2019) 88-92.

Slow-positron beamline temperature rise reduction at Kyoto University Research Reactor

A. Yabuuchi, R. Naka, K. Sato, Q. Xu and A. Kinomura

*Nuclear Instruments and Methods in Physics Research Section B: Beam Interactions with Materials and Atoms* **461** (2019) 137-141.

Swamps of Hydrogen in Equiatomic FeCuCrMnMo Alloys: First-Principles Calculations

X. L. Ren, P. H. Shi, W. W. Zhang, X. Y. Wu, Q. Xu and Y. X. Wang

*Acta Materialia* **180** (2019) 189-198.

Synchrotron-radiation-based Mössbauer absorption spectroscopy with high resonant energy nuclides  
R. Masuda, K. Kusada, T. Yoshida, S. Michimura, Y. Kobayashi, S. Kitao, H. Tajima, T. Mitsui, H. Kobayashi, H. Kitagawa and M. Seto  
*Hyperfine Interactions* **240(1)** (2019) 120.

Understanding diffraction patterns of glassy, liquid and amorphous materials via persistent homology analyses  
Y. Onodera, S. Kohara, S. Tahara, A. Masuno, H. Inoue, M. Shiga, A. Hirata, K. Tsuchiya, Y. Hiraoka, I. Obayashi, K. Ohara, A. Mizuno and O. Sakata  
*Journal of the Ceramic Society of Japan* **127** (2019) 853-863.

Chemical Environment and Magnetic Moment Effects on Point Defect Formation in CoCrNi-Based Concentrated Solid-Solution Alloys  
H.Q. Guan, S.S. Huang, J.H. Ding, F.Y. Tian, Q. Xu and J.J. Zhao  
*Acta Materialia* **187** (2020) 122-134.

Contribution of cadmium to the total amount of positron creation in a reactor-based slow positron beamline  
A. Yabuuchi, T. Yoshiie and A. Kinomura  
*Nuclear Instruments and Methods in Physics Research Section B: Beam Interactions with Materials and Atoms* **463** (2020) 40-49.

Influence of Helium Ion Irradiation Damage Behavior after Laser Thermal Shock of W-2%Vol Y<sub>2</sub>O<sub>3</sub> Composites  
G. Yao, X.Y. Tan, L.M. Luo, X. Zan, Y. Xu, Q. Xu, X.Y. Zhu, K. Tokunaga and Y.C. Wu  
*Progress in Nuclear Energy* **121** (2020) 103241.

Significant growth of vacancy-type defects by post-irradiation annealing in neon ion-irradiated tungsten probed by a slow positron beam  
A. Yabuuchi, M. Tanaka and A. Kinomura  
*Journal of Nuclear Materials* **531** (2020) 152018-1\_152018-5.

Vacancy formation enthalpy in CoCrFeMnNi high-entropy alloy  
K. Sugita, N. Matsuoka, M. Mizuno and H. Araki  
*Scripta Materialia* **176** (2020) 32-35.

Deuterium irradiation resistance and relevant mechanism in W-ZrC/Sc<sub>2</sub>O<sub>3</sub> composites prepared by spark plasma sintering  
G. Yao, H.Y. Chen, M.Q. Fu, L.M. Luo, X. Zan, Q. Xu, K. Tokunaga, X.Y. Zhu and Y.C. Wu  
*Progress in Nuclear Energy* **120** (2020) 103215.

Evolution of Defects with Isochronal Annealing in Helium-Irradiated 316L Studied by Slow Positron Beam  
L.G. Song, B.Y. Wang, T. Zhu, Y.H. Gong, Q. Xu, L.P. Guo, S.X. Jin, P. Zhang, Y.M. Song and X.Z. Cao  
*Nuclear Instruments and Methods in Physics Research Section B: Beam Interactions with Materials and Atoms* **467** (2020) 80-85.

A Power Metallurgy Route to Fabricate CNT-Reinforced Molybdenum-Hafnium-Carbon Composites  
Y. Wei, L.M. Luo, H.B. Liu, X. Zan, J.P. Song, Q. Xu, X.Y. Zhu and Y.C. Wu  
*Materials & Design* **190** (2020) 108635.

Crystal structure, microhardness, and toughness of biomineral CaCO<sub>3</sub>  
K. Iwase and K. Mori  
*Crystal Growth & Design* **20(3)** (2020) 2091-2098.

Effect of C on the Formation of Cu Precipitates and Vacancy Clusters in Neutron-Irradiated Fe-Cu Alloys  
S. Huang and Q. Xu  
*Journal of Nuclear Materials* **533** (2020) 152085.

Transport Parameters and Permeation Behavior of Hydrogen Isotopes in the First Wall Materials of Future Fusion Reactors  
Y. Xu, Z.S. Wu, L.M. Luo, X. Zan, X.Y. Zhu, Q. Xu and Y.C. Wu  
*Fusion Engineering and Design* **155** (2020) 111563.

## Proceedings

Effect of gamma irradiation dose on radiation damage in polystyrene and fused quartz  
S. Konishi, H. Minagawa, S. Nakagawa, Q. Xu, and H. Tsuchida  
Proceedings of 4th Japan-China Joint Workshop on Positron Science Nara, Japan (Oct.28-Nov.2, 2019).

Development of AMOC measurement system for radiation damage in materials under ion irradiation  
H. Minagawa, S. Konishi, S. Nakagawa and H. Tsuchida  
Proceedings of 4th Japan-China Joint Workshop on Positron Science Nara, Japan (Oct.28-Nov.2, 2019).

Vacancy migration behavior in a CoCrFeMnNi high entropy alloy  
K. Sugita, R. Ogawa, M. Mizuno, H. Araki, A. Yabuuchi and A. Kinomura  
MATERIALS RESEARCH MEETING 2019 Yokohama, Japan (Oct.10-14, 2019).

Irradiation-induced vacancy defects and its recovery behavior in 5N-purity tungsten and 3N-purity tantalum  
M. Tanaka, A. Yabuuchi and A. Kinomura  
18th International Conference on Positron Annihilation (ICPA-18) Orlando, USA (Dec.27, 2019)  
050014-1\_050014-4.

Magnetic Doppler broadening measurement on Gadolinium-doped GaN  
M. Maekawa, S. Sakai, S. Hagiwara, A. Miyashita, K. Wada, A. Kawasuso, A. Yabuuchi and S. Hasegawa  
18th International Conference on Positron Annihilation (ICPA-18) Orlando, USA (Dec.27, 2019)  
050007-1\_050007-4.

粒子線照射された化合物合金中の欠陥による水素捕獲/  
Hydrogen trapping behavior at defects introduced by irradiation into compound alloys  
F. Hori, A. Takano, K. Sugita, Y. Sumikura, Q. Xu and K. Ohsawa  
Proceedings of the 54th KURNS Scientific Meeting Kumatori, Japan (Feb.5-6, 2020) 26. (in Japanese)

中性子放射化分析法による岩絵具に含まれる微量元素分析/  
Analysis of trace elements in natural mineral pigments by instrumental neutron activation analysis  
N. Hagura, Y. Okada, T. Uchiyama and Y. Minai  
Proceedings of the 54th KURNS Scientific Meeting Kumatori, Japan (Feb.5-6, 2020) 29. (in Japanese)

イオン濃度調整による 線照射還元 Cu 系合金ナノ粒子の合成制御 /  
Synthesis of Cu base alloy nanoparticles by gamma-ray irradiation reduction with various ion concentration ratio  
Y. Uchimura, S. Toda, T. Yamada, T. Matsui, Q. Xu and F. Hori  
Proceedings of the 54th KURNS Scientific Meeting Kumatori, Japan (Feb.5-6, 2020) 35. (in Japanese)

ジルコニウムとトランスフェリンの錯生成に関する研究 /  
Study on complexation of zirconium and transferrin  
T. Suzuki, T. Kobayashi and T. Sasaki  
Proceedings of the 54th KURNS Scientific Meeting Kumatori, Japan (Feb.5-6, 2020) 36. (in Japanese)

ガンマ線環境下の伝送線路において生成する励起電流の評価/  
Estimation of the current generated in cables under gamma-ray irradiation  
Y. Gotoh, Y. Okuno, N. Sato, M. Akiyoshi, M. Imaizumi, T. Kobayashi and T. Okamoto  
Proceedings of the 54th KURNS Scientific Meeting Kumatori, Japan (Feb.5-6, 2020) 50. (in Japanese)

Positron Annihilation Spectroscopy Characterization of Formation of Helium/Hydrogen-Vacancy Nano-Clusters in FeCr Alloy  
T. Zhu, B.Y. Wang, X.N. Lian, S.X. Jin, R.S. Yu, X.Z. Cao and Q. Xu  
Proceeding of the 15th Workshop on Slow Positron Beam Techniques and Applications (Sept.2-6, 2019) 235-237.

## Reviews

マルチキャピラリーX線レンズを用いた顕微メスバウアー分光/  
Mössbauer microspectrometer with a multicapillary X-ray lens  
篠田 圭司, 小林 康浩/  
K. Shinoda and Y. Kobayashi  
岩石鉱物科学/  
Japanese Magazine of Mineralogical and Petrological Sciences **47(4)** (2019) 163-167. (in Japanese)

量子ビーム実験と構造モデリングによる亜鉛リン酸塩ガラスの熱膨張係数異常の起源の解明  
小野寺陽平, 小原真司, 正井博和  
放射光 **32** (2019) 67-74. (in Japanese)

混合アニオン層状化合物  $\text{Sr}_2\text{CrFeAsO}_{3-\delta}$  の電子磁気相図/  
Electronic and Magnetic Phase Diagram of Mixed Anion Layered Compound  $\text{Sr}_2\text{CrFeAsO}_{3-\delta}$   
日本磁気学会論文特集号/  
山口 道太郎, 藤岡 弘孝, 大塚 貴史, 瀬戸 誠, 北尾 真司, 的場 正憲, 神原 陽一/  
Transaction of the Magnetics Society of Japan Special Issues **3(1)** (2019) 28-33. (in Japanese)

Synchrotron Radiation-Based Quasi-Elastic Scattering Using Mössbauer Gamma Ray with neV-Energy Resolution  
M. Saito, T. Kanaya and R. Mashita  
High-Resolution Inelastic X-Ray Scattering [Working Title] (2019).

## Books

錯体化合物事典  
大川尚士, 海崎純男, 齋藤太郎, 佐々木陽一, 中村 晃, 宗像 惠, 山内 脩, 脇田久伸  
錯体化学会  
朝倉出版 (2019). (in Japanese)

基礎高分子科学  
井上倫太郎  
高分子学会  
東京化学同人(2020). (in Japanese)

## Other

Hydrogen trapping of defects introduced by irradiation in intermetallics  
F. Hori, Y. Sumikura, K. Sugita, A. Takano, A. Iwase, M. Maekawa, A. Kawasuso, Q. Xu and K. Ohsawa  
QST Takasaki Annual Report 2018 QST-M-23 (2020) 39.

Synthesis of Au stabilized Cu nanoparticles by gamma-ray irradiation reduction method  
F. Hori, Y. Uchimura, S. Toda, T. Matsui, A. Iwase, N. Taguchi, S. Tanaka and Q. Xu  
Photon Factory Activity Report 2018 (2019) 36-39.

後藤康仁, 奥野泰希, 佐藤信浩, 秋吉優史, 今泉 充, 小林知洋, 岡本 保  
放射線環境下のセンサ出力を伝送する線路において生成するガンマ線励起電流の評価  
電子情報通信学会 技術研究報告 119(305) (2019) 39-42. (in Japanese)

## 5. Geochemistry and Environmental Science

### Papers

EFFECT ON MICROBIAL PRODUCTS ON CAESIUM ELUTION BEHAVIOUR FROM CLAY MINERALS  
T. Kimura, S. Fukutani, K. Yamaji, M. Ikegami and M. Yoneda  
Radiation Protection Dosimetry **184(3-4)** (2019) 385-387.

Gastrointestinal Absorption Rate in Rats for Radiocesium in Soil Collected near Fukushima Power Plant or Doped Artificially with  $^{134}\text{CsCl}$   
K. Iwata, T. Takahashi, S. Tanaka, T. Kubota, S. Fukutani, Y. Kinashi, M. Konno, Mitsuyuki, S. Mizuno and S. Takahashi  
Japanese Journal of Health Physics **54(1)** (2019) 66-71.

Scaling Relationships of Source Parameters of Inland Crustal Earthquakes in Tectonically Active Regions  
K. Miyakoshi, K. Somei, K. Yoshida, S. Kurahashi, K. Irikura and K. Kamae  
Pure and Applied Geophysics **1** (2019) 13.

Vertical Migration of  $^{137}\text{Cs}$  in Japanese Orchards after the Fukushima Daiichi Nuclear Power Plant Accident  
M. Sato, K. Matsuoka, T. Takase, N.I. Kobayashi, H. Kikunaga, D. Takata, K. Tanoi, T. Ohtsuki, S. Kusaba and K. Yamaguchi  
The Horticulture Journal **88 (2)** (2019) 150-163.

Y. Ohtsuka, M. Aoyama, Y. Takaku, Y. Igarashi, M. Hattori, K. Hirose and S. Hisamatsu  
 $^{240}\text{Pu}/^{239}\text{Pu}$  and  $^{242}\text{Pu}/^{239}\text{Pu}$  atom ratios of Japanese monthly atmospheric deposition samples during 1963–1966  
Scientific Reports **9(1)** (2019) 8105.

Correlation between Different Type of Caesium Carrier in The Radiocaesium Interception Potential Measurement for Forest Soils

H.A Pratama, M. Yoneda, Y. Shimada, S. Fukutani and M. Ikegami  
Journal of Physics: Conference Series **1198(2)** (2019) 022026.

Aerosol mixing state revealed by transmission electron microscopy pertaining to cloud formation and human airway deposition

J. Ching, K. Adachi, Y. Zaizen, Y. Igarashi and M. Kajino  
npj Climate and Atmospheric Science **2** (2019) 22.

人工構造物周辺の地下水流動及び水質変動解析

谷口文紀, 藤川陽子, 国分宏城, 橋本芳, 村沢直治, 尾崎博明

第 25 回地下水・土壌汚染とその防止対策に関する研究集会講演集 **25** (2019) 455-459. (in Japanese)

地下水中の放射性セシウム—福島県浜通り, 中通りおよび会津での調査結果

藤川陽子, 谷口文紀, 国分宏城, 橋本芳, 村沢直治, 静間清

第 25 回地下水・土壌汚染とその防止対策に関する研究集会講演集 **25** (2019) 408-412. (in Japanese)

振動計測に基づく傾斜基盤上に建つ免震建物の振動性状に関する検討/

Dynamic Properties of a Seismically-Isolated Building Constructed on Soil with Inclined Bedrock from Vibration Measurements

西浦 遼, 永野正行, 飛田喜則, 上林宏敏/

R. Nishimura, M. Nagano, Y. Tobita and H. Uebayashi

日本地震工学会論文集/

Journal of Japan Association for Earthquake Engineering **19(6)** (2019) 181-192. (in Japanese)

福島第一原子力発電所事故により 1 号機から放出された放射性エアロゾルの物理・化学的性状の解明/

Investigation of Physical and Chemical Characteristics of Radioactive Aerosols Emitted From Reactor Unit 1 by Fukushima Daiichi Nuclear Power Plant Accident

S. Onozaki, Y. Abe, I. Nakai, K. Adachi, Y. Igarashi, Y. Oura, M. Ebihara, T. Miyasaka, H. Nakamura, K. Sueki, H. Tsuruta and Y. Moriguchi

BUNSEKI KAGAKU **68(10)** (2019) 757-768. (in Japanese)

S. Yokoyama, T. Takahashi, M. Ota, H. Kakiuchi, S. Sugihara, S. Hirano, N. Momoshima, T. Tamari, N. Shima, M. Atarashi-Andoh, S. Fukutani, S. Nakasone, M. Furukawa, M. Tanaka and N. Akata

Development of Field Estimation Technique and Improvement of Environmental Tritium Behavior Model

Plasma and Fusion Research **14** (2019) 3405099-1\_3405099-4.

Petit-spot volcanoes on the oldest portion of the Pacific plate

N. Hirano, S. Machida, H. Sumino, K. Shimizu, A. Tamura, T. Morishita, H. Iwano, S. Sakata, T. Ishii, S. Arai, S. Yoneda, T. Danhara and T. Hirata

Deep Sea Research Part I: Oceanographic Research Papers **159** (2019) 103142.

Tritium separation from heavy water using a membrane containing deuterated manganese dioxide Journal of

H. Koyanaka, S. Fukutani and H. Miyatake

Radioanalytical and Nuclear Chemistry **322(3)** (2019) 1889-1895.

放射性核種の大気放出と大気中動態の理解の現状/

Recent Understanding on the Release of Radionuclides and Their Behavior in the Atmosphere

山澤弘実, 五十嵐康人/

H. Yamazawa and Y. Igarashi

RADIOISOTOPES **69** (2019) 19-30. (in Japanese)

## Proceedings

Petit-spot and seamount rejuvenation overprinting western Pacific plate

N. Hirano and H. Sumino

AGU Fall Meeting 2019 San Francisco, California, USA (Dec.9-13, 2019) V11E-0142.

Performance of a 500 L SNAP reactor placed in the downstream of biological filtration system for removal of arsenic from groundwater

Y. Fujikawa, Ph. D. Hung, D. Hira, T. Fujii, H. Ozaki and K. Furukawa

Proceedings of 4th International Symposium IANAS2019 Osaka, Japan (Nov.13-15, 2019) 226-231.

Microbiome analysis of samples from a single stage partial nitrification - anammox reactor used for treatment of groundwater  
Y. Fujikawa, D. Hira, I. Suzuki, Ph. D. Hung, T. Fujii, K. Kokubun and K. Furukawa,  
Proceedings of 4th International Symposium IANAS2019 Osaka, Japan (Nov.13-15, 2019) 274-279.

福島原発事故で放出された放射性微粒子の分析および模擬生成実験/  
Analysis and simulated generation  
experiment for radioactive particles released by the Fukushima nuclear accident  
Makoto Inagaki, Ryo Sato, Shun Sekimoto, Koichi Takamiya, Yuichi Oki, Tsutomu Ohtsuki  
Proceedings of the 54th KURNS Scientific Meeting Kumatori, Japan (Feb.5-6, 2020) 30. (in Japanese)

核分裂生成物と溶液エアロゾル粒子の静電相互作用による吸着挙動/  
Attachment behavior of fission products on solution aerosol by electrostatic interaction  
Y. Takeuchi, T. Takeuchi, K. Takamiya, M. Inagaki, S. Sekimoto, Y. Oki and T. Ohtsuki  
Proceedings of the 54th KURNS Scientific Meeting Kumatori, Japan (Feb.5-6, 2020) 53. (in Japanese)

核分裂生成物と溶液エアロゾル粒子の静電相互作用による吸着挙動/  
Attachment behavior of fission products on solution aerosol by electrostatic interaction  
T. Takeuchi, Y. Takeuchi, K. Takamiya, M. Inagaki, S. Sekimoto, Y. Oki and T. Ohtsuki  
Proceedings of the 54th KURNS Scientific Meeting Kumatori, Japan (Feb.5-6, 2020) 54. (in Japanese)

放射性物質の大気沈着・拡散および陸域からの再浮遊について/  
Atmospheric deposition and diffusion of radioactive materials from the FINPP accident and their resuspension  
Y. Igarashi  
Proceedings of the 54th KURNS Scientific Meeting Kumatori, Japan (Feb.5-6, 2020) 71-73. (in Japanese)

## Reviews

Accurate determination of three halogen elements (Cl, Br, and I) in U.S. Geological Survey geochemical reference materials by radiochemical neutron activation analysis and an exhaustive comparison with literature data: a review  
S. Sekimoto and M. Ebihara  
Journal of Nuclear and Radiochemical Science **20** (2020) 12-19.

山澤弘実, 五十嵐康人/  
H. Yamazawa and Y. Igarashi  
放射性核種の大気放出と大気中動態の理解の現状/  
Recent Understanding on the Release of Radionuclides and Their Behavior in the Atmosphere  
RADIOISOTOPES **69(1)** (2019) 19-30. (in Japanese)

木村建貴, 福谷 哲, 山路 恵子, 池上 麻衣子/  
T. Kimura, S. Fukutani, K. Yamaji and M. Ikegami  
シデロホアによる粘土鉱物中セシウムの脱離現象に関する研究/  
A STUDY OF CESIUM ELUTION BEHAVIOR FROM CLAY MINERALS TRIGGERED BY SIDEROPHORES  
土木学会論文集 G(環境)/  
Journal of Japan Society of Civil Engineers, Ser. G (Environmental Research) **7** (2019) 503-508. (in Japanese)

A review of Cs-bearing microparticles in the environment emitted by the Fukushima Dai-ichi Nuclear Power Plant accident  
Y. Igarashi, T. Kogure, Y. Kurihara, H. Miura, T. Okumura, Y. Satou, Y. Takahashi and N. Yamaguchi  
Journal of Environmental Radioactivity **205-206** (2019) 101-118.

## Books

Environmental Contamination from the Fukushima Nuclear Disaster  
Part I. Dynamics of Radioactive Materials in the Environment: I. Introduction – basic concepts regarding the Fukushima accident, radiation and radioactivity  
T. Nakajima, T. Ohara, M. Uematsu, Y. Onda, M. Ebihara, A. Shinohara, Y. Hamajima, Y. Igarashi, T. Aono, M. Aoyama, M. Takigawa and K. Saito, T. Nakajima, T. Ohara, M. Uematsu and Y. Onda  
Cambridge University Press (2019).

大気環境の事典  
原発事故による環境影響  
五十嵐康人  
大気環境学会 (編)  
朝倉書店(2019). (in Japanese)

## 6. Life Science and Medical Science

### Papers

Catalytic Hydrolysis of Phosphate Monoester by Supramolecular Phosphatases Formed from a Monoalkylated Dizinc(II) Complex, Cyclic Diimide Units, and Copper(II) in Two-Phase Solvent System  
A.B Rahman, H. Imafuku, Y. Miyazawa, A. Kafle, H. Sakai, Y. Saga and S. Aoki  
*Inorganic Chemistry* **58(9)** (2019) 5603-5616.

Structural Insights into the Inhibition of Amyloid Fibril Formation by Fibrinogen via Interaction with Prefibrillar N. Yamamotoi, T. Akai, R. Inoue, M. Sugiyama, A. Tamura and E. Chatani  
*Intermediates Biochemistry* **58(24)** (2019) 2769-2781.

Structural characterization of the N-terminal kinase-interacting domain of an Hsp90-cochaperone Cdc37 by CD and solution NMR spectroscopy  
F. Ihama, M. Yamamoto, C. Kojima, T. Fujiwara, K. Matsuzaki, Y. Miyata and M. Hoshino  
*Biochimica et Biophysica Acta (BBA) - Proteins and Proteomics* **1867(9)** (2019) 813-820.

Catalytic Hydrolysis of Phosphate Monoester by Supramolecular Complexes Formed by the Self-Assembly of a Hydrophobic Bis(Zn<sup>2+</sup>-cyclen) Complex, Copper, and Barbitol Units That Are Functionalized with Amino Acids in a Two-Phase Solvent System  
Y. Miyazawa, A.B. Rahman, Y. Saga, H. Imafuku, Y. Hisamatsu and S. Aoki  
*Micromachines* **710(7)** (2019) 452.

Design, Synthesis, DNA/HSA Binding, and Cytotoxic Activity of Half-Sandwich Ru(II)-Arene Complexes Containing Triarylamine-Thiosemicarbazone Hybrids  
M. Muralisankar, R. Dheepika, J. Haribabu, C. Balachandran, S. Aoki, N.S.P. Bhuvanesh and S. Nagarajan  
*ACS Omega* **4(7)** (2019) 11712-11723.

Dynamic Views of the Fc Region of Immunoglobulin G Provided by Experimental and Computational Observations  
S. Yanaka, R. Yogo, R. Inoue, M. Sugiyama, S.G. Itoh, H. Okumura, Y. Miyanoiri, H. Yagi, T. Satoh, T. Yamaguchi and K. Kato.  
*Antibodies* **8(3)** (2019) 39.

NHC-catalyzed green synthesis of functionalized chromones: DFT mechanistic insights and in vitro activities in cancer cells  
N. Muruges, J. Haribabu, K. Arumugam, C. Balachandran, R. Swaathy, S. Aoki, A. Sreekanth, R. Karvembu and S. Vedachalam.  
*New Journal of Chemistry* **43** (2019) 13509-13525.

Design, synthesis, and anticancer activity of iridium(III) complex-peptide hybrids that contain hydrophobic acyl groups at the N-terminus of the peptide units  
K. Naito, K. Yokoi, C. Balachandran, Y. Hisamatsu and S. Aoki.  
*Journal of Inorganic Biochemistry* **199** (2019) 110785.

A New Class of  $\beta$ -Pyrrolidino-1,2,3-Triazole Derivatives as  $\beta$ -Adrenergic Receptor Inhibitors: Synthesis, Pharmacological, and Docking Studies  
M. Easwaramoorthi, J.A Rajendran, K.C. Rao, C. Balachandran, Y. Arun, S.M. Mahalingam, N. Arumugam, A. Almansour, R.S. Kumar, D.M. Al-thamili and S. Aoki  
*Molecules* **24(19)** (2019) 3501.

Cisplatin Facilitates Radiation-Induced Abscopal Effects in Conjunction with PD-1 Checkpoint Blockade Through CXCR3/CXCL10-Mediated T-cell Recruitment  
R. Luo, E. Firat, S. Gaedicke, E. Guffart, T. Watanabe and G. Niedermann  
*Clinical Cancer Research* **23** (2019) 7243-7255.

- Purified F-ATP synthase forms a  $\text{Ca}^{2+}$ -dependent high-conductance channel matching the mitochondrial permeability transition pore  
A. Urbani, V. Giorgio, A. Carrer, C. Franchin, G. Arrigoni, C. Jiko, K. Abe, S. Maeda, K. Shinzawa-Itoh, J.F.M. Bogers, D.G.G McMillan, C. Gerle, I. Szabó and P. Bernardi  
*Nature Communications* **1** (2019) 4341.
- Crystal structure of pantoate kinase from *Thermococcus kodakarensis*  
A. Kita, A. Kishimoto, T. Shimosaka, H. Tomita, Y. Yokooji, T. Imanaka, H. Atomi and K. Miki  
*Proteins: Structure, Function, and Bioinformatics* **88(5)** (2020) 718-724.
- Regulation of plant ER oxidoreductin 1 (ERO1) activity for efficient oxidative protein folding  
M. Matsusaki, A. Okuda, K. Matsuo, K. Gekko, T. Masuda, Y. Naruo, A. Hirose, K. Kono, Y. Tsuchi and R. Urade  
*Journal of Biological Chemistry* **49** (2019) 18820-18835.
- The design and green synthesis of novel benzotriazoloquinolinyl spirooxindolopyrrolizidines: antimycobacterial and antiproliferative studies  
V. Pogaku, V.S. Krishna, C. Balachandran, K. Rangan, D. Sriram, S. Aoki and S. Basavoju  
*New Journal of Chemistry* **44** (2019) 17511-17520.
- Ubiquitin carboxyl-terminal hydrolase L1 promotes hypoxia-inducible factor 1-dependent tumor cell malignancy in spheroid models  
X. Li, A. Hattori, S. Takahashi, Y. Goto, H. Harada and H. Kakeya  
*Cancer Science* **111** (2019) 239-252.
- Increased  $^{14}\text{C}$ -acetate accumulation in IDH-mutated human glioblastoma: implications for detecting IDH-mutated glioblastoma with  $^{11}\text{C}$ -acetate PET imaging  
S. Koyasu, Y. Shimizu, A. Morinibu, T. Saga, Y. Nakamoto, K. Togashi and H. Harada  
*Journal of Neuro-Oncology* **145(3)** (2019) 441-447.
- Structural Studies of Overlapping Dinucleosomes in Solution  
A. Matsumoto, M. Sugiyama, Z. Li, A. Martel, L. Porcar, R. Inoue, D. Kato, A. Osakabe, H. Kurumizaka and H. Kono  
*Biophysical Journal* **118(9)** (2019) 2209-2219.
- Adding Indoximod to Hypofractionated Radiotherapy with Anti-PD-1 Checkpoint Blockade Enhances Early NK and  $\text{CD8}^+$  T-Cell-Dependent Tumor Activity  
T. Watanabe, S. Gaedicke, E. Guffart, E. Firat and G. Niedermann  
*Clinical Cancer Research* **26(4)** (2020) 945-956.
- One-pot synthesis of cyclic oligosaccharides by the polyglycosylation of monothioglycosides  
H. Someya, T. Seki, G. Ishigami, T. Itoh, Y. Saga, Y. Yamada and S. Aoki  
*Carbohydrate Research* **487** (2020) 107888.
- Supramolecular tholos-like architecture constituted by archaeal proteins without functional annotation  
M. Yagi-Utsumi, A. Sikdar, C. Song, J. Park, R. Inoue, H. Watanabe, R.N. Burton-Smith, T. Kozai, T. Suzuki, A. Kodama, K. Ishii, H. Yagi, T. Satoh, S. Uchiyama, T. Uchihashi, K. Joo, J. Lee, M. Sugiyama, K. Murata and K. Kato  
*Scientific Reports* **10** (2020) 1540-1540.
- Unprecedented formation of palladium(II)-pyrazole based thiourea from chromone thiosemicarbazone and  $[\text{PdCl}_2(\text{PPh}_3)_2]$ : Interaction with biomolecules and apoptosis through mitochondrial signaling pathway  
J. Haribabu, C. Balachandran, M.M. Tamizh, Y. Arun, N. S.P. Bhuvanesh, S. Aoki and R. Karvembu  
*Journal of Inorganic Biochemistry* **205** (2020) 110988.
- Current status and near future plan of neutron protein crystallography at J-PARC  
I. Tanaka, T. Chatake, S. Fujiwara, T. Hosoya, K. Kusaka, N. Niimura, T. Yamada and N. Yano  
*Methods in Enzymology* **634** (2020) 101-123.
- Disturbance in the regulation of miR 17-92 cluster on HIF-1- $\alpha$  expression contributes to clinically relevant radioresistant cells: an in vitro study  
M.H. Roudkenar, M. Fukumoto, A.M. Roushandeh, Y. Kuwahara, Y. Uroshihara, H. Harada and M. Fukumoto  
*Cytotechnology* **20(1)** (2020) 141-153.

A single Asp isomer substitution in an  $\alpha$ A-crystallin-derived peptide induces a large change in peptide properties  
K. Magami, I. Kim and N. Fujii  
Experimental Eye Research **192** (2020) 107930.

## Proceedings

Development of a proton range-verification method using ionoacoustic waves generated from spherical metal markers  
T. Takayanagi, T. Uesaka, Y. Nakamura, M. B. Unlu, Y. Kuriyama, T. Uesugi, Y. Ishi, K. Umegaki, H. Shirato and T. Matsuura  
The 58th Annual Conference of the Particle Therapy Co-Operative Group (PTCOG58) Manchester, UK (June10-15, 2019).

Development of Glass-Beads Filters for the Isolation, Culture, and Re-collection of Cancer Cells  
S. Aoki, B. Shashni, S. Ariyasu, H. Takemura, K. Akimoto, N. Aikawa, K. Iwasaki, T. Nakanishi, A. Yasumori, T. Osaki and N. Itoh  
International e-Conference on Cancer Research 2019 (e-ICCR 2019) London, United Kingdom (June10-11, 2019).

CTCs extraction method based on frequency-domain filtering from microscope images  
K. Yoshida, Y. J. Chen, L. S. Lu, S. Aoki, and N. Aikawa,  
23rd IEEE International Conference on Signal Processing: Algorithms, Architectures, Arrangements, and Applications Poznan, Poland (Sept.18-20, 2019) 186-191.

Hydrogen/deuterium exchange behavior in tetragonal hen egg-white lysozyme crystals analyzed by the neutron diffraction methods  
A. Kita and Y. Morimoto  
6th International Symposium on Diffraction Structure Biology Osaka, Japan (Oct.17-20, 2019).

Hydrogen/deuterium exchange behavior in tetragonal hen egg-white lysozyme crystals  
A. Kita and Y. Morimoto  
16th Conference of the Asian Crystallographic Association Singapore (Dec.17-20, 2019).

Structural analysis of ligand binding mechanism of L-lactate oxidase from *Aerococcus viridans* by use of ligand soaking crystals  
Y. Morimoto, N. Furubayashi, M. Kamo, Y. Umena, A. Kita, T. Matsuoka and K. Inaka  
16th Conference of the Asian Crystallographic Association Singapore (Dec.17-20, 2019).

マルチドメインタンパク質のコントラスト同調中性子小角散乱解析のためのキメラ重水素化タンパク質作製法の確立/  
Establishing the method of chimera-deuterated protein synthesis for contrast-matching SANS  
A. Okuda, K. Morishima, N. Sato, R. Inoue, R. Urade and M. Sugiyama  
Proceedings of the 54th KURNS Scientific Meeting Kumatori, Japan (Feb.5-6, 2020) 21. (in Japanese)

アミロイド核形成メカニズムの解明を目指した核形成中間体の捕捉と構造解析/  
Trapping and structural analysis of nucleation intermediates aimed at clarifying amyloid nucleation mechanisms  
Y. Yoshikawa, N. Yamamoto, R. Inoue, K. Morishima, M. Sugiyama, A. Tamura and E. Chatani  
Proceedings of the 54th KURNS Scientific Meeting Kumatori, Japan (Feb.5-6, 2020) 23. (in Japanese)

マルチドメイン蛋白質の階層的な動的構造とダイナミクス/  
Solution structure of multi-domain protein  
H. Nakagawa, T. Saio, M. Sugiyama, R. Inoue, M. Nagao and T. Tominaga  
Proceedings of the 54th KURNS Scientific Meeting Kumatori, Japan (Feb.5-6, 2020) 24. (in Japanese)

X線小角散乱によるアミロイド線維前駆中間体発達の時分割追跡/  
Monitoring structural formation of amyloid prefibrillar intermediates by small-angle X-ray scattering  
N. Yamamoto, T. Akai, R. Inoue, M. Sugiyama, N. Shibayama and E. Chatani  
Proceedings of the 54th KURNS Scientific Meeting Kumatori, Japan (Feb.5-6, 2020) 25. (in Japanese)

古細菌の集合シャペロン様タンパク質 PbaA の動的構造解析/  
Dynamical structure of archaeal homolog of proteasome-assembly chaperone PbaA  
M. Y. Utsumi, R. Inoue, M. Sugiyama and K. Kato  
Proceedings of the 54th KURNS Scientific Meeting Kumatori, Japan (Feb.5-6, 2020) 27. (in Japanese)

Solution structure of the circadian clock protein complex characterized by a combination approach involving solution scattering and computational methods

Y. Yunoki, H. Yagi, K. Morishima, J. Matsumoto, N. Sato, L. Porcar, A. Martel, R. Inoue, T. Kazuki, H. Kono, K. Kato and M. Sugiyama

Proceedings of the 54th KURNS Scientific Meeting Kumatori, Japan (Feb.5-6, 2020) 28. (in Japanese)

メタン菌由来 sHsp の温度依存性機構の解明/

Study on the temperature dependency of sHsps from methanogens

M. Yohda, A. Kanno, R. Inoue, N. Sato, K. Morishima and M. Sugiyama

Proceedings of the 54th KURNS Scientific Meeting Kumatori, Japan (Feb.5-6, 2020) 37. (in Japanese)

溶液状態を反映した、重水素化タンパク質の中性子線結晶構造解析/

Neutron crystallographic studies for deuterated protein that reflects the solvent state

A. Kita and Y. Morimoto

Proceedings of the 54th KURNS Scientific Meeting Kumatori, Japan (Feb.5-6, 2020) 41. (in Japanese)

海藻由来フコイダンによるアミロイド凝集抑制機構の解析/

Inhibitory mechanism of amyloid fibril formation by sea-weed fucoidan

M. Hoshino, Y. Kato, K. Morishima, R. Inoue, M. Subiyama and H. Yagi

Proceedings of the 54th KURNS Scientific Meeting Kumatori, Japan (Feb.5-6, 2020) 42. (in Japanese)

小角散乱法と分析超遠心によるタンパク質溶液散乱からの凝集除去解析/

Aggregation elimination analysis of protein solution scattering with small angle scattering and analytical ultracentrifugation

Y. Miyamoto, K. Morishima, R. Inoue, N. Sato, A. Okuda, R. Urade and M. Sugiyama

Proceedings of the 54th KURNS Scientific Meeting Kumatori, Japan (Feb.5-6, 2020) 48. (in Japanese)

植物小胞体での新生タンパク質の酸化的フォールディング機構/

Mechanism of oxidative folding in plant endoplasmic reticulum

R. Urade

Proceedings of the 54th KURNS Scientific Meeting Kumatori, Japan (Feb.5-6, 2020) 61-63. (in Japanese)

休止期腫瘍細胞特性と癌幹細胞性との関連性解析と癌治療への応用

増永慎一郎, 真田悠生, 田野恵三

第 22 回菅原・大西記念癌治療増感シンポジウム 奈良(Feb.8-9, 2020). (in Japanese)

IDO inhibition strongly enhances effects of combined hRT and PD1/PD-L1 checkpoint blockade

T. Watanabe and G. Niedermann

Radiotherapy and Oncology Milan, Italy (Apr.26-30, 2019) S72-S73.

Indoximod Strongly Enhances Effects of Combined Hrt and PD1/PD-L1 Checkpoint Blockade

T. Watanabe and G. Niedermann

International Journal of Radiation Oncology, Biology, Physics Chicago, USA (Sept.15-19, 2020) E652.

## Book

タンパク質のアモルファス凝集と溶解性—基礎研究からバイオ産業・創薬研究への応用まで—

黒田 裕, 有坂文雄, 白木賢太郎, 岩下和輝, 三村真大, 宗 正智, 後藤祐児, 今村比呂志, 渡邊秀樹, 千賀由佳子, 本田真也, 太田里子, 杉山正明, 城所俊一, 若山諒大, 内山 進, デミエン ホール, 廣田奈美, 五島直樹, 河村義史, 廣瀬修一, 野口 保, 丹羽達也, 田口英樹, 伊豆津健一, 津本浩平, 伊倉貞吉, 池口雅道, 荒川 力, 江島大輔, 浅野竜太郎, 赤澤陽子, 萩原義久, 小澤大作, 武内敏秀, 永井義隆, 安藤昭一郎, 石原智彦, 小野寺 理, 加藤昌人, 米田早紀, 鳥巢哲生, 黒谷篤之, 柴田寛子, 石井明子, 黒田裕, 有坂文雄

第Ⅱ編 第4章 小角散乱法

(株)シーエムシー出版 (2019). (in Japanese)

## Reviews

杉山 正明, 井上 倫太郎, 中川 洋, 齋尾 智英

中性子溶液散乱：現在・過去・未来

(特集 波紋刊行 30 年記念特集 これからの中性子科学コミュニティの在り方とは)

波紋：Neutron network news **30(1)** (2020) 16-25. (in Japanese)

## 低酸素バイオロジーの創造と進展

原田浩

放射線生物研究 **55(1)** (2020) 61-67. (in Japanese)

## 水晶体内クリスタリン中のアスパラギン酸残基の異性化/

The spontaneous isomerization of aspartate residues in lens crystallin

高田匠, 藤井紀子/

T. Takata and N. Fujii

生化学/

Journal of Japanese Biochemical Society **91(3)** (2019) 322-328. (in Japanese)

## がん治療における Particle Therapy の現状と展望

石川仁, 中井啓, 野中哲生, 櫻井英幸

癌と化学療法 **46(8)** (2019) 1219-1225. (in Japanese)

ヒト水晶体加齢モデル蛋白質の熱安定性とシャペロン様機能の測定

高田匠, 藤井紀子

Jasco Report **61(2)** (2019) 1-6. (in Japanese)

## ストレス誘発細胞老化は炎症・がん細胞増殖促進に関与する/

Stress-induced Cellular Senescence Contributes to Chronic Inflammation and Cancer Progression Thermal

小橋川 新子, 坂口 義彦, 増永 慎一郎, 森 英一朗/

S. Kobashikawa, Y. M. Sakaguchi, S. Masunaga and E. Mori

Medicine **35(4)** (2019) 41-58. (in Japanese)

## 7. Neutron Capture Therapy

### Papers

Design, Synthesis, and Evaluation of Lipopeptide Conjugates of Mercaptoundecahydrododecaborate for Boron Neutron Capture Therapy

A. Isono, M. Tsuji, Y. Sanada, A. Matsushita, S. Masunaga, T. Hirayama and H. Nagasawa

ChemMedChem **14(8)** (2019) 823-832.

Development of proton beam irradiation system for small animals using FFAG accelerator

H. Tanaka, T. Takata, Y. Ishi, T. Uesugi, Y. Kuriyama, T. Watanabe, Y. Sakurai, S. Kawabata, S.-I. Masunaga and M. Suzuki.

Nuclear Instruments and Methods in Physics Research Section A: Accelerators, Spectrometers, Detectors and Associated Equipment **922** (2019) 230-234.

Depth distributions of RBE-weighted dose and photon-isoeffective dose for boron neutron capture therapy

T. Sato, S.-I. Masunaga, H. Kumada and N. Hamada

Radiation Protection Dosimetry **183(1-2)** (2019) 247-250.

Intracellular target delivery of cell-penetrating peptide-conjugated dodecaborate for boron neutron capture therapy (BNCT)

I. Nakase, M. Katayama, Y. Hattori, M. Ishimura, S. Inaura, D. Fujiwara, T. Takatani- Nakase, I. Fujii, S. Futaki and M. Kirihata

Chemical Communications **55(93)** (2019) 13955-13958.

Preparation of pentagamaboronon-0 and its fructose and sorbitol complexes as boron carrier for boron neutron capture therapy (BNCT) application

E. Meiyanto, R.A. Susidarti, R.Y. Utomo, L. Qodria, R.D. Ramadani, Y. Ohta, Y. Hattori and M. Kirihata

Research in Pharmaceutical Sciences **14(4)** (2019) 286.

A design study of application of the CsI self-activation method to the neutron rem-counter technique

T. Ueki, A. Nohtomi, G. Wakabayashi, J. Fukunaga, T. Kato and S. Ohga

Radiation Measurements **128** (2019) 106181.

Usefulness of combination with both continuous administration of hypoxic cytotoxin and mild temperature hyperthermia in boron neutron capture therapy in terms of local tumor response and lung metastatic potential

S.I. Masunaga, Y. Sakurai, H. Tanaka, T. Takata, M. Suzuki, Y. Sanada, K. Tano, A. Maruhashi and K. Ono

International Journal of Radiation Biology **95(12)** (2019) 1708-1717.

- In Vitro* Evaluation System of Pharmacokinetics and Irradiation Effect in Boron Neutron Capture Therapy (BNCT) Using Three-Dimensional Artificial Human Tumor Tissue Model  
S. Ishiyama, Y. Asano, M. Suzuki, A. Mitsuru and H. Shimoda  
Journal of Cancer Therapy **10(10)** (2019) 835-845.
- Radiation Sensitivity of *in Vitro* Evaluation System of Pharmacokinetics in Boron Neutron Capture Therapy (BNCT) Using Three-Dimensional Artificial Human Tumor Tissue Model  
S. shiyama and M. Suzuki  
Journal of Cancer Therapy **10(12)** (2019) 1025-1035.
- Boron neutron capture therapy (BNCT): a unique role in radiotherapy with a view to entering the accelerator-based BNCT era  
M. Suzuki  
International Journal of Clinical Oncology **25(1)** (2020) 43-50.
- Boron nitride ( $^{10}\text{BN}$ ) a prospective material for treatment of cancer by boron neutron capture therapy (BNCT)  
M. Kaur, P. Singh, K. Singh, U.S. Gaharwar, R. Meena, M. Kumar, F. Nakagawa, S. Wu, M. Suzuki, H. Nakamura and A. Kumar  
Materials Letters **259** (2020) 126832.
- Poly(vinyl alcohol) boosting therapeutic potential of p-boronophenylalanine in neutron capture therapy by modulating metabolism  
T. Nomoto, Y. Inoue, Y. Yao, M. Suzuki, K. Kanamori, H. Takemoto, M. Matsui, K. Tomoda and N. Nishiyama  
Science Advances **6(4)** (2020) eaaz1722.
- Design and construction of an accelerator-based boron neutron capture therapy (AB-BNCT) facility with multiple treatment rooms at the Southern Tohoku BNCT Research Center  
T. Kato, K. Hirose, H. Tanaka, T. Mitsumoto, T. Motoyanagi, K. Arai, T. Harada, A. Takeuchi, R. Kato, S. Yajima and Y. Takai  
Applied Radiation and Isotopes **156** (2020) 108961.
- Enhanced MRI-Guided Gadolinium (III) Neutron Capture Therapy by Polymeric Nanocarriers Promoting Tumor Accumulation and Intracellular Delivery  
C. Qin, X. Hou, T. Khan, N. Nitta, M. Yanagawa, Y. Sakurai, M. Suzuki, S.-I. Masunaga, H. Tanaka, Y. Sakurai, H. Takahashi, I. Aoki, H. Yanagie and H. Cabral  
ChemNanoMat **6(3)** (2020) 412-419.
- Growth and scintillation properties of a new red-emitting scintillator  $\text{Rb}_2\text{HfF}_6$  for the fiber-reading radiation monitor  
S. Kodama, S. Kurosawa, Y. Morishita, H. Usami, T. Torii, M. Hayashi, M. Sasano, T. Azuma, H. Tanaka, V. Kochurikhin, J. Pejchal, R. Kra, M. Yoshino, A. Yamaji, S. Toyoda, H. Sato, Y. Ohashi, Y. Yokota, K. Kamada, M. Nikl and A. Yoshikawa  
IEEE TRANSACTIONS ON NUCLEAR SCIENCE 2020.
- Carrier proteins-based boron delivery to tumor  
S. Kikuchi, S. Sato and H. Nakamura  
Applied Radiation and Isotopes **157** (2020) 109011.
- Evaluation of PHITS for microdosimetry in BNCT to support radiobiological research  
N. Hu, H. Tanaka, T. Takata, S. Endo, S. Masunaga, M. Suzuki and Y. Sakurai  
Applied Radiation and Isotopes **161** (2020) 109148.
- Fiber-read radiation monitoring system using an optical fiber and red-emitting scintillator for ultra-high-dose conditions  
S. Kodama, S. Kurosawa, M. Ohno, Y. Morishita, H. Usami, M. Hayashi, M. Sasano, T. Azuma, H. Tanaka, V. Kochurikhin, A. Yamaji, M. Yoshino, S. Toyoda, H. Sato, Y. Ohashi, K. Kamada, Y. Yokota and A. Yoshikawa  
Applied Physics Express **13(4)** (2020) 047002.
- Microdosimetric quantities of an accelerator-based neutron source used for boron neutron capture therapy measured using a gas filled proportional counter  
N. Hu, H. Tanaka, T. Takata, K. Okazaki, R. Uchida and Y. Sakurai  
Journal of radiation research **61(2)** (2020) 214-220.

Clinical results: patients with head and neck squamous cell carcinoma who have no other treatment options.  
-Japanese experiences-

I. Kato

Neutron Capture Therapy - Principles and Applications (2nd edition): Wolfgang Sauerwein, Andrea Wittig, Ray Moss, Yoshinobu Nakagawa, Koji Ono Editors (2020) in press.

## Proceedings

Synthesis and Biological Evaluation of S-Octylsulfoniodecaborate Containing L-Amino Acids for Boron Neutron Capture Therapy

Y. Hattori, M. Ishimura, Y. Ohta, H. Takenaka, K. Matsumoto, K. Uehara, T. Asano and M. Kirihata  
Peptide Science 2019 Tokyo, Japan (Oct.23-25, 2019).

新規ホウ素薬剤開発に向けた研究開発/

Preclinical study for development of new drug for NCT

M. Suzuki

Proceedings of the 54th KURNS Scientific Meeting Kumatori, Japan (Feb.5-6, 2020) 1. (in Japanese)

BNCT 適応拡大に向けた探索的臨床研究/

Clinical research on explorations into new application of BNCT

M. Suzuki

Proceedings of the 54th KURNS Scientific Meeting Kumatori, Japan (Feb.5-6, 2020) 2. (in Japanese)

経路阻害剤は放射線照射と抗 PD1 抗体阻害剤の併用効果を NK 細胞・CD8<sup>+</sup>T 細胞を介して増強する/

Better early NK and CD8<sup>+</sup>T cell-dependent tumor control by adding IDO pathway inhibitor to hypofractionated radiotherapy plus Anti-PD1 checkpoint blockade

T. Watanabe, G. Niedermann and M.Suzuki

Proceedings of the 54th KURNS Scientific Meeting Kumatori, Japan (Feb.5-6, 2020) 3-5. (in Japanese)

BNCT に関する総合的線量評価システムの構築/

Establishment of integrated system for dose estimation in BNCT

Y. Sakurai, A. Uritani, M. Ishikawa, A. Nohtomi, S. Endo, K. Tanaka, K. Shinsho, M. Oita, S. Hayashi, H. Tanaka, S. Kurosawa, T. Tanimori, S. Nakamura, T. Takata, H. Yasuda, S. Uno, H. Michiue and I. Murata

Proceedings of the 54th KURNS Scientific Meeting Kumatori, Japan (Feb.5-6, 2020) 6-10. (in Japanese)

ホウ素中性子捕捉療法用新規ホウ素薬剤送達ツールとしての二重特異性抗体の抗原認識能/

Recognition of double antigen by using a bispecific antibody for boron delivery in boron neutron capture therapy

T. Kanai, T. Tachibana, T. Nakanishi and T. Nagasaki

Proceedings of the 54th KURNS Scientific Meeting Kumatori, Japan (Feb.5-6, 2020) 18. (in Japanese)

Hif-1 $\alpha$  遺伝子欠損が BNCT の殺細胞効果を増強する/

Disruption of Hif-1 $\alpha$  enhances the sensitivity to BNCT in murine squamous cell carcinoma

Y. Sanada, T. Takata, Y. Sakurai, H. Tanaka, K. Tano and S. Masunaga

Proceedings of the 54th KURNS Scientific Meeting Kumatori, Japan (Feb.5-6, 2020) 38. (in Japanese)

## Reviews

中性子捕捉療法のためのホウ素薬剤研究開発の進展：ホウ素薬剤が今後の適応疾患拡大の鍵を握る! (役に立つ放射線：医療への利用)/

Recent Advances in the Development of Boron Agents for Neutron Capture Therapy

中村 浩之

アトモス：日本原子力学会誌/

Ατομοσ : journal of the Atomic Energy Society of Japan **62(1)** (2020) 18-22. (in Japanese)

皮膚悪性腫瘍に対するホウ素中性子捕捉療法(BNCT)の現状

平塚純一, 神谷伸彦, 河田裕二郎, 笹岡俊輔, 桑原千晶, 田中了

Skin Cancer **34(2)** (2019) 116-120. (in Japanese)

【 $\alpha$ 線治療とDDS】4.ホウ素中性子捕捉療法:がん細胞内で $\alpha$ 線を発生させる次世代放射線治療  
中村浩之  
DDS学会誌 **35(2)** (2020) 129-136. (in Japanese)

【 $\alpha$ 線治療とDDS】5.悪性軟部腫瘍への新たな治療オプションとしての中性子捕捉療法の現状と可能性  
安藤 徹, 市川 秀喜, 藤本 卓也, 鈴木 実  
DDS学会誌 **35(2)** (2020) 137-145. (in Japanese)

加速器中性子源を用いた中性子捕捉療法の現状と今後の展望  
中村浩之  
BIO Clinica **34** (2019) 431-434. (in Japanese)

有望な放射線治療について  
佐々木良平, 出水祐介, 吉村亮一, 加藤逸郎  
日本口腔腫瘍学会誌 **32(4)** (2019). (in Japanese)

## 8. Neutron Radiography and Radiation Application

### Papers

Effects of p53 Status of Tumor Cells and Combined Treatment With Mild Hyperthermia, Wortmannin or Caffeine on Recovery From Radiation-Induced Damage  
S.-I. Masunaga, K. Tano, Y. Sanada, M. Suzuki, A. Takahashi, K. Ohnishi and K. Ono  
World Journal of Oncology **10(3)** (2019) 132-141.

中性子イメージングを用いた高強度コンクリート内部の脱水に関する研究  
小山拓, 西尾悠平, 伊藤大介, 兼松学  
コンクリート工学論文集 **41** (2019) 1013-1018. (in Japanese)

An experimental setup for creating and imaging  $^4\text{He}_2^*$  excimer cluster tracers in superfluid helium-4 via neutron- $^3\text{He}$  absorption reaction  
V. Sonnenschein, Y. Tsuji, S. Kokuryu, W. Kubo, S. Suzuki, H. Tomita, Y. Kiyonagi, T. Iguchi, T. Matsushita, N. Wada, M. Kitaguchi, H. Shimizu, K. Hirota, T. Shinohara, K. Hiroi, H. Hayashida, W. Guo, D. Ito and Y. Saito  
Review of Scientific Instruments **91(3)** (2020) 033318.

### Proceedings

Development of multiphase flow imaging technique using neutrons and x-ray  
D. Ito, K. Ito and Y. Saito  
Proceedings of the 10th International Conference on Multiphase Flow Rio de Janeiro, Brazil (May19-24, 2019).

Velocity vector measurement of LBE flows by using neutron imaging  
Y. Saito and D. Ito  
Proceedings of the 10th International Conference on Multiphase Flow Rio de Janeiro, Brazil (May19-24, 2019).

Design and Construction of an Imaging beamline at the Nagoya University Neutron Source  
K. Hirota, S. Awano, T. Fujiie, S. Fukumura, M. Hishida, G. Ichikawa, S. Imajo, I. Itoh, Y. Iwashita, M. Kitaguchi, Y. Kiyonagi, Y. Kuriyama, K. Morikawa, Y. Niinomi, H. M. Shimizu, K. Tsuchida, Y. Tsuchikwa, Y. Tsurita, A. Uritani, K. Watanabe, Y. Yamagata, N. Yamamoto, A. Yamazaki, S. Yoshihashi and T. Yoshioka  
8th International Meeting of Union for Compact Accelerator-Driven Neutron Sources (UCANS8) Paris, France (July 8-10, 2019)

Improvement of high-speed neutron imaging for visualization of reflooding phenomena  
D. Ito, K. Ito and Y. Saito  
Proceedings of Specialists Workshop on Advanced Instrumentation and Measurement Techniques for Experiments related to Nuclear Reactor Thermal Hydraulics and Severe Accidents Livorno, Italy (Oct.22-25, 2019).

Effects of water distribution on the electrical characteristics of polymer electrolyte fuel cell  
H. Murakawa, S. Sakihara, A. Shirakawa, K. Sugimoto, H. Asano, D. Ito and Y. Saito  
Proceedings of International Conference on Power Engineering-2019 Kunming, China (Oct.21-25, 2019) 1081-1084.

Evaluation of Meltwater Behavior During the Defrosting Process by Using X-ray radiography  
T. Shiokawa, R. Matsumoto, Y. Nishiura, Y. Saito and D. Ito  
Proceedings of the 2019 Energy and Refrigerating Air-Conditioning Conference Taipei, TAIWAN ERAC2019  
(Oct.26-27, 2019) IS003.

X-Ray Radiography and Numerical Simulation of Gas Bubble Behavior in Centrifugal Pump  
R. Xiong, K. Ito, D. Ito, Y. Saito, H. Ushifusa, M. Shinozaki, Y. Asai and M. Sato  
Proceedings of the 11th International Symposium on Measurement Techniques for Multiphase Flow  
Zhenjiang, Jiangsu, China (Nov.3-17, 2019).

Quantitative Measurement of Reflooding Process by Using Neutron Radiography  
H. Umekawa, K. Saito, H. Fujiwara, H. Sakai, T. Ami, Y. Saito and D. Ito  
Proceedings of the 11th International Symposium on Measurement Techniques for Multiphase Flow  
Zhenjiang, Jiangsu, China (Nov.3-17, 2019).

## 9. TRU and Nuclear Chemistry

### Papers

Measurements of thermal-neutron capture cross-section and resonance integral of neptunium-237  
S. Nakamura, F. Kitatani, A. Kimura, A. Uehara and T. Fujii  
Journal of Nuclear Science and Technology **56(6)** (2019) 493-502.

Enhanced Thermoelectric Properties of Ga and Ce Double-Filled p-Type Skutterudites  
J. Kim, Y. Ohishi, H. Muta and K. Kurosaki  
MATERIALS TRANSACTIONS **60(6)** (2019) 1078-1082.

Structural Approach to Understanding the Solubility of Metal Hydroxides  
T. Kobayashi, S. Nakajima, R. Motokawa, D. Matsumura, T. Saito and T. Sasaki  
Langmuir **35(24)** (2019) 7995-8006.

Iodine-rich mixed composition perovskites optimised for tin(IV) oxide transport layers: the influence of halide ion ratio, annealing time, and ambient air aging on solar cell performance  
M. Ozaki, Y. Ishikura, M.A. Truong, J. Liu, I. Okada, T. Tanabe, S. Sekimoto, T. Ohtsuki, Y. Murata, R. Murdey and A. Wakamiya  
Journal of Materials Chemistry A **7(28)** (2019) 16947-16953.

Leaching behavior of gamma-emitting fission products, calcium, and uranium from simulated MCCI debris in water  
T. Sasaki, S. Sakamoto, D. Akiyama, A. Kirishima, T. Kobayashi and N. Sato  
Journal of Nuclear Science and Technology **56(12)** (2019) 1092-1102.

Spin-triplet superconductivity in the paramagnetic UCoGe under pressure studied by <sup>59</sup>Co NMR  
M. Manago, S. Kitagawa, K. Ishida, K. Deguchi, N. K. Sato and T. Yamamura  
Physical Review B **100(3)** (2019) 035203.

Effects of the nuclear structure of fission fragments on the high-energy prompt fission  $\gamma$ -ray spectrum in U<sup>235</sup>(n<sub>th</sub>,f)  
H. Makii, K. Nishio, K. Hirose, R. Orlandi, R. Léguillon, T. Ogawa, T. Soldner, U. Köster, A. Pollitt, F.-J. Hamsch, I. Tsekhanovich, M. Aïche, S. Czajkowski, L. Mathieu, C. M. Petrache Astier A., Guo S., T. Ohtsuki, S. Sekimoto, K. Takamiya, R.J.W. Frost and T. Kawano.  
Physical Review C **100(4)** (2019) 44610.

Neutron activation analysis of carbonate reference materials: coral (JCp-1) and giant clam (JCt-1)  
S. Sekimoto, Y. Homura, V. D. Ho, M. Inagaki, N. Shirai and T. Ohtsuki  
Journal of Radioanalytical and Nuclear Chemistry **322** (2019) 1579-1583.

Superconductivity at the Pressure-Induced Ferromagnetic Critical Region in UCoGe  
M. Manago, S. Kitagawa, K. Ishida, K. Deguchi, N. K. Sato and T. Yamamura  
Journal of the Physical Society of Japan **88(11)** (2019) 113704.

Thermodynamic interpretation of uranium(IV/VI) solubility in the presence of  $\alpha$ -isosccharinic acid  
T. Kobayashi, T. Sasaki and A. Kitamura  
The Journal of Chemical Thermodynamics **138** (2019) 151-158.

Direct observation of vanadium ion permeation behavior through Nafion 117 using  $^{48}\text{V}$  radiotracer for all-vanadium redox flow battery

K. Shirasaki and T. Yamamura

Journal of Membrane Science **592** (2019) 117367.

Production of  $^{47}\text{Sc}$ ,  $^{67}\text{Cu}$ ,  $^{68}\text{Ga}$ ,  $^{105}\text{Rh}$ ,  $^{177}\text{Lu}$ , and  $^{188}\text{Re}$  using electron linear accelerator

M. Inagaki, S. Sekimoto, W. Tanaka, T. Tadokoro, Y. Ueno, Y. Kani and T. Ohtsuki

Journal of Radioanalytical and Nuclear Chemistry **3** (2019) 1703-1709.

Dispersal Rate of Radon-219 from Aqueous Radium-223 Solution Containing Sodium Chloride/Citrate

K. Nagata, K. Shirasaki, A. Toyoshima, K. Ooe, T. Yamamura, A. Shinohara and T. Yoshimura

Radiation Safety Management **19** (2020) 1-9.

## Proceedings

化学交換法によるモリブデン同位体濃縮/

Isotope separation of Molybdenum by chemical exchange method

K. Tanoshiro, C. Kato, S. Fukutani, S. Sekimoto, T. Otsuki, T. Ohno, S. Umehara and T. Fujii

Proceedings of the 54th KURNS Scientific Meeting Kumatori, Japan (Feb.5-6, 2020) 15. (in Japanese)

MA/REE 分離用抽出剤を用いた希土類元素の抽出機構に関する研究/

Research on extraction mechanism of rare earth elements using extractants for MA/REE separation

Y. Yoneda, T. Kawakami, S. Ogawa, T. Matsumura, H. Suzuki, S. Fukutani, C. Kato and T. Fujii

Proceedings of the 54th KURNS Scientific Meeting Kumatori, Japan (Feb.5-6, 2020) 17. (in Japanese)

ノーベリウム研究に向けた2族元素の水酸化物および硫酸沈殿実験/

Hydroxide and sulfate precipitation experiment of Group 2 elements toward the chemical study of nobelium

S. Hayami, E. Watanabe, H. Ninomiya, K. Tonai, Y. Kasamatsu and A. Shinohara.

Proceedings of the 54th KURNS Scientific Meeting Kumatori, Japan (Feb.5-6, 2020) 22. (in Japanese)

使用済み燃料再処理工程におけるモリブデンの酸化還元挙動/

Redox behavior of molybdenum in spent fuel reprocessing process

S. Shinya, S. Yatsugi, H. Sugihara, A. Uehara, C. Kato and T. Fujii

Proceedings of the 54th KURNS Scientific Meeting Kumatori, Japan (Feb.5-6, 2020) 39. (in Japanese)

新規抽出剤を用いた硝酸溶液からのセレンの溶媒抽出特性/

Solvent extraction of selenium in nitric acid solutions using novel extractants

T. Kawakami, Y. Yoneda, S. Ogawa, T. Matsumura, Y. Tsubata, K. Morita, S. Fukutani, A. Uehara, C. Kato and

T. Fujii

Proceedings of the 54th KURNS Scientific Meeting Kumatori, Japan (Feb.5-6, 2020) 45. (in Japanese)

硝酸溶液に溶存するバナジウムの分光電気化学分析/

Spectroelectro-chemical study of vanadium in nitric acid solution

S. Yatsugi, A. Uehara, S. Sato, H. Sugihara, C. Kato and T. Fujii

Proceedings of the 54th KURNS Scientific Meeting Kumatori, Japan (Feb.5-6, 2020) 47. (in Japanese)

模擬燃料デブリの溶出に関する実験的研究 /

Experimental study on leaching behavior from simulated fuel debris

R. Tonna, Y. Kodama, T. Kobayashi, T. Sasaki, N. Sato, A. Kirishima, D. Akiyama, S. Sekimoto and R. Okumura

Proceedings of the 54th KURNS Scientific Meeting Kumatori, Japan (Feb.5-6, 2020) 49. (in Japanese)

化学交換法における同位体分別研究/

Study of isotope separation via chemical exchange reaction

R. Hazama, T. Yoshimoto, Y. Sakuma, T. Fujii, S. Fukutani and Y. Shibahara

Proceedings of the 54th KURNS Scientific Meeting Kumatori, Japan (Feb.5-6, 2020) 51. (in Japanese)

## 10. Health Physics and Waste Management

### Papers

DEVELOPMENT OF A PELTIER TYPE CLOUD CHAMBER WITH WIDE VIEW FIELD

T. Toda, M.M. Hasan, Y. Igarashi, E.W. Katengeza and T. Iimoto

Radiation Protection Dosimetry **184(3-4)** (2019) 539-542.

コロイドの存在を考慮した Cs の森林土壌中移動メカニズムに関する研究  
島田 洋子, 下川 諒, 米田 稔, 池上 麻衣子, 福谷 哲, 颯田 尚哉, 菅原 大輔  
土木学会論文集 G(環境) **75** (2019) 117-125. (in Japanese)

Iron oxide nanoparticle core-shell magnetic microspheres: Applications toward targeted drug delivery  
S. Ayyanaar, M.P. Kesavan, C. Balachandran, S. Rasala, P. Rameshkumar, S. Aoki, J. Rajesh, T.J. Webster and G. Rajagopal  
Nanomedicine: Nanotechnology, Biology and Medicine **24** (2020) 102134.

## Proceedings

Current Status of KURAMA-II  
M. Tanigaki  
Proceedings of 17th Biennial International Conference on Accelerator and Large Experimental Physics Control Systems New York, USA (Oct.5-11, 2019) 1-3.

Nuclear Waste Inventory Calculations from Fuel Cycle with Fast Reactors by a Reactor Physics Code System CBZ  
Y. Kobayashi and G. Chiba  
Proceedings of Reactor Physics Asia Conference 2019 (RPHA2019) Osaka, Japan (Dec.2-3, 2019) 123-126.

堺市で観測した大気エアロゾル粒径別元素成分の長期観測結果/  
Long term observation of element concentration in the atmospheric aerosols at Sakai, Osaka,1995-2017  
N. Ito, A. Mizohata, Y. Iimura and R. Okumura  
Proceedings of the 54th KURNS Scientific Meeting Kumatori, Japan (Feb.5-6, 2020) 16. (in Japanese)

ヒストンバリエント H2A.B を含むヌクレオソームの自発的なヒストン交換機構解析/  
Spontaneous histone exchange activity of histone variant H2A.B nucleosome  
R. Hirano, Y. Arimura, T. Kujirai, R. Inoue, A. Okuda, K. morishima, M. Sugiyama and H. Kurumizaka  
Proceedings of the 54th KURNS Scientific Meeting Kumatori, Japan (Feb.5-6, 2020) 31. (in Japanese)

Prediction of Municipal Solid Waste Composition and Estimation of Impact on Incineration Process in Depopulation and Aging Society  
S. Hayasaki, K. Oshita, K. Kawai and M. Takaoka  
The 6th 3R International Scientific Conference on Material Cycles and Waste Management Tsukuba, JAPAN (Mar.16-18).

## Review

Activities and Development for NS&T HRD Focusing on Secondary School Levels in Asia Pacific Region \_ Case of Japan  
T. Iimoto, T. Kakefu, R. Takaki, T. Toda, I. Takahashi, G. Wakabayashi, H. Iizuka, K. Makabe and T. Koashi  
Journal of Radiation Emergency Medicine **8(1)** (2019) 33-38.

Application of a Hand-made Air GM Counter as a Radiation Education Training Material for Secondary School Education  
E. W. Katengeza, R. A. C. N. Ranasinghe, S. Ozaki and T. Iimoto  
Japanese Journal of Health Physics **54(4)** (2020) 206-211.

国際規制物資(少量核燃料物質)に係る教育のあり方/  
Concept of Internal Education Regarding the Use of International Controlled Material for Small Amount of Nuclear Materials  
安田 幸司, 高橋 賢臣, 飯本 武志, 木村 圭志, 稲垣 昌代, 山西 弘城 /  
K. Yasuda, M. Takahashi, T. Iimoto, K. Kimura, M. Inagaki and H. Yamanishi  
RADIOISOTOPES **69(2)** (2020) 55-65.

Development of radiation literacy among secondary school students in SRI LANKA  
N. Ranasinghe, U. Perera, P. Mahakumara, N. Rathnaweera, P. Rathnayake, T.Toda and T. Iimoto  
Journal of Environment and Safety **10(2)** (2019) 37-40.

## 11. Accelerator Physics

### Papers

AC Losses in HTS Coils of Superferric Dipole and Combined-Function Magnets  
Y. Sogabe, M. Yasunaga, Y. Fuwa, Y. Kuriyama, T. Uesugi, Y. Ishi and N. Amemiya  
IEEE Transactions on Applied Superconductivity **29(5)** (2019) 8629310.

## Proceedings

### Beam Optics Study on FFA-MERIT Ring

H. Okita, Y. Ishi, Y. Kuriyama, Y. Mori, Y. Ono, A. Taniguchi, T. Uesugi, N. Ikeda, Y. Yonemura, M. Kinsho, K. Okabe, M. Yoshimoto, Y. Miyake, M. Muto and A. Sato  
10th International Particle Accelerator Conference (IPAC2019) Melbourne, Australia (May19-24, 2019).

### Remodeling of 150 MeV FFAG Main Ring at KURNS to Pion Production Ring

K. Suga, Y. Fuwa, Y. Ishi, Y. Kuriyama, Y. Mori, H. Okita and T. Uesugi  
10th International Particle Accelerator Conference (IPAC2019) Melbourne, Australia (May19-24, 2019).

### Longitudinal Tomography in a Scaling FFA

D.J. Kelliher, C. Brown, J.-B. Lagrange, S. Machida, C.R. Prior, C.T. Rogers, Y. Ishi, Y. Kuriyama, H. Okita, T. Uesugi and S.L. Sheehy  
10th International Particle Accelerator Conference (IPAC2019) Melbourne, Australia (May19-24, 2019).

### Study of Beam Injection Efficiency in the Fixed Field Alternating Gradient Synchrotron at KURNS

T. Uesugi, Y. Fuwa, Y. Ishi, Y. Kuriyama, Y. Mori, H. Okita and K. Suga  
10th International Particle Accelerator Conference (IPAC2019) Melbourne, Australia (May19-24, 2019).

### Updates on the Inspection System for SRF Cavities

Y. Iwashita, H. Tongu, H. Hayano and Y. Kuriyama  
The 19th International Conference on RF Superconductivity (SRF2019) Dresden, Germany (Jun.30-July5, 2019).

### Proposal of a 1-ampere-class deuteron single-cell linac for nuclear transmutation

H. Okuno, H. Sakurai, Y. Mori, R. Fujita and M. Kawashima  
Proceedings of the Japan Academy, Series B (July, 2019) 430-439.

### Recent Experimental Results of the Accelerator Drive System with a Sub-Critical Nuclear Reactor (ADS) Program

Y. Ishi, Y. Fuwa, Y. Kuriyama, Y. Mori, H. Okita, K. Suga and T. Uesugi  
International Conference on Cyclotrons and their Applications (CYC2019) CapeTown, South Africa (Sept.22-27, 2019).

## 12. Others

### Papers

複雑な 3 次元波動場の P,SV 及び SH 波への地表面地震動を用いた分離 (数値実験に基づく時間-空間領域における手法の評価)/

DECOMPOSITION OF SURFACE SEISMOGRAMS IN THE COMPLEX FULL-WAVEFIELD INTO P-, SV- AND SH-WAVES

上林宏敏/Hirotoshi UEBAYASHI

日本建築学会構造系論文集/

Journal of Structural and Construction Engineering (Transactions of AIJ) **18(5) 513** (2019) 521. (in Japanese)

Determination of the electric field gradient tensor of Fe<sup>3+</sup> in the M1 site of aegirine by single crystal Mössbauer spectroscopy

K. Shinoda and Y. Kobayashi

Journal of Mineralogical and Petrological Sciences **114(3) (2019)** 130-141.

### CubeSat bus interface with Complex Programmable Logic Device

T. Tumenjargal, S. Kim, H. Masui and M. Cho

Acta Astronautica **160** (2019) 331-342.

### Development of Near-Infrared Fluorescent Probes with Large Stokes Shifts for Non-Invasive Imaging of Tumor Hypoxia

H. Nagasawa, K. Okuda, B. G. M. Youssif, R. Sakai, T. Ueno, T. Sakai, T. Kadonosono, Y. Okabe, O. I. A. R. Salem, A. M. Hayallah, M. A. Hussein and S. Kizaka-Kondoh  
HETEROCYCLES **101(2)** (2019) 559.

PD-L1 and PD-L2 expression in the tumor microenvironment including peritumoral tissue in primary central nervous system lymphoma

M. Furuse, H. Kuwabara, N. Ikeda, Y. Hattori, T. Ichikawa, N. Kagawa, K. Kikuta, S. Tamai, M. Nakada, T. Wakabayashi, M. Wanibuchi, T. Kuroiwa, Y. Hirose and S.-I. Miyatake  
BMC Cancer **20(1)** (2020) 277.

The effect of body waves on phase-velocity determined by the spatial autocorrelation (SPAC) method, evaluated using full-wave modelling

H. Uebayashi, I. Cho, M. Ohori, K. Yoshida and H. Arai  
Exploration Geophysics **1** (2020) 11.

コヒーレント共鳴後方回折放射による準単色テラヘルツ光源の研究

清 紀弘, 高橋俊晴

日本赤外線学会誌 **29(2)** (2020) 49-56. (in Japanese)

Design, Synthesis, and Conformation-Activity Study of Unnatural Bridged Bicyclic Depsipeptides as Highly Potent Hypoxia Inducible Factor-1 Inhibitors and Antitumor Agents

K. Koike, M. Nagano, M. Ebihara, T. Hirayama, M. Tsuji, H. Suga and H. Nagasawa  
Journal of Medicinal Chemistry **63(8)** (2020) 4022-4046.

High-count-rate  $^3\text{He}$  position-sensitive detector system: NEUNET-HCR

S. Sato, T. Seya, H. Oshita, H. Kato, N. Hikida, K. Ishizawa, A. Yamaguchi and M. Matsuura  
EPJ Web of Conferences **231** (2020) 05004.

## Proceedings

Research of coherent edge radiation generated by electron beams oscillating free-electron lasers

N. Sei, H. Ogawa, T. Tanaka, Y. Hayakawa, T. Sakai, Y. Sumitomo, Y. Takahashi, K. Hayakawa, K. Nogami, H. Zen and H. Ohgaki

Journal of Physics: Conference Series Conference Melbourne, Australia (May19-24, 2019) 12039.

The change in characteristics of soil and Cs elution by heat treatment

M. Ikegami, K. Kuroki, S. Fukutani, Y. Shimada and M. Yoneda

5th International Conference on Environmental Radioactivity ENVIRA 2019 Czech (Sept.8-13, 2019) 25-26.

Study of gas-gain saturation and cross-talk effect by low energy proton with a prototype chamber for the COMET CDC

H. Yoshida, M. Aoki, M. Dobouchet, M. Moritsu, A. Sato, Y. Ishi, Y. Kuriyama, T. Uesugi and Y. Mori  
J-PARC Symposium 2019 Tsukuba, Japan (Sept.23-26, 2019).

## Books

がん生物学イラストレイテッド 第2版

近藤 夏子, 平田 英周, 渋谷 正史, 湯浅 保仁

第9章 6. 脳腫瘍

羊土社 (2019). (in Japanese)

## Review

国内外の原子力教育事情(2)京都大学原子核工学専攻・原子核工学コース

高木郁二, 中島健

日本原子力学会誌(アトムス) **61** (2019) 143-145. (in Japanese)

京都大学「原子炉実験所」から「複合原子力科学研究所」へ/

From Research Reactor Institute to Institute for Integrated Radiation and Nuclear Science, Kyoto University  
川端祐司/

Yuji Kawabata

保健物理/Japanese Journal of Health Physics **53(4)** (2019) 205-206. (in Japanese)

---

KURNS Progress Report 2019

Issued in August 2020

Issued by the Institute for Integrated Radiation and Nuclear Science,  
Kyoto University  
Kumatori-cho, Sennan-gun, Osaka 590-0494 Japan

Tel. +81-72-451-2300

Fax. +81-72-451-2600

In case that corrections are made, an errata will be provided  
in the following webpage:

<https://www.rii.kyoto-u.ac.jp/PUB/report/PR/ProgRep2019/ProgRep2019.html>

Publication Team

IINUMA, Yuto  
INOUE, Rintaro (Subchief)  
KINASHI, Yuko  
KITAMURA, Yasunori  
MORI, Kazuhiro (Chief)  
NAKAYAMA, Chiyoko  
SAKURAI, Yoshinori (Subchief)  
SANO, Hiroaki  
TAKATA, Takushi  
TOMINAGA, Yuta  
TSURUTA, Yachiyo  
YOKOTA, Kaori